

# A study of microporous polymeric materials for electronic applications

Patrick Heasman



Department of Chemistry  
Lancaster University

March 2020

A thesis submitted to Lancaster University for the degree of  
Doctor of Philosophy in the Faculty of Science and Technology

*Supervised by Dr. Abbie Trewin*

*For Carys.*



---

## Abstract

In this thesis we look at two microporous polymer materials and their respective electronic properties.

We firstly assess the electronic properties of pyrene-based conjugated microporous polymers (CMPs). The research revolves around the hypothesis that unique structures, called here "molecular rings", are the influencing factor of their luminescent properties. Here we showed that the introduction of a linear co-monomer greatly reduced the number of molecular rings observed in a pyrene-based CMP (S0). With this in mind, we designed two further materials, S1 and S2, that use non-linear co-monomers (1,3-dibromobenzene and 1,2-dibromobenzene, respectively). These were computationally generated and subsequently synthesised. The rationalisation of the co-polymeric CMPs S1 and S2 demonstrated a rapid increase in molecular rings. The synthesised CMPs showed luminescence consistent with our computational predictions. Further investigation into the formation mechanism of these materials has led to an "*inference*" technique that could be utilised for a qualitative assessment of the incorporation of monomers, and their electronic properties.

The second set of materials studied the diffusive behaviour of the newly introduced OSPC-1 material as an anode for lithium ion batteries, and also as anodes for alternate ion batteries (sodium, potassium, magnesium, and calcium). We have also predicted a novel set of materials to expand upon the OSPC family. OSPC-0 introduces a carbon framework with reduced  $sp^3$ - $sp^3$  node distances, whereas OSPC-2 and OSPC-3 have increasing  $sp^3$ - $sp^3$  node distances (node-to-node distance: OSPC-0 < OSPC-1 < OSPC-2 < OSPC-3). Overall, the *active diffusion* rate of lithium ions increased with an increase of node-to-node distance. However, the trend established for the ions is more complex, with the *active diffusion* rate being determined by a combination of ionic radius and node-to-node distance.

---

## Acknowledgements

I would firstly like to thank Abbie Trewin for putting up with me and for supporting me throughout this PhD. My aspirations and stubbornness has led to me following in her footsteps of biting off more than I can chew. It will always be a privilege to work with her, and she truly is somebody I highly admire and respect.

Vilius Franckevičius and Pierre Fayon have also been great assets towards my understanding and skill development. You have been great mentors and it has been a pleasure working with you. I would also like to thank Prof. Teng Ben for allowing me to visit his research group in China, and the collaborative work we have published. Additionally, Carol, who has made the process much easier to handle. You have had the patience of a saint with my progress and have always been one to keep my spirits high.

I most definitely have to thank my Mum, my Dad, and my Nan who have never once doubted my abilities, and have supported me (mostly financially) when things have become difficult. And I would like to thank my brother, Tim, and my friends who were always there to make things fun, enduring my stupidity over the many years we've known each other. Be it London, Lancaster, or the many cities you all live in, a pint (or ten) and a chat was always appreciated.

And lastly, somebody that deserves much more than just a mention: my beautiful daughter Carys. She doesn't, and will never know how much she has impacted my life. She will never know how proud I am to call her my daughter, and that I have made sure to finish this for her. Everything I have done, and will continue to do, will be to honour her legacy. Carys has been the light in my life when times were tough, and the memory of that tiny bag of sugar has always got me through. I will always love Carys, and I will never give up and always do her proud. Thank you for giving me the strength I never knew I had.

---

*\*An additional special thanks to those not mentioned by name - A round of tap water is on me!*

---

---

## Declaration

I declare that the thesis has been composed by myself, and that the work has not be submitted for any other degree or professional qualification. I confirm that the work submitted is my own, with the exception of collaborative work and publications where specifically indicated.

---

## Publications

- P. Heasman, A. Trewin, "Uptake and Diffusion of Ions in Organically Synthesized Porous Carbon for Battery Anode Applications", *J. Phys. Chem. C.*, vol. 123, pp. 25603-25610, 2019.
- Z. Zhao, S. Das, G. Xing, P. Fayon, P. Heasman, M. Jay, S. Bailey, C. Lambert, H. Yamada, T. Wakihara, A. Trewin, T. Ben, S. Qui, V. Valtchev, "A 3-D Organically Synthesized Porous Carbon Material for Lithium-Ion Batteries", *Angew. Chemie. Int. Ed.*, vol. 57, pp. 1-6, 2018.
- S. Das, P. Heasman, T. Ben, S. Qui, "Porous Organic Materials: Strategic Design and Structure Function Correlation", *Chem. Rev.*, vol. 117, no. 3, pp. 1515-1563, 2017.

### - In preparation -

- J.M.H. Thomas, L. Turner, P. Heasman, P. Fayon, A. Trewin, "Artificial Synthesis of Conjugated Microporous Polymers via Sonogashira-Hagihara Coupling."
- P. Heasman, P. Fletcher, J.M.H. Thomas, P. Fayon, M. Peach, A. Trewin, "Band Gap Engineering Strategy for Amorphous Pyrene-based Conjugated Microporous Polymers: Targeted Design, Synthesis, and Rationalisation."
- P. Heasman, A. Trewin, "Uptake and Diffusion of Ions in Predicted Family of Organically Synthesised Porous Carbon Materials for Battery Applications."

# Contents

Abstract . . . . .	i
Acknowledgements . . . . .	ii
Publications . . . . .	iv
Contents . . . . .	ix
<b>1 Introduction</b>	<b>1</b>
1.1 Porous Materials . . . . .	1
1.2 Inorganic Microporous Materials . . . . .	2
1.2.1 Zeolites . . . . .	2
1.2.2 Metal-organic frameworks (MOFs) . . . . .	2
1.2.3 Zeolitic imidazolate frameworks (ZIFs) and metal-organic zeo- lites (MOZs) . . . . .	5
1.3 Organic Microporous Materials . . . . .	5
1.3.1 Covalent organic frameworks (COFs) . . . . .	6
1.3.2 Hyper-cross-linked polymers (HCPs) . . . . .	7
1.3.3 Polymers of intrinsic microporosity (PIMs) . . . . .	9
1.3.4 Porous organic molecules . . . . .	12
1.3.5 Conjugated microporous polymers (CMPs) . . . . .	14
1.3.6 Covalent triazine-based frameworks (CTFs) . . . . .	19
1.3.7 Porous aromatic frameworks (PAFs) . . . . .	22
1.3.8 Organically synthesised porous carbon . . . . .	24
1.4 Computational characterisation and design of porous materials . . . . .	25

---

1.4.1	Energetics and parameterisation . . . . .	26
1.4.2	Structural prediction and design of porous materials . . . . .	27
1.5	Overview and Research . . . . .	32
<b>2</b>	<b>Methodology</b>	<b>33</b>
2.1	Synthesis of conjugated microporous polymers . . . . .	33
2.1.1	<i>Method 1:</i> General method of CMP synthesis . . . . .	33
2.1.2	<i>Method 2:</i> Interval extraction method . . . . .	34
2.1.3	<i>Method 3:</i> Synthetic procedure for UV-vis analysis . . . . .	35
2.2	Gas sorption and diffusion . . . . .	36
2.2.1	Adsorption isotherms . . . . .	36
2.2.2	Langmuir adsorption model . . . . .	38
2.2.3	Brunauer-Emmett-Teller sorption model . . . . .	39
2.3	Gas sorption and surface area analysis . . . . .	41
2.3.1	Gas diffusion . . . . .	41
2.3.2	Active diffusion . . . . .	44
2.4	X-Ray diffraction . . . . .	46
2.4.1	Single crystal X-ray diffraction . . . . .	46
2.4.2	Powder X-ray diffraction . . . . .	47
2.4.3	Fourier transform infra-red spectroscopy (FTIR) . . . . .	48
2.4.4	Nuclear magnetic resonance (NMR) . . . . .	48
2.4.5	UV-Vis spectroscopy . . . . .	49
2.5	Theoretical methodology . . . . .	49
2.5.1	Molecular mechanics . . . . .	49
2.5.2	Energy minimisation . . . . .	50
2.5.3	Molecular dynamics . . . . .	50
2.5.4	Surface area calculations . . . . .	54
2.5.5	AmBuild . . . . .	55
2.5.6	DL_POLY . . . . .	60

---

---

2.5.7	Materials Studio . . . . .	61
<b>3</b>	<b>Pyrene-based conjugated microporous polymers</b>	<b>62</b>
3.1	Introduction . . . . .	62
3.2	Molecular Ring Theory . . . . .	64
3.2.1	Molecular ring formation in YPy . . . . .	66
3.2.2	Molecular ring formation in YDBPy . . . . .	73
3.2.3	Molecular ring formation in YDPPy . . . . .	75
3.2.4	Design of pyrene-based CMPs . . . . .	77
3.3	Synthesis and characterisation of pyrene-based CMPs . . . . .	83
3.3.1	Synthesis of rationalised CMPs . . . . .	83
3.3.2	Ring formation mechanism analysis of YPy . . . . .	94
3.3.3	Ring formation mechanism analysis with co-monomer inclusion	100
3.4	Electronic structure analysis . . . . .	106
3.4.1	Electronic structure comparison and HOMO-LUMO analysis .	106
3.4.2	Orbital analysis of the pyrene-based clusters . . . . .	110
3.5	Conclusion . . . . .	122
<b>4</b>	<b>Development of organic porous carbon structures for lithium ion batteries</b>	<b>125</b>
4.1	Introduction . . . . .	125
4.2	Background . . . . .	126
4.2.1	Experimental Research . . . . .	126
4.2.2	Conductivity and Lithium Ion Uptake . . . . .	127
4.2.3	Structural Modelling and Molecular Dynamics . . . . .	128
4.2.4	Diffusion of lithium ions within OSPC-1 . . . . .	129
4.3	Ion migration simulations . . . . .	131
4.3.1	Migration of lithium ions through OSPC-1 . . . . .	134
4.3.2	Conclusion . . . . .	145
4.4	Alternative OSPC-based materials . . . . .	146

---

---

4.4.1	OSPC-0 and lithium ion migration . . . . .	150
4.4.2	OSPC-2 and lithium ion migration . . . . .	161
4.4.3	OSPC-3 and lithium ion migration . . . . .	175
4.5	Comparison . . . . .	187
4.6	Reproducibility . . . . .	191
4.7	Conclusion . . . . .	193
<b>5</b>	<b>Alternate battery technology development using OSPC</b>	<b>194</b>
5.1	OSPC-1 . . . . .	194
5.1.1	Sodium-ion batteries . . . . .	195
5.1.2	Potassium-ion batteries . . . . .	202
5.1.3	Magnesium-ion batteries . . . . .	208
5.1.4	Calcium-ion batteries . . . . .	213
5.1.5	Conclusion . . . . .	218
5.2	OSPC-0 . . . . .	222
5.2.1	Sodium-ion batteries . . . . .	222
5.2.2	Potassium-ion batteries . . . . .	227
5.2.3	Magnesium-ion batteries . . . . .	233
5.2.4	Calcium-ion batteries . . . . .	237
5.2.5	Conclusion . . . . .	241
5.3	OSPC-2 and OSPC-3 . . . . .	244
5.3.1	Sodium-ion batteries . . . . .	244
5.3.2	Potassium-ion batteries . . . . .	252
5.3.3	Magnesium-ion batteries . . . . .	258
5.3.4	Calcium-ion batteries . . . . .	264
5.3.5	Comparison . . . . .	269
5.4	Ion Comparison . . . . .	271
<b>6</b>	<b>Conclusion</b>	<b>275</b>
6.1	Summary . . . . .	275

---



---

6.2	Future work . . . . .	278
<b>A</b>	<b>Appendix</b>	<b>300</b>
A.1	Chapter: 3 . . . . .	300
A.2	Chapter: 4 . . . . .	302
A.3	Chapter: 5 . . . . .	312
A.3.1	OSPC-1 . . . . .	312
A.3.2	OSPC-0 . . . . .	320
A.3.3	OSPC-2 . . . . .	329
A.3.4	OSPC-3 . . . . .	337

*"If we knew what we were doing, it wouldn't be called research."*

---

— Albert Einstein

# Chapter 1

## Introduction

### 1.1 Porous Materials

This introduction discusses the various porous materials from published literature. The electronic applications of the materials studied have been discussed within the relevant chapters.

Porous materials have been widely studied due to their exceptional capabilities in gas sorption and separation,<sup>1–4</sup> catalysis,<sup>5–8</sup> energy storage,<sup>9–15</sup> and a wide series of alternative applications.<sup>8,16–22</sup> Porous materials develop through the inefficient packing of building blocks, forming cavities within the internal structure.<sup>23–25</sup> Porous materials can be defined by the size of the pores; macroporous materials have pore sizes greater than 50 nm, mesoporous materials have pore sizes between 2 and 50 nm, and microporous materials have pore sizes less than 2 nm.<sup>26,27</sup> Porous materials can be categorised as crystalline or amorphous. The exact atomic structure of crystalline materials can be determined via X-Ray diffraction techniques due to their highly ordered nature. Amorphous porous materials on the other hand are more difficult to characterise as they lack this long-range order. There are multiple classes of porous material. The first established microporous material were naturally occurring zeolites.<sup>28–30</sup> However, alternative synthetic materials have emerged subsequently. Metal-organic frameworks (MOFs),<sup>31</sup> covalent organic frameworks (COFs),<sup>32</sup> polymers of intrinsic microporos-

ity (PIMs),<sup>33</sup> conjugated microporous polymers (CMPs),<sup>34</sup> covalent triazine-based frameworks (CTFs),<sup>35</sup> porous organic cages,<sup>36</sup> and porous organic molecules<sup>37</sup> are amongst the many differing families of microporous materials known to date.

## 1.2 Inorganic Microporous Materials

### 1.2.1 Zeolites

Zeolites are naturally occurring porous materials, and have been extensively studied. Their composition results from a tetrahedral atom bonded to oxygen ( $\text{TO}_4$ ), typically silicon in nature. Replacement of silicon in silicate materials ( $\text{SiO}_2$ ) with aluminium gives rise to voids developing throughout the material, and the formation of tectoaluminosilicate frameworks. Tectoaluminosilicates are negatively charged due to the imbalance of oxidation states. Countercations, such as  $\text{Na}^+$  or  $\text{K}^+$ , are in place to balance the overall charge, and these can undergo ion exchange with alternative cations, making zeolites beneficial for separation. Synthetic zeolites can be tailored to possess larger voids that are applicable towards catalysis. The synthesis of zeolites has typically mimicked geological conditions (replicating the natural development of the materials), and solvothermal synthesis, making high pressure and temperature a necessity for their formation.<sup>38</sup>

### 1.2.2 Metal-organic frameworks (MOFs)

Metal-organic frameworks (MOFs) are created through the bonding of inorganic elements with organic compounds, forming strong, rigid structures. They possess extended crystalline structures in one-, two-, or three-dimensional constructs controlled through the geometry of the metal centre and the secondary building block.<sup>39–42</sup>

By defining appropriate building blocks, MOFs with desired properties can be produced, tailoring the pore size and shape to give highly selective functionality. *Reticular synthesis*<sup>43</sup> was proposed for the design of new MOF materials, with such

shown in Figure 1.1. The trends that these materials follow, and the types of linkers used between the metal centres, can be advanced for the developed of novel MOFs and more porous materials.

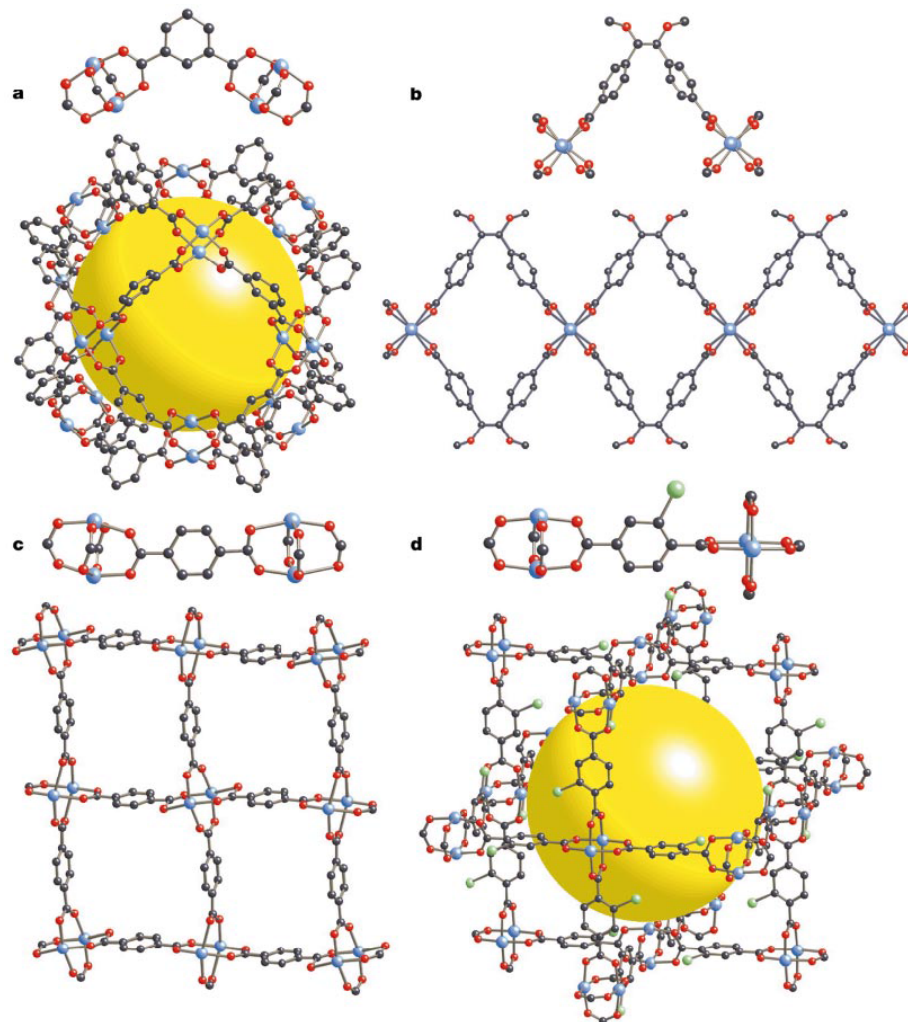


**Figure 1.1:** Fragments of assembled structures of (a) MOP-1,<sup>44</sup> (b) MOF-222, (c) MOF-2, and (d) MOF-101. C, black; O, red; Br, green; Metal, blue. One linker is shown above each structure. Yellow sphere represents the central cavity in MOP-1 and MOF-101. (The metal-organic polyhedra, MOP-1, is a type of porous organic polymer discussed in section 1.3). Figure replicated from reference 43.<sup>43</sup>

Similarly, MOF-5 has been exploited through extension of its structure and functionalisation to develop a series of isorecticular MOFs (IRMOFs) (Figure 1.2).<sup>31</sup> MOF-200 and MOF-210 both exhibit high surface areas; MOF-200,  $SA_{\text{BET}}$  of  $4530 \text{ m}^2 \text{ g}^{-1}$ , and MOF-210,  $SA_{\text{BET}}$  of  $6240 \text{ m}^2 \text{ g}^{-1}$ . Both display a larger Langmuir surface area

( $SA_{Lang}$ ) of  $10400 \text{ m}^2 \text{ g}^{-1}$ . The selection of organic linkers, and in the case of MOF-210 the inclusion of a tertiary building block, which means that the large pore sizes and large surface areas can be achieved.<sup>45</sup>

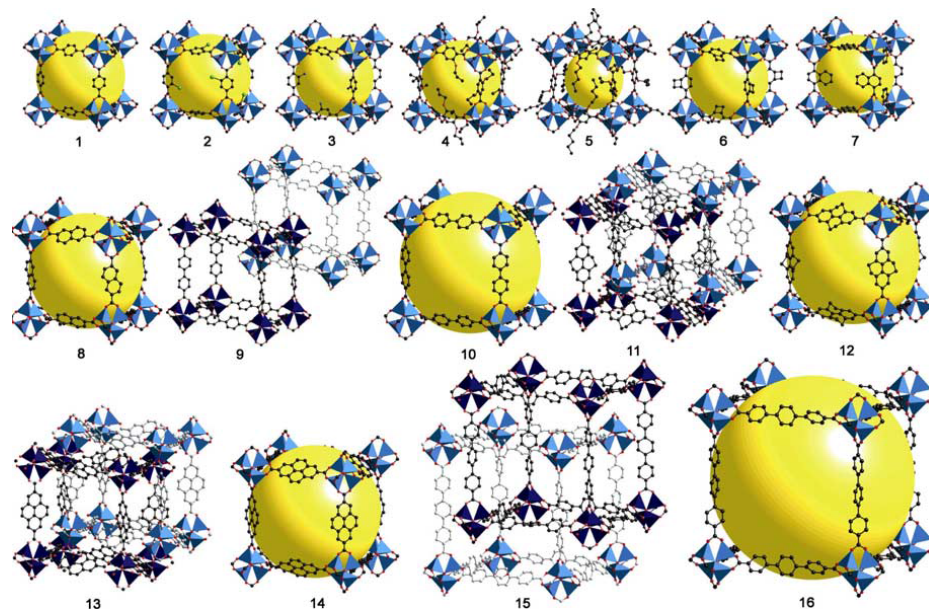


**Figure 1.2:** A series of IRMOFs with the same cubic topology, but differing organic linkers. The yellow sphere represents the available voids within the construct. Replicated from reference 31.<sup>31</sup>

MOFs have gained high interest due to their porosity and potential applications. They first showed promise in catalytic processes,<sup>46,47</sup> and now show potential for various other applications including gas storage and separation,<sup>48</sup> and sensing technologies.<sup>49</sup> It is highly desirable to rationally design and synthesise new MOF materials. However, due to the complexity of the organic linker and secondary building units, the prediction of structure, porosity, topology, and functionality becomes difficult. Advances through symmetry-guided approaches and the implementation of pre-synthetically designed organic linkers, MOFs of predetermined structure and behaviour can be produced. More recently, MOFs are being studied for electronic applications. Luminescent sensors,<sup>50</sup> supercapacitors,<sup>51</sup> and development into battery technologies<sup>52</sup> are some of the developments made thus far.

### 1.2.3 Zeolitic imidazolate frameworks (ZIFs) and metal-organic zeolites (MOZs)

Zeolitic imidazolate frameworks (ZIFs) and metal-organic zeolites are new breeds of metal-organic framework. ZIFs are constructed of imidazolate linkers and metal ions, with structures based on zeolites. Much like MOFs, ZIFs can be applied in a variety of applications,<sup>53</sup> with their most famous being gas separation.<sup>54,55</sup>

MOZs possess very similar behaviour to ZIFs. However, their composition does not include imidazolate, but rather the topology of zeolites built through selectivity of metal ions and organic linkers. MOZ-1 displays a surface area ( $SA_{\text{BET}}$ ) of close to  $2000 \text{ m}^2 \text{ g}^{-1}$ , similar to that of ZIF-67 ( $SA_{\text{BET}} 1832 \text{ m}^2 \text{ g}^{-1}$ ).<sup>56</sup> And similarly can be applied to a series of applications.

## 1.3 Organic Microporous Materials

Organic microporous polymers (which have accrued many abbreviations over the time, but shall be referred to here as MOPs: microporous organic polymers) are porous materials strictly comprised of organic elements; boron, carbon, nitrogen, and oxygen. The use of organic elements has shown to have a range of advantages over inorganic porous materials; comparably, most inorganic-based materials are sensitive in air whereas the majority of organic-based are not, and also MOPs are insoluble in a wide variety of solvents.<sup>57</sup>

MOPs can be found in crystalline forms, such as covalent organic frameworks, and amorphous materials, some including porous aromatic frameworks, hyper-cross-linked polymers, and conjugated microporous polymers.<sup>58</sup> Much like their inorganic propinquity, they can be developed and tailored to approach a variety of applications, including gas storage, molecular separation, catalysis, energy storage and conversion, and sensing technologies.

### 1.3.1 Covalent organic frameworks (COFs)

Covalent organic frameworks (COFs) are porous, crystalline materials constructed by the covalent bonding of organic molecules. The crystallinity of COFs arises from the reversible reactions applied to the synthesis of the materials, forming thermodynamically stable materials. The variety of available building blocks, coupled with the functionality of the monomeric units, enables COFs to adopt a variety of applications, including gas storage and separation, catalysis, energy storage, and many others.

COF-1 and COF-5 were the initial COF materials developed. COF-1 was synthesised through the self-condensation reaction of 1,4-benzenediboronic acid, and COF-5 through the co-condensation of 1,4-benzenediboronic acid with 2,3,6,7,10,11-hexahydroxytriphenylene.

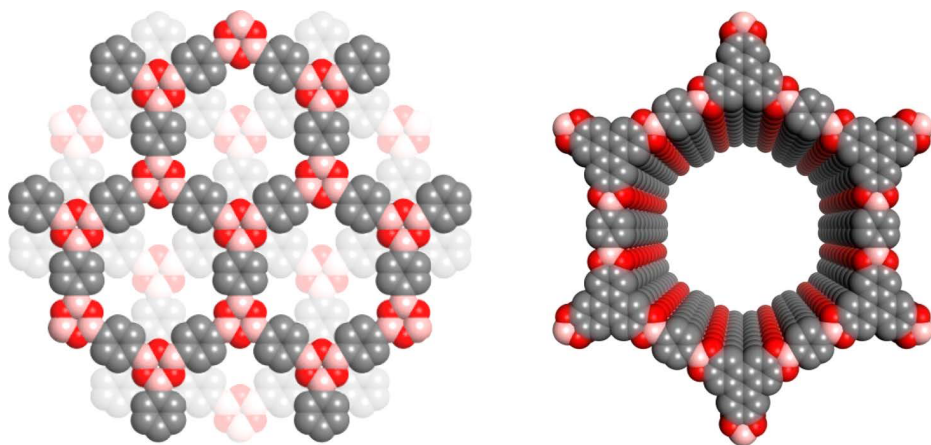


**Figure 1.3:** Structural models of (left) COF-1 and (right) COF-5. Carbon, grey; Boron, pink; Oxygen, red; Hydrogen, white. Replicated from reference 57.<sup>59</sup>

Figure 1.3 shows the structure of COF-1 and COF-5. As can be seen the topology of these materials differ greatly. X-ray diffraction determined the materials to be graphite-like, having layered sheets. COF-1 ( $\text{SA}^{\text{BET}}$  711  $\text{m}^2 \text{g}^{-1}$ ) has a staggered layering, whereas the layers COF-5 ( $\text{SA}^{\text{BET}}$  1590  $\text{m}^2 \text{g}^{-1}$ ) stack in an eclipsed fashion.<sup>32</sup>

Further development into these materials from Yaghi *et al.* gave rise to three-dimensional frameworks of COF-102, COF-105, and COF-108,<sup>60</sup> displaying surface areas ( $\text{SA}^{\text{BET}}$ ) of over 3000  $\text{m}^2 \text{g}^{-1}$  (COF-2,  $\text{SA}^{\text{BET}}$  3472  $\text{m}^2 \text{g}^{-1}$ ). Reticular synthesis

was also established for the development of the two-dimensional frameworks COF-6, COF-8, and COF-10 ( $S_{\text{BET}}$  1049 m<sup>2</sup> g<sup>-1</sup>, 986 m<sup>2</sup> g<sup>-1</sup>, and 976 m<sup>2</sup> g<sup>-1</sup> respectively), following on from the topology of COF-1 and COF-5.<sup>61</sup>

Aside from boron-comprising COFs, imine- and imide-based COFs have also been reported. COF-300 ( $S_{\text{BET}}$  1360 m<sup>2</sup> g<sup>-1</sup>)<sup>62</sup> and 3D-COF-Py ( $S_{\text{BET}}$  1290 m<sup>2</sup> g<sup>-1</sup>)<sup>63</sup> are two of the produced imine-based COFs. They show great promise towards further development of COF materials due to their impressive stabilities and ease of post-synthetic functionalisation. PI-COF-4 ( $S_{\text{BET}}$  2403 m<sup>2</sup> g<sup>-1</sup>) and PI-COF-5 ( $S_{\text{BET}}$  1876 m<sup>2</sup> g<sup>-1</sup>) are two imide-based COFs. These have shown apt capabilities for drug delivery.<sup>8</sup>

There has also been further development into chiral COFs, using chiral building blocks. Xu *et al.* first reported the synthesis of chiral COFs in 2016.<sup>64</sup> Since then, development has shown chiral COFs with surface areas up to 1000 m<sup>2</sup> g<sup>-1</sup><sup>65–67</sup> for applications such as asymmetric catalysis, chiral separation, and many more. Similar to MOFs, COFs are being utilised further within electronic applications, typically energy storage.<sup>68</sup>

### 1.3.2 Hyper-cross-linked polymers (HCPs)

Hyper-cross-linked polymers (HCPs) are amorphous polymers with high surface areas, microporosity, and low density. They are typically synthesised through Friedel-Crafts alkylation, differing from alternative porous materials. HCPs are developed through cross-linking of polymer chains. The cross-linking of the polymer chains is a result of complete dissolution or swelling of the precursor, alongside post-crosslinking treatment (Figure 1.4).<sup>69</sup> Davankov *et al.* first established these porous materials, and furthered their research through the use of polystyrene as a precursor, displaying BET surface areas over 1000 m<sup>2</sup> g<sup>-1</sup>.<sup>70–72</sup>



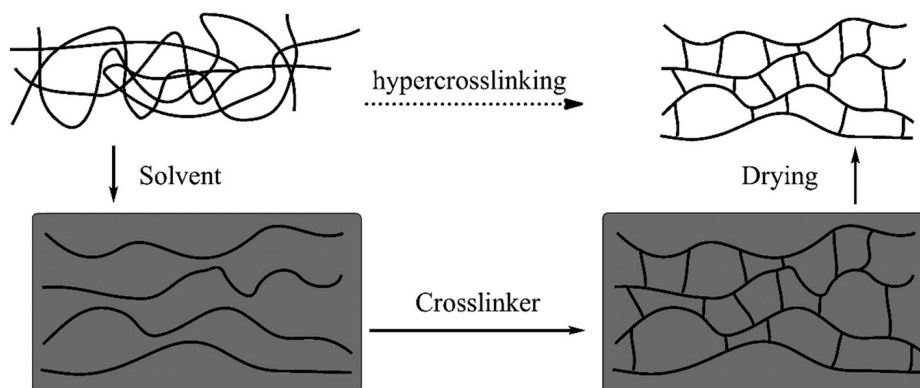


**Figure 1.4:** Representation of the hypercrosslinking process of HCPs.<sup>73</sup>

In an attempt to further increase the surface area of HCPs, polystyrene-divinylbenzene<sup>74,75</sup> and vinylbenzyl chloride-divinylbenzene<sup>76–78</sup> as precursors have produced HCPs with surface areas up to  $2000 \text{ m}^2 \text{ g}^{-1}$ .<sup>78</sup> Progress into ascertaining improvements on the pore size and surface areas of HCPs came from varying the divinylbenzene content within the divinylbenzene-vinylbenzene chloride precursors.<sup>79</sup> The resulting surface areas ranged through  $1260 \text{ m}^2 \text{ g}^{-1}$  to  $2060 \text{ m}^2 \text{ g}^{-1}$  (surface areas varied between 0–10% divinylbenzene content; greatest surface produced was from 2% divinylbenzene).

Improvements towards HCP applications have been a major focal point in recent research. Hydrogen storage was enhanced through the incorporation of platinum nanoparticles,<sup>80</sup> enhancing the hydrogen storage capacity of HCPs to 0.21 wt% (298K, 19 bar) with 2 wt% Pt nanoparticles, and  $\text{CO}_2$ , through the development of a robust mesoporous framework of phenolic resin polymers.<sup>81</sup>

Newer strategies into the crosslinking of polymer chains has brought about the process of "*Knitting*" (Figure 1.5).<sup>82</sup> Tan *et al.* demonstrated the process of cross-linking aromatic ring-containing small molecules using dimethoxymethane (FDA: formaldehyde dimethyl acetal). The results showed high thermal stability in HCPs, with surface areas of up to  $1391 \text{ m}^2 \text{ g}^{-1}$ , and increased  $\text{H}_2$  and  $\text{CO}_2$  uptakes of up to 1.58 wt% and 15.9 wt% respectively. The "*Knitting*" process was applied using several different aromatic heterocycles, including thiophene, pyrrole, and furan,<sup>83</sup> as well as

fused heterocycles such as benzothiophene,<sup>84</sup> benzofuran,<sup>84</sup> dibenzofuran,<sup>84</sup> triazine,<sup>85</sup> tricarbazolyltritycene,<sup>86</sup> and carbazole.<sup>84,85,87</sup> The use of carbazole in particular has shown great advancements in CO<sub>2</sub> adsorption. With surface areas (SA<sub>BET</sub>) ranging up to 1845 m<sup>2</sup> g<sup>-1</sup>, carbazole-based HCPs demonstrate up to 18 wt% CO<sub>2</sub> uptake, which is comparably close to materials with greater surface area.<sup>85</sup>

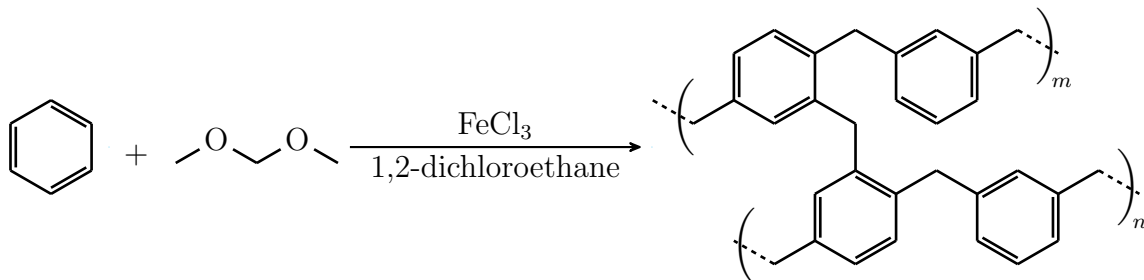


**Figure 1.5:** The "Knitting" process involving benzene and FDA. The benzene is coupled and FDA are heated with a catalyst at 45 °C for 5 hours, then heated again at 80 °C for 19 hours to complete the condensation reaction. The FDA couples at multiple locations on the benzene, allowing for the bridging of polymer chains, and therefore the HCP network.

As well as "Knitting" differing aromatic heterocyclic monomers, alternate external cross-linkers have been used for the development of HCPs. Bhaumik *et al.* introduced a hypercrosslinked supermicroporous polymer (HMP-1).<sup>88</sup> The polymer presented a lower surface area (SA<sub>BET</sub> 913 m<sup>2</sup> g<sup>-1</sup>) than others, yet showed great potential for low temperature catalytic processes.

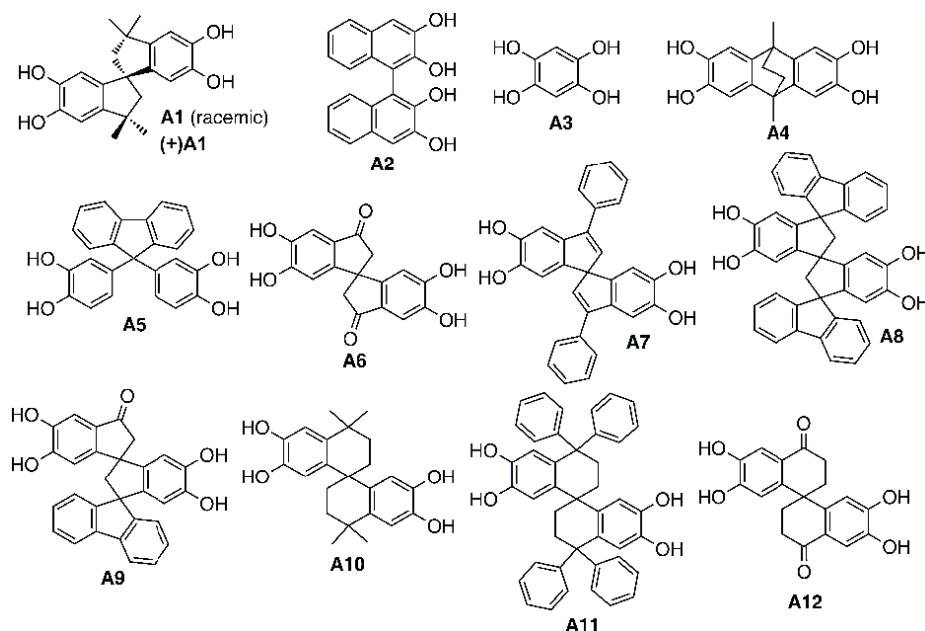
### 1.3.3 Polymers of intrinsic microporosity (PIMs)

Polymers of intrinsic porosity (PIMs) are amorphous polymers with highly rigid chains. They differ greatly from other porous media as they do not possess a framework, but instead rely on inefficient packing resulting from the contortion of the rigid chain. Maintaining the microporosity requires strong hinderance of rotation, preventing uniform packing of the polymer chains.

PIMs are generally synthesised using a "low temperature method". This involves mixing monomers of equimolar quantities in dimethyl formamide (DMF) with potassium carbonate at 50-60 °C. The low temperature is ideal so as the DMF does not

decompose, interfering with the polymerisation reaction. Alternatively, a "rapid high temperature method"<sup>89,90</sup> can be used. This involves intense stirring of a monomer combination in dimethyl acetamide at 155 °C, or another approach suggested by Skupov *et al.* for synthesising PIM-1 was to use dimethylsulfoxide at 120 °C.<sup>91</sup> Both techniques yield high molecular masses, leading to robust films, as well as high CO<sub>2</sub> permeability.

McKeown *et al.* reported the synthesis of PIM-1, prepared from the monomers 5,5',6,6'-tetrahydroxy-3,3,3',3'-tetramethyl-1,1'-spirobisindane and 2,3,5,6-tetrafluoroterephthalonitrile.<sup>92</sup> PIM-1 had a surface area ( $SA_{\text{BET}}$ ) of 850 m<sup>2</sup> g<sup>-1</sup> as well as great stability and lifespan. McKeown *et al.* reported that the porosity was close to unchanged after heating to 300 °C or stored for over a year. PIMs 1-6 demonstrate great processability. Each material was readily soluble in organic polar solvents, offering further potential applications as thin-film, membrane materials.<sup>93</sup> Monomers A1-A3 and B1-B3 were used to synthesise PIMs 1-6 (Figure 1.6). The largest surface area determined came from PIM-1 ( $SA_{\text{BET}}$  up to 850 m<sup>2</sup> g<sup>-1</sup>). Using the monomers of A8 and B1 produced a PIM with enhanced surface area comparable to PIM-1 ( $SA_{\text{BET}}$  895<sup>94</sup>).



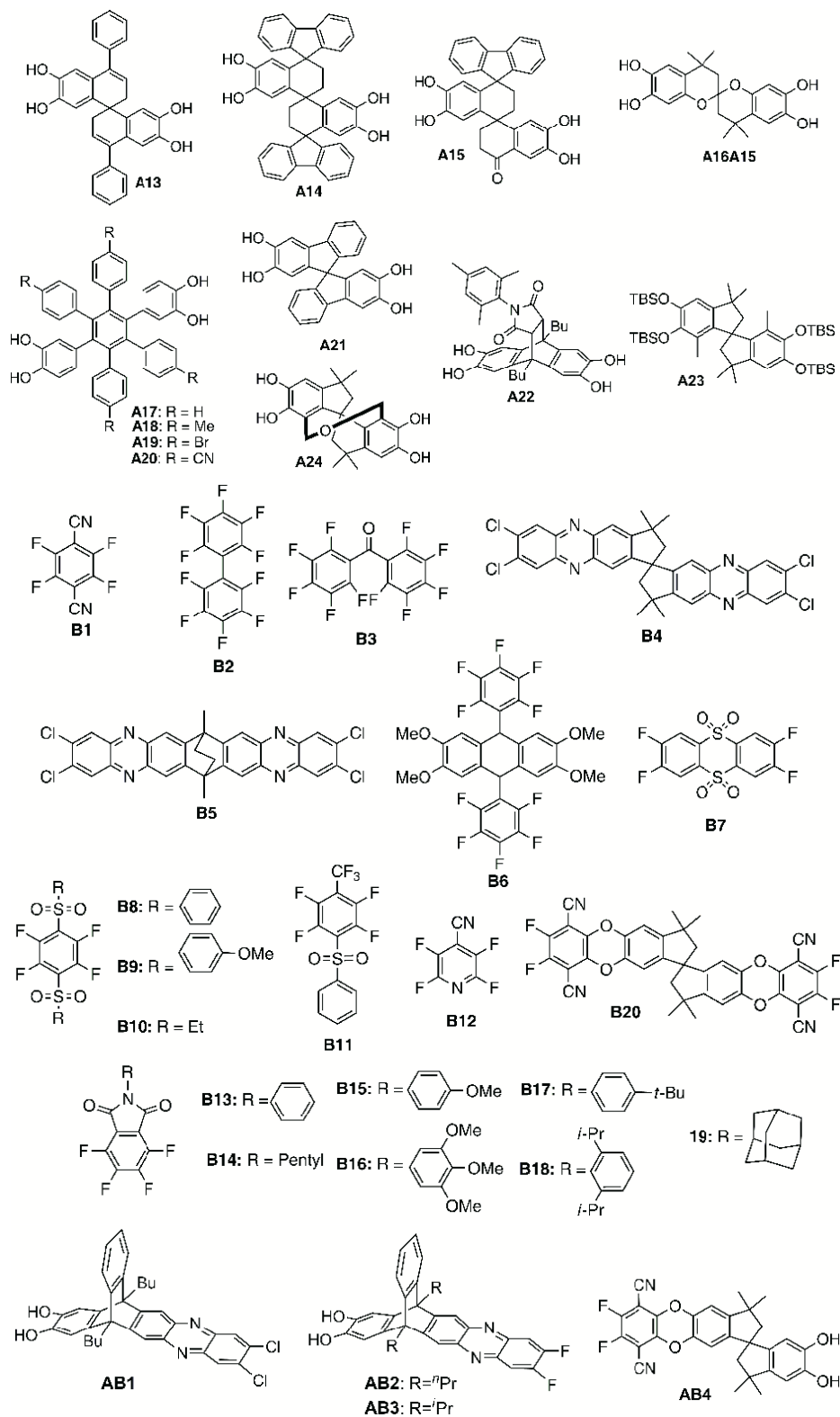


**Figure 1.6:** Typical structures of PIM monomers; A1-3 and B1-3 used for the synthesis of PIMs 1-6. Figure extracted from reference 94.<sup>95</sup>

The lack of framework leads to great solubility, making PIMs readily processable into thin films and coatings. The processability of PIMs opens up a wide variety of applications, such as sensors,<sup>96,97</sup> gas separation,<sup>98</sup> and electrochemical applications.<sup>99,100</sup>

### 1.3.4 Porous organic molecules

Molecular solids demonstrate porous properties that are not only porous but can also be soluble, making them ideal candidates for membrane processing.<sup>101</sup> Dianin's compound is a prime example of a porous molecule. The crystal structure possesses cavities between the molecules in which guest molecules can become trapped.<sup>102,103</sup> Figure 1.7 shows the hourglass cavities present within the crystal structure.

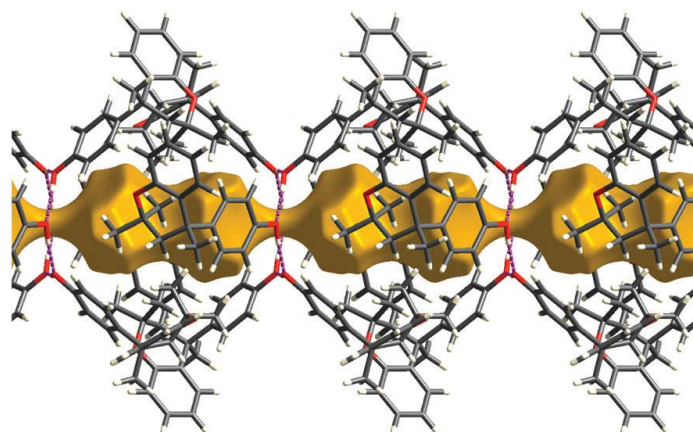


**Figure 1.7:** Representation of the hourglass-shaped cavities present between the Dianin's compound (yellow). Six Dianin's compound molecules for a single cavity, with intermolecular bonds shown as the red dashed lines. Figure reproduced from reference<sup>103</sup>

The porosity of porous organic cages can arise from either intrinsic porosity, to which the molecular cages contain a central void within them, or extrinsically due to inefficient packing of the molecules.<sup>104</sup> In some cases, these materials can possess both intrinsic and extrinsic porosity, making them ideal candidates for molecular storage and separation.

Difficulties arise with porous molecules when desolvation is performed. Removal of the occupying solvent post-synthesis leads to further packing of the molecules,

resulting in dense solids containing only intrinsic porosity.<sup>105</sup>

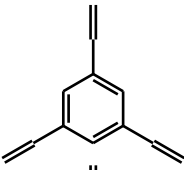
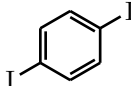
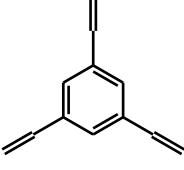
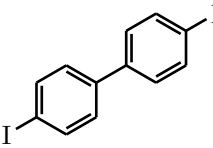
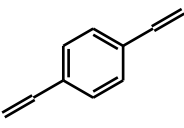
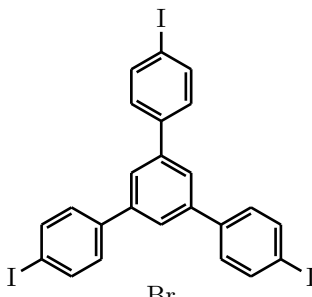
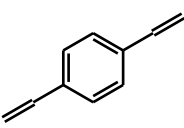
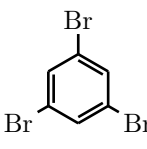
Inorganic cage compounds have already been well established.<sup>106,107</sup> These materials have high symmetry, and are widely used for small molecule storage, or as reaction vessels. High yielding organic cages based on imine-linked structures were synthesised through the condensation of 1,3,5-triformylbenzene and 1,2-ethylenediamine as host structures for small molecules.<sup>108,109</sup> These materials, with their intrinsic and extrinsic porosity, display surface areas ( $SA_{\text{BET}}$ ) up to  $650 \text{ m}^2 \text{ g}^{-1}$ .

Porous cages of varying topology have been explored. Cooper *et al.* reported porous cages of tetrahedral topology, synthesised through a template-free-one-pot technique.<sup>110</sup> Development of the structure has led to further insight for development of more complex porous cage materials. The greatest challenge face when developing highly porous cage materials is the structural collapse of the systems. This generally arises on the removal of present solvent in the systems. However, careful removal of the solvent can lead to some exceptionally high surface areas. Rigid triptycene derivatives can self-assemble through intermolecular bonds, the slow removal of occupying solvent (dimethylsulfoxide) through solvent exchange allowed for the rigid structure to be retained, leaving an accessible surface area ( $SA_{\text{BET}}$ ) of  $2796 \text{ m}^2 \text{ g}^{-1}$ .<sup>111</sup> Another method has been proposed for increasing porous molecule surface area, via freeze drying to promote crystallisation. The resulting surface area of the porous cages virtually doubled from this technique ( $SA_{\text{BET}}$   $409 \text{ m}^2 \text{ g}^{-1}$  to  $859 \text{ m}^2 \text{ g}^{-1}$ ).

The solubility of the materials makes them more processable into porous thin-films or membranes. The inclusion of functionality within the cage molecules offers great potential for selective properties, as well as co-crystallisation for multifunctional materials.

### 1.3.5 Conjugated microporous polymers (CMPs)

Conjugated microporous polymers (CMPs) are porous organic materials comprised of highly conjugated building blocks, resulting in extended  $\pi$ -conjugation through the porous polymer. The alternation of  $\pi$ - and  $\sigma$ - bonds through the networks allows CMPs to be readily utilised for electronic applications. CMPs have been synthesised through a series of different techniques. Some examples include Suzuki coupling,<sup>112,113</sup> Yamamoto,<sup>114,115</sup> and Sonogashira-Hagihara<sup>116</sup> coupling reactions.

	Alkyne monomer	Halogen monomer	SA <sub>BET</sub> (m <sup>2</sup> g <sup>-1</sup> )
CMP-1			834
CMP-2			634
CMP-3			522
CMP-4			744

**Table 1.1:** Brunauer-Emmett-Teller surface area of the synthesised CMPs;<sup>117</sup> Surface area calculated from N<sub>2</sub> adsorption isotherm.

The first CMPs synthesised were introduced in 2007 by Cooper *et al.*<sup>117</sup> formed from poly(aryleneethynylene) (PAE) (Table 1.1). CMP-1 (Figure 1.8), -2, -3, and -4 gave insight into the new techniques for developing porous materials, as well as the

use of  $\pi$ -electron donating monomers that produce the conjugated framework. The amorphous materials display BET surface areas between  $500 \text{ m}^2 \text{ g}^{-1}$  and  $850 \text{ m}^2 \text{ g}^{-1}$ . The CMPs were produced using iodo-substituted benzene monomers, with CMP-4 involving a bromo-substituted monomer. CMP-1 contains smaller node-to-node strut yet possess the highest surface area ( $\text{SA}_{\text{BET}} 834 \text{ m}^2 \text{ g}^{-1}$ ), whereas CMP-3, with the larger node-to-node strut, possesses the lowest surface area ( $\text{SA}_{\text{BET}} 522 \text{ m}^2 \text{ g}^{-1}$ ). This behaviour is due to the increased flexibility of the struts with increased length. This was displayed by the introduction of CMP-0 and CMP-5.

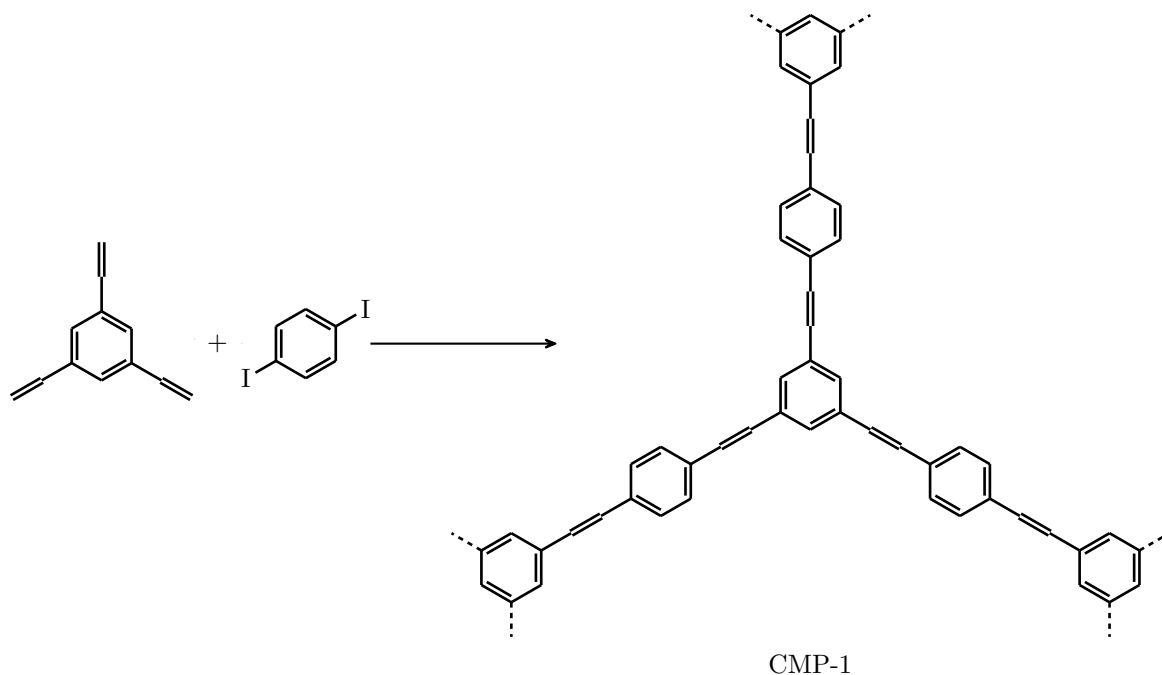


**Figure 1.8:** Schematic representation of the formation of the poly(aryleneethynylene) framework, CMP-1. Synthesised using the Sonogashira-Hagihara coupling reaction of 1,3,5-triethynylbenzene and 1,4-diiodobenzene.

CMP-0 and CMP-5 demonstrated how manipulation and selection of the monomeric building blocks can tailor the structural properties of porous materials.<sup>118</sup> Increasing the linker length from 0.82 nm in CMP-0 to 2.55 nm in CMP-5 (1.11, CMP-1; 1.53, CMP-2; 1.90, CMP-3) leads to a decrease in surface area ( $\text{SA}_{\text{BET}} 1018 \text{ m}^2 \text{ g}^{-1}$ , CMP-0;  $834 \text{ m}^2 \text{ g}^{-1}$ , CMP-1;  $634 \text{ m}^2 \text{ g}^{-1}$ , CMP-2;  $522 \text{ m}^2 \text{ g}^{-1}$ , CMP-3;  $512 \text{ m}^2 \text{ g}^{-1}$ , CMP-5), with an increase in pore size. This indicates that a shorter linker resulted in a microporous structure, whereas a larger linker resulted in a more mesoporous structure. Hydrogen



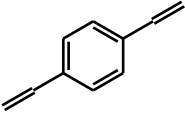
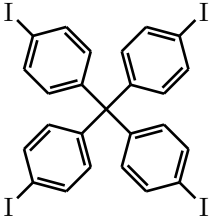
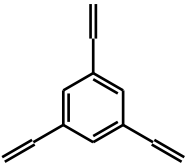
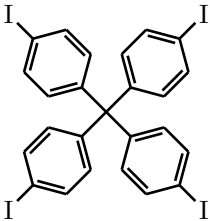
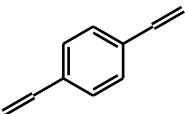
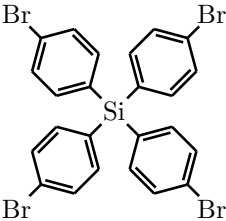
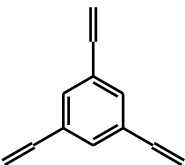
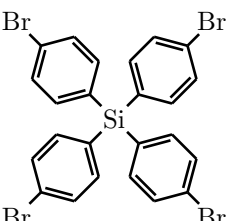
isotherms of these CMPs were determined. CMP-0, with the largest surface area, displayed the largest uptake of H<sub>2</sub> of 1.4 wt% at 1 bar and 77 K. The introduction of metal nanoparticles previously mentioned for HCPs has been explored with CMPs. Incorporating palladium nanoparticles into the CMP-0 framework increased the H<sub>2</sub> uptake at 298 K and 1.13 bar from 0.006 wt% in CMP-0 to 0.069 wt% with 9.5 wt% of Pd nanoparticles.<sup>119</sup>

CMPs with greater BET surface areas have been developed through the use of tetrahedrally-based monomers. Tetrakis(4-iodophenyl) methane and tetrakis(4-bromophenyl) silane coupled with 1,4-diethynylbenzene to produce CMPs with BET surface areas of 1213 m<sup>2</sup> g<sup>-1</sup> and 1093 m<sup>2</sup> g<sup>-1</sup> respectively (E1 and E3 Table 1.2).<sup>120</sup>

The surface areas of CMPs can be manipulated through many methods. Changing the reaction solvent during the Sonogashira-Hagihara coupling reaction can raise or lower the BET surface area. 1,3,5-triethynylbenzene coupled with 2,5-dibromobenzene-1,4-diol in varying solvents of toluene, dioxane, tetrahydrofuran (THF), and dimethylformamide (DMF) produced CMPs with surface areas of 761 m<sup>2</sup> g<sup>-1</sup>, 778 m<sup>2</sup> g<sup>-1</sup>, 847 m<sup>2</sup> g<sup>-1</sup>, and 1043 m<sup>2</sup> g<sup>-1</sup> respectively.<sup>121</sup>

Alternatively, the molar ratio of catalyst used for the formation of these materials can influence the size of pores produced in the systems. Covalent triazine-based frameworks (CTFs) are a derivative of CMPs. Use of aromatic or conjugated monomers can result in an overall conjugated framework consisting of triazine nodes (see Covalent Triazine-based Frameworks).

Antonietti *et al.* displayed studies of various CTF materials altering the ratio of ZnCl<sub>2</sub> for synthesis.<sup>122</sup> Increasing the number of catalyst equivalents from 10 to 20 for the polymerisation of 4,4''-dicyanoterphenyl (DCTP) gave an increase in surface area from 495 m<sup>2</sup> g<sup>-1</sup> to 1900 m<sup>2</sup> g<sup>-1</sup>. They also demonstrated the effects of increasing reaction temperature. 1,4-dicyano-benzene (DCB), used for the formation of CTF-1 (see Section 1.3.6), with ZnCl<sub>2</sub> at temperatures of 400 °C, 500 °C, 600 °C, and 700 °C resulted in porous framework formations with surface areas of 920, 1600, 1750, and 2530 m<sup>2</sup> g<sup>-1</sup> respectively.

	Alkyne monomer	Halogen monomer	SA <sub>BET</sub> (m <sup>2</sup> g <sup>-1</sup> )
E1			1213
E2			488
E3			1093
E4			925

**Table 1.2:** Brunauer-Emmett-Teller surface area of the synthesised PAE networks;<sup>120</sup> Surface area calculated from N<sub>2</sub> adsorption isotherm.

Similarly, CMPs produced from phenazine monomers (Aza-CMPs) observed similar effects. Increasing the reaction temperature can finely tune the surface area and pore size. This was apparent with the condensation of 1,2,4,5-benzenetetramine with triquinoylhydrate at 300 °C, 350 °C, 400 °C, 450 °C, and 500 °C, resulting in porous

frameworks with BET surface areas 24, 546, 1029, 1086, and 1227 m<sup>2</sup> g<sup>-1</sup> respectively, and pore sizes decreasing from 1.65 to 1.40, 0.90, and 0.85 (for both 450 °C and 500 °C) respectively.<sup>123</sup>

Porosity and surface area have been explored with pyrene-based CMPs.<sup>124</sup> The CMPs of YPy (1,3,6,8-tetrabromopyrene), YDBPy (1,3,6,8-tetrabromopyrene coupled with 1,4-dibromobenzene), and YDPPy (1,3,6,8-tetrabromopyrene coupled with 4,4'-dibromobiphenyl) were synthesised via *Yamamoto* coupling, producing surface areas of 1508 m<sup>2</sup> g<sup>-1</sup>, 1069 m<sup>2</sup> g<sup>-1</sup>, and 303 m<sup>2</sup> g<sup>-1</sup> respectively. These CMPs not only possess a porous, conjugated framework, but also strong luminescent properties, opening up opportunities in the likes of organic electronics and photocatalysis. Cooper *et al.* demonstrated how the introduction and extension of linear linkers can manipulate the porosity of a structure, but also the electronic properties. Through the introduction of phenyl or biphenyl linkers the band gap was tailorable, as shown in Table 1.3.

CMP	SA <sup>BET</sup> (m <sup>2</sup> g <sup>-1</sup> )	$\lambda^{\max}$ (nm)	Band gap (eV)
YPY	1508	620	1.84
YDPPy	303	602	1.90
YDBPy	1069	545, 582	2.05

**Table 1.3:** Surface areas, photoluminescence peak, and band gap for the corresponding CMPs of YPy, YDBPy, and YDPPy.

CMPs have gained great interest due to their chemical properties and functionalisation. Designing CMPs for specific applications lies with the choice of monomers as well as the synthetic procedures performed. Recent advances have seen the control over pore size in CMPs offer high selectivity of small molecules, as well as catalysis.<sup>125,126</sup> However, their unique properties make the materials more ideal for electronic applications. Their conductivity can be utilised for photoelectronic, photocatalysis, and optoelectronic applications.<sup>127–129</sup>

The studies performed on pyrene-based CMPs for electronic applications has led to the research into the further development on these materials in this thesis.

### 1.3.6 Covalent triazine-based frameworks (CTFs)

As previously mentioned, covalent triazine-based frameworks are a sub-class of covalent organic frameworks (COFs) that can be related to conjugated microporous polymers (CMPs). They were first reported in 2008 with the introduction of CTF-1 (Figure 1.9).<sup>130</sup> The ionothermal strategy employed for the development of CTF gave rise to the first crystalline and microporous CTF. 1,4-dicyanobenzene was subjected to ionothermal synthesis with  $\text{ZnCl}_2$ . A 1.0 monomer/ $\text{ZnCl}_2$  ratio gave rise to a BET surface area of  $791 \text{ m}^2 \text{ g}^{-1}$ . However, as previously discussed for CMP development, the BET surface area of this material was enhanced with an increase in catalyst equivalents. A 0.1 monomer/ $\text{ZnCl}_2$  ratio produced a porous polymer with BET surface area of  $1123 \text{ m}^2 \text{ g}^{-1}$ . Albeit, the ionothermal reaction performed within this literature also yielded amorphous materials.

The reaction of CTF-1 was also studied with varying temperatures.<sup>131</sup> Performing the reaction at high temperatures resulted in a porous CTF with a BET surface area up to  $3270 \text{ m}^2 \text{ g}^{-1}$ .  $400^\circ\text{C}$  resulted in a BET surface area of  $920 \text{ m}^2 \text{ g}^{-1}$ . Increasing the temperature through 500, 600, and  $700^\circ\text{C}$  offered surface areas increased to 1600, 1750, and  $2530 \text{ m}^2 \text{ g}^{-1}$  respectively. However, the largest surface area established was through a combination of temperatures ( $400^\circ\text{C}$  for 20 h, then  $600^\circ\text{C}$  for 96 h), displaying  $3270 \text{ m}^2 \text{ g}^{-1}$ .

Thomas *et al.* reported the synthesis of the crystalline porous organic polymer CTF-2. CTF-2 was produced using the same ionothermal conditions as CTF-1, with 2,6-naphthalene dinitrile monomer.<sup>132</sup> The BET surface area of the resulting structure was comparatively small, being only  $90 \text{ m}^2 \text{ g}^{-1}$ . However, altering the monomer/ $\text{ZnCl}_2$  ratio and increasing the temperature of the reaction resulted in a considerable increase in BET surface area ( $\text{SA}_{\text{BET}} 2255 \text{ m}^2 \text{ g}^{-1}$ ), yet this affected the long range order exhibited initially, leaving a multimodal micro- and mesoporous amorphous material.

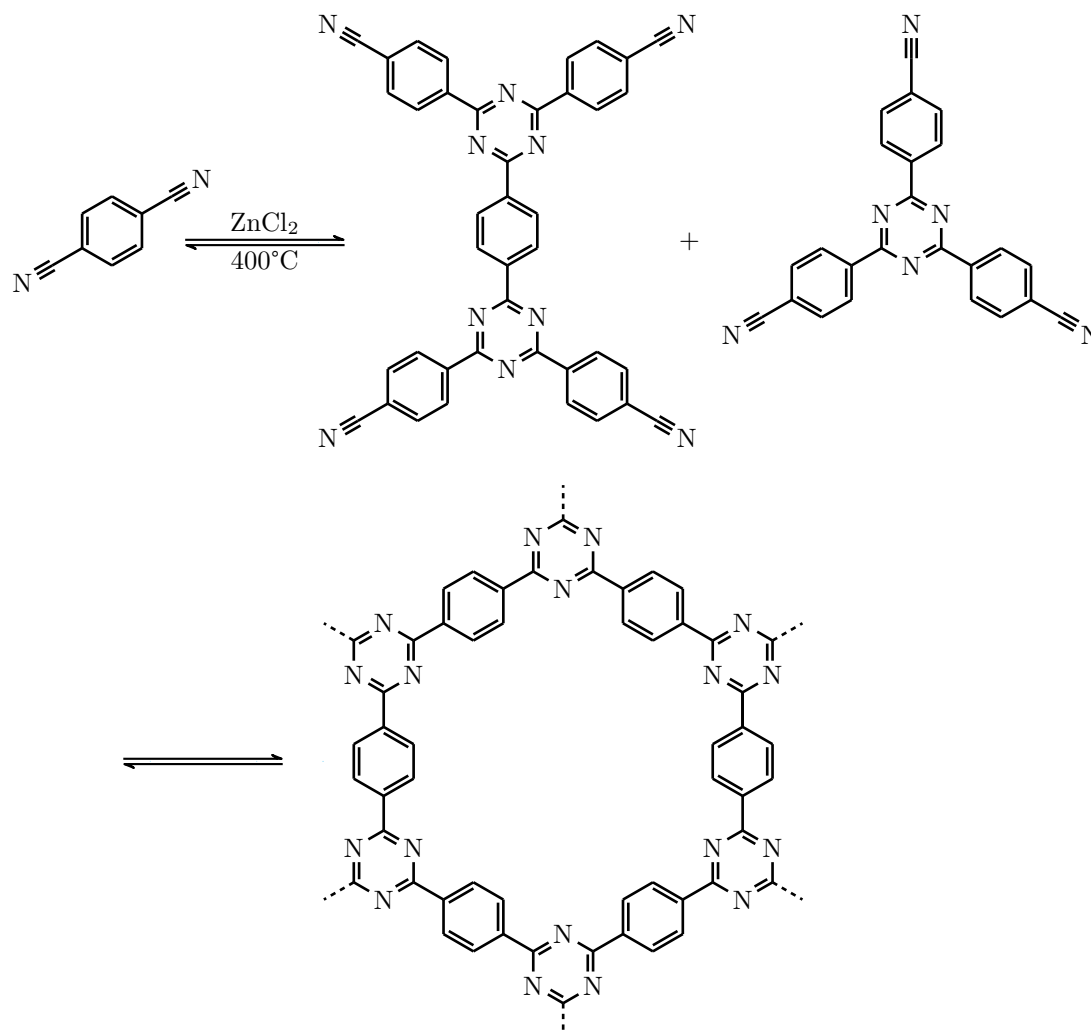


**Figure 1.9:** Trimerisation of dicyanobenzene with  $\text{ZnCl}_2$  for the formation of oligomers and then to CTF-1.<sup>130</sup>

CTF-0 was produced from 1,3,5-tricyanobenzene (Figure 1.10).<sup>35</sup> A 1:1 ratio of monomer :  $\text{ZnCl}_2$  at 400 °C resulting in a porous polymer with BET surface area of 546  $\text{m}^2 \text{g}^{-1}$ . However, adopting the multi-temperature process observed with CTF-1 (400 °C followed by 600 °C) results in an great increase in surface area, from 546 to 2011  $\text{m}^2 \text{g}^{-1}$ . CTF-0 showed to be a promising candidate for carbon dioxide capture and storage. Using the technique giving the greatest surface area (5 mol. equivalents of  $\text{ZnCl}_2$ , 400 °C for 20 hours, 600 °C for 20 hours), the resulting polymer has a  $\text{CO}_2$  uptake of 15.7 wt%.

Although the process produces very robust and highly porous materials, the ionother-

mal synthesis of CTFs poses many problems, including prolonged synthesis times, high temperatures, and the removal of  $\text{ZnCl}_2$ . To overcome these challenges Cooper *et al.* introduced a series of CTFs synthesised using trifluoromethanesulfonic acid (triflic acid) at room temperature and through microwave assisted conditions.<sup>133</sup>

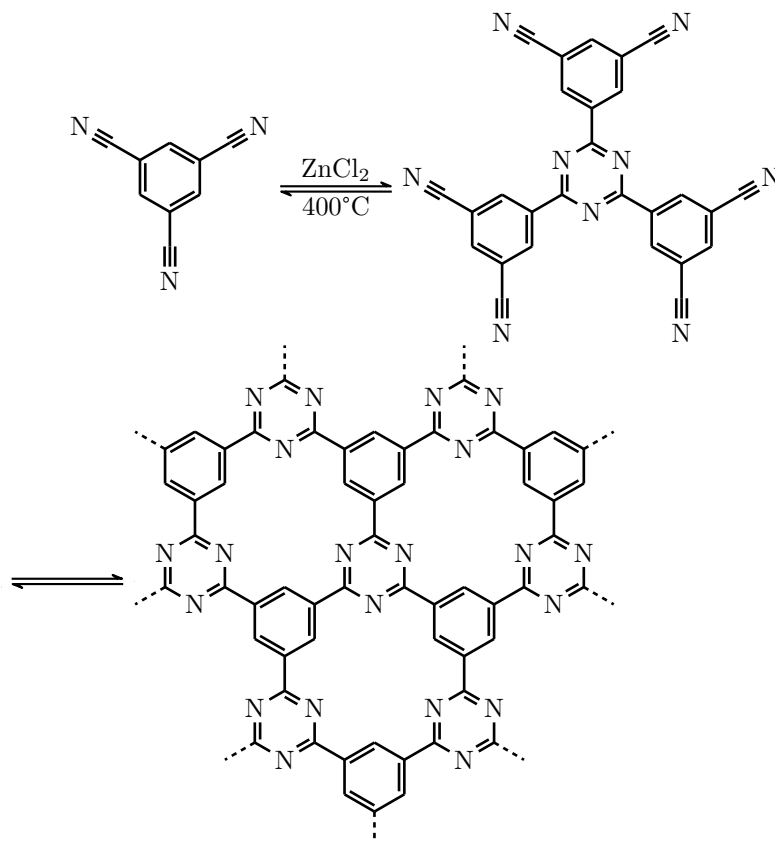


**Figure 1.10:** Trimerisation of 1,3,5-tricyanobenzene with  $\text{ZnCl}_2$  for the formation of oligomers and then CTF-0.<sup>35</sup>

This process was adapted from the formation of symmetrical triazine compounds synthesised through metal-free catalysis.<sup>134</sup> The CTFs produced (P1-P6 and P1M-P6M) were found to be amorphous. P1 and P1M were synthesised using 1,4-dicyanobenzene. The BET surface areas produced were negligible in comparison to the of CTF-1, with both techniques showing less than  $10 \text{ m}^2 \text{ g}^{-1}$ . However, the tetrahedral monomer of 4,4',4'',4'''-methanetetrayltetrabenzonitrile displayed promising BET surface areas of  $1152 \text{ m}^2 \text{ g}^{-1}$  via the room temperature method, and  $947 \text{ m}^2 \text{ g}^{-1}$  via the microwave assisted method.

Additionally, this process has been applied to the synthesis of CTF membranes based on 4,4'-biphenyldicarbonitrile<sup>135</sup> and letrozole (4,4'-((1h-1,2,4-triazol-1-yl)methylene)dibenzonitrile).<sup>136</sup> The materials showed BET surface areas close to that of CTF-1 (TFM-1, 738 m<sup>2</sup> g<sup>-1</sup>; <sup>135</sup> TFMT-550, 421 m<sup>2</sup> g<sup>-1</sup><sup>136</sup>) and great CO<sub>2</sub> permeability.

The use of strong Lewis and Brønsted acids offers less harsh reaction conditions for the formation of triazine-based compounds<sup>137</sup> and CTFs. Both techniques for CTF synthesis have produced highly porous materials, displaying great CO<sub>2</sub> adsorption. They have also been studied for their electronic properties, incorporating triazine rings within CMPs to offer high surface areas and extended conjugation (TNCMP-2, 995 m<sup>2</sup> g<sup>-1</sup>).<sup>138</sup> The use of reduced reaction conditions with strong acid catalysis has led to the development of novel CTFs that possess a degree of conjugation presented in this thesis.

### 1.3.7 Porous aromatic frameworks (PAFs)

Porous aromatic frameworks are open frameworks comprised of solely organic elements. They bear outstanding surface areas and a high level of stability. PAFs were first introduced with the synthesis of PAF-1. PAF-1 shows to have a BET surface area of 5600 m<sup>2</sup> g<sup>-1</sup> and incredibly high H<sub>2</sub> and CO<sub>2</sub> storage capacities.<sup>139</sup> PAF-1 is synthesised through the homo-coupling of tetrakis(4-bromo-phenyl)methane via the *Yamamoto* coupling reaction, as shown in Figure 1.11. The high rigidity and size of the monomer used gives rise to the immense stability and lack of interpenetration within the PAF-1 polymer. Trewin and Cooper established computational models for the rationalisation of PAF-1 structure. The basis of a diamond-like structure was employed due to the shape of the monomer, offering a strong open framework. The established results from these simulations led to a surface area of over 5000 m<sup>2</sup> g<sup>-1</sup> and a density as low as 0.315 g cm<sup>-3</sup>. Regardless, PAF-1 was experimentally determined as amorphous, lacking in long range order but maintaining a uniform pore diameter.<sup>140</sup> This synthetic strategy was adopted for the synthesis of both PAF-3 and PAF-4 using tetrakis(4-bromophenyl)silane and tetrakis(4-bromophenyl)germane respectively.

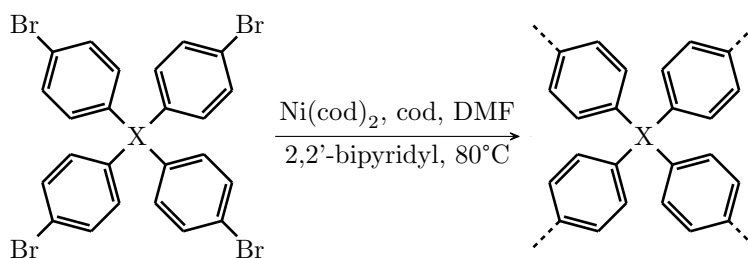


**Figure 1.11:** *Yamamoto* coupling reaction for the synthesis of porous aromatic frameworks. For PAF-1, PAF-3, and PAF-4, X = C, Si, Ge, respectively.

Both of these materials possess BET surface areas of  $2932\text{ m}^2\text{ g}^{-1}$  for PAF-3, and  $2246\text{ m}^2\text{ g}^{-1}$  for PAF-4.<sup>141</sup> Advancements on these PAF materials have shown dramatic increase to their surface areas. PAF-3 and PAF-4 (under the names PPN-4 and PPN-5) have demonstrated increased surface areas of  $6461$  and  $4267\text{ m}^2\text{ g}^{-1}$  respectively through the alteration of the synthetic procedure.<sup>142</sup> PAF-5 is another example of porous aromatic frameworks synthesised through *Yamamoto* coupling. The amorphous powder developed from 1,3,5-tris(4-bromophenyl)-benzene building blocks giving a BET surface area of  $1503\text{ m}^2\text{ g}^{-1}$ , and displaying high stability and a high affinity for the absorption of organic chemical pollutants.<sup>143</sup>

The use of alternate synthetic procedures have also been explored. PAF-2, with a BET surface area of  $891\text{ m}^2\text{ g}^{-1}$ , was synthesised via the trimerisation of tetrakis(4-cyanophenyl) methane.<sup>144</sup> PAF-11, with a BET surface area of  $704\text{ m}^2\text{ g}^{-1}$ , was synthesised via the *Suzuki-Miyaura* coupling reaction of tetrakis(4-bromophenyl)methane with 4,4'-biphenyldiboronic acid.<sup>145</sup> JUC-Zs (Jilin University, China Zeolites) were produced via a *Yamamoto*-type *Ullman* cross coupling. JUC-Z1 displayed a BET surface area of  $283\text{ m}^2\text{ g}^{-1}$  alongside high selectivity for benzene, making it a promising candidate for environmental pollutant applications.<sup>146</sup> JUC-Z2 displayed a larger surface area of  $2081\text{ m}^2\text{ g}^{-1}$  with strong electroactive properties, making it an ideal candidate for electrochemical applications.<sup>147</sup>



### 1.3.8 Organically synthesised porous carbon

Organically synthesised porous carbon materials are a new age for porous materials. OSPC-1 was first introduced by Zhao *et al.*<sup>148</sup> OSPC-1 is produced through the Eglinton homocoupling of ethynyl methane. This in turn produces a microporous structure, with *sp*<sup>3</sup>-hybridised carbon nodes connected with struts consisting of two ethyne groups. Figure 1.12 shows the reaction process for producing OSPC-1

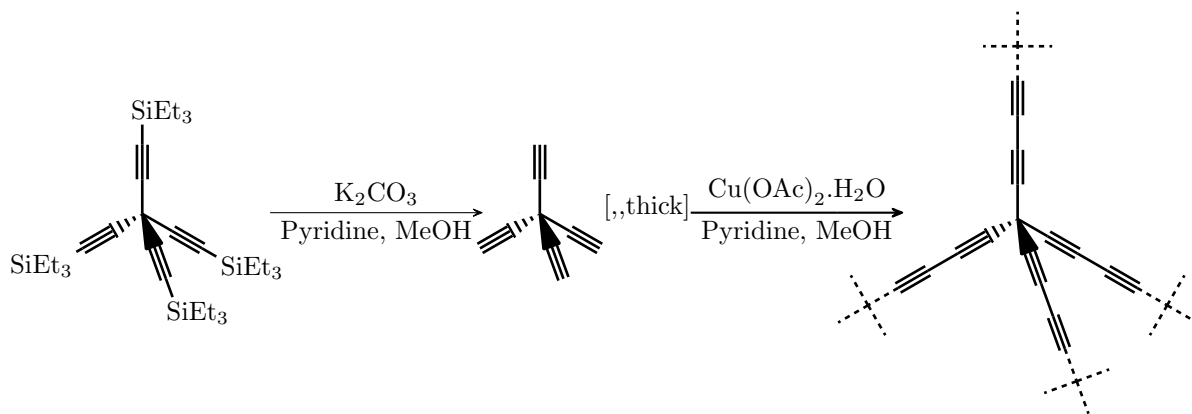


**Figure 1.12:** Reaction process for the formation of OSPC-1 via Eglinton homocoupling.

The unique structure of OSPC-1 has not only created to a newly developed porous material. It also introducing a new reaction process for manufacturing porous polymers and a highly electronic porous polymer. The surface area is not comparable to the exceptional surface areas of many other materials (for example PAF-1), determined to  $766 \text{ m}^2 \text{ g}^{-1}$ . Its unique structure has made it a suitable candidate as an anode for lithium ion batteries.

Graphite is a commonly used anode for lithium ion batteries, demonstrating a reversible lithium ion capacity of  $324 \text{ mA h g}^{-1}$  at  $200 \text{ mA g}^{-1}$ . However, material swelling and the formation of lithium dendrites are great causes to the short lifetime of these batteries. Therefore, materials that can resolve these issues are a necessity. OSPC-1, under the same conditions, surpasses graphite and many other materials, demonstrating a reversible lithium ion capacity of  $748 \text{ mA h g}^{-1}$ . Figure 1.13 illustrates the efficiency and rate capabilities of OSPC-1.

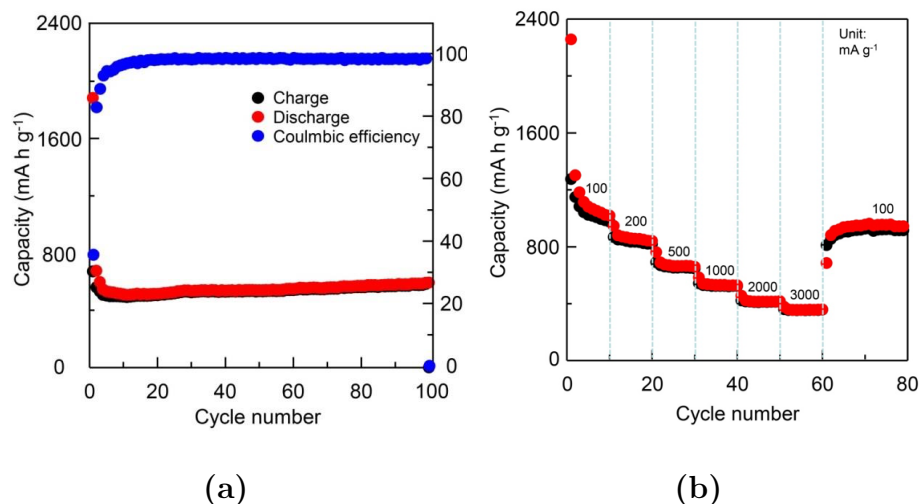


**Figure 1.13:** (a) Cycling performance of OSPC-1 showing discharge capacity (red), charge capacity (black), and coulombic efficiency (blue); current density of 200 mA g<sup>-1</sup> for 100 cycles. (b) Rate capability of OSPC-1 using varying current densities between 100 and 3000 mA g<sup>-1</sup>; discharge capacity (red) and charge capacity (black).

The efficiency of OSPC-1 as an anode for lithium ion batteries makes it a strong candidate for further battery development. Additionally, the synthetic technique, along with the electronic properties of the OSPC-1 material, offer insight into future development of carbon anode materials. OSPC-1 and further battery development is discussed further in Chapters 4 and 5.

## 1.4 Computational characterisation and design of porous materials

Computational techniques have redesigned materials development. The structural properties of porous materials, and properties such as surface area, pore size distribution (PSD) and volume, and gas uptake can be simulated. These techniques allow for ease of characterisation for materials synthesised, as well as rationalising materials with unique properties. Rationalisation of porous materials prior to experimental attempts is highly beneficial for screening porosity, meaning potential structural properties can be foreseen. Computational techniques can be highly cost effective if the

synthetic procedure for developing novel porous polymers is expensive.

Using computational techniques for characterising crystalline porous materials is a straightforward process as the structural properties correspond to the predetermined crystal structure. However, any deviation between the adsorption isotherms of these molecular systems and the experimental data can indicate deficiencies from either the molecular force field, the material samples itself, or inherent errors in the characterisation techniques. Comparably, amorphous materials require a larger characterisation data set to model against. Adsorption isotherms, PSD, density, and elemental data are such examples used when modelling amorphous porous materials. However, as there is limited structural data to compare to, any deviation from the experimental data typically indicates inadequacies with the simulated model.

### 1.4.1 Energetics and parameterisation

The energetics of porous materials can be defined through either coarse-graining methods,<sup>14,149,150</sup> electronic structure calculations, or molecular mechanics techniques. Electronic structure calculations use quantum mechanics to describe the electronic distribution of a system, which therefore can offer insight into optical, electronic, and magnetic properties. One method for calculating these properties is through density functional theory.<sup>151,152</sup>

Force fields are a requirement for computational simulations. A force field is a determined set of interatomic potentials used to describe the potential energy of an atom and the interactions between atoms. Force field development has advanced the prediction capabilities for structural and dynamic properties of a system. These incorporate set potential parameters and functional forms to describe the potential energy surface (PES) of a system. The parameters can be derived from a combination of experimental data and quantum mechanical calculations. The use of force fields is computationally less expensive than other approaches, yet they lack in accuracy if poorly parameterised. There are a number of commercially available force fields, most of which are only viable towards qualitative analysis. This means that the FF

needs to be well suited and parameterised for the system in question, and type of simulation applied. The universal force field (UFF), COMPASS,<sup>153</sup> and the polymer consistent force field (PCFF)<sup>154</sup> are typical examples of commercially available force fields applied to the modelling of porous materials. Derived from the CFF91 force field, and due to it being parameterised against a wide variety of organic and inorganic compounds and polymers, the PCFF force field is extensively used within the simulations performed throughout this thesis.

### 1.4.2 Structural prediction and design of porous materials

Porous materials are found both in nature, with the likes of zeolites and porous carbons, and also by synthetic design. Efforts have been made to tailor the development of porous materials and their functionality, with materials having function led design.<sup>58</sup> Designing porous materials through computational modelling has become very useful for the scientific community. Masterlerz *et al.* demonstrated the rationalisation of a porous material which exhibits a BET surface area of 2796 m<sup>2</sup> g<sup>-1</sup> through self-assembly hydrogen bonding of reactively accessible organic compounds.<sup>111</sup>

Through study of the molecular components of published porous materials, it is possible to extrapolate structural and functional properties for the design of new materials. Following the ideology of structural formatting, the inclusion of C<sub>2</sub>, C<sub>3</sub>, C<sub>4</sub>, and C<sub>6</sub> category monomers can be used to design porous materials structurally.<sup>155</sup> Using such techniques expands the database of potential porous materials, and screening of building blocks with unique properties can improve the evolution of functional materials. Snurr *et al.* have demonstrated the use of high throughput computational screening for the rationalisation of MOFs, to which they were able to generate over 130,000 theoretical structures of MOFs for methane storage.<sup>156,157</sup>

More recent advances in computational screening sees the determination of materials for selective properties. Cooper *et al.* demonstrated the use of electronic structure calculations coupled with molecular dynamics to screen porous organic molecules for xenon and krypton separation.<sup>158</sup> This led to the CC3 porous organic cage continues

to show the most promise for this separation, yet also highlighting the potential of Noria compounds for Xe/Kr separation.<sup>159,160</sup>

Computational techniques for the characterisation of structure and properties for crystalline materials are well established and have been widely used in the design of novel materials.<sup>161</sup> Using the knowledge and understanding of how these materials are compiled aids in the rationalisation process of novel materials. One process for the development of crystalline materials is the automated assembly of secondary building units (AASBU) introduced by Ferey *et al.*, offering a suitable process for modelling and predicting the formation and packing of zeolitic materials.<sup>162</sup> Crystalline porous materials can be readily characterised through computational techniques, as the experimental data can be aligned with the computational output. The design of metal-organic frameworks has proven to be straightforward using modelling techniques. Snurr *et al.* proposed the method for rationalising structure for methane storage.<sup>163,164</sup> Crystalline materials can be depicted as squares or cuboids when considering their structure, with the vertices of the shape given as each metal centre. Figure 1.14 illustrates the rationalisation of the 2-dimensional metal-organic frameworks topology.

Using the idea that crystalline porous materials follow this pattern, materials can be designed for a multitude of applications. The rigid organic linker incorporated into the system introduces both the 3-dimensional properties of the complex, as well as the functionality of the system. Therefore, it is necessary to consider carefully the building blocks of the porous material for a proposed application.

Hupp *et al.* demonstrate this further, illustrating the different topologies of the materials, as well as the selection of linkers available.<sup>165</sup> Applying linkers designed to preclude interpenetration and catenation can further the development of MOFs with desired porosity, surface area, and functionality.

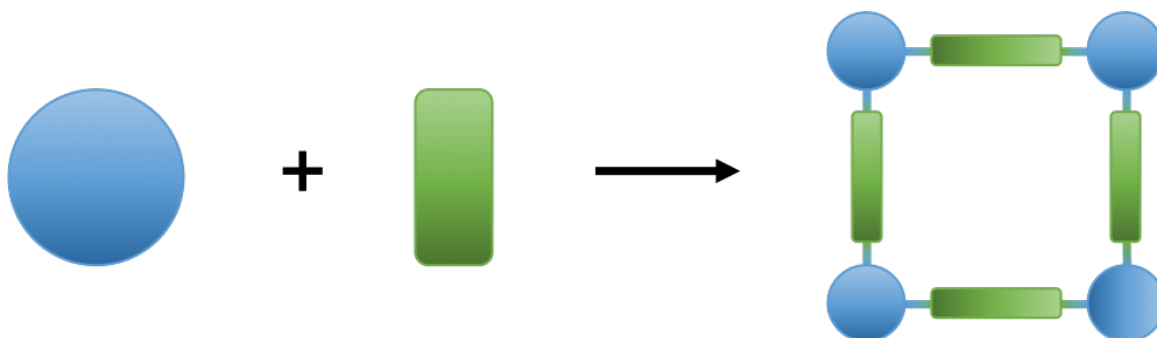


**Figure 1.14:** Rational design of metal-organic frameworks using a metal complex centre (blue circles) and rigid organic linkers (green rectangles).

Computational rationalisation of crystalline porous materials relies on the study of interactions between linkers and metal complexes, similar to studies performed on designing non-porous materials.<sup>166</sup> Early studies of crystalline material prediction presented techniques that incorporated calculating the relative energies for a vast array of known crystal structures.<sup>167</sup> Applying this technique alongside experimental analysis enables a more thorough throughput of crystal structure prediction.<sup>168,169</sup> Models of materials can be constructed and analysed for their porous properties. Yaghi *et al.* demonstrate initial design of MOFs through reticular design.<sup>170</sup> However, it is more challenging for molecular porous crystals due to the lack of strong coordination bonds within the system. Day *et al.* proposed the use of crystal structure prediction and DFT energy calculations to establish energy-function-structure maps for the prediction of porous crystal structures.<sup>171,172</sup> Although the pore size and topology of crystalline porous materials can be readily characterised through simple modelling techniques, the functionality and properties of materials designed require electronic calculations and MD simulations for their performance in certain applications.<sup>173</sup>

Because of the predictability of synthetic approaches for metal-organic materials, and the vast quantity of varying building blocks, molecular modelling has grown to be an attractive approach for material design. This process is transferable towards the rationalisation and design of amorphous materials. However, because of the unpredictable formation of amorphous materials, and lack of long range order, it becomes

more difficult to characterise materials through computational techniques.

Crystalline materials are produced through synthetic processes that result in thermodynamically stable products, whereas amorphous materials are kinetically controlled. Exact atomic structure of crystalline materials can be readily determined, amorphous materials require an alternate approach as experimental characterisation data is limited. Materials Studio<sup>174</sup> has proven to be a useful tool for the development and characterisation of structural models. Trewin *et al.* demonstrated atomistic simulations for the characterisation of Nitrogen-containing microporous polymers (NCMPs) and poly(aryleneethynylene) networks via the use of Materials Studio. Characterisation of these amorphous materials was made possible by applying atomistic simulations alongside the experimental data collected.<sup>120,175,176</sup> Although the stepwise approach performed can be applied to predict the structural properties of porous polymers, the approach does not replicate the internal structure of materials, excluding catenation and interpenetration which leads to overestimation of pore size and volumes. Zwijnenburg *et al.* applied an *ab initio* approach similar to that of crystal structure prediction, by screening low-energy conformers of small fragments for the study on pyrene models.<sup>177</sup> Coupled with DFT calculations, they were able to establish the structural and functional differences between the porous network and analogous soluble pyrene chains.

Interest in the development of computational software for studying the structural properties of amorphous porous polymers has grown significantly with the expansion of materials published. Colina *et al.* have presented a computational technique for the structural formation of amorphous polymers (Polymatic).<sup>178,179</sup> United atom models from the polymer consistent force field (PCFF) and Lennard-Jones potentials were utilised to understand the structural formation of the pyrene-based CMPs.<sup>124</sup> The models generated in this manner presented strong correlation to the experimental data published. Alternatively, Trewin *et al.* have developed a similar technology for the structural analysis of amorphous material. AmBuild (see Chapter 2) has been applied for the structural interpretation for PAF-1 and its formation mechanism, as well as the

understanding of lithium ion uptake and diffusion of the OSPC-1 material.<sup>148,180,181</sup>

Computational modelling of amorphous materials further enhances the characterisation of materials synthesised. It is also beneficial where rationalised materials produce unexpected outcomes. Trewin proposed the formation of novel polyamic acids through modelling of different topologies. Where crystallinity is predicted, the presence of two amic acid conformations has the potential to decrease the crystallinity of the overall framework.<sup>173</sup> Similarly, computational characterisation was applied to clarify the topology and structural properties of aza-CMP; where the experimental rationalisation offered a crystalline outcome, the structure was in fact amorphous. Figure 1.15 shows the reaction mechanism, with expected monomer bonding, and the overall generated system showing the occurring defects that result in the amorphous polymer.

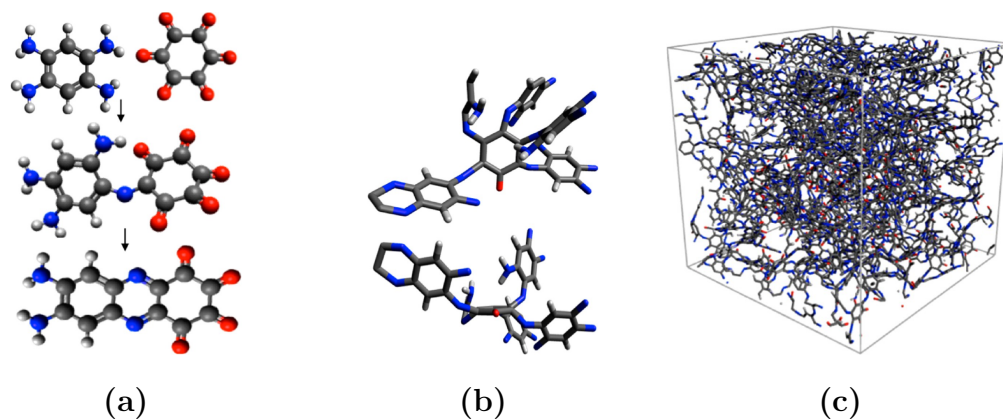


**Figure 1.15:** The monomers and resulting output of the AmBuild simulation for the generation of aza-CMP. (a) shows the reaction mechanism for the formation of aza-CMP, (b) shows an example of the defects present within the structure, showing multiple molecules of the 1,2,4,5-benzenetetramine monomer binding to the triquinoyl hydrate, inducing disorder into the structure, and (c) shows the generated aza-CMP structure within a 100 Å<sup>3</sup> cell. Figures extracted from reference<sup>181</sup>



## 1.5 Overview and Research

The development of porous materials has expanded greatly since their first discovery. Crystalline materials, such as MOFs and COFs, offer great surface areas along with potential functionalisation to give properties tailorable for many applications, with the likes of molecular separation and storage, catalysis, and energy storage. Amorphous materials are being more widely studied due to the ease of reaction process and reduced reaction conditions compared to thermodynamically stable crystalline materials. The likes of PIMs and HCPs have already offered exceptionally high surface areas. However, CMPs, CTFs, PAFs, and the newly introduced OSPC-1 opens up potential for amorphous porous polymers within the energy field.

This thesis will describe the synthesis process for newly developed amorphous porous polymers via computational and synthetic approaches. Pyrene-based CMPs have been studied through the *Yamamoto*-coupling synthetic procedure for their uses within photocatalysis, attempting to engineer the band-gap with the introduction of co-monomers such as 1,2-dibromobenzene and 1,3-dibromobenzene (Chapter 3). Finally, further studies based upon OSPC-1 for the development of anode materials for lithium ion batteries (Chapter 4) and alternate battery technologies (Chapter 5).

*"Chemistry, unlike other sciences, sprang originally from delusions and superstitions, and was at its commencement exactly on a par with magic and astrology."*

---

—Thomas Thomas

## Chapter 2

# Methodology

### 2.1 Synthesis of conjugated microporous polymers

The synthetic procedure applied to the synthesis of the conjugated microporous polymers was the *Yamamoto* coupling reaction.<sup>182</sup> Nickel(0)bis(cyclooctadiene)<sub>2</sub>, 2,2'-bipyridine, and cyclooctadiene were used in stoichiometric quantities for each reaction. 1,3,5,8-tetrabromopyrene was the denoting monomer for each reaction, combined with a 2:1 ratios in favour of the co-monomer where applicable.

*Method 1*, *2*, and *3* outline the synthetic procedures performed. *Method 1* is the synthetic procedure for synthesising CMPs and also PAF-1.<sup>124,139</sup> *Method 2* and *3* follow the steps of *Method 1* without running to completion.

#### 2.1.1 *Method 1*: General method of CMP synthesis

A 250 mL two-neck round bottom flask, a two-directional tap, and *Subaseal* were degassed and refilled with N<sub>2</sub> within a glove-box. The catalytic reagents of nickel(0)bis-(cyclo-octadiene)<sub>2</sub> (Ni(cod)<sub>2</sub>, 5.2 mmol, 1.43 g), cyclooctadiene (cod, 5.3 mmol, 0.67 mL), and 2,2'-bipyridine (bipy, 5.2 mmol, 0.811 g) were added to the round bottom flask, then the *Subaseal* and tap were connected accordingly to either neck of the flask. Additionally, a single-neck 100 mL round bottom flask and *Subaseal*

were used for the monomers.

Both flasks were taken from the glove box to the fumehood. They were both evacuated and refilled with N<sub>2</sub> or Ar gas. Dimethylformamide (DMF) (50 mL) was added to the catalytic reagent vessel, and the was solution heated to 80 °C for 1 hour. In the meantime, DMF (50 mL) was also added to the vessel containing the monomers, and left to stir for 1 hour to allow for dissolution of the reagents. The monomer solution was added to the catalytic solution, and heated at 80 °C for 24 hours. The reaction was allowed to cool to room temperature and conc. hydrochloric acid (HCl) (15 mL) was added drop-wise to the reaction vessel, and the mixture was left to stir for 1 hour. The solid product was collected by suction filtration and washed on the filter with chloroform (CHCl<sub>3</sub>) (3 x 100 mL), H<sub>2</sub>O (3 x 100 mL), and tetrahydrofuran (THF) (3 x 100 mL). Further purification was carried out via Soxhlet extraction with THF for 24 hours. The solid product was then dried *in vacuo* at 120 °C.

### 2.1.2 *Method 2: Interval extraction method*

A 250 mL two-neck round bottom flask, a two-directional tap, and *Subaseal* were degassed and refilled with N<sub>2</sub> or Ar gas within a glove-box. The catalytic reagents of Ni(cod)<sub>2</sub> (5.2 mmol, 1.43 g), cod (5.3 mmol, 0.67 mL), and bipy (5.2 mmol, 0.811 g) were added to the round bottom flask, with the *Subaseal* and tap connected. Additionally, a single-neck 100 mL round bottom flask and *Subaseal* were used for the monomers.

Both flasks were taken from the glove box to the fumehood. They were both evacuated and refilled with N<sub>2</sub> or Ar gas. DMF (50 mL) was added to the catalytic reagent vessel, and the solution was heated to 80 °C for 1 hour. Additionally, DMF (50 mL) was also added to the vessel containing the monomers and the solution was left to stir for 1 hour. The monomer solution was added to the catalytic solution, and the reaction heated at 80 °C. 10 mL extractions were taken over varying time periods. The first set of product extractions were collected with incrementing hourly

intervals (1 hour, 2 hours, 4 hours, 8 hours, 12 hours) with the remainder of the reaction solution left to complete the 24 hour synthesis duration. Once cooled to room temperature, conc. HCl (15 mL) was added to each extraction. These were left to stir for 1 hour before collecting the solid product via suction filtration. Each solid product was washed with  $\text{CHCl}_3$  (100 mL),  $\text{H}_2\text{O}$  (100 mL), and THF (100 mL), and dried *in vacuo* at 120 °C.

### 2.1.3 Method 3: Synthetic procedure for UV-vis analysis

A 250 mL two-neck round bottom flask, a two-directional tap, and *Subaseal* were degassed and refilled with  $\text{N}_2$  or Ar gas within a glove-box. The catalytic reagents of  $\text{Ni}(\text{cod})_2$  (5.2 mmol, 1.43 g), cod (5.3 mmol, 0.67 mL), and bipy (5.2 mmol, 0.811 g) were added to the round bottom flask, with the *Subaseal* and tap connected. Additionally, a single-neck 100 mL round bottom flask and *Subaseal* were used for the monomers.

Both flasks were taken from the glove box to the fumehood. They were both evacuated and refilled with  $\text{N}_2$  or Ar gas. DMF (50 mL) was added to the catalytic reagent vessel, and the solution was heated to 80 °C for 1 hour. Additionally, DMF (50 mL) was also added to the vessel containing the monomers and the solution was left to stir for 1 hour. Prior to mixing the reagents, a UV-vis probe was set to measure the UV-vis emission of the solution, then the monomer solution was added to the catalytic solution, and the reaction heated at 80 °C. UV-vis spectra were recorded at intervals of 5 minutes from the initial addition of the monomer (0 minutes) for a period of 24 hours. The reaction was allowed to cool to room temperature, and conc. HCl (15 mL) was added to the mixture. The solid products were collected via suction filtration, and the products washed with  $\text{CHCl}_3$  (3 x 100 mL),  $\text{H}_2\text{O}$  (3 x 100 mL), and THF (3 x 100 mL), and then dried *in vacuo* at 120 °C.

## 2.2 Gas sorption and diffusion

Various techniques were used for the characterisation of these porous polymers. Gas sorption analysis is a method to determine the gas uptake properties of a material. Using this technique, information on the bonding between the surface of a solid material (sorbent) and gas molecules (sorbate) can also be extracted. Gas sorption is heavily used for the characterisation of porous materials. When the sorbate adheres to the sorbent strongly, the sorbent and sorbate can chemically bond. This is referred to as chemisorption. Alternatively, the sorbent and sorbate can bond through weaker interactions, primarily through van der Waals forces. This is referred to as physisorption. Unlike chemisorption, physisorption is a reversible process, meaning gases can enter the porous structure and be removed readily.

### 2.2.1 Adsorption isotherms

The adsorption of gases into a porous material can be described through adsorption isotherms. Gas sorption isotherms describe the amount of gas adsorbed onto a surface as a function of pressure at a fixed temperature. They are typically obtained with nitrogen ( $N_2$ ) at 77 K, and pressures up to 1 bar. Desorption isotherms are calculated as the pressure of the system is reduced.

There are several classifications of isotherm to describe the manner of gas uptake (I - VI), as seen in Figure 2.1. *Type I* is the typical classification observed for microporous materials (pore size  $< 2$  nm). Gas adsorption is greatest at lower pressures, and becomes saturated at higher pressures (*saturation pressure*). *Type II* isotherms deviate from the Langmuir model; the shallow gradient corresponds to monolayer formation. These isotherms are typically observed for macroporous and non-porous systems. *Type III* isotherms show very low gas uptake at lower pressures, and increase in an exponential manner towards the saturation pressure.

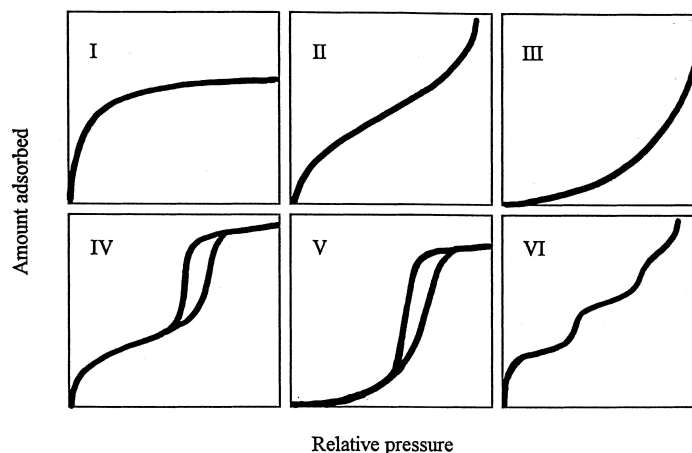


**Figure 2.1:** The IUPAC classifications of adsorption isotherms with respect to increasing pressure. Figure extracted from reference.<sup>183</sup>

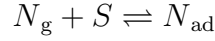
This is due to adsorbate multilayer formation; the first layer acts as a surface substrate for the next layer to adsorb to, with each layer using its predecessor in a continuous process. The ratio of covered surface against the total surface area is constant with each layer of adsorbate, resulting in a convergence of adsorbate uptake following the principles of a geometric series. *Type III* isotherms can be found with both non-porous and microporous systems.

Like *Type II* isotherms, *Type IV* isotherms show greater adsorption occurrence at lower pressures. This is then followed by the formation of a multilayer, and then an increase in uptake due to the condensation of gas within mesopores (capillary condensation). The hysteresis occurs from a deviation of desorption from the adsorption isotherm. *Type V* isotherms follow a similar trend to that of the *Type III* isotherm; monolayer-multilayering adsorption. Capillary condensation is also visible with the presence of the hysteresis. *Type IV* and *V* isotherms are familiar to mesoporous systems, and are very system specific. They both involve multilayer adsorption and capillary condensation. The *Type VI* isotherm occurs from a step-wise adsorption process. Individual monolayers are formed with the incrementing pressure. This type of isotherm is seen as a theoretical adsorption process in homogeneous and non-porous systems.

### 2.2.2 Langmuir adsorption model

One type of model used to describe the adsorption of molecules onto surfaces is the Langmuir model.<sup>184</sup> The Langmuir model assumes the sorbate behaves under ideal gas conditions, and the adsorption process occurs on a single layer.

At constant temperatures and pressures, the rate of adsorption ( $N_{ads}$ ) of the molecules ( $N_g$ ) to the solid surface ( $S$ ) and the rate of desorption are in equilibrium:



The rates of adsorption and desorption are assumed to behave like elementary processes. Hence, the rates are given as:

$$r_{ads} = k_{ads} \cdot P_N \cdot [S]$$

$$r_{des} = k_{des} \cdot [N_{ads}]$$

Rearrangement of these constant equations gives an overall constant as:

$$K = \frac{k_{ads}}{k_{des}}$$

To determine the amount of sorbate adsorbed onto the sorbent surface, a combination of the rate equilibrium equation and the concentration of total sites ( $[S_0]$ ) can give:

$$[S_0] = [S] + [N_{ads}]$$

$$[S_0] = \frac{[N_{ads}]}{K \cdot P_N} + [N_{ads}] = \frac{1 + K \cdot P_N}{K \cdot P_N} \cdot [N_{ads}]$$

From this, the ratio of adsorbed molecules ( $\theta_N$ ) can be defined:

$$\theta_N = \frac{[N_{\text{ads}}]}{[S_0]}$$

which is therefore given as:

$$\theta_N = \frac{K \cdot P_N}{1 + K \cdot P_N}$$

which is defined as the Langmuir theorem.

Experimentally, the Langmuir equation is defined by the fractional occupancy of adsorption sites ( $\theta_N$ ), where the volume of gas adsorbed ( $V$ ) is divided by the volume of the monolayer ( $V_m$ ):

$$\theta_N = \frac{V}{V_m}$$

The surface area of the sorbent can be calculated by plotting the linear form of the Langmuir equation ( $P/V_{\text{ads}}$ ), and multiplying the volume of the monolayer ( $V_m$ ) by the area of a molecule ( $A$ ):

$$P_N/V_{\text{ads}} = \frac{1}{K \cdot V_m} + \frac{P_N}{V_m}$$

$$SA_{\text{Lang}} = V_m \cdot A$$

### 2.2.3 Brunauer-Emmett-Teller sorption model

Another type of isotherm model used to calculate the surface area of porous materials is the Brunauer-Emmett-Teller (BET) sorption model.<sup>185</sup> This model is an



adaptation of the Langmuir model used to describe multilayer adsorption. The BET theory follows the assumptions that gas molecules physically adsorb onto solid layers infinitely, the gas molecules can only interact with adjacent layers, and that the Langmuir theorem can be applied to each of the layers within the system.

This is written as:

$$\frac{1}{v[(P_0/P) - 1]} = \frac{c - 1}{v_m \cdot c} \cdot \frac{P}{P_0} + \frac{1}{v_m \cdot c}$$

$$c = e^{\left(\frac{E_{\text{ads}} - E_{\text{liq}}}{RT}\right)}$$

$P_0$  is the equilibration pressure and  $P$  is the saturation pressure of the sorbates at the 77 K,  $v$  is the quantity of adsorbed gas in volumetric units, and  $v_m$  is the monolayer adsorbed gas quantity.  $c$  is the BET constant calculated using the enthalpy of adsorption onto the first layer ( $\Delta E_{\text{ads}}$ ) and the enthalpy of adsorption onto the following layers, which is equal to the enthalpy of liquefaction ( $\Delta E_{\text{liq}}$ ) ( $R$  and  $T$  being the ideal gas constant and temperature).

Plotting the BET equation ( $\frac{1}{v[(P_0/P) - 1]}$  against  $\frac{P}{P_0}$ ) produces a curve with largely linear trend, from which the gradient  $\frac{c-1}{v_m}$  and intercept  $\frac{1}{v_m \cdot c}$  can be derived via linear regression. From this the BET surface area can be calculated. The total surface area ( $SA_{\text{total}}$ ) and the specific surface area ( $SA_{\text{BET}}$ ) are given as:

$$S_{\text{total}} = \frac{v_m \cdot N \cdot s}{V}$$

$$S_{\text{BET}} = \frac{S_{\text{total}}}{M}$$

with  $N$  being Avogadro's constant,  $s$  being the adsorption cross section of the sorbate,  $V$  the molar volume of sorbate, and  $M$  the mass of sorbent being analysed.

Typically, the Langmuir adsorption model follows a *Type I* isotherm (*Type I* isotherms are sometimes referred to Langmuir isotherms), whereas BET adsorption model can follow the latter isotherms; a BET model is mostly recognised as a *Type II* isotherm.

## 2.3 Gas sorption and surface area analysis

Nitrogen gas sorption isotherms for the CMP networks produced were externally performed and collected by Dr. Darren Bradshaw of Southampton University, Dr. Robert Dawson of Sheffield University, and in tandem by the Dr. Ziqiang Zhao of Jilin University, China, and the author. Approximately 100 mg was used for the sorption analysis, and was weighed accurately before and after the degassing stages. All samples were degassed at 120 °C for a minimum of eight hours in vacuo. Polymer surface areas ( $SA_{\text{BET}}$ ) were measured through nitrogen adsorption at 77.3 K. The BET surface areas were calculated using 5 point isotherm measurements.

### 2.3.1 Gas diffusion

The diffusion of gases through porous solids is beneficial for a series of applications. The rate of diffusion is crucial in determining the selective properties of a system, i.e. molecular separation and catalysis. Fick's law is used to describe the relationship between the diffusion flux vector ( $\bar{J}$ ) and the negative concentration gradient ( $-\nabla \cdot n$ ):

$$\bar{J} = -D \cdot \nabla \cdot n = -D \frac{\partial c}{\partial x}$$

$D$  = the diffusion coefficient.

$c$  = the concentration.

$x$  = position or diffusion length.

$\nabla$  is used to denote the diffusion gradient when diffusion occurs in multiple dimensions.

Fick's law correlates to the transport diffusion of particles in a system,  $D_t(n)$ . Transport diffusivity<sup>186–188</sup> can be used to describe the diffusion of a particle in a macroscopic system:

$$D_t(c) = D_0(n) \left[ \frac{\partial \ln f}{\partial \ln c} \right]_r$$

where the partial derivative involves the concentration of adsorbate and the bulk phase fugacity,  $f$ .  $D_0(c)$  is the corrected diffusivity.  $D_t(c)$  is more readily described for isotropic systems, but can also be generalised for anisotropic systems. Figure 2.2 shows the transport diffusion of particles in a system from high concentration to low concentration.

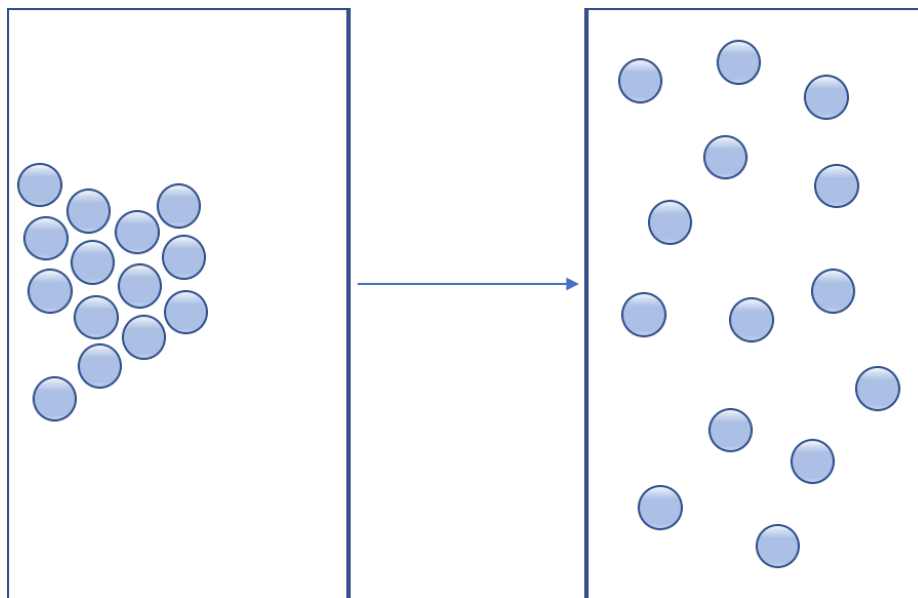


**Figure 2.2:** Scheme of transport diffusion of particles moving from high concentration to low concentration.

Self-diffusion describes the movement of particles (most commonly gas molecules) in a system during equilibration, as shown in Figure 2.3. The self-diffusion of particles,  $D_s(c)$ , in a three-dimensional system can be calculated by using the mean squared displacement (MSD) of molecular trajectories.

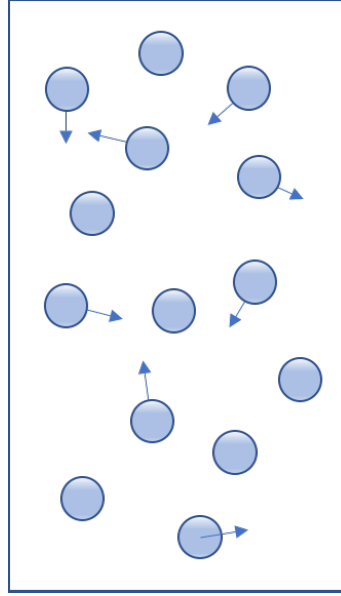


**Figure 2.3:** Scheme of self-diffusion of particles.

This is calculated through the Einstein expression with respect to the total particle concentration:

$$D_s(c) = \lim_{t \rightarrow \infty} \frac{1}{6t} \left\langle \left| \vec{r}(t) - \vec{r}(0) \right|^2 \right\rangle$$

This can equivalently be described in terms of the velocity autocorrelation function of the particle:<sup>189,190</sup>

$$D_s(c) = 1/3 \int_0^\infty \left\langle \vec{v}(0) \cdot \vec{v}(t) \right\rangle \partial t$$

where  $\vec{r}(t)$  and  $\vec{v}(t)$  are the position and velocity of the particle respectively at time  $t$ . Similar to transport diffusion, these expressions are described for an isotropic system, but can be readily generalised for an anisotropic system.<sup>186–188</sup>

Molecular dynamics (MD) simulations can be used to calculate the MSD and therefore the self-diffusion of particles. When  $t$  is small, the motion of particles is considered ballistic, with a logarithmic slope tending towards 2.

The equation can then be written as:

$$\left\langle \left| \vec{r}(t) - \vec{r}(0) \right|^2 \right\rangle \sim t^2$$

Single file diffusion occurs at an intermediary point in the MSD plot, where the slope of the logarithmic plot is 0.5. And normal diffusion is seen when the logarithmic plot tends towards 1. Here, the MSD should increase in a linear fashion with respect to time. Figure 2.4 shows the different diffusion modes.

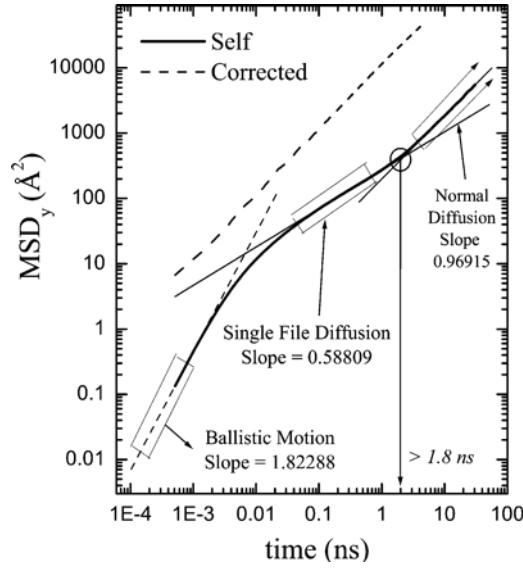


**Figure 2.4:** Example of MSD against time for  $\text{CF}_4$  in zeolite materials. The solid curve represents the self-diffusion data, and the upper dashed curve represents the corrected diffusion. This shows when the normal diffusion occurs during. The gradient of the slope can be used to calculate the diffusion coefficient. Extracted from reference.<sup>188</sup>

### 2.3.2 Active diffusion

This thesis observes what shall be defined as *active diffusion* to study the structural pathways within the system, and the capabilities of ions to diffuse through. *Active diffusion* applies a charge bias, in the form of charged graphene sheets, to the simulation cell. Each simulation contains a graphene sheet at either end of the Z-axis, enforcing an attraction and repulsion technique representing the movement of electrons in the battery. Figure 2.5 shows the setup of the simulation cell.

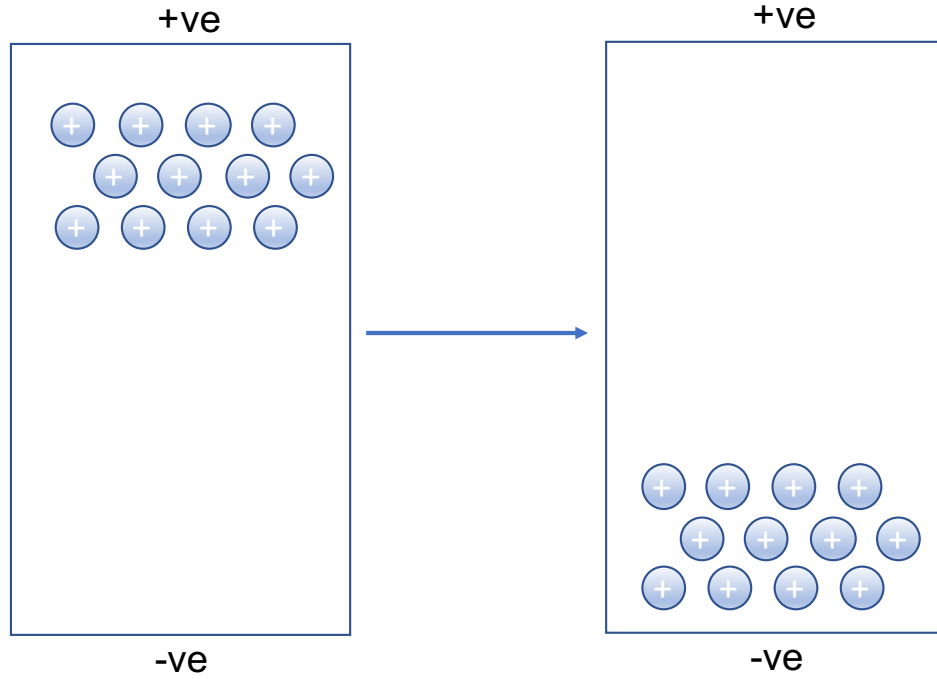


**Figure 2.5:** Representation of the *active diffusion* performed for the diffusion of ions in a system. The positive and negative charges are applied to enforce the attraction and repulsion of ions in the system. Each ion observed in this thesis possesses a positive charge, with the ions placed near the positively charged graphene sheet.

*Active diffusion* can be translated from *electrical mobility*. Charged ions migrate through a system with the application of an electric field, given by the positively and negatively charged boundaries of the simulation cell.

The mobility of these ions is calculated using the equation:

$$v_d = \mu \cdot E$$

where  $v_d$  is the drift velocity of the particle,  $\mu$  is the mobility of the particle, and  $E$  is the magnitude of the electric field. Together with Coulomb's law, the mobility of the particles migrating from the positively charged boundary to the negatively charged boundary can be calculated.

$$E = \frac{kQ}{r^2}$$

$$\mu = \frac{v_d}{E} = v_d \cdot \frac{kQ}{r^2}$$

where  $k$  is Coulomb's constant,  $Q$  is the magnitude of the source charge relative to the atomic charge of a particle of molecular structure, and  $r$  is the magnitude of distance between the two charged boundaries of the simulation cell.

To maintain correlation to the diffusion of ions, the mobility rates calculated in this thesis use the units  $\text{cm s}^{-1}$ , and we calculated from the distance of ion movement in the z-axis from their origin.

## 2.4 X-Ray diffraction

X-ray diffraction (XRD) is a useful technique for characterising structural properties of materials. Properties such as the unit cell parameters, space groups, and atomistic positions are revealed through XRD. Two XRD techniques can be used to characterise solid materials. Single crystal XRD is readily used for crystalline materials that have ordered repeating unit cells. Power XRD (PXRD) has used to characterise solids when crystal growth is weak, or the reaction product is a powder.<sup>191</sup>

### 2.4.1 Single crystal X-ray diffraction

When analysing single crystal samples diffraction of the X-rays occurs when the wavelength of the X-rays is similar to the value of the interatomic distance of the crystal. The diffraction of X-rays can be defined using Bragg's law.

The distance between atomic planes ( $d$ ) can be calculated through the difference in path length ( $\Delta_{\text{pathlength}}$ ) and the angle of reflectance and incidence ( $\theta$ ) (Figure 2.6). Therefore, to calculate the difference in path length we use:

$$\Delta_{\text{pathlength}} = AB + BC = 2d \cdot \sin\theta$$

This can further be transcribed into Bragg's law:

$$n \cdot \lambda = 2d \cdot \sin\theta$$

where  $n$  is an integer and  $\lambda$  represents the wavelength of the X-rays. The diffracted x-rays from the sample are detected in such a manner that gives rise to a diffraction

pattern. This pattern is then interpreted using Bragg's law to give the structural information of the solid crystal.

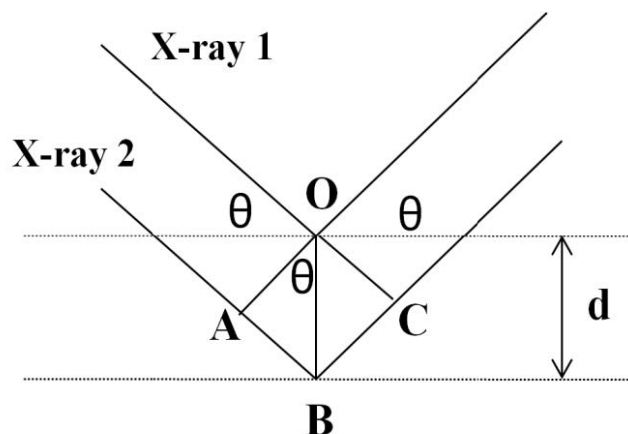


**Figure 2.6:** Bragg diffraction of two x-rays on a single crystal with two planes.  $\theta$  is the angle of reflectance and incidence, A, B, and C represent the points of reflectance and the x-ray pathways, and  $d$  is the distance between atomistic planes. Extract from reference.<sup>192</sup>

## 2.4.2 Powder X-ray diffraction

Powder XRD (PXRD) differs to single-crystal XRD as it analyses a powder of many individual crystals rather than a single crystal. X-rays diffract off of each of these crystallites, giving rise to a diffraction pattern at specific angles.

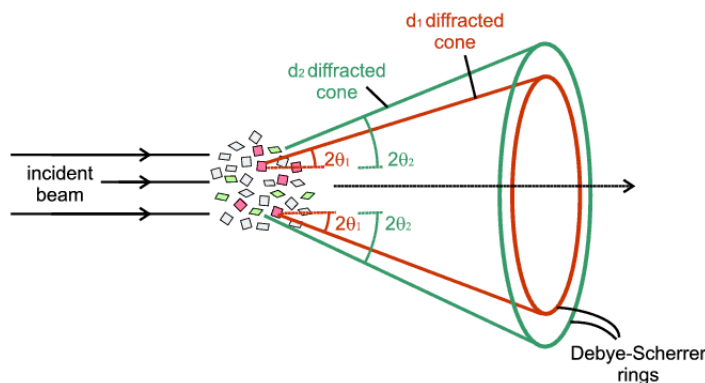


**Figure 2.7:** Powder X-ray diffraction.  $d_1$  and  $d_2$  are the diffraction reflectance pathways, or cones, from the powder sample, producing the Debye-Scherrer rings for the X-ray diffraction pattern. Figure replicated from reference.<sup>193</sup>



The produced pattern is a series of rings; Debye-Scherrer rings (Figure 2.7). These rings reflect the structural information of the material, such as unit cell dimensions and sample purity, and also the crystal structure using Rietveld refinement where growth of a larger single crystal is not possible.

PXRD analysis was performed on a Rigaku Smartlab multipurpose X-ray diffractometer. Solid powder samples were ground and loaded on to quartz plates.

### 2.4.3 Fourier transform infra-red spectroscopy (FTIR)

FTIR spectra display the adsorption of IR radiation at different frequencies by a material. It is used to identify the chemical bonding within the material through the vibrational frequencies observed of different functional groups. Infra-red spectra of the CMP samples were collected using an Agilent Cary 630 FTIR spectrometer to determine the presence of monomer in the product material, and also the presence of bromine within the materials.

### 2.4.4 Nuclear magnetic resonance (NMR)

NMR is used to characterise the molecular structure of organic compounds. It is suitable for defining the atomistic environments within molecules from their electromagnetic signals produced from the perturbation of the nuclei magnetic field. It is a process that can be performed in both solution and solid states. The insolubility of the porous media produced lead to the use of solution state NMR to evaluate the dryness and purity of each product. The samples were prepared by washing the polymers in deuterated dimethylsulfoxide and deuterated chloroform, then filtered into NMR tubes.  $^1\text{H}$  NMR spectra and  $^{13}\text{C}$  spectra were collected using a Bruker Avance 400 NMR.

### 2.4.5 UV-Vis spectroscopy

UV-Vis analysis is the absorption or reflectance of light between the visible and ultraviolet regions of the spectrum (10 nm to ~800 nm). It is used for the quantitative determination of analytes within a sample, such as transition metals and conjugated compounds. UV-Vis spectra for solid samples were taken using an Avantes standard reflectance probe within a dark box at room temperature. The spectra of each materials analysed was collected using Avantes AvaSpec-2048FT spectrometer and ThorLabs SLS201/M stabilized fiber-coupled light source.

## 2.5 Theoretical methodology

### 2.5.1 Molecular mechanics

Molecular mechanics applies classical mechanics (the motion of objects) for the prediction of energy for a molecule as a function of its conformation. Molecular mechanics models follow the rules that each simulated atom is an individual particle, each particle has a charge and radius, typically van der Waals radii, assigned to it, and each bonding atom have a spring-like motion, with equilibrium distance equal to the calculated bond length.

Molecular simulations typically apply the Born-Oppenheimer approximation, meaning electronic and nuclear motions are defined as individual entities, and therefore the total energy can be defined as a function of nuclear coordinates.<sup>194</sup> Consequently, if these coordinates were to change, the overall energy of the system would change. The total energy of a system can be expressed as a sum of all covalent and non-covalent potential energy terms: stretches, bends, torsion angle, van der Waals, electrostatic:

$$E = E_{covalent} + E_{non-covalent}$$

$$E = E_{str} + E_{bend} + E_{tor} + E_{vdw} + E_{el}$$

In molecular simulations, it is possible to determine energy expense of specific parameters. Each of these potential energy parameters (stretch, bend, etc.) is set to define a systems force field (FF), as well as the potential energy of a system. This potential energy can be described as a function of a molecules geometry via both molecular and quantum mechanics. This is defined as the *potential energy surface* (PES), profiling energy changes on a multidimensional surface.

### 2.5.2 Energy minimisation

Finding the most reduced energy of a system computationally has proven to be considerably problematic. Many problems have been a result of a minimisation of a multidimensional function.<sup>195</sup> Optimising and minimising the energy of a molecular within computational strategies is necessary to produce models of materials as they are found naturally. Using a set of atoms and vectors,  $r$ , to describe the atom positions, the energy minima can be calculated as a derivative of energy with respect to each  $r$  variable. At an energy minimum, the first derivative of the function  $E$  is equal to zero, and the second derivative has all positive eigenvalues:

$$\begin{aligned}\frac{\partial E}{\partial r} &= 0 \\ \frac{\partial^2 E}{\partial r^2} &> 0\end{aligned}$$

### 2.5.3 Molecular dynamics

Molecular dynamics (MD) is the study of time-dependent behaviour of molecular systems. MD simulations are used to understand the kinetic and diffusive properties of

systems, and also structural movement and conformational changes observed. Atom trajectory and velocity is determined through Newton's laws, which is expressed as:

$$F_i = m_i a_i$$

$F$  = force of particle  $i$ .

$m$  = mass of particle  $i$ .

$a$  = acceleration of particle  $i$ .

The forces of all present particles are required to run a MD simulation, which are calculated using the first derivative of the energy. Calculating the trajectory of a particle with the system is performed using the derivative equation:

$$\frac{\partial^2 x_i}{\partial t^2} = \frac{F \cdot x_i}{m_i}$$

A finite differences method is normally applied for the integration of Newton's laws. The integration is broken down into smaller stages, all separated by a fixed time interval,  $\partial t$ . The total force is initially calculated and assumed to be constant. The force at time  $t$  is calculated as a sum of interactions between additional particles in the system. Positions and velocities at time  $t$  can be calculated from the acceleration of a particle,  $a$ , and using the particles current position,  $r$ , combined with its velocity,  $v$ , acceleration can be used to determine new positions and velocities at  $t + \delta t$ . With a constant force it is possible to describe accurately how a system evolves over time; accuracy is dependent on the size of the time-step:

$$r(t + \delta t) = r(t) + \delta t \cdot v(t) + 1/2 \cdot \delta t^2 \cdot a(t) + 1/6 \cdot \delta t^3 \cdot b(t) + \dots$$

$$v(t + \delta t) = v(t) + \delta t \cdot a(t) + 1/2 \cdot \delta t^2 \cdot b(t) + 1/6 \cdot \delta t^3 \cdot c(t) + \dots$$

$$a(t + \delta t) = a(t) + \delta t \cdot b(t) + 1/2 \cdot \delta t^2 \cdot c(t) + \dots$$

The *Verlet* algorithm<sup>196</sup> can be used to integrate the equations of motion. This uses the particle position and acceleration at time  $t$  and the previous step,  $r(t-\delta t)$ , to calculate the new position  $r(t+\delta t)$ , and can be written as:

$$r(t + \delta t) = r(t) + \delta t \cdot v(t) + \frac{1}{2} \cdot \delta t^2 \cdot a(t) + \dots$$

$$r(t - \delta t) = r(t) - \delta t \cdot v(t) + \frac{1}{2} \cdot \delta t^2 \cdot a(t) + \dots$$

with a combination of the two written as:

$$r(t + \delta t) = 2r(t) - r(t - \delta t) + \delta t^2 \cdot a(t)$$

The velocities of the particle(s) are not established within these equations, but can be readily calculated from the difference in position at times  $t + \delta t$  and  $t - \delta t$ :

$$v(t) = \frac{r(t + \delta t) - r(t - \delta t)}{2\delta t}$$

Alternatively, the velocities can be calculated from the half-step of the simulation:

$$v(t + \frac{1}{2}\delta t) = \frac{r(t + \delta t) - r(t)}{\delta t}$$

A major disadvantage of the Verlet algorithm is that the velocities are not explicitly calculated, meaning it lacks precision, and also it is not self-starting, meaning the velocities can not be determined when  $t = 0$ . Variations of the *Verlet* algorithm aim to establish the velocities more accurately from the beginning of the simulation. The *Leapfrog*<sup>197</sup> and the *velocity Verlet*<sup>198</sup> algorithms can be applied to increase the accuracy of the calculated velocities.

The *Leapfrog* algorithm calculates the velocity at each half-step:

$$v(t + 1/2 \cdot \partial t) = v(t - 1/2 \cdot \partial t) + \partial t \cdot a(t)$$

The positions at  $r(t + \delta t)$  can be calculated from the velocities at  $v(t + 1/2 \cdot \delta t)$  and position  $r(t)$ :

$$r(t + \partial t) = r(t) + \partial t \cdot v(t + 1/2 \cdot \partial t)$$

These can then be used to calculate the velocity at time  $t$ :

$$v(t) = 1/2 \cdot [v(t + 1/2 \cdot \partial t) + v(t - 1/2 \cdot \partial t)]$$

The aptly named algorithm stems from the velocities 'leaping' over the positions to give newly calculated values;  $t + 1/2 \cdot \partial t$ . The positions are then calculated in a similar manner, thus offering a highly precise calculation of position and velocity.

The *velocity Verlet* algorithm is comparably more computationally expensive to the *Leapfrog* algorithm. It calculates the position, velocity, and acceleration of a particle simultaneously.

MD simulations are performed using a variety of ensembles with a combination of constant pressure (P), volume (V), total energy (E), and number of particles (N). MD simulations using the macrocanonical ensemble (NVE) are isolated from changes in number of particles (N), volume (V), and total energy (E), and is derived from Newton's equation. The canonical ensemble (NVT) involves constant number of particles, volume, and temperature, with the energy calculated through use of a thermostat. And the isothermal-isobaric ensemble (NPT) consists of constant number of particles, pressure, and temperature. Methods for controlling the temperature of a system include thermostat techniques such as the *Nosé-Hoover* thermostat or the *Berendsen* thermostat.<sup>199,200</sup>

### 2.5.4 Surface area calculations

Surface areas are a key property that define a porous material. Experimental surface areas are determined through nitrogen isotherms using the BET model. The surface area of molecular models can be determined through computational techniques. The solvent surface area (SSA) determines the surface area of the porous model by rolling a solvent molecule (probe) along the surface of the generated structure. The surface area is calculated from the centre of the solvent molecule. The Connolly surface area (CSA) is determined by using the solvent probe to roll across the surface or the material. The surface area is calculated by measuring the contact surface between the probe molecule and the porous polymer surface.<sup>201,202</sup> A probe radius of 1.82 Å was used to determine the SSA and CSA of the materials discussed in this thesis. 1.82 Å represents the approximate kinetic radius of a nitrogen molecule, in correlation to experimental nitrogen isotherms. Figure 2.8 illustrates the method of calculating the surface area.

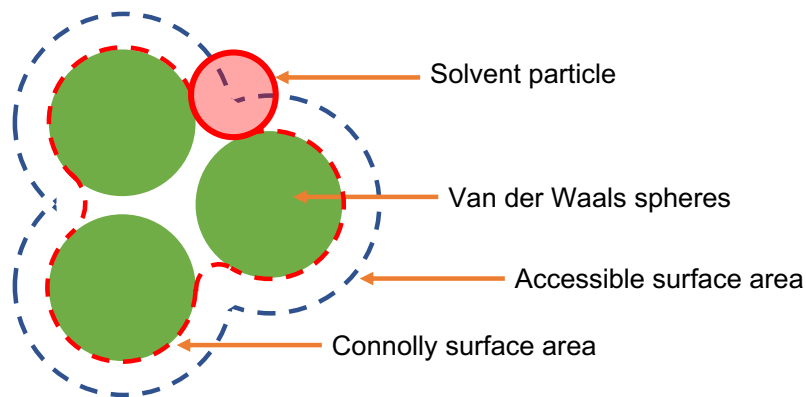


**Figure 2.8:** Illustration of surface area calculations. The green circles represent the van der Waals spheres of the material, the red circle depicts the solvent probe, the blue dotted outline illustrates the solvent accessible surface area for the particle to "roll" around, and the red dotted outline represents the Connolly surface area.

The solvent accessible surface area (SASA) is the surface area calculated from the accessible areas of the material. Compared to the SSA, the SASA measures the surface from the boundaries of the unit cell, representative of the gas molecules entering the system.

### 2.5.5 AmBuild

AmBuild is a Python based program used for the generation of structure development. The program utilises GPU hardware for increased speed and size of the simulations, and integrates HOOMD-Blue and DL\_POLY MD simulation codes for the structure building process.<sup>203–206</sup> The building blocks input into the AmBuild simulation are allocated an endgroup and a cap atom. The endgroup is the binding atom, and the cap atom is the designated leaving group for the building block. These are given in a separate file, declaring all possible bonding formations and leaving groups. Figure 2.9 illustrates the endgroup, cap atom, and resulting bonding formation of a building block.

The parameters of the building block are declared in separate files for the bonds, angles, dihedrals, and van der Waals (pairs) parameters. The bond and angle potentials are described as simple harmonic potentials, the dihedral parameters are cosine harmonic, and the Lennard-Jones potentials are declared for the van der Waals parameters. The PCFF force field is largely used to characterise the atoms in building block. The building blocks are held rigid, so only the bonds, angles, and dihedrals between a joined building blocks are described.

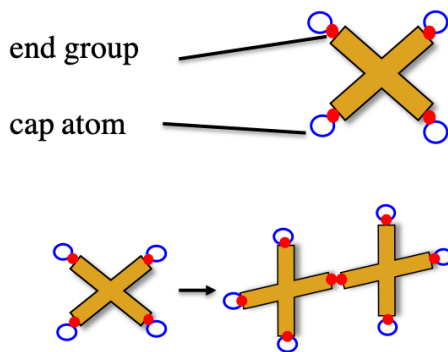


**Figure 2.9:** Illustration of the building block with the highlighted endgroup, cap atom, and bonding formation to a second building block.



AmBuild requires the size of simulation cell, building block coordinates, endgroups, and cap atoms, followed by the forcefield parameters to be declared. This describes the initial setup of the system. All functions are declared after the initial setup has been performed, with the seeding of building blocks or solvent, geometry optimisation, and molecular dynamics. Geometry optimisation and MD cycles are pulled from the HOOMD-Blue GPU-based code, which is easily integrated into the AmBuild system. Shown below is a representative setup for the AmBuild simulation with a methane building block to demonstrate the capabilities of the program (the carbon atom is declared as the endgroup, and the hydrogen atoms are the cap atoms):

```
#!/usr/bin/env python
import sys
sys.path.append("/opt/ambuild/builder")
# Python imports
import cPickle
import csv
import buildingBlocks # Imports building blocks from file
import cell
import util
boxDim = [30,30,30] # Simulation cell size
mycell = cell.Cell(boxDim,atomMargin=0.1,bondMargin=0.5,bondAngleMargin=5,doLog=True,paramsDir="/parameters/directory")
mycell.libraryAddFragment(filename='/blocks/directory/methane.car',fragmentType='Me')
mycell.addBondType('Me:a-Me:a') # Assigns possible bonding formations
mycell.seed(100,fragmentType='Me') # Seeds 100 methane building blocks into simulations cell
mycell.runMD(doDihedral=True,rCut=1,mdCycles=10000000,T=55.0)
mycell.optimiseGeometry(quiet=True) # Runs geometry optimisation without output
for i in range(100):
mycell.zipBlocks(bondMargin=5.0,bondAngleMargin=30,clashCheck=False)
# Runs the ZIP function with desired parameters. clashCheck runs a test of interacting particles in the simulation cell
mycell.dump() # Outputs .pkl file for visualisation
```

The functions included in the AmBuild code allow for the immediate growth of polymers using the *grow blocks* function, and the replication of reactions using the *join blocks* function and *Zip* functions. The latter two are based on the specific parameters declared for the respective atoms within the building blocks (endgroup, cap atom, and bond formation parameters). Figure 2.10 illustrates an example of the distance and angle declared for a bond to be produced.

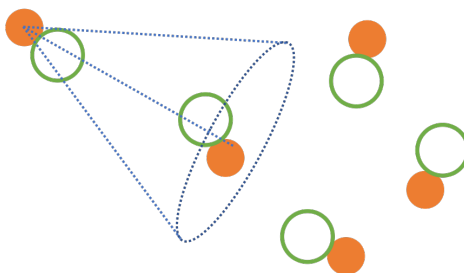


**Figure 2.10:** Illustration of the distance and angle parameters set for two particles to form bonds. The orange circles represent the endgroups of the building blocks and the green circles represent the cap atoms. The blue dotted cone represents the designated parameters for the bonding formation between the building blocks.

The system performs an NVT simulation with defined simulation cell parameters. However, this can result in structures with unrealistic bond lengths. Figure 2.11 shows the formation of the poly-methane structure via the *join blocks* and *Zip* functions. The resulting structure shows stretched bonds after the MD is performed.

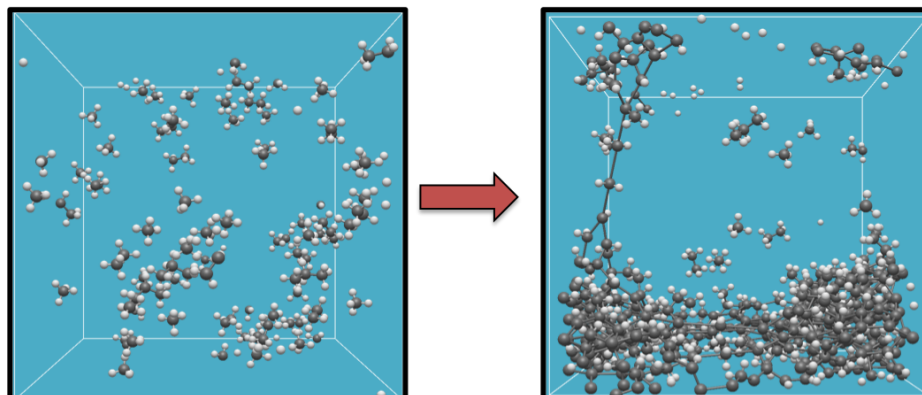


**Figure 2.11:** Example of the formation of a poly-methane structure in AmBuild with stretched bonds after molecular dynamics.

One rectification of this error in structural properties is performing an NPT MD to manoeuvre the methane building blocks into suitable positions, increase the number of building blocks into the system, or alternatively reduce the *Zip* and bonding parameters to smaller distances. Altering these parameters to produce a more suitable and ideal structure gives rise to the polymeric system show in Figure 2.12.

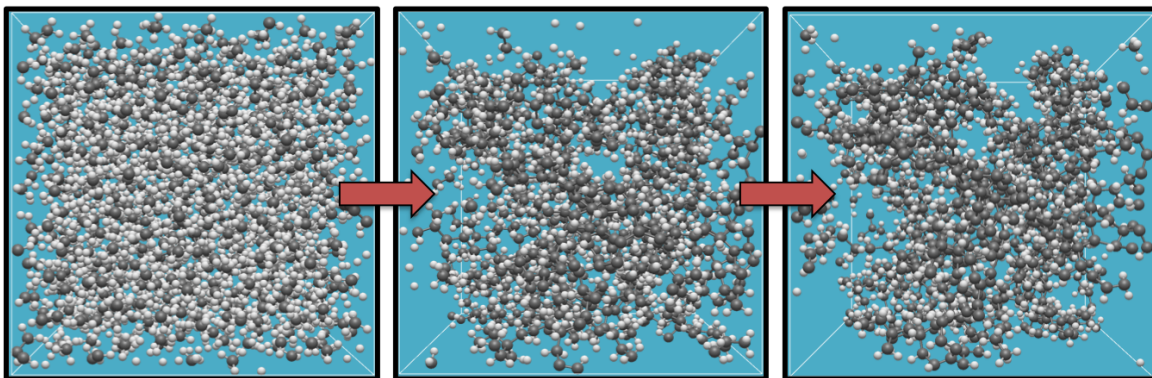


**Figure 2.12:** Formation of a poly-methane structure. System setup involved 1000 methane building blocks with a *Zip* distance of 2 Å, resulting in the overall polymeric structure.

The progress of the simulation and the formation of the polymer can be assessed by the number of *Zip* steps required with each iteration of the functions, and also the number of bonding building blocks. Figure 2.13 shows the number of *Zip* steps performed with each iteration of the functions as well as the percentage of bonds formed with each iteration.

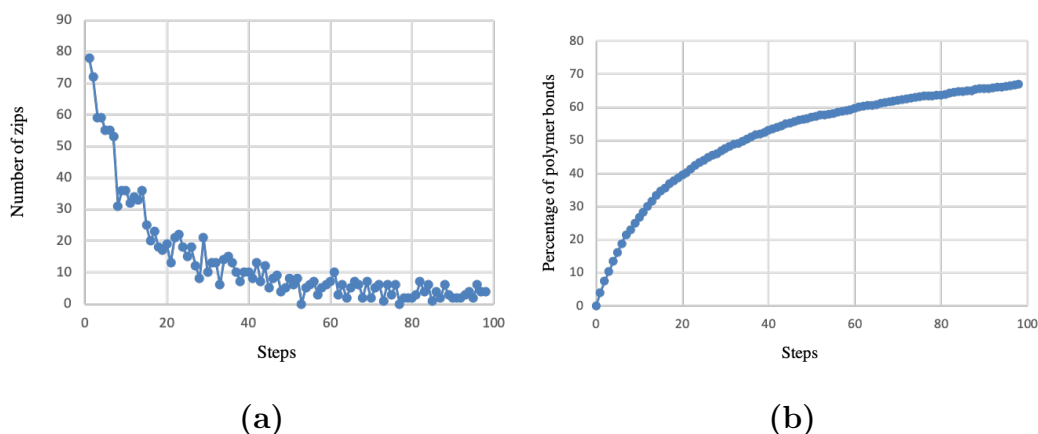


**Figure 2.13:** Plots of (a) the number of *Zip* steps performed and (b) the number of bonding building blocks with each iteration of the functions performed in the AmBuild script. Fewer *Zip* steps are required with the increasing number of bound building blocks in the polymer.

Alternatively, for fast production and simplified MD and optimisation of the structure, the *grow blocks* function can be included. This function is in replacement of the *join blocks* function and directly bonds new building blocks onto the structure at

available binding sites. An example of the *grow blocks* function and the computational process (Figure 2.14) is shown below. This process results in the generation of the cluster shown in Figure 2.15.

```
mycell.see(1,fragmentType='Me')
mycell.runMD(doDihedral=True,rCut=10,mdCycles=1000000,T=55.0)
mycell.optimiseGeometry(quiet=True)
for i in range(100):
    mycell.growBlocks(4,cellEndGroup='Me:a',libraryEndGroup='Me:a')
    mycell.zipBlocks(bondMargin=5.0,bondAngleMargin=30,clashCheck=False)
    mycell.optimiseGeometry(quiet=True)
    mycell.dump()
mycell.runMD(doDihedral=True,rCut=10,mdCycles=1000000,T=55.0)
```

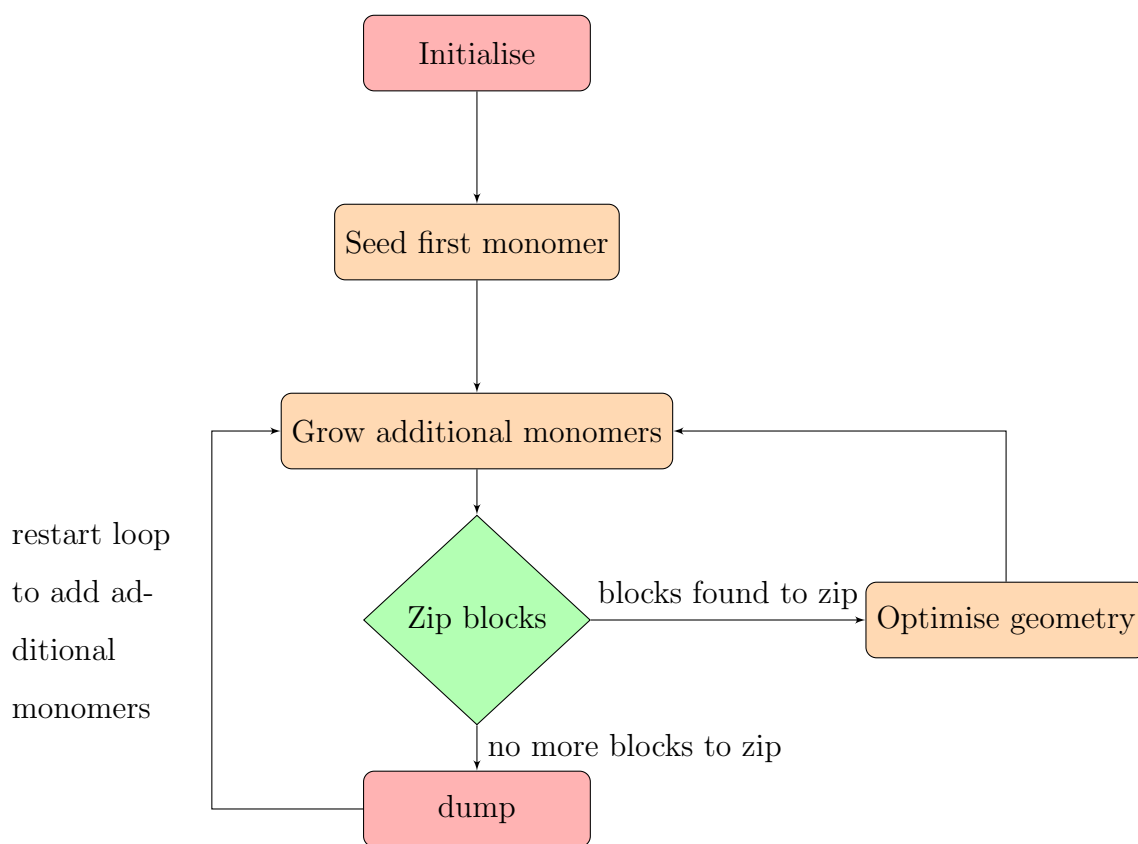


**Figure 2.14:** Flow diagram of the AmBuild structural development process

The simulations performed in this thesis all applied the *grow blocks* function for the fast generation of structures. The CMP clusters were generated in single step increments from a single building block. MD, geometry optimisation, and the *Zip*

function were all applied to produce a realistic representation of the bonding arrangement between the building blocks.

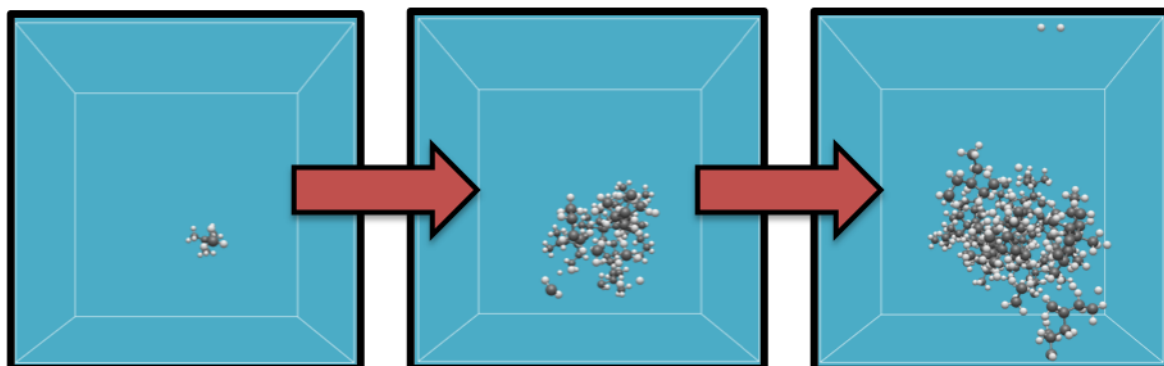


**Figure 2.15:** The formation of a poly-methane structure via the *grow blocks* function. A single methane building block is seeded into the system upon initialisation, and additional building blocks bonded to the available binding sites on the building block to produce the polymer cluster.

The structures generated for the OSPC study applied the *grow blocks* function in greater succession. A single building block was seeded into the simulation cell, followed by the attempt to bind multiple building blocks in a single iteration. The number of building blocks to attempt at growing increased with the number of building blocks in the system. This resulted in fast generation of the OSPC structures.

### 2.5.6 DL\_POLY

DL\_POLY is a molecular dynamics simulation package developed at Daresbury Laboratory.<sup>204,205</sup> The package is designed to facilitate molecular dynamics simulations of varying systems. DL\_POLY Classic was used to performed the ion diffusion simulations of the OSPC systems. The input files were generated using an inbuilt module in AmBuild for the conversion of .pkl files to the CONFIG and FIELD files required for the MD simulations. DL\_POLY does not provide any particular set of forcefield parameters, however the forcefield parameters used in the AmBuild simulation are applied in the DL\_POLY input files upon file conversion. Visual Molecular Dynamics (VMD) was used to display and analyse the trajectories of each simulation.

### 2.5.7 Materials Studio

Materials Studio is a modelling software designed to predict and understand the relationship between a materials structure and its properties and behaviour. In this research Materials Studio is used to generate the building blocks input into AmBuild along with the assignment of forcefield parameters. The Forcite module is used to optimise the structures, and the Discover module was applied to assign the forcefield typing. Materials Studio is also used to calculate solvent accessible surface areas (SASA) and Connolly surface areas (CSA) of the porous polymers.

## Chapter 3

# Pyrene-based conjugated microporous polymers

### 3.1 Introduction

The research within this chapter attempts to expand upon "band gap engineering" of CMPs, first established by Cooper *et al.* using pyrene as the base monomer for CMP development.<sup>124</sup> The pyrene-based CMPs (Figure 3.1) reported exhibited both microporosity and luminescent properties. Porous materials exhibiting luminescent properties have been studied for applications such as organic electronics and optoelectronics. Pyrene-based CMPs in particular have an affinity towards organic electronics and optoelectronics, as well as photocatalysis and also battery technologies.<sup>207</sup>

The polymers named YPy, YDBPy, and YDPPy involve the homocoupling of tetrabromopyrene, the coupling of 1,4-dibromobenzene with tetrabromopyrene, and also 4,4'-dibromobiphenyl with pyrene respectively. The initial observations by Cooper *et al.* showed that the inclusion of co-monomers allowed for the tailoring of the energy band gap with excitation. Figure 3.2 shows the optical differences between the different materials produced, and Table 3.1 shows the differences in band gap between the three materials.

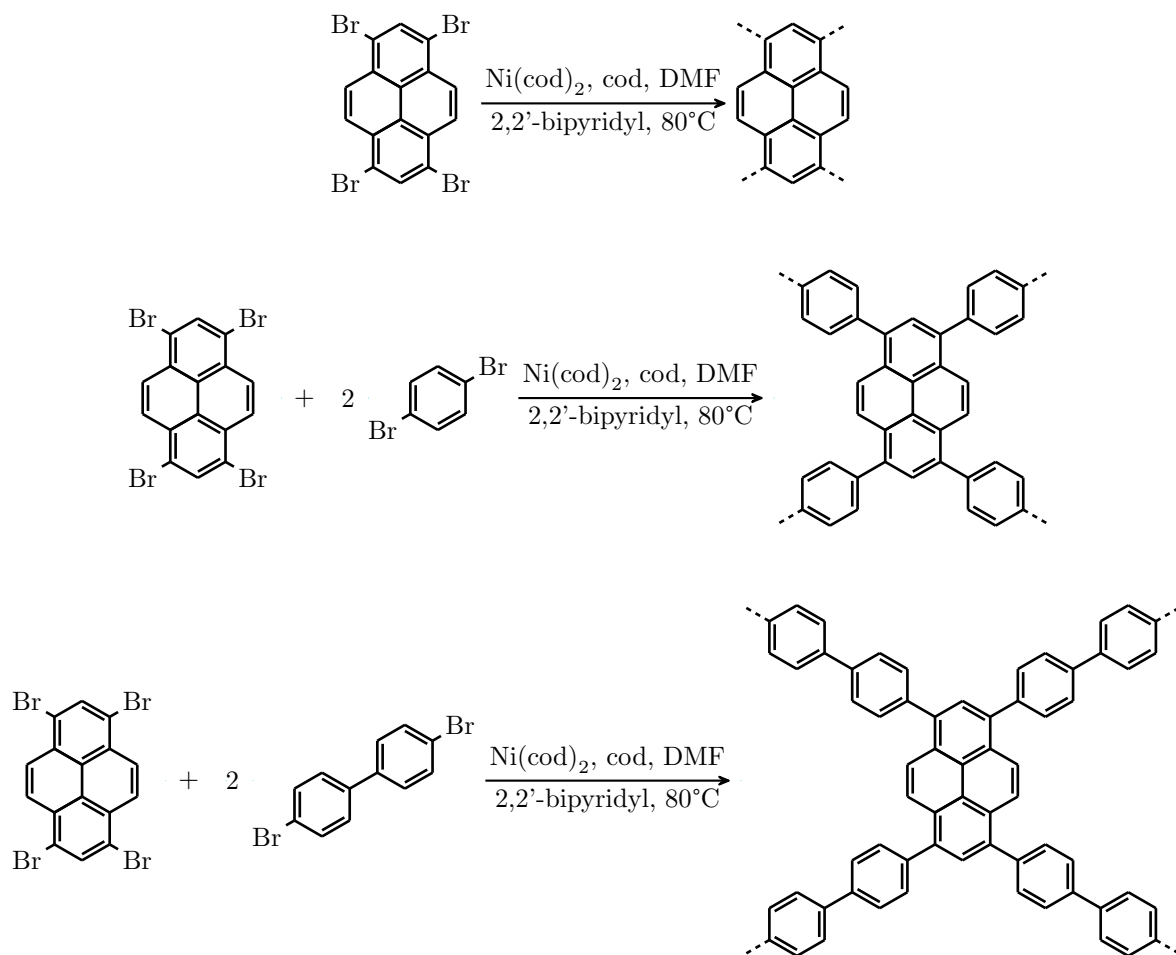


**Figure 3.1:** Hypothetical representation of the synthetic route of pyrene-based CMP synthesis; top to bottom: YPy, YDBPy, and YDPPy

The resulting polymers showed that YPy gives the lowest band gap energy at 1.84 eV, whereas YDBPy, with the inclusion of 1,4-dibromobenzene, gives the highest at 2.05 eV. The difference in band gap between the three structures gives rise to the possible theory that the conjugated system of the porous polymers is affected by the chemical interactions between the monomers. The significance in  $\pi$ -orbital overlap is key to tailoring the band gap of the materials.<sup>208</sup>



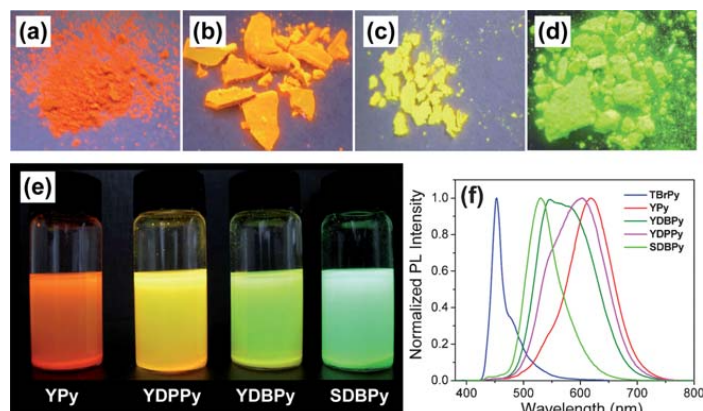


**Figure 3.2:** The optical analysis of the solid materials (a) YPy, (b) YDBPy, (c) YDPPy, and (d) SDBPy under UV irradiation ( $\lambda_{\text{excit}} = 365$  nm). (e) shows the optical analysis of the materials in a suspension of the polymers in THF, and (f) shows the photoluminescence spectra of the materials, as well as the monomer TBrPy ( $\lambda_{\text{excit}} = 360$  nm). Figure taken from reference.<sup>124</sup>

CMP	SA <sub>BET</sub> (m <sup>2</sup> g <sup>-1</sup> )	Band Gap (eV)
YPy	1508	1.84
YDPPy	303	1.90
YDBPy	1069	2.05

**Table 3.1:** Brunauer-Emmett-Teller surface area of the synthesised CMP networks and band gap energy calculated from the UV-Visible spectra.<sup>105</sup>

## 3.2 Molecular Ring Theory

Following up from the research performed by Cooper *et al.*, it was suggested that a potential factor that plays a role in the luminescence, and thus the difference in band gap, is the presence of smaller molecular structures within the CMP networks that possess localised electron density. This localised energy resides over macrocyclic structural entities, named here as *molecular rings*. Figure 3.3 shows a representation of these smaller structures containing pyrene building blocks.

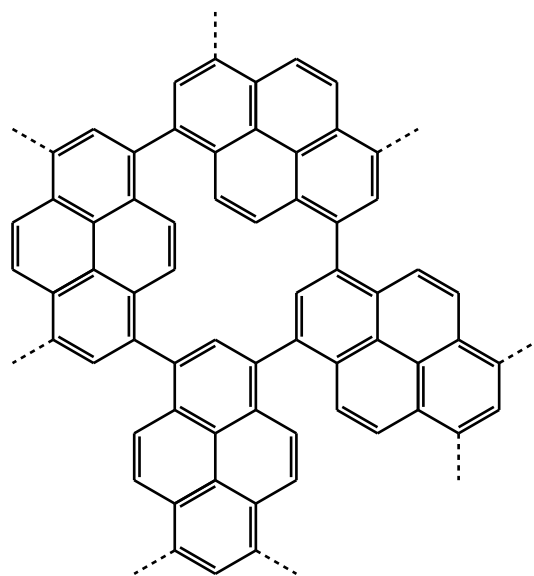


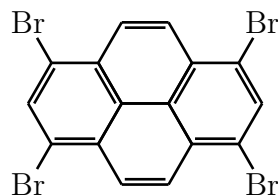
**Figure 3.3:** An example of the molecular ring formation in YPy with four pyrene building blocks.

Zwijnenburg *et al.*<sup>177</sup> determined that the strain induced on these ring structures is a microscopic link to the spectroscopic shift. The fewer pyrene building blocks in present in the rings causes a greater  $\pi$ -overlap due to the structure being flatter. It is postulated that the presence of these molecular rings, together with extended conjugation, contribute to how these CMP materials luminesce. The quantity of smaller structures within the overall CMP, as well as the size of the molecular rings formed, gives potential strategies on how the band gap can be tailored for applications.

From the initial data published on these polymers, along with the hypothesis of molecular rings influencing their electronic properties, computational studies on the structural development of the three materials (YPy, YDBPy, and YDPPy) were performed. AmBuild<sup>180,181</sup> was used to generate three-dimensional clusters of each CMP in order to understand the structural differences and formation of the macrocycles. A statistical analysis of the structural forms was used to understand the extent at which the macrocycles appear throughout the extended structures.

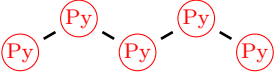
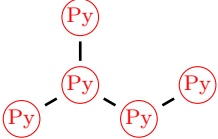
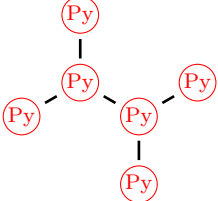
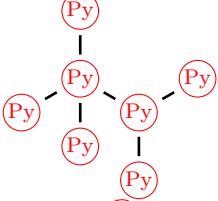
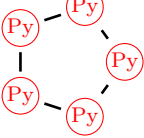
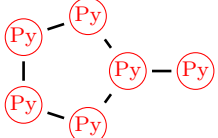
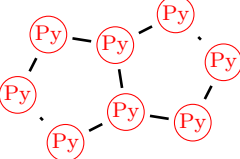
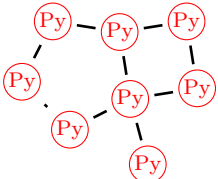
### 3.2.1 Molecular ring formation in YPy

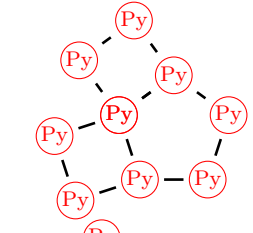
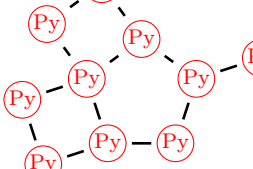
The generation and resulting polymer fragment structure of YPy was first examined. To gain an understanding of the general structure formation process, clusters were generated with and without the presence of solvent to determine the best method for computational analysis. Figure 3.4 shows the pyrene building blocks. YPy is formed via a *Yamamoto* coupling reaction, and so the building blocks are linked via the bromine end groups. AmBuild was used to generate clusters of YPy with incrementing pyrene building blocks. The bromine groups are defined as the *cap-atom*, with the bonded carbons as the *end-groups*, giving the pyrene monomer four potential binding sites. Each size of cluster was repeated 100 fold and the structures generated were classified by their type and configuration. These structures were defined as: *linear*, *branched*, *double-branched*, *multi-branched*, *single ring (pure and branched)*, *double ring (pure and branched)*, and *triple ring (pure and branched)*, as shown in Table 3.2.



**Figure 3.4:** 1,3,5,8-Tetrabromopyrene monomer

Statistical data was collected from the AmBuild MD simulations from three pyrene units up to ten. This gives rise to different bonding arrangements within the assay due to the multiple possible CMP configurations.

Structure name	Structure code	Structure
LC	LC	
Branched chain	LC1B	
Double branched chain	LC2B	
Multi-branched chain	LCXB	
Pure single ring	RS1P	
Branched single ring	RS1B	
Pure double ring	RS2P	
Branched double ring	RS2D	

Structure name	Structure code	Structure
Pure triple ring	RS3P	
Branched triple ring	RS3B	

**Table 3.2:** Classification of the structure types determined from the AmBuild simulations. The red **Py** atoms represent the individual pyrene molecules covalently binding to produce the clusters.

The different types of structure, and the statistical values determined, determined for YPy without the presence of solvent are shown in Table 3.3.

	Pyrene monomers							
	3	4	5	6	7	8	9	10
LC	100	66	34	10	5	1	-	-
LC1B	-	28	49	52	39	26	12	4
LC2B	-	-	1	7	15	23	26	19
LCXB	-	-	-	-	-	2	7	13
RS1P	-	6	1	-	-	-	-	-
RS1B	-	-	15	29	37	39	40	44
RS2P	-	-	-	1	-	-	-	-
RS2B	-	-	-	1	3	7	13	17
RS3P	-	-	-	-	-	-	-	-
RS3B	-	-	-	-	1	2	2	3
Straight chain	100	94	84	69	59	52	45	36
Ring structure	-	6	16	31	41	48	55	64

**Table 3.3:** Statistical analysis of ring structures produced within YPy clusters; pyrene monomers increasing from three units to ten units.

The number of molecular rings greatly increases with the addition of building blocks, and in turn the number of linear chain structures observed reduced greatly. A single ring was observed with as few as five pyrene building blocks, and with a total of ten pyrene building blocks, we see over 50 % of the structures containing a minimum of one molecular ring.

Visualisation of these statistics, and the increase of molecular ring structures is presented in Figure 3.5. As there are no other entities within the simulations cell for the clusters to interact with, the clusters were able fold into a more favourable, closely packed conformations. The close interaction with the available binding sites of the clusters led to the formation of the molecular rings at an earlier stage. These structures followed the same, or similar, conformation to that illustrated in Figure 3.3.

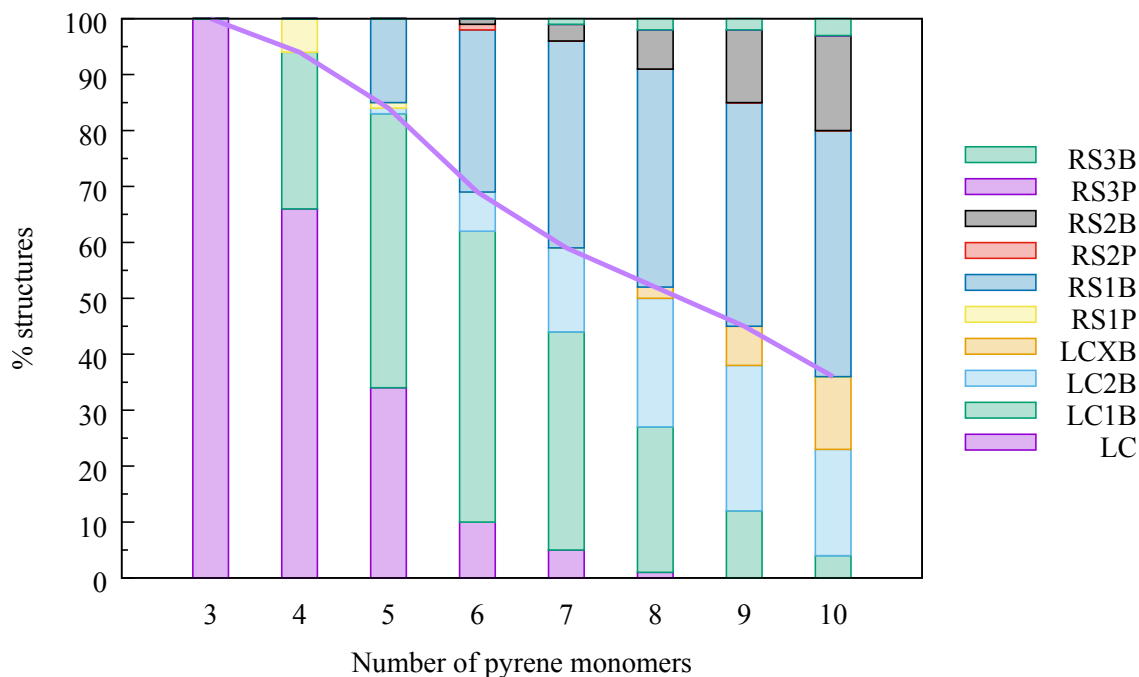


**Figure 3.5:** Histogram of the individual structures presented with each additional monomer for YPy without solvent; from three pyrene monomers to ten pyrene monomers. The purple line represents the total number of chain structures with each increment of pyrene building blocks, and the separation of chain structures (below) and ring structures (above).

There was a great increase of molecular rings up to the tenth pyrene building block. These ring structure consist of one to three rings in a single cluster.

Exclusion of the solvent from the simulations allowed for fast simulation times as there were fewer atoms, and it also meant that the pyrene building blocks were able to move freely about the simulation cell, allowing them to produce the ring structures from an early stage. However, the simulations were not representative of the experimental conditions, therefore MD simulations were performed with the solvent included. In the case of these *Yamamoto* coupling reactions, dimethylformamide (DMF) is used as the solvent. Having the solvent introduced into the system interferes with the movement of the clusters generated. This greatly affects the formation of the ring structures (Table 3.4). The structural generation and difference in ring structures to chain structures is also presented in Figure 3.6.

	Pyrene monomers							
	3	4	5	6	7	8	9	10
LC	100	74	40	13	6	3	-	-
LC1B	-	26	46	53	38	22	14	4
LC2B	-	-	3	19	26	28	22	16
LCXB	-	-	-	-	4	7	7	12
RS1P	-	-	5	-	-	-	-	-
RS1B	-	-	6	15	25	32	43	41
RS2P	-	-	-	-	-	-	-	-
RS2B	-	-	-	-	1	8	14	27
RS3P	-	-	-	-	-	-	-	-
RS3B	-	-	-	-	-	-	-	-
Straight chain	100	94	84	69	59	52	45	36
Ring structure	-	6	16	31	41	48	55	64

**Table 3.4:** Statistical analysis of ring structures produced within YPy clusters; pyrene monomers increasing from three units to ten units.

The molecular rings were not seen until a cluster of five pyrene units was formed. Additionally, the extent to which the rings developed is lessened by the solvent presence. The maximum number of rings observed within a single structure is two, whereas, without the solvent present, up to three rings develop within a cluster. This indicated that the solvent affected the movement of the atoms within the clusters, and therefore the formation of the molecular rings. Both simulations performed show similar results with respect to the number of molecular rings produced at the final stage. This infers that even with the solvent present these structural configurations are able to form. However, the solvent greatly affects the initial development and the extent at which the rings are seen with ten pyrene units. The interference from the solvent on the dynamics of the system hindered the interaction between the available reactive groups on the cluster, resulting in the reduction of number of rings observed in a single cluster compared to the study without DMF.

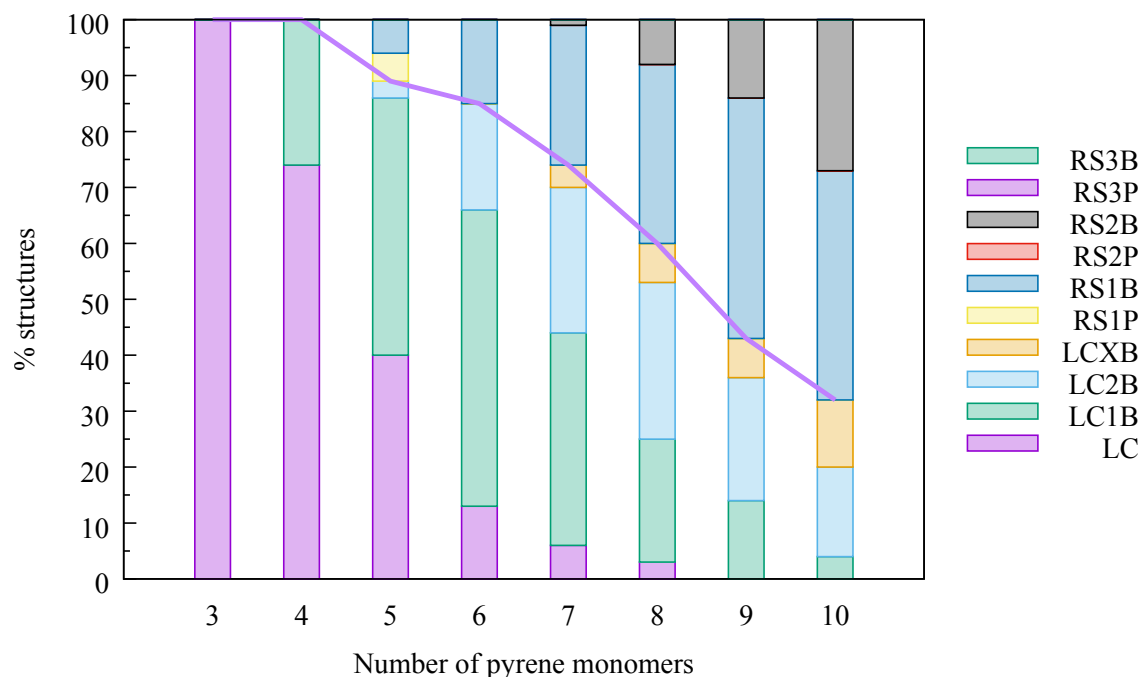


**Figure 3.6:** Histogram of the individual structures presented with each additional monomer for YPy the with DMF solvent; from three pyrene monomers to ten pyrene monomers. The purple line represents the total number of chain structures with each increment of pyrene building blocks, and the separation of chain structures (below) and ring structures (above).



The quantity of ring structures produced both with and without the solvent present do not differ greatly. However, it is to the extent to which these rings formed in a single structure that differs. The solvent has proven to hinder the formation of rings in a single structure, with a maximum of two rings being observed. Overall, the number of rings observed within the structures did not increase greatly, yet there was an increase in generated clusters containing the ring formation. Although the solvent affects the formation of the rings, it is vital to include within the simulations to coincide with the experimental procedure. DMF also plays a key role in pore formation. The DMF molecules can interact with each other, and offer a templating effect on the formation of pores, and consequently the molecular ring formation. This was previously observed by Cooper *et al.*, studying the importance of solvent choice for the formation of CMPs.<sup>209</sup> Figure 3.7 shows the DMF molecules present within a formed pore of a larger YPy structure generated. These DMF molecules congregated together, to which the CMP cluster had folded around to produce the molecular ring.

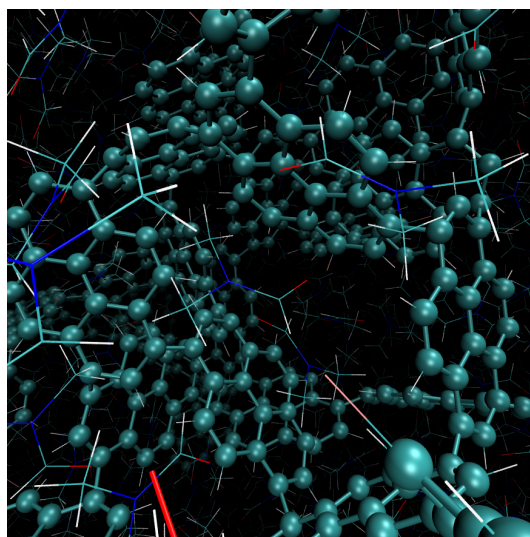


**Figure 3.7:** Graphical representation of DMF presence within the porous structure of YPy. The close proximity of the DMF molecules within this pore lead to the templating effect, offering potentially larger pores in areas of the structure.

### 3.2.2 Molecular ring formation in YDBPy

Now that we understand the effects that the solvent has on the structure formation of YPy clusters, it was deemed necessary to retain the solvent within all following structure generations. YDBPy (tetrabromopyrene with 1,4-dibromobenzene) was next generated to understand how the formation of molecular rings differs to that of YPy. The surface area determined experimentally was smaller than that of YPy. This is due to the inclusion of a linear monomer, extending the distance between the pyrene nodes and potentially allowing for more network interpenetration. Regardless of the decrease in surface area, the simulations performed here YDBPy showed the formation of molecular rings. Table 3.5 shows the statistical analysis of the structures generated involving the YDBPy monomers (pyrene and 1,4- coordinated benzene).

	Pyrene monomers							
	3	4	5	6	7	8	9	10
LC	12	-	-	-	-	-	-	-
LC1B	47	32	9	3	1	-	-	-
LC2B	33	33	32	18	9	1	-	-
LCXB	8	35	57	76	85	93	91	91
RS1P	-	-	-	-	-	-	-	-
RS1B	-	-	2	3	5	6	9	9
RS2P	-	-	-	-	-	-	-	-
RS2B	-	-	-	-	-	-	-	-
RS3P	-	-	-	-	-	-	-	-
RS3B	-	-	-	-	-	-	-	-
Straight chain	100	100	98	97	95	94	91	91
Ring structure	-	-	2	3	5	6	9	9

**Table 3.5:** Statistical analysis of ring structures produced within YDBPy clusters; pyrene monomers increasing from three units to ten units.

The experimental procedure of YDBPy suggests a 2:1 ratio of monomers in favour of the 1,4-dibromobenzene. Therefore the simulations were performed with this ratio,

yet still with the same number of pyrene building blocks as for YPy. It is clear that the inclusion of a linear co-monomer affects the formation of the molecular rings. The YDBPy clusters observed show ring formation with a minimum of five pyrene building blocks, yet the most rings seen in a single system is one. Most of the structures establish a multi-branched configuration. Figure 3.8 shows the comparison between the different structures produced, as well as the difference in total number of straight chain structures and ring structures generated. Less than 10 % of the clusters generated show ring development with ten pyrene building blocks. As mentioned, the linear building block extends the distance between the pyrene units. This structural property, coupled with the steric interactions of the solvent, reduce the chances of cyclisation.

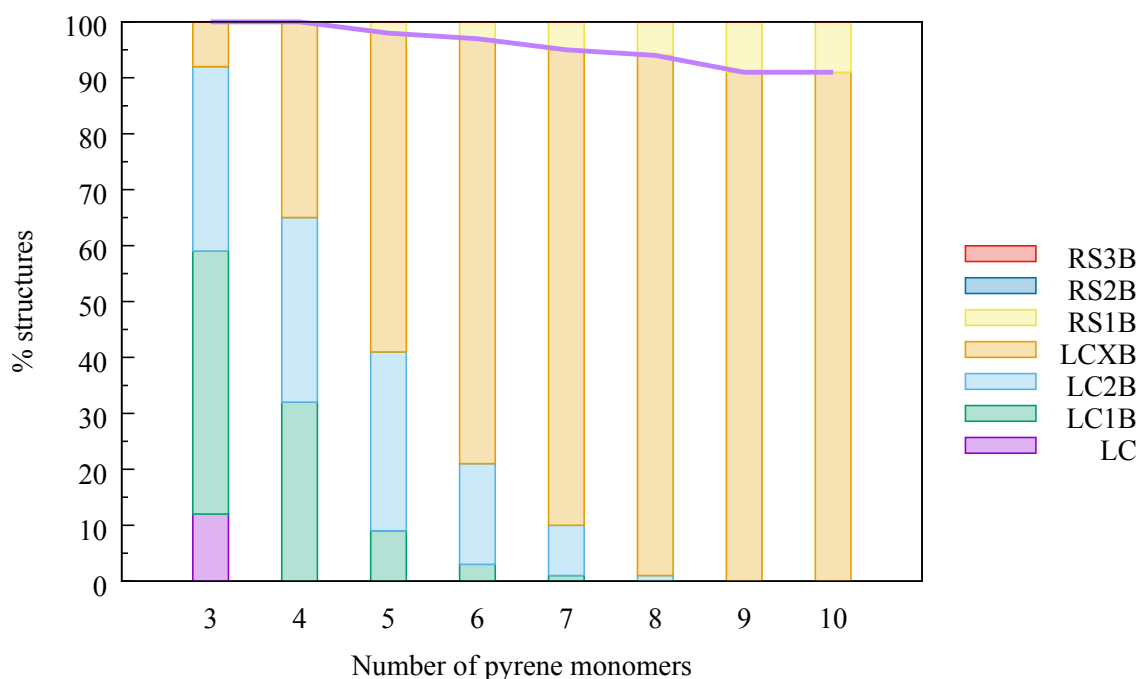


**Figure 3.8:** Histogram of the individual structures presented with each additional monomer for YDBPy with DMF solvent; from three pyrene monomers to ten pyrene monomers. The purple line represents the total number of chain structures with each increment of pyrene building blocks, and the separation of chain structures (below) and ring structures (above).

Comparing the structures produced, the molecular rings developed consist of more building blocks to those of the YPy clusters. The development of branched structures

occurs at an earlier stage for YDBPy. With an increase in branched clusters with fewer pyrene building blocks, one can speculate that multiple molecular rings could develop as clusters chemically bond within the synthetic procedure. The introduction of a linear co-monomer offers an extension upon where the available binding sites are in space, and therefore the potential to develop larger molecular rings within a larger system.

### 3.2.3 Molecular ring formation in YDPPy

The generation process of YDPPy was performed in a similar manner to YDBPy (2:1 in favour of the biphenyl linker), yet shows no formation of molecular rings as the number of building blocks is increased. Table 3.6 shows the statistical analysis of clusters generated for the YDPPy system.

	Pyrene monomers							
	3	4	5	6	7	8	9	10
LC	15	6	1	-	-	-	-	-
LC1B	42	23	9	5	-	-	-	-
LC2B	31	35	29	13	9	3	1	1
LCXB	12	36	61	82	92	97	99	99
RS1P	-	-	-	-	-	-	-	-
RS1B	-	-	-	-	-	-	-	-
RS2P	-	-	-	-	-	-	-	-
RS2B	-	-	-	-	-	-	-	-
RS3P	-	-	-	-	-	-	-	-
RS3B	-	-	-	-	-	-	-	-
Straight chain	100	100	100	100	100	100	100	100
Ring structure	-	-	-	-	-	-	-	-

**Table 3.6:** Statistical analysis of ring structures produced within YDPPy clusters; pyrene monomers increasing from three units to ten units.

As it can be seen, the inclusion of a much larger linker reduces the potential molecular formation even further. Figure 3.9 shows the comparison of structure types generated during the simulations, and the comparison in total number of straight chain structures and ring structures generated.

The clusters generated do not possess any molecular ring formation. This is due to the increase in the size of linker introduced into the system. Similar to the clusters generated for YDBPy, the pyrene nodes are much further apart and therefore the probability of forming the macrocycles is greatly reduced. The number of straight chain structures is statistically similar to those of the YDBPy clusters generated, leading to the probability that further increase in building blocks would lead to larger molecular rings forming. However, the difference in experimental surface areas (YDBPy,  $1069 \text{ m}^2 \text{ g}^{-1}$ ; YDPPy,  $303 \text{ m}^2 \text{ g}^{-1}$ ) suggests that the number of macrocyclic structures developed is less than that of YDBPy.

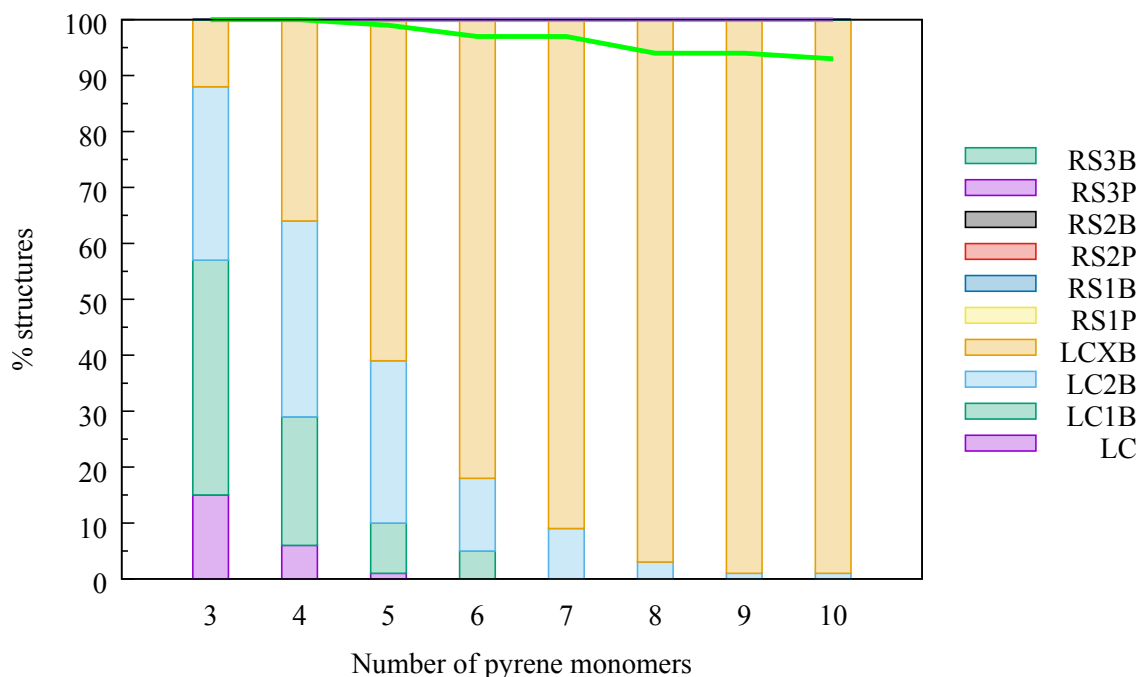


**Figure 3.9:** Histogram of the individual structures presented with each additional monomer for YDPPy with DMF solvent; from three pyrene monomers to ten pyrene monomers. The purple line and green line represent the total number of chain structures with each increment of pyrene building blocks for YDPPy with and without DMF solvent respectively, and the separation of chain structures (below) and ring structures (above).

Additionally, the presence of solvent hinders the "folding" process during the MD stages, preventing the available binding sites on the cluster to come in contact with one another. The statistical analysis of these materials shows how the formation of molecular rings is affected by the inclusion of a co-monomer, and furthermore the size of the molecular rings correlating with the size of the linear co-monomer introduced. The quantity of molecular rings produced greatly decreases with the inclusion of a linear co-monomer, seeing YPy possess the greatest quantity of molecular rings and YDPPy showing the fewest. The degrees of freedom for the building blocks incorporated into the structure increases with the inclusion of co-monomers of increasing size. With the increase in degrees of freedom, the probability that molecular rings develop decreases, along with the formation of strained systems as proposed by Zwijnenburg *et al.*<sup>177</sup>

### 3.2.4 Design of pyrene-based CMPs

To assess how the band gap could be tailored further, structures were generated with pyrene alongside co-monomers with differing structural properties to promote the formation of molecular rings. Ortho-, meta-, and para-substituted benzene building blocks (1,2-dibromobenzene, 1,3-dibromobenzene, and 1,4-dibromobenzene; Figure 3.10) offer potentially different structural properties, with the potential for increased molecular ring formation. This is in direct comparison with YDBPy (which will be referred to as *S0* from here on) to assess how the geometry of a co-monomer of similar size can affect the formation of molecular rings, and therefore affecting the band gap energies. Inclusion of these directional co-monomers has potential to increase upon the strain observed within the structures, increasing the  $\pi$ -overlap and thus the conjugation within the system.

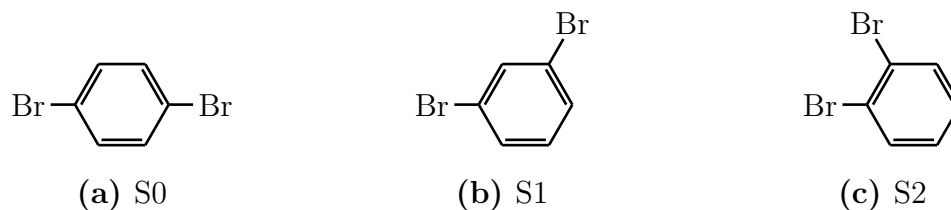


**Figure 3.10:** Phenyl co-monomer for the formation of S0 (YDBPy), and the chosen monomers for the rationalisation of pyrene-based CMPs; (a) 1,4-dibromobenzene (S0) (b) 1,3-dibromobenzene and (c) 1,2-dibromobenzene.

The configuration of these groups can influence the directionality of the polymer chains, allowing for tighter packing of building blocks, and affecting the quantity of molecular rings observed. Figure 3.11 shows the potential binding of the benzene co-monomers to the pyrene building block.

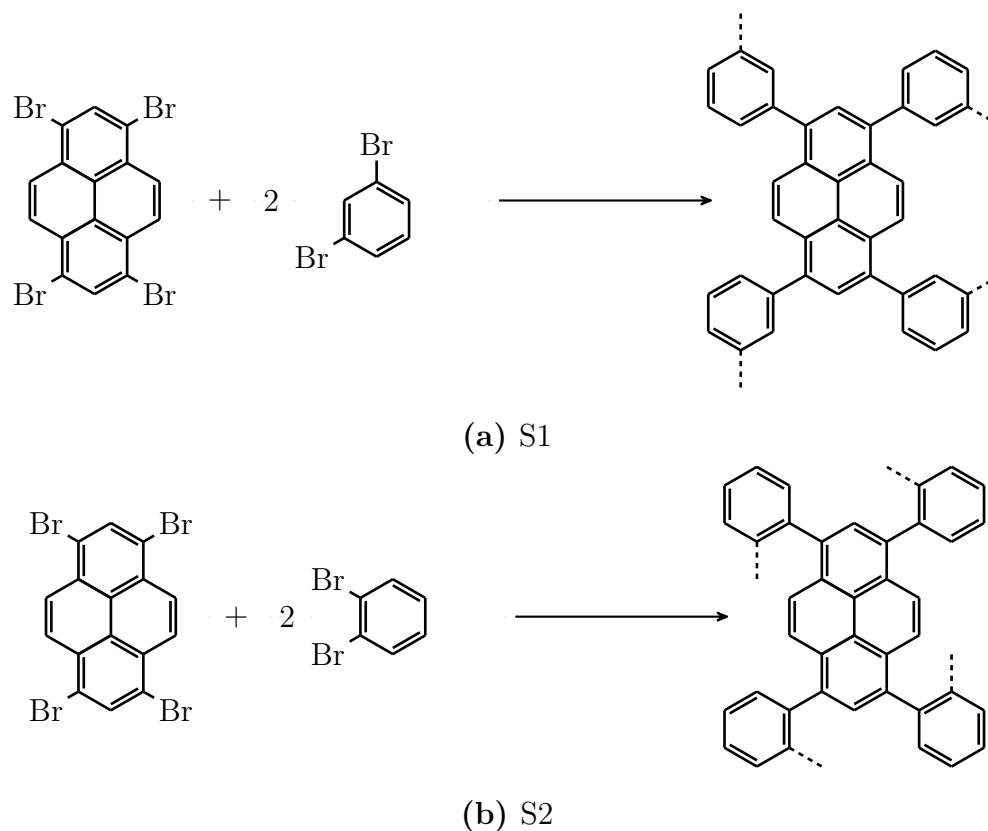


**Figure 3.11:** Formation of the rationalised CMP materials; (a) S1: tetrabromopyrene with 1,3-dibromobenzene, and (b) S2: tetrabromopyrene with 1,2-dibromobenzene.

The generation of clusters for the S1 and S2 structures was performed in the same manner as that of YDBPy. The pyrene building blocks were initially seeded, and the growth steps performed with a 2:1 ratio in favour of the benzene co-monomers. Initially observing the S1 structures, there is a distinct difference between the structures generated and the structures of S0.

Table 3.7 shows the statistical analysis of the structures generated from the S1 MD simulations.

	Pyrene monomers							
	3	4	5	6	7	8	9	10
LC	12	3	2	1	-	-	-	-
LC1B	42	22	12	4	1	-	-	-
LC2B	20	25	11	8	2	-	-	-
LCXB	8	25	41	47	51	45	34	25
RS1P	-	-	-	-	-	-	-	-
RS1B	17	23	30	29	35	36	37	32
RS2P	-	-	-	-	-	-	-	-
RS2B	1	1	2	9	8	15	24	30
RS3P	-	-	-	-	-	-	-	-
RS3B	-	1	2	2	3	3	4	10
RS4P	-	-	-	-	-	-	-	-
RS4B	-	-	-	-	-	1	-	2
RS5P	-	-	-	-	-	-	-	-
RS5B	-	-	-	-	-	-	1	1
Straight chain	82	75	66	60	54	45	34	25
Ring structure	18	25	34	40	46	55	66	75

**Table 3.7:** Statistical analysis of ring structures produced within S1 clusters; pyrene monomers increasing from three units to ten units.

The number of molecular rings dramatically increases with the introduction of the 1,3-coordinated benzene building block. Similar to the S0 analysis, fewer linear structures are generated with the presence of a co-monomer. However, there is greater



diversity in structures with as few as three pyrene monomers and ring formation occurring from the initial observations. The maximum number of rings observed in a single structure is five. With all of the monomers placed in the system, 75 % of the generated structures contain at least one molecular ring.

Figure 3.12 shows the generated ring structure development for the S1 system as the number of pyrene units increased.

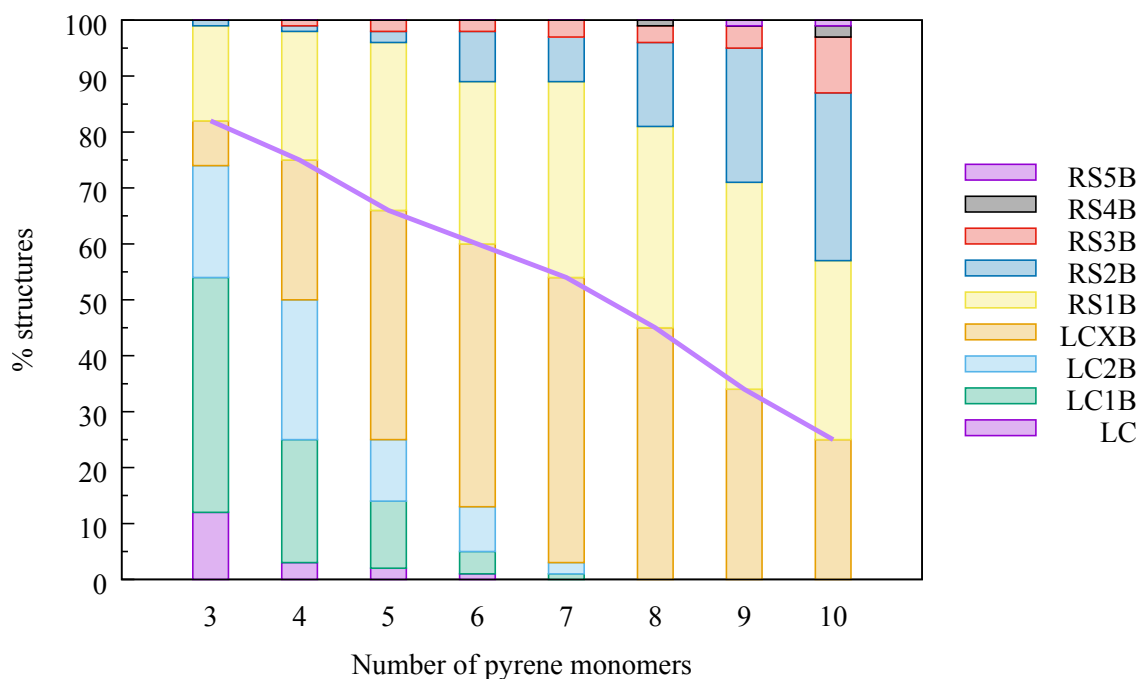


**Figure 3.12:** Histograms of (a) the overall tally of individual structures observed within the S1 material development; from three pyrene monomers to ten pyrene monomers. The purple line represents the total number of chain structures with each increment of pyrene building blocks, and the separation of chain structures (below) and ring structures (above).

The number of ring structures generated is far greater compared to those of S0, and also show further ring development compared to the YPy structures generated. As the ring structures develop from an early stage, the overall system will exhibit a large number of molecular rings. The incorporation of a co-monomer with directionality shows greater numbers of these macrocyclic substructures. Table 3.8 shows the statistical analysis of structures generated for the S2 system.

	Pyrene monomers							
	3	4	5	6	7	8	9	10
LC	6	1	-	-	-	-	-	-
LC1B	29	13	7	1	-	-	-	-
LC2B	15	18	4	3	-	-	-	-
LCXB	7	17	29	27	16	8	7	4
RS1P	-	-	-	-	-	-	-	-
RS1B	37	38	38	37	45	38	28	20
RS2P	-	-	-	-	-	-	-	-
RS2B	6	13	19	22	20	27	34	34
RS3P	-	-	-	-	-	-	-	-
RS3B	-	-	3	10	18	21	20	20
RS4P	-	-	-	-	-	-	-	-
RS4B	-	-	-	-	1	6	7	13
RS5P	-	-	-	-	-	-	-	-
RS5B	-	-	-	-	-	-	3	6
RS6P	-	-	-	-	-	-	-	-
RS6B	-	-	-	-	-	-	1	3
Straight chain	57	49	40	31	16	8	7	4
Ring structure	43	51	60	69	84	92	93	96

**Table 3.8:** Statistical analysis of ring structures produced within S2 clusters; pyrene monomers increasing from three units to ten units.

The clusters generated of the S2 system exhibit even greater molecular ring formation compared to both S0 and S1. The majority of structures produced contain a ring from the minimum number of building blocks, and almost all of the structures contain a molecular ring by the final stage. Figure 3.13 shows the comparison in structures produced and the progression of ring formation in the S2 clusters.

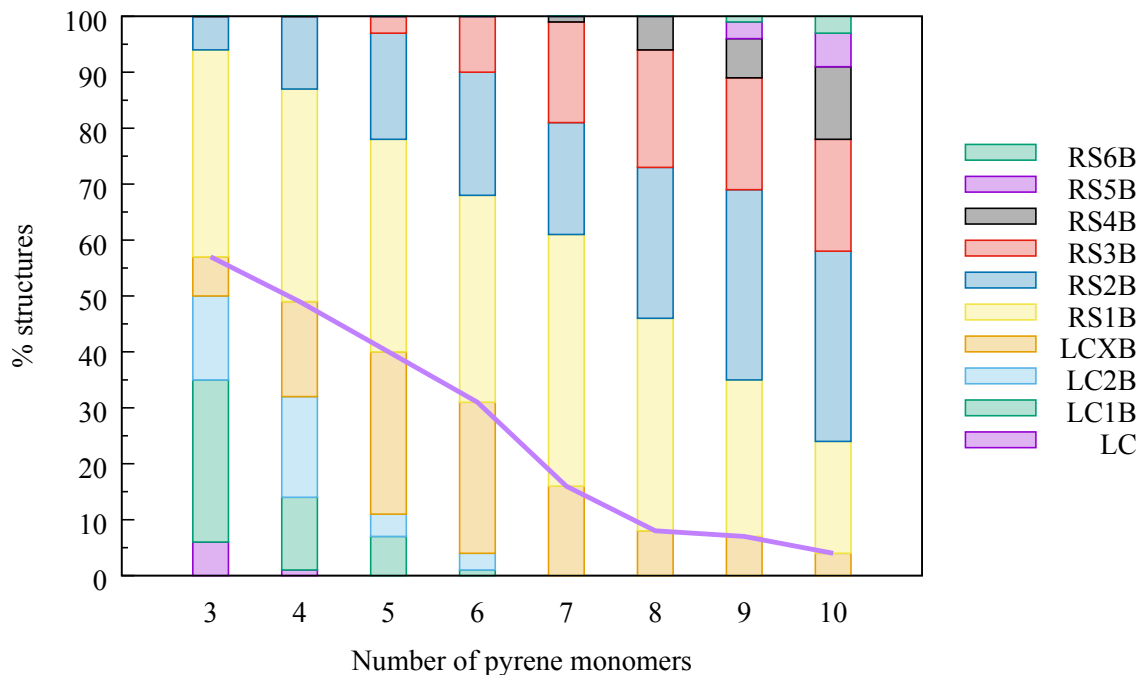


**Figure 3.13:** Histograms of (a) the overall tally of individual structures observed within the S2 material development; from three pyrene monomers to ten pyrene monomers. The purple line represents the total number of chain structures with each increment of pyrene building blocks, and the separation of chain structures (below) and ring structures (above).

The number of different structures observed is much more diverse. The S2 clusters see up to six rings forming within a single structure. The tight angle of the benzene co-monomer means the building blocks can pack more tightly, therefore making the reactive groups closer in space. The S2 clusters show very little straight chain structures by the end of the simulations. The straight chain structures that are formed by the end are all highly branched due to the number of monomers present.

The diverse number of molecular rings formed in both the S1 and S2 structure give insight into how the electronic band gap can potentially be tailored further. Increasing the number of molecular rings within the porous structure could shift the band gap in to much lower energy levels. This could also alter the photoluminescence of the materials, shifting the absorption of light to higher wavelengths. However, through simulating the structure generation process, these additional co-monomers pose several challenges towards synthetic development. For example, the tight angle

between reactive bromine groups on the S2 linker leads to a very tightly packed system. The tight packing of building blocks can render the materials non-porous. As the pyrene building block is larger than that of the benzene, the secondary coupling process to the benzene becomes inhibited from the bulky group already attached to it. It is highly likely that homo-coupling will occur, which will result in fewer molecular ring structures, indicated here.

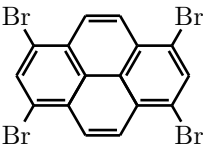
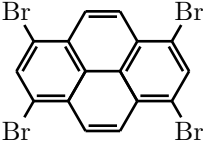
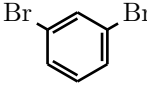
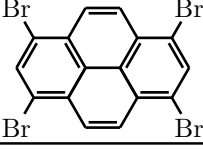
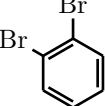
### 3.3 Synthesis and characterisation of pyrene-based CMPs

Each material of YPy, S0, S1, and S2 was synthesised using the *Yamamoto* coupling reaction,<sup>182</sup> applying a 2:1 ratio in favour of the benzene co-monomers. Knowing that YPy and S0 (YDBPy) were previously synthesised,<sup>124</sup> the synthesis of S1 and S2 should also be possible. Additionally, the reactivity of the ortho-, meta-, and para-substituted benzene has an order of  $o- > m- > p-$ , indicating that the *o*- (S1) and *m*-dibromobenzene (S2) should be reactive.<sup>210</sup>

The reaction process itself differs from that of the initial publication which uses a Radley's reactor. However, the process applied here was adopted from the synthesis of PAF-1 within Teng Ben's group at Jilin University, where the initial materials were synthesised.<sup>139</sup>

#### 3.3.1 Synthesis of rationalised CMPs

The CMP YPy was initially attempted to replicate the properties and data produced from the original publication.<sup>124</sup> It was also used to assess the capabilities of the reaction process, and how the reaction can be performed using more conventional laboratory techniques for the purpose of operational simplicity. Alongside YPy, S1 and S2 were also synthesised. Table 3.9 shows the initial three reactions performed and the respective surface areas determined.

Reaction <sup>a</sup>	Monomer	Linker	SA <sub>BET</sub> (m <sup>2</sup> g <sup>-1</sup> )
<b>1</b>		-	< 10
<b>2</b>			< 10
<b>3</b>			514

**Table 3.9:** Reactions and Brunauer-Emmett-Teller surface areas of **(1)** YPy, **(2)** S1, and **(3)** S2. <sup>a</sup>All reactions were performed using *Method 1*.

Reaction **3** yielded a product showing porous properties. The SA<sub>BET</sub> of the polymer produced was 514 m<sup>2</sup> g<sup>-1</sup>. Reactions **1** and **2** on the other hand did not yield porous materials, with reaction **1** giving a product with a BET surface area of < 10 m<sup>2</sup> g<sup>-1</sup> and the yield of material from reaction **2** was far too small to perform analysis on. However, all materials produced bear similar optical and physical properties to those observed originally.<sup>124</sup> Figure 3.14 shows the products of reactions **1** - **3** in a suspension of THF under UV irradiation.

The materials luminesce under UV irradiation. Reaction **2**, S1, and reaction **3**, S2, were readily dispersed in solution giving the clear colour of their luminescence. Reaction **1**, YPy, does not readily disperse in solution yet the solid is shown to luminesces under irradiation. The optical differences between the products are that the product of reaction **2** shows a colour change, whereas the solid materials of reaction **1**, YPy, and reaction **3**, S2 have a very similar orange colour.

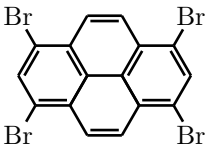
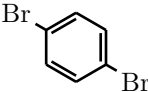
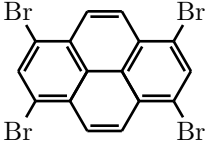
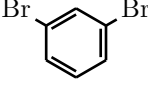
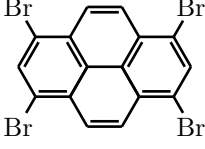
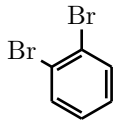
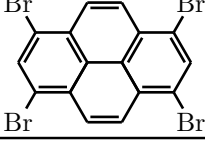


**Figure 3.14:** Products of reactions **1**, **2**, and **3** subjected to UV light (365 nm) in THF; Left to right: THF, reaction **1**, reaction **3**, and reaction **2**.

Having rationalised the structures prior to synthetic analysis (*vide supra*, section 3.2.4), the structures of S1 and S2 formed during the simulation process showed high degrees of strain, and the atomic positions would not be kinetically favourable. Therefore, it is speculated that the product given from reaction **3** is largely comprised of pyrene homo-coupling. However, due to time constraints and availability of analytical equipment within the Jilin University research laboratories, no further analysis was achievable for these materials.

To attain reproducibility of the published data, and the materials produced from reactions **1** - **3**, further synthesis was performed on the formation of YPy, S0, S1, and S2. Table 3.10 shows the further reactions performed on the synthesis of these CMPs. Reactions **4** and **8** for the synthesis of S0 produced materials with much lower porosity in comparison to that of YDBPy ( $1069 \text{ m}^2 \text{ g}^{-1}$ ). The additional reactions yielded products with surface areas ranging between  $< 10 \text{ m}^2 \text{ g}^{-1}$  and  $40 \text{ m}^2 \text{ g}^{-1}$ . The techniques applied to the synthesis of these CMPs greatly differ to those reported previously.<sup>124</sup>

The efficiency of exclusion of air, given that the catalyst is highly air and moisture sensitive, and the rate at which reagents are mixed are important factors to assess for these reactions as they can greatly affect the synthetic process and the reproducibility of results.

Name	Reaction <sup>a</sup>	Monomer	Linker	SA <sub>BET</sub> (m <sup>2</sup> g <sup>-2</sup> )
S0	4 / 8 / 10			247 / 336 / < 10
S1	5 / 6			34 / < 10
S2	7			34
YPy	9		-	< 10

**Table 3.10:** Second stage reactions and Brunauer-Emmett-Teller surface areas of S0 (4/8/10), S1 (5/6), S2 (7), and YPy (9). <sup>a</sup>All reactions performed using *Method 1*.

The lack of airtight vessels, that may be necessary as the catalytic reagent is highly air and moisture sensitive, or the rate at which reagents are mixed, may greatly affect the synthetic process, and therefore result in non-porous materials.

PXRD patterns of the materials produced by reactions 4 to 8 (S0 to S2) confirmed their amorphous nature (Appendix A.1). The broad peak indicates the amorphicity of the materials. The products of reactions 4 and 8 (S0) show a sharp peak at  $2\theta = 20$ . This sharp peak can correlate to  $\pi$ - $\pi$  stacking of aromatic monomers. Although amorphicity is not proportional to porosity, it indicates the formation of a polymeric system. These materials also look visually different to the starting reagents of the reaction (Appendix A.2). The resulting dark orange powders are similar to that of YPy. However, we were able to infer that the co-monomers had been incorporated into the structures of S0, S1, and S2 by <sup>13</sup>C solid-state NMR. Figures 3.15 to 3.23

show the  $^{13}\text{C}$  solid-state NMR spectra for the YPy, S0, S1, and S2 products produced (reactions **9**, **4**, **6**, and **7**, respectively). The key peaks observed occur between 120 ppm to 133 ppm and 133 ppm to 138 ppm. Figures 3.15 and 3.16 show the  $^{13}\text{C}$  solid-state NMR spectrum for YPy (reaction **9**) and a theoretical  $^{13}\text{C}$  NMR spectrum of a generated fragment of the YPy structure.

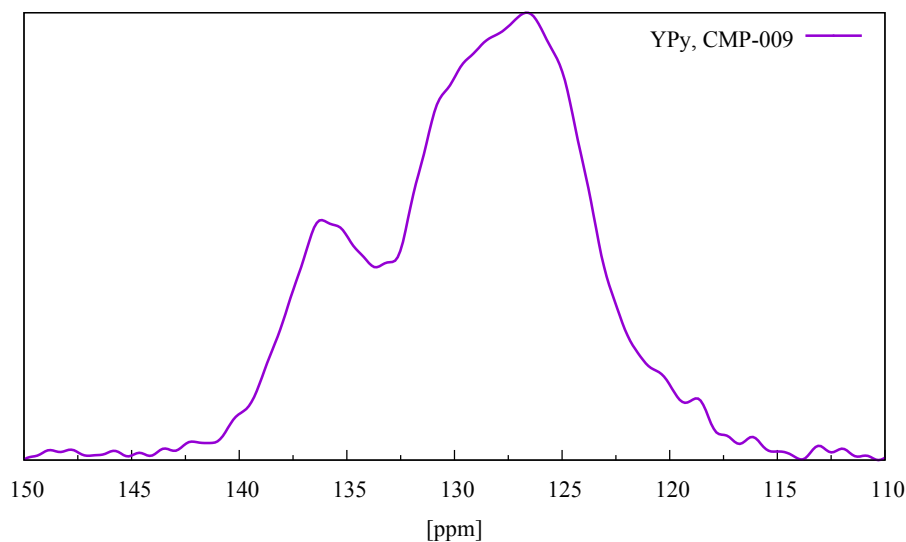


**Figure 3.15:** The  $^{13}\text{C}$  solid-state NMR spectrum of YPy (reaction **9**).

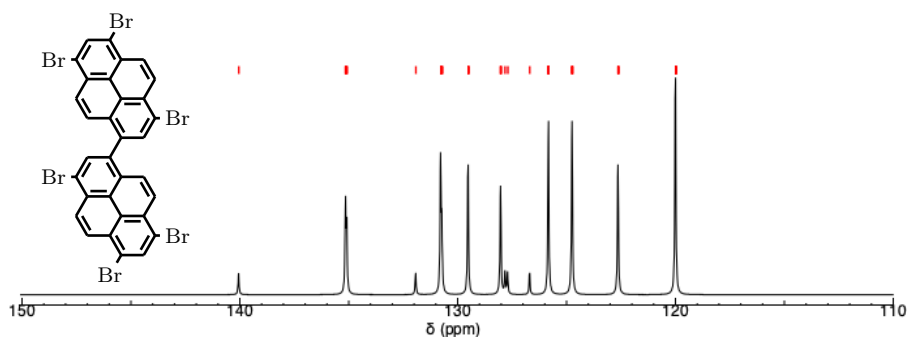


**Figure 3.16:** Theoretically expected  $^{13}\text{C}$  NMR spectrum of a fragment of the YPy structure.

The NMR spectrum of the YPy product provides a reference point to determine the inclusion of the co-monomers by means of NMR. The theorised  $^{13}\text{C}$  NMR spectrum of the YPy fragment allows us to correlate the peaks of the monomers to the solid-state  $^{13}\text{C}$  NMR spectrum. Figures 3.17 and 3.18 show the  $^{13}\text{C}$  solid-state NMR spectrum



of the S0 product (reaction 4) and a theoretical  $^{13}\text{C}$  NMR of a generated fragment of the S0 structure.

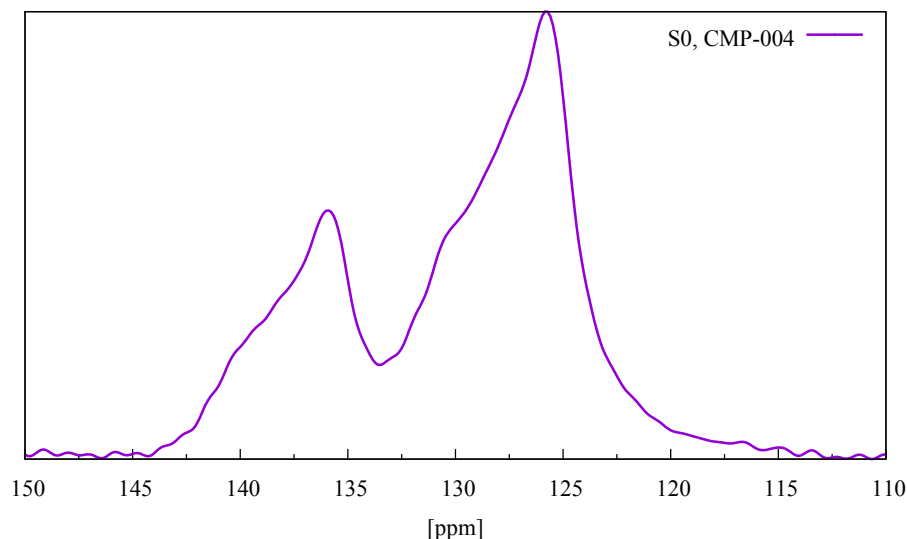


**Figure 3.17:** The  $^{13}\text{C}$  solid-state NMR spectra of S0 (reactions 4).

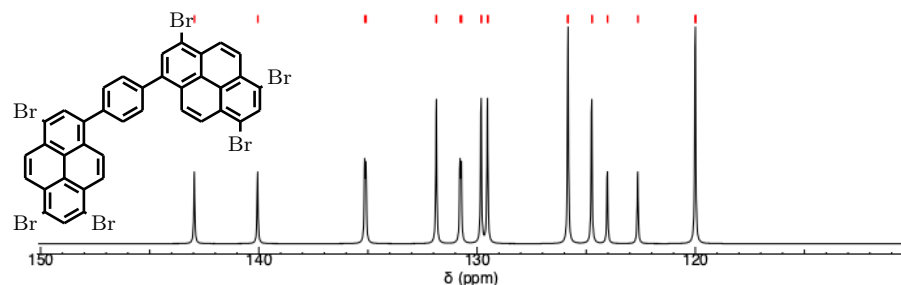


**Figure 3.18:** Theoretically expected  $^{13}\text{C}$  NMR spectra of a fragment of the S0 structure.

There is a difference between the intensities of the observed peaks in the spectrum of S0 compared to that of YPy. Alongside this, the peak observed at 142 - 133 ppm is broader than that seen in the YPy spectrum; both of these observations suggest that structural configurations other than homocoupled pyrene are present in S0 product. This is a similar case for the S1 product. Figures 3.19 and 3.20 display the  $^{13}\text{C}$  solid-state NMR spectrum of S1 (reaction 6) and a theoretical  $^{13}\text{C}$  NMR spectrum of a generated fragment of the S1 structure.

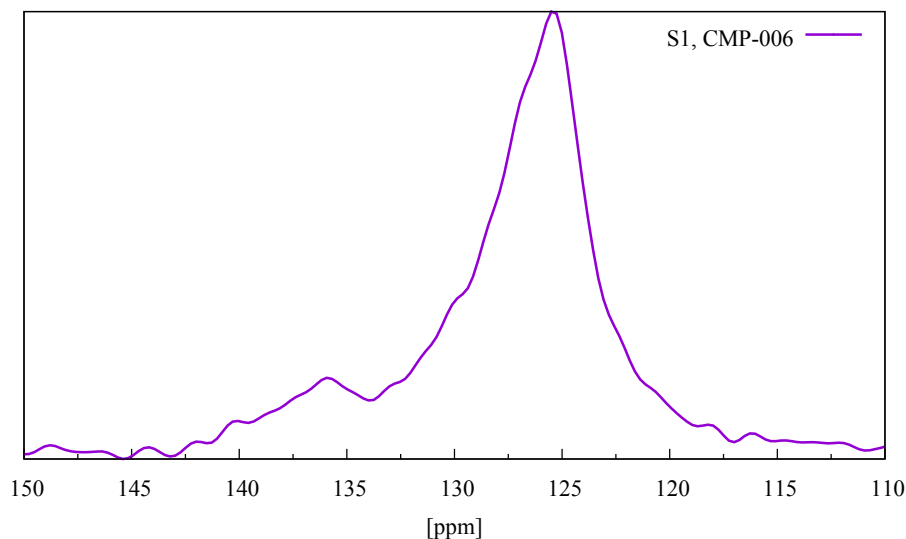


**Figure 3.19:** The  $^{13}\text{C}$  solid-state NMR spectrum of S1 (reactions **6**).

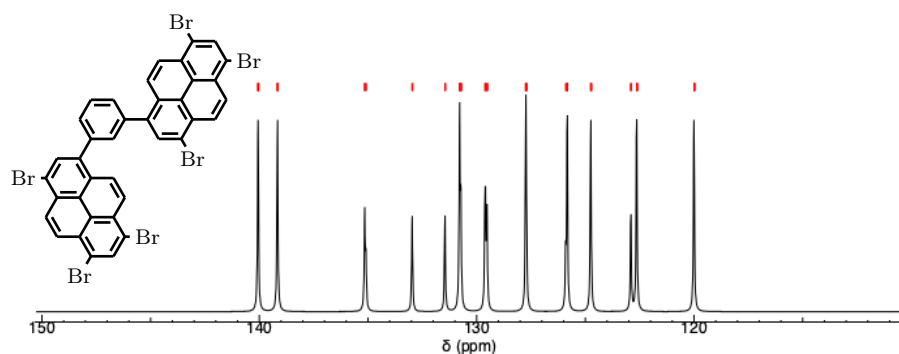


**Figure 3.20:** Theoretically expected  $^{13}\text{C}$  NMR spectrum of a fragment of the S1 structure.

The increase in intensity of the peaks between 133 ppm and 122 ppm follows a similar trend to that observed for the S0 product. However, there is a weaker peak between 140 ppm and 133 ppm. In light of the capricious nature of this synthetic procedure, it can be speculated that there is a presence of homo-coupled pyrene monomers within the material.

The S2 product (reaction **7**) shows a weaker intensity of the resonance between 133 ppm and 120 ppm (Figure 3.21, yet multiple peaks are seen between 142 ppm and 135 ppm. Comparing the  $^{13}\text{C}$  solid-state NMR spectrum with the theorised  $^{13}\text{C}$  NMR spectrum, the presence of these additional peaks suggests that the phenyl co-monomer

is included into the system. Figure 3.22 displays the theorised  $^{13}\text{C}$  solid-state NMR spectrum of the S2 product.

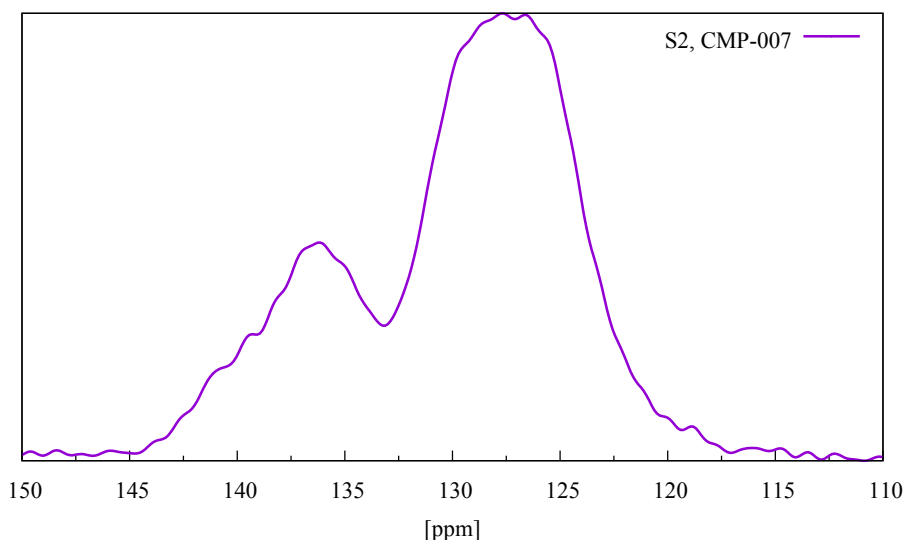


**Figure 3.21:** The  $^{13}\text{C}$  solid-state NMR spectra of S2 (reactions 7).

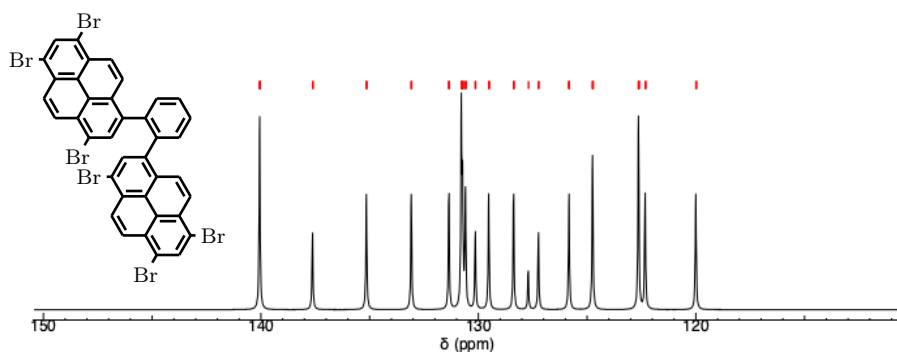


**Figure 3.22:** Theoretically expected  $^{13}\text{C}$  NMR spectra of a fragment of the S2 structure.

It is possible that the phenyl co-monomers are present within the co-polymers synthesised from the expected peaks of small bonded clusters. The peaks observed shown in the theoretical NMR spectrum at 140 ppm and 138 ppm arise from the aromatic carbons in the phenyl co-monomer. The differences between the  $^{13}\text{C}$  solid-state NMR spectra can be seen in Figure 3.23. The shift between the YPy product and the co-polymers correlates with the theoretical  $^{13}\text{C}$  NMR spectra determined for

each system, offering further evidence that the co-monomers have been incorporated into the products.

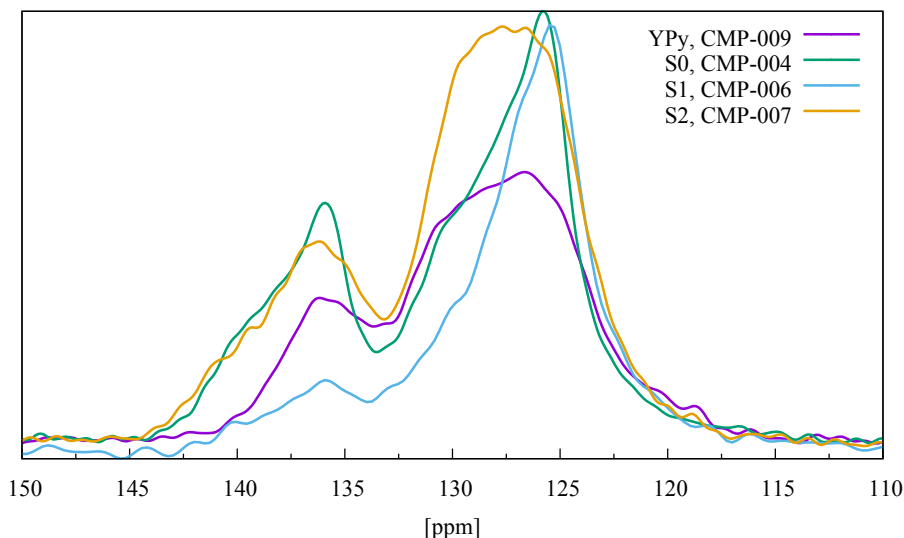


**Figure 3.23:** The  $^{13}\text{C}$  solid-state NMR spectra of YPy, S0, S1, and S2 (reactions **9**, **4**, **6**, and **7** respectively).

The greater intensity peaks between 133 ppm and 120 ppm correspond to the pyrene carbon atoms in the fragment, whereas the less intense peaks at 143 ppm and 140 ppm correspond to the carbon atoms of the phenyl linkers bonded to the pyrene unit. The correlation of the spectra of S0, S1, and S2 to that of the synthesised YPy material suggests that there is presence of homo-coupled pyrene within the co-polymer products. However, the shift in resonance signals from 140 ppm to 138 ppm suggests the inclusion of the phenyl co-monomers. This same shift is present in the spectrum of S1, however, the shallow peak indicates that the co-monomer is present to a lesser extent than in the S0 and S2 products. Overall, this NMR study gives some indication that there is incorporation of the phenyl linker into the co-polymer systems.

Although visually there is little difference between the S0, S1, and S2 materials, despite the inclusion of different co-monomers, under UV irradiation the materials are luminescent (Figure 3.24).

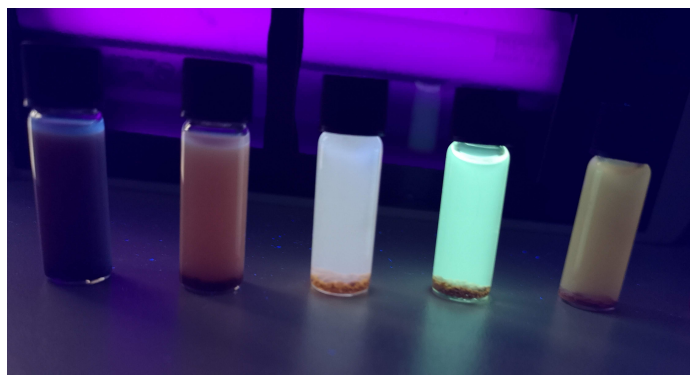


**Figure 3.24:** Reactions **4** to **8** under UV radiation; Left to right: **4**, **5**, **6**, **7**, and **8**, with UV lamp wavelength 365 nm.

Observing the products in a THF suspension shows how the materials activate under UV light. The product of reaction **7** (S1) displays the strongest emission when subjected to UV irradiation, whereas the products of reactions **4**, **5**, **6**, and **8** show weaker luminescence. More concentrate suspensions of each sample also show strong luminescence (Figure 3.25). The luminescence of the products is much more prominent than that of the tetrabromopyrene (TBrPy) starting reagent. Figure 3.26 shows the TBrPy monomer and samples from reaction **9** and reaction **10**, under UV irradiation.



**Figure 3.25:** UV observations of reactions **4** to **8** in more concentrate solutes of THF; (a) Left to right: **4**, **5**, **6**, **7**, **8**, with UV lamp wavelength 365 nm; (b) left to right: **8**, **7**, **6**, **5**, **4**, with UV lamp wavelength 365 nm.

The product of reaction **16** showed to be non-porous. The material optically resembles the pyrene monomer and this correlates to when the samples are subjected to UV radiation (Figure 3.26).



**Figure 3.26:** Samples of tetrabromopyrene (left), YPY (reaction **9**) (middle), and S0 (reaction **10**) (right) under UV exposure.

The product of reaction **9** fluoresces strongly under UV irradiation. The prominent colour change and the visual difference from the pyrene monomer indicates polymer formation. Understanding the differences between the materials produced and the luminescence of the products is key to understanding the reaction process for the generation of pyrene-based CMPs. Comparing the UV-vis spectra of these products provides evidence for the formation of new materials, and the incorporation of the phenyl co-monomers into the structures (Figure 3.27). There is a shift in  $\lambda_{\text{max}}$  between the monomer and produced materials. A minor shoulder appears at approximately 440 nm, where the TBrPy monomer and product overlap.

The difference in  $\lambda_{\text{max}}$  is more visible within the product of reaction **160**. The TBrPy peak is clearly visible along with the product peak. This shift is key to the formation of polymeric systems, although this is not an indication for the incorporation of all reaction reagent; the UV-vis spectra of the co-polymers closely resembles that of YPy (reaction **9**).

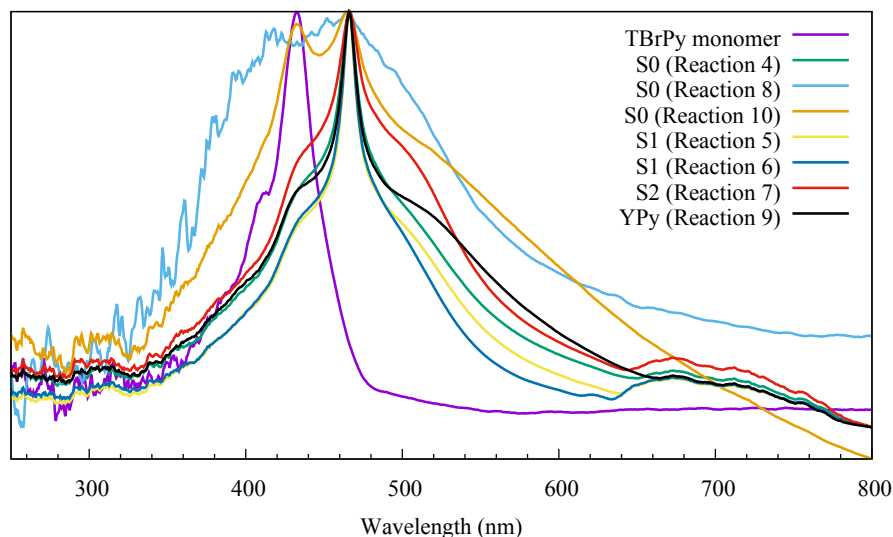


**Figure 3.27:** UV-vis plots of TBrPy, S0, S1, and S2, normalised to the maximum peak observed of TBrPy.

Each co-polymer exhibits a red shift in the the respective UV-vis spectra regardless of co-monomer geometry. This red shift is similar to that observed of the YPy material synthesised. There is little different in the visual appearance of the materials, yet a secondary peak is apparent between  $\sim 480$  nm to  $\sim 550$  nm.

There is a similar red shift between the UV-vis spectra of the co-polymer products, and each material displays a similar shift to that of the YPy material synthesised. This similarity in UV-vis shows that each material is different to that of the TBrPy monomer, yet the absorbency suggests that structural properties similar to that of YPy are present in each material synthesised.

The differences in reagents and similarities between their resulting properties warrants further investigation of the *Yamamoto* coupling reaction in more detail.

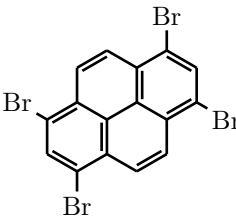
### 3.3.2 Ring formation mechanism analysis of YPy

In light of the theory that molecular rings are important for the band gap leads to the question of how ring formation can be promoted during the reaction. We surmised that by identifying any optical difference between the reagents and product during the polymerisation reaction, it mat be possible to gain insight into the rate of ring

formation and any differences in properties between YPy, S0, S1, and S2.

To determine at what stage the materials, and therefore the molecular rings, are formed, polymerisation reaction times were varied. More specifically, the reactions were independently repeated and terminated at varying times. Table 3.11 shows the reaction reagents and termination times applied for each reaction towards YPy formation. Reaction **11** was performed in the same manner with each iteration.

The duration differed between each of the reactions performed to assess the formation of CMPs at varying stages, from 20 minutes up to 1 week. Each reaction was taken to termination time and a full workup undertaken to result in solid products. With each reaction performed in exactly the same manner (*Method 2, section 2.1.3*), the limiting factors for the success of the reaction should stem from catalyst performance.

Reaction	Time (min)	Monomer
<b>11a</b>	20	
<b>11b</b>	40	
<b>11c</b>	60	
<b>11d</b>	120	
<b>11e</b>	240	
<b>11f</b>	7 days	

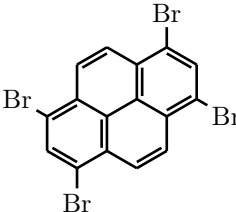
**Table 3.11:** Reaction **11** was performed according to *Method 2* with differing time intervals of 20 minutes, 40 minutes, 60 minutes, 120 minutes, 240 minutes, and 7 days.

The reaction vessels were kept air tight under an inert atmosphere. However, the products of these reactions differed greatly visually (Appendix A.3). Optical observations were necessary to determine the basis of reactivity. The initial reaction (reaction **11a**) performed for 20 minutes produced a dark orange / brown powder. This was similar to the product of reaction **11f** which had a duration of 1 week. Similarly, the products of reactions **11b** and **11e** were visually identical. The orange powders produced share a similar resemblance to those reported previously, namely YPy.<sup>124</sup> While products from reactions **11c** and **11d** appeared similar they closely



resemble the starting material. These observations suggest that reactions **11d** and **11e** did not proceed, and a polymeric system was not produced.

It was therefore apparent that the *Yamamoto* reaction is an unpredictable process, yielding irreproducible results. The excess of catalytic reagents means polymerisation can begin at an early stage, yet the activity and reactivity of these reagents is affected by external factors, resulting in poor catalysis and therefore no polymerisation. Because of these limiting factors, the materials produced can differ greatly, as seen with reaction **11**, and an alternative method for measuring the rate of ring formation was required. Therefore, as an alternative, samples were extracted from a single reaction at regular intervals. Reaction **12** (Table 3.12) followed the general *Yamamoto* coupling procedure with aliquots taken at specific time intervals in order to determine the extent of product formation over the course of the reaction.

Sample	Time (min)	Monomer
<b>12a</b>	20	
<b>12b</b>	40	
<b>12c</b>	60	
<b>12d</b>	120	
<b>12e</b>	240	
<b>12e</b>	480	
<b>12f</b>	12-hours	

**Table 3.12:** Reaction **12** was performed according to *Method 2* with aliquots take at time intervals of 20 minutes, 40 minutes, 60 minutes, 120 minutes, 240 minutes, and 7 days.

Taking samples from a single pot could be used to determine the reactivity of the reagents, at what stage the reaction process begins, and the performance of the reaction itself. Figure 3.28 shows the products of reaction **12**.

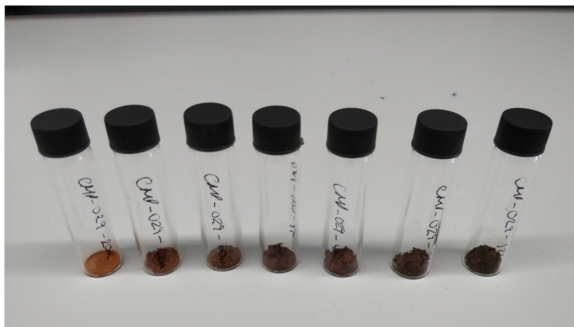
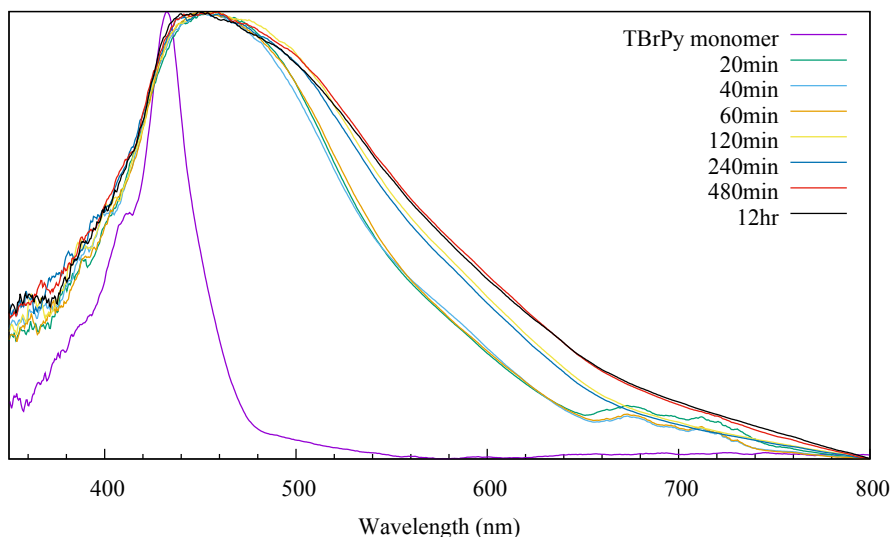


**Figure 3.28:** Samples of reaction **12**; Left to right: (**12a**) 20 minutes, (**12b**) 40 minutes, (**12c**) 60 minutes, (**12d**) 120 minutes, (**12e**) 240 minutes, (**12f**) 480 minutes, and (**12g**) 12-hours.

The extracts of the reaction mixture following work-up were visually different. The products from reaction **12** can be seen transitioning from lighter to darker shades of orange. This indicates that the reaction begins within the first minutes of monomer addition, and that the reaction itself is fast. The product at 20 minutes is visually different to that of the TBrPy monomer, suggesting that the reaction yields a material different to the monomer this early into the reaction. To gain a more thorough understanding on the rate of the reaction, UV-vis spectra were collected of these samples (Figure 3.29). There is an observable shift in absorption compared to the TBrPy monomer. Albeit, each extract spectrum shows an overlap with that of the TBrPy monomer, which absorbs at approximately 425 nm. The maximum absorbance occurs at 457 nm within each extract, yet the distinguishing shift occurs at approximately 550 nm where the extracts taken post 60 minutes show a shoulder. This shoulder is consistent for the extracts taken from 120 minutes to 12-hours and is an indication that the reaction is furthering completion.

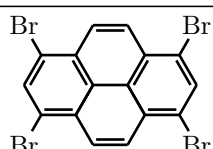
However, there is no observable change in the spectra between 480 minutes to 12-hours, suggesting that the extracts at 480 minutes and 12-hours are very similar. Reaction **12** was utilised to establish the rate of formation of the pyrene-based CMP, YPy. The optical analysis of the solid products shows a red shift from the tetrabromopyrene absorption, indicating a change in electronic structure. Through this method we were able to predict the rate of polymerisation and, therefore, the ring formation within these materials via analysis of solid samples. However, further

analysis is required to understand the mechanism of the formation of rings during the reaction process.



**Figure 3.29:** UV-Vis absorbance spectra of the solid extractions taken during reaction **12**, and the tetrabromopyrene monomer, normalised to the maximum peak of TBrPy.

Reaction **12** was used to determine the differences in extracted material with different reaction times. This showed that a product different to that of the TBrPy monomer was produced after 20 minutes, and observed further changes up to 2-hours. To assess the rate at which the CMPs begin to form *in situ*, Reaction **13** was performed. UV-vis spectra of the reaction mixture were collected at specific time intervals over a 2-hour period (Table 3.13).

Reaction	Monomer	Linker
<b>13</b>		-

**Table 3.13:** Reaction **12** was performed according to *Method 3*. UV-vis spectra of the reaction mixture were collected at specific time intervals over a 2-hour period.

Figure 3.30 shows the UV-vis spectra collected for reaction **13** over a 2-hour period, starting from the moment the monomers were added to the reaction vessel. The

product of reaction **13** is a dark orange/brown powder, as show in Figure 3.31. This is similar to that of reaction **9** (YPy). The reduction in intensity therefore represents an absorption shift from the UV to the infrared wavelength.

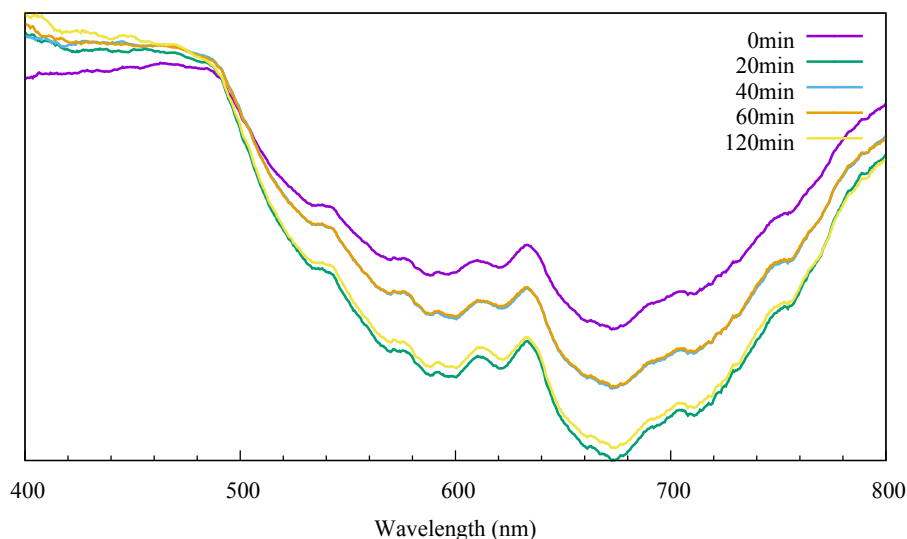


**Figure 3.30:** UV-vis absorbance of reaction **13** (YPy). Plot displays the UV-vis spectra of readings taken at 0 minutes, 20 minutes, 40 minutes, 60 minutes, and 120 minutes.

There is a distinct difference in intensity of the absorption peaks during the reaction process. However, each measurement taken over the 120 minute period shows no change in wavelength absorbance. The reaction mixture absorbs visible light within the 500 nm to 800 nm range. This coincides with the purple colour of the catalytic reagent solution. The intensity of the peaks decreases with time, indicating a transition from the catalytic reagent solution to the formation of a polymer. By comparing the UV-vis spectra of both the solid extracts from reaction **12** and the solution of reaction **13**, the change in absorption with time suggests that small oligomers are being formed in the earlier stages, followed by the formation of larger fragments as the reaction time surpasses 60 minutes. The absorption of light by the reaction mixture decreases with time, suggesting either the bonding of monomers, or the increased absorption of the materials produced. With this in mind, the UV-vis spectra during the early stages of the reaction would show if molecular rings are a key factor.

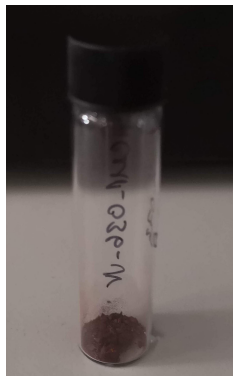


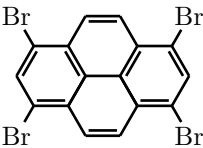
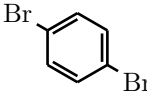
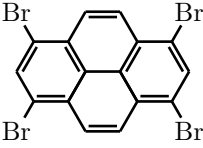
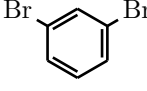
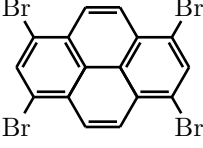
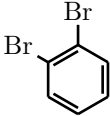
**Figure 3.31:** Product from reaction **13**. Work-up performed after the 2-hour reaction time.

### 3.3.3 Ring formation mechanism analysis with co-monomer inclusion

As a result of studying the formation of YPy within the reaction mixture, we have also monitored the formation of S0, S1, and S2 via UV-vis spectroscopy. The computational study on these materials showed that S0 formed far fewer molecular rings compared to YPy, S1, and S2. This suggests that the S0 materials should, therefore, show little to no difference in UV-vis spectra of the reaction mixture during these early stages (*vide supra* Section 3.2).

These studies have demonstrated how the analysis of the UV-vis absorption of both solid samples and the reaction solution can be used to predict polymerisation, and, therefore, ring formation if these structural properties are hypothesised to affect the band gap of pyrene-based CMPs. To test this idea in practice, UV-vis spectra of reaction **14** were collected to understand the differences in ring formation and band gap between the materials of YPy, S0, S1, and S2 (Table 3.14).

Concerning the formation of S0, there is little difference in absorbance within the first 20 minutes of the reaction, although differences in the UV-vis spectra arise as the reaction progresses further (Figure 3.32).

Reaction	Monomer	Linker	
<b>14a</b>			247 / 336 / < 10
<b>14b</b>			34 / < 10
<b>14c</b>			34

**Table 3.14:** Reaction **14** was performed according to *Method 3*, measuring the UV-vis absorption of the reaction mixture over a 2-hour period; reaction **14a**, YPy, reaction **14b**, S0, reaction **14c**, S1, and reaction **13d**, S2.

The initial spectra collected (0 minutes) and at 20 minutes are very similar, with a sharp peak at approximately 470 nm. This peak corresponds to the absorbance of the monomer. As the reaction is in its early stages, the difference in intensity can be assumed to be an instrumental factor, but the overall spectra are the same. As the reaction continues, however, the spectra begin to change substantially in intensity, and a broad shoulder is observed between 500 and 650 nm at 120 minutes. This coincides with the absorbance of the product being stronger than that of the reaction solution and monomers. In comparison to reaction **13**, reaction **14a** displays differing absorption throughout the synthesis. Compared to the visual appearance of the solid YPy material obtained after work-up (reaction **13**), the visual appearance of the solid S0 material from reaction **14a** differed, which suggests a difference in UV-vis spectrum. However, the UV-vis spectrum of the reaction mixture does not show any signs of polymer formation in the early stages. Comparably, the physical appearances of S0 from reaction **14a** to the products arising from the previous reactions (*vide supra* Section 3.3.1) suggests the completion of the reaction, and the formation of

a different material to that of the TBrPy starting material. However, the UV-vis spectrum collected from reaction **14a** does not clarify at what stage polymerisation occurs.

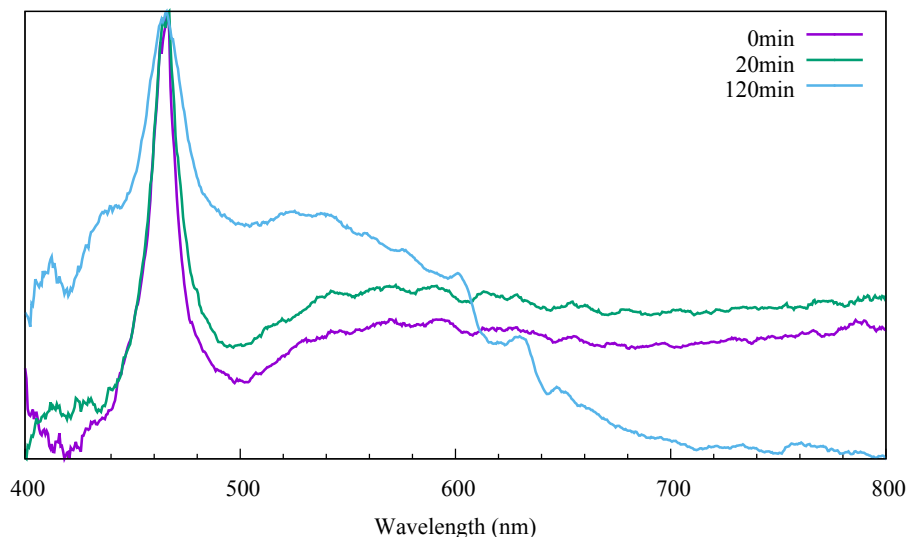


**Figure 3.32:** Normalised UV-vis absorbance of reaction **14a** (S0). Plot displays the UV-vis spectra of readings taken at 0 minutes, 20 minutes, 40 minutes, 60 minutes, and 120 minutes.

The hypothesis that molecular rings are the impacting factor towards the band gap of these materials would suggest that S1 would show signs of polymer formation, and changes in the UV-vis spectra from an earlier stage than that of S0. The UV-vis spectra collected for S1 (reaction **14b**) showed little presence of the TBrPy monomer from the initial reading, yet showed little change in absorbance after the first 20 minutes of the reaction (Figure 3.33). These changes in absorption differed to those seen previously in reactions **13** and **14a**. However, the peaks at approximately 640 nm that were observed in reactions **13** and **14a** are visible as the reaction progresses, whereas the initial UV-vis spectrum collected at 0 minutes contains a broad shoulder between 500 nm and 650 nm.

The S1 material produced post-work-up of reaction **14b** differs in physical appearance to the materials of the previous reactions. Although the UV-vis spectra collected *in situ* indicate a change in chemistry within the reaction mixture, the product bears visual similarities to that of the monomer, and not what was observed for S1 in re-

actions **5** and **6**. However, it was possible to isolate an insoluble product, suggesting the possible formation of oligomers or larger fragments and not a complete polymeric system.

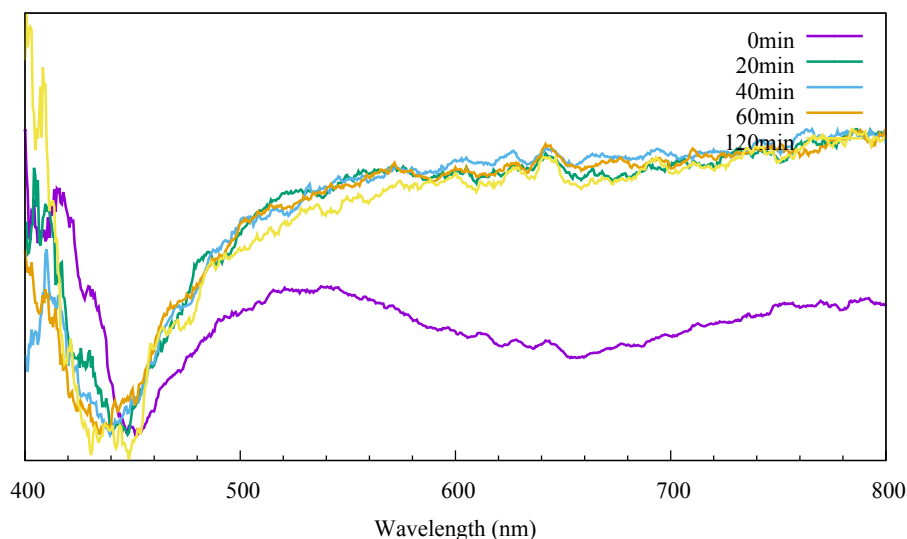


**Figure 3.33:** Normalised UV-vis absorbance of reaction **14b** (S1). Plot displays the UV-vis spectra of readings taken at 0 minutes, 20 minutes, 40 minutes, 60 minutes, and 120 minutes.

The final reaction was the formation of S2 (reaction **14c**). Similar to S1, and looking back at the rationalised structures observed in Section 3.2, it would be expected that immediate changes in the UV-vis spectra would be observed from the early stages of the reaction. Figure 3.34 shows the UV-vis spectra collected of the reaction mixture for reaction **14c**. The peak observed at  $\sim 640$  nm within the previous reactions of **13**, **14a**, and **14b** is present in the the UV-vis spectra of reaction **14c**, and a broad shoulder at  $\sim 475$  nm became more visible as the reaction progressed. There is little difference in absorbance from 0 minutes to 20 minutes. Although, a peak at 425 nm is observed at 0 minutes, which corresponds to the TBrPy monomer, and becomes less visible as the reaction progresses.



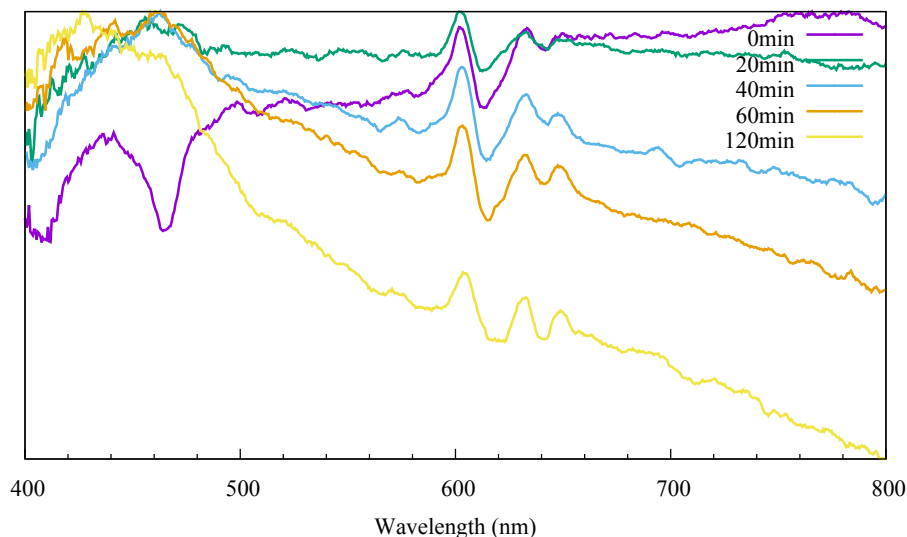


**Figure 3.34:** Normalised UV-vis absorbance of reaction **14b** (S2). Plot displays the UV-vis spectra of readings taken at 0 minutes, 20 minutes, 40 minutes, 60 minutes, and 120 minutes.

The intensity of the absorption peaks substantially reduce as the reaction progresses to 2-hours. The peaks observed between 600 nm and 650 nm reduced, and the broad shoulder observed from 450 nm becomes more visible. This change in UV-vis spectra suggests a reduction in catalyst absorption, with the S2 dominating the UV-vis absorption. Alternatively, it could be an indication that the catalyst is becoming inactive, showing a reduction in available catalyst molecules as bromine groups or monomers could not be released. However, this change is apparent after 40 minutes, and continues to change up to 2-hours.

The UV-vis spectra collected from reactions **13** and **14** show how the catalyst absorbs less intensely over the 2-hour reaction time. This suggests that the monomers *in situ* are reacting and producing material that absorbs more strongly as the reaction progresses. The visual appearance of the products obtained in reaction **14** all differ (Figure 3.35). The visible colour of S2 (reaction **14c**) closely resembles that of the TBrPy monomer. This is more apparent as the material isolated was soluble in H<sub>2</sub>O. S0 (reaction **14a**) and S1 (reaction **14b**) show some change in visible colour, with S0 bearing more resemblance to the products previously obtained (reactions **4 - 9**).

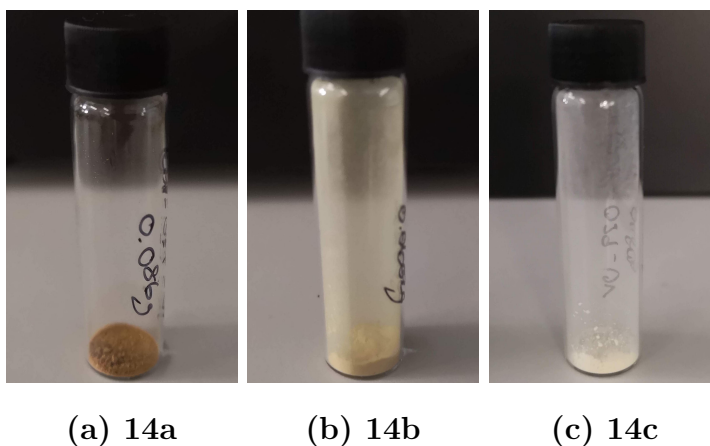


**Figure 3.35:** Solid products of reaction 14.

We have been able to observe the reaction mixture for YPy, S0, S1, and S2, to determine the formation of the CMPs and any potential molecular ring formation. The shifts in UV-vis absorption observed from reaction 13, YPy, suggested the formation of a material with different optical properties to both the catalytic mixture and the starting materials. This was similar for S0. The monomers could be seen more prominently for the first 20 minutes followed by a shift at 2-hours. S1 and S2 showed a similar shift, although the products obtained were both visually and optically similar to the pyrene starting material. Using this method, we had the potential to determine the rate of polymerisation, and thus infer at what point molecular rings were beginning to form.

This study showed that we were able to infer polymer formation during the reaction process for YPy, S0, S1, and S2. The changes in absorption of the UV-vis spectra were observed after the first 20 minutes for S1. The change in spectra was slower for S2, which showed a difference at 40 minutes into the reaction. However, there were no definitive differences between the UV-vis spectra of S0 collected at 0 minutes and 20 minutes, showing a prominent presence of starting material. The broadening of the peak at  $\sim 550$  nm was not seen until the end of the reaction at 120 minutes. This correlated with the computational theory that S0 would not display molecular rings within the early stages of the reaction.

## 3.4 Electronic structure analysis

### 3.4.1 Electronic structure comparison and HOMO-LUMO analysis

TD-DFT calculations were performed by Dr. Michael Peach and Peter Fletcher on the pyrene-based CMP structures originally generated through MD simulations. To reduce time and cost for each calculation the bromine end groups were replaced with hydrogen atoms. TD-DFT calculations were performed on the structures of YPy, S0, S1, and S2 to assess their electronic activity. The molecular mechanical structure generation showed the large difference in molecular rings between each material, with the S2 structures containing the most rings with each increase of building blocks, and S0 containing the least. The end groups were changed to hydrogen atoms in each case, and the structures remained non-optimised post-construction. Table 3.15 shows the excitation energies for the YPy clusters containing seven building blocks, and the calculated HOMO-LUMO gap.

Type	YPy		% structures generated
	Excitation energy (eV)	HOMO-LUMO gap (eV)	
Branched double ring	3.3693	5.31	1
Branched single ring	3.2872	5.14	25
Multi-branched chain	3.5258	5.42	30
Singularly branched chain	3.5047	5.41	38
Linear chain	3.6429	5.51	6
Average	3.4659	5.36	

**Table 3.15:** First singlet excitation energies and HOMO-LUMO gap of the varying structures for YPy; seven pyrene building blocks. The structure percentages are representative of the YPy structures generated with solvent.

The energetics of these clusters decreases from a straight chain structure to a structure containing a molecular ring, and the structure containing one molecular

ring within its structure shows the lowest energy. The difference between the one ring and two rings in the system is approximately 0.08 eV. This difference is a result of the conformation and configuration of the structure containing two rings as it is more strained to that of the single ring. The excitation energies calculated for the YPy clusters are in correlation to that of the reported literature.<sup>177</sup> The generated structures are larger than the previously observed structures, although the energy range calculated is between 3.3 and 3.6 eV, decreasing with the presence of molecular rings.

The inclusion of a linear co-monomer in the S0 structures generated affects the types of structure observed and therefore the excitation energies observed for the material. Table 3.16 shows the energies calculated for the available structures containing seven pyrene building blocks in S0.

Type	S0		
	Excitation energy (eV)	HOMO-LUMO gap (eV)	% structures generated
Branched single ring	3.0759	4.98	5
Multi-branched chain	3.3199	5.17	95
Linear chain	3.6198	3.6198	-
Average	3.3077	5.16	

**Table 3.16:** First singlet excitation energies and HOMO-LUMO gap of the varying structures for S0; seven pyrene building blocks. The structure percentages are representative of the S0 structures generated. The linear chain was included for comparison.

As it is shown, the more highly branched structure of S0 has a lower energy to the branched structures of YPy. This is also the case for the ring structure. The inclusion of a linear phenyl linker results in a less strained system, with few steric interactions. Therefore offering a much less energetic system. It would be expected that S1 does not follow this trend due to the system being more contorted and, therefore, more strained. Although, the system of S1 does show a reduction in energy from the chain clusters to the clusters with molecular rings present. Table 3.17 shows the energetics

of the S1 structures involving seven pyrene building blocks.

Type	S1		
	Excitation energy (eV)	HOMO-LUMO gap (eV)	% structures generated
Branched single ring	2.9651	4.54	35
Branched double ring	2.9630	4.72	8
Branched triple ring	2.7348	4.32	3
Multi-branched chain	3.0029	4.66	51
Double branched chain	3.3058	4.98	2
Singularly branched chain	3.2676	4.83	1
Linear chain	3.4972	5.31	-
Average	3.1052	4.77	

**Table 3.17:** First singlet excitation energies and HOMO-LUMO gap of the varying structures for S1; seven pyrene building blocks. The structure percentages are representative of the S1 structures generated. The linear chain was included for comparison.

There is a further reduction in energy in the S1 system. The energy difference between the ring structures and straight chain structures follows the same trend as S0 and YPy, with the linear chain having the greatest energy. The energetics between the types of structure presented reduce as the number of rings is increased, with the structure containing three rings having the lowest energy. This differs to that of the YPy structures as the energy rises with an increase in number of macrocyclic structures.

Table 3.18 shows the energetics of the S2 structures generated. More rings were able to form within the S2 structure, but to draw a comparison the maximum number of ring structures observed in the DFT calculations was four.

Type	S2		% structures generated
	Excitation energy (eV)	HOMO-LUMO gap (eV)	
Branched single ring	2.9115	4.30	45
Branched double ring	2.5081	4.34	20
Branched triple ring	2.6787	4.42	18
Branched quadruple ring	2.6805	4.61	1
Multi-branched chain	3.0799	4.55	16
Linear chain	3.3834	5.17	-
Average	2.8734	4.57	

**Table 3.18:** First singlet excitation energies and HOMO-LUMO gap of the varying structures for S2; seven pyrene building blocks. The structure percentages are representative of the S2 structures generated. The linear chain was included for comparison.

The structure containing two molecular rings has a much lower energy to that of S1 structure of the same configuration (2.508 eV and 2.963 eV respectively). The energy increase as the number of rings in the structures increases. The acute angle between the reactive groups on the 1,2-dibromobenzene linker means the building blocks are in closer proximity to each other, as well as the ring structures produced being very small and therefore highly strained.

The differences in HOMO-LUMO gap shows how the structures differ electronically as the number of molecular rings increases. The structures generated for YPy present the greatest energy gap despite having fewer building blocks in the system. Comparably, the structures containing two rings within the S1 and S2 structures show the lowest energies, whereas the singular ring has the lowest energy in YPy.

The structures generated for each material can differ conformationally. The structures containing a single ring in each material can be formed with four building blocks or greater, meaning that the strain exhibited by these structure can also vary resulting in the difference in energy. The generated systems of S0, S1, and S2 illustrate how the inclusion of a co-monomer can affect the excitation energy of the system, and

therefore the band gap of the overall material. The size and strain induced on the molecular rings causes the excitation energies to decrease. The larger system of S0 shows a HOMO-LUMO gap of 4.98 eV, whereas this decreases as the geometry of the co-monomer decreases (S1, 4.54 eV; S2, 4.30 eV). This in turn suggests a potential difference in energetics experimentally.

### 3.4.2 Orbital analysis of the pyrene-based clusters

To gain a more precise representation of the overall structure for the YPy, S0, S1, and S2 materials, the energetics of the representative structure types were calculated for each material. As there were a greater number of differing structures for S1 and S2, eleven clusters of differing type were selected from the data sets. Oscillation strengths and singlet excitation energies were calculated to understand distribution of energies with the variation in structural configuration. It was determined that the structures of YPy, S0, and S1 show a uniform distribution between 2.8 and 3.6 eV, which converted to a range of 440 nm to 340 nm. The maximum oscillator strengths are observed at 400 nm (3.1 eV) for each material. These lower energies arise from first singlet states of the structures with greater number of molecular rings as well as the configuration of the rings. A structure containing two molecular rings presents an energy and oscillator strength of its first singlet state similar to both the structure containing five and six molecular rings. Tables 3.19 to 3.22 shows the exact values calculated for the singlet states of each structure observed.

Structure type	Excitation wavelength (nm)	Oscillator energy (eV)
Branched 1	388.6	1.212
Double branched 1	422.1	2.848
Multi-branched 1	385.8	0.001
Multi-branched 2	402.1	2.433
Branched single ring 1	422.1	1.100
Branched single ring 2	395.7	1.485
Branched single ring 3	437.2	0.414
Branched single ring 4	401.9	2.002
Branched double ring 1	429.5	3.546
Branched double ring 2	436.4	2.495
Branched double ring 3	430.1	0.1297
Range	385 - 437	0 - 3.5

**Table 3.19:** Oscillator strengths and first singlet excitation wavelength, calculated from excitation energies, of the YPy structures containing seven pyrene building blocks.

Structure type	Excitation wavelength (nm)	Oscillator energy (eV)
Multi-branched 1	383.2	0.000
Multi-branched 2	386.9	0.001
Multi-branched 3	378.7	0.000
Multi-branched 4	386.6	2.089
Multi-branched 5	390.5	0.001
Multi-branched 6	387.9	0.001
Multi-branched 7	382.5	0.000
Multi-branched 8	385.4	0.008
Multi-branched 9	380.9	4.493
Branched single ring 1	386.6	0.001
Branched single ring 2	408.8	0.034
Range	378 - 408	0 - 2.1

**Table 3.20:** Oscillator strengths and first singlet excitation wavelength, calculated from excitation energies, of the S0 structures containing seven pyrene building blocks.



Structure type	Excitation wavelength (nm)	Oscillator energy (eV)
Multi-branched 1	418.1	1.675
Multi-branched 2	400.9	0.450
Branched single ring 1	405.1	0.731
Branched single ring 2	414.1	1.377
Branched single ring 3	396.4	0.830
Branched double ring 1	423.9	1.308
Branched double ring 2	440.8	2.119
Branched double ring 3	430.7	0.268
Branched triple ring 1	424.1	0.789
Branched quadruple ring 1	434.4	0.425
Branched quintuple ring 1	396.4	0.901
Range	396 - 434	0.2 - 2.1

**Table 3.21:** Oscillator strengths and first singlet excitation wavelength, calculated from excitation energies, of the S1 structures containing seven pyrene building blocks.

Structure type	Excitation wavelength (nm)	Oscillator energy (eV)
Multi-branched 1	386.7	0.003
Branched single ring 1	418.9	1.030
Branched single ring 2	406.4	1.185
Branched double ring 1	427.7	3.221
Branched double ring 2	456.7	0.043
Branched double ring 3	503.9	0.158
Branched triple ring 1	420.6	1.607
Branched triple ring 2	429.4	1.590
Branched quadruple ring 1	410.2	1.556
Branched quintuple ring 1	498.5	0.263
Branched sextuple ring 1	511.2	1.404
Range	386 - 511	0 - 3.2

**Table 3.22:** Oscillator strengths and first singlet excitation energies of the S2 structures containing seven pyrene building blocks.

The distribution of oscillator strengths for each of the CMP structures are shown in Figure 3.36.

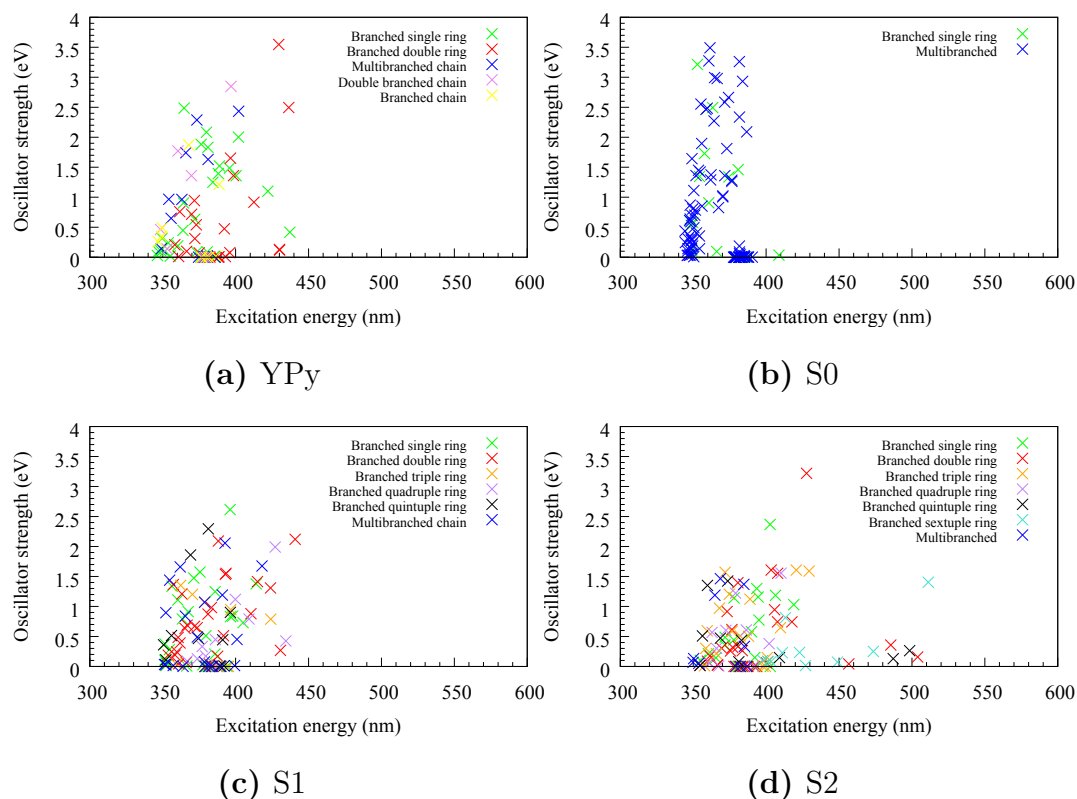


**Figure 3.36:** representative data plots of excitation wavelength vs. oscillator strengths for each material containing seven pyrene building blocks; (a) YPy, (b) S0, (c) S1, and (d) S2.

The limited number of structure types for S0 shows the energy profile for the branched chains that can form within the early stages of the reaction process. The oscillator strengths for each singlet are all situated between 344 nm and 400 nm, absorbing at lower wavelengths, and having greater excitation energies to the ring structures present in the structures of YPy, S1, and S2. The highly branched chains present in S0 have the highest excitation energies (lower excitation wavelengths) and HOMO-LUMO gap, and the ring structures present in the S2 structures show the lowest excitation energies (thus higher excitation wavelengths). This indicates how the ring structures affect the electronic structure of each system, as well as how the ring structures are highly favourable within these system. The larger number of rings

in a system is more favourable with an increase in building blocks, yet these can pose to be highly strained or contorted. There is a difference of 0.31 eV between the straight chain structures and the ring structures. The difference in energy between the S0 structures is minimal. However, ring structures can vary greatly in size, which suggests that the ring structures do not greatly influence the electronic properties of the S0 system. On the other hand, the structures generated of the S2 structure show a great difference. The energy decrease with the molecular ring increase shows that the rings are affecting the electronic structure. This coincides with the original theory that the molecular rings, and the strain induced between the building blocks on their formation, affects the overall energetics of the system. Observing the distribution of structures compared to their oscillator strengths it can be possible to construct an assumption on the differences in absorption (Figure 3.37).

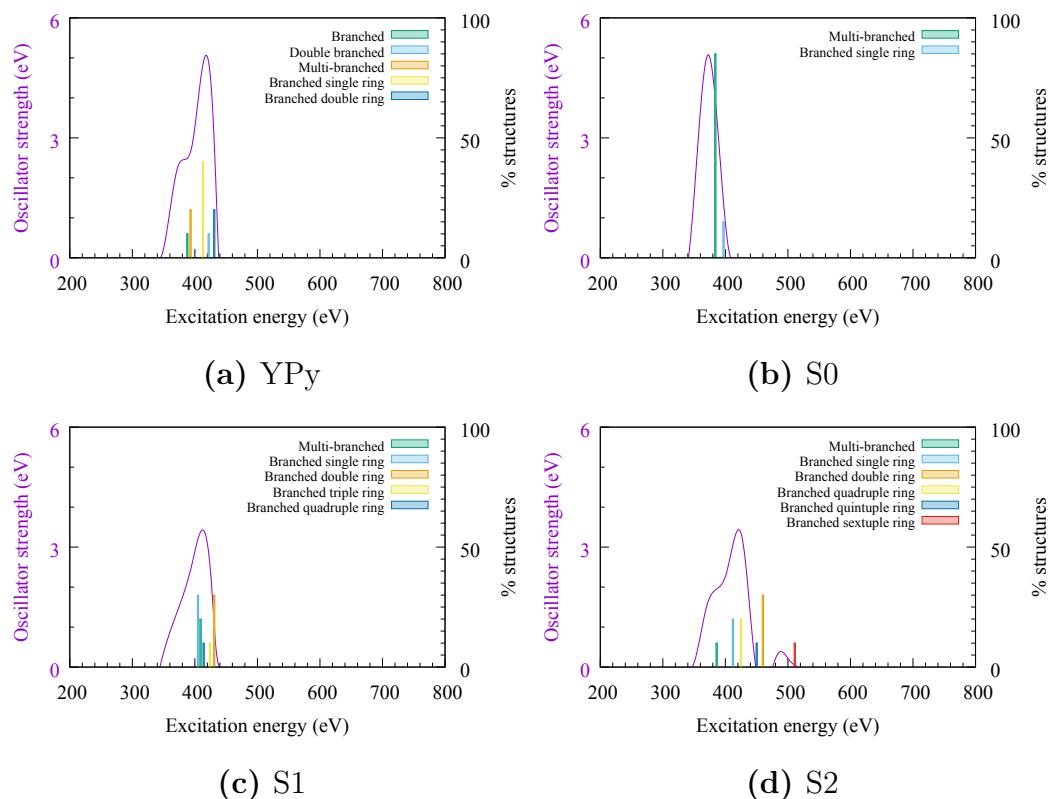


**Figure 3.37:** Comparison of structure types and the oscillator strength distribution against excitation energy. (a) YPy - (d) S2.

Previous analysis and calculations performed on pyrene molecules presented an experimental absorption peak at 334 nm, and a theoretical absorption peak at 328.5 nm.<sup>211</sup> With this in mind, we could infer a shift in absorption peak from the calculated excitation energies of the hydrogen substituted clusters generated to represent the bromo-substituted pyrene CMP. The UV-vis absorption spectrum of TBrPy collected gave a maximum peak at 432.5 nm, indicating a difference of 88.5 nm. Applying this difference to the excitation energies of the structures generated, we were able to infer the presence of the differing types of structure observed throughout the simulations within the synthesised product.

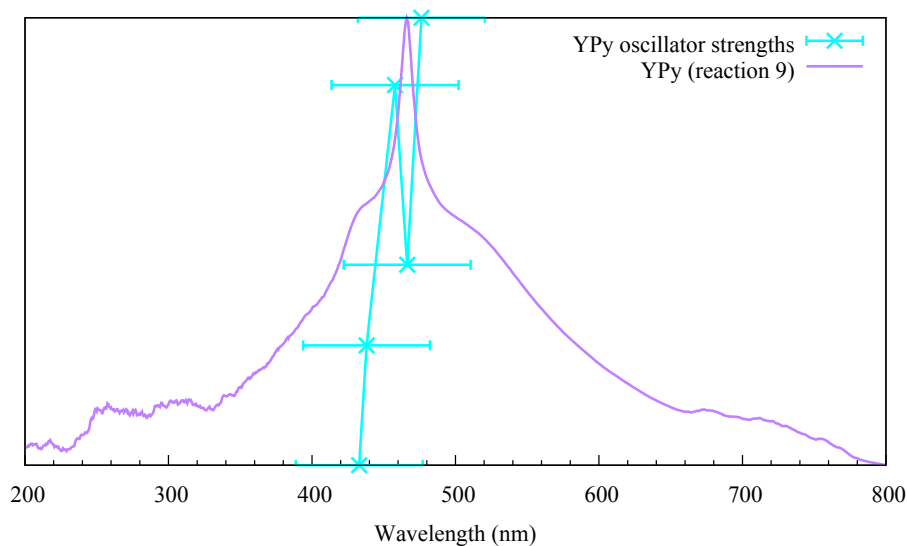


**Figure 3.38:** Comparison between the experimental UV-vis absorption peak of the YPy product (reaction **9**) and the observed oscillator strengths from the generated clusters of YPy. The error bars illustrate the suggested absorption range for YPy, with the minima calculated from the oscillator strengths calculated, and the maxima calculated from the difference in absorption between pyrene and the bromine substituted pyrene monomer.

Taking the average oscillator strengths of the generated structures types of YPy and multiplying these by the percentage of structural type generated, it was possible to obtain a representative absorption spectrum. Because the clusters generated contain a greater percentage of bromine endgroups to that of the reported materials,<sup>124</sup> the synthesised products are assumed to absorb within a wavelength range between the calculated energies of the hydrogen substituted clusters, and the difference in shift

between the pyrene and the tetrabromopyrene molecules (380 nm - 520 nm). This gives a peak at  $\sim$ , which coincides with the experimental data collected for YPy (reaction 9), shown in Figure 3.38.

Additionally, we were able to observe the differences in absorption between the types of structure generated. The clusters generated containing molecular rings displayed lower excitation energies to the branched chains, thus translating to a greater wavelength. With the inclusion of the shift, the observed experimental UV-vis and simulation oscillator strengths aligned. The inferred range from the excitation energies and oscillator strengths indicated that the ring structures would be visible between 500 nm and 520 nm. This coincided with the broad shoulder observed at  $\sim$ 510 nm of the YPy experimental UV-vis spectrum. Comparing the differences in excitation energy between the generated structures, it could be inferred that there was a mixture of monomer, chain structures, and ring structures present in the synthesised material.

If the calculated oscillator strengths and excitation energies of the varying structures correlate to the experimental data of YPy, we could infer the presence and extent to which the molecular rings have formed within the materials of S0, S1, and S2. There was a change in absorption between YPy, S0, S1, and S2 at approximately 510 nm. The observed shoulder is present within YPy, S1, and S2, but is not apparent in S0 (Figure 3.39).

In reference to the oscillator strengths calculated, we observe peaks in the materials of YPy, S1, and S2 that could be inferred towards the presence of molecular rings in the products (Figure 3.40). Because of the weaker absorbance in the UV-vis spectra at approximately 510 nm, it could be speculated that rings were being formed, yet their presence within the structure are much farther apart spatially, which would suggest that the largest peak observed experimentally indicates a more open, chain-like structure.

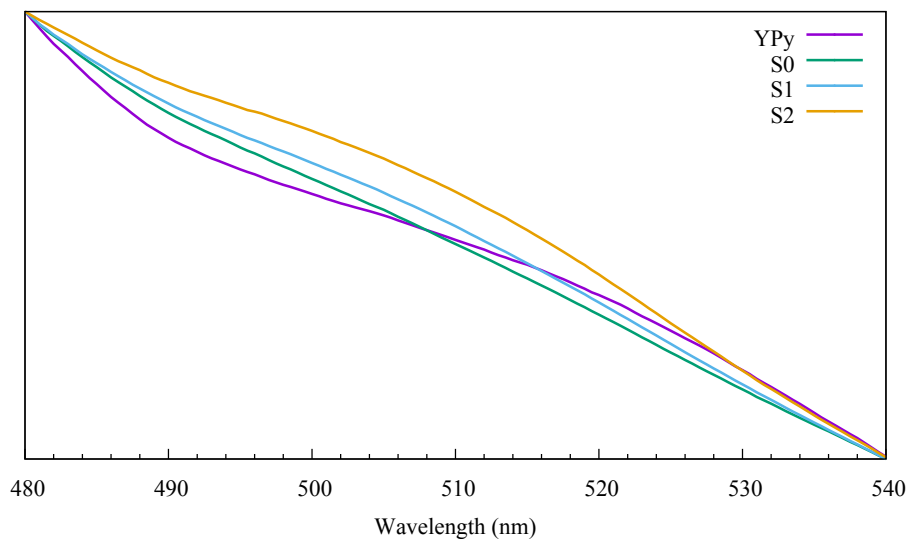


**Figure 3.39:** Comparison between the experimental UV-vis absorption peak of the YPy, S0, S1, and S2 within the range of 450 nm to 540 nm.

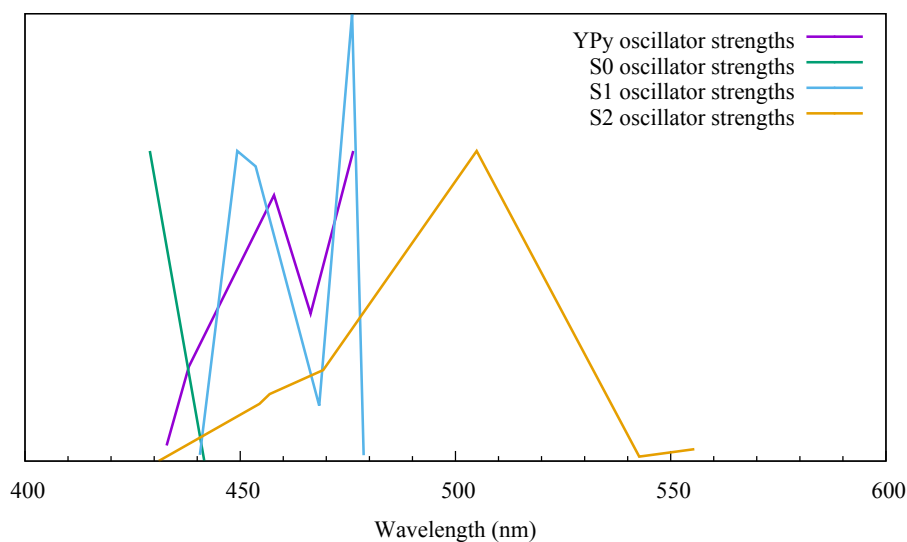


**Figure 3.40:** A comparison of the oscillator strength vs. the wavelength calculated for the materials of YPy, S0, S1, and S2, and their respective representative structures.

The structures generated for S1 and S2 displayed a greater number of molecular rings than YPy and S0, and also the lowest energetic structures. However, the predicted absorption of S0 was greater than that of YPy despite the lack of molecular rings observed within the structures generated. Analysis of the orbitals of these struc-

tures suggested that it was not only the molecular rings within the structures that are having an influence on the band gap for these CMPs. Figure 3.42 shows the electron density for the first singlet of the YPy system.

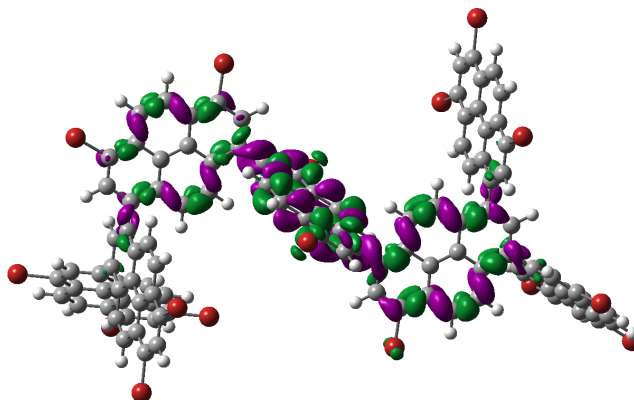


**Figure 3.41:** Electron density distribution for the first singlet excitation state of a branched YPy structure.

The only building blocks in the YPy structure are the pyrene monomers, which therefore shows the electron density residing over the polycyclic aromatic units. This is also the case for the triplet excitation states. (Figure ??).

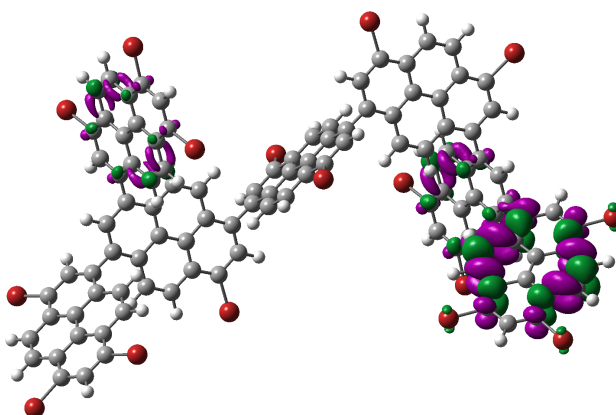


**Figure 3.42:** Electron density distribution for the first triplet excitation state of a branched YPy structure.

Observing the higher triplet states showed the electron density moving across the structure, but is still localised to the pyrene units. Figure 3.43 shows the electron density distribution for the fourth, seventh, and ninth triplet states of the YPy cluster.

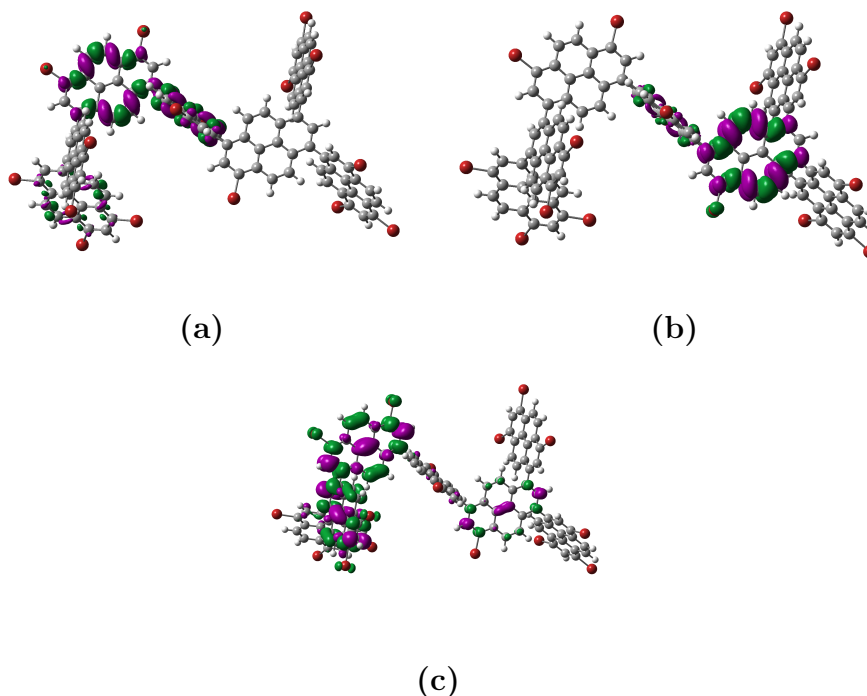


**Figure 3.43:** Electron density distribution of the branched YPy structure. (a) fourth triplet excitation state, (b) seventh triplet excitation state, and (c) ninth triplet excitation state.

The electron density distribution across the YPy cluster showed how the energetics of the system differ between the types of structure present within the overall construct. The shift between excitation states is a representation of how the electron density was shifted throughout the structure, and how conjugated the overall system is.

Electron density distribution calculations were also observed for the S1 structures to understand how the introduction of a linker can affect the electronic structure, and thus the band gap of the materials. Figure 3.44 shows the electron density of the first triplet excitation state of a branched S1 cluster. The electron density continues to reside over the pyrene building blocks with the inclusion of a co-monomer. This represents how the materials optical properties and band gap differ with the different



monomers, as the distance between electron density increases between the published materials of YPy, YDBPy, and YDPPy.

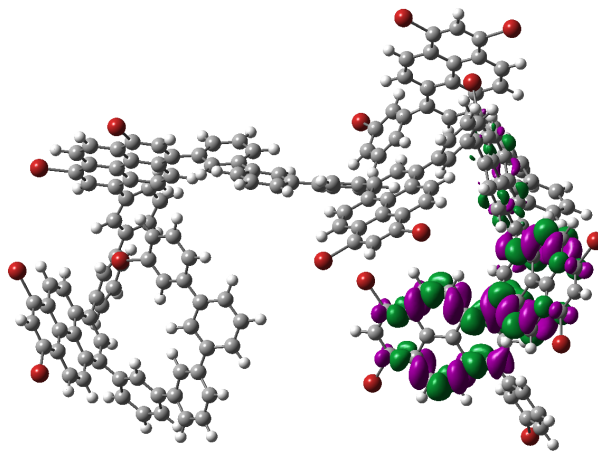


**Figure 3.44:** Electron density distribution for the first triplet excitation state of a branched S1 structure.

Observing the ring structures produced of the S1 material also gives further insight into how these molecular rings affect the electronic activity of the materials. Figure 3.45 shows the electron density distribution for the first triplet state of an S1 structure with a singular molecular ring. Similar to the straight chain structures observed of YPy, the electron density resides over the pyrene units.

Jiang *et al.* proposed how the delocalisation of CMP systems is disrupted with the inclusion of a co-monomer.<sup>212</sup> YPy, having no co-monomer, has a more delocalised system to that of the S0, S1, and S2 systems. With this in mind, the idealistic structures to tailor the band gap would be formed with pyrene building blocks in close proximity. Calculating the distances between the pyrene building blocks present in each structures shows how the pyrene building block can be further in space, removing the potential for orbital overlap. Statistically ordered structures were generated to assess the spacial distance between each pyrene building block.

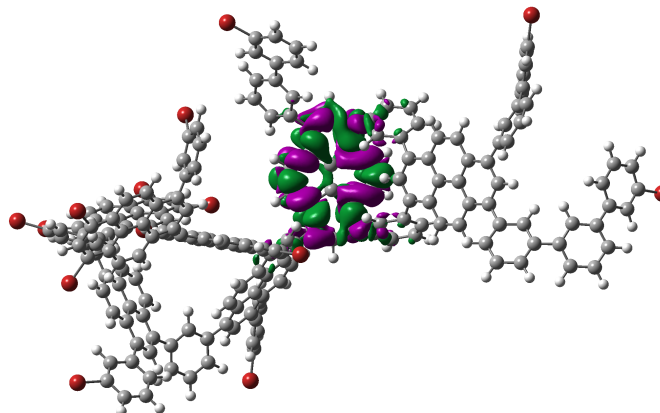


**Figure 3.45:** Electron density distribution for the first triple excitation state of an S1 structure containing a single ring.

The S0 and S1 structures show to be more spread into space compared to the YPy and S2 structures. This results in the pyrene building blocks having a greater distance apart from one another. Measuring the distance between the pyrene building blocks shows how the folding and dynamics of the structure, coerced by the directionality of the building blocks, can lead to the pyrene units being closer in space as seen with the YPy and S2 structures generated. The structures generated using AmBuild possess more realistic pyrene distances that would be found within the physical materials. Figure 3.46 shows the distances between pyrene nodes from the generated structures.

The distances between the pyrene building blocks becomes reduced as the structures are randomly constructed. As shown in Figure 3.46, the S2 structures illustrates the shortest distances between each node. The variation in distances between the pyrene nodes with the inclusion of a co-monomer means there is a lack of orbital overlap between the pyrene units. This therefore results in the localisation of electron density, leading towards a lack of overall conjugation.

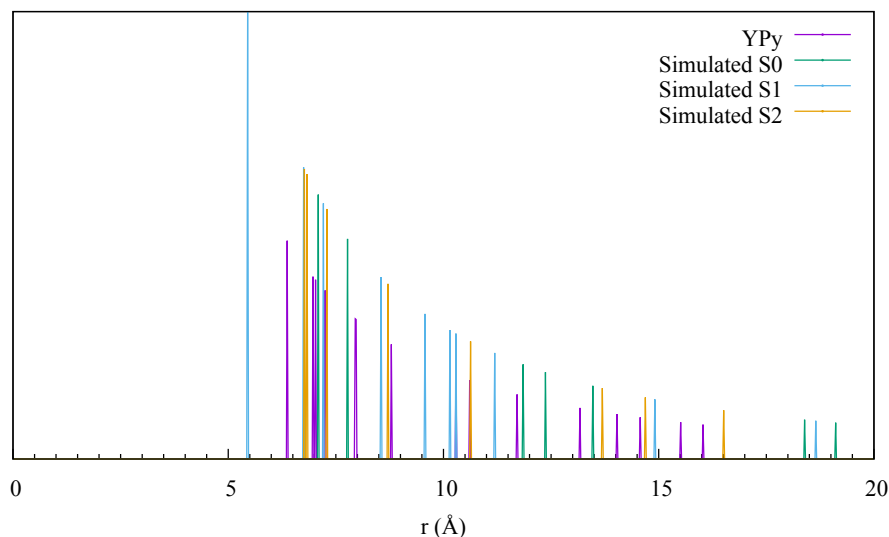


**Figure 3.46:** Distance between pyrene building blocks within the structures of YPy, S0, S1, and S2. RDF of the structures generated using AmBuild containing seven pyrene building blocks.

The strain on the molecular rings is also unpredictable. The structure of YPy can possess highly strained molecular rings contained of solely pyrene, which states how the band gap energy differs greatly to that of S0. The directional co-monomers of S1 and S2 can induce strain, yet the electron density has shown to localise across the pyrene units. It is because of this that there is no visible difference in material produced and the band gap calculated.

## 3.5 Conclusion

This research focuses on band gap tailoring of conjugated microporous polymers. It attempts to understand the differences in band gap observed with co-monomers of increasing size, as well as the attempt at synthesising novel materials to tailor this band gap further. The materials of S1 and S2 possess benzene linkers with differing configuration to influence the formation of the macrocyclic structures thought to be the limiting factor of the CMPs luminescent properties.

Analysis of the structural development between these materials showed how the number of molecular rings differed between the published YPy, YDBPy and YDPPy

materials. The inclusion of directionality with 1,3- and 1,2-dibromobenzene led to a great increase in number of molecular rings. The increase in molecular rings within these structures was the basis of understanding how the band gap can be manipulated further.

These materials were idealised in accordance to the hypothesis that the molecular rings present influence the luminescent properties. Materials were synthesised via the *Yamamoto* coupling reaction of the YPy, S0, S1, and S2 CMPs. However, due to unknown factors during the synthetic procedure, the reactions performed yielded non-porous materials. Analysis of the optical properties showed that the synthesised materials differed, although the UV-vis analysis showed a similar red shift with each product. An understanding of how the reaction process performs for the formation of porous media showed the fast formation of products from as little as 20 minutes into the reaction. As the reaction is fast acting, it is likely that the materials synthesised incorporated greater quantities of the monomers involved, and therefore increasing the packing and density of the materials. Studying the absorption of materials synthesised and the excitation energies for the structure computationally generated, we have been able to devise a tool for predicting the potential UV-vis absorptions for these materials. Imploring the idea that these materials can be experimentally synthesised, the UV-vis absorptions predicted display a great shift between the YPy structure, S0, S1, and S2 (469 nm, 498 nm, 551 nm, 586 nm respectively).

Reflecting on the hypothesis of how ring structures present within a structure could affect the band gap between these materials, the observation that the electron density resides over the pyrene building suggests that pyrene monomers are the influencing factor for the differences in band gap. This correlates with the optical properties of the materials synthesised. Each material possesses very similar colour transitions, as well as a red shift in the UV-vis absorption spectra between 420 nm and 480 nm as shown with reactions **4** to **9**, which indicates that the inclusion of linear linkers, increasing the distance between pyrene nodes, is a cause towards the differences between the porosity and photoluminescence. Although the structures of

S1 and S2 possess a increased number of molecular rings, orbital overlap is greatly reduced. The original hypothesis declared that fewer pyrene monomers included in the molecular rings would induce strain, planarizing the molecular rings to allow for orbital overlap. The structures produced for the S2 material possess highly strained rings in greater numbers. However, the orientation of the building blocks results in an axial configuration, and therefore reduces the potential for orbital overlap.

*"The most exciting phrase to hear in science,  
the one that heralds new discoveries, is not  
'Eureka!' but 'That's funny...'"*

---

—Arthur C. Clarke

## Chapter 4

# Development of organic porous carbon structures for lithium ion batteries

### 4.1 Introduction

Carbon is a very useful element as it has many biological and technological applications. Alongside its naturally occurring forms of diamond and graphite, synthetic allotropes include nanotubes, graphene, and graphite. The first allotropes synthetically developed were fullerenes by Kroto *et al.*<sup>213</sup> This has led to the development of a vast array of carbon allotropes with varying  $sp^2$ - and  $sp^3$ - hybridisation.

Graphite is the most widely used commercial anode in lithium ion batteries. However, graphite swells upon lithium ion uptake, and thus results in fractures and destruction of the crystal structure. Also, the formation of lithium dendrites on the graphite-electrolyte interface can cause the battery to short circuit. In addition, graphite has a low theoretical capacity ( $\sim 350\text{mAh g}^{-1}$ ). There is therefore a need for alternative carbon-based materials to act as alternative anodes materials for battery technologies.<sup>214,215</sup> Alternative anode materials include metal-oxide anodes,<sup>216–218</sup> lay-

ered sheets,<sup>219</sup> micro and nano constructs,<sup>219</sup> porous nanocages,<sup>220</sup> metal-oxide porous nanosheets,<sup>221</sup> and metal-organic frameworks.<sup>222</sup>

The polymer OSPC-1 (organically synthesised porous carbon) was developed with the intent to develop a porous polymer that can be applied as a new anode material. The synthesised polymer showed to be a pure carbon porous material ( $766 \text{ m}^2 \text{ g}^{-1}$ ), demonstrating high lithium ion uptake to make it a strong contender as an anode material in lithium ion batteries.<sup>148</sup>

## 4.2 Background

### 4.2.1 Experimental Research

All experimental research was performed by Ben *et al.* at the Department of Chemistry, Jilin University, Zhuhai, China. They synthesised the amorphous OSPC-1 polymer via a catalytic Eglinton homo-coupling<sup>223</sup> of ethynyl methane (Figure 4.1). The PXRD pattern shows an amorphous structure, as no Bragg diffraction peaks are observed (Appendix A.4).

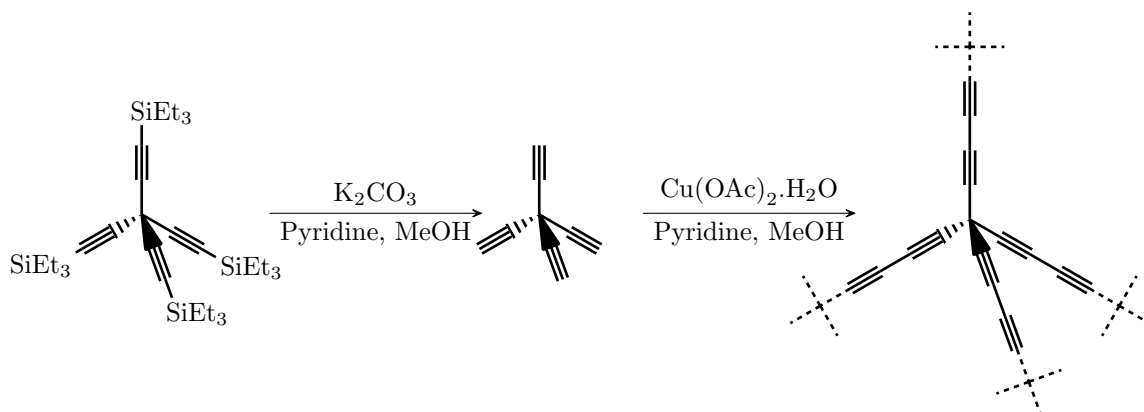


**Figure 4.1:** Synthesis of the OSPC-1 framework via Eglinton homo-coupling of ethynyl methane

A BET surface area of ( $\text{SA}_{\text{BET}}$ )  $766 \text{ m}^2 \text{ g}^{-1}$  was determined via analysis of the nitrogen uptake isotherm. The isotherm follows the type II trend, as seen in Figure 4.2, with rapid uptake at low relative pressures, indicating microporosity within the

structure.

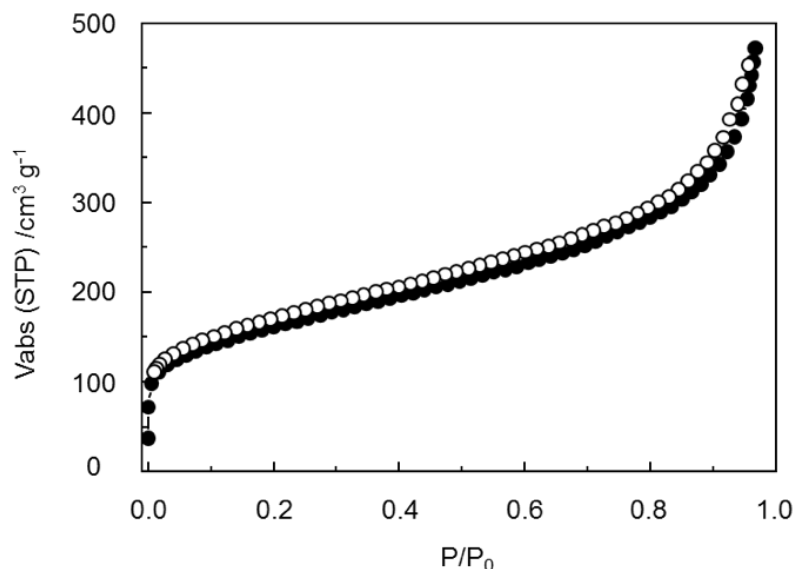


Figure 4.2: N<sub>2</sub> sorption isotherm of OSPC-1 at 77 K

### 4.2.2 Conductivity and Lithium Ion Uptake

Graphene and graphite possess electron conducting ability due to the highly delocalised orbitals of  $sp^2$  hybridised carbon bonding, offering a highly connected, open pathway for electron conduction. On the other hand, diamond, with its highly localised  $sp^3$  hybridised network, acts as an insulator. OSPC-1 has  $sp$  and  $sp^3$  hybridisation, with the  $sp^3$  carbons residing at the centre of nodes between each monomer. Therefore, one would expect very little in terms of conduction throughout the OSPC-1 framework. However, conductivity measurements on the material show a conductivity of  $\sigma = 1.2 \times 10^{-4} \text{ S cm}^{-1}$ , making OSPC-1 a semiconducting carbon material. This is attributed to a quantum tunnelling effect between the  $sp$ - orbitals of an adjacent strut of the same node.

A reversible lithium ion uptake of  $748 \text{ mAh g}^{-1}$  is obtained at a current density of  $200 \text{ mA g}^{-1}$  over 100 cycles (Figure 4.3a). In comparison, this exceeds many alternative materials, with the likes of C<sub>60</sub> ( $2.5 \text{ mAh g}^{-1}$ ), carbon nanotubes ( $324 \text{ mAh g}^{-1}$ ), and graphite ( $324 \text{ mAh g}^{-1}$ ). There is reversible capacity at higher current densities. Figure



4.3b illustrates the reversible capacities of 530 mAh g<sup>-1</sup>, 416 mAh g<sup>-1</sup>, and 356 mAh g<sup>-1</sup> at 1000 mA g<sup>-1</sup>, 2000 mA g<sup>-1</sup>, and 3000 mA g<sup>-1</sup>, respectively. More notably, upon reducing the current density back to 100 mA g<sup>-1</sup>, a very similar capacity is obtained to the initial cycle, offering a rate capacity of 944 mAh g<sup>-1</sup>.

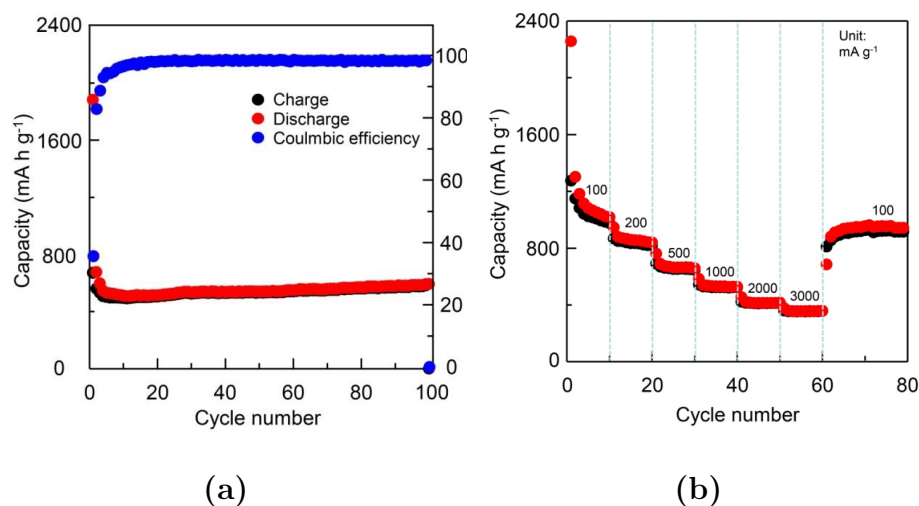


**Figure 4.3:** (a) Cycling performance of OSPC-1 showing discharge capacity (red), charge capacity (black), and coulombic efficiency (blue); current density of 200 mA g<sup>-1</sup> for 100 cycles. (b) Rate capability of OSPC-1 using varying current densities between 100 and 3000 mA g<sup>-1</sup>; discharge capacity (red) and charge capacity (black).

Overall, the newly developed carbon-based structure offers strong potential experimentally to outperform current lithium ion batteries. The long cycle life and high capacity demonstrate the stability of the interactions with lithium ions, along with its open framework, giving rise to a large internal storage space. To rationalise the uptake of cations, computational models were developed to illustrate the capabilities of this porous framework.

### 4.2.3 Structural Modelling and Molecular Dynamics

OSPC-1 monomers were produced via the use of Materials Studio,<sup>174</sup> and resulting periodic systems of the OSPC frameworks were developed through the in-house code AmBuild.<sup>224</sup> Trewin *et al.* produced a series of amorphous models and were able to simulate the lithium-ion capacity through simulated annealing using the *Sorption*

module in Materials Studio, offering a theoretical capacity of lithium ion uptake. Models-1a-e had a capacity of 1000 lithium ions, which equates to 420-579 mAh g<sup>-1</sup> (Table 4.1) as calculated using *Faraday's Law* shown in Figure 4.4. The generated models and their sorption of lithium ions is illustrated in Appendix A.5.

$$Q_T = \frac{1000 \times nF}{3600 \times Mw}$$

**Figure 4.4:** *Faraday's Law* for the calculation of theoretical capacity of the OSPC-1 models.  $Q_T$  units mAh s<sup>-1</sup>;  $n$  is the number of lithium ions (1000);  $F$  is *Faraday's constant*, units A s mol<sup>-1</sup>;  $Mw$  is molecular weight of the OSPC-1 system developed.

Model	Lithium ion uptake (mAh g <sup>-1</sup> )
Model-1a	420
Model-1b	579
Model-1c	457
Model-1d	579
Model-1e	420

**Table 4.1:** Theoretical lithium ion uptake for models 1a-e. Uptakes calculated using *Faraday's Law* and the molecular weights of the respective models.

Each model shows the uptake of lithium ions, and the possible locations for each individual ion to reside within the OSPC-1 framework. These models reflect the microporous properties of the OSPC-1 structure, and do not take into account the mesoporous regions of the material. Based upon the ratio of volume within the microporous and mesoporous areas obtained through the nitrogen uptake isotherm, a total capacity of 786 mAh g<sup>-1</sup> is obtained, in high agreement with the experimental value of 748 mAh g<sup>-1</sup>.

#### 4.2.4 Diffusion of lithium ions within OSPC-1

Trewin *et al.* performed Molecular Dynamics (MD) simulations consisting of ten lithium ions, seeded into the simulation box at random positions. Their trajectory

was followed during a 10 ns simulation, and lithium ions with different radii were used (1.39 Å and 1.46 Å) representing the minimum and maximum radius of lithium ions used previously. It can be seen in Figure 4.5 the trajectory of the individual atoms with radius of 1.39 Å, and this is a very similar case for those with 1.46 Å. The lithium ions comfortably diffuse throughout the volume of the OSPC-1 framework, diffusing more freely through the larger pores of the system, and gradually through the smaller pores.

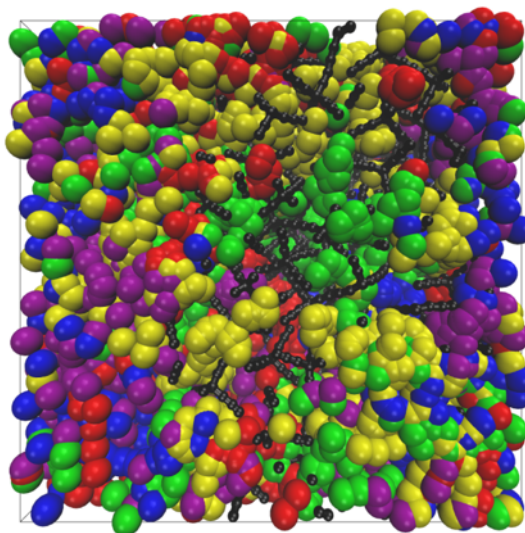


**Figure 4.5:** Trajectory of individual lithium ions (coloured) within the porous OSPC-1 system (black). Lithium ion radius of 1.39 Å.

For the lithium ions with a radius of 1.39 Å the calculated mean squared displacement was  $4.4 \times 10^{-10} \text{ m}^2 \text{ s}^{-1}$  and the diffusion coefficient was  $3.6 \times 10^{-10} \text{ m}^2 \text{ s}^{-1}$ . For the lithium ions with a radius of 1.46 Å the calculated mean squared displacement was  $4.2 \times 10^{-10} \text{ m}^2 \text{ s}^{-1}$  and the diffusion coefficient was  $3.4 \times 10^{-10} \text{ m}^2 \text{ s}^{-1}$ . These ion diffusion simulations correlate to those of lithium ion diffusion in alternate materials; for example, polyelectrolyte solution.<sup>225</sup> However, they significantly differ compared to nonporous materials, with the likes of graphite-Ni alloys ( $10^{-12} \text{ m}^2 \text{ s}^{-1}$ ),<sup>226</sup> Lithium oxides ( $10^{-12}$ - $10^{-17} \text{ m}^2 \text{ s}^{-1}$ ),<sup>79</sup> and graphite ( $10^{-13}$ - $10^{-14} \text{ m}^2 \text{ s}^{-1}$ ).<sup>227</sup>

### 4.3 Ion migration simulations

To assess the how lithium ions move through the OSPC-1 structure under the influence of a charge bias, which is termed here as **active diffusion**(Section 2.3.2), MD simulations were performed using DLPoly Classic with OSPC-1 structures produced using the Ambuild code previously described. The simulation cell has fixed dimensions of 30 Å x 40 Å x 70 Å, and models were produced in Materials Studio with graphene sheets layered on both XY periodic planes; Z=0 Å and z=70 Å. The initial simulation cells containing the graphene sheets is presented in Figure 4.6.

The PCFF<sup>154</sup> forcefield was used to generate the structures within AmBuild, and generate the input files for the MD simulations in DLPoly.<sup>228</sup>

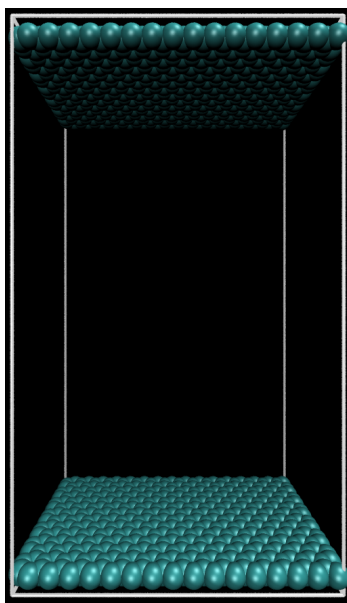


**Figure 4.6:** Initialised simulation cell contain the two graphene sheets across both X-Y planes; Z=0 and 70 Å

This model acts as the input for the periodic cell. The resulting OSPC-1 structures were produced using AmBuild, allowing individual monomers to grow between the graphene sheets. The OSPC models possess periodicity in the x- and y- directions, but growth in the z-direction is limited by the placement of the graphene sheets at the head and base of the simulation cell. Below is the basis of the OSPC-1 genera-

tion through AmBuild. The parameters and methodology were chosen to offer rapid growth of the systems. A fragment of the structural development using AmBuild is shown below:

```
#Here the input file containing the graphene sheets and lithium to give simulation cell.

mycell = cell.Cell(filepath='/opt/ambuild/blocks/Graphite-Lithium-1.car', atomMargin=0.1, bondMargin=0.5, bondAngleMargin =15,
doLog=False)

#Next, the building blocks of the OSPC-1 polymer are imported, and the available bonding groups - in this case it is the termi-
nating carbon atoms.

mycell.libraryAddFragment( filename='/opt/ambuild/blocks/tetra-1.car', fragmentType='tetra' )
mycell.addBondType( tetra:a-tetra:a)

#The system is initialised by the inclusion of the first monomer.

mycell.seed( 1, fragmentType='tetra', center=True)

#The OSPC-1 framework is developed by looping over the growth zip steps.

for i in range(200):
    if i == 1:
        x=i
        print str(x)+" dinosaur"
        mycell.growBlocks( 1, cellEndGroups=None, libraryEndGroups=['tetra:a'], maxTries=500 )
        mycell.zipBlocks(bondMargin=2.0, bondAngleMargin=70, clashCheck=False)
        i=i+1

#The parameters set in the Zip function allow the closed system to develop, bonding together any monomers within these param-
eters to another.

#After each growth cycle, a file with the updated atoms and coordinates is exported.

mycell.dump()
```

Each individual simulation was performed with the intent to maximise packing and bonding within the system, resulting in a cell filled with the OSPC-1 structure. It was necessary to increment the number of blocks input into the system with each bonding cycle to maximise the number of building blocks in the OSPC-1 structure. Figure 4.7 illustrates the building block used for the generation of the OSPC-1 framework, and Figure 4.8 illustrates the filled cell, with the lithium ions presented as pink van der Waals spheres.

The lithium ions were seeded into the simulation cell at designated positions at the top of the simulation cell. They were placed as closely as possible to the graphene

sheet so as not to interact with the OSPC-1 structure. Their positioning was also distributed across the x- and y- plane to fully explore the channels available through the OSPC-1 structure.

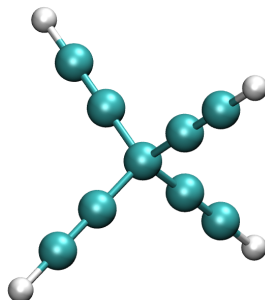


**Figure 4.7:** OSPC-1 monomer used for structural development; Built using Materials Studio, the blue spheres represent each carbon atom, and the white spheres represent the hydrogen atoms.

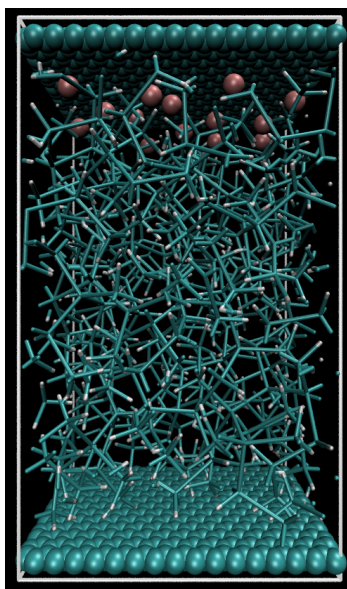


**Figure 4.8:** Simulated OSPC-1 structure between two graphene sheets with  $\text{Li}^+$  ions in situ

A total of 15 lithium ions were included in each simulation to explore all of the available pathways through the generated structure, and each MD simulation was performed using an optimisation and equilibration prior to charge application:

```

#These are the initial equilibration parameters for the simulation.
Simulation NVT
ensemble nvt hoover 0.1 1.0
steps 200000
equilibration 200000
traj 1 100 0
timestep 1.00E-4

#This is for running the simulation with charge bias applied.
Simulation NVT
restart
temperature zero
ensemble nvt hoover 0.1 1.0
steps 1000000

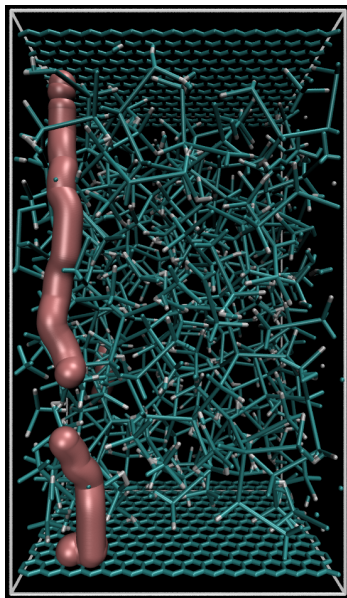
traj 1 100 0 timestep 1.00E-4

```

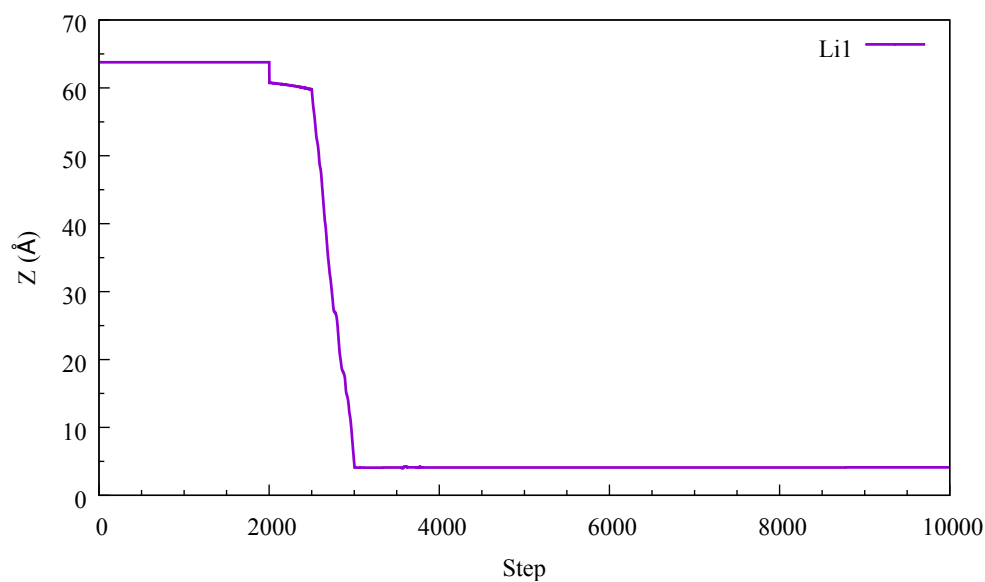
The graphene sheets were initially kept uncharged to minimise any interactions between themselves and the lithium ions. The uncharged graphene sheets allows for normal diffusion of the lithium ions during the initial steps. Applying the charge initialises the *active diffusion* of the lithium ions for the determination of their diffusion pathways.

### 4.3.1 Migration of lithium ions through OSPC-1

Each lithium ion in the simulation cell was readily able to migrate through the OSPC-1 structure generated from the positively charged graphene sheet to the negatively charged graphene sheet. The first lithium ion was able to establish a direct pathway through the structure with little sign of blockage or interference from the OSPC-1 structure (Figure 4.9). The movement of Li1 through the z-axis proved possible and demonstrated the porosity and available channels within the OSPC-1 structure. Figure 4.10 illustrates the z-axis movement of Li1 during the MD simulation. Although the lithium ion is required to manoeuvre around the carbon framework, its movement in the z-axis was fast, taking approximately 1000 steps to diffuse through towards the negatively charged graphene sheet. Initially, the lithium ion moves more slowly, which is down to Li1 moving around the first carbon atoms to determine its pathway. Li1 slowly establishes its pathway before traversing the z-axis through to the negatively charged graphene sheet (Figure 4.11).



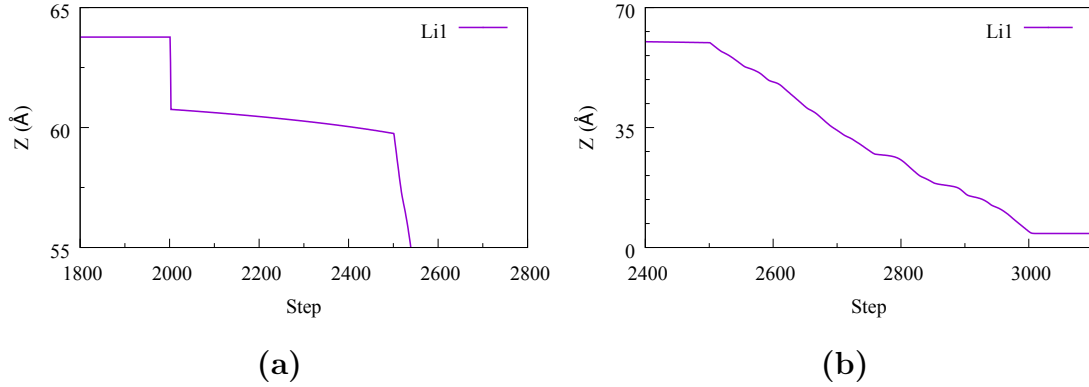
**Figure 4.9:** Lithium ion diffusion of a single lithium ion (Li1) through the OSPC-1 framework.



**Figure 4.10:** Plotted movement through the z-axis for the lithium ion diffusion through the OSPC-1 structure; Li(1).

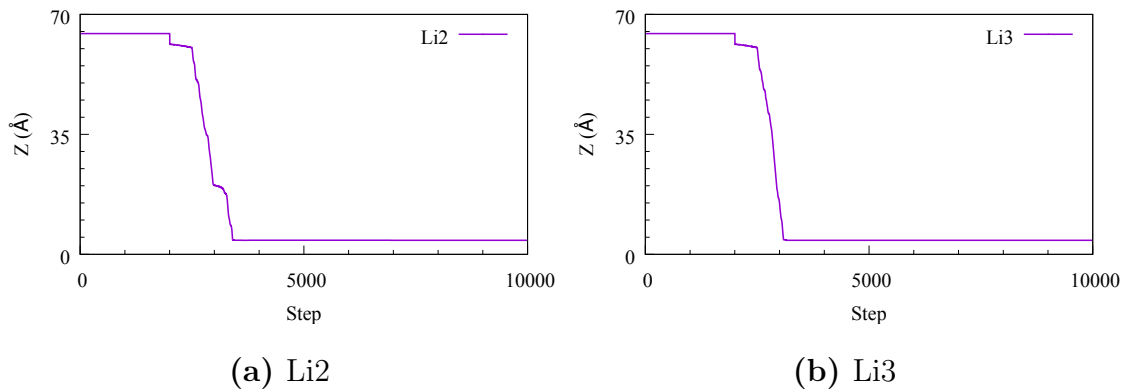
These commencing steps after the charge is applied do not discourage the movement of the lithium ion through the OSPC-1 structure generated, but they have illustrated an area of tightly packed building blocks, and highlighted that OSPC-1 can possess these dense areas within its internal structure.

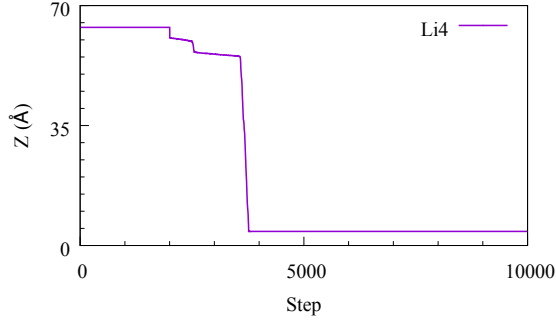




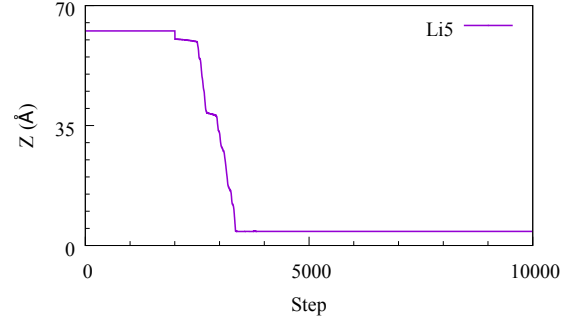
**Figure 4.11:** Enlargement of the post equilibration steps immediately after charge bias is applied at step 2000 for Li1 in OSPC-1. **(a)** Showing the movement between  $Z = 65$  Å to 55 Å and **(b)** showing the diffusion between steps 2400 and 3100.

The additional lithium ions within the system demonstrate very similar migrational behaviour through the OSPC-1 structure generated. Each ion is able to migrate completely through the structure towards the negatively charged graphene sheet (Appendix A.6l). The z-axis movement of each ion illustrates each lithium ions ability to establish a pathway through the system. Figure 4.12 illustrates the x-axis movement for the lithium ions Li2 to Li15. Each ion goes through the same establishment procedure as Li1, showing slow movement for the first several steps after the charge is applied. However, several ions exhibit areas of the OSPC-1 structure similar to that which Li1 had.

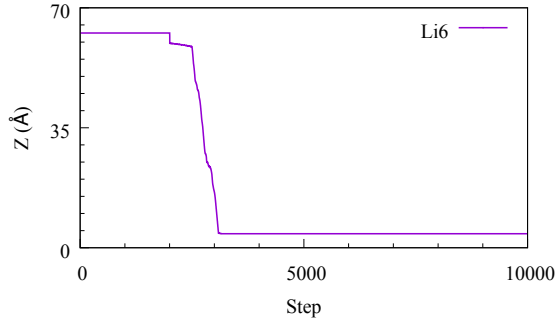




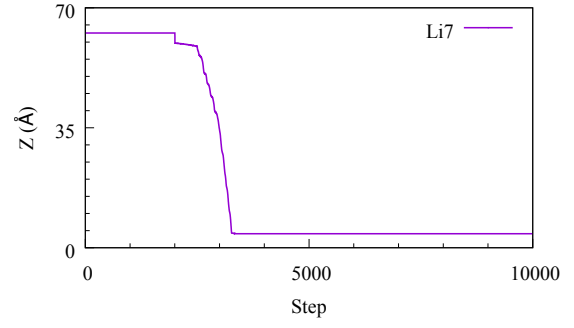
(c) Li4



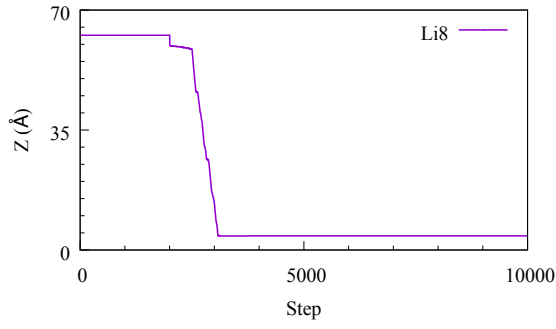
(d) Li5



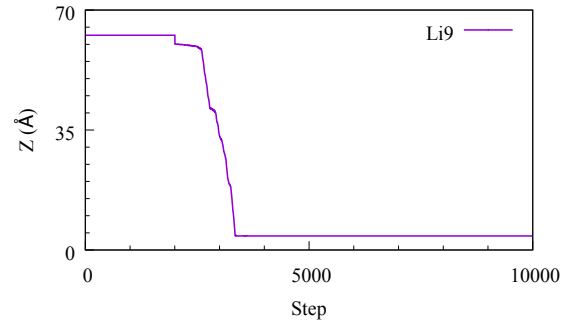
(e) Li6



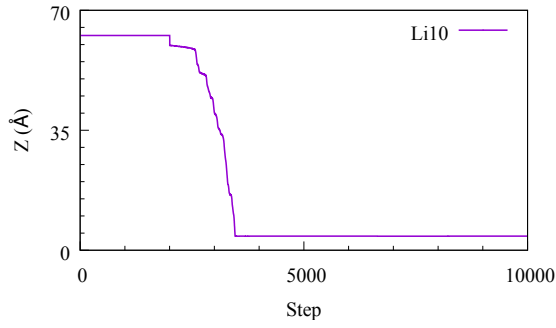
(f) Li7



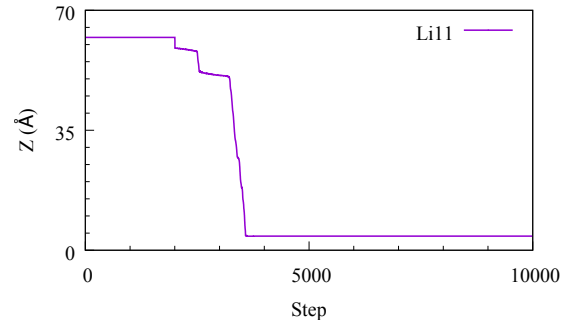
(g) Li8



(h) Li9



(i) Li10



(j) Li11

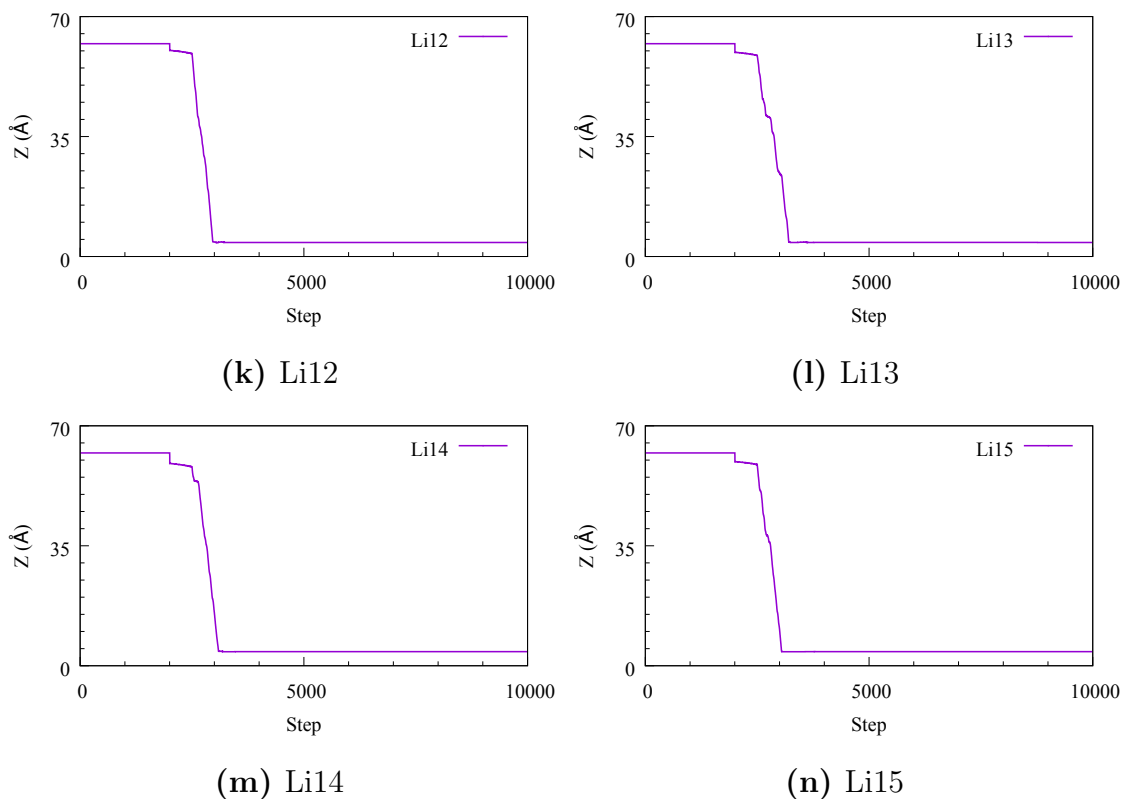


**Figure 4.12:** Migration plots of the individual lithium ions within the simulation cell of OSPC-1; (a) Li2 - (n) Li15.

Li4 and Li11 (Figures 4.12c and 4.12j, respectively) were examples of the lithium ions becoming trapped in tightly packed areas of the OSPC-1 structure. They were able to move approximately 10 Å from their origin, but their established pathway contains a blockage, with each ion showing reduced movement for several hundred steps. However, both were able to establish a new pathway that is highly direct, giving it a very short transport time from this point; Li4 showed an almost instantaneous move from  $\sim 55$  Å to the negatively charge graphene.

The remaining ions observed all showed particular positions in the z-axis with slightly reduced movement. Although, their transport from the positively charge graphene to the negatively charged graphene is much faster than that of Li4 and Li11. The rates at which these ions move through the OSPC-1 structure generated a shown in Table 4.2. These rates are calculated for the *active diffusion* of the lithium ions from step 2000 of the simulation.

Lithium ion	Ion mobility rate ( $\times 10^4 \text{ cm s}^{-1}$ )
Li1	5.88
Li2	4.22
Li3	5.47
Li4	3.32
Li5	4.25
Li6	5.30
Li7	4.55
Li8	5.36
Li9	4.28
Li10	3.95
Li11	3.61
Li12	5.94
Li13	4.75
Li14	5.24
Li15	5.48
Average	4.78

**Table 4.2:** Mobility rates of the individual lithium ions within the OSPC-1 system; diffusion rates calculated from the activation of the charges on each graphene sheet at step 2000.

Due to these diffusion rates being calculated from the active diffusion, they are comparably larger to the charge-free and experimental diffusion coefficients ( $4 \times 10^{-4} \text{ cm}^2 \text{ s}^{-1}$ ). Therefore, the rates are used to demonstrate the available pathways within OSPC-1, and also how the structure can affect the movement of lithium ions through its confines. Figure 4.13 illustrates further how each lithium ion differs in diffusion rate, and how each differs to the average rate calculated from the simulation.

The size of the charge applied, along with the flexibility of the node-to-node struts between the  $sp^3$  carbons allows for the lithium ions to establish pathways through the network.

The applied charge means that the lithium ions move towards the anode and will impose a force upon the carbon atoms of the framework that are in their path.

However, the microporous system does contain pockets in which the ions become trapped as the lithium ions cannot find a way out, as shown with Li4 and Li11. The rate at which the lithium ions diffused is greatly affected by these pockets, although, as shown with the diffusion simulation, these lithium ions were able to completely diffuse through the OSPC-1 structure generated.

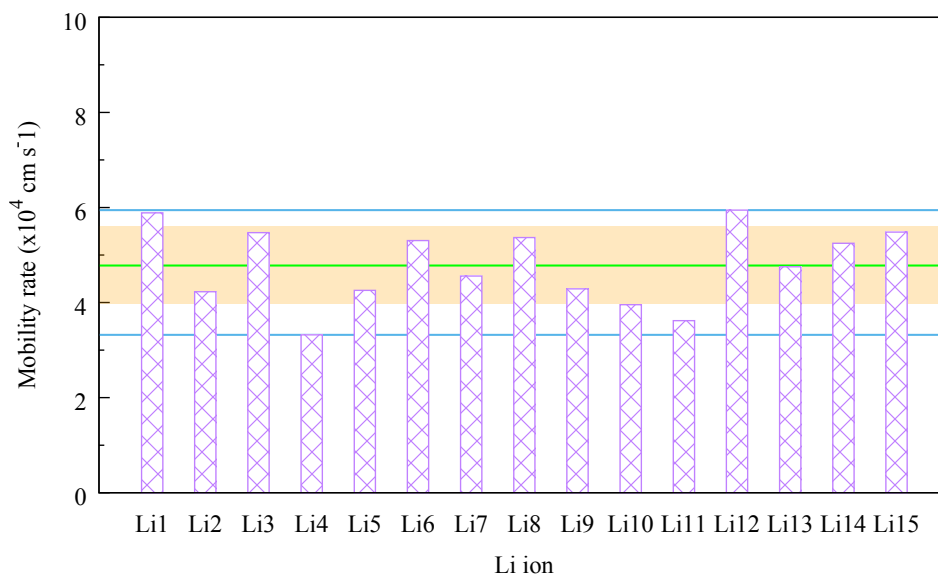


**Figure 4.13:** Plot of diffusion rates for the individual lithium ions within the OSPC-1 system; the green line represents the average diffusion rate, the upper and lower blue lines represent the maximum and minimum calculated rates respectively, and the highlighted region depicts the standard deviation of the mobility rate.

To determine how the carbon framework is affected by the movement of the lithium ions, and vice versa, the distance between the fastest moving and slowest moving lithium ions (Li12 and Li4, respectively) and the nearest carbon atoms were measured (Figure 4.14). The distance of the closest carbon was determined for every 50 steps of the simulation. There is little difference between the two lithium ions as they traverse the OSPC-1 system. However, Li12 shows an increase in distance at approximately 3000 steps. This is an indication towards its movement away from the carbon framework and closer to the negatively charged graphene sheet. On the other hand, Li4 shows displays close distances to the carbon framework up to  $\sim 3500$  steps, where it increases its distance greatly.

The difference in mobility rate, and the movement in z-axis of both Li4 and Li12 give indication towards the size of the pathways they both established. Li4 is unable to move for several hundreds of steps, whereas Li12 is able to establish a direct pathway much more freely (Figure 4.15).

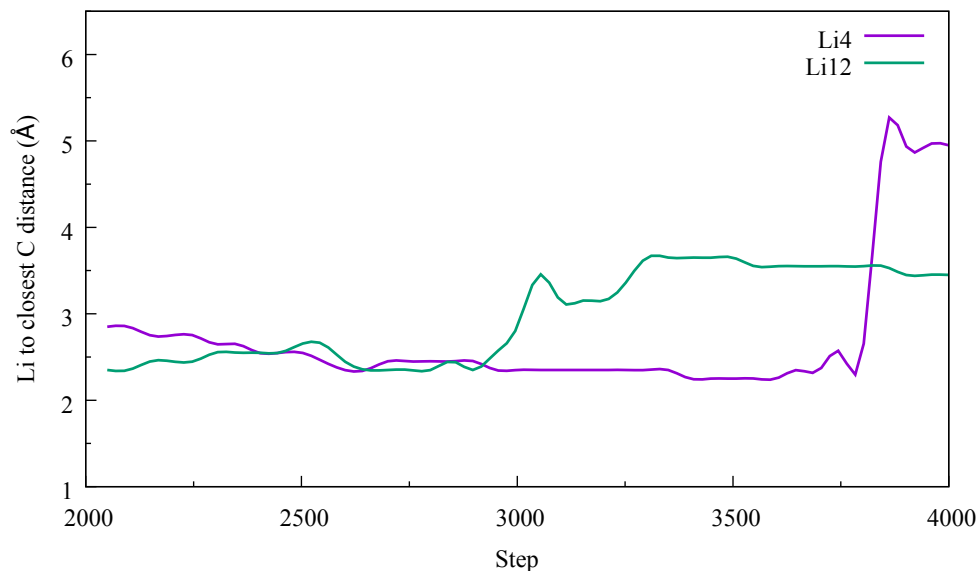


**Figure 4.14:** Distance between the lithium ions and the closest carbon of the OSPC-1 structure generated, collected over two thousand frames; Li4 (slowest) and Li12 (fastest).

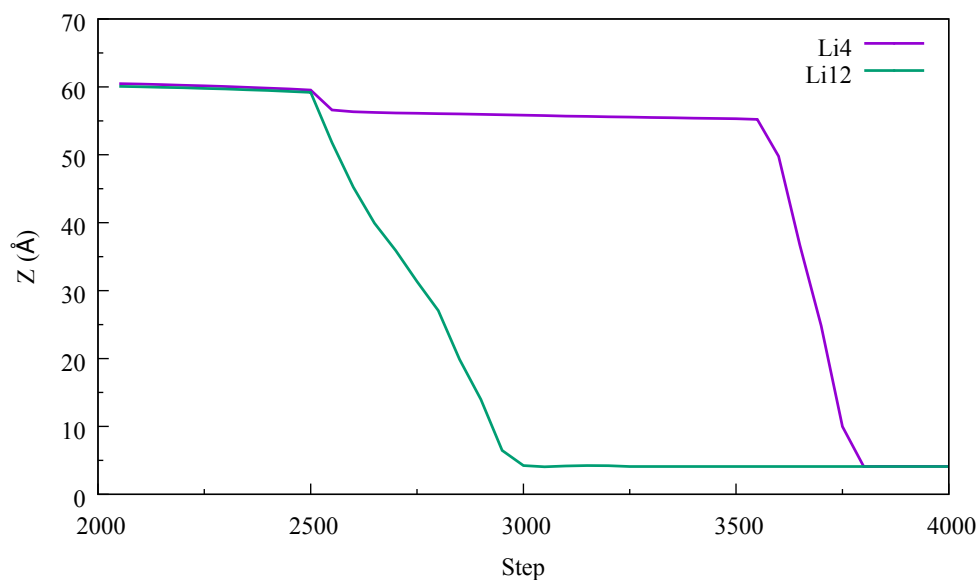


**Figure 4.15:** Li12 vs. Li4 migration; distance vs. simulation time

In addition, the distance between the lithium ions and the carbon framework give further indication to where the lithium ions surpass the opposite end of the structure, reaching the negatively charged graphene sheet.

Observing their movement through the OSPC-1 structure, Li12 displayed a greater distance from the carbon atoms to that of Li4. Both ions showed fluctuations in distance as they travel through the system, yet the faster ion (Li12,  $5.94 \times 10^4$ ; Li4,  $3.32 \times 10^4$ ) displays a minorly greater distance throughout its migration (Figure 4.16). Due to the availability of open pathways for the lithium ion to traverse, Li12 was able to determine a more open channel than that of Li4, which observed a stationary period closer to the positively charged graphene sheet. Therefore, the mobility rate can be related to the interactions with the framework, and thus the available pathways for the ions to travel.

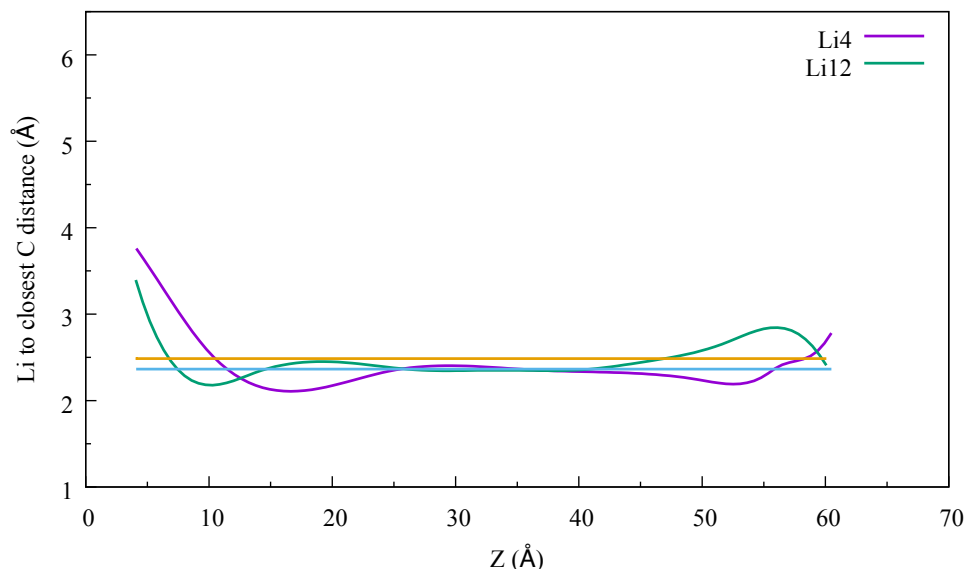


**Figure 4.16:** Measured distance between the lithium ions (Li4 and Li12) to the closest carbon atom of the OSPC-1 framework. The blue and yellow lines represent the average distance for Li4 and Li12 respectively.

As established, Li12 established a wider pathway, which had an average of 2.486 Å, whereas Li4 has a much narrower pathway (average 2.364 Å), and therefore establishing a more difficult path for the lithium ion to traverse. With lithium having a radius of the lithium ion is 1.4 Å, Li4 is unable to move through along the narrower

pathway, and was only able to force its way through at approximately step 3750.

Due to the greater negative and positive charges of the graphene sheets, the lithium ion was strongly attracted to the negative charge. Due to this, it applies great force onto the structure of OSPC-1, which forced the OSPC-1 structure to move and therefore allowing the lithium ion to pass. This is shown in Figure 4.17. The distance between these specific carbon atoms of OSPC-1 increase as the lithium ion passes between them, proving how the flexibility of the *node-to-node* struts allows the carbon structure to shape around the lithium ions as they pass through the system.

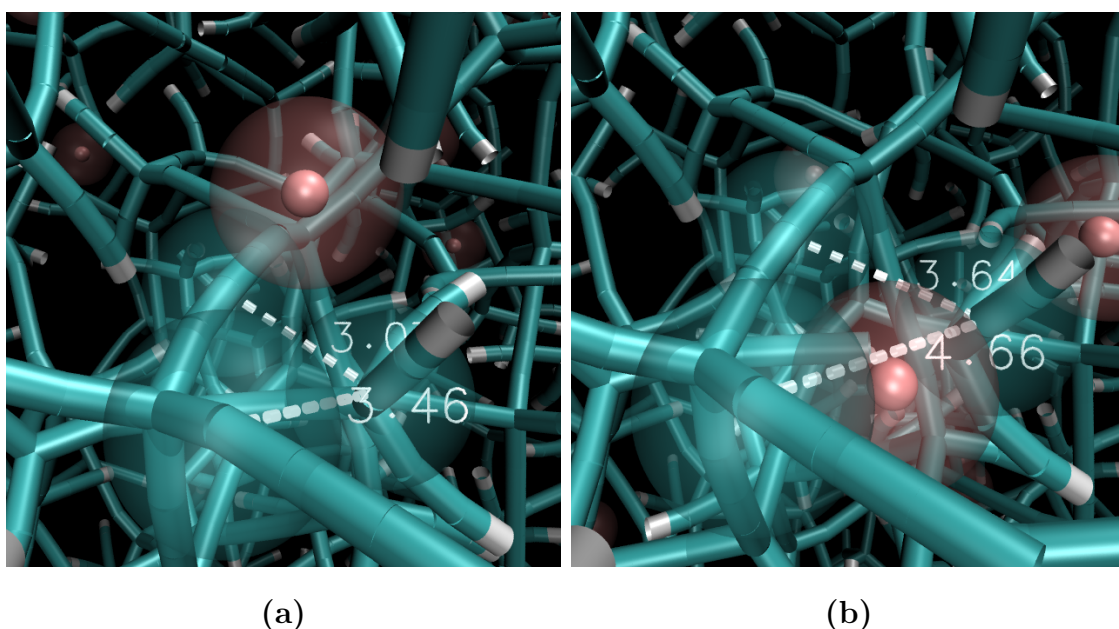


**Figure 4.17:** Carbon movement with lithium ion migration within OSPC-1; (a) initial distance and (b) movement with lithium ion diffusion.

Several **carbon-carbon** distances have been observed during the lithium ion migration simulation. Figure 4.18 shows these separations over the simulation period at which the lithium ions migrate from the positively charged to the negatively charged graphene sheets. The structure of OSPC-1 contains available channels for the lithium ions to travel, however, there are pathways in which several ions travel that are narrower in comparison. The  $sp^3$ - $sp^3$  struts bend and flex to allow the passage of ions through the system.



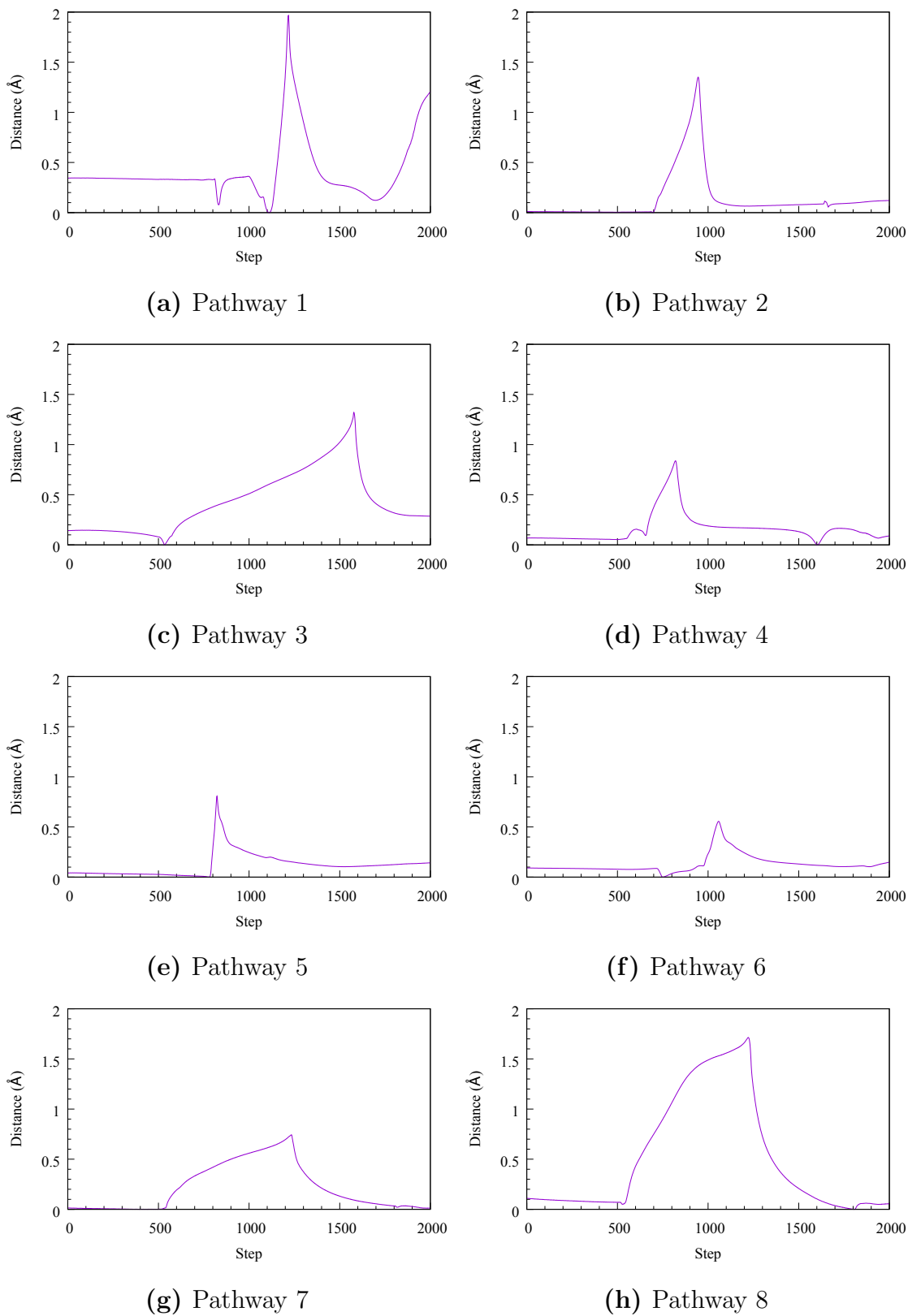


**Figure 4.18:** Distance movement of carbon atoms within the lithium ion pathways of OSPC-1.

The flexibility of the OSPC-1 structure allows the lithium ions to establish a more open volume within the material, therefore allowing the lithium ions to readily migrate through the system. The charge bias influences the movement of the carbon atoms of OSPC-1 as the lithium ions are being forced in one direction. Table 4.3 shows the  $\Delta_{\text{Distance}}$  between the carbon atoms observed.

Pathway	Max displacement ( $\Delta\text{\AA}$ )
1	1.966
2	1.351
3	1.321
4	0.838
5	0.807
6	0.556
7	0.743
8	1.714
Average	1.162

**Table 4.3:** Max displacement of the carbon atoms within the OSPC-1 structure during lithium ion diffusion.

This movement shows that the pathways available within the OSPC-1 structure are still not wide enough to allow lithium ions to pass through. The *active diffusion* of the simulation forces the lithium ions through the system, which in turn moves the OSPC-1 structure to allow passage. The average movement of the carbon atoms is 1.162  $\text{\AA}$ . This also describes how these materials behave internally with the presence of a guest material.

### 4.3.2 Conclusion

OSPC-1 shows great potential as a lithium-ion battery. The migration simulations performed demonstrate the potential performance of lithium ion diffusion through the framework with a charge bias, giving an average mobility rate of  $4.78 \times 10^4 \text{ cm s}^{-1}$ . The inclusion of charged graphene sheets within the simulation introduces a *push-*

*pull* behaviour, forcing the lithium ions through the structure towards the negatively charged graphene sheet. However, the internal porous properties of the material do not inhibit the transport of ions through the system, as direct pathways are established for each individual lithium ion input into the system.

These pathways vary in size. The narrower pathways require the lithium ions to move the structure of OSPC-1 to allow passage through the system. From the pathways observed, the average distance the carbon atoms have to separate by is 1.162 Å. The movement and flexibility of the structure creates the available channels for lithium ion diffusion.

## 4.4 Alternative OSPC-based materials

To demonstrate the potential of OSPC-1 as an anode for lithium-ion batteries, and to expand upon this family of materials, several similar structures, based on the OSPC-1 topology, have been proposed. Differing the length between the  $sp^3$  carbon nodes may change the porous structure in comparison to that of the OSPC-1 framework. Extension of the struts between nodes potentially gives rise to larger pore sizes, and greater pore volumes, which, in turn, produces larger pore channels. However, with longer struts and larger pore channels comes the potential for interpenetration within the network. This will reduce the pore diameter, and therefore potentially affect the rate of ion diffusion.

On the other hand, reducing the length between the  $sp^3$  carbon nodes offers a greater surface for small molecules to interact with. The downside of a greater surface area is that the pores within the network are potentially not large enough for molecules to channel through. This technicality is ideal for selectivity and separation, tailoring the pore sizes to specific sizes to allow only specific molecules through. There is potential to tailor the OSPC structure for specific ions, including lithium ions.

Here three polymers based on OSPC-1 are proposed. OSPC-0 reduces the  $sp^3$ - $sp^3$  distance by reducing the node-to-node distance with a reduction of alkyne bonds in the

strut, from two to one. OSPC-2 and OSPC-3 increase the node-to-node distance by including additional alkyne bonds between the  $sp^3$ -carbon nodes, giving a potentially greater pore size distribution. The alkyne struts between the  $sp^3$  nodes is illustrated in Figure 4.19 for OSPC-2 and OSPC-3.

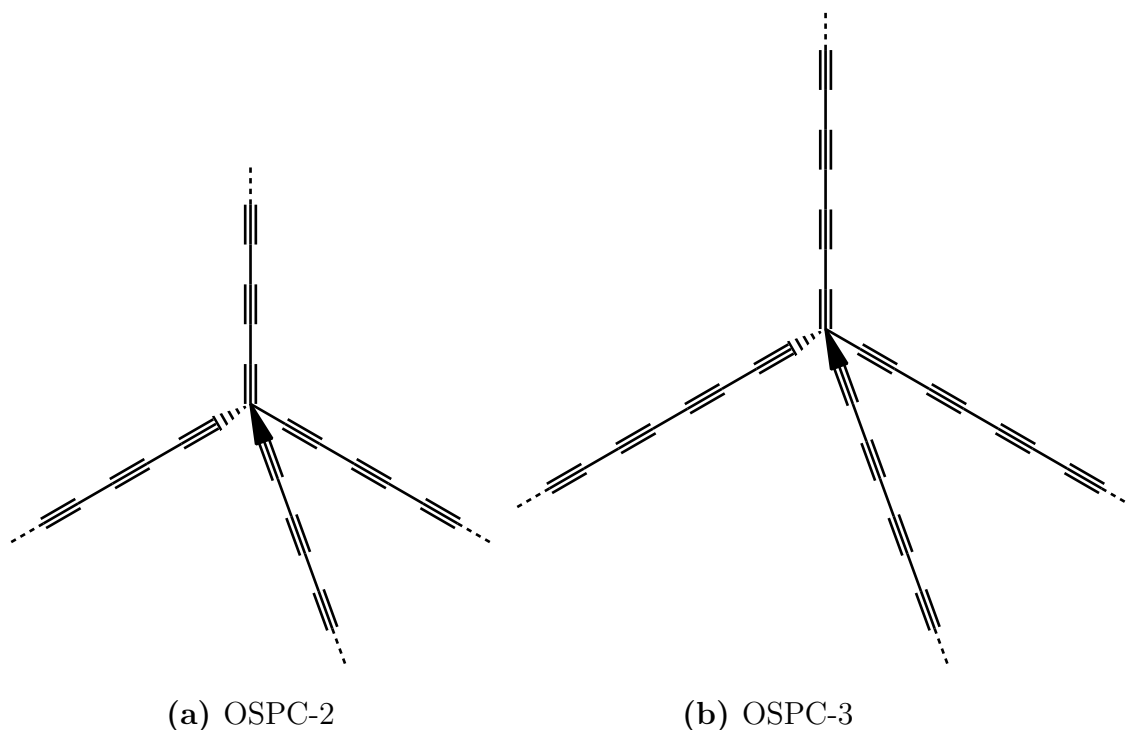


**Figure 4.19:** Theoretical representations of the  $sp^3$  nodes and the incorporated linkers for (a) OSPC-2, and (b) OSPC-3.

While these are hypothetical materials, we still need to ensure that they are synthetically viable. Hence here we discuss potential synthetic pathways. For OSPC-2 and -3, the basis of the synthetic methodology is derived from that of OSPC-1. The building block of OSPC-1 is a TES-protected tetrathynylmethane. This can then be unprotected using the same process given for OSPC-1 (Figure 4.1; potassium carbonate, with pyridine and methanol) to give monomer **1**. This process can be utilised further to produce monomer **2**. The key steps of which are shown in Figures 4.20 and 4.21.

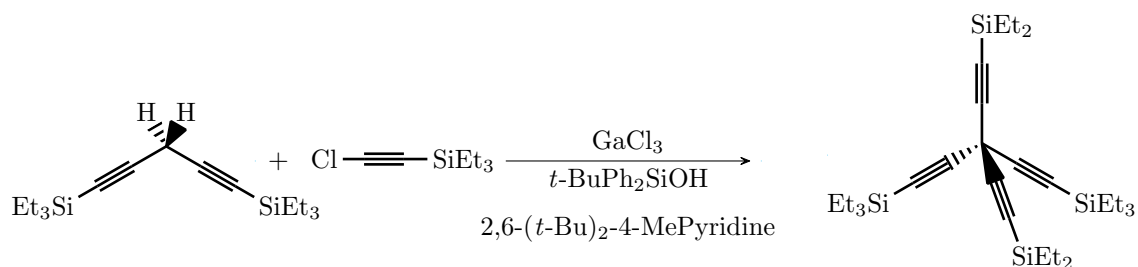


**Figure 4.20:** Synthesis of TES-protected tetraethynylmethane<sup>229</sup>

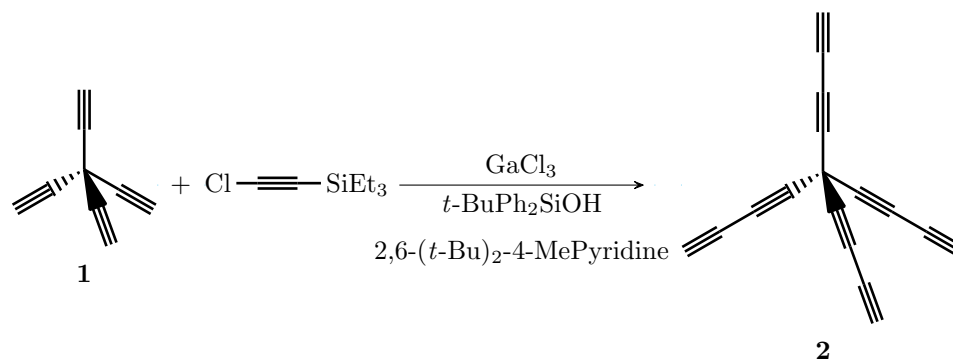


**Figure 4.21:** Rationalisation of extended tetraethynylmethane monomer (**2**) from the tetraethynylmethane monomer (**1**), via  $\text{GaCl}_3$ -promoted ethynylation.

For OSPC-2, where there are three alkyne groups present within the  $sp^3$ - $sp^3$  struts, the proposed method is to combine the monomers of **1** and **2** (Figure 4.21). However, this will result in a random combination of the monomers, and therefore a variation of two, three, and four alkyne groups linking each  $sp^3$  carbon in the framework (Figure 4.22). With this combination of monomers, it would be assumed that the porosity of the material would also deviate from that of OSPC-1, dependent on the reactivity of the monomers in solution.

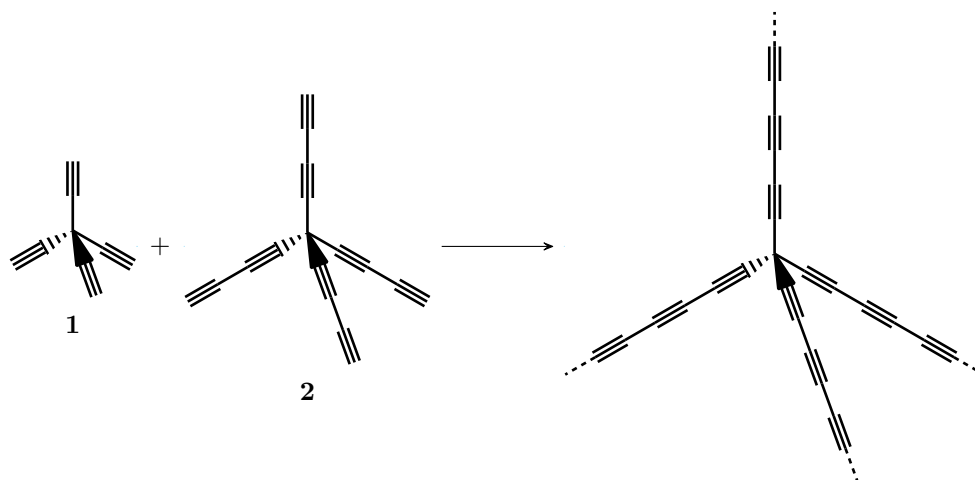


**Figure 4.22:** Rationalised synthesis of OSPC-2, via Eglinton Coupling; Co-coupling of monomers **1** and **2**.

For the synthesis of OSPC-3 we have recommended the homo-coupling of monomer **2** via the proposed synthetic procedure used for OSPC-1. This would result in structure proposed in Figure 4.23, where four alkyne groups make up the struts between the  $sp^3$ - $sp^3$  carbon nodes.

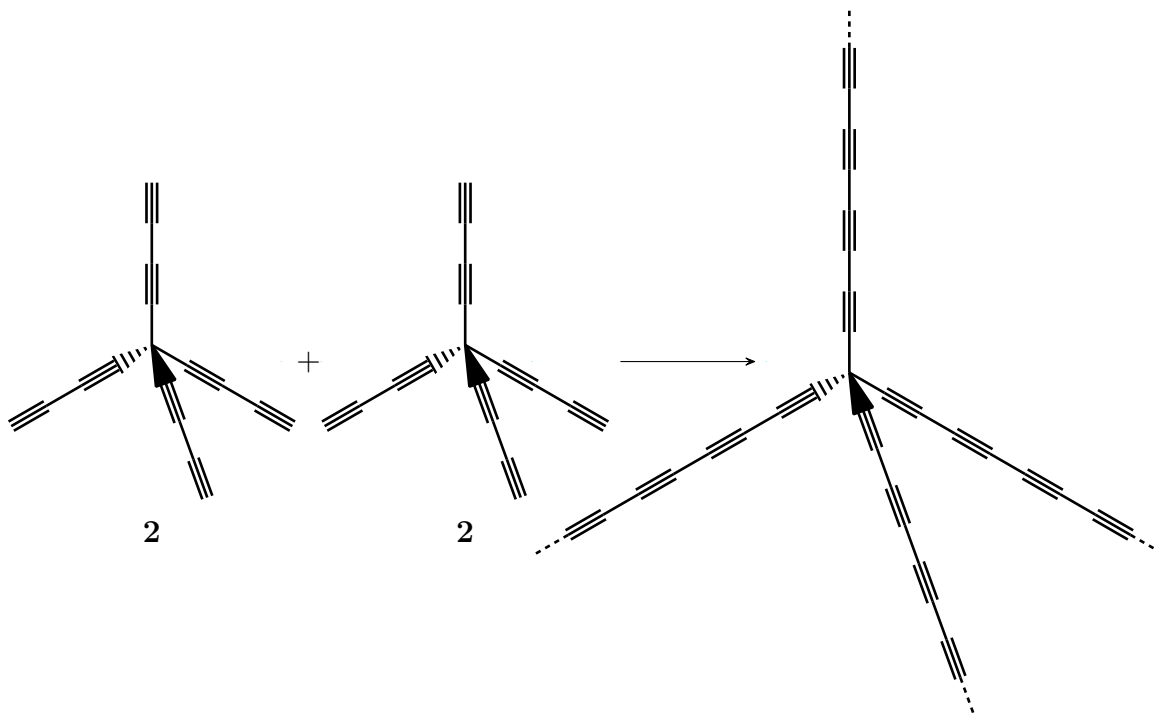


**Figure 4.23:** Rationalised synthesis of OSPC-3, via Eglinton Coupling; Homo-coupling of monomer **2**.

The synthesis of a porous carbon-based framework with fewer alkyne groups between each node poses more of a challenge. Rationalisation of the synthetic procedure has led to a potential method involving cross-coupling using halogenated compounds.

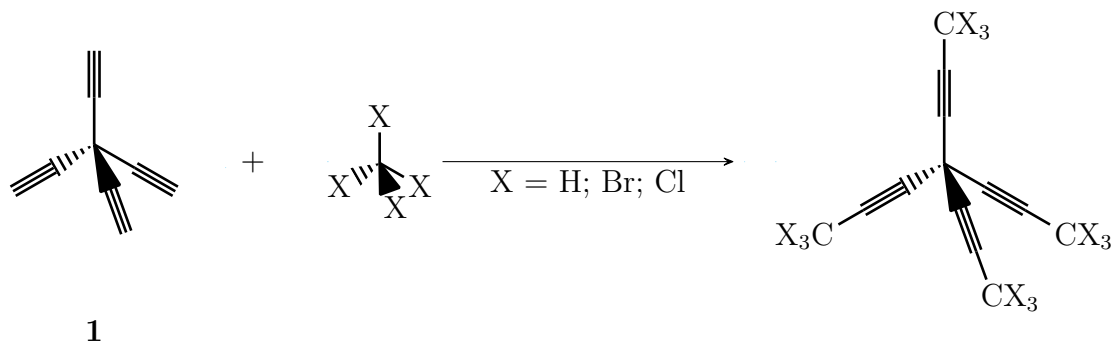


**Figure 4.24:** Proposed synthesis of OSPC-0 with monomer **1** and a halogenated methane.

As shown in Figure 4.24, the basic generation of the porous framework could be performed via synthetic procedures involving halogenated methane, similar to that of Suzuki coupling.<sup>230</sup> To obtain the single  $Csp-Csp$  strut, a cross coupling method is most ideal. However, further investigation into the synthesis of this material is required.

In an overview of each material, the potential bonding arrangements have been considered. The preliminary rationalisation of the synthetic procedures, coupled with the amorphous nature of the materials leads to different bonding arrangements for each structure observed. This is shown in Table ???. The bonding arrangements of OSPC-0 have been established from the proposed synthetic procedure.

#### 4.4.1 OSPC-0 and lithium ion migration

Ambuild was used to build the OSPC-0 structure using the methodology similar to that used for OSPC-1. The coupling process and building block used for the development of OSPC-0 is shown in Figure 4.25. Here we generate the network using the atom types defined by what they will be in the network, rather than the atom

types and bonding present within the monomers. Hydrogen atoms are attached to the terminating carbons to act as leaving groups.

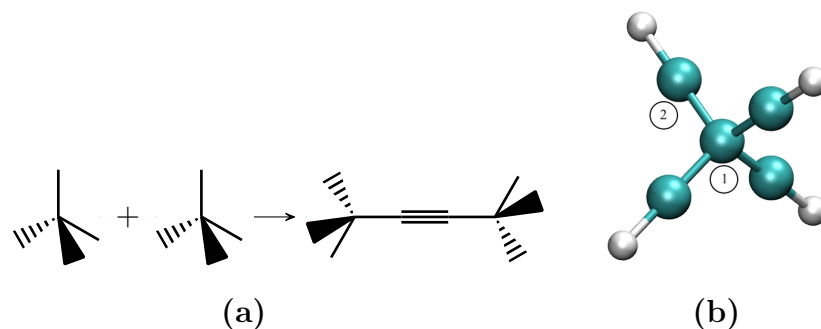


**Figure 4.25:** OSPC-0 monomers and structural definition; (a)Computational formation of the alkyne bond, (b)Tetrahedral monomer used for structural development (built using Materials Studio) with (1) being the  $sp^3$ -hybridised carbon atom, and (2) being the  $sp$ -hybridised carbon atom.

C2 is defined as a  $sp$ -hybridised carbon, which when a bond is formed between two monomers, forms an alkyne bonded strut. Figure 4.26 shows a small cluster of the OSPC-0 formation. The hydrogen atoms are in place as leaving groups from the monomers, bonding to  $sp$ -hybridised carbons to produce the highly rigid alkyne struts. The triple bond is defined by the typing of the individual carbon atoms, and thus cannot be seen.

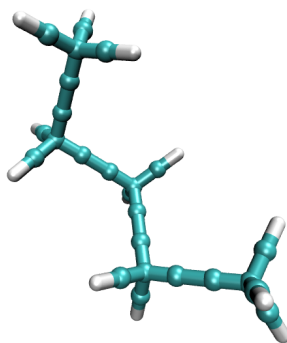


**Figure 4.26:** Structural formation of the OSPC-0 framework; An oligomer of four monomers is shown.

Periodic structures of OSPC-1 and OSPC-0 in a 30 Å x 40 Å by 50 Å cell were produced and their accessible surface area were calculated using Materials Studio



(Figure 4.27). shows the OSPC-0 structure in comparison to OSPC-1. The OSPC-0 structure is more densely packed, with a density of  $0.865 \text{ g cm}^{-3}$ , and much tighter channels in comparison to OSPC-1, with a density of  $0.817 \text{ g cm}^{-3}$ . This is apparent as OSPC-1 had a greater solvent accessible surface area ( $5,130 \text{ \AA}^2$ ) than that of OSPC-0 ( $2,324 \text{ \AA}^2$ ). This suggests that the monomers of OSPC-0 produced a more tightly packed system, and therefore narrower pore channels which may inhibit the migration of lithium ion diffusion. With this in mind, it would be expected that OSPC-0 will contain more narrow pathways, and that the lithium ions will diffuse much more slowly through the structure. The AmBuild structure generated of OSPC-0 between the two graphene sheets is shown in Figure 4.28. Visually, the OSPC-0 structure generated was denser than that of OSPC-1.

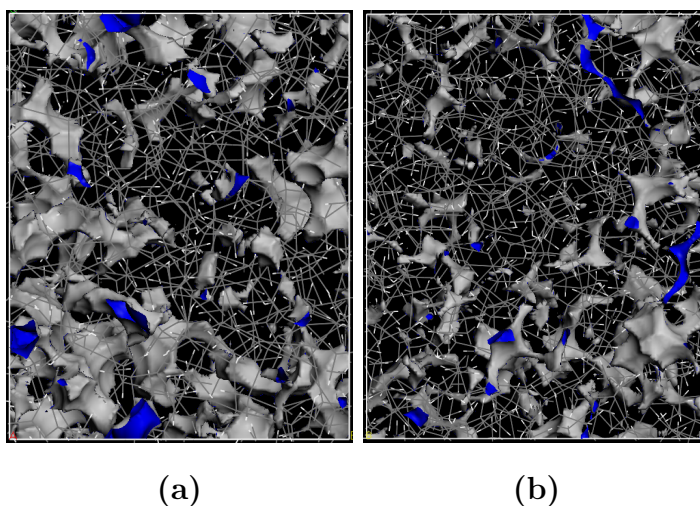


**Figure 4.27:** Solvent accessible surface area of (a) OSPC-1 and (b) OSPC-0; calculated using Materials Studio with a surface probe diameter of  $1.82 \text{ \AA}$ .

Once the charge was applied to the graphene sheet, Li1 was able to determine a pathway through the tighter channels of OSPC-0 (Figure 4.29). The lithium ion can be seen moving through Z-axis towards the negatively charged graphene sheet. However, due to tight packing and narrow channels within the OSPC-0 structure generated, the lithium ion only able to migrate  $\sim 20 \text{ \AA}$  through the simulation cell towards the negatively charged graphene sheet, and therefore a complete migration is

not achieved. The simulation cells and visualisation of the additional lithium ions is shown in Appendix A.7.

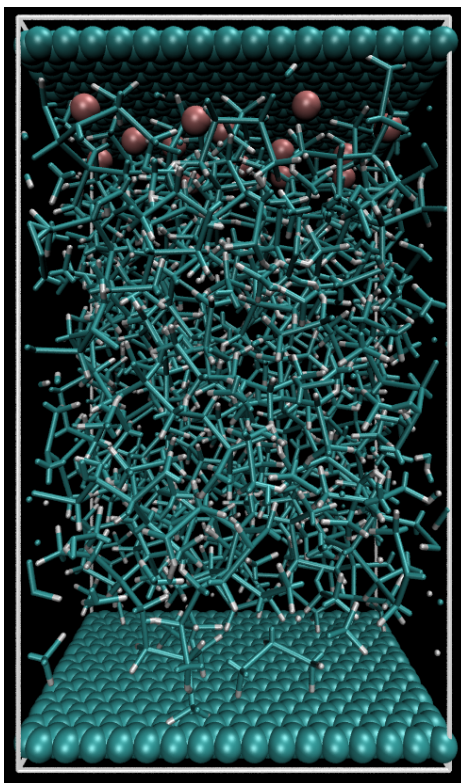


**Figure 4.28:** Developed system of the OSPC-0 framework; Graphene sheets and lithium ions are show in VDW representation.

Not all of the lithium ions were able to migrate through the system. Many of the lithium ions were required to establish new pathways at multiple points within the structure as they were blocked or too narrow to pass through. The incomplete migration of the lithium ion, Li1, was visualised by measuring its movement in the z-axis. The movement in the z-axis of lithium ion 1 (Li1) was observed in Figure 4.30. This illustrates how the ion moved through the structure, and more so the point where the ion becomes stuck during the simulation and is unable to establish a direct pathway through the system.

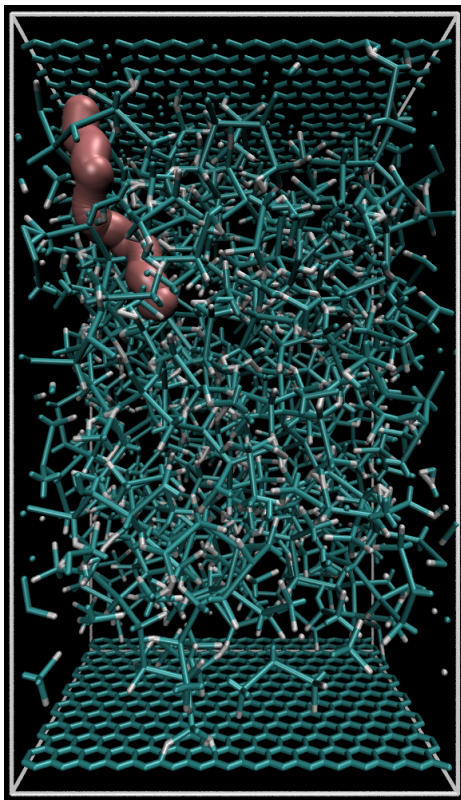


**Figure 4.29:** Lithium ion diffusion of a single lithium ion (Li1) through the OSPC-0 framework.

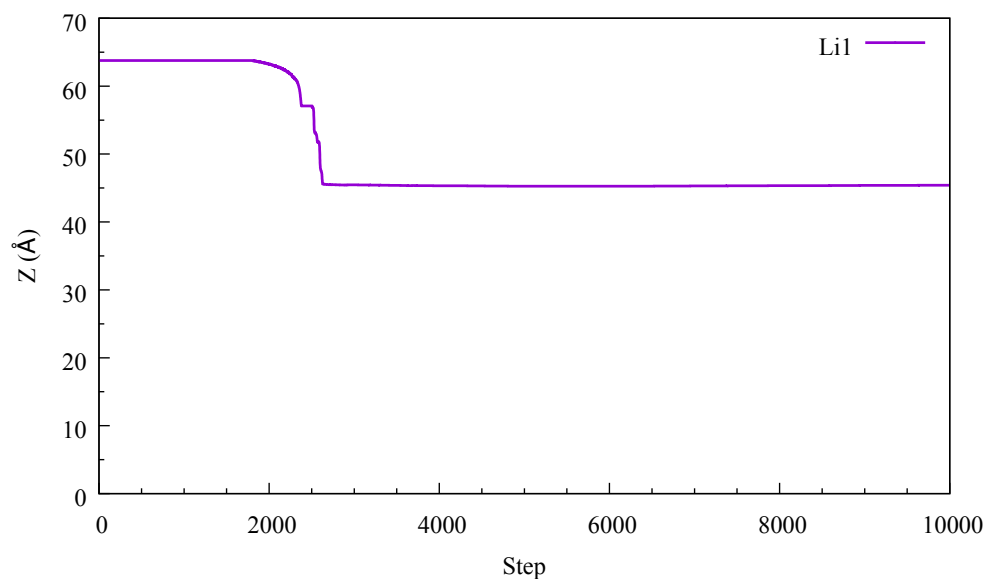


**Figure 4.30:** Plotted movement through the z-axis for the lithium ion diffusion through the OSPC-0 structure; Li(1).

The ion was seen slowly moving through the structure once the charge was applied. However, the reduced movement at  $\sim 58$  Å and  $\sim 55$  Å indicates where the lithium ion becomes trapped, and is unable to migrate farther through the OSPC-0 structure generated. This is the case for many of the additional lithium ions in the system (Figure 4.31)).

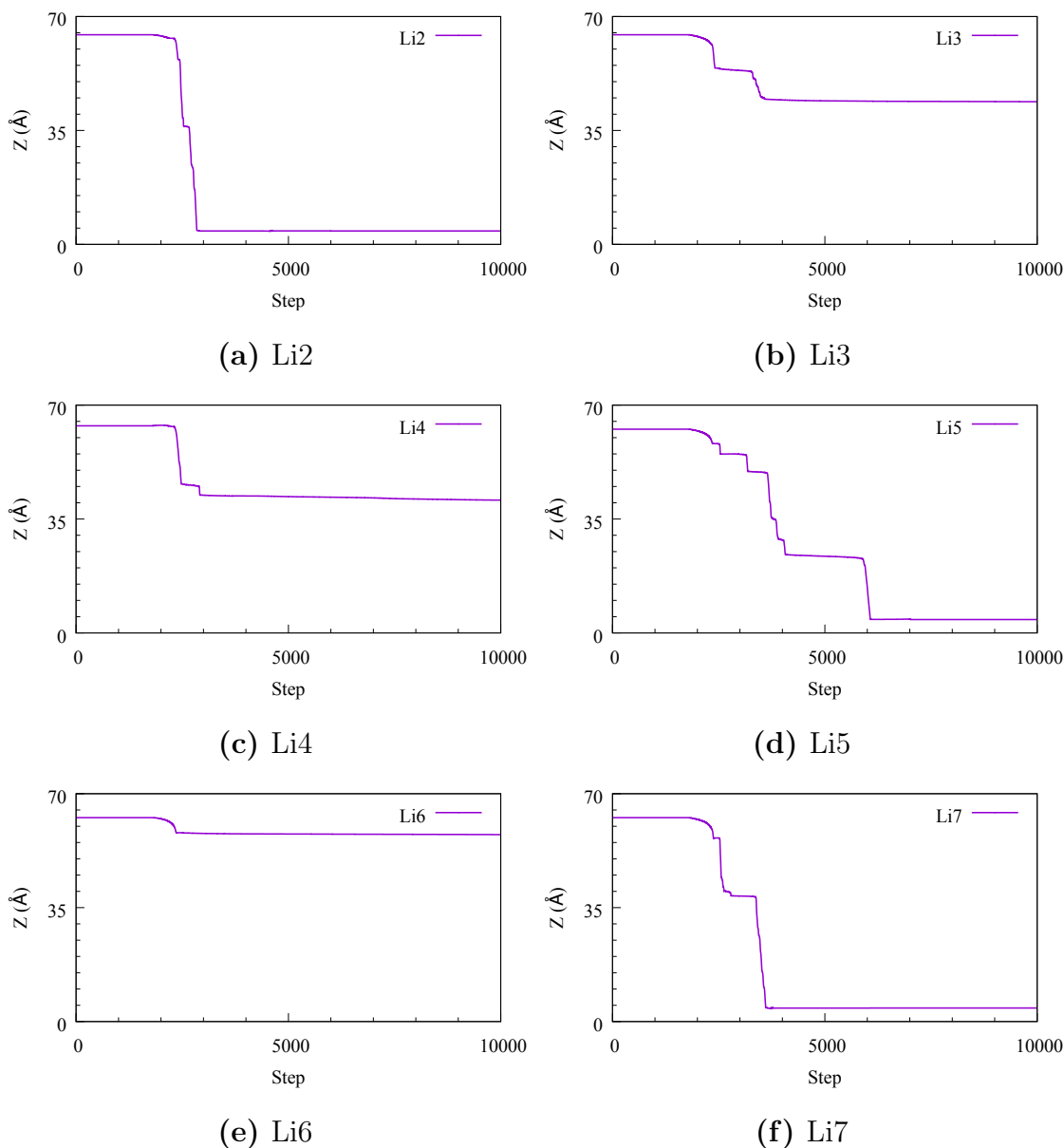
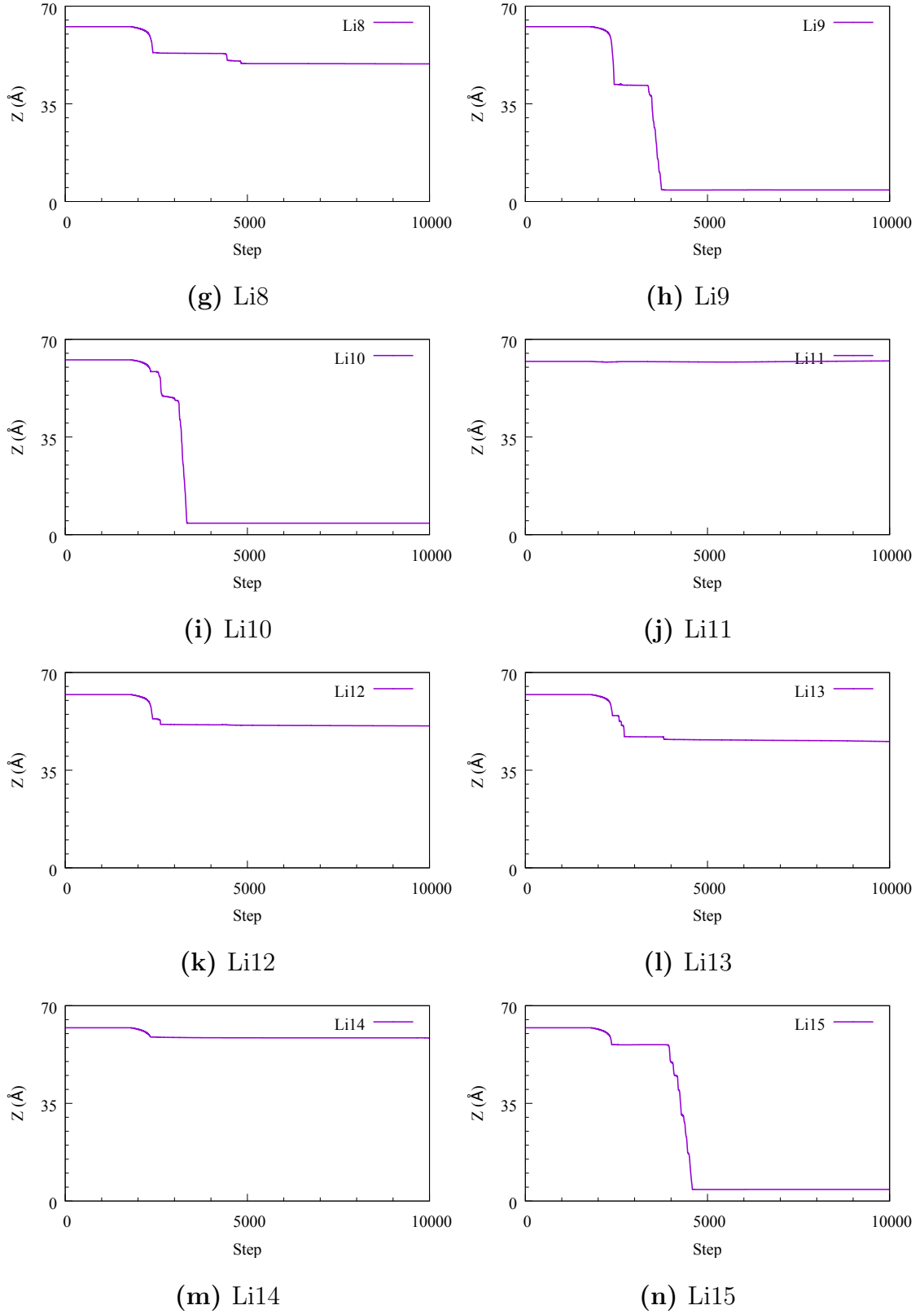


Figure 4.31



**Figure 4.31:** Migration plots of the individual lithium ions within the simulation cell of OSPC-0; (a)Li1 - (n)Li14.

The lithium ions Li8, Li11, and Li14 (Figures 4.31g, 4.31j, and 4.31m respectively) displayed the shortest movement during *active diffusion*. Li8 and Li14 are only able to move approximately 5 Å before becoming trapped, whereas Li11 became trapped immediately, and was unable to move through from its initial position.

Lithium ion	Ion mobility rate ( $\times 10^4$ cm s $^{-1}$ )
Li1	0.17
Li2	7.07
Li3	0.19
Li4	0.22
Li5	1.42
Li6	0.04
Li7	3.59
Li8	0.12
Li9	3.32
Li10	4.32
Li11	0.00
Li12	0.10
Li13	0.15
Li14	0.02
Li15	2.21
Average	1.53

**Table 4.4:** Mobility rates of the individual lithium ions within the OSPC-0 system

Li2, Li5, Li7, Li9, Li10, and Li15 were able to completely migrate through the OSPC-0 structure. However, the pathways they established are not direct. For example, Li5 showed several periods of slow movement and fast movement. This is due to the lithium ion following a very narrow pathway, and having to force its way through (Figure A.7d). As predicted, the more packed system and narrower pores of OSPC-0 greatly affected the rate at which the lithium ions migrated under *active diffusion*, and further clarifies that the system would greatly affect the diffusion of lithium ions. The mobility rates calculated were much slower than those calculated

within the OSPC-1 system. This is shown in Table 4.4.

The average mobility rate of the ions within the OSPC-0 system was calculated at  $1.53 \times 10^4 \text{ cm s}^{-1}$ , whereas the OSPC-1 structure gave an average mobility rate of  $4.78 \times 10^4 \text{ cm s}^{-1}$ . The calculated mobility rate of the lithium ions with the OSPC-0 system gave an estimation towards how the material would perform experimentally. The ions that were able to migrate completely through the system displayed mobility rates similar to those observed in OSPC-1. However, a large majority of the lithium ions gave substantially slow mobility rates, reducing the average mobility rate of the system (Figure 4.32).

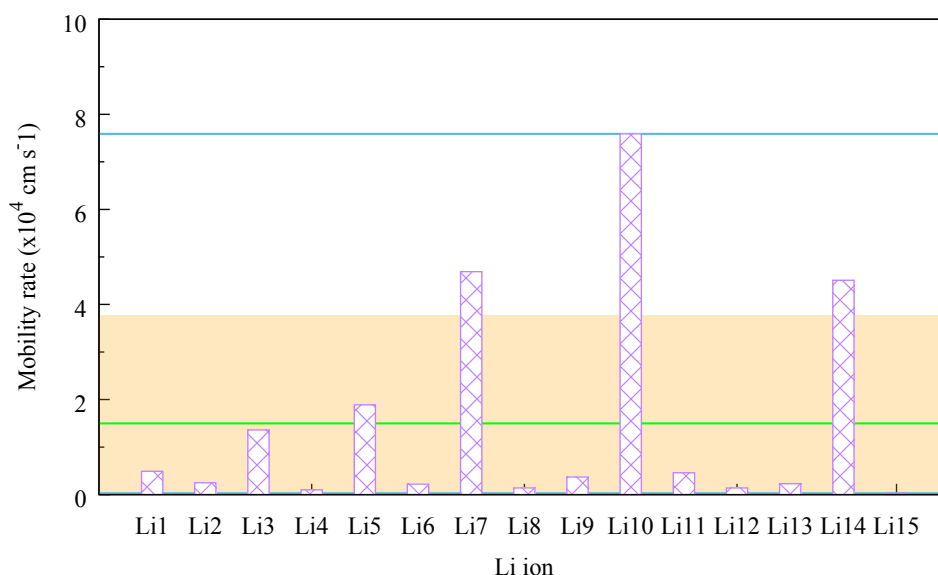


**Figure 4.32:** Plot of diffusion rates for the individual lithium ions within the OSPC-0 system; the green line represents the average diffusion rate, the upper and lower blue lines represent the maximum and minimum calculated rates respectively, and the highlighted region depicts the standard deviation of the mobility rate.

Comparing the fastest (Li2) and slowest (Li11) moving lithium ions, we can visualise the difference between their position in the system. Figure 4.33 displays the z-axis movement of Li2 and Li11. As Li2 is able to migrate farther through OSPC-0, it would be presumed that it was able to maintain a greater distance from the carbon atoms of the construct. Figure 4.33 displays the distance between the lithium ions, Li2 and Li11, and the closest carbon atoms of OSPC-0.

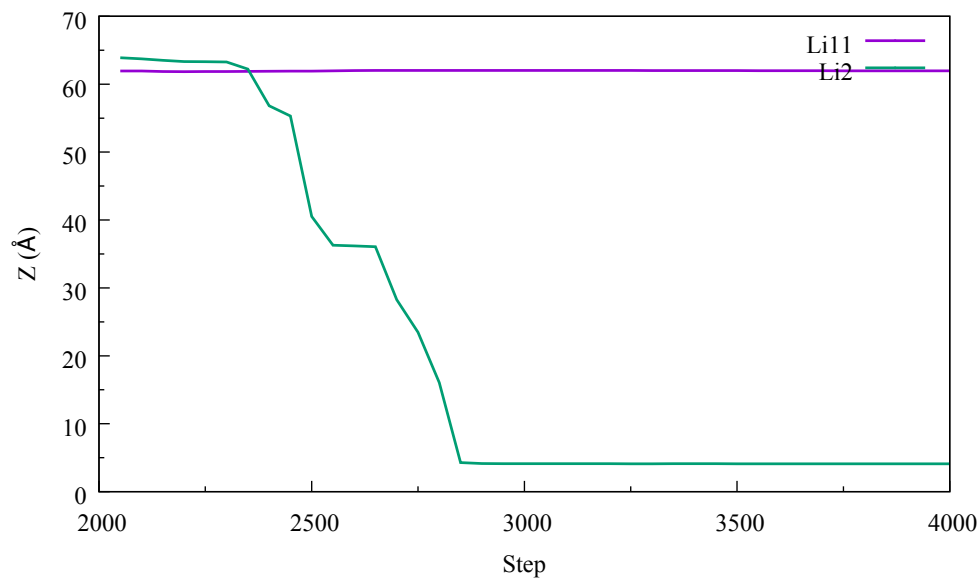


**Figure 4.33:** Li2 and Li11 diffusion within the OSPC-0 simulation; distance vs. simulation time.

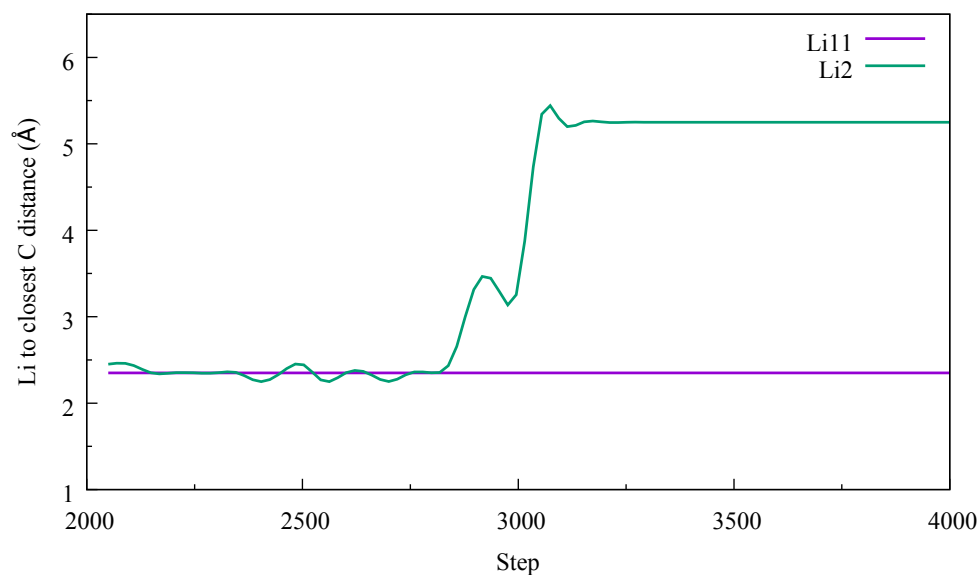


**Figure 4.34:** Radial distribution function of OSPC-0 collected over two thousand frames; Li11 (slowest) and Li2 (fastest).

As Li11 was unable to move through the system, it showed a constant distance from the carbon atoms. However, Li2 is able to increase its distance at the points where it established a new pathway, and increasing this distance farther as it moves



towards the negatively charged graphene. This is an example of how the small OSPC-0 monomer formed tightly packed areas within the system, forming densely populated areas.

Although the mobility rate for Li2 was comparably greater through the system, the average distance calculated between Li2 and the carbon structure showed no difference from that of Li11 (Figure 4.35). This further clarified that the building blocks of OSPC-0 bonded to produce narrow pathways to which lithium ions were or were not able to diffuse along.

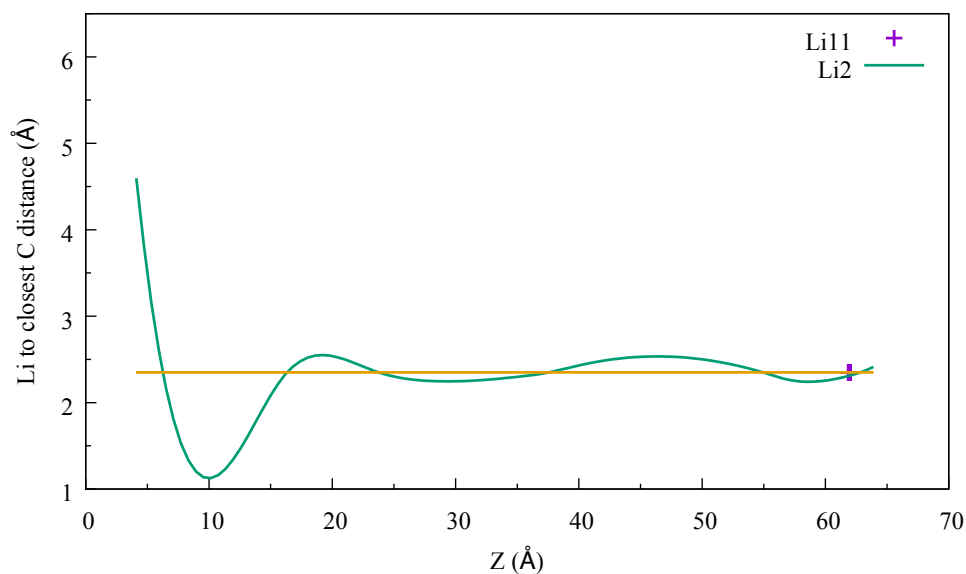


**Figure 4.35:** Radial distribution function of Li2 and Li11 against their position in the simulation z-axis; Yellow line represents the average distance from Li2 to the closest carbon atom.

Due to Li11 becoming trapped within the system, it is not possible to collect the data necessary to visualise the contact distance during the diffusion simulation. However, the distance between these lithium ions and OSPC-0 demonstrated how OSPC-0 and OSPC-1 possessed variations in channel and pore size.

This research demonstrated the tailoring of the OSPC-1 structure by reducing the distance between the  $sp^3$  carbon atoms of the structure. The OSPC-0 structure generated showed much narrower pathways for the lithium ions to migrate through, which resulted in much slower mobility during the MD simulation. Several lithium ions

were able to migrate completely through the OSPC-0 structure generated, whereas the additional ions became trapped within tightly packed areas of OSPC-0, preventing their migration further through the system. Because of this, OSPC-0 has limited suitability as an anode for lithium ion batteries.

#### 4.4.2 OSPC-2 and lithium ion migration

OSPC-2 includes the monomer of OSPC-1 coupled with a monomer involving an additional alkyne group along the branches. The co-polymerisation results in a random arrangement of building blocks with the structure, connecting the  $sp^3$  carbon nodes with one, two, or three alkyne groups along the struts. The inclusion of monomers with differing sizes offers the possibility of multiple different structure sets within the framework, producing a diverse assortment of diffusion channel sizes.

Figure 4.36 illustrates the bond formation process between these two differing monomers to produce the statistical bond structure, as well as a cluster generated of OSPC-2 illustrating the three types of bonding that can arise from the coupling of the building blocks.

The OSPC-1 monomer undergoes homo-coupling to produce two alkyne groups (1), a co-coupling with the secondary monomer to produce three alkyne groups (2), and a homo-coupling of the secondary monomer to produce four alkyne groups (3). Opening up the framework with larger monomers would potentially offer more available pathways for the lithium ions to diffuse completely through, and would also allow for faster, and more fluid movement of ion transport. The increase in  $sp^3$ - $sp^3$  distance could open up the overall framework, increasing the size of the pores within the structure.

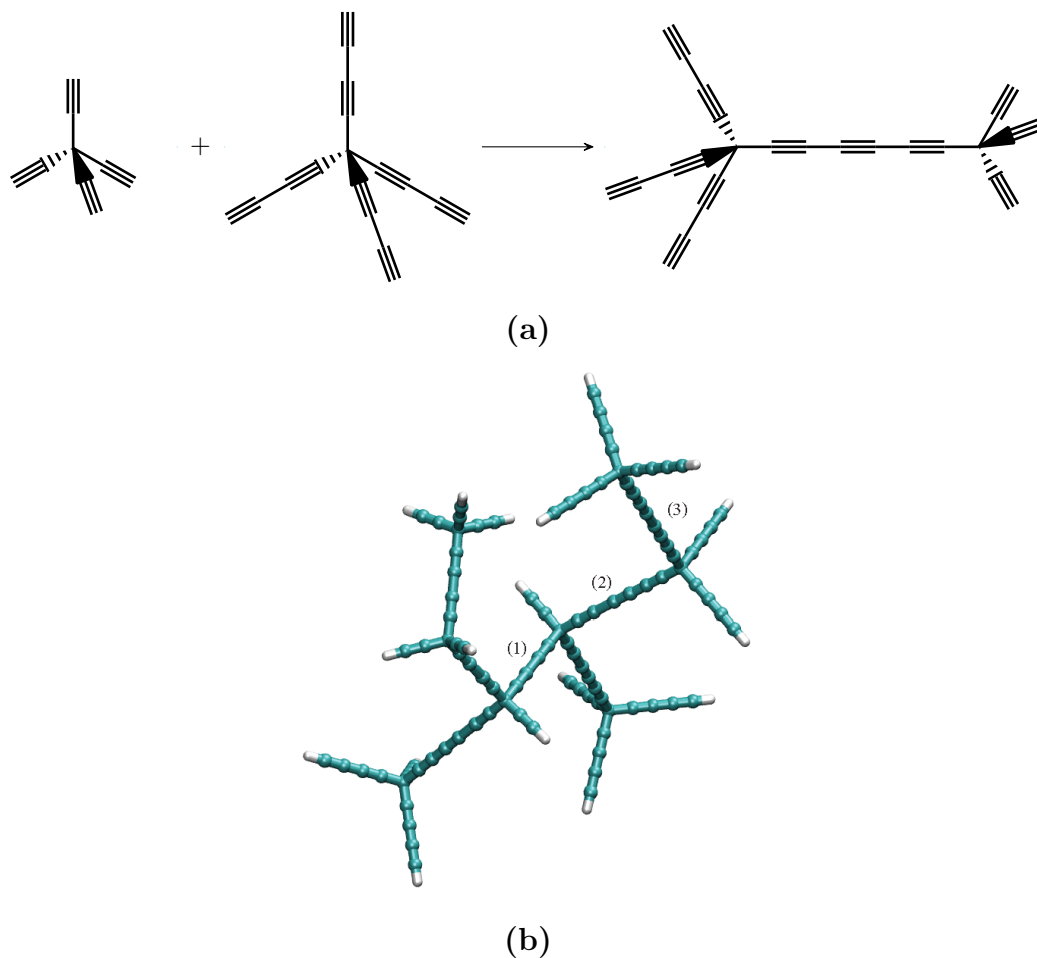


**Figure 4.36:** OSPC-2 monomers and structural definition; (a) The co-coupling of monomers **2** and **1** for the formation of a pure OSPC-2 linkage, and (b) a generated fragment of OSPC-2 illustrating the types of bonding that could form.

The accessible surface area of OSPC-2 (Figure 4.37) is greater than that of the OSPC-1 framework, having  $11719 \text{ \AA}^2$ , whereas the OSPC-1 structure shows to have an accessible surface area of  $5130 \text{ \AA}^2$ . A larger accessible surface area signifies a more open microporous network, and therefore more accessible channels for ion diffusion. Although the OSPC-2 structure has a more accessible surface, its density is slightly greater to that of OSPC-1. The models produced showed OSPC-2 to have a density of  $0.842 \text{ g cm}^{-3}$ , whereas the OSPC-1 models presented a density of  $0.817 \text{ g cm}^{-3}$ .

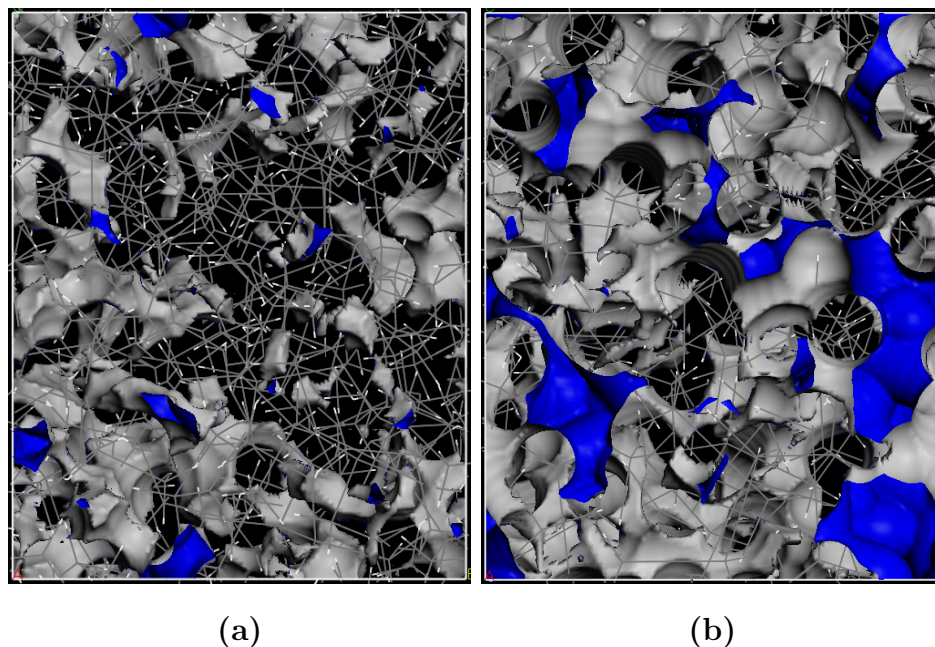


**Figure 4.37:** Solvent accessible surfaces of (a)OSPC-1 and (b)OSPC-2

OSPC-2 was generated using AmBuild between the two graphene sheets, and the lithium ions placed in the same positions as those previously observed for OSPC-1 and OSPC-0 (*vide supra* Sections 4.3.1 and 4.4.1). Figure 4.38 shows the structure generated and the movement of the first lithium ion, Li1, through the OSPC-2 structure generated. This lithium ion was able to establish a pathway that allowed it to completely migrate through the structure to the negatively charged graphene sheet.

The visualised movement of the additional lithium ions is shown in Appendix A.8.

Similar to the OSPC-1 structure, each individual lithium ion achieves complete migration through the OSPC-2 network, and all lithium ions in the system established pathways that showed few obstacles and tightly packed areas of the OSPC-2 structure that could trap the ions.

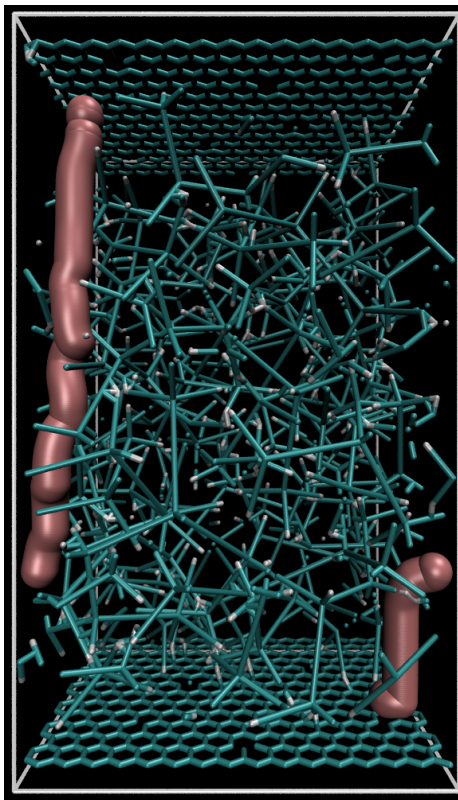


**Figure 4.38:** Lithium ion diffusion of a single lithium ion (Li1) through the OSPC-2 framework.

To determine the rate at which the lithium ions migrated through the generated structure, their movement in the z-axis was observed. Although Li1 migrated quickly through OSPC-2, it had encountered blockages that required it to change direction and establish an alternative pathway. This is apparent where the ions movement became slower at various positions in the simulation cell (Figure 4.39).

The additional lithium ions in the system presented similar z-axis movement through OSPC-2. Figure 4.40 shows the z-directional movement of the lithium ions (Li2-Li15) during *active diffusion*. Several ions display direct pathways through the system. Lithium ions 11 and 13 (Figures 4.40j and 4.40l respectively) illustrate a lapse in trajectory through the z-axis. The migration of ions through the OSPC-2 network is similar to that of OSPC-1, whereas migration is more restricted in OSPC-0 compared to both OSPC-1 and OSPC-2.

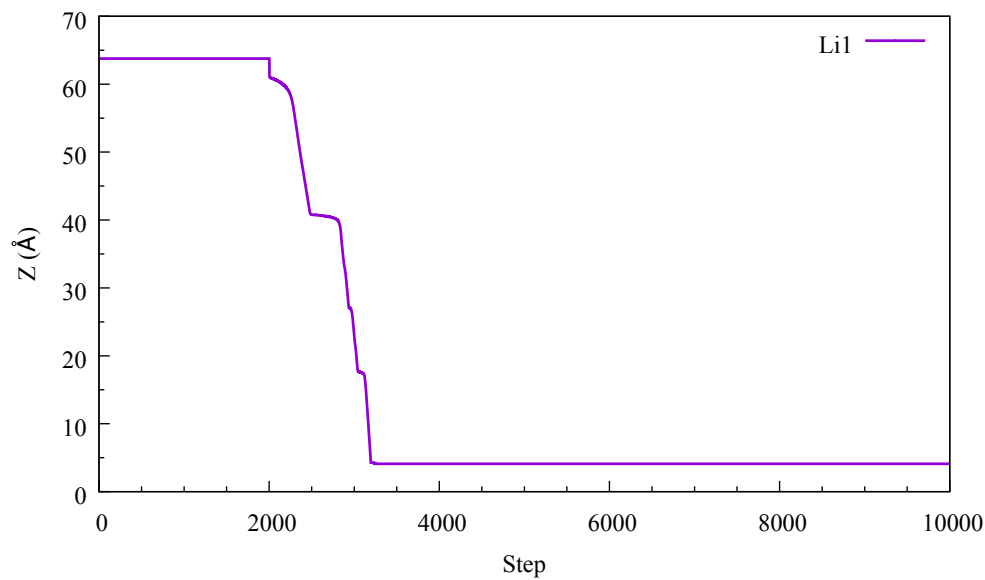
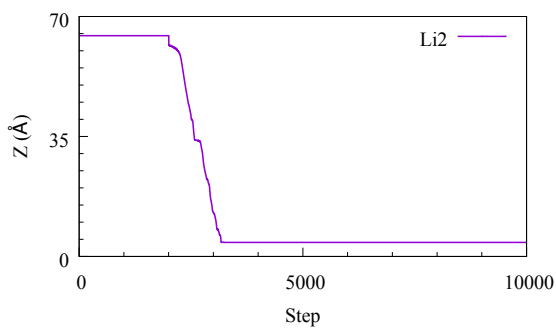
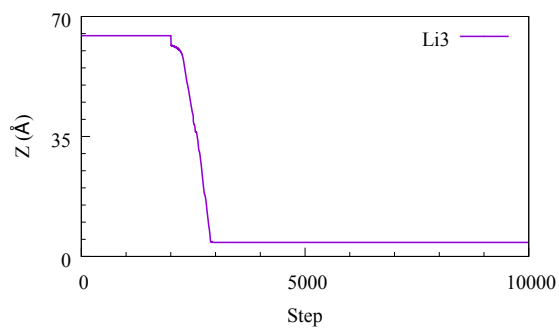


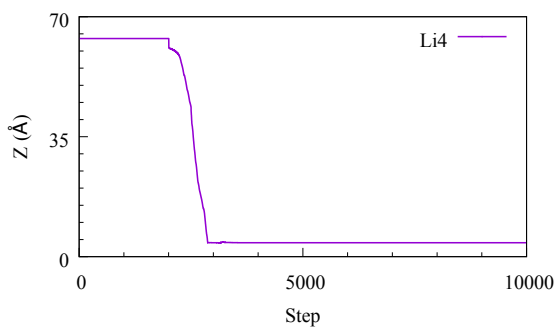
**Figure 4.39:** Plotted movement through the z-axis for the lithium ion diffusion through the OSPC-2 structure; Li(1).



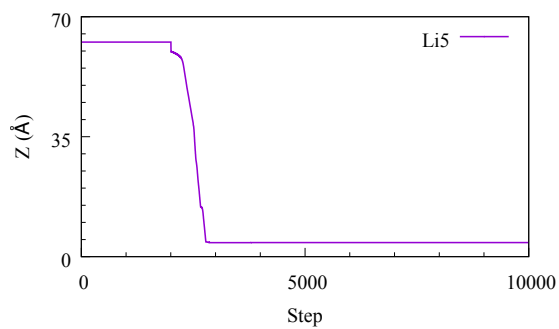
(a) Li2



(b) Li3



(c) Li4



(d) Li5

**Figure 4.40**

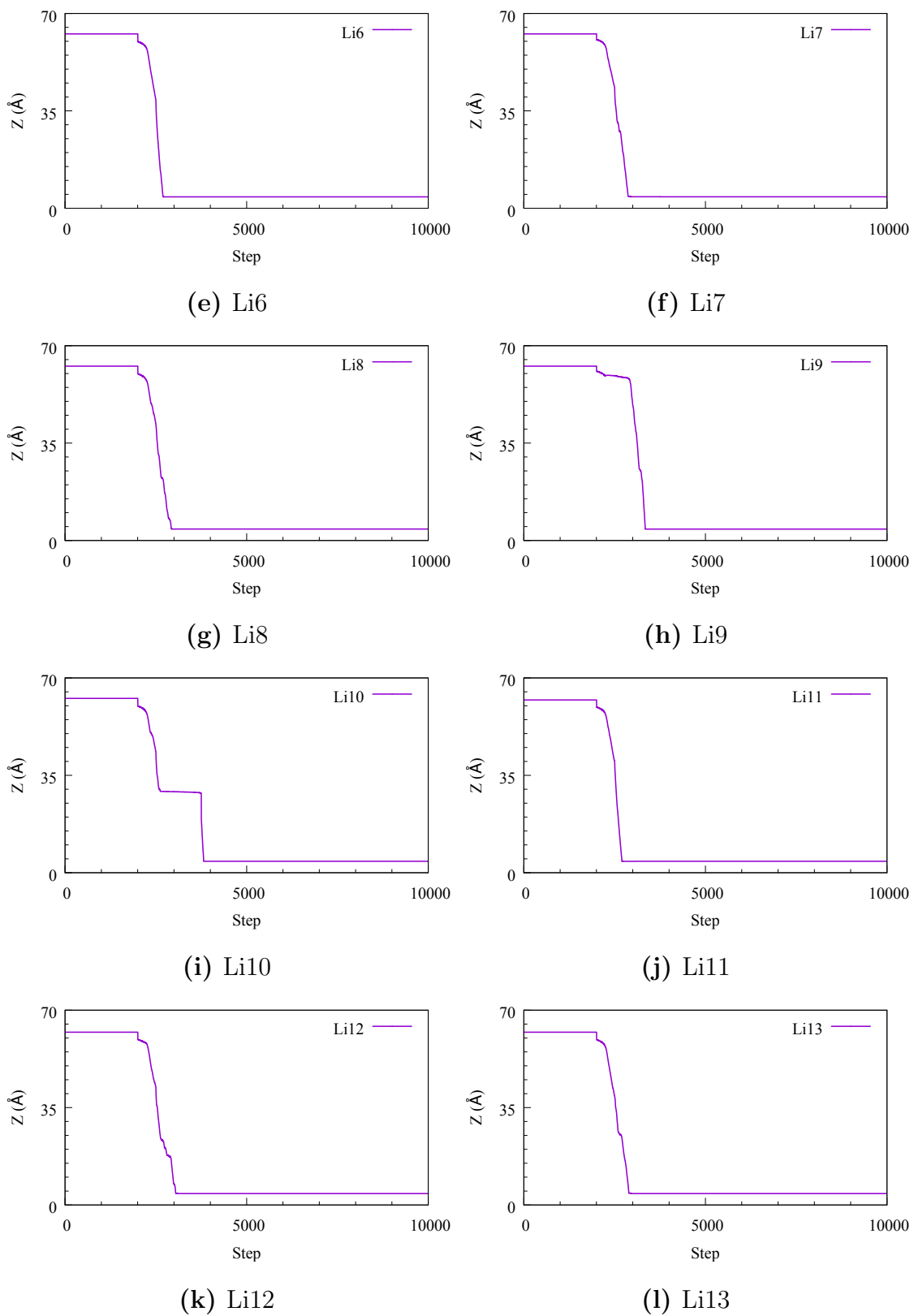
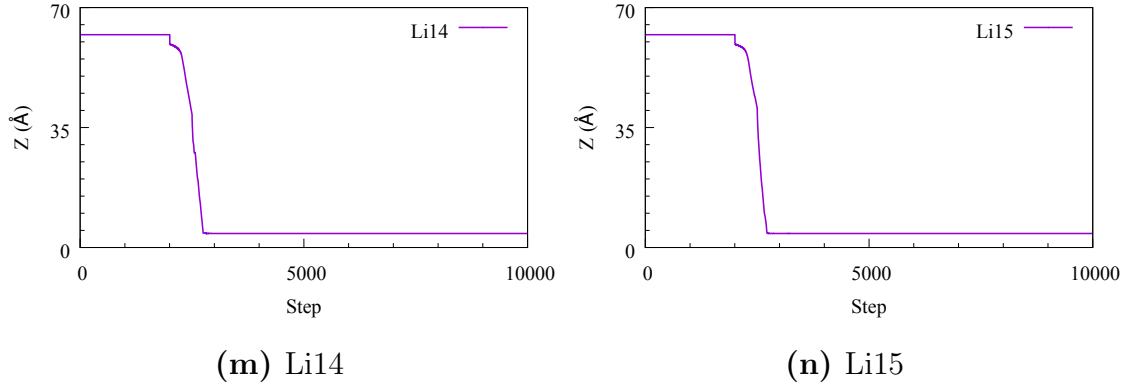


Figure 4.40



**Figure 4.40:** Migration plots of the individual lithium ions within the simulation cell of OSPC-2; (a) Li2 - (n) Li15.

The mobility rates shown in Table 4.5 for the lithium ions in the OSPC-2 network are greater than that of both the OSPC-1 and OSPC-0 systems. OSPC-2 displays an average mobility rate of  $6.36 \times 10^4 \text{ cm s}^{-1}$ , whereas OSPC-1 displays an average mobility rate of  $4.78 \times 10^4 \text{ cm s}^{-1}$ . The increase in  $sp^3$ - $sp^3$  distances offers an increase in micropore size, which in turn allows for a faster migration of lithium ions from the positively charged to the negatively charged graphene sheet. The maximum mobility rate of the OSPC-2 system shows to be  $8.34 \times 10^4 \text{ cm s}^{-1}$ , whereas the OSPC-1 has a maximum of  $5.94 \times 10^4 \text{ cm s}^{-1}$ . Figure 4.41 shows a comparison of the mobility rates for each lithium ion. With the exception of Li9, the mobility rates calculated for the lithium ions through OSPC-2 were all greater than  $4 \times 10^4 \text{ cm s}^{-1}$ .



Lithium ion	Ion mobility rate ( $\times 10^4$ cm s $^{-1}$ )
Li1	4.93
Li2	5.08
Li3	6.71
Li4	6.77
Li5	7.39
Li6	8.34
Li7	6.65
Li8	6.27
Li9	4.30
Li10	3.18
Li11	8.19
Li12	5.48
Li13	6.42
Li14	7.67
Li15	7.99
Average	6.36

**Table 4.5:** Mobility rates of the individual lithium ions within the OSPC-2 system

The inclusion of a co-monomer within this amorphous system shows improvement on the diffusive capabilities, and the random nature of this amorphous material produces areas of differing sizes of the microporous regions. This generated more open channels for the ions to diffuse through. However, the homo-coupling of the OSPC-1 monomer resulted in areas of reduced channel sizes, and similar to OSPC-1, the potential for indirect diffusion pathways through the system.

The increase in pore size leads to an increase in diffusion pathway width. This means that the distance between the lithium ions and carbon atoms of the OSPC-2 network is increased, reducing the potential for lithium ions to become stuck within the structure. Figure 4.42 shows the variation in distances between the lithium ions of Li10 and Li6 (the slowest and fastest diffusing lithium ion within the OSPC-2 simulation respectively).

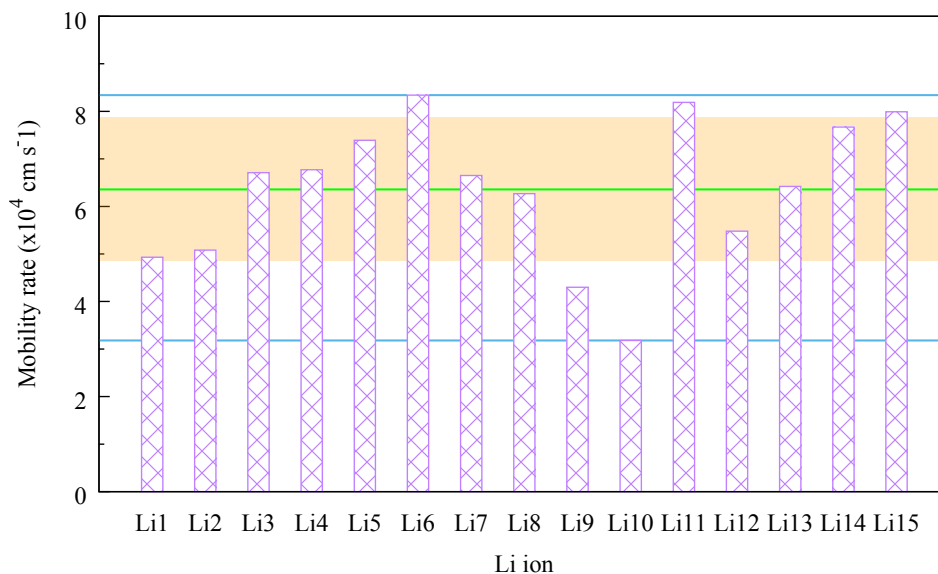


**Figure 4.41:** Plot of diffusion rates for the individual lithium ions within the OSPC-2 system; the green line represents the average diffusion rate, the upper and lower blue lines represent the maximum and minimum calculated rates respectively, and the highlighted region depicts the standard deviation of the mobility rate.

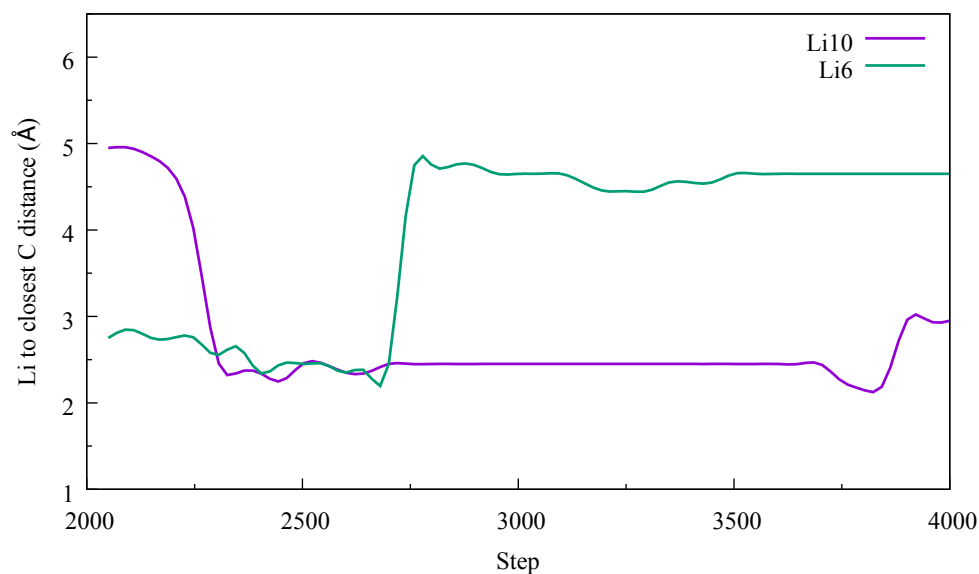


**Figure 4.42:** Radial distribution function of OSPC-2 collected over two thousand frames; Li10 (slowest) and Li6 (fastest).

There is variation in the distances observed throughout the simulation. This indicates that the lithium ions are moving from narrower to more open volumes within

the OSPC-2 structure. Li6 finds a more direct pathway than Li10, and is able to diffuse quickly through the structure. However, Li10 moves from locations of empty space with little volume into space with larger volume. This accounts for the sharp spikes in the distance calculated. The closes distance is not too dissimilar to that of OSPC-1, between 2-3 Å. However, the variation in pore size and available space means that the lithium ions are able to move out of tighter pathways and into more open pathways more readily.

The distance between these lithium ions (Li6 and Li10) and the nearest carbon are similar, although the pathway determined for Li6 is more direct, and encounters less obstructions from the OSPC-2 network. This is shown in Figure 4.45 between the steps of approximately 2600 and 3800 Li10. Li10 is attempting to move out of a narrower pathway and determine a more open one. This correlates with the spikes presented in Figure 4.42.

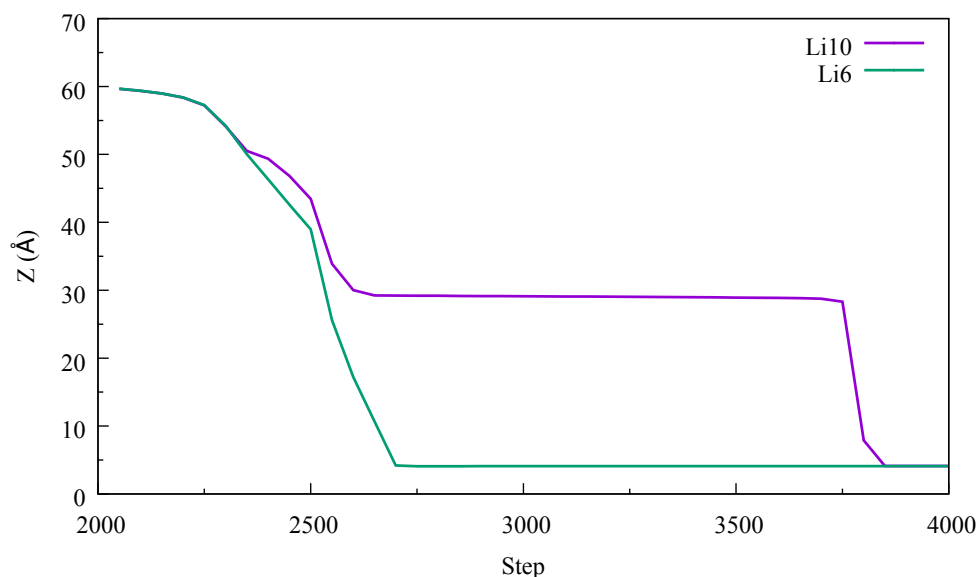


**Figure 4.43:** Radial distribution function of OSPC-2 collected over two thousand frames; Li10 (slowest) and Li6 (fastest).

Due to the random nature of OSPC-2, a greater build-up of smaller monomers can occur. The maximum and minimum diffusion rates for the lithium ions observed can be correlated to the occurrence of a build-up of small building blocks, leading to

more tortuous and narrower pathways being determined. This is apparent with Li6 (fastest) and Li10 (slowest). Figure 4.44 shows the two pathways of Li6 and Li10 established, to which Li10 was seen traversing a pathway more tortuous than that of Li6.

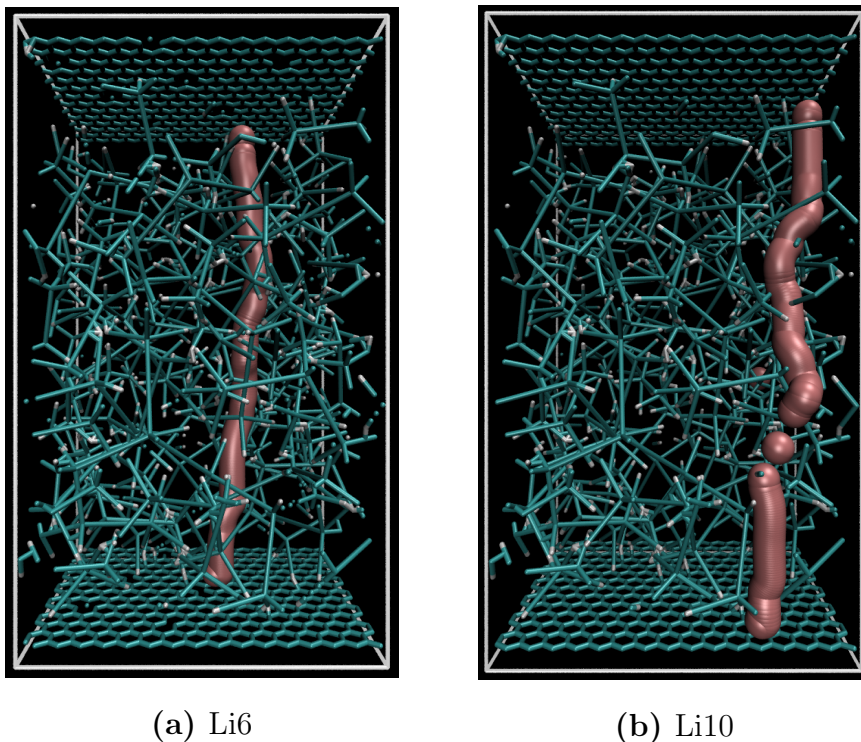


**Figure 4.44:** The diffusion pathways of (a) Li6 and (b) Li10. Li6 shows a less tortuous pathway than that of Li10.

An average distance between the lithium ions (Li6 and Li10) during the *active diffusion* shows that the pathway determined by Li10 is much narrower than that of Li6. Measuring the distance between the lithium ions and the carbon structure, we can see the differences in determined pathway for each of these lithium ions (Figure 4.45).

Li6 maintained a greater distance from the OSPC-2 carbon atoms to that of Li10. Between 40 Å and 3 Å of the simulation cell, both lithium ions showed approximately the same distance from the structure. This suggests that these regions share a similar distribution of carbon atoms. The distance between Li10 and the OSPC-2 carbon atoms reduces greatly as the ion moves through the first 20 Å of the simulation

cell, with a sharp increase where the ion establishes a more open pathway. The minor movement of Li10 between steps 2600 and 3800, and the increase in distance at approximately  $Z=30$  Å links directly with the presence of sharp peaks seen in Figure 4.42. This is the point where Li10 is re-establishing its pathway, moving between tighter and more open spaces.

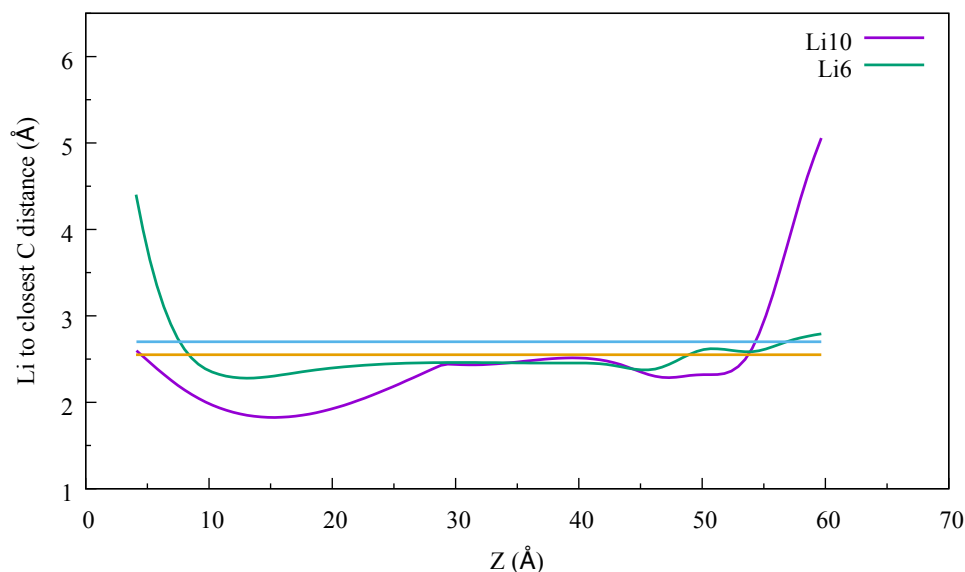
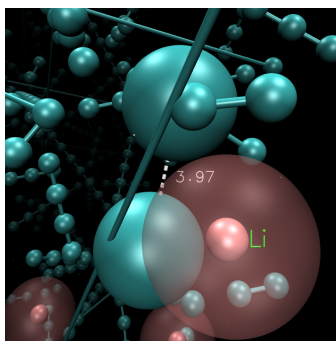


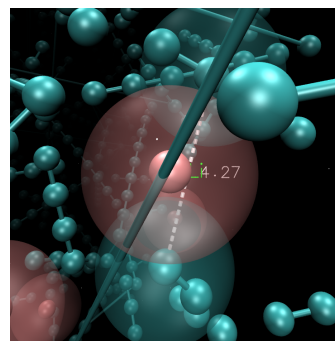
**Figure 4.45:** Radial distribution function of OSPC-2 collected over two thousand frames; Li10 (slowest) and Li6 (fastest). Yellow and blue lines represent the average distance between lithium ions of Li10 and Li6 and the closest carbon atoms to them respectively.

The establishment of pathway and movement between narrower and more open spaces can be linked to the movement of the OSPC-2 structure. As observed with OSPC-1, the atoms within the structure are able to move, allowing the lithium ions to pass between them (Figure 4.46).

The distance between two carbon atoms is shown to increase as the lithium ion, Li10, gets closer to them. Several additional carbon-carbon distances were observed throughout the simulation. The change in distance between these carbon atoms is presented in Figure 4.47.

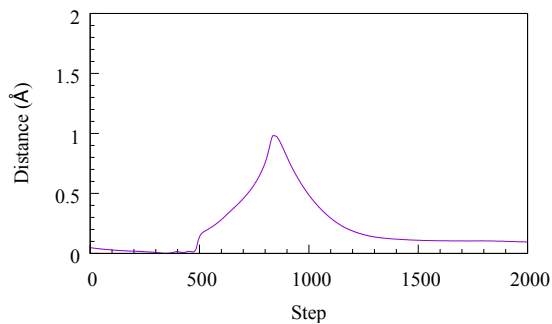


(a)

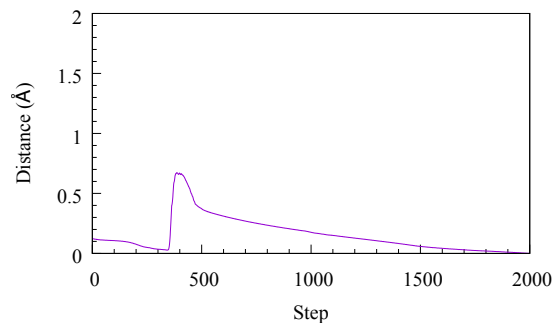


(b)

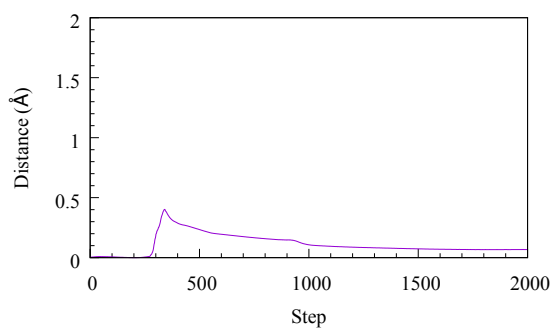
**Figure 4.46:** Carbon movement with lithium ion diffusion within OSPC-2; (a) initial distance and (b) movement with lithium ion diffusion.



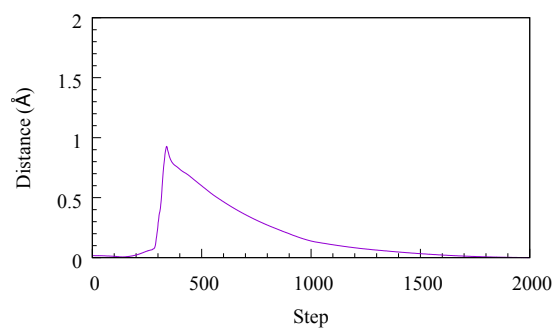
(a) Pathway 1



(b) Pathway 2



(c) Pathway 3



(d) Pathway 4

**Figure 4.47**

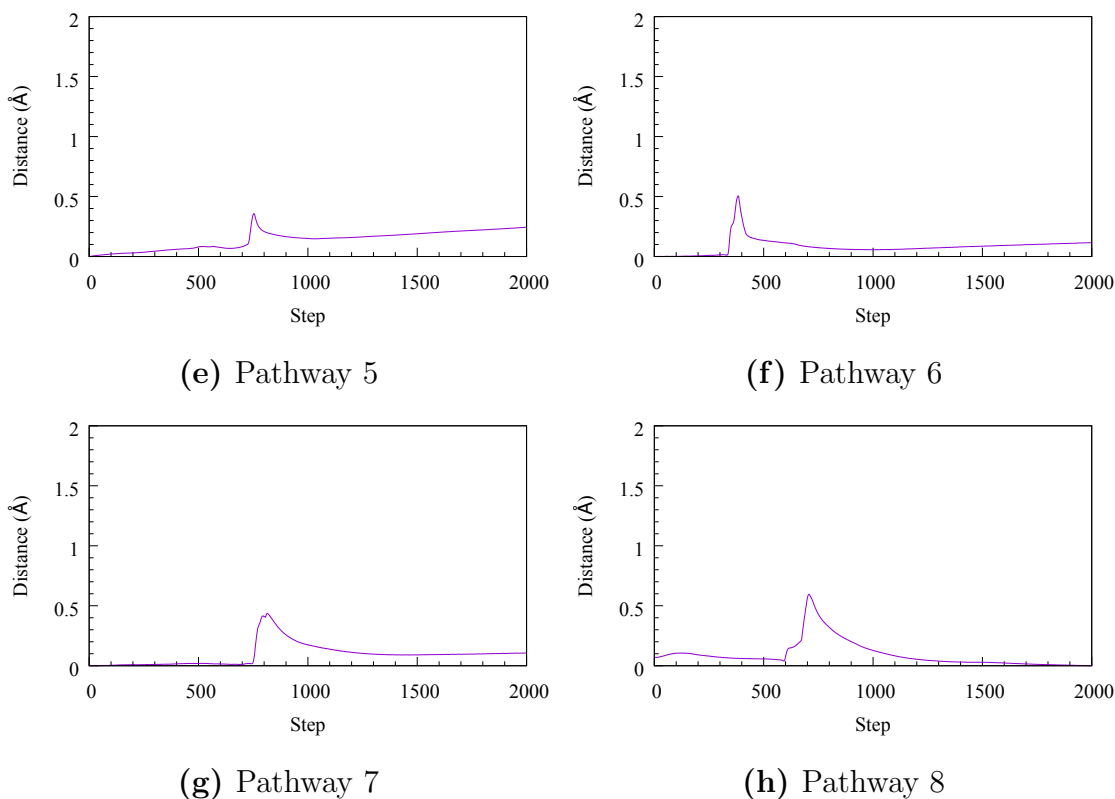


**Figure 4.47:** Distance movement of carbon atoms in separate struts from lithium ion passage within the OSPC-2 framework.

The carbon movement is shown in Table 4.6. The average distance moved is 0.609 Å, whereas OSPC-1 displays a greater average movement of 1.162 Å. This reduction in movement was due to the structure of OSPC-2 containing more open channels, therefore requiring less movement to allow the lithium ions to pass through.

The movement of carbon atoms represents the OSPC-2 structures ability to flex to allow ion passage. Each carbon-carbon distance sharply increases as lithium ions pass between them, and further relaxing back to their distance minima. The relaxation and return to their natural position indicates that the OSPC-2 structure is able to change accordingly with guest presence and return to its previous state with removal of the guest material.

Pathway	Max displacement ( $\Delta\text{\AA}$ )
1	0.983
2	0.672
3	0.402
4	0.925
5	0.357
6	0.504
7	0.435
8	0.595
Average	0.609

**Table 4.6:** Max displacement of the carbon atoms within the OSPC-2 structure during lithium ion diffusion.

This showed the capabilities of OSPC-2 as an anode for lithium ion batteries, and the further tailoring of the OSPC-1 structure to offer greater pore sizes and faster diffusion of ions

### 4.4.3 OSPC-3 and lithium ion migration

OSPC-3 is constructed using monomer **2** via homo-coupling. The bonding of the monomer results in four alkyne groups between the  $sp^3$ - $sp^3$  nodes (Figure 4.48).

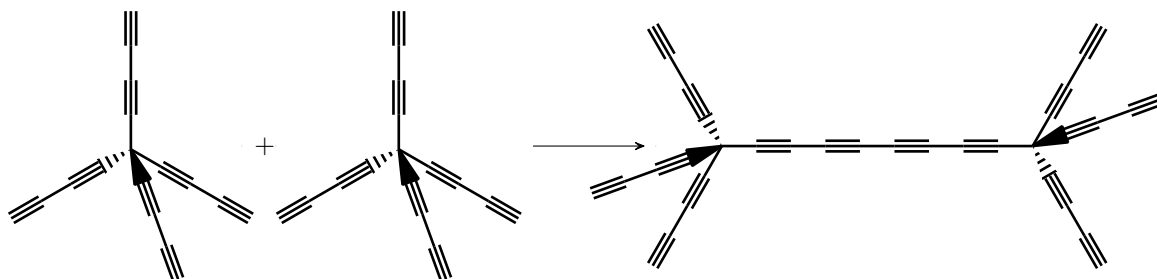


**Figure 4.48:** Formation of OSPC-3 via homo-coupling of monomer **2** to produce an  $sp^3$ - $sp^3$  strut with four alkyne groups.

The homo-coupling of the larger monomer will potentially give rise to a more open structure to those of OSPC-1 and OSPC-2. Calculating the accessible surface area of the OSPC-3 structure generated showed that OSPC-3 contained more free volume



within compared to OSPC-0, OSPC-1, and OSPC-2 (Figure 4.49). As determined previously (*vide supra* Section 4.4.2), OSPC-2 ( $11719\text{\AA}^2$ ) possessed a greater accessible surface areas to that of OSPC-1. In turn, OSPC-3 displayed a further increase in accessible surface area to OSPC-1 and OSPC-2, which was calculated to be  $10616\text{\AA}^2$ .

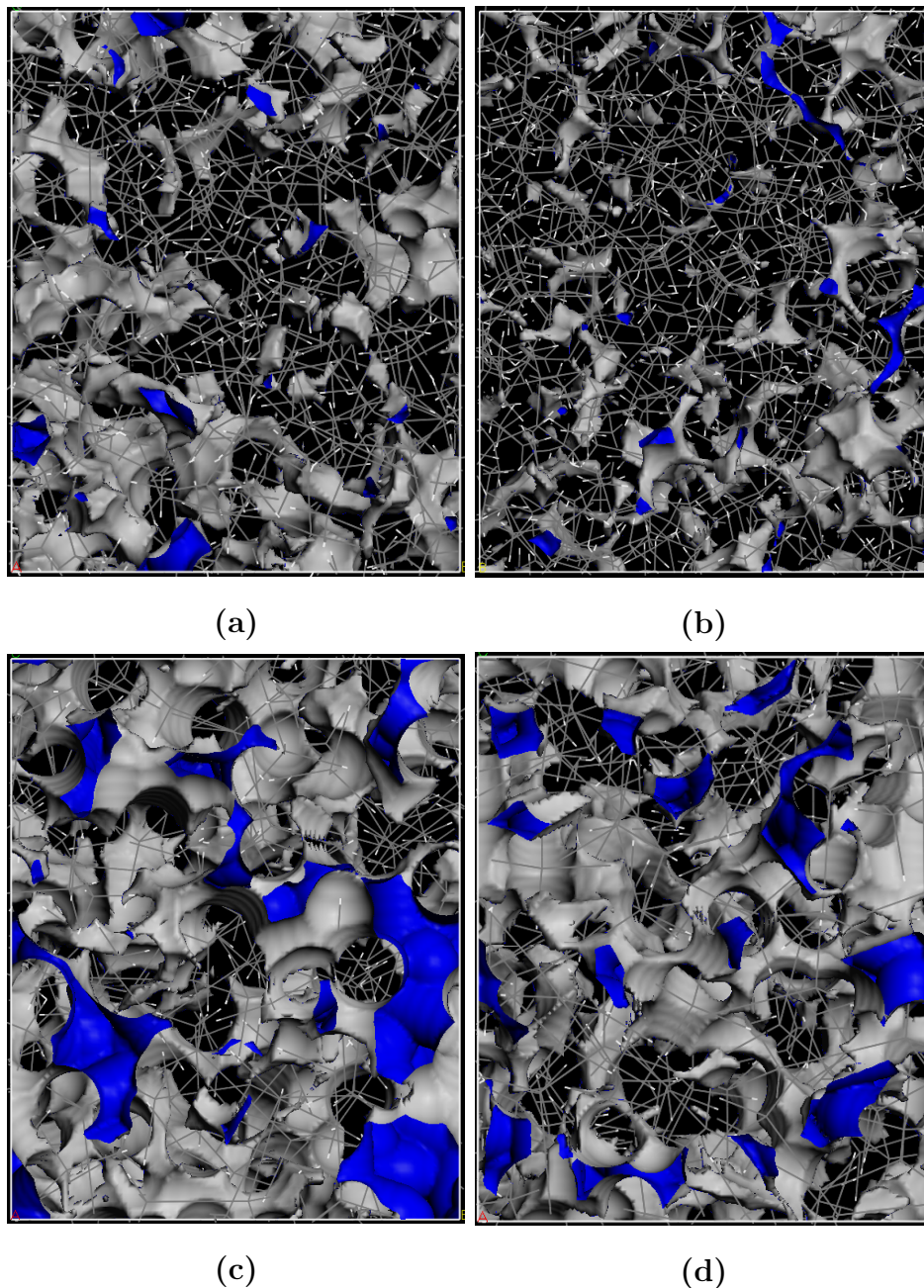


**Figure 4.49:** Solvent accessible surface areas of (a)OSPC-1, (b)OSPC-0, (c)OSPC-2, and (d)OSPC-3.

To determine how OSPC-3 behaves as an anode for lithium ion batteries, MD simulations were performed in a similar manner to those performed previously. The OSPC-3 structure was generated using AmBuild, with the structure itself being formed between the two graphene sheets, and the fifteen lithium ions were placed in the same positions to the OSPC-0, OSPC-1, and OSPC-2 simulations.

Visually, the OSPC-3 structure generated appeared more open to its predecessors. The lithium ions were readily able to establish direct diffusion pathways through the OSPC-3 network, and each lithium ion completely diffused through the structure towards the negatively charged graphene sheet. Li1, shown in Figure ??, established a direct pathway and diffuses from the positively charged graphene sheet to the negatively charge graphene sheet.

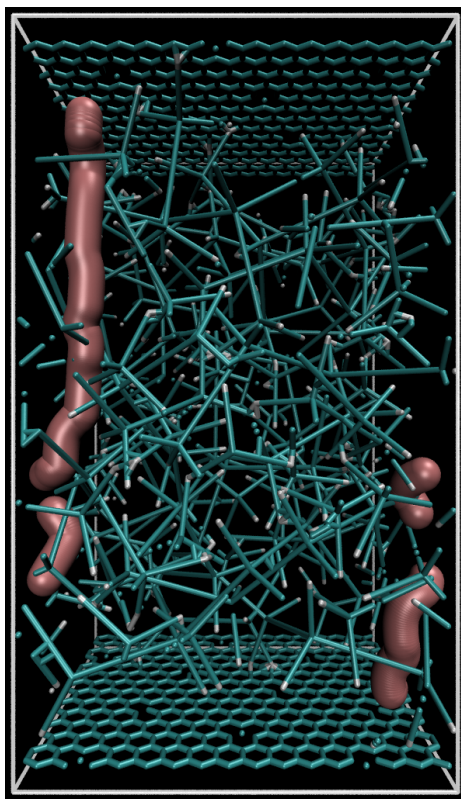


**Figure 4.50:** Lithium ion diffusion of a single lithium ion (Li1) through the OSPC-3 network

Monitoring the diffusion of Li1 through the z-axis showed that the lithium ion was able to establish a pathway allowing for complete diffusion through OSPC-3

(Figure 4.51). The pathway of Li1 showed to be direct for the first  $\sim 40$  Å and then encountered a blockage to which its movement reduced. Despite becoming blocked within the structure, Li1 was able to establish an alternate pathway to complete its transport.

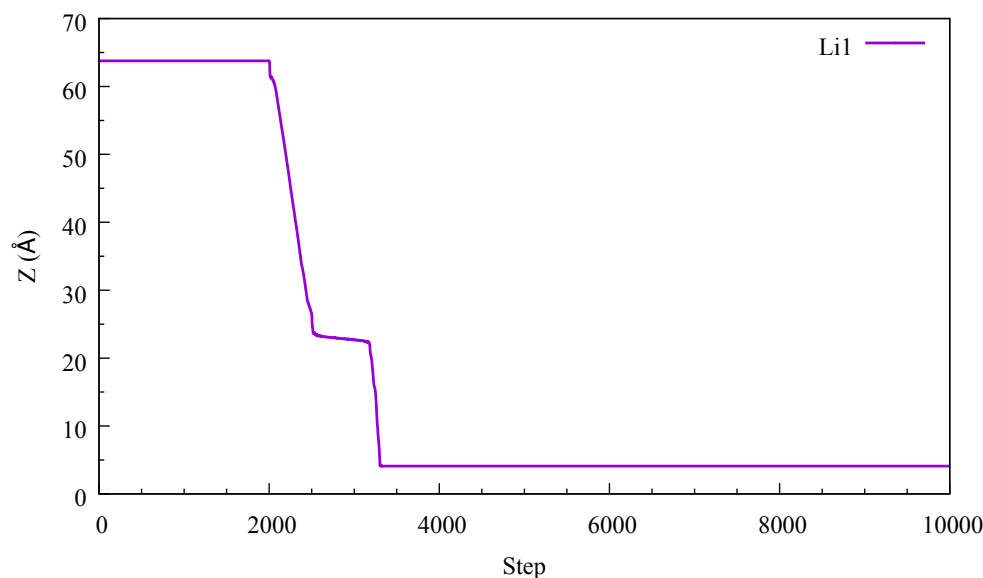


**Figure 4.51:** Plotted movement through the z-axis for the lithium ion diffusion through the OSPC-3 structure; Li1.

The reduction in movement was a result of the lithium ion attempting to diffuse through a area of tightly packed carbon atoms, requiring Li1 to manoeuvre around OSPC-3 to continue along its path. This was shown to be similar for several of the additional lithium ions, as shown for Li2, Li9, and Li11, which encounter areas along their diffusion pathway that reduce their movement through the system. However, each lithium ion was able to achieve complete diffusion through the system (Figure 4.52).

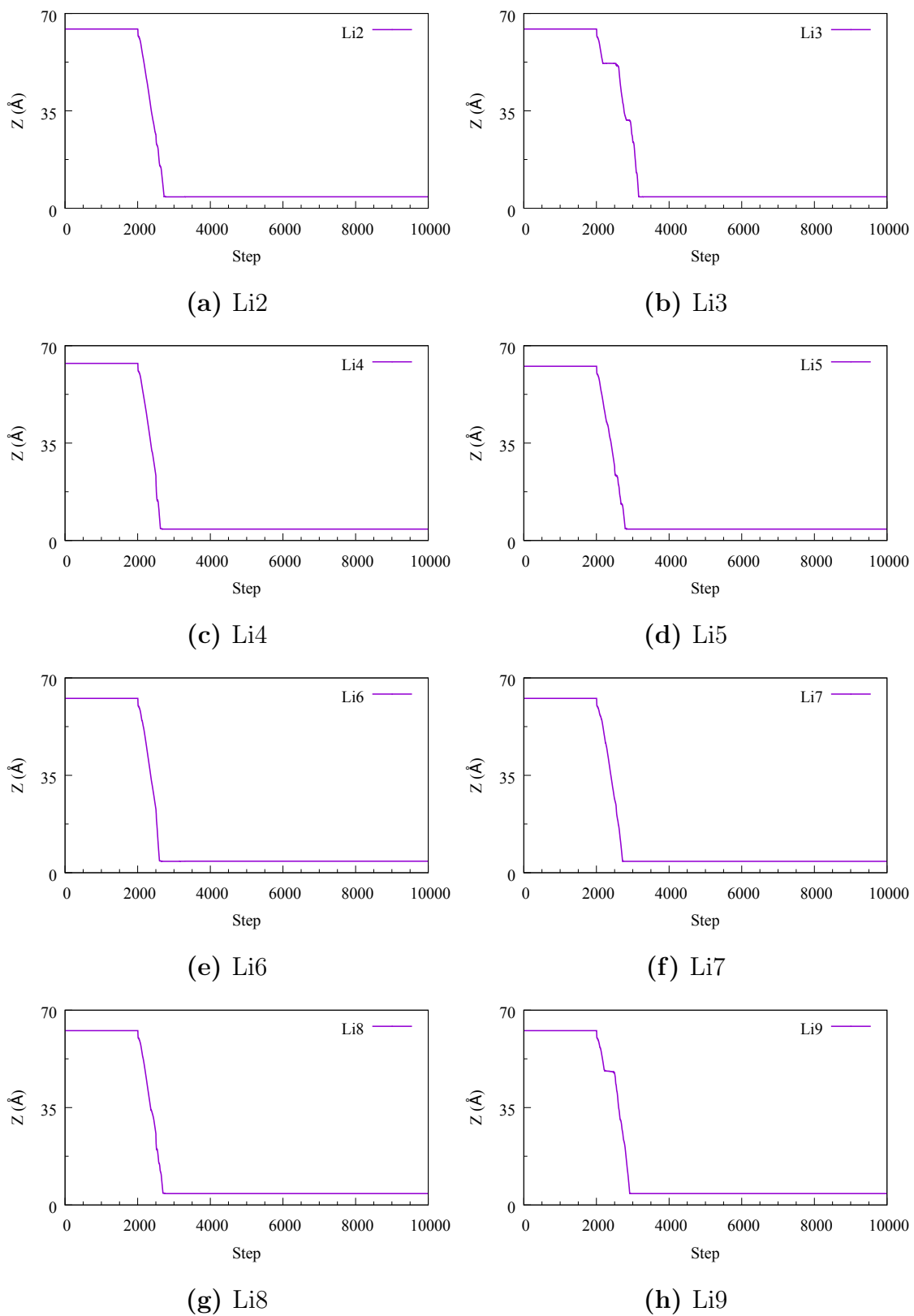
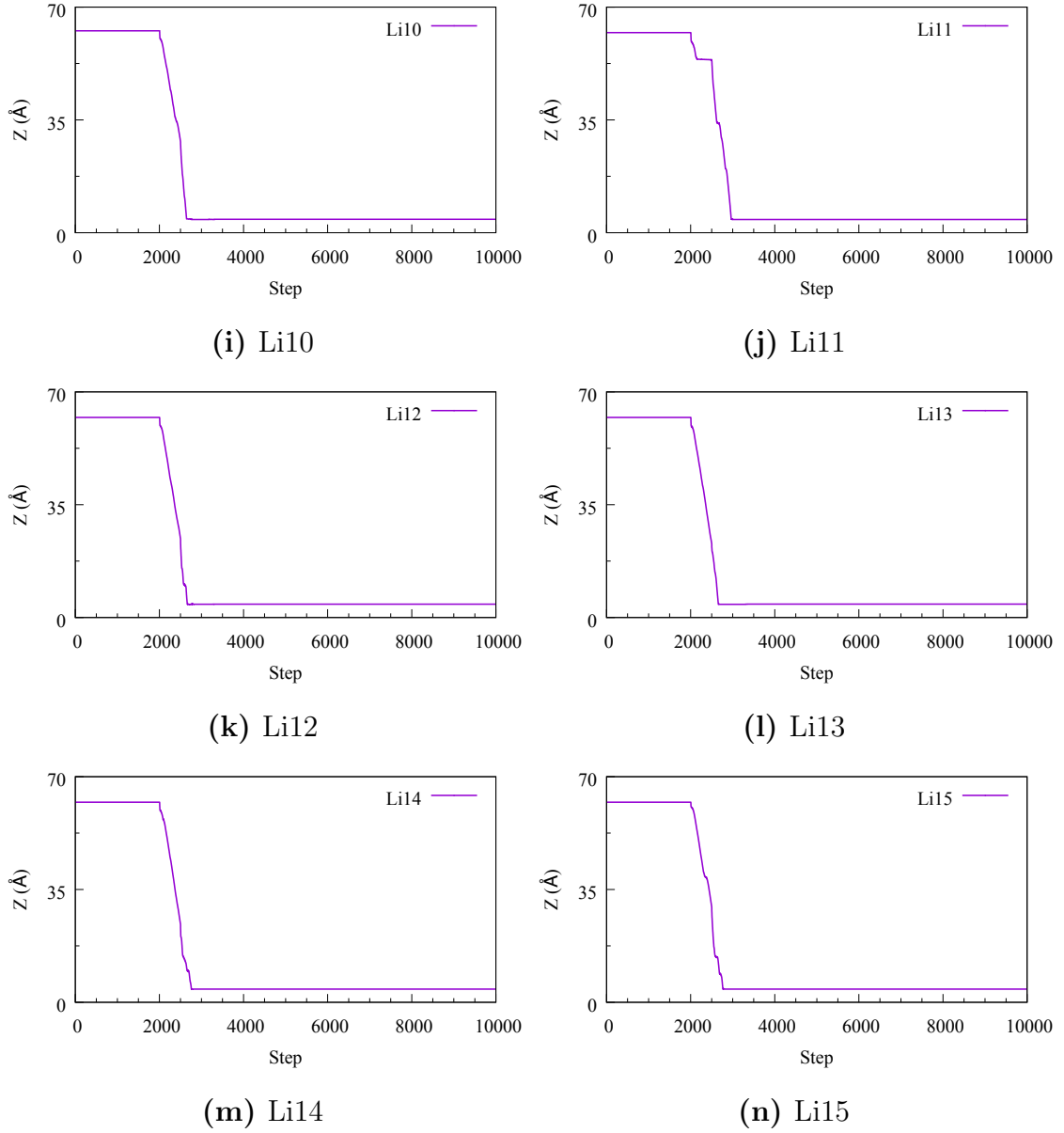


Figure 4.52



**Figure 4.52:** Migration plots of the individual lithium ions within the simulation cell of OSPC-3; (a)Li2 - (n)Li14.

The much less densely packed system allows the ions to establish direct pathways with far greater ease. The calculated diffusion rates of the lithium ions through OSPC-3 were substantially faster compared to both OSPC-1 and OSPC-2. As previously mentioned, Li2, Li9, and Li11 each exhibit reduced movement in areas of the structure. However, due to its chosen pathway, Li1 was the slowest ion to diffuse through the structure. The diffusion rates of the individual lithium ions through OSPC-3 is shown

in Table 4.7 and Figure 4.53. In comparison to OSPC-0, OSPC-1, and OSPC-2, the lithium ions diffuse at a greater rate through OSPC-3. The average rate of diffusion of the lithium ions within the OSPC-3 system is almost twice as fast in comparison to those within the OSPC-1 system (OSPC-3,  $7.63 \times 10^4 \text{ cm s}^{-1}$ ; OSPC-1,  $4.78 \times 10^4 \text{ cm s}^{-1}$ ).

Lithium ion	Ion mobility rate ( $\times 10^4 \text{ cm s}^{-1}$ )
Li1	4.52
Li2	8.23
Li3	5.13
Li4	9.42
Li5	7.32
Li6	9.68
Li7	8.08
Li8	8.33
Li9	6.32
Li10	8.99
Li11	5.94
Li12	8.69
Li13	8.74
Li14	7.58
Li15	7.50
Average	7.63

**Table 4.7:** Mobility rates of the individual lithium ions within the OSPC-3 system

The increased distance between  $sp^3$  nodes offered the potential for larger pore sizes and larger channels for the lithium ions to move through. Observing the interaction and close contact between the lithium ions and the carbon structure of OSPC-3, the diffusion rates of the lithium ions can be deemed relative to the free volume within OSPC-3, which resulted in these lithium ions displaying greater diffusion rates in comparison to the previous structures of OSPC-0, OSPC-1, and OSPC-2.

Having larger *node-to-node* struts, the distances between the lithium ions and

carbon atoms were assumed to be greater than those observed for OSPC-1 and OSPC-2. The distances of the fastest (Li6) and slowest (Li1) lithium ions against the closest carbon atoms were calculated for this comparison (Figure 4.54).

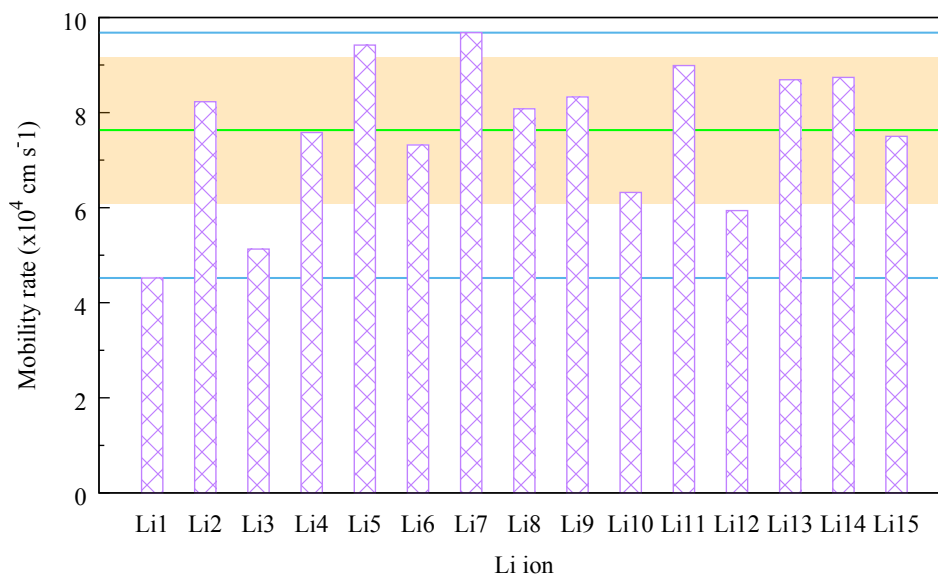


**Figure 4.53:** Plot of diffusion rates for the individual lithium ions within the OSPC-3 system; the green line represents the average diffusion rate, the upper and lower blue lines represent the maximum and minimum calculated rates respectively, and the highlighted region depicts the standard deviation of the mobility rate.

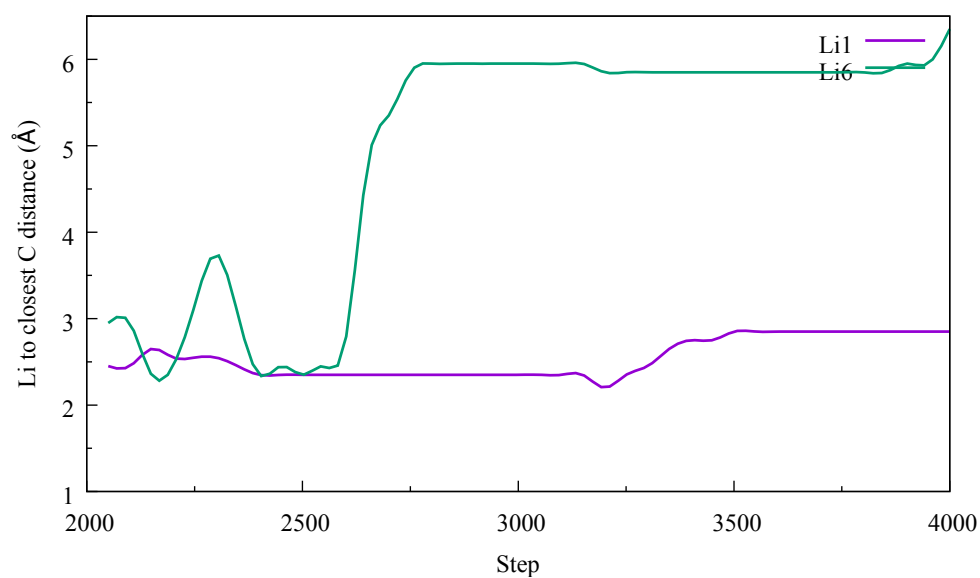


**Figure 4.54:** Radial distribution function of OSPC-3 collected over two thousand frames; Li1 (slowest) and Li6 (fastest).

Li1 maintained a close distance to OSPC-3 during its diffusion. Between 2500 and 3000 steps this distance remained unchanged because the lithium ion became trapped. In comparison, the distance of Li6 from OSPC-3 fluctuated as it diffused. The spikes in distance seen at  $\sim 2300$  and  $\sim 2600$  steps indicates where the pathway of the lithium ion widens. This correlates to the differences in diffusion rate and their movement through the z-axis (Figure 4.55). The increase in  $Li-C$  distance of Li6 correlates with the lithium ion increasing its movement at  $\sim 45$  Å, and also  $\sim 25$  Å. On the other hand, where the  $Li-C$  distance of Li1 plateaus correlates to the reduction in movement of the lithium ion. Additionally, the further decrease, followed by increase, in this distance coincides with Li1 establishing an alternate pathway.

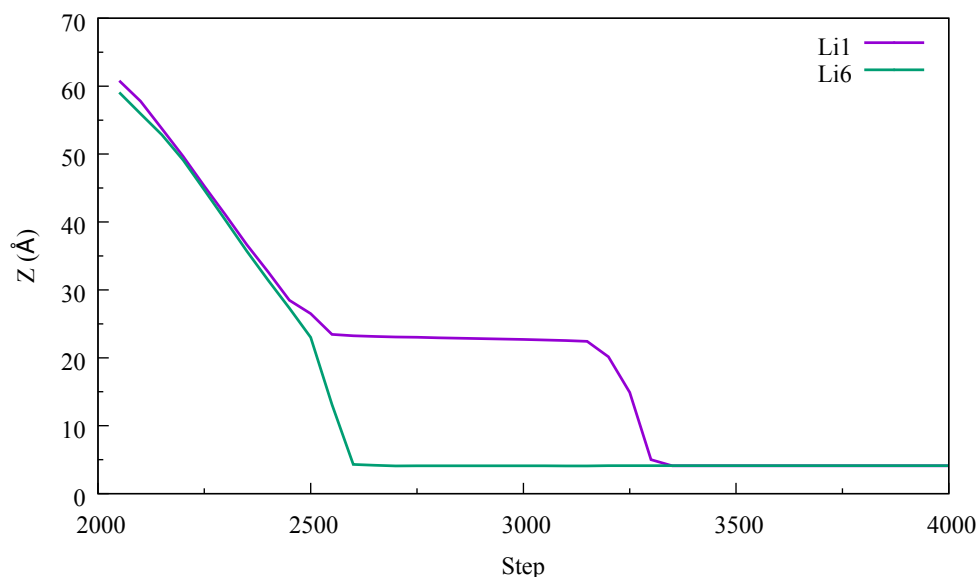


**Figure 4.55:** Li1 and Li6 diffusion pathways; distance vs. simulation time.

As we have seen with the generated structures of OSPC-0, OSPC-1, and OSPC-2, these carbon frameworks were not wholly open. The area at which Li1 displayed reduced movement is due to the generated OSPC-3 structure possessing an area of tightly packed atoms similar to those seen previously, resulting in the lithium ion becoming trapped for several hundred steps. This particular area is shown in Figure 4.56.



There is the potential of interpenetration within the OSPC-3 network as the possibility of large open voids increases with larger monomers. As a result, this could potentially lead to slower diffusion rates, with such examples including Li1, Li3, and Li11. However, uniform packing can result in large pores and wide channels for the lithium ions to diffuse.

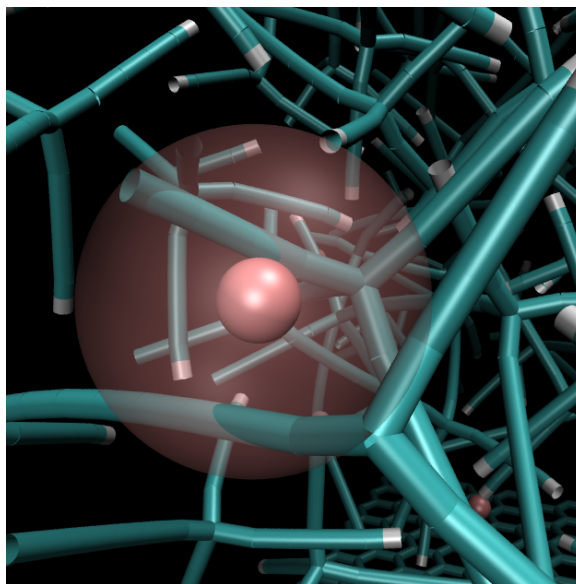


**Figure 4.56:** Visualisation of Li1 trapped with a framework pocket.

Observing the distance between the lithium ions and the carbon atoms in relation to their position shows where the ions of Li1 and Li6 were required to navigate narrower channels. Figure 4.57 shows the difference in distance from the carbon atoms between Li1 and Li6.

The *Li-C* distance of Li6 showed to increase at 40 Å, and again at 15 Å, whereas the *Li-C* distance of Li1 decreases as it moves through OSPC-3 before increasing as it reached the negatively charged graphene sheet. This resulted in an average measure distance for Li6 being greater than that of Li1. This illustrated how OSPC-3 could possess pores and channels of varying sizes, affecting the diffusion rate of individual lithium ions.

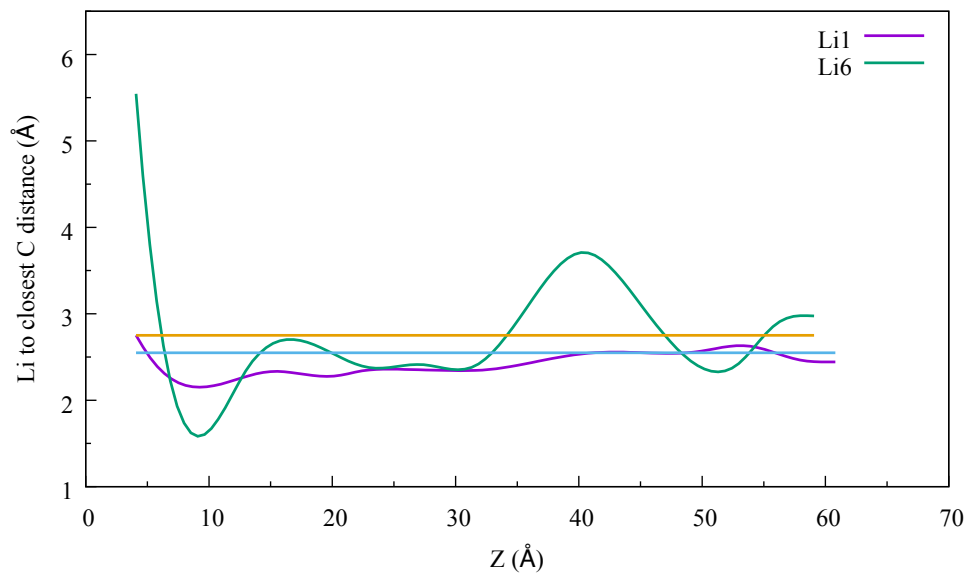


**Figure 4.57:** Radial distribution function of Li1 and Li6 against their position in the simulation z-axis.

Several carbon-carbon distances were measured to determine how much movement occurred of the OSPC-3 structure generated. Figure 4.58 displays the changes in carbon-carbon distances as lithium ions pass between them.

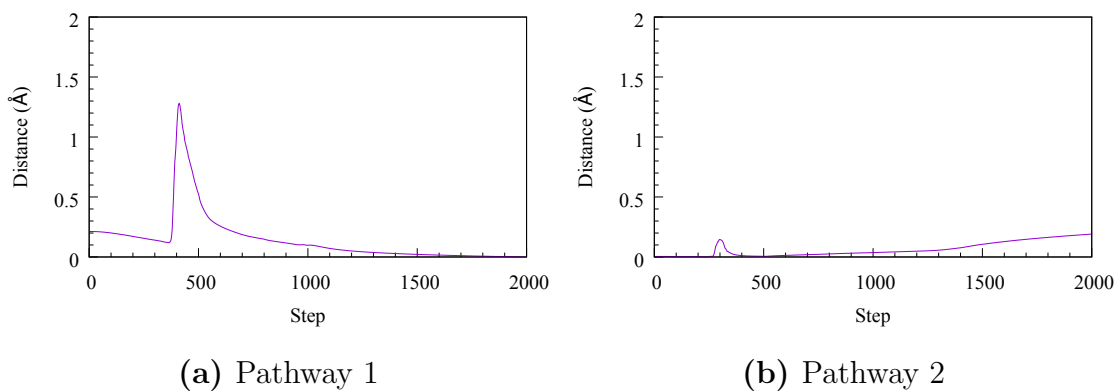


**Figure 4.58**

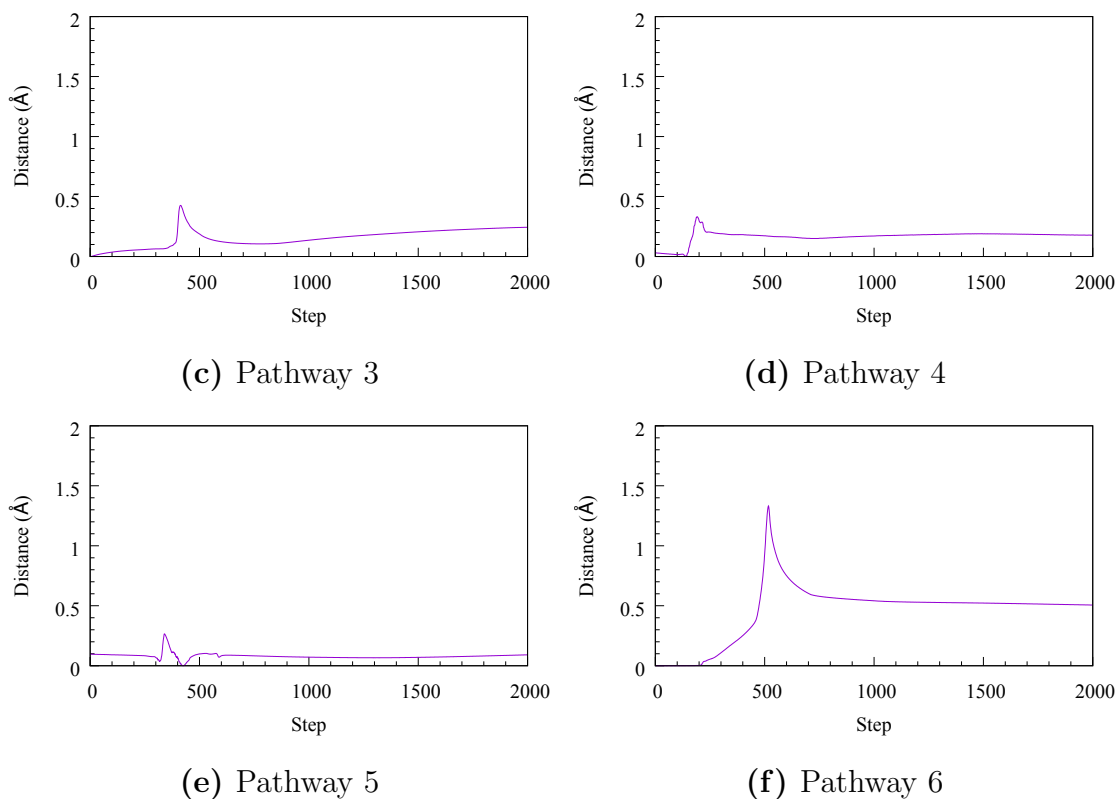


**Figure 4.58:** Distance movement of carbon atoms in separate struts from lithium ion passage within the OSPC-3 framework.

Due to the increased distance between the lithium ions and the carbon atoms of the OSPC-3 structure, the lithium ions did not interfere with the structure during diffusion, and in turn the diffusion of the lithium ions was not interrupted by the OSPC-3 structure. The carbon-carbon distances 2-5 show no greater than 0.5 Å in movement when the lithium ions pass between them, demonstrating the size of the available pathways within the structure. However, there is still a large increase in distance in carbon-carbon distance for pathway 1 and pathway 6. These are a representation of the tighter pathways present, and also the close packing of the atoms within the system. The increase in distance between these carbon atoms is presented in Table 4.8.

Pathway	Max displacement ( $\Delta$ Å)
1	1.280
2	0.190
3	0.425
4	0.331
5	0.264
6	1.332
Average	0.637

**Table 4.8:** Max displacement of the carbon atoms within the OSPC-3 structure during lithium ion diffusion.

The average movement is not dissimilar to that of OSPC-2 (0.609 Å). However, the data set collected from OSPC-3 is smaller, with two large changes in C-C distance. The size of the data set is representative to the free volume present in OSPC-3, allowing for the lithium ions to readily diffuse through.

This study demonstrated how the further increase in *node-to-node* distance potentially offers a more open framework. The diffusion of the lithium ions through the structure showed to be greater than previously observed in OSPC-0, OSPC-1, and OSPC-2. The free volume within OSPC-3 allows for the fast diffusion of the lithium ions, with little interference, demonstrating the capabilities of OSPC-3 as an anode for lithium ion batteries.

## 4.5 Comparison

Structures rationalised from the OSPC-1 have been designed and simulated to show comparison novel materials as anodes for lithium ion batteries, and also offering further insight into these OSPC and carbon-based porous networks. The smaller monomer of OSPC-0 gave rise to a more tightly packed construct, with smaller microporous channels for the lithium ions to traverse, and thus resulting in the much slower diffusion of ions through the system. OSPC-2, composed of the co-polymerisation of

the OSPC-1 monomer and a larger monomer containing additional alkyne groups, gave rise to a similar throughput of lithium ions to that of the OSPC-1. However, with the random nature of the materials constructed, the microporous structure involved diverse micropore sizes, resulting in a range of diffusion rates of the lithium ions. And lastly, OSPC-3, which involves four alkyne groups between the  $sp^3$ - $sp^3$  struts. This demonstrated a much faster diffusion of lithium ions as a result of its larger monomer, and, therefore, a more open framework.

Comparing the average diffusion rates calculated from each simulation, it was clear that increasing the distance between the  $sp^3$  carbons, and thus using larger monomers, gave the greatest diffusion of lithium ions. Figure 4.59 displays this comparison by showing how the diffusion rate is proportional to the  $sp^3$ - $sp^3$  node distance.

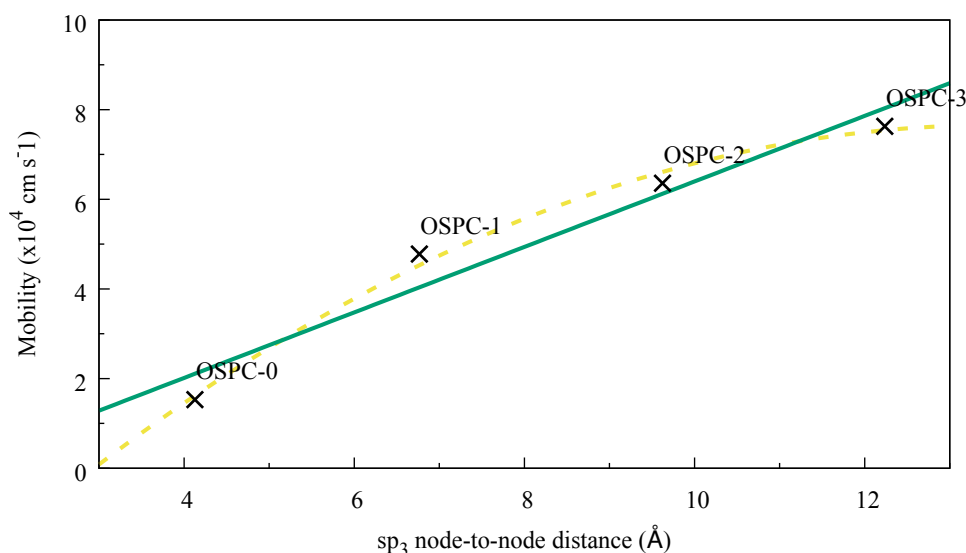


**Figure 4.59:** A comparison of lithium ion diffusion rates for OSPC-0, OSPC-1, OSPC-2, and OSPC-3, as a function of  $sp^3$  node-to-node distance (Å). The green line represents a linear trend with respect to the increasing node-to-node distance, and the yellow dashed line represents a trend that follows the changes in diffusion rate with increasing node-to-node distance.

This is also visible from the comparison of the normal distribution for each of the materials studied. Figure 4.60 shows how the diffusion rates differ between the structures, and displaying further how the increase in node-to-node distance affects

not only the average mobility rates observable with these structures, but also how alterations within the structure can give rise to broader ranges of mobility rates. OSPC-1 shows the greatest consistency in mobility rate compared to those of OSPC-0, OSPC-2, and OSPC-3. Additionally, the distribution of mobility rates through OSPC-2, with the variable node-to-node distances, overlap those of both OSPC-1 and OSPC-3.

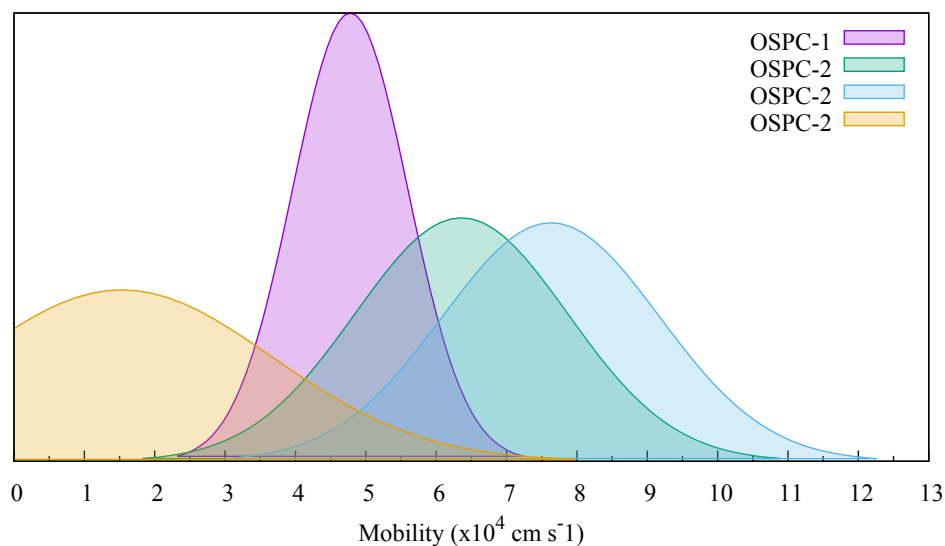


**Figure 4.60:** Normal distribution of lithium ion mobility rates through OSPC-1, OSPC-2, OSPC-3, and OSPC-0.

Increasing the distance between the  $sp^3$  carbons resulted in more open frameworks, with OSPC-2 and OSPC-3 having greater accessible surface areas than those of OSPC-1 and OSPC-0. The reduced interpenetration of the pores gave rise to more available and wider pathways for the lithium ions to traverse. However, several ions within each simulation encountered blockages and areas of densely packed carbon atoms, giving insight into the differences in pathway within each structure, and resulting in reduced movement and diffusion rates.

The co-polymerisation to produce OSPC-2 showed how this structure could possess characteristics similar to both OSPC-1 and OSPC-3. Controlling the structural development of OSPC-3 could potentially give rise to a structure wholly comprised of three-alkyne-long struts, and therefore offering a further comparison for lithium ion

diffusion.

The MD simulations entailing lithium ion diffusion with a charge bias has offered insight into how the OSPC materials may perform as an anode for lithium ion batteries. Differing diffusion rates were obtained between the three structures, with a strong correlation between diffusion rate and monomer size. OSPC-0, with a smaller monomer, produces a much more densely packed system with tighter channels and pathways, giving rise to an average diffusion rate of  $1.53 \times 10^4 \text{ cm s}^{-1}$ . OSPC-1 demonstrates a much larger diffusion rate of  $4.78 \times 10^4 \text{ cm s}^{-1}$ , due to the larger  $sp^3$  node-to-node distance. Increasing this distance farther with OSPC-2 and OSPC-3 increased the average diffusion rate observed, with OSPC-2 showing an average diffusion rate of  $6.36 \times 10^4 \text{ cm s}^{-1}$ , and OSPC-3 having a diffusion rate of  $7.63 \times 10^4 \text{ cm s}^{-1}$ .

Additionally, the flexibility of the alkyne struts within these materials plays a key role in the diffusion of ions through the systems. A more flexible strut showed to allow the structures to bend and move to open up pathways for the ions to traverse. However, this flexibility initially offered wider pathways, as shown by OSPC-3. Although, This flexibility is subjective of the length of alkyne strut. OSPC-0 possessed the shortest strut, making it the most rigid structure of the series, whereas OSPC-3 possessed the longest strut, which is freely able to flex within the structure. A comparison of the average angle of the struts within each structure is shown in Figure 4.61.

The measurements calculated showed that the struts within OSPC-3 were more acute than those observed in OSPC-0, OSPC-1, and OSPC-2. There was also little difference in angle between OSPC-1 and OSPC-2. The structure of OSPC-2 contains a variety of different strut lengths, which resulted in the average angle being very close to that of OSPC-1.

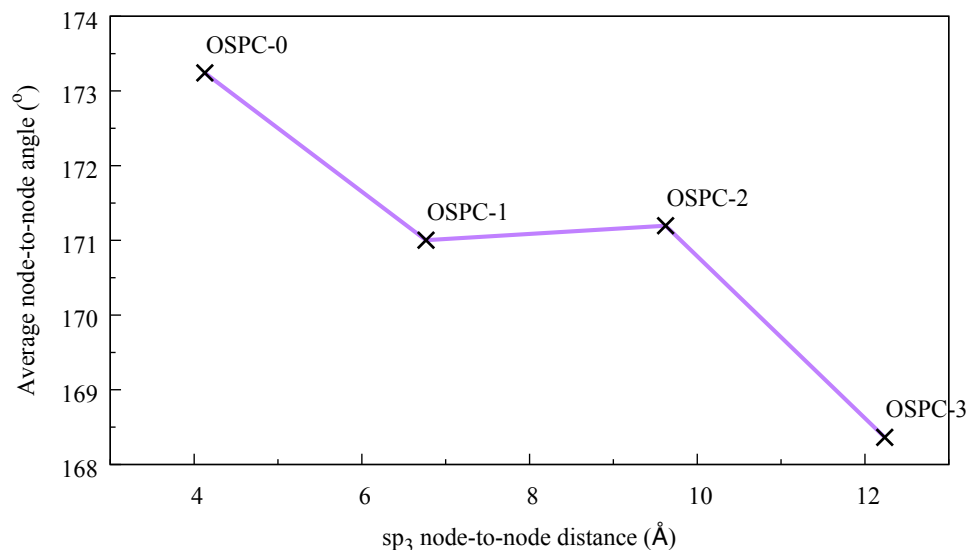


**Figure 4.61:** Average bond angle of the  $sp^3$ - $sp^3$  struts within OSPC-0, OSPC-1, OSPC-2, and OSPC-3.

## 4.6 Reproducibility

To demonstrate the reproducibility of AmBuild, and to give a representative data set for the internal structure of the porous carbon networks, two models of OSPC-0, OSPC-1, OSPC-2, and OSPC-3 were generated. The first models were subjected to lithium ion diffusion with DLPOLY as shown in Chapter 4, and the results compared prior to understanding their capabilities as anodes for alternative ion battery technologies. Due to the formation process involved using AmBuild, the building blocks are seeded and grown with random coordinates. This can result in several structures being generated that possess differing porous properties. The two structures generated had comparable diffusive properties for lithium ions. Table 4.9 displays the calculated diffusion rates of lithium ions through the two structures generated of OSPC-0, OSPC-1, OSPC-2, and OSPC-3. The former structure of OSPC-3 (RUN1, *vide supra* Section 4.4.3) gave a slower average diffusion rate of lithium ions compared to the latter (RUN2). However, the diffusion rates calculated for OSPC-0, OSPC-1, and OSPC-2 are very similar, showing that these structures did not differ greatly in



structural properties, and that the lithium ions were able to diffuse at the same rates through newly generated structures.

Although the differences in diffusion rate were minimal in comparison to OSPC-3, the diffusion rates of lithium ions through the structures of OSPC-0, OSPC-1, and OSPC-2 were slightly different. This demonstrates how the internal composition of each of these materials can differ throughout the polymers, and also that the generation of these amorphous materials using AmBuild is reproducible.

Lithium ion	Ion mobility rate ( $\times 10^4$ cm s $^{-1}$ )							
	OSPC-0		OSPC-1		OSPC-2		OSPC-3	
	RUN1	RUN2	RUN1	RUN2	RUN1	RUN2	RUN1	RUN2
Li1	0.17	0.49	5.88	5.14	4.96	5.83	4.52	7.97
Li2	7.07	0.25	4.22	4.86	5.08	7.69	8.23	8.35
Li3	0.19	1.36	5.47	4.90	6.71	3.71	5.13	3.64
Li4	0.22	0.10	3.32	3.58	6.77	9.00	9.42	7.41
Li5	1.42	1.89	4.25	4.81	7.39	7.87	7.32	8.57
Li6	0.04	0.22	5.30	3.30	8.34	5.18	9.68	7.64
Li7	3.59	4.69	4.55	5.93	6.65	7.17	8.08	6.26
Li8	0.12	0.14	5.36	4.25	6.27	7.08	8.33	5.41
Li9	3.32	0.37	4.28	5.06	4.30	6.50	6.32	7.27
Li10	4.32	7.59	3.95	5.55	3.18	5.97	8.99	4.45
Li11	0.00	0.46	3.61	5.05	8.19	7.41	5.94	6.52
Li12	0.10	0.14	5.94	4.48	5.48	7.63	8.69	5.01
Li13	0.15	0.23	4.75	5.41	6.42	6.81	8.74	4.73
Li14	0.02	4.51	5.24	4.98	7.67	8.24	7.58	7.81
Li15	2.21	0.03	5.48	5.73	7.99	6.26	7.50	2.50
Average	1.53	1.50	4.78	4.87	6.36	6.82	7.63	6.24
Range	0.00 - 7.07	0.03 - 7.59	3.32 - 5.94	3.30 - 5.93	3.18 - 8.34	3.71 - 9.00	4.52 - 9.68	2.50 - 8.57

**Table 4.9:** Mobility rates of the individual lithium ions within the generated systems of OSPC-0, OSPC-1, OSPC-2, and OSPC-3.

## 4.7 Conclusion

A new carbon-based framework has been introduced that possess strong lithium ion diffusion capabilities. The long cycle life and high capacity make it an ideal construct for development into lithium ion batteries. Here we have determined the available diffusion pathways for lithium ions through the structure of OSPC-1. The fifteen lithium ions observed diffusion completely through the OSPC-1 network with a charge bias at opposing ends of the simulation cell. The average diffusion rate calculated was  $4.78 \times 10^4 \text{ cm s}^{-1}$ .

Additionally, three alternative and novel structures based off OSPC-1 have been rationalised, and their diffusive behaviour studied. OSPC-0 has a reduced  $sp^3$ - $sp^3$  node distance, resulting in tighter packing of the building blocks, and therefore resulting in a structure with smaller pore and channel sizes in comparison to OSPC-1. The resulting average diffusion rate was calculated to be  $1.53 \times 10^4 \text{ cm s}^{-1}$ . On the other hand, increasing the  $sp^3$ - $sp^3$  distance with co-polymerisation with OSPC-2, and homo-coupling of larger monomers with OSPC-3, results in structures with more open frameworks, and therefore wider channels for the lithium ions to diffuse through. The resulting average diffusion rates for OSPC-2 and OSPC-3 were calculated to be  $6.36 \times 10^4 \text{ cm s}^{-1}$  and  $7.63 \times 10^4 \text{ cm s}^{-1}$  respectively.

This research and these structures give insight into new cathode materials for lithium ion batteries, and how increasing pore size can affect the rate of lithium ion diffusion. Experimental research into these rationalised materials could open up the OSPC family further and expand the development into lithium ion batteries.

*"Now I'm a scientific expert; that means I  
know nothing about absolutely everything."*

---

—Arthur C. Clarke

## Chapter 5

# Alternate battery technology development using OSPC

### 5.1 OSPC-1

Research into ion batteries is ever expanding. The discovery and anticipated development of OSPC-1 opens the doorway for the introduction of other organically synthesised porous anode carbon materials for ion batteries. Tailoring the physical properties of these materials can potentially offer a diverse series of properties and behaviours that can be utilised for specificity.

The development of new battery materials is key for technology progression. Due to the growing portable device industry, lithium ion batteries are becoming of high demand, with lithium ion supplies depleting at a fast rate. As alternatives to lithium ion batteries, batteries of sodium,<sup>231,232</sup> potassium,<sup>231,233</sup> calcium,<sup>234,235</sup> and magnesium<sup>236</sup> have been studied.

Due to its incredible performance as an anode for lithium-ion batteries, it is interesting to establish how OSPC-1 behaves for these alternative ions. The materials of OSPC-0, OSPC-1, OSPC-2, and OSPC-3 were generated between two graphene sheets using AmBuild. Sodium, potassium, magnesium, and calcium ions were placed as close as possible to one graphene sheet, and DLPOLY was used to monitor the

*active diffusion* through each system, along with any structural changes. The force field parameters of each ion were input into the AmBuild system. Sodium, potassium, and calcium PCFF<sup>154</sup> parameters are readily available and were used here, however the parameters from the COMPASS force field<sup>153</sup> were required for magnesium.

### 5.1.1 Sodium-ion batteries

Sodium ion batteries (SIBs) have been a concept for many years. Early studies showed how sodium ions ( $\text{Na}^+$ ) could be incorporated into carbon structures such as graphite, offering capacities from 30 mA h g<sup>-1</sup> to 140 mA h g<sup>-1</sup>.<sup>237</sup> Recent studies have shown the development of graphene-based, and many carbon-based anode materials for sodium ion batteries.<sup>238–240</sup> Several nitrogen-doped materials have shown charge capacities of up to 1000 mA h g<sup>-1</sup> with a current density of 0.1 A g<sup>-1</sup>.<sup>241</sup> Porous materials have also been studied for their potential as sodium-ion batteries. Ji *et al.* displayed the charge capacity capabilities of porous carbon frameworks.<sup>242</sup> This porous material displayed a charge capacity of 290 mA h g<sup>-1</sup> with a current density of 0.2 A g<sup>-1</sup>. Similarly, a mesoporous soft carbon material has shown great recyclability over 3000 cycles (103 mA h g<sup>-1</sup> at 0.5 A g<sup>-1</sup>). The maximum charge capacity of this material exceeded that of the porous carbon framework with 331 mA h g<sup>-1</sup> at 0.03 A g<sup>-1</sup> charge density.<sup>243</sup>

This research focussed on the diffusion capabilities of OSPC-1, OSPC-0, OSPC-2, and OSPC-3 as anodes for sodium ion batteries. Sodium ions possess an ionic radius larger than that of lithium ( $\text{Na}^+$ , 1.16 Å;  $\text{Li}^+$ , 0.9 Å). To analyse the diffusive behaviour of OSPC-1 and the rationalised materials, *active diffusion* migrations simulations were performed with the lithium ions positioned in RUN2 replaced with sodium ions, and the DLPOLY MD simulations performed accordingly.

The first sodium ion observed (Na1) was able to migrate completely through the OSPC-1 structure generated. The simulation cell and the migration pathway of Na1 are shown in Figure 5.1.

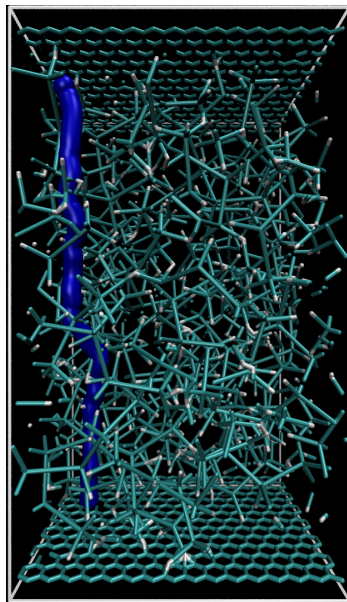


**Figure 5.1:** Graphical representation of the individual sodium ion, Na1, migrating through the OSPC-1 system. This representation is extracted from the complete migrations of the ion within the system, and onset as individual overlays with Van der Waals spheres.

Na1 had established a pathway that allowed it to migrate completely through the OSPC-1 structure generated with ease. Upon calculating the mobility rate via the movement in the z-axis, the pathway showed little to no reduction in movement, being able to navigate freely around OSPC-1 (Figure 5.2).

All of the 15 sodium ions observed in this simulation were able to completely migrate through OSPC-1 towards the negatively charged graphene sheet. This showed that the OSPC-1 structure generated is capable of allowing ions with larger ionic radius to pass through its structure. The mobility in z-axis of the additional sodium ions are shown in Appendix A.10.

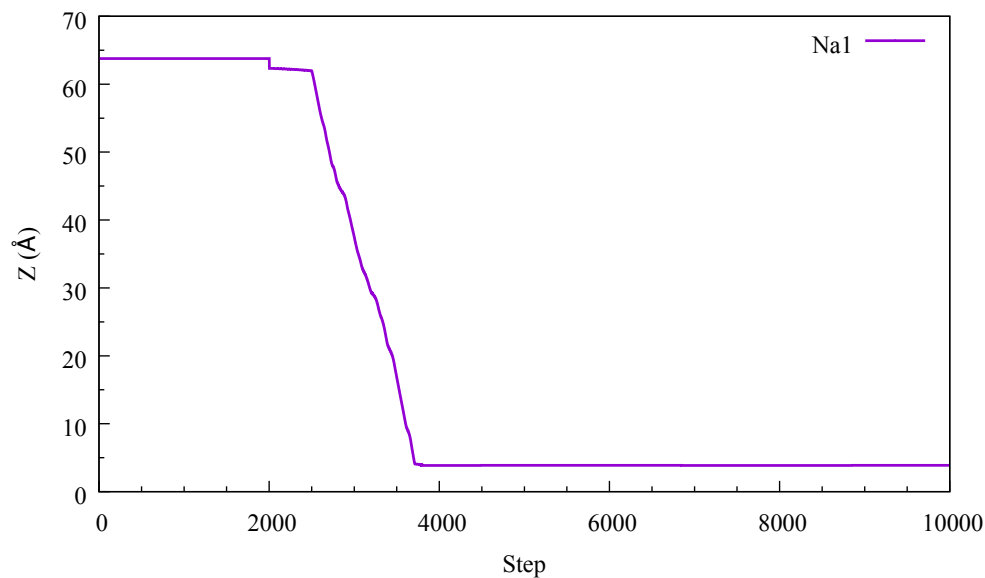


**Figure 5.2:** Movement in the z-axis during *active diffusion* of sodium 1 (Na1).

Many of the pathways established by the sodium ions observe little obstruction and reduced movement due to OSPC-1. However, Na3 (Appendix A.10b) and Na4 (Appendix Figure A.10c) encounter areas of the structure generated to which they were required to establish an alternate route to migrate through, resulting in a reduction in mobility rate. Both Na3 and Na4 had slower mobility rates to the additional sodium ions (Table 5.1), with Na4 displaying the slowest mobility rate of  $2.37 \times 10^4$  cm s<sup>-1</sup>.

Sodium ion	Mobility rate ( $\times 10^4 \text{ cm s}^{-1}$ )
Na1	$3.46 \times 10^4$
Na2	$3.08 \times 10^4$
Na3	$2.79 \times 10^4$
Na4	$2.37 \times 10^4$
Na5	$3.48 \times 10^4$
Na6	$3.58 \times 10^4$
Na7	$3.45 \times 10^4$
Na8	$3.02 \times 10^4$
Na9	$3.31 \times 10^4$
Na10	$3.18 \times 10^4$
Na11	$3.53 \times 10^4$
Na12	$3.21 \times 10^4$
Na13	$4.00 \times 10^4$
Na14	$3.53 \times 10^4$
Na15	$3.50 \times 10^4$
Average	$3.30 \times 10^4$
Range	$2.37\text{-}4.00 \times 10^4$

**Table 5.1:** Mobility rates of the individual sodium ions through the OSPC-1 system.

The mobility rate of the sodium ions was much slower in comparison to the lithium ion migration. The average mobility rate of the lithium ions was  $4.78 \times 10^4 \text{ cm s}^{-1}$ , whereas the average sodium ion mobility rate was  $3.30 \times 10^4 \text{ cm s}^{-1}$ . Expectedly, the ions of larger ionic radius migrated more slowly, in which the sodium ions were required to manoeuvre around OSPC-1 and establish wider pathways to migrate through. Comparing the movement of Li1 to Na1, it is shown that both ions encounter an obstruction at  $\sim 45 \text{ \AA}$ , although Li1 was able to move faster in the z-axis to that of Na1, thus resulting in a greater mobility rate (Figure 5.3). This demonstrates that ionic radius is also a determining factor for ion migration, and therefore diffusion, through OSPC-1, alongside the construction and formation of the porous network.

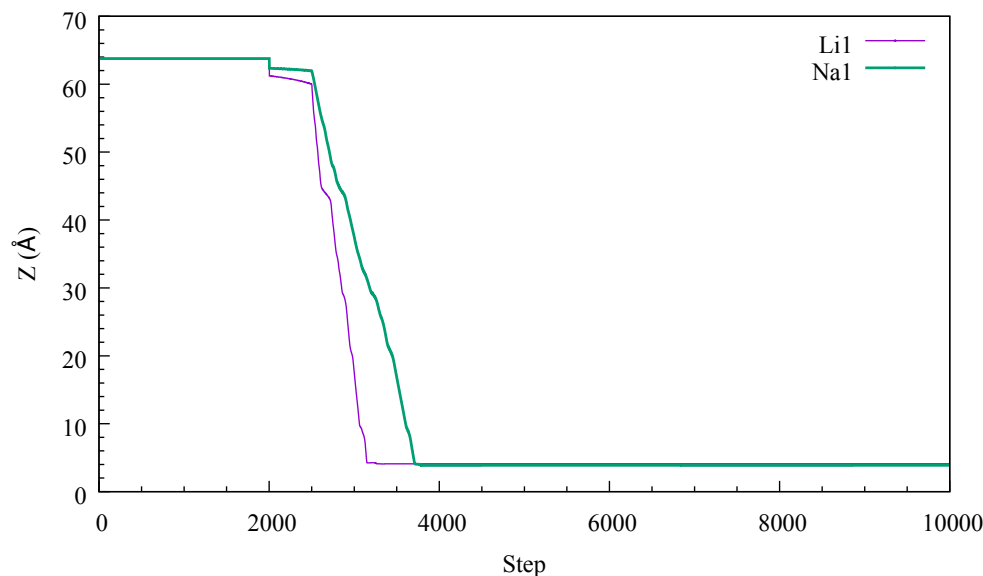


**Figure 5.3:** Difference in movement through the z-axis of Li1 and Na1 through the OSPC-1 structure generated.

This was apparent for each sodium ion observed. The sodium ions migrated at slower rates to their lithium ion counterparts (with the exception of Na6, having a mobility rate that was slightly greater than that of Li6). There was a difference of  $\sim 1.50 \times 10^4 \text{ cm s}^{-1}$  between the average mobility rate of lithium ions and sodium ions, and the maximum mobility rate observed of the sodium ions did not surpass  $4 \times 10^4 \text{ cm s}^{-1}$ . Figure 5.4 illustrates the difference in calculated mobility rates between the sodium ions and lithium ions through OSPC-1.

As the respective ions have the same starting position, the comparable mobility rates were therefore dependent on the size of the ion and the pathway established by each ion in the simulation. Comparing the migrations pathways of Na1 and Li1 (Figure 5.5), we can see that they were able to establish almost identical pathways through OSPC-1. However, as was established, the size of the sodium ion resulted in it moving at a slower rate through the structure than that of the lithium ion.



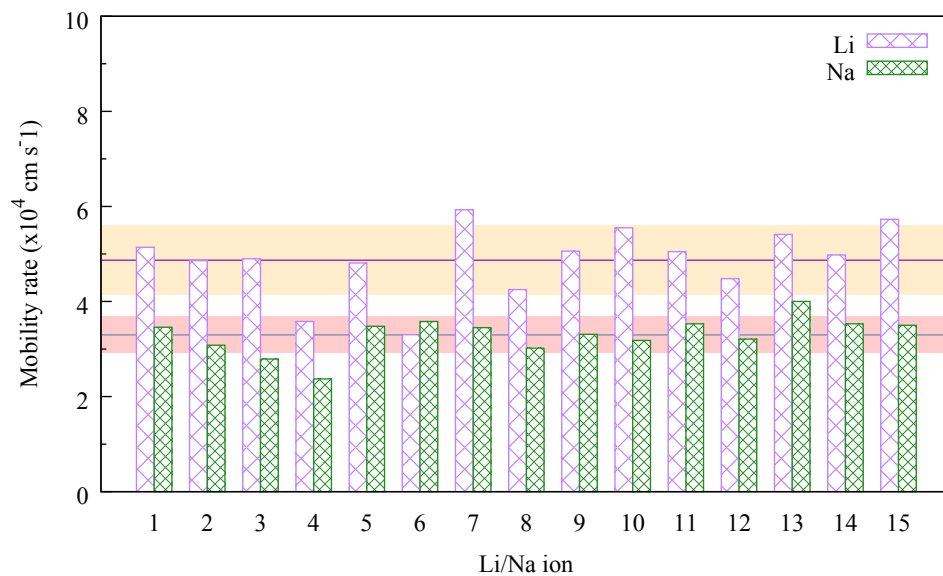


**Figure 5.4:** Comparison of the mobility rates for the sodium ion and lithium ion migration through the OSPC-1 framework. The pink line represents the average mobility rate of the lithium ions, the blue line represents the average mobility rate of the sodium ions, and the highlighted regions depict the standard deviation of the mobility rate for both lithium (orange) and sodium (red).

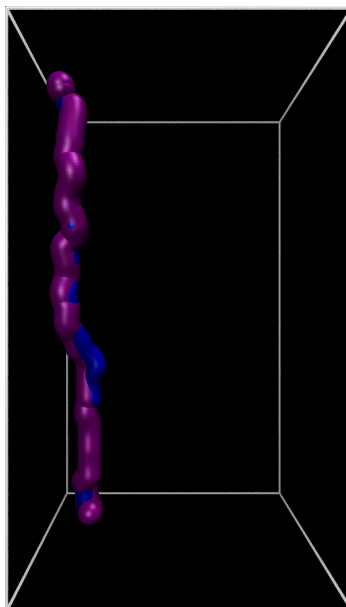


**Figure 5.5:** Overlay of atoms illustrating the migration pathways for Li1 (purple) and Na1 (blue) through the generated OSPC-1 structure.

The OSPC-1 structure generated allowed both ions to follow similar pathways through its construct. The pathway proved to be wide enough for both the lithium and sodium ions. However, the sodium ion was not able to pass through the structure once the charges had been applied, as is shown in Figure 5.4 where the sodium ion appeared to have no movement between 2000 and  $\sim 2500$  steps, and the lithium ion showed reduced movement. After 2500 steps the lithium ion was able to move rapidly once it had overcome its first obstacle. At 2770 steps we could see the difference in position between the two different ions as they traversed the system. Figure 5.6 displays the positions of both Na1 and Li1 at step 2770.

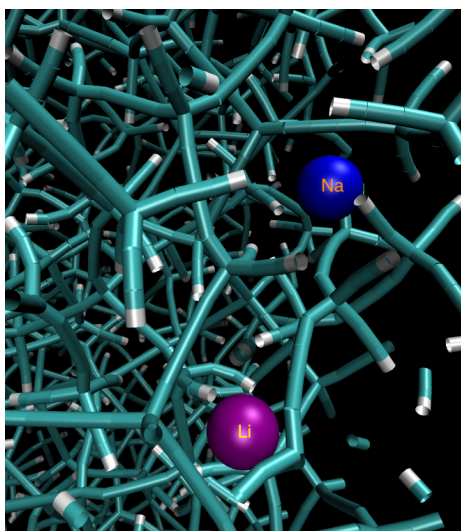


**Figure 5.6:** Li1 (purple) and Na1 (blue) position in the simulation cell at 2770 steps of the *active diffusion* simulation.

Although the mobility rate is slower for the sodium ions in comparison to the lithium ions observed, a complete migration was possible for the sodium ions through OSPC-1. The pathways determined for each sodium ion do not differ greatly from those established by the lithium ions. This showed that OSPC-1 was a potential as an anode for sodium ion batteries, offering pathways for the sodium ions to migrate through. However, the ions encountered more obstructions and had a slower mobility rate due to their ionic radius.

### 5.1.2 Potassium-ion batteries

Potassium-ion batteries (KIBs) have received much interest recently due to the availability and affordability of resources. Recent advancements have seen the development of 3-dimensional carbon frameworks as anode materials for potassium ion batteries.<sup>244</sup> KIBs based on a perylene-tetracarboxylic acid-dianhydride (PTCDA) cathode<sup>245</sup> and dipotassium terephthalate ( $K_2TP$ )<sup>246</sup> anode have shown great promise towards stable cycling performance. PTCDA based KIBs showed a specific capacity of  $131 \text{ mA h g}^{-1}$  with a potential range of 1.5-3.5 V vs.  $K/K^+$ , and retained a stable cycling performance over 200 cycles. This particular material demonstrated a great increase in capacity with a potential of 0.01 V vs.  $K/K^+$  ( $753 \text{ mA h g}^{-1}$ ). The  $K_2TP$  anode demonstrated a high capacity retention of 94.6 % over 500 cycles, and a specific capacity of  $249 \text{ mA h g}^{-1}$ . Jiang *et al.* have introduced several CMP materials that include benzothiadiazole.<sup>212</sup> These materials exhibit great band gap changes from changing the phenyl linker to benzothiadiazole. A prime example is the material produced involving pyrene. The band gap reduced from 2.37 eV to 1.95 eV. This has already been shown with the inclusion of longer linkers.<sup>124</sup> However, there is a movement of electron density by incorporation of benzothiadiazole, allowing  $K^+$  to readily interact with the electron rich sites. This results in a capacity of  $428 \text{ mA h g}^{-1}$ .

The capacities of these materials as KIBs are still comparably smaller to LIBs, although potassium ions possess larger ionic radii to both lithium and sodium ions. A large volume change commonly ensues from the size of potassium ions resulting in poor cyclability in comparison to lithium ion batteries.

Here we examine the diffusive capabilities of OSPC-1 as an anode for KIBs. The OSPC-1 structure generated for RUN2 of the lithium ion migration (*vide supra* Section 4.6) was used and the lithium ions replaced with potassium ions for the *active diffusion* simulation. Similar to the lithium ions and sodium ions, each potassium ion was able to migrate completely through the structure generated to the negatively charged

graphene sheet. K1 (Figure 5.7) was able to establish a migration pathway similar to that of Na1 and Li1.

However, in comparison to the calculated mobility rates and movement in the z-axis, K1 migrated more slowly than Li1 and Na1 through OSPC-1. The potassium ion showed a further reduction in movement for the first several hundred steps post charge application, followed by a further reduction in movement through the construct. Figure 5.8 shows the movement of K1 in the z-axis. The potassium ion completed its migration over approximately 2000 steps ( $\sim 4000$  steps total), whereas Li1 and Na1 migrated to the negatively charged graphene sheet at  $\sim 3200$  and  $\sim 3800$  steps, respectively.

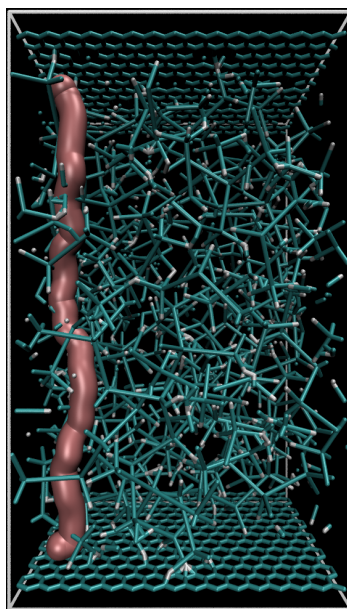


**Figure 5.7:** Graphical representation of the individual potassium ion, K1, migrating through the OSPC-1 framework. This representation is extracted from the complete migration of the ion within the system, and onset as individual overlays with Van der Waals spheres.

The increased size of the potassium ions resulted in slower mobility rates and reduced movement through OSPC-1. However, the porous construct of OSPC-1 posed no challenge for the potassium ions to pass through, with each ion completing its migration. The movement in the z-axis of each ion is shown in Appendix A.11. Although each ion was able to completely migrate through OSPC-1, several ions

showed periods of reduced movement where they were required to navigate blockages or narrower channels.

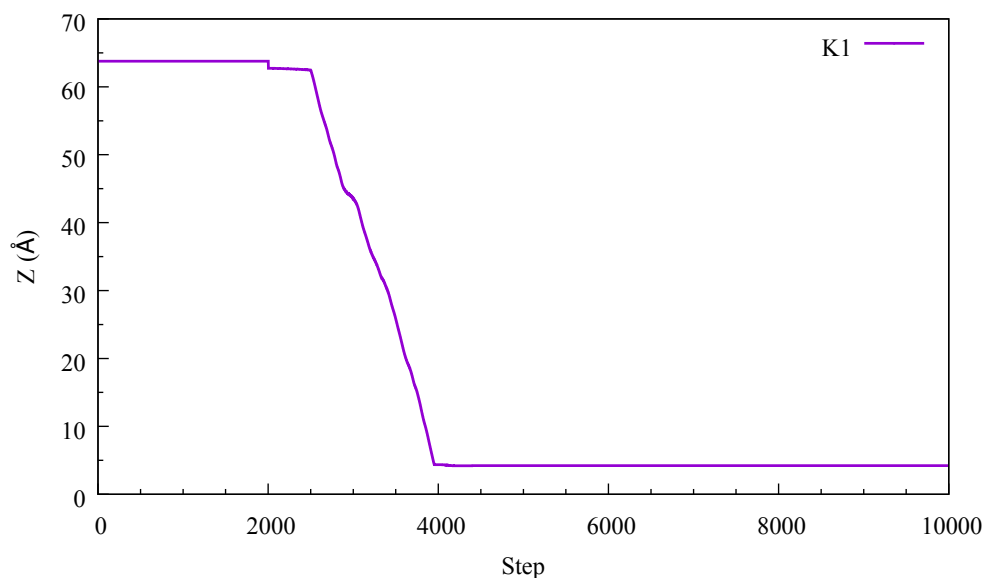


**Figure 5.8:** Plot of migration through the z-axis of K1; OSPC-1.

K4 is an example of a potassium ion encountering a blockage along its pathway. Li4 also encounters this obstruction, although the duration in which the potassium ion took to overcome the blockage, and continue on its migration pathway is greater than that of the lithium ion. Li4 becomes blocked for approximately 500 steps, whereas K4 takes over 1000 steps to establish an alternate route. The comparison between the z-axis movement of K4 and Li4 is shown in Figure 5.9. Li4 showed to migrate at a greater rate before becoming trapped, and then continued to migrate at a great rate once released. K4, on the other hand, migrated at a slower rate to begin with, but displayed a greater rate of mobility once it had navigated the blockage.

As well as becoming trapped for a longer duration than Li4, K4 was required to establish a different route to that of Li4 (Figure 5.10). The potassium ion can be seen following a similar pathway to Li4 before the blockage, and then diverts onto a differing path to complete its migration. The potassium ion was unable to follow the lithium ion along the same pathway due to its larger ionic radius, and the size of the pathway.

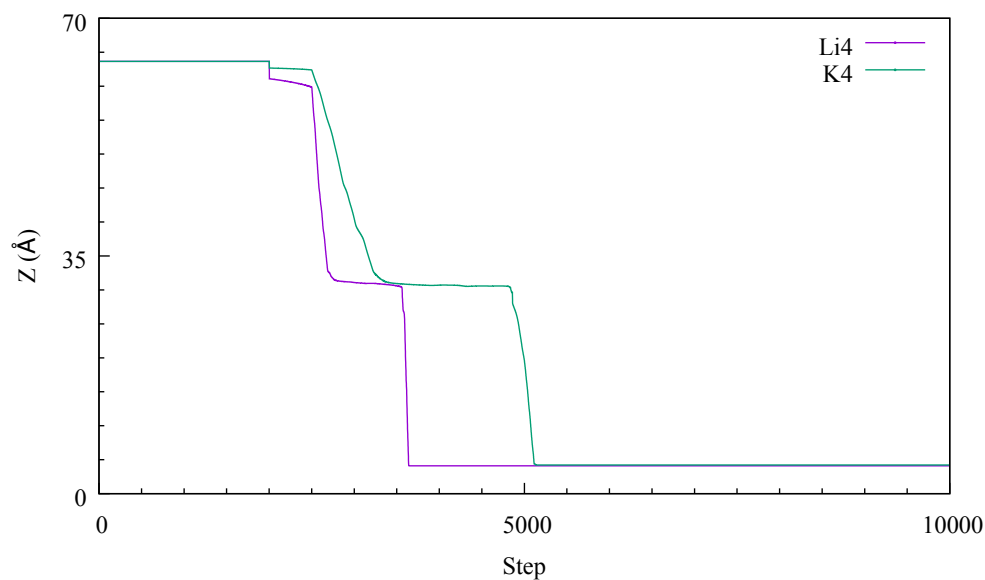


**Figure 5.9:** Comparison of the z-axis movement for Li4 (purple) and K4 (green).

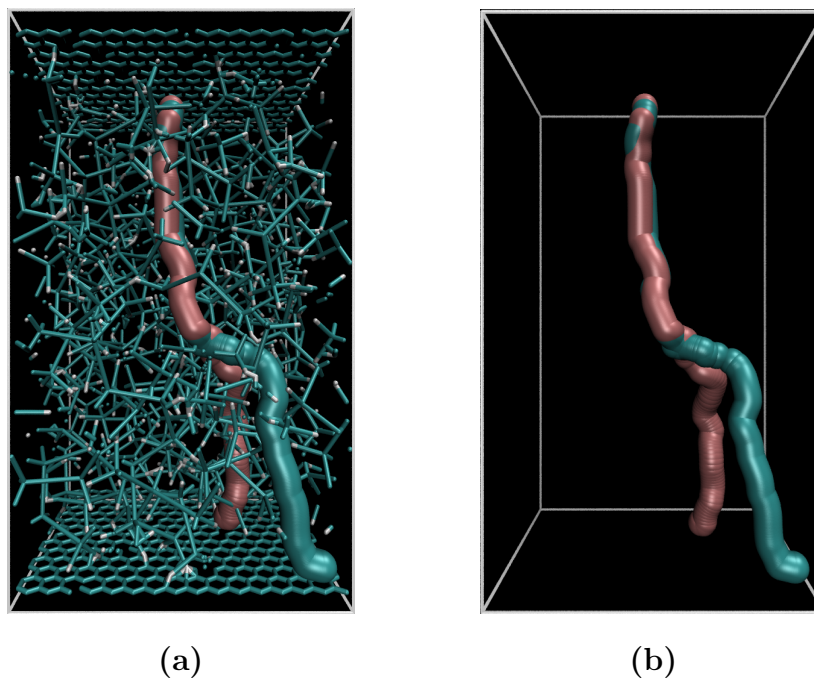


**Figure 5.10:** Migration pathways for Li4 (pink) and K4 (blue) during the respective OSPC-1 migration simulations.

The change in migration pathway illustrated the potential pathway sizes available in OSPC-1, and also gave evidence towards further reduction and diversion of pathway for ions of much larger ionic radius.

The mobility rates calculated for the potassium ions did not surpass the mobility rates of any of the lithium ions (Table 5.2).

Potassium ion	Ion mobility rate ( $\times 10^4 \text{ cm s}^{-1}$ )
K1	$3.02 \times 10^4$
K2	$2.60 \times 10^4$
K3	$2.73 \times 10^4$
K4	$1.88 \times 10^4$
K5	$2.65 \times 10^4$
K6	$2.23 \times 10^4$
K7	$2.96 \times 10^4$
K8	$2.39 \times 10^4$
K9	$2.81 \times 10^4$
K10	$2.71 \times 10^4$
K11	$2.76 \times 10^4$
K12	$2.33 \times 10^4$
K13	$3.06 \times 10^4$
K14	$2.36 \times 10^4$
K15	$3.13 \times 10^4$
Average	$2.64 \times 10^4$

**Table 5.2:** Mobility rates of the individual potassium ions through the OSPC-1 system.

The average mobility rate for of the potassium ions was calculated at  $2.64 \times 10^4 \text{ cm s}^{-1}$ , whereas the average mobility rate for the lithium ions was  $4.78 \times 10^4 \text{ cm s}^{-1}$ . Comparably, the average mobility rate of the sodium ion migration was calculated to be  $3.30 \times 10^4 \text{ cm s}^{-1}$ . This study of group 1 ions migrating through the OSPC-1 structure generated demonstrates that the ionic radius of the ions is a highly impacting factor on their migration, and therefore a potential impactor on ion diffusion. The average mobility rate decreases going down the group from lithium ions to potassium ions.

The comparison between the individual lithium ions and potassium ions through OSPC-1 is shown in Figure 5.11. As previously observed, K4 becomes trapped within

the OSPC-1 structure, forcing the ion to establish a new direction. Because of this obstruction, K4 was the slowest potassium ion to migrate through ( $1.88 \times 10^4 \text{ cm s}^{-1}$ ), whereas K15 was the fastest to migrate through, at  $3.13 \times 10^4 \text{ cm s}^{-1}$ . The mobility rate of K15 was much slower in comparison to both Li15 and Na15 ( $5.73 \times 10^4$  and  $3.30 \times 10^4 \text{ cm s}^{-1}$ , respectively), demonstrating how the size of pores within the microporous structure, as well as the size of ionic radius, affect the transport of ions.

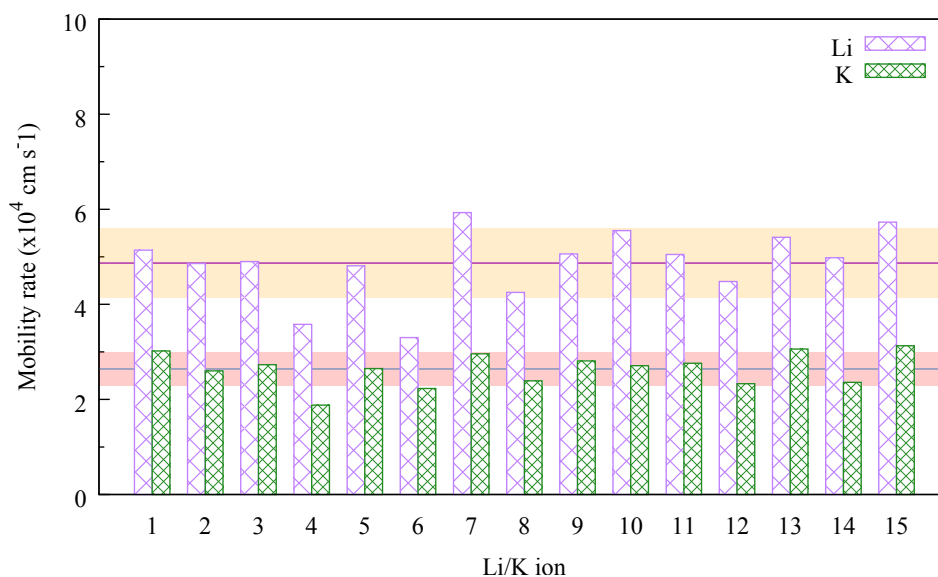


**Figure 5.11:** Comparison of mobility rates for the individual lithium and potassium ions during the OSPC-1 simulations. The pink line represents the average mobility rate of the lithium ions, the blue line represents the average mobility rate of the potassium ions, and the highlighted regions depict the standard deviation of the mobility rate for both lithium (orange) and potassium (red).

This study showed that OSPC-1 has the capacity to allow potassium ion migrate through its structure, and therefore a potential candidate as an anode for KIBs. However, the larger ionic radius of the potassium ions resulted in a slower mobility rate. Additionally, the pathways available for the lithium ions were not as readily accessible for the potassium ions (as seen with Li4 and K4), which presented obstructions and blockage to which the potassium ions were required to deviate from the lithium ion pathway.



### 5.1.3 Magnesium-ion batteries

Magnesium ion battery technology (MIBs) is still young in comparison to LIBs. Magnesium is a suitable choice as an anode material due to its much lower price and toxicity. In comparison to lithium, magnesium as an anode provides a considerably high volumetric energy density alongside its high volumetric capacity ( $2200 \text{ mA h g}^{-1} / 3800 \text{ mA h cm}^{-3}$ ).<sup>247</sup> However, the main difficulties of developing MIBs has been the electrolyte solution, as proton donating nor accepting show to be unsuitable, and also the choice of cathode material, as magnesium is not easily intercalated into many hosts.<sup>248,249</sup> Aurbach *et al.* first introduced a rechargeable MIB with a capacity of  $\sim 122 \text{ mA h g}^{-1}$ .<sup>250</sup> Since then, research has focused on developing materials that approach the challenges MIBs face. Doi *et al.* showed the capabilities of potential positive electrodes for MIBs, demonstrating their high electrical conductance.<sup>251</sup> More recent advances have seen the development of rechargeable MIBs displaying rate capabilities up to  $200 \text{ mA h g}^{-1}$ .<sup>252,253</sup>

The following simulations were performed to determine the diffusive capabilities of magnesium ions through the OSPC-1 structure, establishing its suitability as an anode for MIBs. In the same manner as the sodium ion and potassium ion simulations performed (*vide supra* Sections 5.1.1 and 5.1.2), the lithium ions of the OSPC-1 structure generated for RUN2 were replaced with  $\text{Mg}^{2+}$  ions, and the *active diffusion* migration simulations were performed accordingly. Each of the magnesium ions in the simulation were able to completely migrate through OSPC-1 to the negatively charged graphene sheet, establishing migration pathways that presented minor obstructions as they traversed the system. Figure 5.12 shows the migration pathway of Mg1 through OSPC-1. Mg1 was able to establish a pathway through OSPC-1 that showed a high degree of linearity through the construct. This is shown also in Figure 5.13. The magnesium ion encountered a similar obstacle to that of Li1 at the beginning of its migration, having started to follow the same pathway as that of the lithium ion.

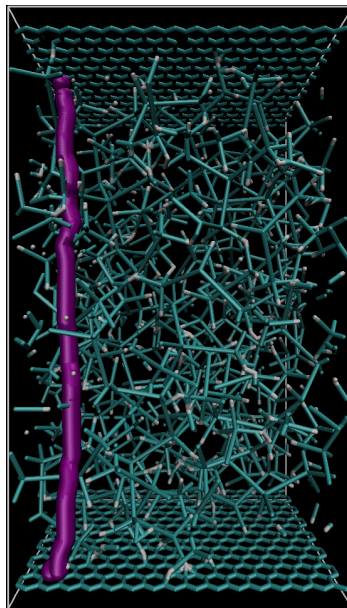


**Figure 5.12:** Graphical representation of the individual magnesium ion, Mg1, migrating through the OSPC-1 framework. This representation is extracted from the complete migration of the ion within the system, and onset as individual overlays with Van der Waals spheres.

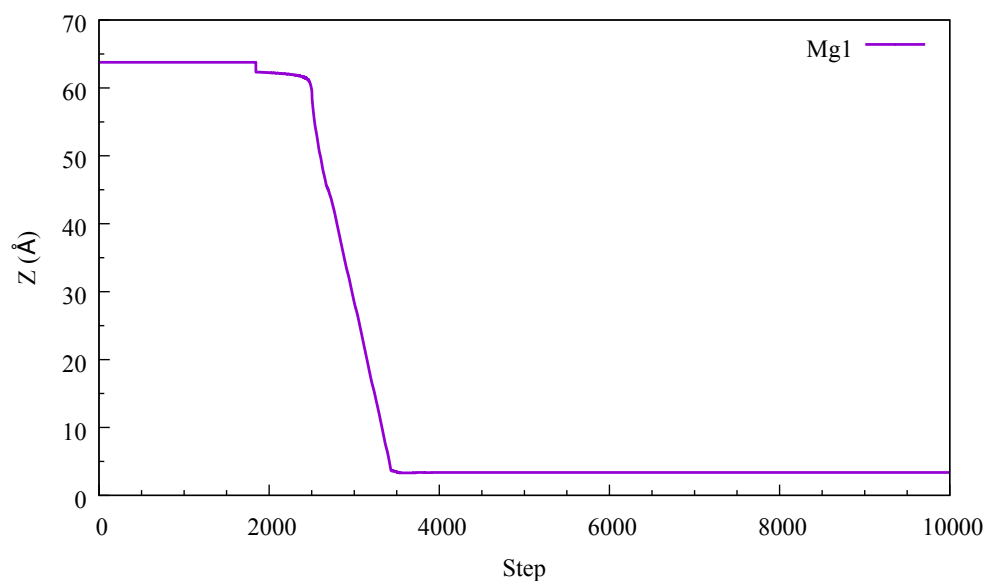


**Figure 5.13:** Migration through the z-axis of Mg1; OSPC-1.

However, Mg1 diverted from that pathway and established a different route, to which it had encountered very few obstacles as it traversed the system, resulting in a final position that was different to that of the lithium ion at the negatively charged

graphene. Despite the ionic radius of the magnesium ions being similar to that of the lithium ions, the migration pathway of Mg1 greatly differed. Another example of the magnesium ions establishing a different migration pathway to their respective lithium ions is Mg3. The magnesium ion diverts from the lithium ions pathway within the early stages of the simulation. However, both ions converge to a very similar position at the negatively charged graphene sheet (Figure 5.14).

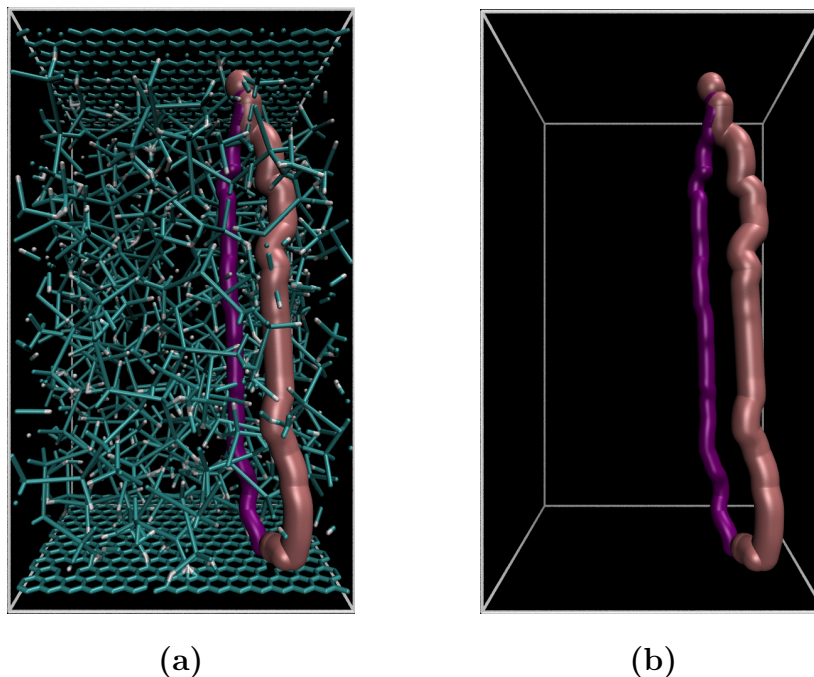


**Figure 5.14:** Migration pathways for Li3 (pink) and Mg3 (purple) during the respective OSPC-1 *active diffusion* simulation.

The migration pathway established for Li3 appeared to be more contorted compared to that of Mg3. However, the chosen migration pathway for Mg3 contained more obstructions. This was apparent from their mobility rates and movement through the z-axis (Figure 5.15). Mg3 showed a reduction in movement at approximately 55 Å, but was able to continue its migration without further obstruction. The rate at which it migrated through after overcoming the obstacle was still slower than that of Li3, resulting in the ion reaching the negatively charged graphene sheet in over  $\sim 2000$  steps, whereas Li3 achieved this in less than 1500 steps.

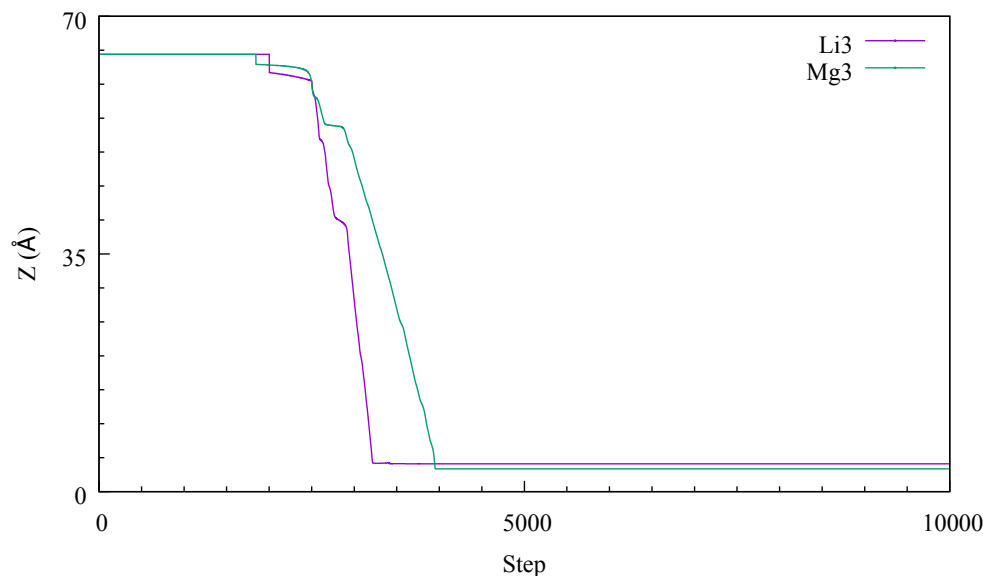


**Figure 5.15:** Comparison of the z-axis movement between Li3 and Mg3 through the OSPC-1 structure. Li3 shown in purple and Mg3 shown in green.

This was similar for the additional magnesium ions (Appendix A.12). The majority of magnesium ions established direct pathways through OSPC-1, although, such examples as Mg3, Mg9, and Mg11 encountered more obstructions during their migration. With the exception of Mg4 and Mg6, the mobility rates calculated for each magnesium ion were slower than their respective lithium ions. The individual calculated mobility rates of the magnesium ions are shown in Table 5.3.

Due to its obstruction, Mg3 presented the slowest mobility rate of all the magnesium ions with  $3.09 \times 10^4 \text{ cm s}^{-1}$ , whereas Mg13 showed the fastest mobility rate of the series with  $4.79 \times 10^4 \text{ cm s}^{-1}$ . In comparison to the lithium ions, the average mobility rate is slower. The lithium ions presented an average mobility rate of  $4.87 \times 10^4 \text{ cm s}^{-1}$ , compared to  $3.94 \times 10^4 \text{ cm s}^{-1}$  of the magnesium ions (Figure 5.16).

Magnesium ion	Ion mobility rate (x10 cm s <sup>-1</sup> )
Mg1	4.18 x10 <sup>4</sup>
Mg2	3.68 x10 <sup>4</sup>
Mg3	3.09 x10 <sup>4</sup>
Mg4	4.20 x10 <sup>4</sup>
Mg5	3.35 x10 <sup>4</sup>
Mg6	3.69 x10 <sup>4</sup>
Mg7	4.56 x10 <sup>4</sup>
Mg8	3.80 x10 <sup>4</sup>
Mg9	3.26 x10 <sup>4</sup>
Mg10	3.80 x10 <sup>4</sup>
Mg11	3.34 x10 <sup>4</sup>
Mg12	4.41 x10 <sup>4</sup>
Mg13	4.79 x10 <sup>4</sup>
Mg14	4.15 x10 <sup>4</sup>
Mg15	4.75 x10 <sup>4</sup>
Average	3.94 x10 <sup>4</sup>

**Table 5.3:** Mobility rates of the individual magnesium ions through the OSPC-1 system.

The maximum mobility rate observed of the magnesium ions did not surpass the average mobility rate calculated of the lithium ions through OSPC-1. However, the magnesium ion mobility rates were greater than those calculated of the sodium ions and potassium ions  $3.30 \times 10^4$  and  $2.64 \times 10^4$  cm s<sup>-1</sup>, respectively). This was due to the ionic radius of magnesium being smaller than both sodium and potassium, resulting in a greater mobility rate than both of the group 1 ions. Additionally, magnesium holds a 2+ charge, which is more strongly attracted to the negatively charged graphene sheet than the group 1 ions, allowing it to move through OSPC-1 and force any bond movement of the carbon structure.

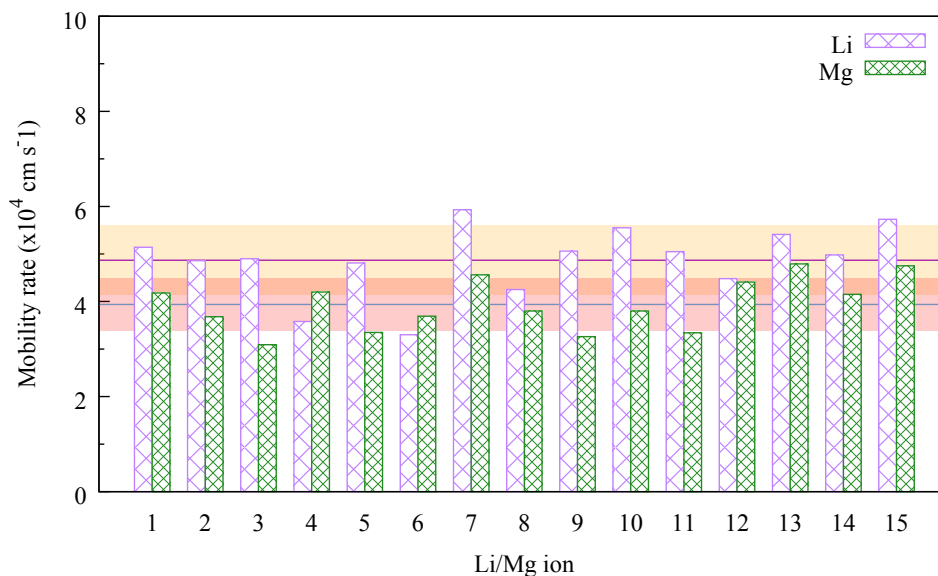


**Figure 5.16:** Comparison of mobility rates for the individual lithium and magnesium ions during the OSPC-1 simulations. The pink line represents the average mobility rate of the lithium ions, the blue line represents the average mobility rate of the magnesium ions, and the highlighted regions depict the standard deviation of the mobility rate for both lithium (orange) and magnesium (red).

This study showed that OSPC-1 is capable of allowing magnesium ions to pass through its structure. As well as this, the magnesium ions migrated at a greater rate than the group 1 ions of sodium and potassium. Lithium ions, with their smaller ionic radius, maintained a greater mobility rate than the magnesium ions. However, each magnesium ion was able to completely migrate through OSPC-1, demonstrating the capabilities of the carbon structure as an anode for MIBs.

#### 5.1.4 Calcium-ion batteries

Calcium ions show great potential within the field of battery technologies.<sup>235</sup> However, additional research is required for them to reach their full potential, and to demonstrate properties that lithium-ion batteries have displayed. Development of calcium-ion batteries (CIBs) has faced several challenges, one including the lack of redox processes at room temperature, although the greater abundance of calcium available compared to lithium proves to be a beneficial factor towards CIB progres-

sion.<sup>254,255</sup> Here we investigate the capabilities of OSPC-1 as an anode for CIBs, and the pathways available for calcium ions. MD simulations using the OSPC-1 structure generated for RUN2 were performed, replacing the lithium ions previously observed with  $\text{Ca}^{2+}$  ions. Firstly observing the migration pathway of Ca1 (Figure 5.17), the calcium was able to completely migrate through OSPC-1 towards the negatively charged graphene sheet. The pathway observed closely resembles that established by Mg1 (*vide supra* Section 5.1.3), finishing in a very similar position to the magnesium ion.

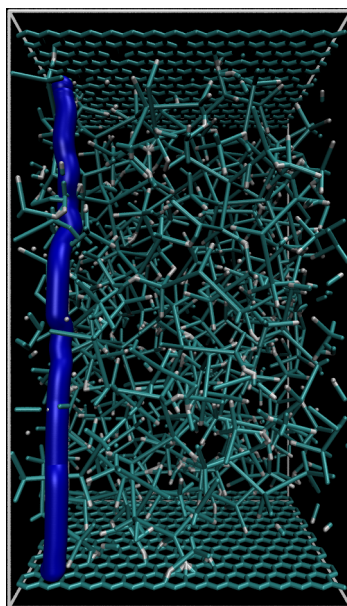


**Figure 5.17:** Graphical representation of the individual potassium ion, Ca1, migrating through the OSPC-1 framework. This representation is extracted from the complete migration of the ion within the system, and onset as individual overlays with Van der Waals spheres.

Calcium has a much larger ionic radius out of the two divalent ions observed. However, this does not restrict the migration of calcium ions. Each individual ion was able to establish a pathway through the OSPC-1 structure that allowed for their complete migration (Appendix A.13. The divalent ions are more strongly attracted to the negatively charged graphene sheet, which has potential to enforce movement in the OSPC-1 structure. However, the size of these ions inhibits their trajectory, as previously seen with the larger of the group 1 ions (*vide supra* Section 5.1.2). Observing the movement Ca6 through the structure, it is apparent that the size of

the ion affects the rate at which it migrates, although the greater charge in comparison to that of lithium ions ( $\text{Li}^{1+}$ ) reduces the obstructions encountered by the ion. As shown in Figure 5.18, the calcium ion moves steadily through the structure once the charge is applied. Whereas, in comparison, the lithium ion, Li6, moves in a step-like fashion, displaying fast mobility before encountering blockages at several regions along its migration pathway. Both ions appear to arrive at the same positions in z-axis at within the same time period. However, due to the faster movement of the lithium ion after each blockage, it was able to migrate at a greater rate than that of the calcium ion.

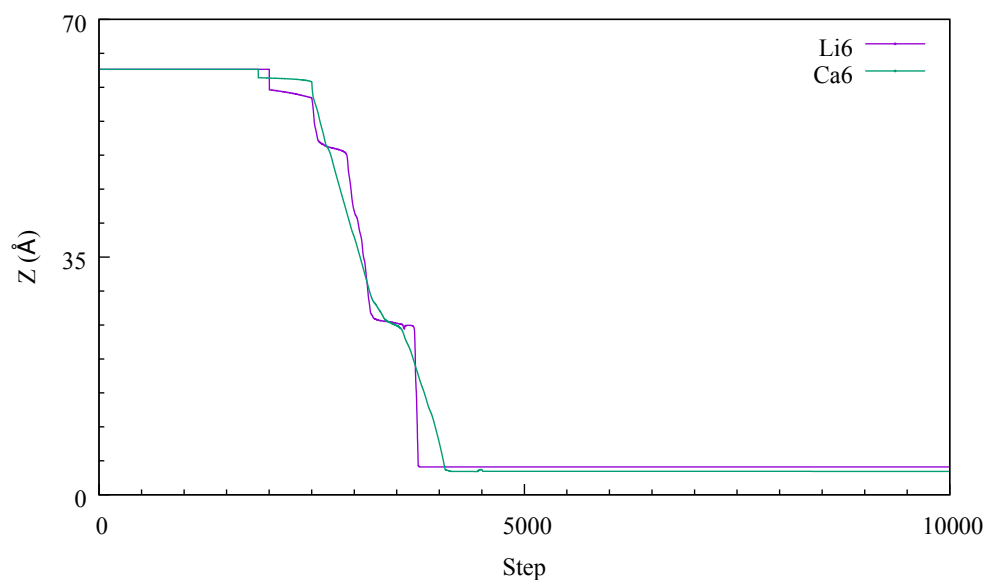


**Figure 5.18:** Comparison of ion movement in the z-axis between Li6 and Ca6 through the OSPC-1 structure.

The pathways established by Li1 and Ca1 are almost identical for the first 35 Å through OSPC-1. It was at this point where the calcium ion deviated from the pathway taken by Li1, and was able to establish an alternate pathway to complete its migration. The area in which they both encountered had blocked the lithium ion from continuing its migration, whereas the calcium ion was able to encourage the movement of the OSPC-1 framework, allowing it to continue along its desired pathway. Figure 5.19 displays the area where the lithium ion becomes trapped, and the calcium ion overtaking the lithium ion during its migration. As the calcium ion possess a stronger



attraction and repulsion to the graphene sheets, it was able to force its way through the construct. The lithium ion, on the other hand, became trapped for approximately 200 steps before it could release itself. However, the steady movement of the calcium ion compared to the rapid movement of the lithium results in Ca6 migrating at a slower rate to that of Li6.

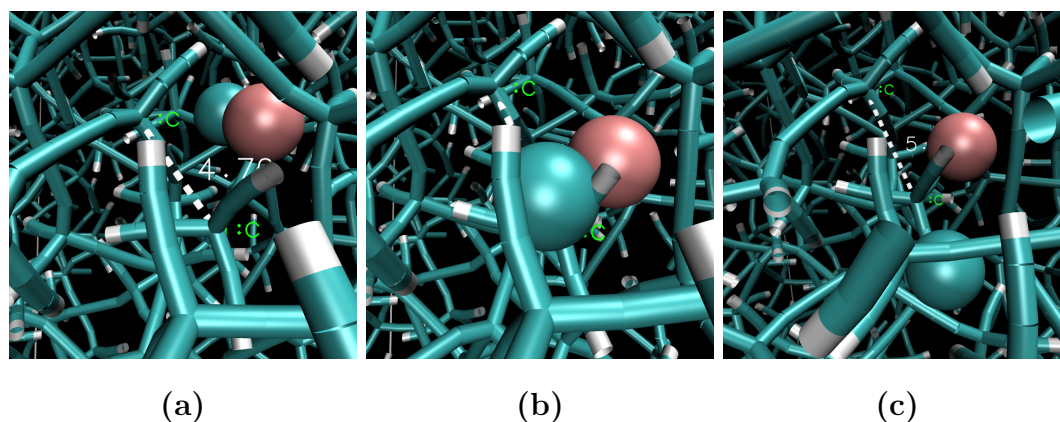


**Figure 5.19:** Graphical representation of the ions Li6 and Ca6 migrating through the OSPC-1 structure at  $\sim 25$  Å. (a) and (b) illustrate the position at which both ions become trapped, and (c) illustrates where the calcium ion is able to take a different pathway to the lithium ion and continue to migrate through the system.

In comparison, the mobility rate of Ca6 was calculated at  $2.83 \times 10^4$  cm s<sup>-1</sup> (Table 5.4), whereas Li6 displayed a mobility rate of  $3.30 \times 10^4$  cm s<sup>-1</sup> (Table 4.9). Additionally, the respective calcium ions showed slower mobility rates to the lithium ions, giving a calculated average mobility rate of  $3.06 \times 10^4$  compared to  $4.87 \times 10^4$  cm s<sup>-1</sup> from the lithium ions.

The calcium ions showed to move at continuous rates, encountering only minor obstructions from the OSPC-1 structure generated. They were able to enforce movement in the carbon atoms due to their charge, although their size reduced this rate as they were required to navigate pathways that allowed for them to pass through. The migration of magnesium ions through the system could do so at a much greater rate ( $3.94 \times 10^4$  cm s<sup>-1</sup>), demonstrating again that the size of the ions is a limiting factor for the migration, and therefore diffusion, through this porous material.

Despite having an ionic radius smaller than both of the larger monovalent ions,

the mobility rate calculated of the calcium ions did not surpass that of the sodium ions ( $3.30 \times 10^4 \text{ cm s}^{-1}$ ), which had an ionic radius slightly larger than that of  $\text{Ca}^{2+}$ . However, the calculated average mobility rate of the calcium ions was greater than the average of the potassium ions ( $2.64 \times 10^4 \text{ cm s}^{-1}$ ). Figure 5.20 illustrates the differences in mobility rate between the individual lithium and calcium ions that result in the difference in average mobility rates calculated.

Calcium ion	Ion mobility rate ( $\times 10^4 \text{ cm s}^{-1}$ )
Ca1	$3.04 \times 10^4$
Ca2	$2.63 \times 10^4$
Ca3	$2.44 \times 10^4$
Ca4	$3.20 \times 10^4$
Ca5	$2.66 \times 10^4$
Ca6	$2.83 \times 10^4$
Ca7	$3.56 \times 10^4$
Ca8	$2.80 \times 10^4$
Ca9	$2.88 \times 10^4$
Ca10	$3.35 \times 10^4$
Ca11	$2.59 \times 10^4$
Ca12	$3.37 \times 10^4$
Ca13	$3.64 \times 10^4$
Ca14	$3.26 \times 10^4$
Ca15	$3.67 \times 10^4$
Average	$3.06 \times 10^4$

**Table 5.4:** Mobility rates of the individual calcium ions through OSPC-1.

Overall, the larger divalent ion was able to establish pathways through OSPC-1 that allowed for complete migration, indicating the potential of OSPC-1 as an anode for calcium ions. The larger ion migrated at slower rates than the lithium, sodium, and magnesium ions, but displayed mobility rates great than potassium. This was expected as it has a larger ionic radius than both lithium and magnesium, although its size does not differ greatly to sodium ions, to which the mobility rate was slower,

yet did not differ too greatly. This study further clarified how the pathways available and size of ion affect the mobility rate, and in turn diffusion rate, through OSPC-1.

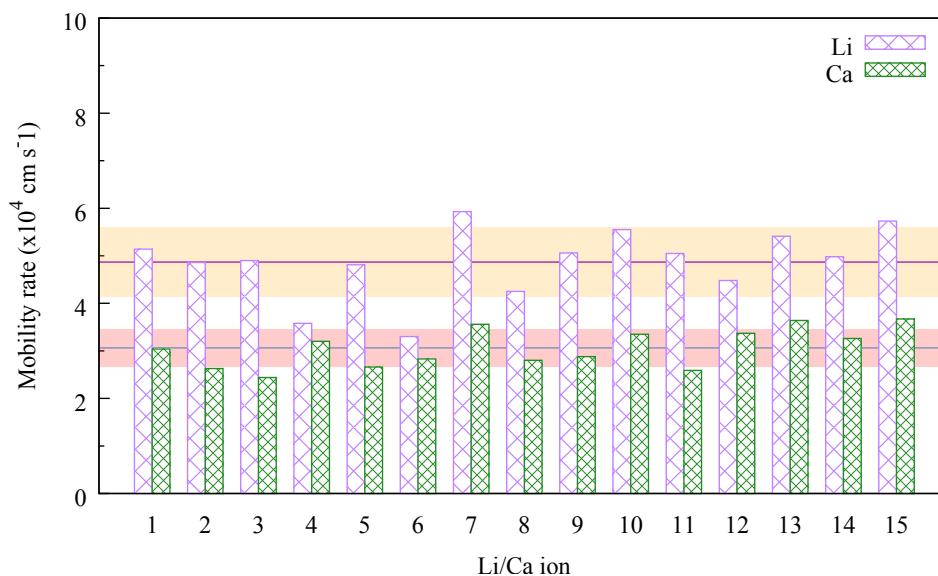


**Figure 5.20:** Comparison of mobility rates for the individual lithium and magnesium ions during the OSPC-1 simulation. The pink line represents the average mobility rate of the lithium ions, the blue line represents the average mobility rate of the calcium ions, and the highlighted regions depict the standard deviation of the mobility rate for both lithium (orange) and calcium (red).

### 5.1.5 Conclusion

The lithium ions observed in this study showed the greatest mobility rate through OSPC-1 in comparison to the alternative metal ions (Table 5.5). The smaller ionic radius allows the  $\text{Li}^+$  to ions find suitable pathways to traverse, without relying too heavily on Van der Waals forces to take effect and force their way through the structures. Analysis of the migration pathways established by the ions in these simulations proved that OSPC-1 was capable of allowing lithium, sodium, potassium, magnesium, and calcium ions to pass through, although the pathways available challenged the migration of ions with larger ionic radius. This resulted in potassium displaying the slowest mobility rate. The increase in ionic radius led to the influence of size and charge coming into effect. Magnesium and calcium possess smaller ionic radii to those of sodium and potassium, allowing them to traverse through smaller microporous chan-

nels. Although, The greater charge that they possess intensifies this potential, as the attraction towards the negatively charged graphene sheet allows them to apply Van der Waals forces to a greater extent, thus manipulating the OSPC-1 structure to a greater extent. This showed that the ionic charge of the ions was a rate determining factor. With the exception of lithium, the divalent ions presented greater mobility rates than their respective monovalent ions in each period ( $\text{Mg}^{2+} > \text{Na}^+$ ;  $\text{Ca}^{2+} > \text{K}^+$ ).

Ion	Average ion mobility rate ( $\times 10 \text{ cm s}^{-1}$ )
Li	$4.87 \times 10^4$
Na	$3.30 \times 10^4$
K	$2.64 \times 10^4$
Mg	$3.94 \times 10^4$
Ca	$3.06 \times 10^4$

**Table 5.5:** The average mobility rates calculated for the each ion observed migrating through OSPC-1.

Although the lithium ions encountered blockages more frequently than the other ions, they were able to exhibit greater mobility when their pathways were more open. In comparison, the calcium ions migrated through the structure at a continuous rate, and showed very few periods of reduced movement along their pathways. The size and charge of the calcium ions compared to the lithium ions introduced a *bull-dozing* effect on the OSPC-1 structure generated. Each ion enforced movement of the carbon framework to allow each ion to pass, although, they navigated these pathways at reduced rates to the lithium. A similar effect was seen with in the migration of magnesium ion, where each ion encountered fewer obstructions, yet moved at a slower pace to the lithium ions.

Comparing the mobility rates of each ion showed the correlation between the size of ionic radius and the diffusive capabilities of OSPC-1 (Figure 5.21). Both the monovalent and divalent ions decreased in mobility rate as the ionic radius increased down the peridoc group. Sodium and calcium possess very similar ionic radii, therefore

offering mobility rates that are closely related of  $3.28 \times 10^4 \text{ cm s}^{-1}$  and  $2.90 \times 10^4 \text{ cm s}^{-1}$ , respectively. On the other hand, magnesium ions display a much greater mobility rate to those of sodium, potassium, and calcium. The reduced ionic radius, alongside the  $+2$  charge, allow them to navigate established migration pathways more readily, giving rise to an average mobility rate of  $3.71 \times 10^4 \text{ cm s}^{-1}$ .

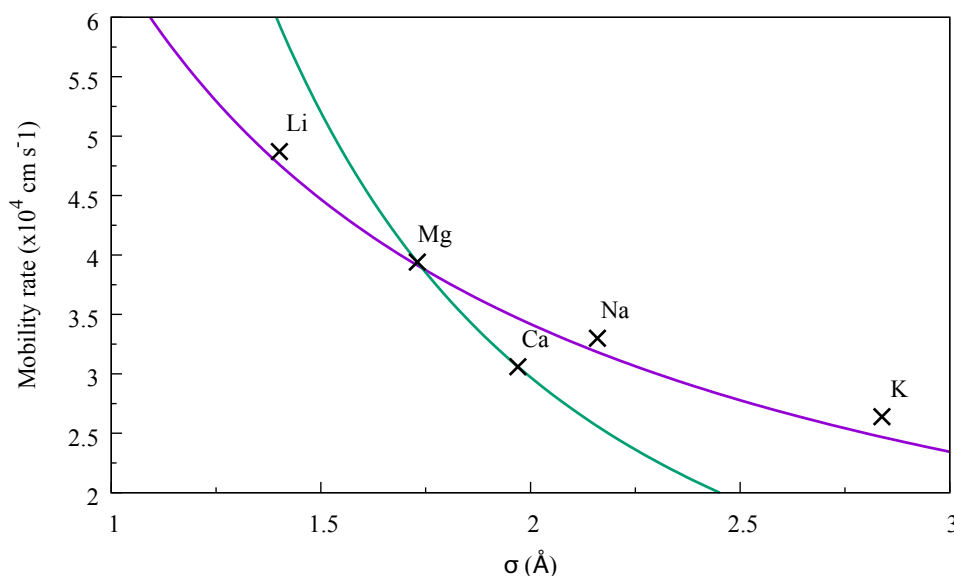


**Figure 5.21:** Comparison of mobility rates for each cation observed in respect to the Van der Waals sigma values applied for the simulations. The blue line represents the fitted trendline

This can be utilised to estimate the mobility rates of more ions within the groups. For example, the plotted curve between the magnesium and calcium ion mobility rates could be extrapolated to estimate the mobility rates of beryllium ions and also strontium ions.

Observing the displacement of the OSCP-1 structure generated, it was shown that, overall, the lithium, sodium, and calcium ions disrupt the carbon framework less than magnesium and potassium. It was noted that the calcium ion observed (*vide supra* 5.1.4) enforced the movement of OSCP-1 to allow it to pass through the structure, although the overall movement enforced by the ions was less than that observed for the magnesium and potassium ions. As the potassium ions possessed the largest ionic

radius, it would be expected that they would enforce greater movement upon the carbon framework of OSPC-1 compared to the alternative ions (Figure 5.22).

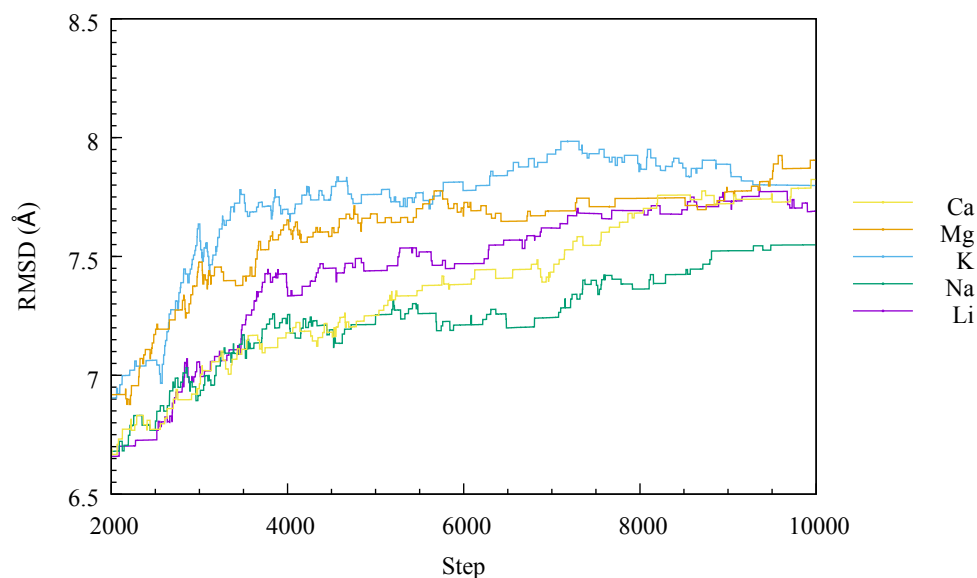


**Figure 5.22:** Root-mean-square deviation of the carbon atoms of the OSPC-1 structure. The RMSD is shown from the activation of the charges, where the ions are migrating through the system.

The carbon network was required to move to allow all of the ions to migrate through. However, the established pathways between all of the ions differ. Because of this, the chosen pathways of the smaller ions contained more blockages, resulting in greater movement of the system.

This study proved how OSPC-1 could be applied for alternative battery technologies: sodium, potassium, magnesium, and calcium ion batteries. All of the ions observed were able to establish pathways through the structure that allowed for complete migration. However, the structure was required to move to a certain degree to allow for the passage of ions. Both the size of the ion and their ionic charge were mobility rate determining factors, as well as affecting the established pathway of each ion in the system.

## 5.2 OSPC-0

The rationalisation of OSPC structures offers further potential in the development of battery technologies. Challenges arose upon the migration of lithium ions (*vide supra Chapter 4*) through OSPC-0. Many of the ions encountered blockages and became stuck, resulting in greatly reduced mobility rates. These characteristics would be expected from the alternative ions, however it would be speculated that the divalent ions, with their stronger attraction to the negatively charged graphene sheet, would be able to overcome this challenge. The OSPC-0 structure generated for the previous *active diffusion* simulations was applied here, with the replacement of lithium ions with the respective ions for this study.

### 5.2.1 Sodium-ion batteries

Firstly, we observed the migration of sodium ions through OSPC-0. Similar to that of the lithium ion, Li1, Na1 was unable to establish a pathway that allowed for complete migration (Figure 5.23). Its movement in the z-axis showed that it struggled to migrate farther than 20 Å through the structure. The tight channels and close proximity building blocks resulted in a blockage that the sodium ion could not overcome, and therefore remained stagnant after 2000 steps of the *active diffusion* simulation. Comparably, many of the additional sodium ions in the system were able to move farther than half-way through the OSPC-0 structure, whereas the remaining ions shared a similar migration pattern to that of Na1 (Appendix A.14). The movement of the sodium ions was staggered as they passed through the generated structure, implying that their migration pathways were very tortuous, and that they encountered many areas of densely packed carbon atoms that they were required to manoeuvre around. The larger ionic radius coupled with the densely packed system of OSPC-0 prevented the ions from establishing direct pathways through the structure towards the negatively charged graphene sheet.

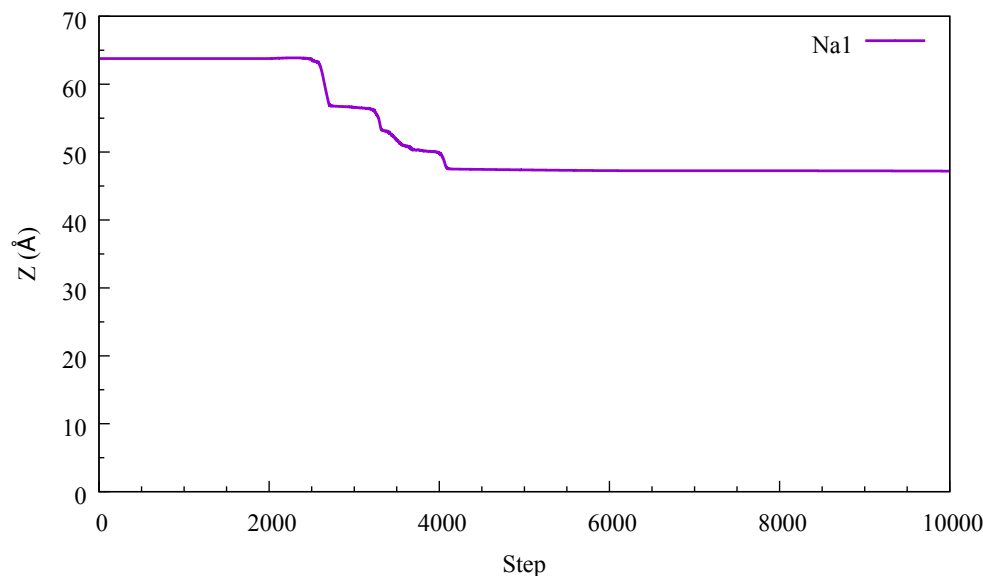


**Figure 5.23:** Z-axis movement of Na1 through the OSPC-0 structure generated.

The established migration pathways of the sodium ions gave rise to a slower mobility rate compared to the lithium ions ( $1.50 \times 10^4 \text{ cm s}^{-1}$ , *vide supra* Section 4.6). Li10 ( $4.51 \times 10^4 \text{ cm s}^{-1}$ , Table 4.9) showed a mobility rate far greater than that of Na10, alongside several other lithium ions having greater mobility than their respective sodium ions. However, this was expected as the sodium ions had a larger ionic radius. Several of the sodium ions observed presented mobility rates greater than, or similar to, their respective lithium ions, with such examples as Na5 having greater mobility rates than Li5. Despite this, the majority of sodium ions gave mobility rates far slower than the lithium ions, resulting in the average mobility rate for the sodium ion migration being slower than the lithium ions, calculated at  $1.22 \times 10^4 \text{ cm s}^{-1}$  (Table 5.6).

Due to the increase in ionic radius, the sodium ions encountered more obstructions along their pathways, and were unable to migrate along pathways similar to those of the lithium ions. The contorted pathways within the OSPC-0 structure generated affected the movement of both the lithium and sodium ions. However, as seen with Na5, there were several sodium ions that were able to completely migrate through, and at rates greater than their respective lithium ions.



Sodium ion	Ion mobility rate ( $\times 10^4$ cm s $^{-1}$ )
Na1	0.15
Na2	2.56
Na3	0.28
Na4	0.45
Na5	2.68
Na6	0.21
Na7	0.46
Na8	0.13
Na9	2.81
Na10	0.95
Na11	2.17
Na12	1.97
Na13	0.20
Na14	2.75
Na15	0.47
Average	1.22

**Table 5.6:** Calculated mobility rates of the sodium ions through OSPC-0.

Na9 showed the greatest mobility of the sodium ions migrating through OSPC-0. It was one of a few ions able to completely migrate to the negatively charged graphene sheet, but still encountered areas of the OSPC-0 structure where the ion was required to establish an alternative route to migrate to the negatively charged graphene sheet. In comparison to the respective lithium ion, Li9, it was able to migrate farther through the structure. Li9 showed periods of fast movement, but inevitably came to a standstill approximately 40 Å along its pathway, and could not pass this position within OSPC-0. In comparison, Na9 progressed through the generated structure at a slow pace, but did not become trapped for prolonged periods of time, continuing on its migration pathway (Figure 5.24). Na9 was able to establish an alternate pathway to that of Li9. They initially followed the same pathway for the first 10-15 Å, at which point the sodium ion was required to divert onto a different route.

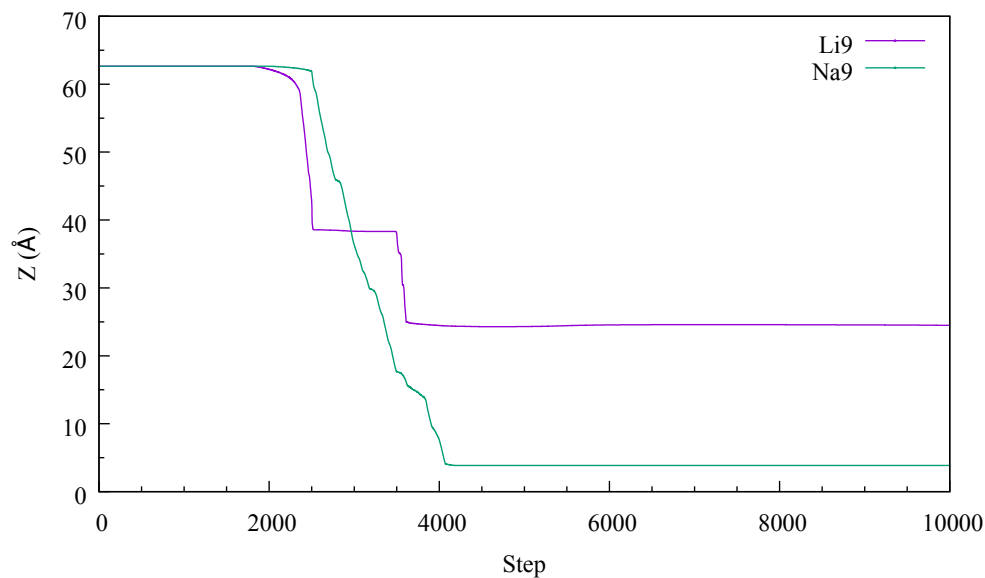


**Figure 5.24:** Comparison of migration pathways for Li9 and Na9 through the OSPC-0 structure.

Both of the migration pathways of Li9 and Na9 (Figure 5.25) displayed the tortuous channels available within OSPC-0. The OSPC-0 structure generated showed to be challenging for both lithium and sodium ions to migrate through.

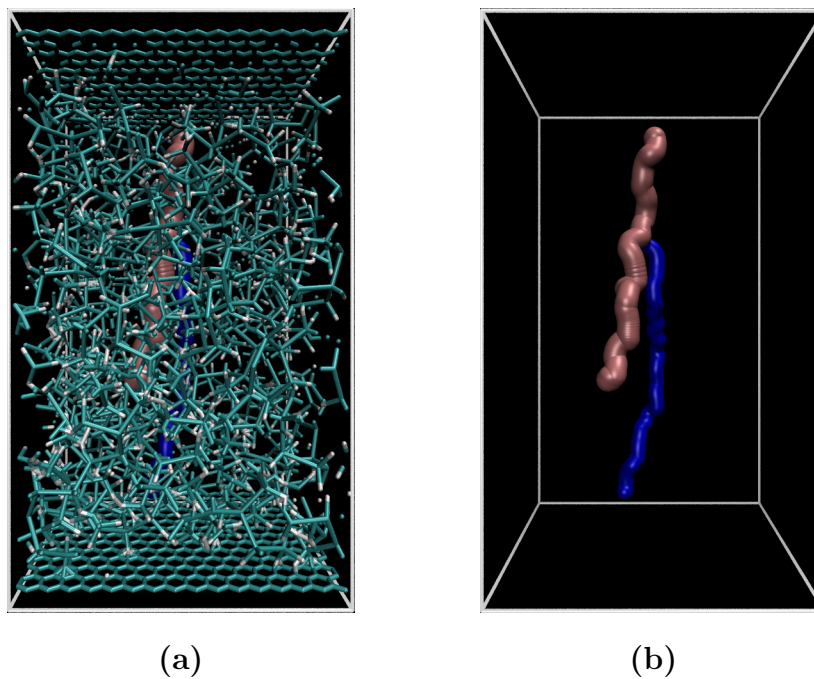


**Figure 5.25:** Comparison of the migration pathways of Li9 (pink) and Na9 (blue) through the OSPC-0 structure.

With its limited availability of direct pathways to the negatively charged graphene sheet, the ions are required to overcome the obstacles of the densely packed carbon atoms in the system.

The number of potential migration pathways was greater for the lithium ions compared to the sodium ions, due to the difference in size. However, these available pathways did not all allow for complete migration, as shown between Li9 and Na9. The OSPC-0 structure generated exhibited structural movements during as the ions passed through it. The sodium ion deviated from the same pathway as the lithium ion pathway due to the OSPC-0 structure shifting and tightening the channel that the lithium ion traverses. Figure 5.26 shows the tightening of this channel between the steps at which the respective ions pass through.

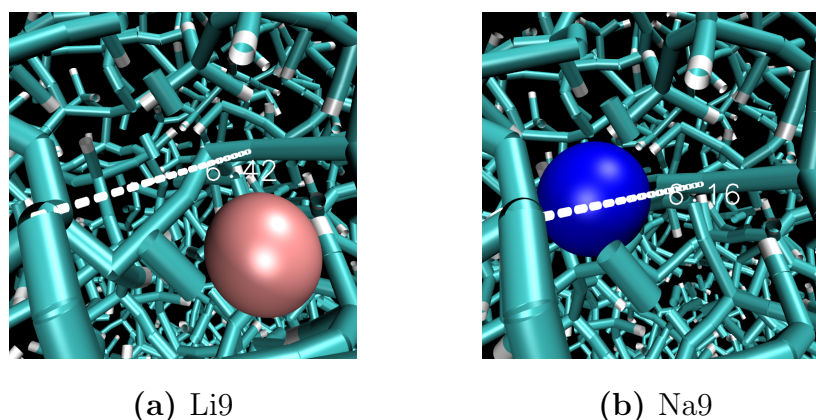


**Figure 5.26:** Graphic representation of the OSPC-0 structural movement during the sodium and lithium ion *active diffusion* simulations. Graphics collected at approximately 2500 steps for Li9, and 2700 steps for Na9.

Figure 5.27 shows the mobility rate comparison between the individual sodium and lithium ions. As can be seen, the average mobility rate for sodium ion migration does not differ too greatly from that of the lithium ions. However, due to the increase in ionic radius, the sodium ions moved at much slower rates in comparison to their lithium ion counterparts. As seen with Na9, several sodium ions establish alternate pathways to those of the lithium ions. This results in several sodium ions being able to completely migrate through the OSPC-0 structure, and therefore have faster mobility rates.

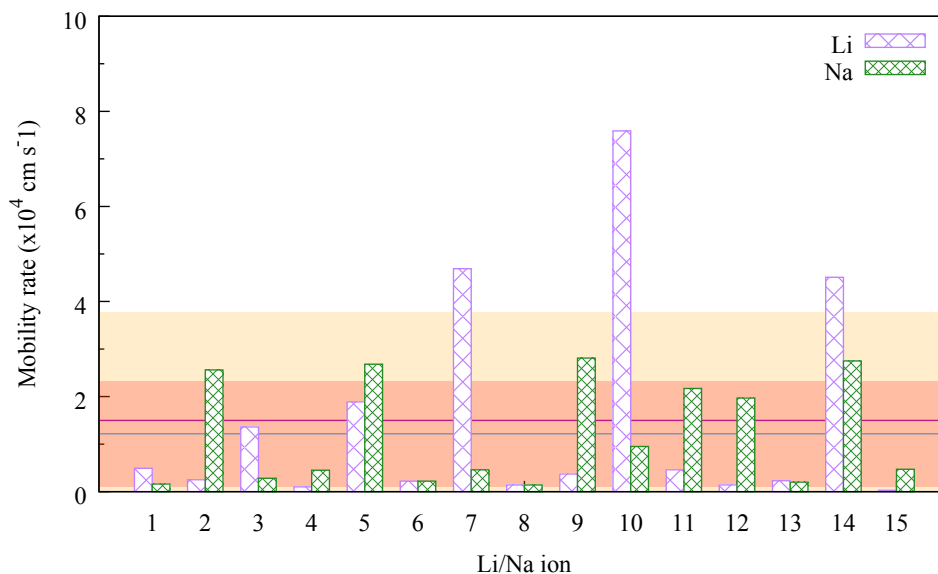


**Figure 5.27:** Comparison of the individual lithium and sodium ion mobility rates through the OSPC-0 structure. The pink line represents the average mobility rate of the lithium ions, the blue line represents the average mobility rate of the sodium ions, and the highlighted regions depict the standard deviation of the mobility rate for both lithium (orange) and sodium (red).

## 5.2.2 Potassium-ion batteries

Here we observed the migration of potassium ions through OSPC-0 with intention on establishing novel anodes for KIBs. The OSPC-0 structure generated for RUN2 was used for the *active diffusion* simulations, having replaced the lithium ions with potassium ions. Firstly, we observed the movement and migration of K1 through the generated structure (Figure A.15). Having determined that the migration of ions through the OSPC-0 structure was challenging for both the lithium ions and sodium ions, it was expected that the potassium ions would share a similar migration pattern. K1 was able to move as far through the structure as that of Na1 (*vide supra* Section 5.2.1). However, its migration pathway contained less obstructions prior to the ion becoming stuck within the confines of OSPC-0. The initial starting position of K1 (as well as Li1 and Na1) proved to be unsuitable as the available pathways resulted in blockages, leaving the ions trapped.

All of the potassium ions were unable to completely migrate through OSPC-0.

K10 and K14 were able to surpass the midpoint of the simulation cell (35 Å), whereas the additional ions do not migrate farther than this half-way point. The movement in the z-axis of the simulation cell of the additional potassium ions is shown in Appendix A.15. As expected, having a larger ionic radius than both the lithium ions and sodium ions, the mobility rate of the potassium ions was far slower compared to the alternative monovalent ions.

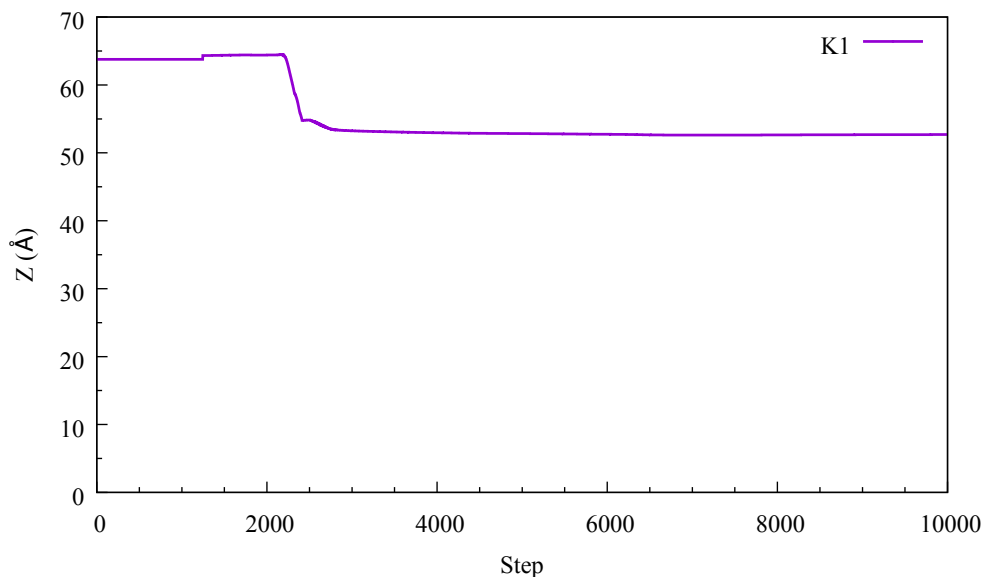


**Figure 5.28:** Movement in the z-axis of K1 through OSPC-0.

Comparably to the migration of lithium ions, several of the potassium ions established different migration pathways, allowing them to move farther through the OSPC-0 structure. This was the case for K2, which was able to migrate farther through OSPC-0 than its respective lithium ion (Figure 5.29). K2 was able to establish a migration pathway more efficiently than Li2. The potassium ion began its migration approximately 100 steps prior to that of the lithium ion, and travelled at a fast rate for the first 20 Å through OSPC-0. In comparison, Li2 travelled at a fast rate for these same 20 Å, although its migration pathway appeared more tortuous than K2. This was apparent from the staggered movement every several steps.

The difference in mobility rate and movement in the z-axis was a result of the potassium ion establishing an alternate migration pathway to Li2.

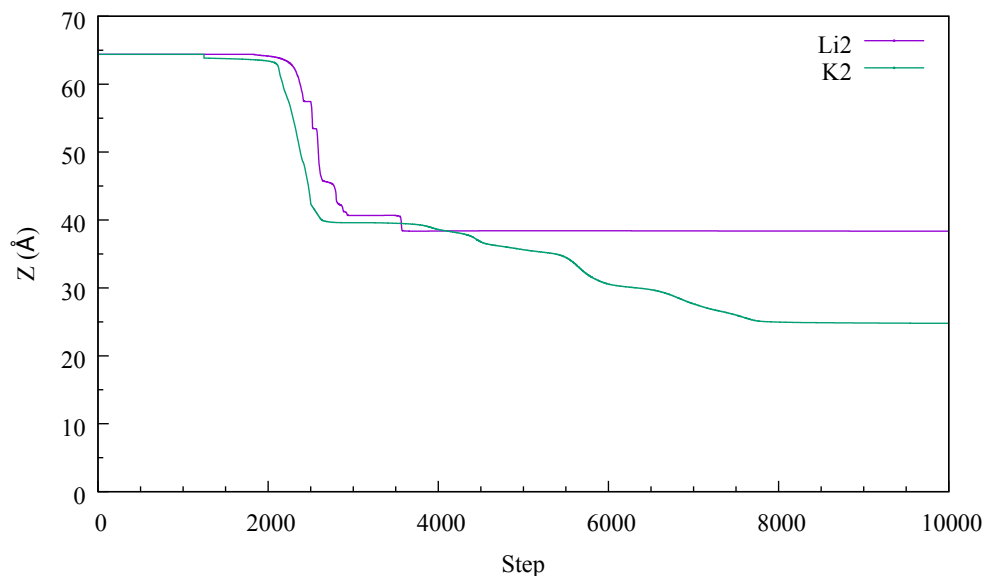


**Figure 5.29:** Difference in z-axis movement for Li2 and K2 through the OSPC-0 structure.

The alternate pathway of K2 is shown in Figure 5.30. The potassium ion immediately started travelling along its alternate route. The pathways of both ions could be seen overlapping at  $\sim 20$  Å, although the potassium ion was able to continue on this path, whereas the lithium ion was unable to. It was suggested that the potassium would completely migrate if the simulation duration were extended. The differences between the migration of potassium ions and the migration of lithium ions are relative to the migration of the sodium ions. The larger ionic radius of the potassium ions results in a difference in established pathway, allowing it to travel farther through the OSPC-0 structure. On the other hand, several of the potassium ions do not migrate as readily as the lithium ions, and several become trapped within the structure at similar positions to those of the lithium ions. K6 shows a slower migration through the OSPC-0 structure, yet becomes trapped within the structure at the same point as Li6 (Figure 5.31).

Li6 greater mobility through the structure compared to K6. However, they both take the same pathway through the structure, resulting in both ions becoming trapped at the same position. This resulted in the calculated mobility rate of Li6 and K6 being similar as they are only able to travel part way through OSPC-0 (Table 5.7).

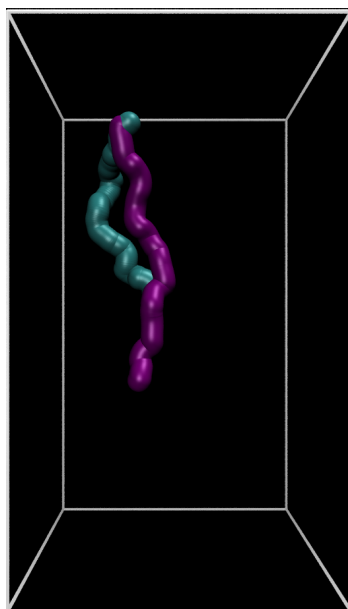


**Figure 5.30:** Comparison of migration pathways for Li2 (turquoise) and K2 (purple) through the OSPC-0 structure.

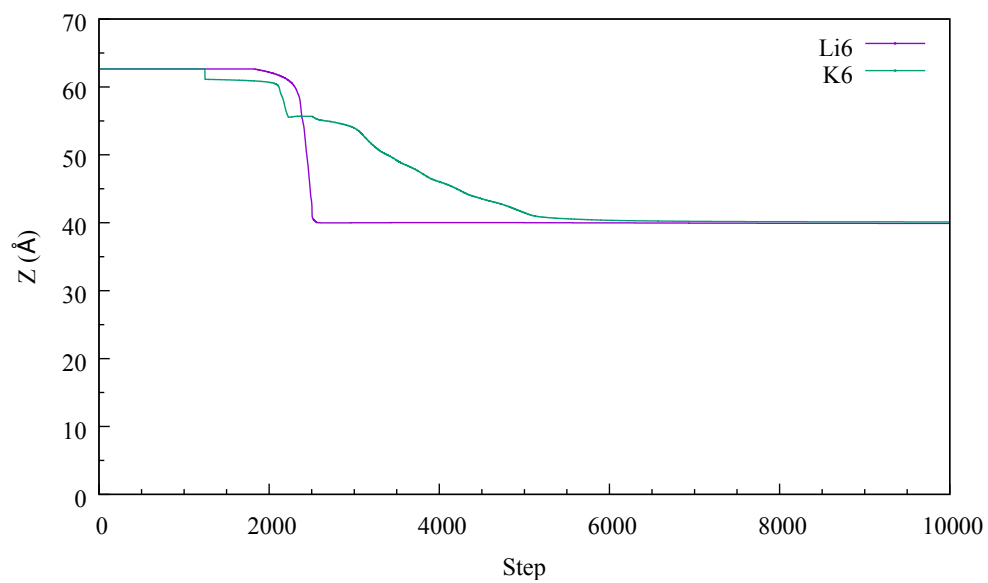


**Figure 5.31:** Comparison of migration and z-axis movement of Li6 and K6 through the OSPC-0 structure.

Potassium ion	Ion mobility rate ( $\times 10^4 \text{ cm s}^{-1}$ )
K1	0.11 $\times 10^4$
K2	0.39 $\times 10^4$
K3	0.23 $\times 10^4$
K4	0.10 $\times 10^4$
K5	0.11 $\times 10^4$
K6	0.22 $\times 10^4$
K7	0.15 $\times 10^4$
K8	0.13 $\times 10^4$
K9	0.35 $\times 10^4$
K10	0.45 $\times 10^4$
K11	0.15 $\times 10^4$
K12	0.14 $\times 10^4$
K13	0.15 $\times 10^4$
K14	0.45 $\times 10^4$
K15	0.20 $\times 10^4$
Average	0.22 $\times 10^4$

**Table 5.7:** Mobility rates of the individual potassium ions through the OSPC-0 system.

In comparison to the lithium and sodium ions observed previously through the OSPC-0 structure, the average mobility rate of the potassium ions is much slower. The migration of lithium ions displays an average of  $1.50 \times 10^4 \text{ cm s}^{-1}$ , and the sodium ions have an average of  $1.22 \times 10^4 \text{ cm s}^{-1}$ . Whereas the potassium ions demonstrate a slower average mobility rate of  $0.22 \times 10^4 \text{ cm s}^{-1}$ . Figure 5.32 displays the comparison between the mobility rates of the potassium ions and lithium ions through the OSPC-0 structure.



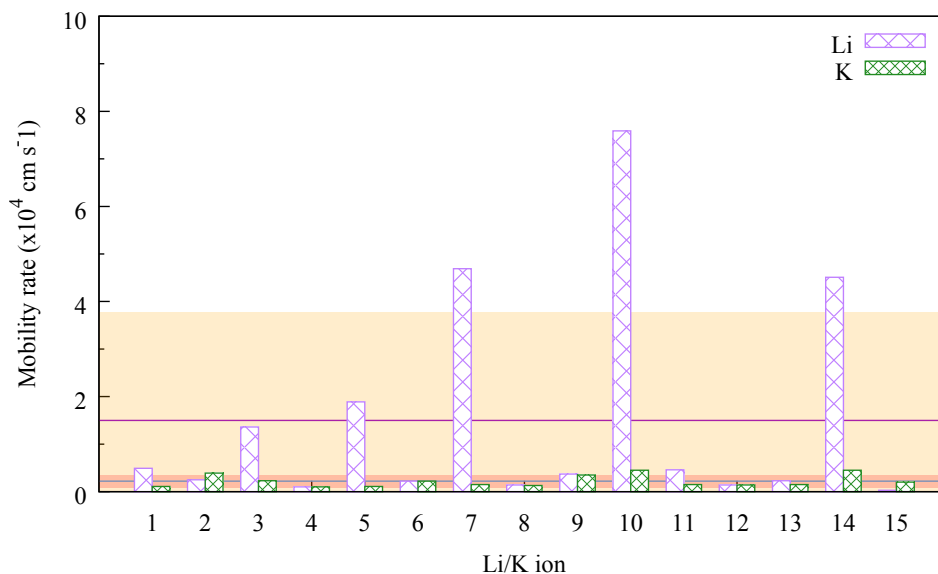


**Figure 5.32:** Comparison of the individual lithium and potassium ion mobility rates through the OSPC-0 structure. The blue and orange lines represent the average mobility rate for the lithium and potassium ions, respectively.

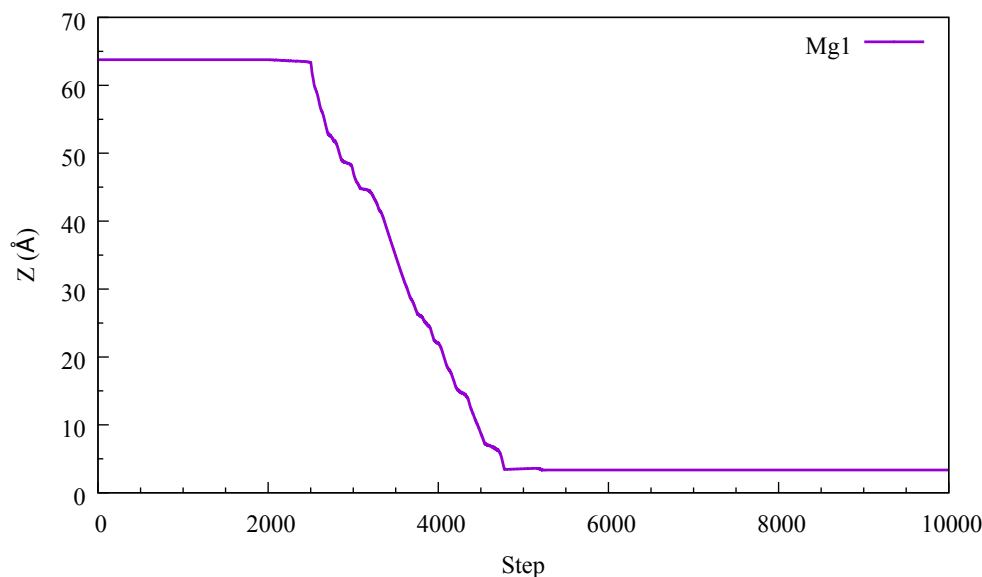
The lithium ions display a variation of mobility rates through the OSPC-0 structure. The lithium ions demonstrating mobility rates greater than their potassium ion counterparts (for example Li5, Li7, Li10, and Li14) are able to migrate through the network towards the negatively charged graphene sheet. Whereas many of the lithium ions, like the potassium ions, became trapped within the system, and are unable to establish a pathway that allows for complete migration.

In tandem with the observed migration patterns of the lithium ions, this representation of the OSPC-0 structure is unsuited for complete migration of monovalent ions through its confines. Therefore, observations on a more representative structure are required to understand how the OSPC-0 material can behave as an anode for monovalent ion batteries. On the other hand, the narrow channels and porous pockets make the OSPC-0 structure a suitable candidate for the uptake of potassium ions, as well as the alternative monovalent ions.

### 5.2.3 Magnesium-ion batteries

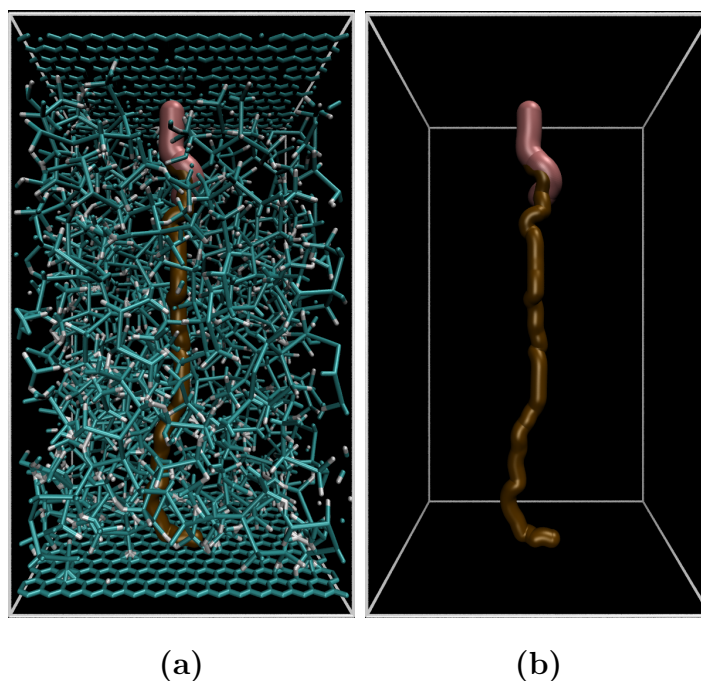
The magnesium simulations were set similarly to those previously observed. The OSPC-0 structure generated between two graphene sheets, and the input of magnesium ions accordingly. As the magnesium ion has an ionic radius close to that of lithium, it would be expected to see this divalent ion to produce similar mobility rates and pathways.

Figure A.16 shows the z-axis movement of magnesium ion, Mg1, through the OSPC-0 structure.



**Figure 5.33:** Movement in the z-axis of Mg1 through OSPC-0.

The z-axis movement of the additional magnesium ions is shown in Appendix A.16. With the exception of Mg14, all of the magnesium ions are able to completely migrate through the OSPC-0 structure. They are also able to progress further through the structure in comparison to the lithium ions. Mg4 completely migrates towards the negatively charge graphene sheet, whereas Li4 becomes trapped within the structure. Figure 5.34 illustrates the movement of Mg4 in comparison to Li4 through OSPC-0.



**Figure 5.34:** Comparison of pathways and movement through the OSPC-0 structure of Li4 (pink) and Mg4 (brown). (a) shows the ion movement with the OSPC-0 structure in place, and (b) shows the ion movement without the OSPC-0 structure.

The increased positive charge of magnesium makes it more strongly attracted to the negatively charged graphene sheet. This results in Mg4 being able to manoeuvre its way through the OSPC-0 structure, forcing the carbon atoms to part to allow the magnesium ion to move through. This is shown further in Figure 5.35.

Mg4 becomes trapped between approximately 3000 and 3800 steps. The ion shows slower movement at the beginning in comparison to Li4, yet is able to establish a new pathway to complete its migration. This results in the large difference in mobility rate between Li4 and Mg4, and similarly between the additional lithium and magnesium ions. Table 5.8 shows the mobility rates for the individual magnesium ions.

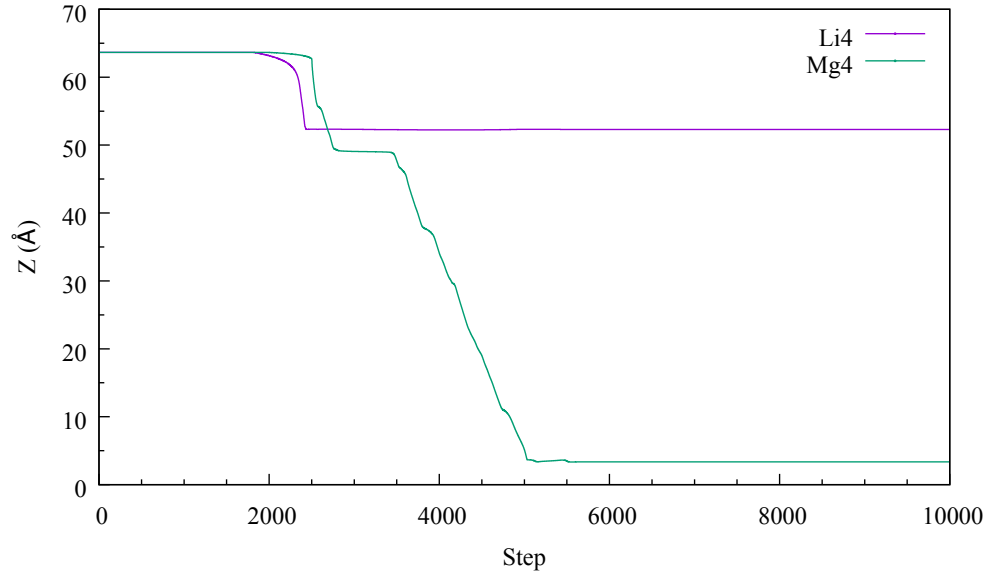


**Figure 5.35:** Comparison of z-axis movement for Li4 and Mg4 through the OSPC-0 structure.

Magnesium ion	Ion mobility rate ( $\times 10 \text{ cm s}^{-1}$ )
Mg1	$2.15 \times 10^4$
Mg2	$2.35 \times 10^4$
Mg3	$3.80 \times 10^4$
Mg4	$1.97 \times 10^4$
Mg5	$4.06 \times 10^4$
Mg6	$0.30 \times 10^4$
Mg7	$3.54 \times 10^4$
Mg8	$2.85 \times 10^4$
Mg9	$3.20 \times 10^4$
Mg10	$4.16 \times 10^4$
Mg11	$3.66 \times 10^4$
Mg12	$2.35 \times 10^4$
Mg13	$2.48 \times 10^4$
Mg14	$0.39 \times 10^4$
Mg15	$2.50 \times 10^4$
Average	$2.65 \times 10^4$

**Table 5.8:** Mobility rates of the individual magnesium ions through OSPC-0.

The average mobility rate of the magnesium ions is  $2.65 \times 10^4 \text{ cm s}^{-1}$ . This is much faster than the lithium ions that have an average of  $1.50 \times 10^4 \text{ cm s}^{-1}$ . Comparing the individual ions, Mg4 displays a mobility rate of  $1.97 \times 10^4 \text{ cm s}^{-1}$  whereas, as Li4 becomes trapped, its mobility rate is much slower ( $1.0 \times 10^3 \text{ cm s}^{-1}$ ). Figure 5.36 illustrates the difference in mobility rates between the individual magnesium ions, as well as a comparison with the mobility rates of the lithium ions.

The mobility rate of the magnesium ions is greatly increased in comparison to the lithium ions, resulting in an increase in average mobility rate. Magnesium ions readily establish pathways through the tortuous channels of the structure. The stronger attraction towards the negatively charged graphene sheet from the divalent cation proves to have great effect over the mobility rates. Following the migration pathway of the Mg4 and Li4, the stronger attraction towards the negatively charged graphene sheet of the magnesium ion forces the carbon network of OSPC-0 to shift, allowing the ion to move through freely, whereas the lithium ion is unable to induce movement of the structure, becoming trapped within the network.

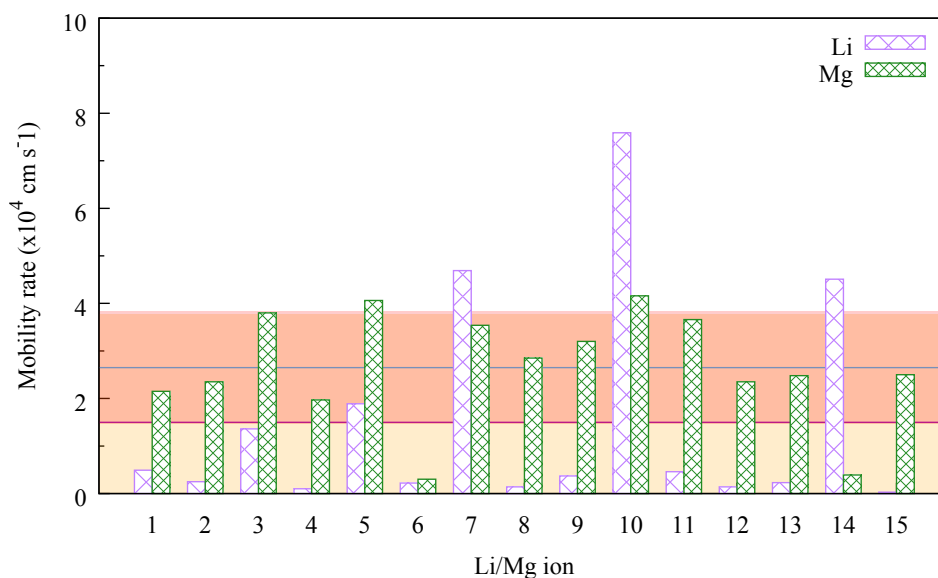


**Figure 5.36:** Comparison of mobility rates between the individual magnesium and lithium ions with the OSPC-0 structure. The blue and orange lines represent the average mobility rate for the lithium and magnesium ions, respectively.

### 5.2.4 Calcium-ion batteries

Calcium ions with their larger ionic radius showed a much slower mobility rate the OSPC-1 compared to lithium. Therefore, it would be expected to have the same effects within the more densely packed structure of OSPC-0.

Figure 5.37 shows the migration pathways and movement of the calcium ion, Ca1, through the OSPC-0 structure.

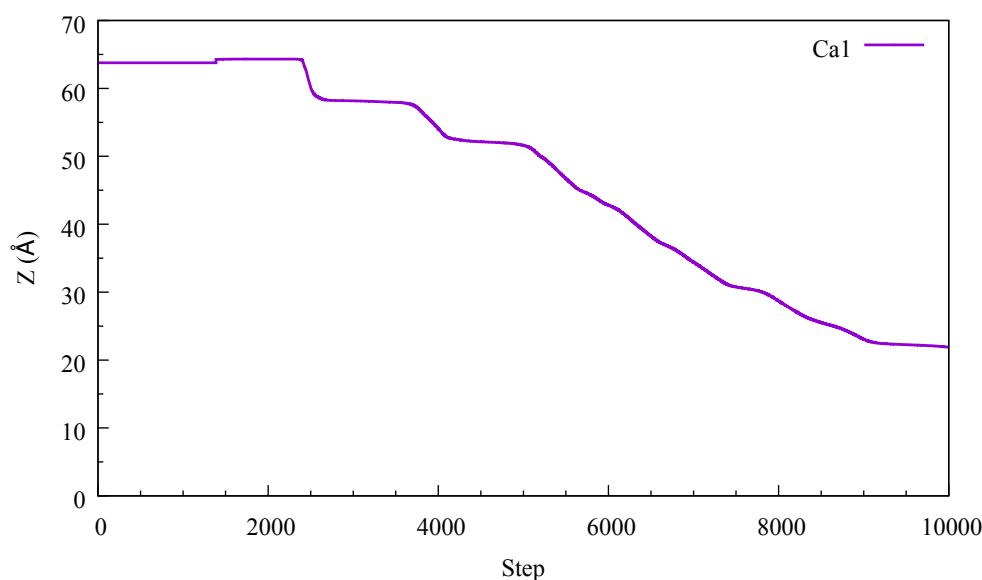


**Figure 5.37:** Plot of the movement in the z-axis of Ca1 through the OSPC-0 structure generated.

The z-axis movement of the additional calcium ions is shown in Appendix A.17. The majority of the calcium ions are able to completely migrate through the OSPC-0 structure (for example Ca5, Ca6, and Ca7). However, several of the ions are unable to completely migrate through to the negatively charged graphene sheet. Ca8 is unable to travel further than  $\sim 10$  Å along its pathway before becoming stuck. Nevertheless, It shows minor movement towards the end of the simulation duration. Given a longer simulation duration, Ca8 may show further migration through the OSPC-0 structure.

Many of the ions display very slow movement. Ca2 becomes trapped within the early phases of the *active diffusion*, and is able to continue travelling along an alternate pathway. However, much like Ca8, it does not completely migrate through OSPC-0,

yet showed to continue along its migration pathway prior to simulation termination.

In comparison to the migration of lithium ions, the migration pathway of the calcium ions is more tortuous. Figure 5.38 shows the difference in z-axis movement between Li2 and Ca2. As can be seen, the lithium ion moves much more quickly through the construct, yet is unable to free itself from the porous pocket it becomes trapped in. However, Ca2 is able to establish new pathways and can free itself to continue on its chosen migration pathway.

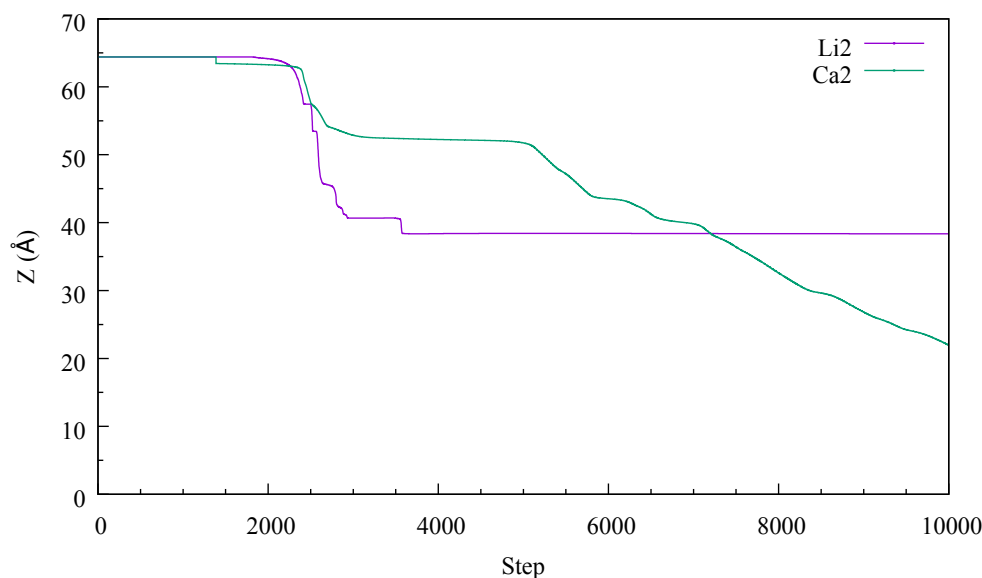


**Figure 5.38:** Comparison of migration and z-axis movement for Ca2 and Li2 through OSPC-0.

Comparably, Ca3 is a calcium ion that was able to completely migrate through the OSPC-0 structure. Ca3 is able to migrate directly through the system whereas Li3 becomes trapped at several points, having to establish several alternate pathways. This is a similar case to the previous ions observed through the OSPC-0 structure, where the calcium ions are able to travel farther through the structure than the lithium ions. This is also illustrated in Figure 5.39. Li3 is able to move much quicker than Ca3. However, it becomes trapped and requires a sideways movement to migrate through fully, which means its overall mobility rate is greatly reduced.

As shown in Figure 5.39, Li3 has a "step-like" migration plot, whereas the movement of Ca3 is a gradual decline.

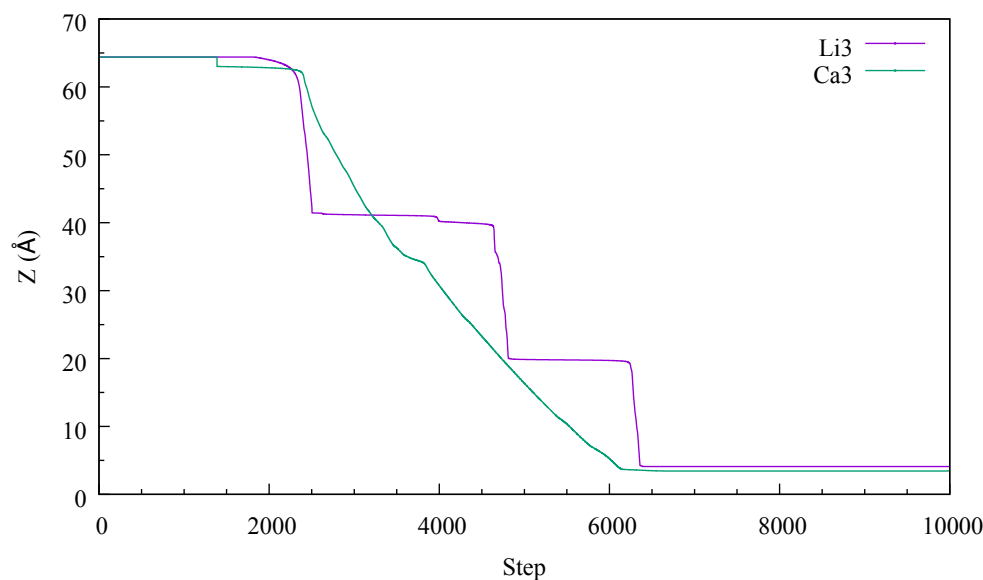


**Figure 5.39:** Comparison of migration and z-axis movement for Ca3 and Li3 through OSPC-0.

The average mobility rate calculated for the migration of calcium ions is slower to that of the lithium ions (Table 5.9);  $1.07 \times 10^4 \text{ cm s}^{-1}$  for calcium in comparison to  $1.50 \times 10^4 \text{ cm s}^{-1}$  for lithium. The mobility rates of the calcium ions do not exceed  $2.00 \times 10^4 \text{ cm s}^{-1}$ , with the maximum observed mobility rate being  $1.74 \times 10^4 \text{ cm s}^{-1}$ . Lithium, sodium, and magnesium ions were able to surpass this, with maximum mobility rates of  $7.59 \times 10^4$ ,  $2.81 \times 10^4$ , and  $4.16 \times 10^4 \text{ cm s}^{-1}$  respectively.



Calcium ion	Ion mobility rate (x10 cm s <sup>-1</sup> )
Ca1	0.41 x10 <sup>4</sup>
Ca2	0.41 x10 <sup>4</sup>
Ca3	1.47 x10 <sup>4</sup>
Ca4	0.72 x10 <sup>4</sup>
Ca5	1.74 x10 <sup>4</sup>
Ca6	1.47 x10 <sup>4</sup>
Ca7	0.99 x10 <sup>4</sup>
Ca8	0.18 x10 <sup>4</sup>
Ca9	1.18 x10 <sup>4</sup>
Ca10	1.62 x10 <sup>4</sup>
Ca11	1.65 x10 <sup>4</sup>
Ca12	0.74 x10 <sup>4</sup>
Ca13	1.01 x10 <sup>4</sup>
Ca14	1.43 x10 <sup>4</sup>
Ca15	1.06 x10 <sup>4</sup>
Average	1.07 x10 <sup>4</sup>

**Table 5.9:** Mobility rates of the individual calcium ions through OSPC-0.

Similar to the previously observed ions (sodium, potassium, and magnesium), several calcium ions demonstrate mobility rates faster than their lithium ion counterparts (Figure 5.40). The pathways established by the calcium ions allow them to migrate directly through the OSPC-0 structure, and not become trapped as often as the lithium ions. The determined pathway, along with the increased size and positive charge affected the mobility rates through this particular structure, resulting in the calcium ions being able to travel farther than the lithium ions.

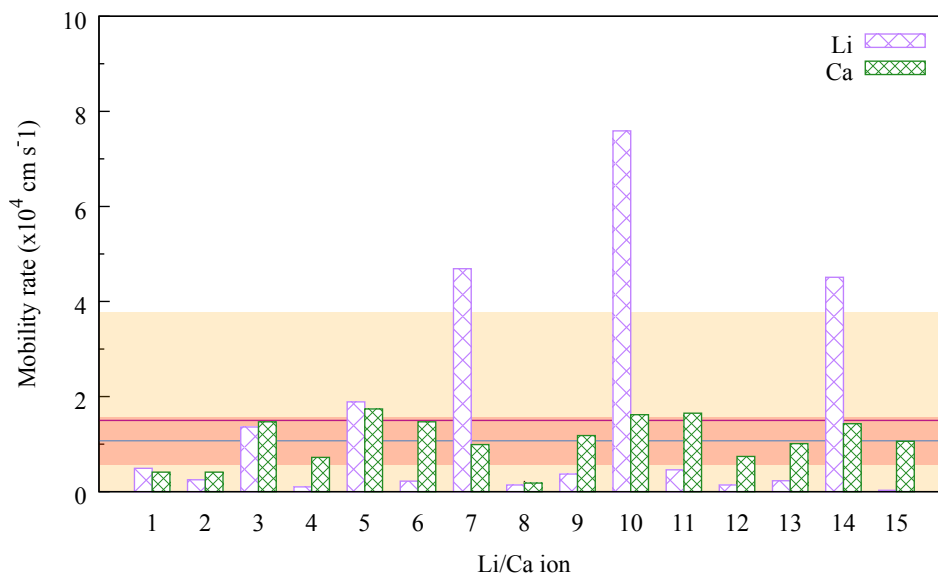


**Figure 5.40:** Comparison of mobility rates between the individual lithium and calcium ions through OSPC-0. The blue and orange lines represent the average mobility rate for the lithium and calcium ions, respectively.

### 5.2.5 Conclusion

The increasing ionic radius of the monovalent ions causes the ions to migrate at a slower rate through the OSPC-0 structure generated. The lithium ions show the fastest mobility rate ( $1.50 \times 10^4 \text{ cm s}^{-1}$ ), followed by the sodium ( $1.22 \times 10^4 \text{ cm s}^{-1}$ ) and potassium ions ( $0.22 \times 10^4 \text{ cm s}^{-1}$ ) respectively. On the other hand, the divalent ions divert from the trend established. Magnesium possesses an ionic radius close to that of lithium. However, the larger positive charge of the ion creates a stronger attraction to the negatively charged graphene sheet, therefore demonstrating a much faster mobility rate ( $2.65 \times 10^4 \text{ cm s}^{-1}$ ). This is similar for calcium ( $1.07 \times 10^4 \text{ cm s}^{-1}$ ), which possesses an ionic radius close to that of sodium. Figure 5.41 shows the comparison between the ion mobility rates through the OSPC-0 structure.

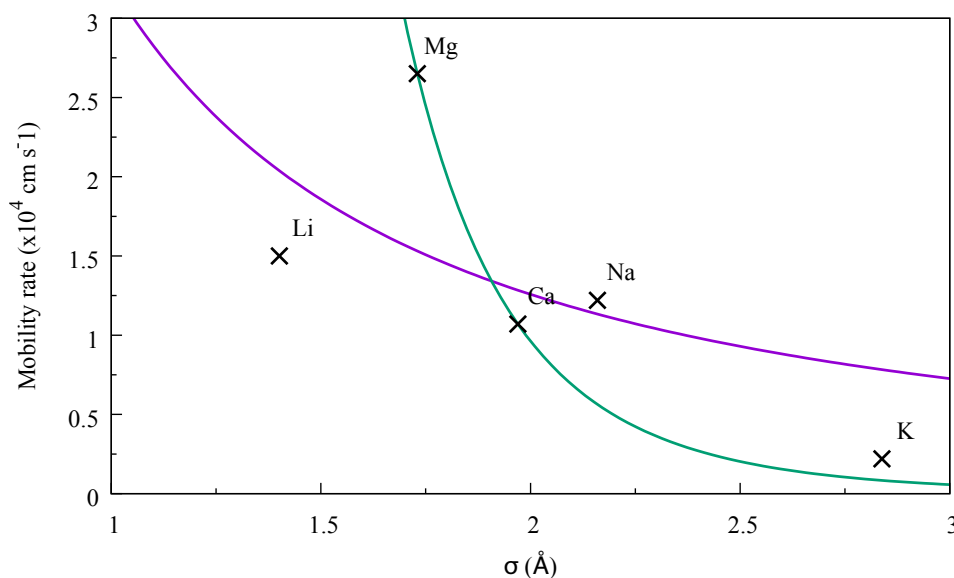


**Figure 5.41:** Comparison of average mobility rates of the ions observed through the OSPC-0 system.

As is shown, the average mobility rate of magnesium ions towards the negatively charged graphene sheet is greater than the additional ions observed. The size and charge of the ion forces the carbon network to move, allowing the ions to navigate along their established pathways. The comparable distances moved for each of the ions indicates three phases of ion behaviour: Lithium ions do not have the size nor charge to influence movement in the OSPC-0 structure; sodium ions possess an ionic radius large enough to induce structural movement, therefore leading to the ions migrating farther through system to those of the lithium ions; magnesium and calcium ions possess both a large enough radius to induce movement, as well as a greater positive charge. This 2+ charge enforces a stronger attraction / repulsion effect, allowing the ions to migrate farther through the system; the potassium ions possess neither a stronger charge or an ideal radius allowing them to migrate through the OSPC-0 structure. Figure 5.42 compares the average distance in Z-axis movement through the OSPC-0 structure between the ions observed.

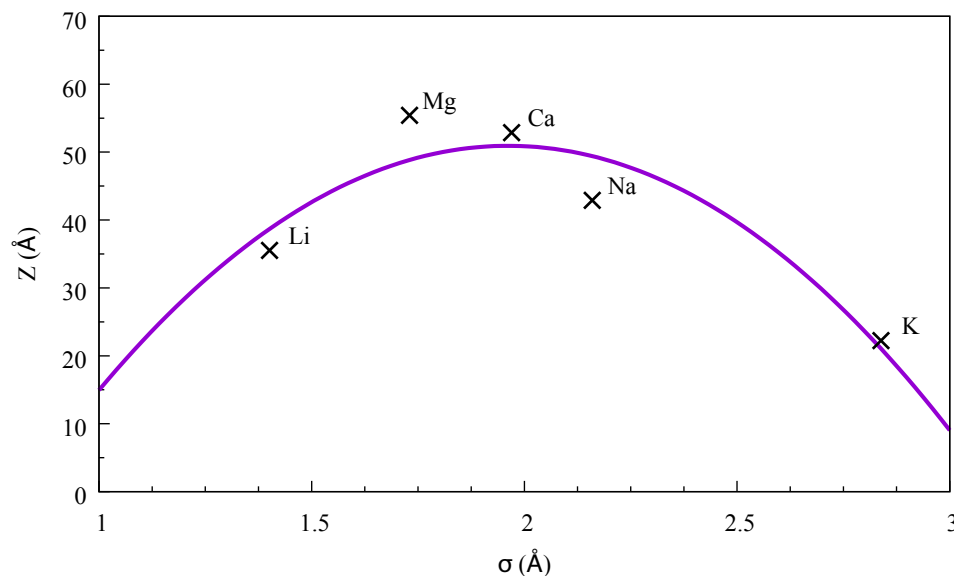


**Figure 5.42:** Average Z-axis migration of each of the ions in the OSPC-0 material with respect to the sigma value applied for the migration simulations.

These simulations indicate idealistic properties for ion migration, and therefore ion diffusion, through the OSPC-0 structure. The divalent ions of magnesium and calcium show a great average movement through the system, whereas the monovalent ions show a lesser distance moved. Within the monovalent ions themselves, there is a key ionic radius that sodium possess, allowing it to move farthest through the system, as well as influencing the movement of the carbon structure. The divalent ions possess both the idealistic ionic radius coupled with the increased positive charge, creating a stronger attraction / repulsion effect with the charged graphene sheets. The difference in mobility rates alongside the observed migration distances of each ion show that the OSPC-0 structure would be more suited as an anode for divalent ion batteries, and more selectively towards magnesium ion batteries, whereas the OSPC-1 structure showed to be more suited as an anode for lithium ion batteries.

## 5.3 OSPC-2 and OSPC-3

OSPC-2 and OSPC-3 proposed more open frameworks than OSPC-1, therefore it was predicted that both structures would allow the ions to migrate through their structures at greater rates compared to the ions observed through OSPC-1. Because of this, the migration of ions through the generated structures were observed and studied. Due to the random connectivity of building blocks in the system, certain areas within the OSPC-2 structure are structurally similar to those observed in the OSPC-1 structure. However, it displayed an average strut length greater to that of OSPC-1, therefore leading to a more open porous structure. On the other hand, OSPC-3 possessed the greatest strut length.

The lithium ions input into the OSPC-2 and OSPC-3 systems were replaced with the respective ions observed, and the MD simulation performed in the same manner as the OSPC-1 and OSPC-0 simulations.

### 5.3.1 Sodium-ion batteries

The sodium ions observed migration through OSPC-2 and OSPC-3 were all able to migrate through OSPC-2 and OSPC-3. Observing the migration of Na1 through both systems, OSPC-3 allowed the sodium ion to travel at a greater rate than OSPC-2. The migration and movement in the z-axis of Na1 through OSPC-2 and OSPC-3 is shown in Figure 5.43. Na1 showed to encounter more obstructions through OSPC-2 compared to OSPC-3. The sodium ion showed reduced movement during the first 20 Å of the simulation cell. The movement in the z-axis of Na1 through OSPC-3 showed little to no reduced movement as it moved through the structure.

Each of the sodium ions were able to completely migrate through both OSPC-2 and OSPC-3 (Appendix A.18 and A.22). There were several ions that encountered obstructions within both of the simulations, although these were much less frequent

compared to the sodium ions observed through OSPC-1 and OSPC-0. Overall, the mobility rate of the sodium ions was greater through OSPC-3 compared to OSPC-2 (Table 5.10). The larger  $sp^3$ - $sp^3$  struts resulted in wider channels for the ions to traverse along. However, the mobility rate of the sodium ion through OSPC-2 and OSPC-3 was slower compared to the lithium ions through the respective systems.

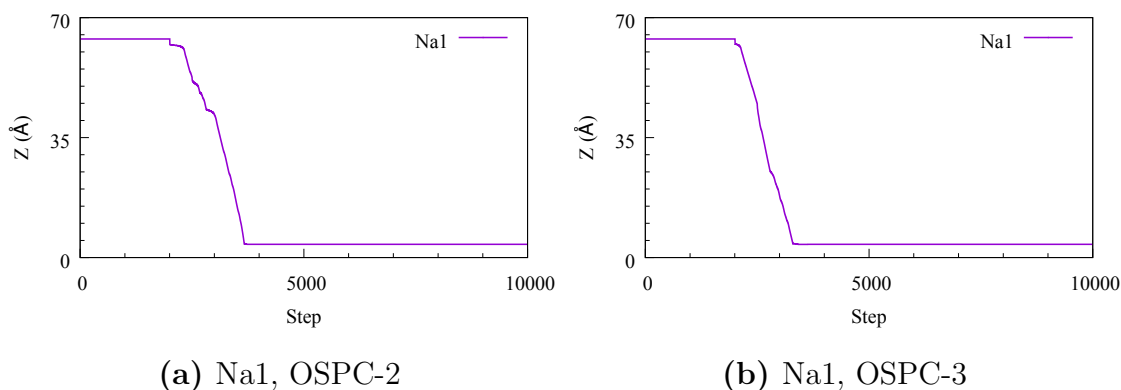


**Figure 5.43:** Movement in the z-axis of Na1 through (a) OSPC-2 and (b) OSPC-3.

The average mobility rate for the sodium ions within the OSPC-2 structure was  $3.79 \times 10^4 \text{ cm s}^{-1}$ , whereas the migration of lithium ions gave a greater mobility rate of  $6.82 \times 10^4 \text{ cm s}^{-1}$ .

Similar to OSPC-2, the average mobility rate of the sodium ions through OSPC-3 ( $3.88 \times 10^4 \text{ cm s}^{-1}$ ) was slower than the average of the lithium ions ( $6.24 \times 10^4 \text{ cm s}^{-1}$ ).

Several of the lithium and sodium ions through OSPC-2 showed large differences in mobility rate. The mobility rate of Na7 ( $3.17 \times 10^4 \text{ cm s}^{-1}$ ) was far slower compared to Li7 ( $7.17 \times 10^4 \text{ cm s}^{-1}$ ). This large difference was not only due to the increased size of the sodium ion, but also the chosen pathways that the ions travelled along. Na7 established a different migration pathway through OSPC-2 to that of Li7 (Figure 5.44). Na7 was required to divert from the same pathway as the lithium ion within the first 5 Å of the simulation.

Sodium ion	Ion mobility rate ( $\times 10^4$ cm s $^{-1}$ )	
	OSPC-2	OSPC-3
Na1	3.55	4.59
Na2	3.10	4.47
Na3	3.97	3.05
Na4	4.98	3.64
Na5	4.32	3.89
Na6	4.12	4.63
Na7	3.17	4.07
Na8	3.95	3.74
Na9	3.29	3.04
Na10	3.62	3.56
Na11	3.99	3.45
Na12	3.38	4.51
Na13	3.32	3.59
Na14	4.35	3.57
Na15	3.79	4.40
Average	3.79	3.88

**Table 5.10:** Mobility rates of the individual sodium ions through OSPC-2 and OSPC-3.

The pathways of Na7 and Li7 are both tortuous, although Na7 encountered more obstructions during its migration compared to the lithium ion, resulting in a slower mobility rate (Figure 5.45).

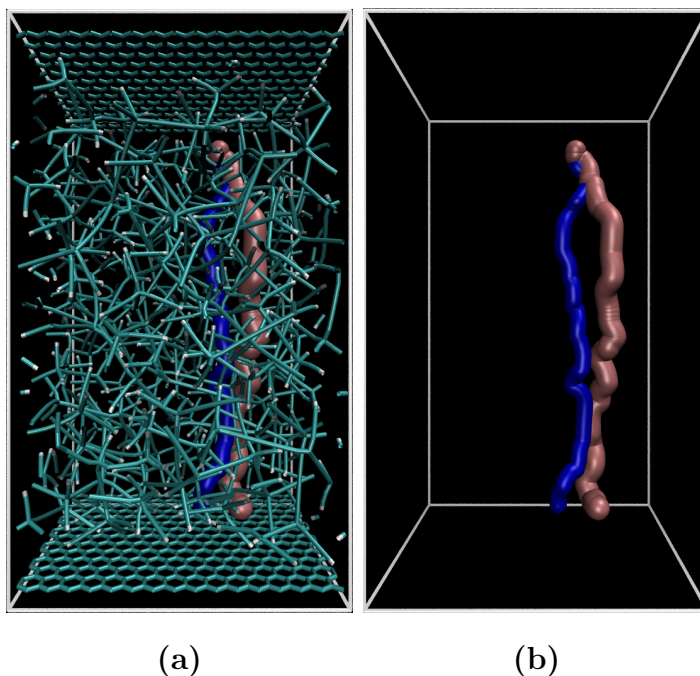


**Figure 5.44:** Migration pathways established for Li7 (pink) and Na7 (blue) with the OSPC-2 structure. (a) With the OSPC-2 structure visible, and (b) without.

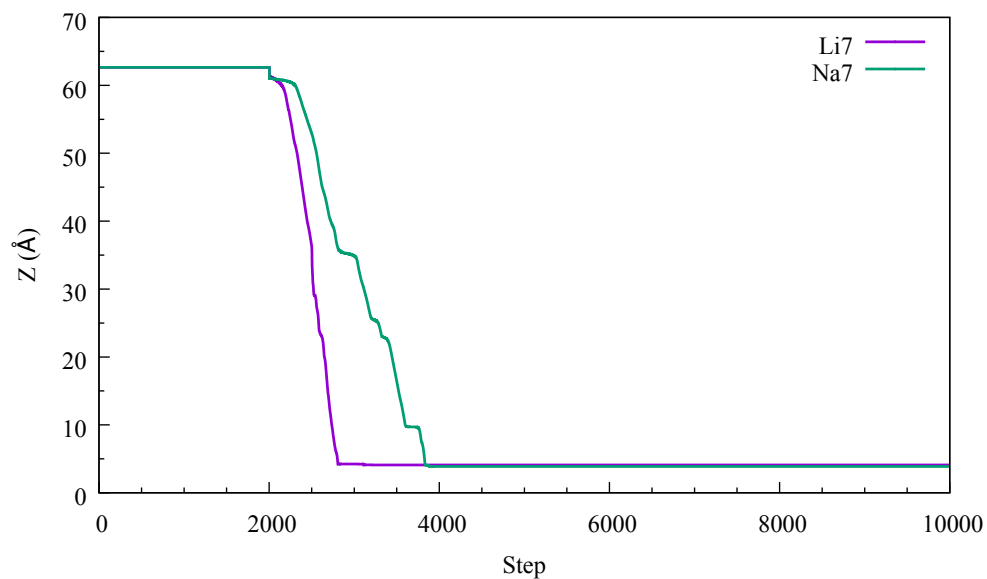


**Figure 5.45:** Comparison of z-axis movement between Li7 and Na7 through the OSPC-2 structure.

Na2 was another example of how the established pathway affected the mobility rate of the sodium ions through OSPC-2. The sodium ion was able to completely



migrate through the structure. However, it had encountered an area of the structure that resulted in a great reduction in its movement (Figure 5.46). The sodium ion moves at a slower rate to the lithium ion, Li2. The plotted movement of the ions showed that the sodium ion becomes stagnant for several hundred steps before being able to continue along its migration pathway.

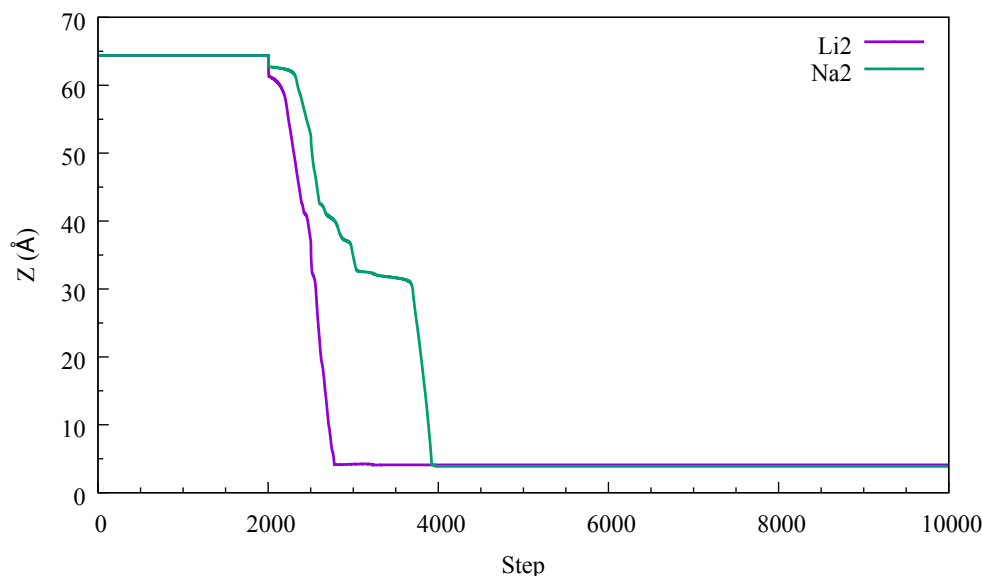


**Figure 5.46:** Comparison of z-axis movement between Li2 and Na2 through OSPC-2.

This reduced movement occurred at  $\sim 30$  Å along its pathway, whereas the migration pathway that Li2 established possessed far fewer obstructions, allowing it to move more freely towards the negatively charged graphene sheet. This was a similar case for the additional sodium ions. Although they all established pathways through OSPC-2 to allow them to reach the negatively charged graphene sheet, the routes they had chosen differ from the lithium ion pathways. This greatly affected the mobility rates calculated for each ion.

This was similar for the migration of sodium ions through OSPC-3. Na9 (Appendix A.25h) showed reduced movement at approximately 35 Å through the structure. However, there were several ions displaying far greater mobility rates in comparison to their lithium counterparts. Na15 was able to establish a pathway that allowed it to mi-

grate through OSPC-3 whilst encountering very few obstructions in the system. On the other hand, Li15 showed great mobility through the first 25 Å of the structure before becoming trapped for  $\sim 1000$  steps. The difference between the movement in z-axis of Na15 and Li15 is shown in Figure 5.47.

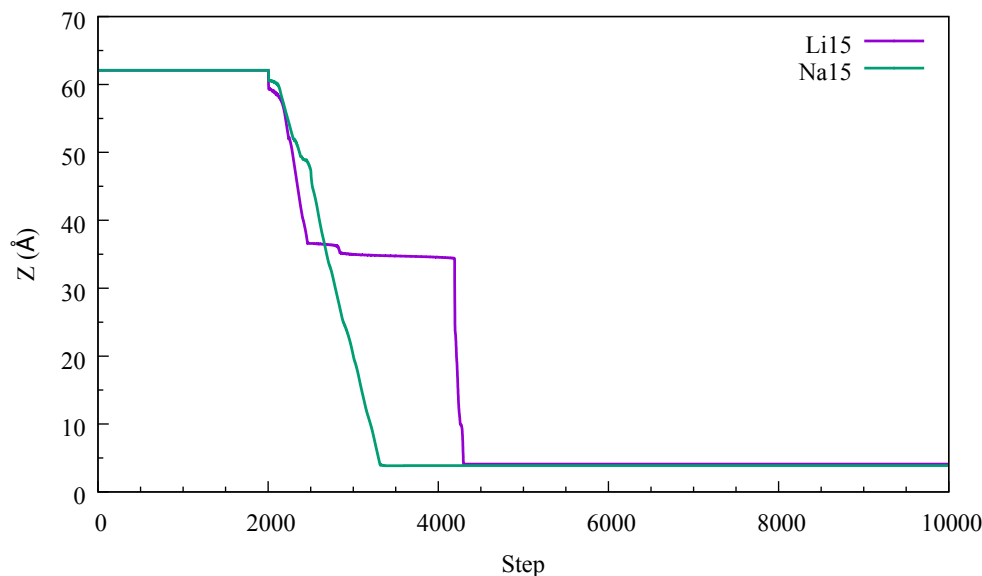


**Figure 5.47:** Comparison of the migration and z-axis movement for Li15 and Na15 through the OSPC-3 structure.

The resulting mobility rate of Na15 was due to its chosen migration pathway. This showed an opposite effect to that observed with Na7 through OSPC-2. The pathway determined by Na15 through OSPC-3 possessed fewer obstructions than Li15, although the migration pathway appeared more tortuous (Figure 5.48). Both ions were following the same direction for the initial 10 Å, after which Na15 established an alternate route. This highlights the potential routes for both ions to traverse along. However, the lithium ions are able to move through narrow channels compared to the sodium ions, which can offer more beneficial results for lithium ion migration, and also diffusion, as seen between Na2 and Li2, and also Na7 and Li7, through OSPC-2, or less beneficial results, as seen between Na15 and Li15 through OSPC-3.

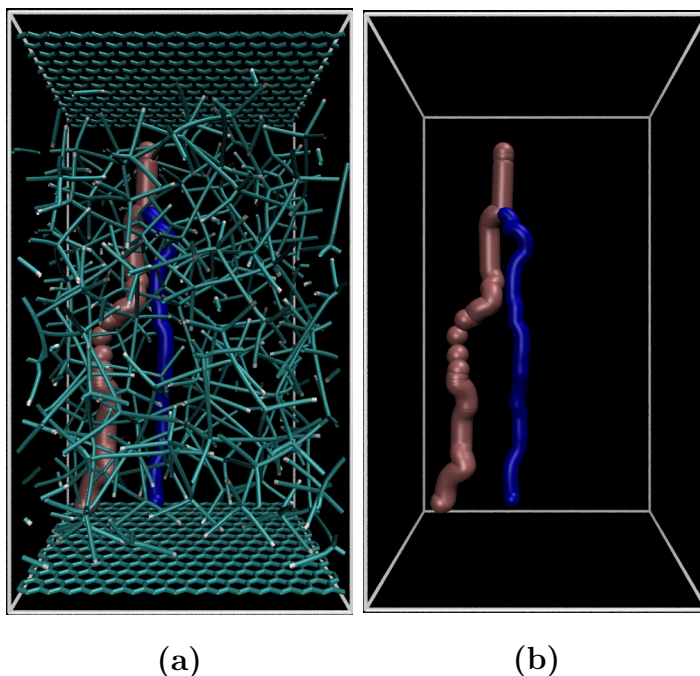


**Figure 5.48:** Comparison of established migration pathways for Li15 (pink) and Na15 (blue). (a) with the OSPC-3 structure present, and (b) without the OSPC-3 structure.

On average, the lithium ions displayed greater mobility rates through both OSPC-2 and OSPC-3 compared to the sodium ions. There was a similar difference between the two ions through each structure, highlighting towards the capabilities of OSPC-2 and OSPC-3 as anodes for lithium ion batteries. Figures 5.49 and 5.50 show the difference in mobility rates between the lithium ions and sodium ions through OSPC-2 and OSPC-3, respectively. However, each sodium ion was able to establish a migration pathway that offered complete migration through the two structure generated. This highlighted the potential of both OSPC-2 and OSPC-3 as anodes for sodium ion batteries. The sodium ions were required to establish migration pathways that differed from those of their respective lithium ions. This was a result of the size of the sodium ions. The lithium ions were able to navigate through narrower channels that had the potential advantage to allow fast migration, or the disadvantage of resulting in obstruction of movement, whereas the sodium ions were required to navigate the wider channels, which also had the same effects on their migration.

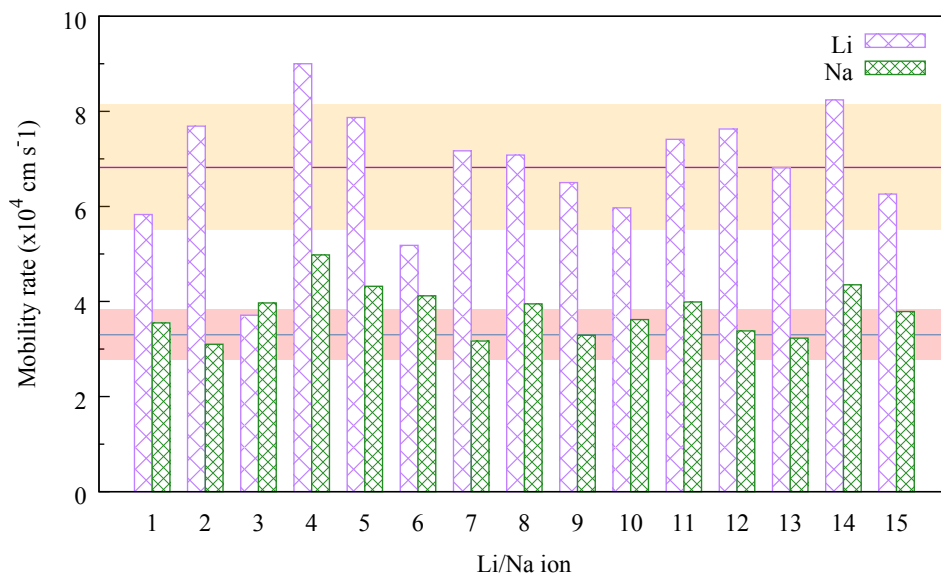


**Figure 5.49:** Comparison of mobility rates for the individual lithium and sodium ions through OSPC-2. The blue and orange lines represent the average mobility rate for the lithium and sodium ions, respectively.

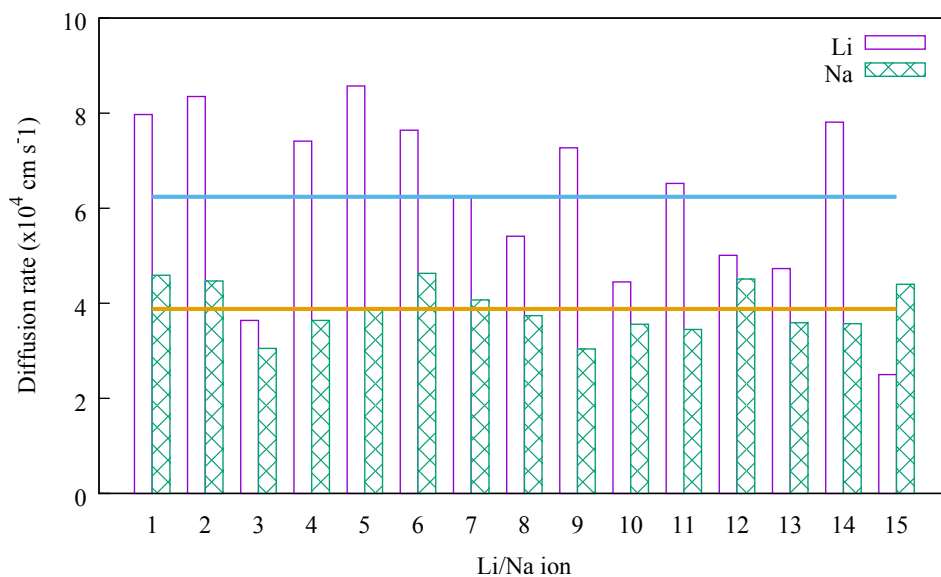


**Figure 5.50:** Comparison of mobility rates for the individual lithium and sodium ions through OSPC-3. The blue and orange lines represent the average mobility rate for the lithium and sodium ions, respectively.

### 5.3.2 Potassium-ion batteries

The larger ionic radius of potassium ions was estimated to follow a similar trend that was previously observed through OSPC-1 (*vide supra* Section 5.1.2). The increased ionic radius of the monovalent ion would show reduced mobility rates compared to lithium and sodium through OSPC-2 and OSPC-3. Each of the potassium ions were able to migrate through both OSPC-2 and OSPC-3 completely. However, many within both simulations encountered obstructions that resulted in them becoming trapped for several hundred steps (OSPC-2, Appendix A.19; OSPC-3, Appendix A.23). As shown in Figure 5.51, K1 was able to completely migrate through OSPC-2 and OSPC-3, encountering very few obstructions.

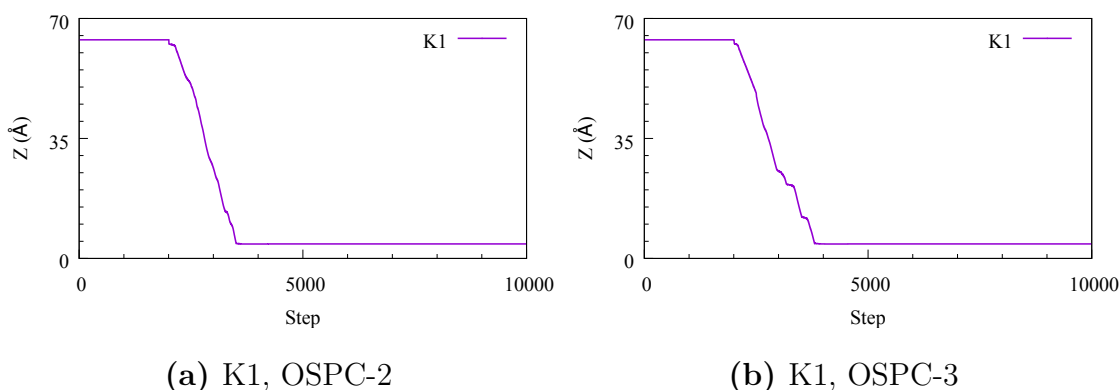


**Figure 5.51:** Migration and movement in the z-axis of K1 through (a) OSPC-2 and (b) OSPC-3.

Because of the greater potential of interpenetration within OSPC-3, Na1 encountered more obstructions through OSPC-3 than through OSPC-2. As a result, the reduced movement of Na1 through OSPC-3 apparent between 5 Å and 25 Å resulted in the ion migrating at a slower rate compared to its migration through OSPC-2. This was similar for the additional potassium ions within the system. The majority of the potassium ions had greater mobility rates through OSPC-2 than through OSPC-3. Such examples are K3 and K13, where the calculated mobility rates through OSPC-2 were almost halved through OSPC-3 (Table 5.11).

Potassium ion	Ion mobility rate ( $\times 10^4 \text{ cm s}^{-1}$ )	
	OSPC-2	OSPC-3
K1	3.92	3.27
K2	3.73	3.42
K3	3.75	1.84
K4	3.31	2.71
K5	2.49	2.88
K6	2.65	3.59
K7	3.27	2.86
K8	2.57	2.42
K9	1.10	3.46
K10	2.12	2.27
K11	3.08	2.90
K12	3.76	2.11
K13	4.00	2.21
K14	2.97	3.17
K15	2.84	2.34
Average	3.04	2.76

**Table 5.11:** Mobility rates of the individual potassium ions through OSPC-2.

In comparison to the migration of lithium and sodium ions through both OSPC-2 and OSPC-3, the potassium ions migrated at much slower rates. The average mobility rate of the potassium ions through OSPC-2 was  $3.04 \times 10^4 \text{ cm s}^{-1}$ , showing a slight reduction compared to the sodium ions ( $3.30 \times 10^4 \text{ cm s}^{-1}$ ), and a far greater reduction compared to the lithium ions ( $6.82 \times 10^4 \text{ cm s}^{-1}$ ). The migration of potassium ions through OSPC-3 showed a greater reduction. The average for the potassium ions was  $2.76 \times 10^4 \text{ cm s}^{-1}$ , whereas the lithium and sodium ions displayed mobility rates of  $6.24 \times 10^4$  and  $3.88 \times 10^4 \text{ cm s}^{-1}$ , respectively.

In a comparison of the individual ions, K9 through OSPC-2 showed a substantially greater reduction in movement through the structure. The potassium ion became trapped at approximately  $10 \text{ \AA}$  through OSPC-2, whereas Li9 and Na9 were able to

establish pathways with fewer obstructions, resulting in a time difference of  $>3000$  steps for the potassium ion to migrate to the negatively charged graphene sheet (Figure 5.52). This was a result of the potassium ion establishing a different pathway to those of both Li9 and Na9 from the initial charge activation.

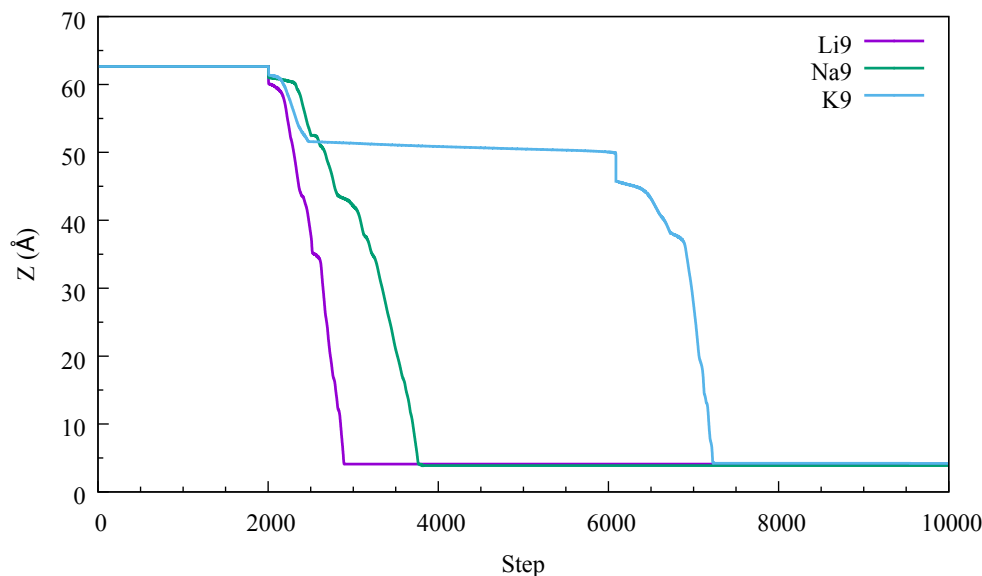


**Figure 5.52:** Comparison of migration and z-axis movement between Li9, Na9, and K9 within OSPC-2 structure.

Li9 and Na9 were able to traverse along almost identical pathways through OSPC-2, whereas K9 established an alternative pathway. This is shown in Figure 5.53, in which the pathways of the lithium and sodium ions almost overlap, and the potassium ion takes an alternate direction. K9 was unable follow the same pathway as Li9 and Na9, and struggled to reestablish a migration pathway once it became trapped because of its larger ionic radius and the available channels it could traverse along. Additionally, Li9 and Na9 illustrate how the mobility rate can be affected by the size of ion migrating through the system as they share almost identical pathways, yet the calculated mobility rate of the lithium ion was greater than the sodium ion.

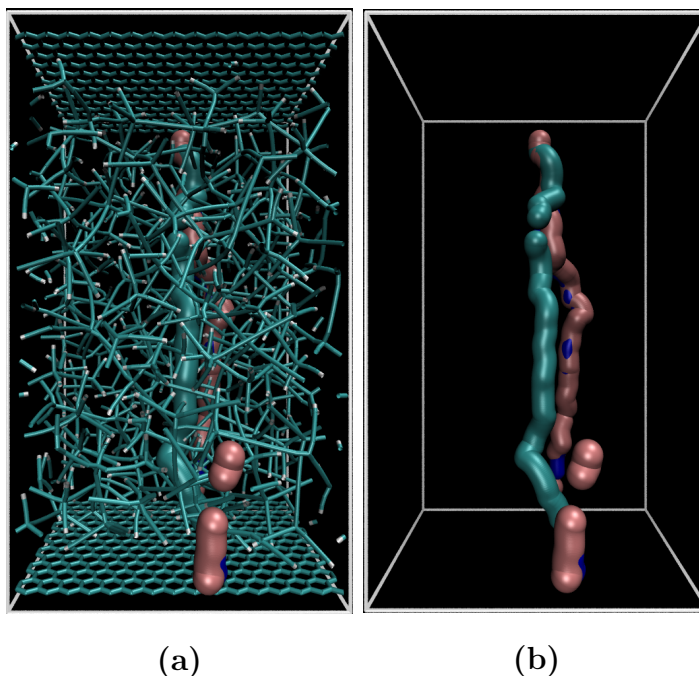


**Figure 5.53:** Comparison of the migration pathways established through the OSPC-2 structure for Li9 (pink), Na9 (blue), and K9 (turquoise).

The OSPC-3 structure generated showed to affect the migration of all monovalent ions observed. K15 was able to establish a pathway that allowed for complete migration through the structure. However, the potassium ion encountered a blockage. This was similar for Li9, yet the lithium ion was able to travel at a greater rate when it had reestablished its pathway (Figure 5.54). The early stages of the migration pathway established by Li15 through OSPC-3 showed to be wide enough for K15 to travel along. However, the potassium ion was required to divert onto an alternate route as it had encountered a blockage that reduced its movement. Na15 diverted on to an alternate pathway through OSPC-3 earlier on. This pathway possessed far fewer obstructions for the ion, which resulted the calculated mobility rate of Na15 to be greater than both Li15 and K15 (Figure 5.55). This highlighted that the increased *node-to-node* length can inhibit the movement of guest molecules within porous systems.



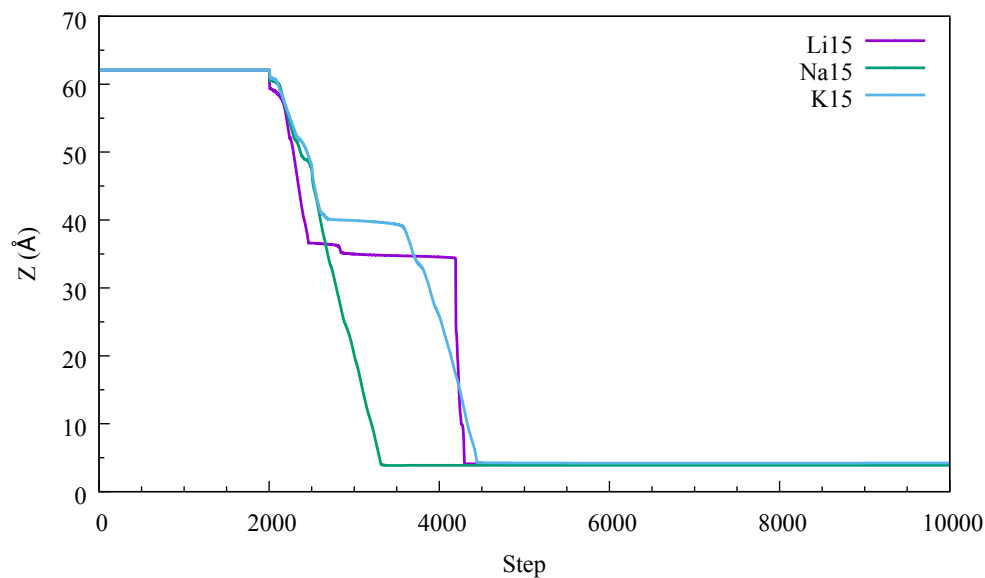


**Figure 5.54:** Comparison of migration and z-axis movement between Li15, Na15, and K15 through OSPC-3.

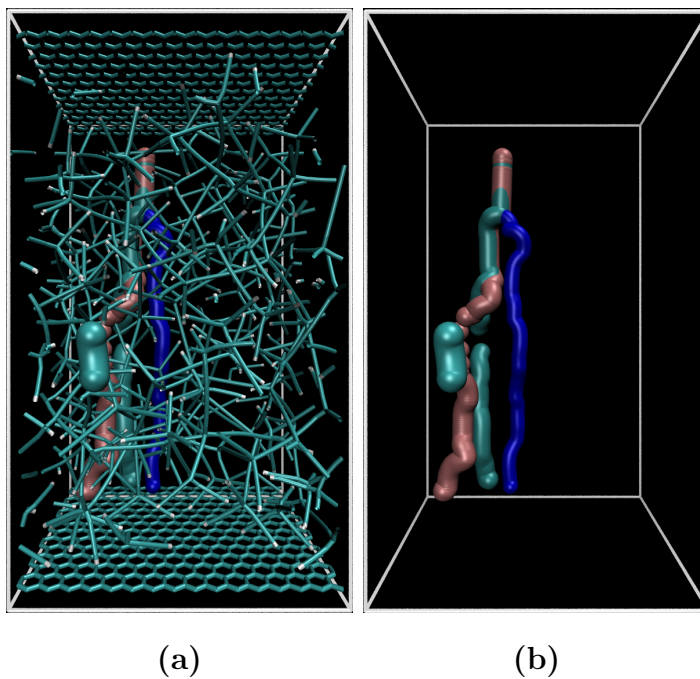


**Figure 5.55:** Comparison of established migration pathways between Li15 (pink), Na15 (blue), and K15 (turquoise) through the OSPC-3 structure. (a) with the OSPC-3 structure shown and (b) without the OSPC-3 structure.

In comparison, the potassium ions were able to establish more direct migration pathways through OSPC-2 than OSPC-3. This resulted in a minor difference in aver-

age mobility rates between the sodium ions and the potassium ions through OSPC-2. However, the difference between the lithium ions and the larger monovalent ions was far greater through OSPC-2 compared to OSPC-3 (Figure 5.56).

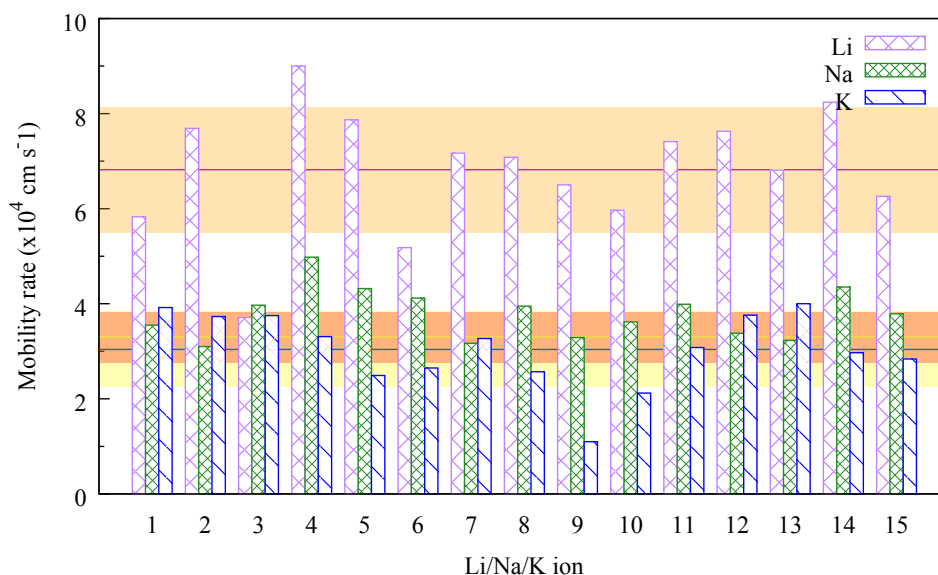


**Figure 5.56:** Comparison of mobility rates between the lithium, sodium, and potassium ions through OSPC-3. The purple line represents the average mobility rate of lithium ions, the yellow line represents the average mobility rate of the sodium ions, the blue line represents the average mobility rate of the potassium ions, and the highlighted regions depicts the standard deviation of the mobility rates for the lithium ions (orange), the sodium ions (red), and the potassium ions (yellow).

The packing of OSPC-3 resulted in the potassium ions showing substantially reduced movement through the structure generated compared to the lithium and sodium ions (Figure 5.57). The lithium ions also showed a reduction in mobility rate through OSPC-3 to that of OSPC-2. Although, the sodium ions were able to migrate at a greater rate.

The increased ionic radius and the establishment of different migration pathways of the potassium ions leads to the ions traversing the system at slower rates in comparison to the alternative monovalent ions of lithium and sodium.

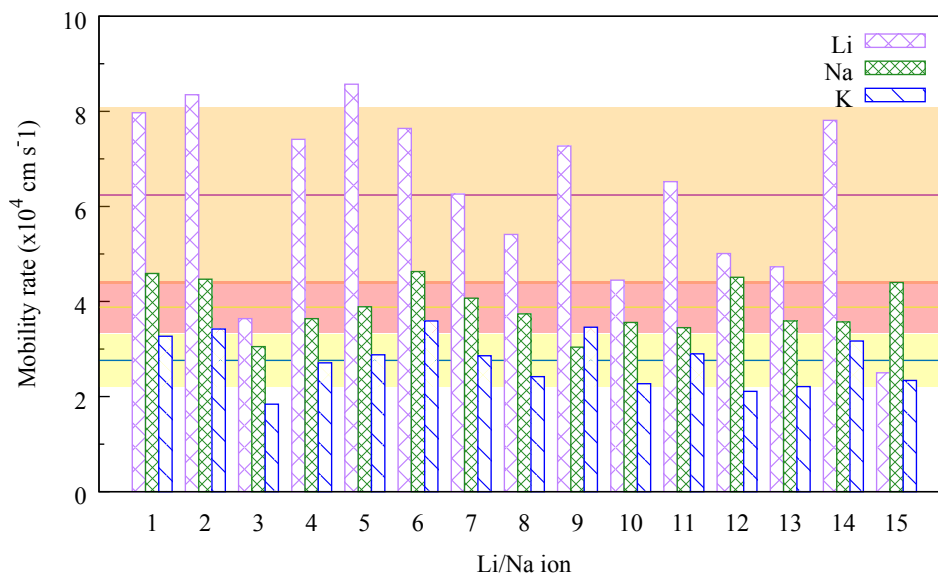


**Figure 5.57:** Comparison of mobility rates between the lithium, sodium, and potassium ions through OSPC-3. The orange line represents the average mobility rate of lithium ion, yellow line represents the average mobility rate of sodium ions, and blue line represents the average mobility rate of potassium ions.

### 5.3.3 Magnesium-ion batteries

Here we investigate the ability of OSPC-2 and OSPC-3 to allow for the migration of magnesium ion. The previously performed simulations had shown that magnesium ions migrate through OSPC-1 and OSPC-0 at greater rates than the monovalent ions, sodium and potassium. This would suggest that the magnesium ions would be able to migrate through OSPC-2 and OSPC-3 similar to that observed in OSPC-1.

Mg1 was able to completely migrate through OSPC-2 and OSPC-3 to the negatively charged graphene sheet. The magnesium ion encountered far fewer obstructions along its chosen pathways compared to the previously observed ions (*vide supra* Sections 5.3.1 and 5.3.2). The movement of Mg1 through OSPC-2 showed to slower compared to its migration through OSPC-3 (Figure 5.58). The pathways available within OSPC-3 were, therefore, suitably wide for the magnesium ion to establish a direct route through the structure. This was different for the potassium ions, although the magnesium ions have an ionic radius smaller than both sodium and potassium,

indicating that the size of the ion greatly affected the mobility of ions through both of these systems.

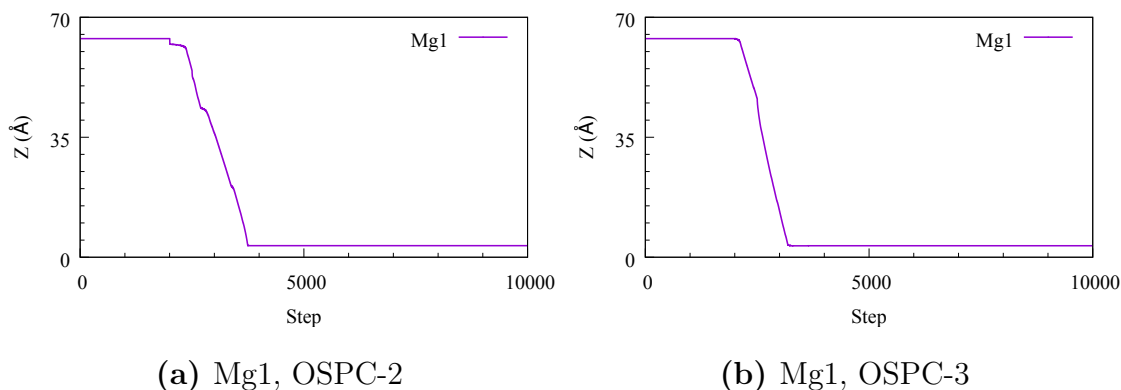


**Figure 5.58:** Movement in the z-axis of Mg1 through (a) OSPC-2 and (b) OSPC-3.

The additional magnesium ions in the simulation were able to establish pathways through OSPC-2 and OSPC-3 that allowed for a complete migration (OSPC-2, Appendix A.20; OSPC-3, Appendix A.24). The movement of the magnesium ions through the system was not hindered by the structures generated, and each ion was able to establish direct pathways that contained very few obstructions, resulting in great mobility through both systems. Because of the availability of pathways, the mobility rates calculated of the magnesium ions did not differ greatly between OSPC-2 and OSPC-3 (Table 5.12).

Compared to the migration of sodium and potassium ions, the magnesium ions showed greater mobility rates through both OSPC-2 and OSPC-3. The migration of magnesium ions did not surpass that of the lithium ions through OSPC-2 ( $6.82 \times 10^4$  cm s<sup>-1</sup>) or OSPC-3 ( $6.24 \times 10^4$  cm s<sup>-1</sup>), with several sharing similar mobility rates or falling short. However, this was expected as the migration of magnesium ions through OSPC-1 was slower than the lithium ions.

Magnesium ion	Ion mobility rate ( $\times 10^4$ cm s $^{-1}$ )	
	OSPC-2	OSPC-3
Mg1	3.42	5.06
Mg2	3.62	3.97
Mg3	3.52	3.51
Mg4	4.21	3.63
Mg5	4.58	4.02
Mg6	4.72	5.12
Mg7	4.84	4.24
Mg8	3.62	4.83
Mg9	3.38	5.36
Mg10	4.42	3.49
Mg11	3.85	3.91
Mg12	3.92	4.38
Mg13	5.09	4.94
Mg14	4.42	4.91
Mg15	4.55	4.38
Average	4.15	4.38

**Table 5.12:** Mobility rates of the individual magnesium ions through OSPC-2 and OSPC-3.

The small difference between the mobility rates of the magnesium ions showed how the difference in strut length of the OSPC structures did not hinder the movement of the divalent ion. The available pathways within OSPC-2 and OSPC-3 were wide enough to allow passage. However, the greater ionic charge did not promote their movement. This was apparent when comparing the pathways of the magnesium ions and lithium ions through both structure.

The migration pathway of Li7 through OSPC-2 appeared more tortuous to that of Mg7 (Figures 5.59 and 5.60). Each ion showed to establish direct routes through the structure generated. However, the initial movement of Mg7 was slower than Li7, and its movement appeared to be slower than that of the lithium ion between 40 and 70 Å through OSPC-2, resulting in a slower mobility rate.

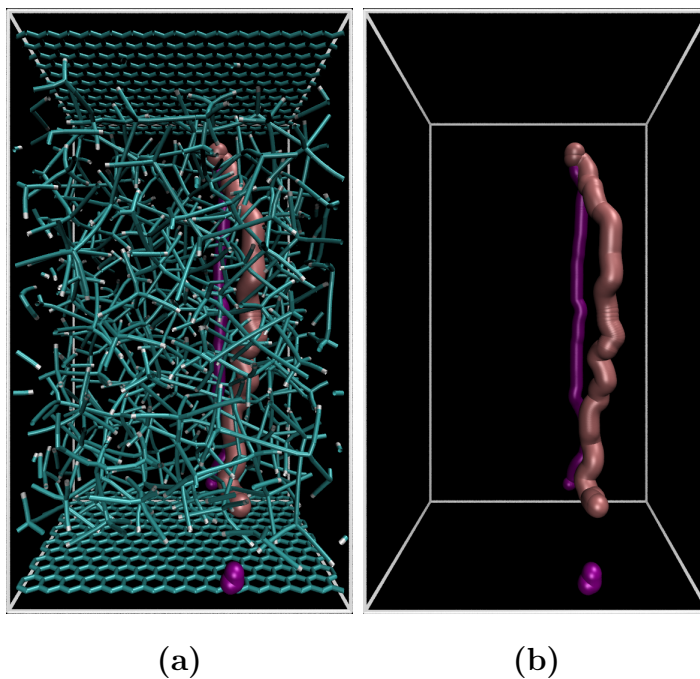


**Figure 5.59:** Comparisons of migration pathways between Li7 (pink) and Mg7 (purple) through the OSPC-2 structure.

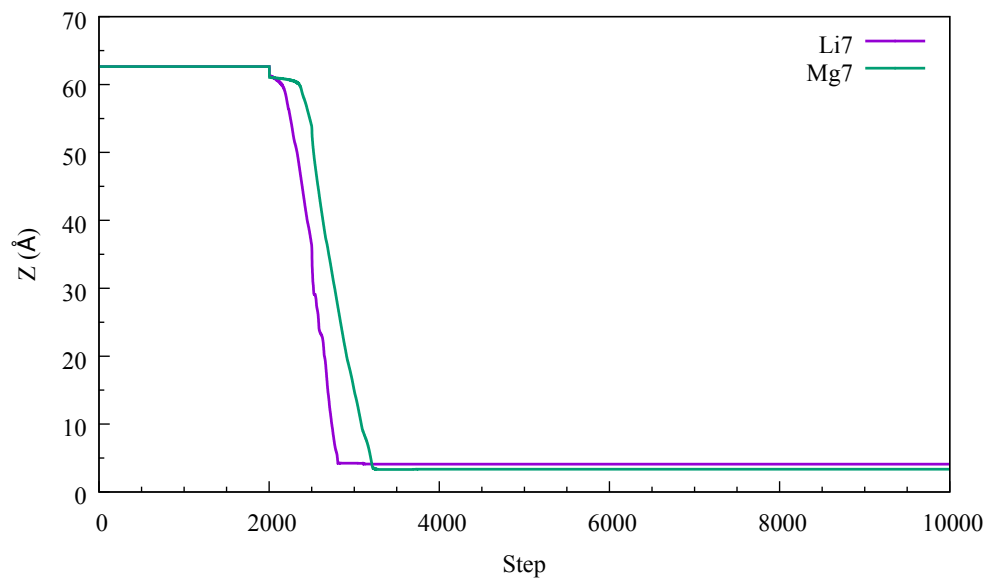


**Figure 5.60:** Comparison of migration and z-axis movement between Li7 and Mg7 OSPC-2.

This was similar for most of the magnesium ions through OSPC-3. Although, there were several magnesium ions that were able to establish migration pathways through the structure that resulted in mobility rates greater than their lithium ion counterparts.

Mg15 through OSPC-3 was able to divert from the same pathway as Li15, taking a more direct route through the structure, whereas the pathway established by Li15 resulted in the ion becoming trapped at the midpoint of the structure. This is shown in Figure 5.61

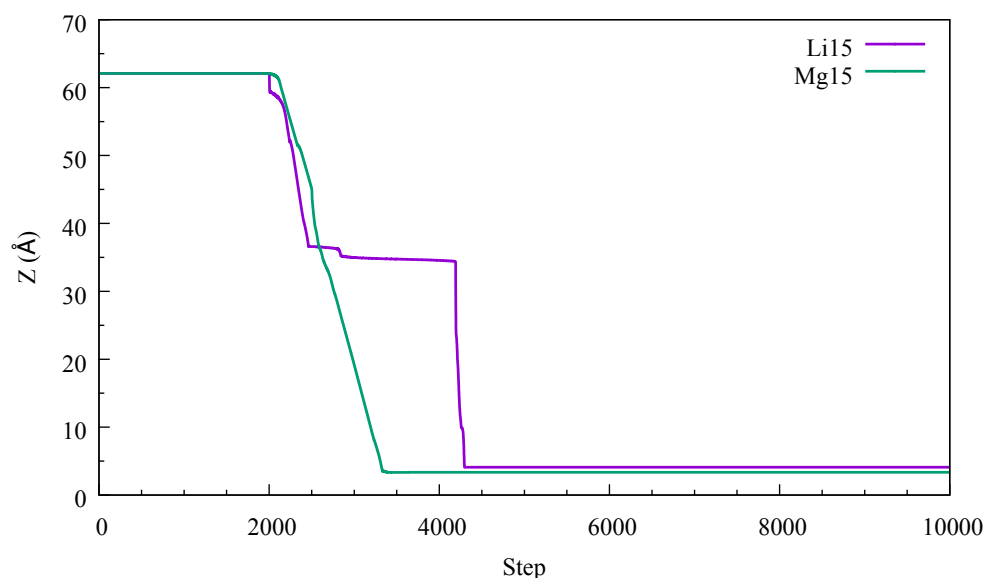


**Figure 5.61:** Comparison of migration and z-axis movement for Li15 and Mg15 through OSPC-3.

Because of the pathway chosen by the magnesium ion, it did not encounter the same obstructions as the lithium ion. However, this was not observed for the migration of magnesium ions through OSPC-2, which had led to a greater difference in average mobility rate between the magnesium and lithium ions through OSPC-2 compared to OSPC-3. Figures 5.62 and 5.63 show the difference in mobility rates between the lithium and magnesium ions through OSPC-2 and OSPC-3, respectively.

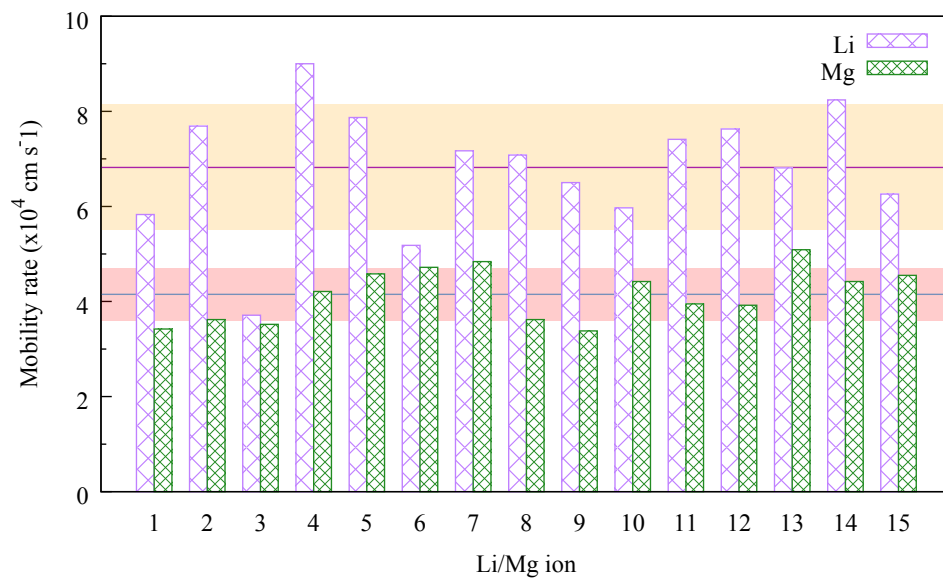


**Figure 5.62:** Comparison of mobility rates for the individual lithium and magnesium ions during the OSPC-2 simulations. The pink line represents the average mobility rate of the lithium ions, the blue line represents the average mobility rate of the magnesium ions, and the highlighted regions depict the standard deviation of both the lithium ions (orange) and the magnesium ions (red).

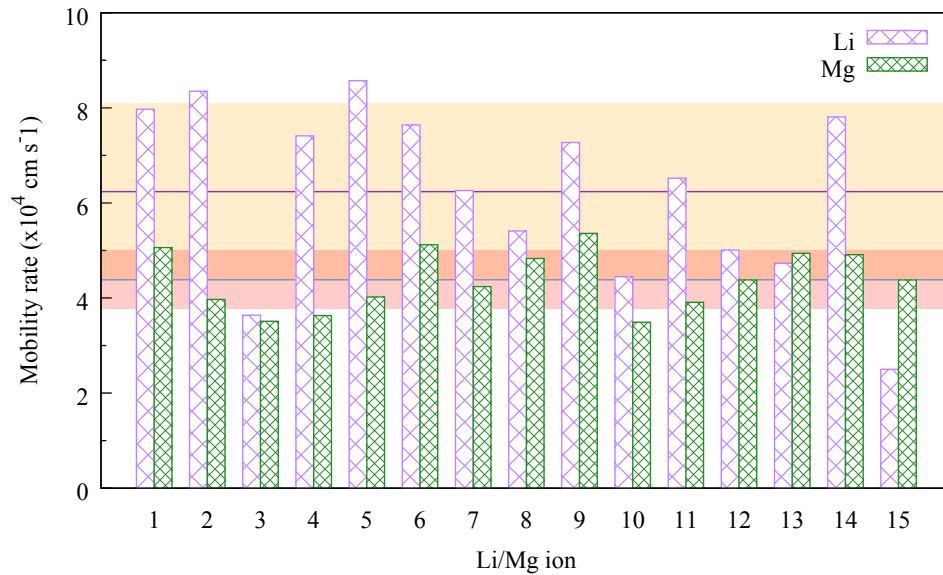


**Figure 5.63:** Comparison of mobility rates for the individual lithium and magnesium ions during the OSPC-3 simulations. The pink line represents the average mobility rate of the lithium ions, the blue line represents the average mobility rate of the magnesium ions, and the highlighted regions depict the standard deviation of both the lithium ions (orange) and the magnesium ions (red).



Comparably, the lithium ions were able to migrate at greater rates through OSPC-2 than OSPC-3. The average mobility rate of the lithium ions through OSPC-2 exceeds that of the magnesium, whereas this difference is smaller between the ions through OSPC-3.

However, the magnesium ions were able to migrate through the OSPC-2 and OSPC-3 structures generated, highlighting the potential of these materials as anodes for MIBs.

### 5.3.4 Calcium-ion batteries

To determine their potential as anodes for alternate divalent ion batteries, the migration of calcium ions through OSPC-2 and OSPC-3 was observed.

Although all of the calcium ions were able to migrate through each structure, their migration appeared to be more challenging compared to the magnesium ions observed. Ca1 was an example of a calcium ion establishing a direct pathway through the constructs (Figure 5.64).

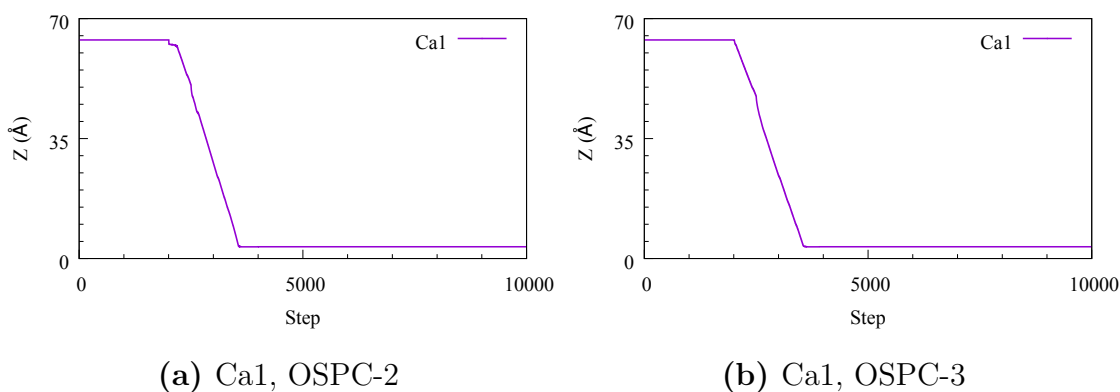


**Figure 5.64:** Movement in the z-axis of Ca1 through (a) OSPC-2 and (b) OSPC-3.

Several of the additional calcium ions presented similar migration patterns to that of Ca1, yet there were several that encountered obstructions through both OSPC-2 and OSPC-3 (OSPC-2, Appendix A.21; OSPC-3, Appendix A.25). Similar to Mg15 through OSPC-3, Ca15 was able to establish a migration pathway through the struc-

ture that offered a greater mobility rate to that of Li15. Figure 5.65 shows how the calcium ion was able to move more freely through the OSPC-3 structure generated. It encountered several obstructions from OSPC-3, yet its migration was not hindered in the same manner as Li15.

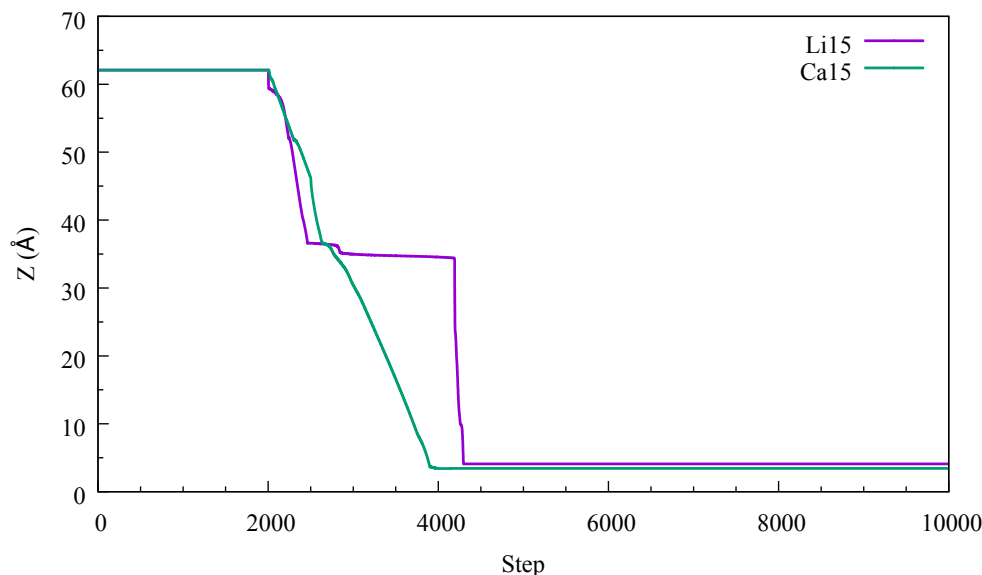


**Figure 5.65:** Comparison of migration and z-axis movement between Ca15 and Li15 through the OSPC-3 structure.

Comparing the two OSPC structures generated, OSPC-2 allowed for faster migration and movement of calcium ions compared to OSPC-3 (Table 5.13). This was different compared to the migration of magnesium ions, where OSPC-3 allowed the ions to travel at greater rates than OSPC-2. Although, there was only a minor difference between the migration of the divalent ions through both systems (OSPC-2, Figure 5.66; OSPC-3, Figure 5.67).

Calcium ion	Ion mobility rate ( $\times 10^4$ cm s $^{-1}$ )	
	OSPC-2	OSPC-3
Ca1	3.84	3.86
Ca2	3.41	3.16
Ca3	3.26	2.66
Ca4	3.65	2.72
Ca5	4.39	2.88
Ca6	3.53	3.69
Ca7	3.92	3.46
Ca8	2.85	3.82
Ca9	2.85	4.12
Ca10	3.55	2.87
Ca11	2.95	3.64
Ca12	2.88	3.48
Ca13	4.41	3.60
Ca14	4.22	3.84
Ca15	3.70	3.06
Average	3.56	3.39

**Table 5.13:** Mobility rates of the individual calcium ions through OSPC-2 and OSPC-3.

The calculated mobility rates of the magnesium ions through OSPC-3 were greater than the calcium ions, whereas there was minor differences between the mobility rates of the calcium and magnesium ions through OSPC-2. Ca1 through OSPC-2 was able to establish a pathway that gave a greater mobility rate than Mg1. The calculated mobility rate of Ca1 through OSPC-3 was slower compared to Mg1 through OSPC-2.

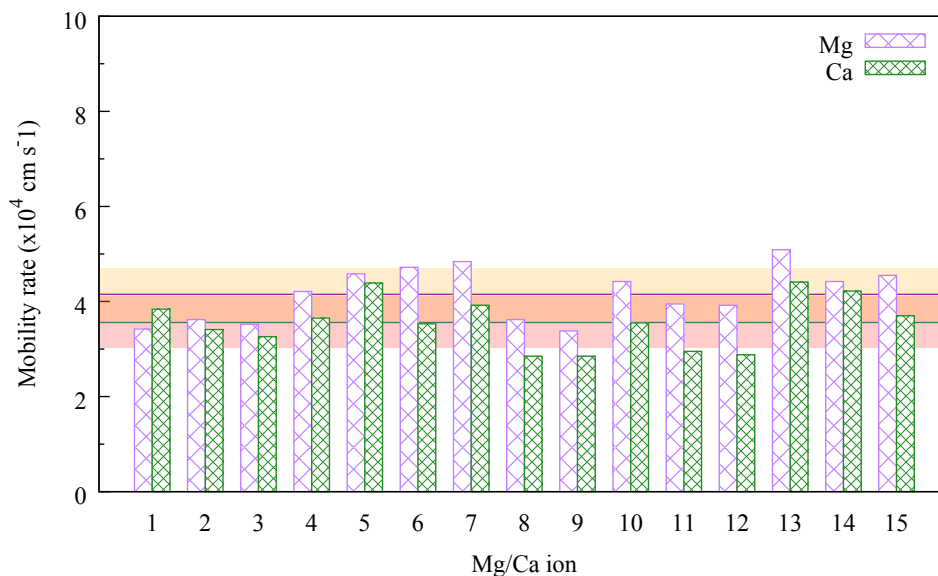


**Figure 5.66:** Comparison of mobility rates for the individual magnesium and calcium ions through OSPC-2. The pink line represents the average mobility rate of the magnesium ions, the blue line represents the average mobility rate of the calcium ions, and the highlighted regions depict the standard deviation of both the magnesium ions (orange) and the calcium ions (red).

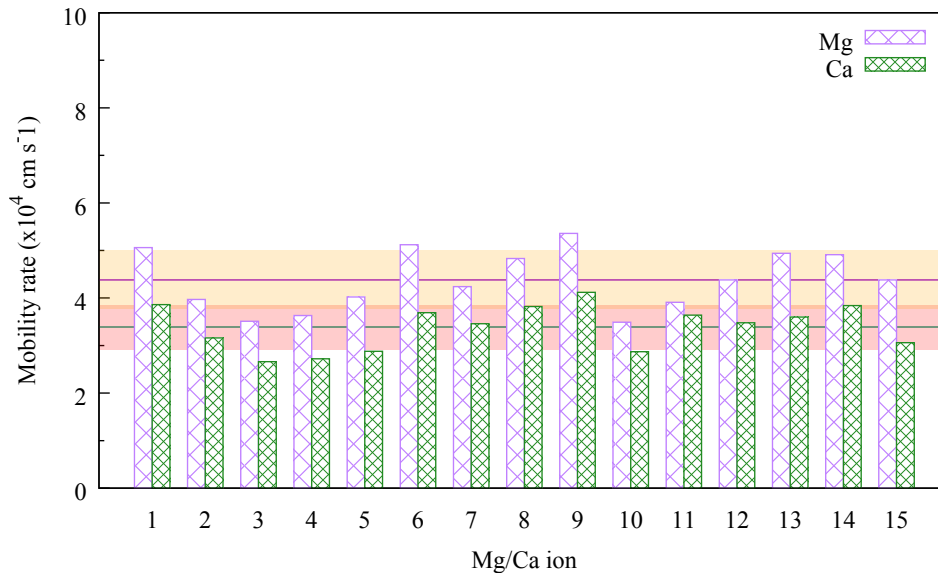


**Figure 5.67:** Comparison of mobility rates for the individual magnesium and calcium ions through OSPC-3. The pink line represents the average mobility rate of the magnesium ions, the blue line represents the average mobility rate of the calcium ions, and the highlighted regions depict the standard deviation of both the magnesium ions (orange) and the calcium ions (red).

In comparison to the migration of lithium ions through both OSPC-2 and OSPC-3, the divalent ions showed greatly reduced mobility rates. Figure 5.68 illustrates the difference in mobility rate between the calcium and lithium ions through OSPC-2, and Figure 5.69 illustrates the difference through OSPC-3. As is shown, the migration of lithium ions was far greater than both divalent ions observed through OSPC-2 (Li,  $6.82 \times 10^4 \text{ cm s}^{-1}$ ; Mg,  $4.15 \times 10^4 \text{ cm s}^{-1}$ ; Ca,  $3.56 \times 10^4 \text{ cm s}^{-1}$ ) and OSPC-3 (Li,  $6.24 \times 10^4 \text{ cm s}^{-1}$ ; Mg,  $4.38 \times 10^4 \text{ cm s}^{-1}$ ; Ca,  $3.39 \times 10^4 \text{ cm s}^{-1}$ ).

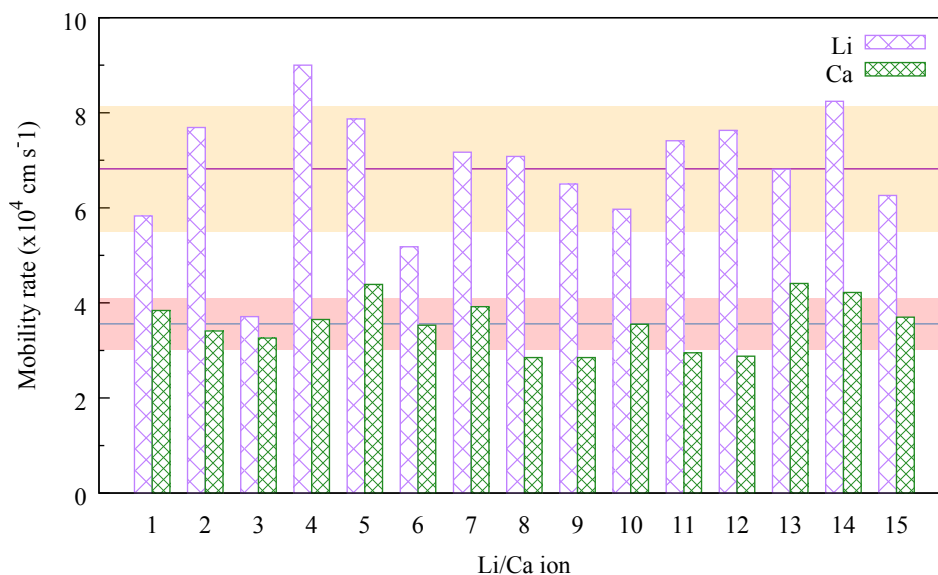


**Figure 5.68:** Comparison of mobility rates for the individual lithium and calcium ions during the OSPC-2 simulations. The pink line represents the average mobility rate of the lithium ions, the blue line represents the average mobility rate of the calcium ions, and the highlighted regions depict the standard deviation of both the lithium ions (orange) and the calcium ions (red).

Similar to OSPC-1, the larger of the divalent ions had slower mobility rates through OSPC-2 and OSPC-3. Not only does the size of the ion continue to affect the mobility rates through these materials, but the established pathways also affect how the ions behave and move through the constructs.

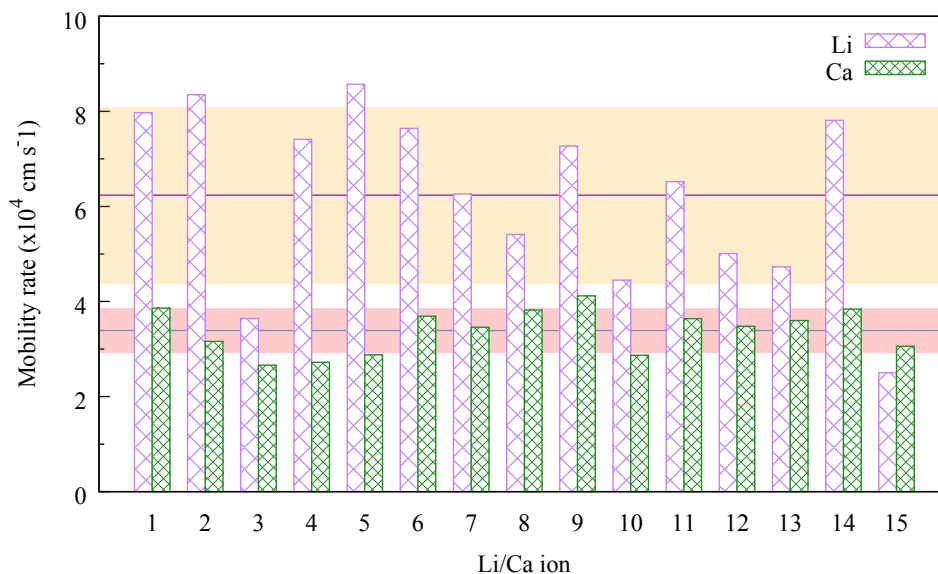


**Figure 5.69:** Comparison of mobility rates for the individual lithium and calcium ions during the OSPC-3 simulations. The pink line represents the average mobility rate of the lithium ions, the blue line represents the average mobility rate of the calcium ions, and the highlighted regions depict the standard deviation of both the lithium ions (orange) and the calcium ions (red).

### 5.3.5 Comparison

Overall, the lithium ions are able to traverse the system of OSPC-2 much more quickly than those of the latter ions (sodium, potassium, magnesium, and calcium). The great difference between the lithium ions and their alternatives lies with not only the size of the ion, but also the established pathway of the individual ions within the system.

The magnesium ions share a very similar ionic radius to the lithium ions. However, their established pathways resulted in an average mobility rate of  $4.15 \times 10^4 \text{ cm s}^{-1}$ , in comparison to the lithium ions which displayed an average mobility rate of  $6.82 \times 10^4 \text{ cm s}^{-1}$ . Furthermore, the increasing ionic radius of the monovalent ions leads to much slower mobility rates. The average mobility rate of the sodium ions was calculated to be  $3.30 \times 10^4 \text{ cm s}^{-1}$ , and for the potassium ions it was calculated to be  $3.04 \times 10^4 \text{ cm s}^{-1}$ . This trend extends into the divalent ions. The average mobility rate for the magnesium and calcium ions was calculated to be  $4.15 \times 10^4$  and  $3.56$

$\times 10^4 \text{ cm s}^{-1}$  respectively. As shown in Figure 5.70, the lithium ions migrated at much greater rates than those of the sodium, potassium, magnesium, and calcium ions. As expected, the mobility rate of the monovalent ions decreases as the ionic radius is increased. This is similar for the divalent ions, although, as previously observed, the size of the ion is not the only factor that affects the mobility rates.

The established pathway for many of the ions differ to those of the lithium ions. This results in the ions moving more slowly through the structure as they want to move through channels that are not as wide as those that the lithium ions establish.

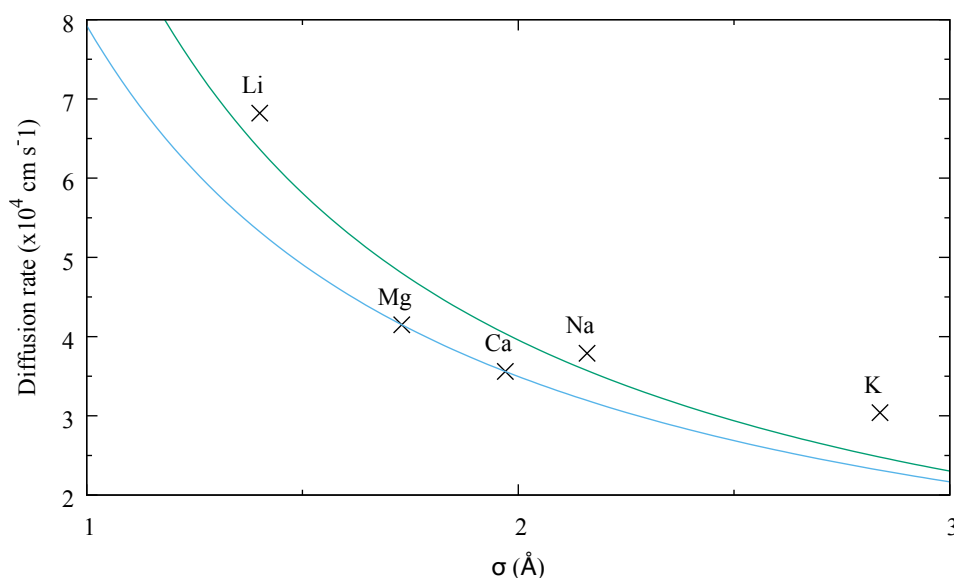


**Figure 5.70:** Comparison of the average mobility rates between the lithium, sodium, potassium, magnesium, and calcium ions observed through OSPC-2. The blue line represents the fitted trend between the calculated rates.

The OSPC-3 structure, with its more open framework and accessible surface area, leads to fast migration of the ions through its confines. In several cases the ions become trapped, as seen with Li15. However, the likes of Mg15 and Ca15 are able to establish direct migration pathways through the structure towards the negatively charged graphene sheet (Figure 5.71).

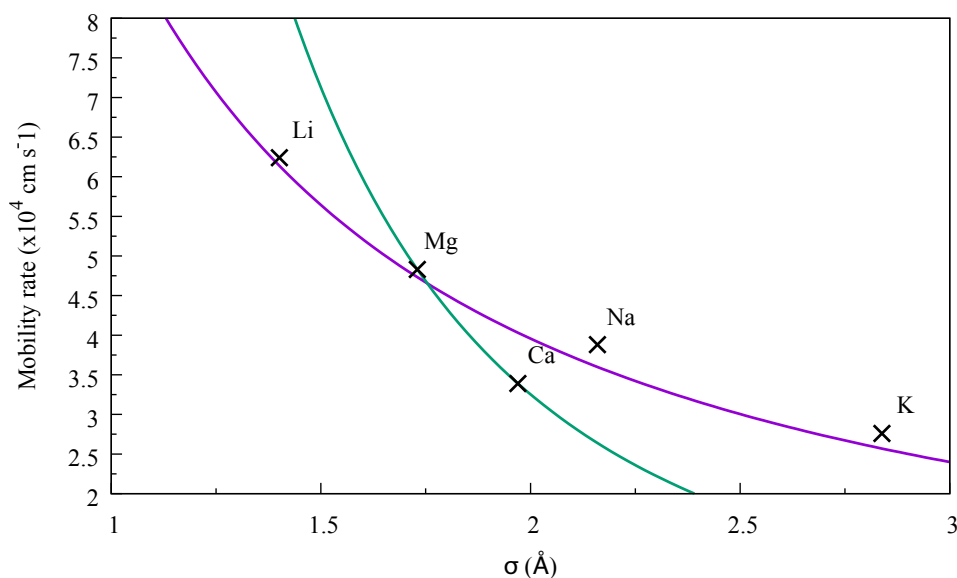


**Figure 5.71:** Comparison between the average mobility rates calculated for each ion observed through the OSPC-3 structure.

As seen with the previous structures, the lithium ions present the fastest mobility rates ( $6.24 \times 10^4$  cm s $^{-1}$ ) and the potassium ions present the slowest mobility rates ( $2.76 \times 10^4$  cm s $^{-1}$ ). Although overall the lithium ions show the greatest mobility rate, the pathway in which Li15 establishes results in its mobility rate being amongst some of the slower ions to migrate through ( $2.50 \times 10^4$  cm s $^{-1}$ ). Nonetheless, due to its larger size, the potassium ions present the slowest mobility rates.

Each ion is able to completely migrate through the system towards the negatively charged graphene sheet, presenting the capabilities of OSPC-3 as an anode for batteries. However, the internal network still contains obstructions and narrower channels, meaning that the pathways in which the ions establish for migration are the limiting factor to the rate of their diffusion.

## 5.4 Ion Comparison

The structures of OSPC-0, OSPC-1, and OSPC-2 generated offered respectively increasing mobility rates for each of the ions. However, the mobility rate of lithium



ions shows to decline through OSPC-3 (Figure 5.72).

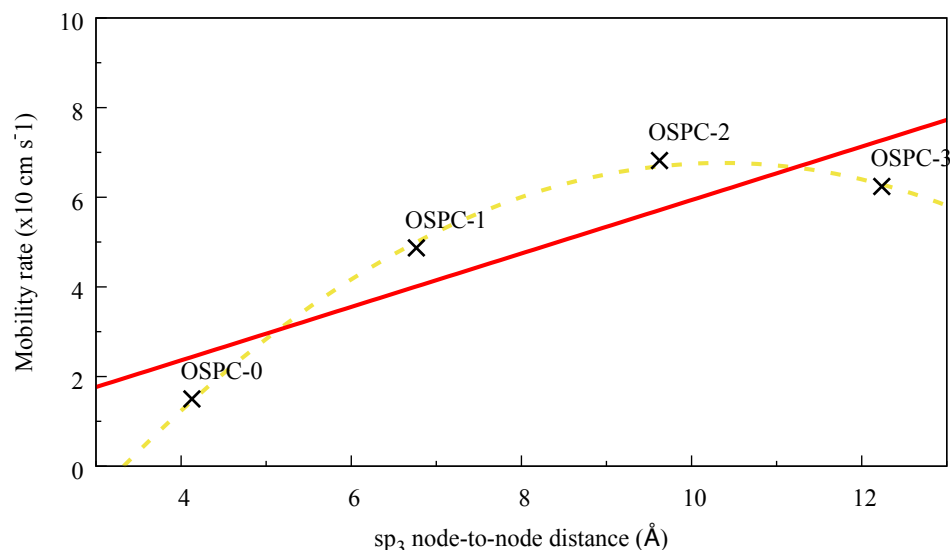


**Figure 5.72:** Comparison of lithium ion mobility rates between the structures of OSPC-0, OSPC-1, OSPC-2, and OSPC-3 in relation to their average  $sp^3$ -node-to-node distances.

The migration of lithium ions through this generated structure of OSPC-3 is reduced in comparison to OSPC-2. The mobility rates of the lithium ions show a linear trend from the OSPC-0 structure to the OSPC-2 structure. However, the OSPC-3 structure outliers from this trend.

The porous structure can differ greatly as it is generated. This can affect the available pathways within its internal confines, leading to blockages and porous pockets in which the ions become trapped. This is shown with Li15, where the lithium ion shows greatly reduced movement for approximate 1000 steps before moving into a more open channel so it can continue on its trajectory.

There is a great difference in mobility rate between each ion across the four structures observed. Lithium demonstrates the fastest mobility rate within OSPC-1, OSPC-2, and OSPC-3, with the mobility rate of lithium ions through OSPC-2 far exceeding both the monovalent and divalent ions studied. Figure 5.73 shows the difference between the mobility rates of each ion for the four structures generated.

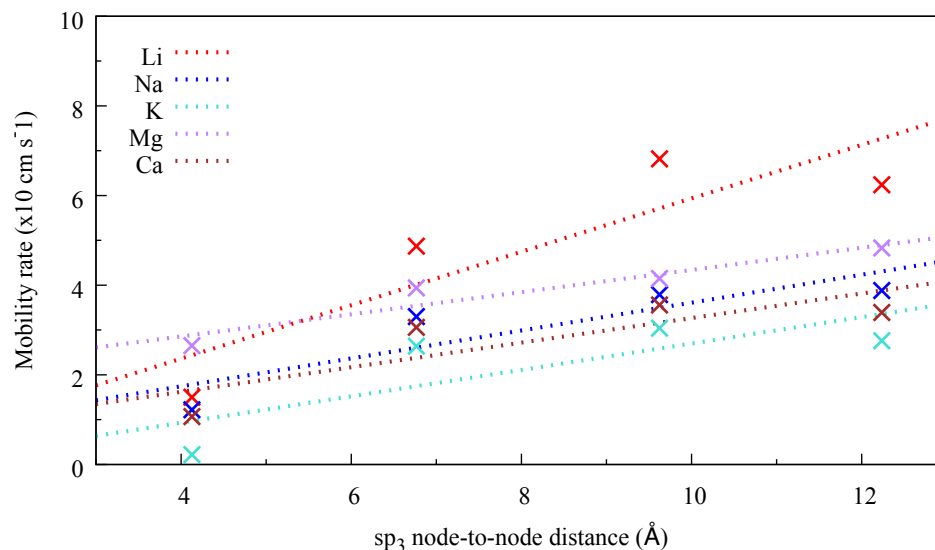


**Figure 5.73:** Comparison of mobility rates between each ion observed through the structures of OSPC-0, OSPC-1, OSPC-2, and OSPC-3 in relation to their average  $sp^3$ -node-to-node distances. Red, lithium; Blue, sodium; Turquoise, potassium; Purple, magnesium; Brown, calcium.

The mobility rates of each ion increase from the OSPC-0 structure generated, and begin to decrease from the OSPC-2 to the OSPC-3 structures generated. The pathways determined for each ion is significant through the structures, and the structural nature of the carbon network generated for OSPC-3 proves to reduce the mobility rate of the ions compared to that of the OSPC-2 structure. However, the magnesium ions present the fastest mobility rate through the OSPC-0 structure. Both the comparable size to lithium ions, and the +2 charge of magnesium drive the ions through the system towards the negatively charged graphene sheet. Whereas the potassium ions presents the slowest mobility rates through each system. Having the largest radius results in the ions become more accustomed to blockages, and therefore becoming unable to completely migrate through the systems.

This research demonstrates how the OSPC-1 material can be utilised as an anode for alternative batteries: sodium ion, potassium ion, magnesium ion, and calcium ion. It also presents rationalised materials to extend the structural possibilities based

upon OSPC-1. These materials have similar functionalisation to that of OSPC-1, which gives reason towards their performance as anodes for lithium ion batteries.

The calculated mobility rates for each ion through each of the structures generated increase with the extension between the  $sp^3$ -carbon nodes. However, the performance drops between OSPC-2 and OSPC-3. Due to each structure having being randomly generated within AmBuild, this is not representative of the overall OSPC-3 structure. However, the mobility rates of the OSPC-3 structure are greater than those calculated within the OSPC-1 structure.

By understanding the diffusion coefficients and the structural formation of these materials, anodes can be designed and synthesised to tailor the uptake of ions as well as the discharge rates for battery technologies.

*"There's two ways to deal with mystery:  
uncover it, or eliminate it.."*

---

—Andrew Ryan

## Chapter 6

# Conclusion

### 6.1 Summary

This research focusses on the electronic properties of pyrene-based conjugated microporous polymers and the newly introduced organically synthesised porous carbon. The original research on these materials illustrates the electronic activity of the materials for photocatalysts and anodes for lithium ion batteries respectively.

The former research project has focussed on the electronic properties of conjugated microporous polymers, and the study of novel materials for electronic applications. Conjugated microporous polymers show great potential in a variety of electronic applications. The conjugated microporous polymers in question have been studied for their luminescent properties and behaviour as photocatalysts. However, to understand the behaviour of these materials in application, it is first necessary to understand how their structural properties can be utilised to tailor their specificity through unique characteristics. The introduced materials of YPy, YDBPy, and YDPPy have shown tailorable band gap properties.<sup>124</sup> The introduction of a linear co-monomer into the structure can be used to alter the photoluminescent properties of a material. Using this knowledge computational simulations have been performed to understand how the difference in structural properties can impact the energetics of the system.

Implementing the hypothesis that unique structures, called here "molecular rings",

are the influencing factor towards their luminescent properties, and thus their band gap energies, an analysis of computational models was performed. The statistical analysis of molecular rings between the structures shows a great reduction with the introduction of linear co-monomers of increasing size. This introduced the idea that co-monomers of non-linear geometry could be implemented to tailor the band gap further within the pyrene-based CMPs. The rationalisation of the co-polymeric CMPs S1 and S2 (including 1,3-dibromobenzene and 1,2-dibromobenzene respectively) demonstrated a rapid increase in molecular rings that encouraged further studies into the synthesis of the materials. Attempts on the synthesis of the CMPs of YPy, YDBPy (S0), S1, and S2 were proven inconsistent with the published literature, enlightening to the fact that these materials are not wholly replicable and that the synthetic procedure is sporadic. Analysis of these materials showed the incorporation of each building block, yet the optical properties of the materials showed no considerable changes. This further encouraged the understanding of how these materials develop, and how the incorporation of a co-monomer could in fact be used to manipulate the energetics of the system.

In collaboration with academics within the Department of Chemistry, Lancaster University, computational calculations were performed to visualise the differences between the structures generated, and to further understand how the energetics of a system could be manipulated. Through this understanding, coupled with the experimental analysis of the synthesised materials, it was possible to produce assumptions as to where optical peaks in the UV-vis spectrum could occur, although the understanding of why they would occur in these places was yet to follow. Visualising orbital analyses of the generated structures, it was possible to follow the electron density of the materials. These studies showed that the electron density of the materials resided over the pyrene building blocks themselves, and that the orbital overlap between pyrene units was an additional factor for the electronic nature of the materials. Together with the molecular ring theory, it can be inferred that the spacing between the pyrene, and the conformation and strain of these molecular rings are the limit-

ing factors to the changes in band gap energy between the pyrene building blocks. The introduction to non-linear co-monomers plays a role in both this spacing and the strain induced upon the rings observed.

The latter research project has observed the nature of the newly introduced OSPC-1 (organically synthesised porous carbon) material, with its application as an anode for lithium ion batteries. Computational models of the OSPC-1 system were generated, and its diffusive behaviour for lithium ions observed.<sup>148</sup> Continuing the studies into this unique material, rationalised materials based upon its structural properties were generated: OSPC-0, OSPC-2, and OSPC-3. These consist over a varying number of triply-bonded  $sp^3$ -carbon nodes to develop systems involving a reduction and an increase in pore volumes between the structures. As OSPC-1 has demonstrated such adept behaviour as an anode for lithium ion batteries, these rationalised materials were subjected to the same diffusive simulations performed on its parent material. As one would expect, an increase in pore volume and size inevitably leads to faster movement of guest materials through its system. *Active diffusion* was applied within these simulations to gain an understanding of the pathways and diffusive rates between the OSPC materials. OSPC-0 with its more tortuous pathways and tighter channels proved to have the least accessible pathways, where as OSPC-3, with its much wider pathways, excelled in its diffusive properties ( $OSPC-0 > OSPC-1 > OSPC-2 > OSPC-3$ ).

To further expand on how these materials could be used in advancing technologies, the lithium ions were replaced with ions of greater abundance between groups 1 and 2: sodium, potassium, magnesium, and calcium. The increasing ionic radius of the ions observed showed that the OSPC structures were greatly suited towards lithium ion diffusion... With the exception of OSPC-0. A unique charge:ionic radius ratio was found to overcome the sterics and highly rigid framework of the OSPC-0, with the diffusion of magnesium ions, calcium ions, and sodium ions surpassing the diffusive rates of the smaller lithium ions.

This thesis introduces new concepts for porous polymers with unique electronic qualities. Expansion upon the rationalised CMPs and the theory behind their unique properties can be utilised in the further development of such materials and their functionalities. Additionally, the diffusive behaviour of the OSPC networks gives insight into rationalised materials for alternate battery technologies.

## 6.2 Future work

Functionalisation of the building blocks could be utilised to further manipulate the band gap energy of pyrene-based CMPs. The simulations performed herein offer an understanding into the energetics of the materials, and how the band-gap is affected with the inclusion of a co-monomer. Performing these simulations with building blocks containing electron withdrawing and electron donating functional groups could greatly affect the  $\pi$ -system, which in turn could lead to changes in the electron density that resides over the pyrene monomer. Additionally, synthesis of the designed OSPC family and the analysis of their structural and electronic properties will further confirm their capabilities as anodes for battery technologies.

# Bibliography

- [1] B. Li, Y. Zhang, R. Krishna, K. Yao, Y. Han, Z. Wu, D. Ma, Z. Shi, T. Pham, B. Space, J. Liu, P. K. Thallapally, J. Liu, M. Chrzanowski and S. Ma, *Journal of the American Chemical Society*, 2014, **136**, 8654–8660.
- [2] T. Hasell, M. Miklitz, A. Stephenson, M. A. Little, S. Y. Chong, R. Clowes, L. Chen, D. Holden, G. A. Tribello, K. E. Jelfs and et al., *Journal of the American Chemical Society*, 2016, **138**, 1653–1659.
- [3] J. Fu, S. Das, G. Xing, T. Ben, V. Valtchev and S. Qiu, *Journal of the American Chemical Society*, 2016, **138**, 7673–7680.
- [4] Q. Song, S. Jiang, T. Hasell, M. Liu, S. Sun, A. K. Cheetham, E. Sivaniah and A. I. Cooper, *Advanced Materials*, 2016, **28**, 2629–2637.
- [5] H. Xu, J. Gao and D. Jiang, *Nature Chemistry*, 2015, **7**, 905–912.
- [6] K. Iwase, T. Yoshioka, S. Nakanishi, K. Hashimoto and K. Kamiya, *Angewandte Chemie International Edition*, 2015, **54**, 11068–11072.
- [7] P. Thomas, C. Pei, B. Roy, S. Ghosh, S. Das, A. Banerjee, T. Ben, S. Qiu and S. Roy, *Journal of Materials Chemistry A*, 2015, **3**, 1431–1441.
- [8] Q. Fang, J. Wang, S. Gu, R. B. Kaspar, Z. Zhuang, J. Zheng, H. Guo, S. Qiu and Y. Yan, *Journal of the American Chemical Society*, 2015, **137**, 8352–8355.
- [9] C. R. DeBlase, K. E. Silberstein, T.-T. Truong, H. D. Abruna and W. R. Dichtel, *Journal of the American Chemical Society*, 2013, **135**, 16821–16824.



- 
- [10] B. Guo, T. Ben, Z. Bi, G. M. Veith, X.-G. Sun, S. Qiu and S. Dai, *Chemical Communications*, 2013, **49**, 4905.
- [11] Y. Li, S. Roy, T. Ben, S. Xu and S. Qiu, *Physical Chemistry Chemical Physics*, 2014, **16**, 12909.
- [12] F. Xu, H. Xu, X. Chen, D. Wu, Y. Wu, H. Liu, C. Gu, R. Fu and D. Jiang, *Angewandte Chemie International Edition*, 2015, **54**, 6814–6818.
- [13] F. Xu, S. Jin, H. Zhong, D. Wu, X. Yang, X. Chen, H. Wei, R. Fu and D. Jiang, *Scientific Reports*, 2015, **5**, 1–6.
- [14] J.-S. M. Lee, T.-H. Wu, B. M. Alston, M. E. Briggs, T. Hasell, C.-C. Hu and A. I. Cooper, *Journal of Materials Chemistry A*, 2016, **4**, 7665–7673.
- [15] C. R. Mulzer, L. Shen, R. P. Bisbey, J. R. McKone, N. Zhang, H. D. Abruña and W. R. Dichtel, *ACS Central Science*, 2016, **2**, 667–673.
- [16] H. Xu, S. Tao and D. Jiang, *Nature Materials*, 2016, **15**, 722–726.
- [17] H. Ma, B. Liu, B. Li, L. Zhang, Y.-G. Li, H.-Q. Tan, H.-Y. Zang and G. Zhu, *Journal of the American Chemical Society*, 2016, **138**, 5897–5903.
- [18] X. Ding, X. Feng, A. Saeki, S. Seki, A. Nagai and D. Jiang, *Chemical Communications*, 2012, **48**, 8952.
- [19] X. Feng, L. Liu, Y. Honsho, A. Saeki, S. Seki, S. Irle, Y. Dong, A. Nagai and D. Jiang, *Angewandte Chemie International Edition*, 2012, **51**, 2618–2622.
- [20] L. Pan, M.-Y. Xu, L.-J. Feng, Q. Chen, Y.-J. He and B.-H. Han, *Polymer Chemistry*, 2016, **7**, 2299–2307.
- [21] K. Venkata Rao, R. Haldar, T. K. Maji and S. J. George, *Physical Chemistry Chemical Physics*, 2016, **18**, 156–163.
-

- 
- [22] S. Dalapati, E. Jin, M. Addicoat, T. Heine and D. Jiang, *Journal of the American Chemical Society*, 2016, **138**, 5797–5800.
- [23] Y. Jiao, F. H. Stillinger and S. Torquato, *Physical Review Letters*, 2008, **100**, 245504.
- [24] Y. Jiao, F. H. Stillinger and S. Torquato, *Physical Review E*, 2009, **79**, 041309.
- [25] R. G. D. Taylor, C. G. Bezzu, M. Carta, K. J. Msayib, J. Walker, R. Short, B. M. Kariuki and N. B. McKeown, *Chemistry - A European Journal*, 2016, **22**, 2466–2472.
- [26] K. S. W. Sing, D. H. Everett, R. A. W. Haul, L. Moscou, R. A. Pierotti, J. Rouquerol and T. Siemieniewska, in *Reporting Physisorption Data for Gas/Solid Systems*, American Cancer Society, 2008, ch. 3.3.1, pp. 1217–1230.
- [27] B. Behera and P. Hari, in *Woven Textile Structure*, ed. B. Behera and P. Hari, Woodhead Publishing, 2010, pp. 413 – 435.
- [28] M. E. Davis, *Industrial & Engineering Chemistry Research*, 1991, **30**, 1675–1683.
- [29] J. Weitkamp, *Solid State Ionics*, 2000, **131**, 175–188.
- [30] R. Xu, W. Pang, J. Yu, Q. Huo and J. Chen, *Chemistry of Zeolites and Related Porous materials: Synthesis and Structure*, John Wiley & Sons (Asia) Pte Ltd, 2007.
- [31] J. L. Rowsell and O. M. Yaghi, *Microporous and Mesoporous Materials*, 2004, **73**, 3–14.
- [32] A. P. Cote, A. I. Benin, N. W. Ockwig, M. O’Keefe, A. J. Matzger and O. M. Yaghi, *Science*, 2005, **310**, 1166–1170.
- [33] N. B. McKeown and P. M. Budd, *Chemical Society Reviews*, 2006, **35**, 675.
-

- 
- [34] A. I. Cooper, *Advanced Materials*, 2009, **21**, 1291–1295.
- [35] P. Katekomol, J. Roeser, M. Bojdys, J. Weber and A. Thomas, *Chemistry of Materials*, 2013, **25**, 1542–1548.
- [36] T. Tozawa, J. T. A. Jones, S. I. Swamy, S. Jiang, D. J. Adams, S. Shakespeare, R. Clowes, D. Bradshaw, T. Hasell, S. Y. Chong and et al., *Nature Materials*, 2009, **8**, 973–978.
- [37] J. R. Holst, A. Trewin and A. I. Cooper, *Nature Chemistry*, 2010, **2**, 915 EP –.
- [38] M. E. Davis and R. F. Lobo, *Chemistry of Materials*, 1992, **4**, 756–768.
- [39] H. Li, M. Eddaoudi, M. O’Keeffe and O. M. Yaghi, *Nature*, 1999, **402**, 276 EP –.
- [40] J. R. Long and O. M. Yaghi, *Chemical Society Reviews*, 2009, **38**, 1213.
- [41] Z. Hao, X. Song, M. Zhu, X. Meng, S. Zhao, S. Su, W. Yang, S. Song and H. Zhang, *Journal of Materials Chemistry A*, 2013, **1**, 11043.
- [42] M. Zhao, Y. Huang, Y. Peng, Z. Huang, Q. Ma and H. Zhang, *Chemical Society Reviews*, 2018, **47**, 6267–6295.
- [43] O. M. Yaghi, M. O’Keeffe, N. W. Ockwig, H. K. Chae, M. Eddaoudi and J. Kim, *Nature*, 2003, **423**, 705 EP –.
- [44] M. Eddaoudi, J. Kim, J. B. Wachter, H. K. Chae, M. O’Keeffe and O. M. Yaghi, *Journal of the American Chemical Society*, 2001, **123**, 4368–4369.
- [45] H. Furukawa, N. Ko, Y. B. Go, N. Aratani, S. B. Choi, E. Choi, A. Ö. Yazaydin, R. Q. Snurr, M. O’Keeffe, J. Kim and O. M. Yaghi, *Science*, 2010, **329**, 424–428.
- [46] B. F. Hoskins and R. Robson, *Journal of the American Chemical Society*, 1990, **112**, 1546–1554.
-

- 
- [47] M. Fujita, Y. J. Kwon, S. Washizu and K. Ogura, *Journal of the American Chemical Society*, 1994, **116**, 1151–1152.
- [48] N. L. Rosi, J. Eckert, M. Eddaoudi, D. T. Vodak, J. Kim, M. O’Keeffe and O. M. Yaghi, *Science*, 2003, **300**, 1127–1129.
- [49] L. E. Kreno, K. Leong, O. K. Farha, M. Allendorf, R. P. Van Duyne and J. T. Hupp, *Chemical Reviews*, 2012, **112**, 1105–1125.
- [50] Y. Zhang, S. Yuan, G. Day, X. Wang, X. Yang and H.-C. Zhou, *Coordination Chemistry Reviews*, 2018, **354**, 28 – 45.
- [51] R. Ramachandran, W. Xuan, C. Zhao, X. Leng, D. Sun, D. Luo and F. Wang, *RSC Advances*, 2018, **8**, 3462–3469.
- [52] G. Xu, P. Nie, H. Dou, B. Ding, L. Li and X. Zhang, *Materials Today*, 2017, **20**, 191 – 209.
- [53] B. Chen, Z. Yang, Y. Zhu and Y. Xia, *J. Mater. Chem. A*, 2014, **2**, 16811–16831.
- [54] J.-R. Li, R. J. Kuppler and H.-C. Zhou, *Chemical Society Reviews*, 2009, **38**, 1477.
- [55] N. Jusoh, Y. F. Yeong, K. K. Lau and A. M. Shariff, *Procedia Engineering*, 2016, **148**, 1259 – 1265.
- [56] Y.-X. Tan, F. Wang and J. Zhang, *Chemical Society Reviews*, 2018, **47**, 2130–2144.
- [57] Z. Chang, D.-S. Zhang, Q. Chen and X.-H. Bu, *Phys. Chem. Chem. Phys.*, 2013, **15**, 5430–5442.
- [58] A. G. Slater and A. I. Cooper, *Science*, 2015, **348**, aaa8075–aaa8075.
- [59] S. Das, P. Heasman, T. Ben and S. Qiu, *Chemical Reviews*, 2017, **117**, 1515–1563.
-

- [60] H. M. El-Kaderi, J. R. Hunt, J. L. Mendoza-Cortés, A. P. Côté, R. E. Taylor, M. O’Keeffe and O. M. Yaghi, *Science*, 2007, **316**, 268–272.
- [61] A. P. Côté, H. M. El-Kaderi, H. Furukawa, J. R. Hunt and O. M. Yaghi, *Journal of the American Chemical Society*, 2007, **129**, 12914–12915.
- [62] F. J. Uribe-Romo, J. R. Hunt, H. Furukawa, C. Klöck, M. O’Keeffe and O. M. Yaghi, *Journal of the American Chemical Society*, 2009, **131**, 4570–4571.
- [63] G. Lin, H. Ding, D. Yuan, B. Wang and C. Wang, *Journal of the American Chemical Society*, 2016, **138**, 3302–3305.
- [64] H.-S. Xu, S.-Y. Ding, W.-K. An, H. Wu and W. Wang, *Journal of the American Chemical Society*, 2016, **138**, 11489–11492.
- [65] X. Han, Q. Xia, J. Huang, Y. Liu, C. Tan and Y. Cui, *Journal of the American Chemical Society*, 2017, **139**, 8693–8697.
- [66] X. Han, J. Huang, C. Yuan, Y. Liu and Y. Cui, *Journal of the American Chemical Society*, 2018, **140**, 892–895.
- [67] X. Han, J. Zhang, J. Huang, X. Wu, D. Yuan, Y. Liu and Y. Cui, *Nature Communications*, 2018, **9**, 1–10.
- [68] S. B. Alahakoon, C. M. Thompson, G. Occhialini and R. A. Smaldone, *ChemSusChem*, 2017, **10**, 2116–2129.
- [69] J. Germain, J. M. J. Fréchet and F. Svec, *Journal of Materials Chemistry*, 2007, **17**, 4989.
- [70] V. A. Davankov, S. V. Rogoshin and M. P. Tsyurupa, *Journal of Polymer Science: Polymer Symposia*, 1974, **47**, 95–101.
- [71] V. A. Davankov, M. M. Ilyin, M. P. Tsyurupa, G. I. Timofeeva and L. V. Dubrovina, *Macromolecules*, 1996, **29**, 8398–8403.

- 
- [72] R. Joseph, W. T. Ford, S. Zhang, M. P. Tsyurupa, A. V. Pastukhov and V. A. Davankov, *Journal of Polymer Science Part A: Polymer Chemistry*, 1997, **35**, 695–701.
- [73] L. Tan and B. Tan, *Chemical Society Reviews*, 2017, **46**, 3322–3356.
- [74] F. Maya and F. Svec, *Polymer*, 2014, **55**, 340 – 346.
- [75] B. Gadwdzik and J. Osypiuk, *Chromatographia*, 2001, **54**, 323–328.
- [76] J. Hradil and E. Králová, *Polymer*, 1998, **39**, 6041 – 6048.
- [77] P. Veverka and K. Jeřábek, *Reactive and Functional Polymers*, 1999, **41**, 21 – 25.
- [78] J.-H. Ahn, J.-E. Jang, C.-G. Oh, S.-K. Ihm, J. Cortez and D. C. Sherrington, *Macromolecules*, 2006, **39**, 627–632.
- [79] H. Li and H. Zhou, *Chem. Commun.*, 2012, **48**, 1201–1217.
- [80] B. Li, X. Huang, R. Gong, M. Ma, X. Yang, L. Liang and B. Tan, *International Journal of Hydrogen Energy*, 2012, **37**, 12813 – 12820.
- [81] J. Zhang, Z.-A. Qiao, S. M. Mahurin, X. Jiang, S.-H. Chai, H. Lu, K. Nelson and S. Dai, *Angewandte Chemie International Edition*, 2015, **54**, 4582–4586.
- [82] B. Li, R. Gong, W. Wang, X. Huang, W. Zhang, H. Li, C. Hu and B. Tan, *Macromolecules*, 2011, **44**, 2410–2414.
- [83] Y. Luo, B. Li, W. Wang, K. Wu and B. Tan, *Advanced Materials*, 2012, **24**, 5703–5707.
- [84] M. Saleh, H. M. Lee, K. C. Kemp and K. S. Kim, *ACS Applied Materials & Interfaces*, 2014, **6**, 7325–7333.
-

- [85] X. Zhu, S. M. Mahurin, S.-H. An, C.-L. Do-Thanh, C. Tian, Y. Li, L. W. Gill, E. W. Hagaman, Z. Bian, J.-H. Zhou, J. Hu, H. Liu and S. Dai, *Chem. Commun.*, 2014, **50**, 7933–7936.
- [86] T.-L. Zhai, L. Tan, Y. Luo, J.-M. Liu, B. Tan, X.-L. Yang, H.-B. Xu and C. Zhang, *Chemistry – An Asian Journal*, 2016, **11**, 294–298.
- [87] X. Yang, M. Yu, Y. Zhao, C. Zhang, X. Wang and J.-X. Jiang, *RSC Adv.*, 2014, **4**, 61051–61055.
- [88] S. Bhunia, B. Banerjee and A. Bhaumik, *Chem. Commun.*, 2015, **51**, 5020–5023.
- [89] J. Song, N. Du, Y. Dai, G. P. Robertson, M. D. Guiver, S. Thomas and I. Pinnau, *Macromolecules*, 2008, **41**, 7411–7417.
- [90] N. Du, J. Song, G. P. Robertson, I. Pinnau and M. D. Guiver, *Macromolecular Rapid Communications*, 2008, **29**, 783–788.
- [91] I. I. Ponomarev, I. V. Blagodatskikh, A. V. Muranov, Y. A. Volkova, D. Y. Razorenov, I. I. Ponomarev and K. M. Skupov, *Mendeleev Communications*, 2016, **26**, 362–364.
- [92] P. M. Budd, B. S. Ghanem, S. Makhseed, N. B. McKeown, K. J. Msayib and C. E. Tattershall, *Chem. Commun.*, 2004, 230–231.
- [93] P. Budd, E. Elabas, B. Ghanem, S. Makhseed, N. McKeown, K. Msayib, C. Tattershall and D. Wang, *Advanced Materials*, 2004, **16**, 456–459.
- [94] M. Carta, K. J. Msayib, P. M. Budd and N. B. McKeown, *Organic Letters*, 2008, **10**, 2641–2643.
- [95] N. B. McKeown, *Science China Chemistry*, 2017, **60**, 1023–1032.
- [96] N. A. Rakow, M. S. Wendland, J. E. Trend, R. J. Poirier, D. M. Paolucci, S. P. Maki, C. S. Lyons and M. J. Swierczek, *Langmuir*, 2010, **26**, 3767–3770.

- [97] Y. Wang, N. B. McKeown, K. J. Msayib, G. A. Turnbull and I. D. W. Samuel, *Sensors*, 2011, **11**, 2478–2487.
- [98] P. M. Budd, N. B. McKeown, B. S. Ghanem, K. J. Msayib, D. Fritsch, L. Staranikova, N. Belov, O. Sanfirova, Y. Yampolskii and V. Shantarovich, *Journal of Membrane Science*, 2008, **325**, 851 – 860.
- [99] E. Madrid, Y. Rong, M. Carta, N. B. McKeown, R. Malpass-Evans, G. A. Attard, T. J. Clarke, S. H. Taylor, Y.-T. Long and F. Marken, *Angewandte Chemie International Edition*, 2014, **53**, 10751–10754.
- [100] Z. Yang, R. Guo, R. Malpass-Evans, M. Carta, N. B. McKeown, M. D. Guiver, L. Wu and T. Xu, *Angewandte Chemie International Edition*, 2016, **55**, 11499–11502.
- [101] J. D. Evans, D. M. Huang, M. R. Hill, C. J. Sumby, A. W. Thornton and C. J. Doonan, *The Journal of Physical Chemistry C*, 2014, **118**, 1523–1529.
- [102] J. L. Flippen, J. Karle and I. L. Karle, *Journal of the American Chemical Society*, 1970, **92**, 3749–3755.
- [103] J. J. Lee, R. O. Fuller, A. N. Sobolev, H. F. Clausen, J. Overgaard, G. A. Koutsantonis, B. B. Iversen and M. A. Spackman, *Chem. Commun.*, 2011, **47**, 2029–2031.
- [104] T. Hasell and A. I. Cooper, *Nature Reviews Materials*, 2016, **1**, 16053 EP –.
- [105] S. Jiang, J. T. A. Jones, T. Hasell, C. E. Blythe, D. J. Adams, A. Trewin and A. I. Cooper, *Nature Communications*, 2011, **2**, 207 EP –.
- [106] P. J. Stang and B. Olenyuk, *Accounts of Chemical Research*, 1997, **30**, 502–518.
- [107] M. Fujita, M. Tominaga, A. Hori and B. Therrien, *Accounts of Chemical Research*, 2005, **38**, 369–378.



- 
- [108] X. Liu, Y. Liu, G. Li and R. Warmuth, *Angewandte Chemie*, 2006, **118**, 915–918.
- [109] M. Mastalerz, *Chem. Commun.*, 2008, 4756–4758.
- [110] T. Hasell, X. Wu, J. T. A. Jones, J. Bacsá, A. Steiner, T. Mitra, A. Trewin, D. J. Adams and A. I. Cooper, *Nature Chemistry*, 2010, **2**, 750 EP –.
- [111] M. Mastalerz and I. M. Oppel, *Angewandte Chemie International Edition*, 2012, **51**, 5252–5255.
- [112] A. Suzuki, *Chem. Commun.*, 2005, 4759–4763.
- [113] A. Suzuki, *Angewandte Chemie International Edition*, 2011, **50**, 6722–6737.
- [114] S. H. Chen, R. F. Horvath, J. Joglar, M. J. Fisher and S. J. Danishefsky, *The Journal of Organic Chemistry*, 1991, **56**, 5834–5845.
- [115] J. Langecker and M. Rehahn, *Macromolecular Chemistry and Physics*, 2008, **209**, 258–271.
- [116] R. Chinchilla and C. Nájera, *Chemical Society Reviews*, 2011, **40**, 5084.
- [117] J.-X. Jiang, F. Su, A. Trewin, C. Wood, N. Campbell, H. Niu, C. Dickinson, A. Ganin, M. Rosseinsky, Y. Khimyak and et al., *Angewandte Chemie International Edition*, 2007, **46**, 8574–8578.
- [118] J.-X. Jiang, F. Su, A. Trewin, C. Wood, H. Niu, J. T. A. Jones, Y. Z. Khimyak and A. I. Cooper, *J. Am. Chem. Soc.*, 2008, **130**, 7710–7720.
- [119] T. Hasell, C. D. Wood, R. Clowes, J. T. A. Jones, Y. Z. Khimyak, D. J. Adams and A. I. Cooper, *Chemistry of Materials*, 2010, **22**, 557–564.
- [120] E. Stöckel, X. Wu, A. Trewin, C. D. Wood, R. Clowes, N. L. Campbell, J. T. Jones, Y. Z. Khimyak, D. J. Adams and A. I. Cooper, *Chem. Commun.*, 2009, 212–214.
-

- 
- [121] R. Dawson, A. Laybourn, Y. Z. Khimyak, D. J. Adams and A. I. Cooper, *Macromolecules*, 2010, **43**, 8524–8530.
- [122] P. Kuhn, A. Thomas and M. Antonietti, *Macromolecules*, 2009, **42**, 319–326.
- [123] Y. Kou, Y. Xu, Z. Guo and D. Jiang, *Angewandte Chemie International Edition*, 2011, **50**, 8753–8757.
- [124] J.-X. Jiang, A. Trewin, D. J. Adams and A. I. Cooper, *Chem. Sci.*, 2011, **2**, 1777–1781.
- [125] Y. Liao, Z. Cheng, W. Zuo, A. Thomas and C. F. J. Faul, *ACS Applied Materials & Interfaces*, 2017, **9**, 38390–38400.
- [126] Y.-B. Zhou, Y.-Q. Wang, L.-C. Ning, Z.-C. Ding, W.-L. Wang, C.-K. Ding, R.-H. Li, J.-J. Chen, X. Lu, Y.-J. Ding and Z.-P. Zhan, *Journal of the American Chemical Society*, 2017, **139**, 3966–3969.
- [127] R. S. Sprick, B. Bonillo, M. Sachs, R. Clowes, J. R. Durrant, D. J. Adams and A. I. Cooper, *Chem. Commun.*, 2016, **52**, 10008–10011.
- [128] C. Su, R. Tandiana, B. Tian, A. Sengupta, W. Tang, J. Su and K. P. Loh, *ACS Catalysis*, 2016, **6**, 3594–3599.
- [129] X.-C. Li, Y. Zhang, C.-Y. Wang, Y. Wan, W.-Y. Lai, H. Pang and W. Huang, *Chem. Sci.*, 2017, **8**, 2959–2965.
- [130] P. Kuhn, M. Antonietti and A. Thomas, *Angewandte Chemie International Edition*, 2008, **47**, 3450–3453.
- [131] P. Kuhn, A. Forget, D. Su, A. Thomas and M. Antonietti, *Journal of the American Chemical Society*, 2008, **130**, 13333–13337.
- [132] M. J. Bojdys, J. Jeromenok, A. Thomas and M. Antonietti, *Advanced Materials*, 2010, **22**, 2202–2205.
-

- [133] S. Ren, M. J. Bojdys, R. Dawson, A. Laybourn, Y. Z. Khimyak, D. J. Adams and A. I. Cooper, *Advanced Materials*, 2012, **24**, 2357–2361.
- [134] A. Ranganathan, B. C. Heisen, I. Dix and F. Meyer, *Chem. Commun.*, 2007, 3637–3639.
- [135] X. Zhu, C. Tian, S. M. Mahurin, S.-H. Chai, C. Wang, S. Brown, G. M. Veith, H. Luo, H. Liu and S. Dai, *Journal of the American Chemical Society*, 2012, **134**, 10478–10484.
- [136] X. Zhu, S. Chai, C. Tian, P. F. Fulvio, K. S. Han, E. W. Hagaman, G. M. Veith, S. M. Mahurin, S. Brown, H. Liu and S. Dai, *Macromolecular Rapid Communications*, 2013, **34**, 452–459.
- [137] A. Herrera, A. Riaño, R. Moreno, B. Caso, Z. D. Pardo, I. Fernández, E. Sáez, D. Molero, A. Sánchez-Vázquez and R. Martínez-Alvarez, *The Journal of Organic Chemistry*, 2014, **79**, 7012–7024.
- [138] S. Ren, R. Dawson, A. Laybourn, J.-x. Jiang, Y. Khimyak, D. J. Adams and A. I. Cooper, *Polymer Chemistry*, 2012, **3**, 928.
- [139] T. Ben, H. Ren, S. Ma, D. Cao, J. Lan, X. Jing, W. Wang, J. Xu, F. Deng, J. Simmons and et al., *Angewandte Chemie International Edition*, 2009, **48**, 9457–9460.
- [140] A. Trewin and A. Cooper, *Angewandte Chemie International Edition*, 2010, **49**, 1533–1535.
- [141] T. Ben, C. Pei, D. Zhang, J. Xu, F. Deng, X. Jing and S. Qiu, *Energy Environ. Sci.*, 2011, **4**, 3991–3999.
- [142] D. Yuan, W. Lu, D. Zhao and H.-C. Zhou, *Advanced Materials*, 2011, **23**, 3723–3725.

- 
- [143] H. Ren, T. Ben, F. Sun, M. Guo, X. Jing, H. Ma, K. Cai, S. Qiu and G. Zhu, *J. Mater. Chem.*, 2011, **21**, 10348–10353.
- [144] H. Ren, T. Ben, E. Wang, X. Jing, M. Xue, B. Liu, Y. Cui, S. Qiu and G. Zhu, *Chem. Commun.*, 2010, **46**, 291–293.
- [145] Y. Yuan, F. Sun, H. Ren, X. Jing, W. Wang, H. Ma, H. Zhao and G. Zhu, *J. Mater. Chem.*, 2011, **21**, 13498–13502.
- [146] Y. Peng, T. Ben, J. Xu, M. Xue, X. Jing, F. Deng, S. Qiu and G. Zhu, *Dalton Trans.*, 2011, **40**, 2720–2724.
- [147] T. Ben, K. Shi, Y. Cui, C. Pei, Y. Zuo, H. Guo, D. Zhang, J. Xu, F. Deng, Z. Tian and S. Qiu, *J. Mater. Chem.*, 2011, **21**, 18208–18214.
- [148] Z. Zhao, S. Das, G. Xing, P. Fayon, P. Heasman, M. Jay, S. Bailey, C. Lambert, H. Yamada, T. Wakihara and et al., *Angewandte Chemie International Edition*, 2018, **57**, 11952–11956.
- [149] V. A. Harmandaris, N. P. Adhikari, N. F. A. van der Vegt and K. Kremer, *Macromolecules*, 2006, **39**, 6708–6719.
- [150] J. P. Dürholt, R. Galvelis and R. Schmid, *Dalton Trans.*, 2016, **45**, 4370–4379.
- [151] E. Runge and E. K. U. Gross, *Phys. Rev. Lett.*, 1984, **52**, 997–1000.
- [152] R. Car and M. Parrinello, *Phys. Rev. Lett.*, 1985, **55**, 2471–2474.
- [153] H. Sun, *The Journal of Physical Chemistry B*, 1998, **102**, 7338–7364.
- [154] H. Sun, *Macromolecules*, 1995, **28**, 701–712.
- [155] Y. Xu, S. Jin, H. Xu, A. Nagai and D. Jiang, *Chemical Society Reviews*, 2013, **42**, 8012.
- [156] C. E. Wilmer, M. Leaf, C. Y. Lee, O. K. Farha, B. G. Hauser, J. T. Hupp and R. Q. Snurr, *Nature Chemistry*, 2011, **4**, 83 EP –.
-

- 
- [157] Y. J. Colón and R. Q. Snurr, *Chem. Soc. Rev.*, 2014, **43**, 5735–5749.
- [158] M. Miklitz, S. Jiang, R. Clowes, M. E. Briggs, A. I. Cooper and K. E. Jelfs, *The Journal of Physical Chemistry C*, 2017, **121**, 15211–15222.
- [159] L. Chen, P. S. Reiss, S. Y. Chong, D. Holden, K. E. Jelfs, T. Hasell, M. A. Little, A. Kewley, M. E. Briggs, A. Stephenson, K. M. Thomas, J. A. Armstrong, J. Bell, J. Busto, R. Noel, J. Liu, D. M. Strachan, P. K. Thallapally and A. I. Cooper, *Nature Materials*, 2014, **13**, 954 EP –.
- [160] R. S. Patil, D. Banerjee, C. M. Simon, J. L. Atwood and P. K. Thallapally, *Chemistry – A European Journal*, 2016, **22**, 12618–12623.
- [161] O. D. Friedrichs, A. W. M. Dress, D. H. Huson, J. Klinowski and A. L. Mackay, *Nature*, 1999, **400**, 644–647.
- [162] C. M. Draznieks, J. M. Newsam, A. M. Gorman, C. M. Freeman and G. Ferey, *Angewandte Chemie International Edition*, 2000, **39**, 2270–2275.
- [163] T. Düren, L. Sarkisov, O. M. Yaghi and R. Q. Snurr, *Langmuir*, 2004, **20**, 2683–2689.
- [164] R. Q. Snurr, J. T. Hupp and S. T. Nguyen, *AIChE Journal*, 2004, **50**, 1090–1095.
- [165] O. K. Farha and J. T. Hupp, *Accounts of Chemical Research*, 2010, **43**, 1166–1175.
- [166] K. T. Butler, J. M. Frost, J. M. Skelton, K. L. Svane and A. Walsh, *Chem. Soc. Rev.*, 2016, **45**, 6138–6146.
- [167] G. M. Day, W. D. S. Motherwell and W. Jones, *Phys. Chem. Chem. Phys.*, 2007, **9**, 1693–1704.
- [168] M. Baias, J.-N. Dumez, P. H. Svensson, S. Schantz, G. M. Day and L. Emsley, *Journal of the American Chemical Society*, 2013, **135**, 17501–17507.
-

- 
- [169] A. B. Fredj and G. M. Day, *Journal of Molecular Modeling*, 2015, **21**, 211.
- [170] M. Eddaoudi, J. Kim, N. Rosi, D. Vodak, J. Wachter, M. O’Keeffe and O. M. Yaghi, *Science*, 2002, **295**, 469–472.
- [171] A. G. Slater, M. A. Little, A. Pulido, S. Y. Chong, D. Holden, L. Chen, C. Morgan, X. Wu, G. Cheng, R. Clowes, M. E. Briggs, T. Hasell, K. E. Jelfs, G. M. Day and A. I. Cooper, *Nature Chemistry*, 2016, **9**, 17 EP –.
- [172] A. Pulido, L. Chen, T. Kaczorowski, D. Holden, M. A. Little, S. Y. Chong, B. J. Slater, D. P. McMahon, B. Bonillo, C. J. Stackhouse, A. Stephenson, C. M. Kane, R. Clowes, T. Hasell, A. I. Cooper and G. M. Day, *Nature*, 2017, **543**, 657 EP –.
- [173] A. Trewin, *CrystEngComm*, 2010, **12**, 2315–2317.
- [174] A. S. Inc., *Materials Studio 5.0*.
- [175] J.-X. Jiang, A. Trewin, F. Su, C. D. Wood, H. Niu, J. T. A. Jones, Y. Z. Khimyak and A. I. Cooper, *Macromolecules*, 2009, **42**, 2658–2666.
- [176] C. Reece, D. J. Willock and A. Trewin, *Phys. Chem. Chem. Phys.*, 2015, **17**, 817–823.
- [177] M. A. Zwijnenburg, G. Cheng, T. O. McDonald, K. E. Jelfs, J.-X. Jiang, S. Ren, T. Hasell, F. Blanc, A. I. Cooper and D. J. Adams, *Macromolecules*, 2013, **46**, 7696–7704.
- [178] L. J. Abbott and C. M. Colina, *Polymatic: A Simulated Polymerization Algorithm*, <https://nanohub.org/resources/17278>, 2013.
- [179] L. J. Abbott, K. E. Hart and C. M. Colina, *Theoretical Chemistry Accounts*, 2013, **132**, 1334.
- [180] J. M. H. Thomas and A. Trewin, *The Journal of Physical Chemistry C*, 2014, **118**, 19712–19722.
-

- 
- [181] P. Fayon and A. Trewin, *Phys. Chem. Chem. Phys.*, 2016, **18**, 16840–16847.
- [182] T. Yamamoto, A. Morita, Y. Miyazaki, T. Maruyama, H. Wakayama, Z. H. Zhou, Y. Nakamura, T. Kanbara, S. Sasaki and K. Kubota, *Macromolecules*, 1992, **25**, 1214–1223.
- [183] M. D. Donohue and G. L. Aranovich, *Advances in Colloid and Interface Science*, 1998, **76-77**, 137–152.
- [184] I. Langmuir, *Journal of the American Chemical Society*, 1916, **38**, 2221–2295.
- [185] S. Brunauer, P. H. Emmett and E. Teller, *Journal of the American Chemical Society*, 1938, **60**, 309–319.
- [186] A. I. Skoulidas and D. S. Sholl, *The Journal of Physical Chemistry B*, 2001, **105**, 3151–3154.
- [187] A. I. Skoulidas and D. S. Sholl, *The Journal of Physical Chemistry B*, 2002, **106**, 5058–5067.
- [188] A. I. Skoulidas and D. S. Sholl, *The Journal of Physical Chemistry A*, 2003, **107**, 10132–10141.
- [189] G. G. Emch, *Journal of Mathematical Physics*, 1973, **14**, 1775–1783.
- [190] O. J. Eder, *The Journal of Chemical Physics*, 1977, **66**, 3866–3870.
- [191] L. E. Smart, *Solid State Chemistry: An Introduction*, CRC Press, 2nd edn., 2005.
- [192] A. R. West, *Basic Solid State Chemistry*, John Wiley & Sons, 2nd edn., 1999.
- [193] P. Barnes, S. Jacques and M. Vickers, *Advanced Certificate in Powder Diffraction on the Web*, <http://pd.chem.ucl.ac.uk/pdnn/diff2/kinemat2.htm>.
- [194] B. Jeziorski, R. Moszynski and K. Szalewicz, *Chemical Reviews*, 1994, **94**, 1887–1930.
-

- 
- [195] F. Jensen, *Introduction to Computational Chemistry*, Wiley, 2013.
- [196] L. Verlet, *Phys. Rev.*, 1967, **159**, 98–103.
- [197] R. Hockney, *Potential Calculations and Some Applications*, 1970.
- [198] N. S. Martys and R. D. Mountain, *Phys. Rev. E*, 1999, **59**, 3733–3736.
- [199] H. J. C. Berendsen, J. P. M. Postma, W. F. van Gunsteren, A. DiNola and J. R. Haak, *The Journal of Chemical Physics*, 1984, **81**, 3684–3690.
- [200] W. G. Hoover, *Phys. Rev. A*, 1985, **31**, 1695–1697.
- [201] M. L. Connolly, *Journal of Applied Crystallography*, 1983, **16**, 548–558.
- [202] M. Connolly, *Journal of Molecular Graphics*, 1993, **11**, 139–141.
- [203] HOOMD-Blue, <http://glotzerlab.engin.umich.edu/hoomd-blue/>.
- [204] W. Smith, C. Yong and P. Rodger, *Molecular Simulation*, 2002, **28**, 385–471.
- [205] I. T. Todorov, W. Smith, K. Trachenko and M. T. Dove, *J. Mater. Chem.*, 2006, **16**, 1911–1918.
- [206] T. D. Nguyen, C. L. Phillips, J. A. Anderson and S. C. Glotzer, *Computer Physics Communications*, 2011, **182**, 2307 – 2313.
- [207] Q. He, C. Zhang, X. Li, X. Wang, P. Mu and J.-X. Jiang, *Acta Chimica Sinica*, 2018, **76**, 202–208.
- [208] L. J. Abbott and C. M. Colina, *Journal of Chemical & Engineering Data*, 2014, **59**, 3177–3182.
- [209] R. Dawson, A. Laybourn, Y. Z. Khimyak, D. J. Adams and A. I. Cooper, *Macromolecules*, 2010, **43**, 8524–8530.
- [210] D. Thoelmann and H. F. Gruetzmacher, *Journal of the American Chemical Society*, 1991, **113**, 3281–3287.
-



- [211] M. D'Abramo, M. Aschi and A. Amadei, *The Journal of Chemical Physics*, 2014, **140**, 164104.
- [212] C. Zhang, Y. Qiao, P. Xiong, W. Ma, P. Bai, X. Wang, Q. Li, J. Zhao, Y. Xu, Y. Chen, J. H. Zeng, F. Wang, Y. Xu and J.-X. Jiang, *ACS Nano*, 2019, **13**, 745–754.
- [213] H. W. Kroto, J. R. Heath, S. C. O'Brien, R. F. Curl and R. E. Smalley, *Nature*, 1985, **318**, 162–163.
- [214] J. M. Tarascon and M. Armand, *Nature*, 2001, **414**, 359 EP –.
- [215] P. Bruce, B. Scrosati and J.-M. Tarascon, *Angewandte Chemie International Edition*, 2008, **47**, 2930–2946.
- [216] H. Wang, Z. Lu, D. Qian, Y. Li and W. Zhang, *Nanotechnology*, 2007, **18**, 115616.
- [217] Y.-M. Lin, P. R. Abel, A. Heller and C. B. Mullins, *The Journal of Physical Chemistry Letters*, 2011, **2**, 2885–2891.
- [218] Z. Bai, N. Fan, C. Sun, Z. Ju, C. Guo, J. Yang and Y. Qian, *Nanoscale*, 2013, **5**, 2442–2447.
- [219] T. Yang, Y. Liu, Z. Huang, Q. Yang, M. Guan, M. Fang and X. Wu, *RSC Adv.*, 2015, **5**, 24486–24493.
- [220] K. Park, J. H. Cho, J.-H. Jang, B.-C. Yu, A. T. De La Hoz, K. M. Miller, C. J. Ellison and J. B. Goodenough, *Energy Environ. Sci.*, 2015, **8**, 2389–2395.
- [221] Y. Feng, X.-Y. Yu and U. Paik, *Chem. Commun.*, 2016, **52**, 6269–6272.
- [222] A. V. Bazilevsky, A. L. Yarin and C. M. Megaridis, *Langmuir*, 2007, **23**, 2311–2314.
- [223] G. Eglinton and A. R. Galbraith, *J. Chem. Soc.*, 1959, 889–896.

- 
- [224] J. M. H. Thomas and A. Trewin, *The Journal of Physical Chemistry C*, 2014, **118**, 19712–19722.
- [225] H. G. Buss, S. Y. Chan, N. A. Lynd and B. D. McCloskey, *ACS Energy Letters*, 2017, **2**, 481–487.
- [226] Y. Wu, E. Rahm and R. Holze, *Journal of Power Sources*, 2003, **114**, 228 – 236.
- [227] P. Yu, B. N. Popov, J. A. Ritter and R. E. White, *Journal of The Electrochemical Society*, 1999, **146**, 1201–1217.
- [228] F. Moučka, M. Lísal and W. R. Smith, *The Journal of Physical Chemistry B*, 2012, **116**, 5468–5478.
- [229] R. Amemiya, K. Suwa, J. Toriyama, Y. Nishimura and M. Yamaguchi, *Journal of the American Chemical Society*, 2005, **127**, 8252–8253.
- [230] N. Miyaura, K. Yamada and A. Suzuki, *Tetrahedron Letters*, 1979, **20**, 3437 – 3440.
- [231] C. D. Wessells, S. V. Peddada, R. A. Huggins and Y. Cui, *Nano Letters*, 2011, **11**, 5421–5425.
- [232] M. D. Slater, D. Kim, E. Lee and C. S. Johnson, *Advanced Functional Materials*, 2012, **23**, 947–958.
- [233] S. Komaba, T. Hasegawa, M. Dahbi and K. Kubota, *Electrochemistry Communications*, 2015, **60**, 172–175.
- [234] R. J. Gummow, G. Vamvounis, M. B. Kannan and Y. He, *Advanced Materials*, 2018, **30**, 1801702.
- [235] A. Ponrouch and M. Palacin, *Current Opinion in Electrochemistry*, 2018, **9**, 1–7.
-

- [236] N. Singh, T. S. Arthur, C. Ling, M. Matsui and F. Mizuno, *Chem. Commun.*, 2013, **49**, 149–151.
- [237] Z. Yang, J. Zhang, M. C. W. Kintner-Meyer, X. Lu, D. Choi, J. P. Lemmon and J. Liu, *Chemical Reviews*, 2011, **111**, 3577–3613.
- [238] S. Li, J. Qiu, C. Lai, M. Ling, H. Zhao and S. Zhang, *Nano Energy*, 2015, **12**, 224 – 230.
- [239] L. Fan and B. Lu, *Small*, 2016, **12**, 2783–2791.
- [240] S. Vadahanambi, H.-H. Chun, K. H. Jung and H. Park, *RSC Adv.*, 2016, **6**, 38112–38116.
- [241] J. Xu, M. Wang, N. P. Wickramaratne, M. Jaroniec, S. Dou and L. Dai, *Advanced Materials*, 2015, **27**, 2042–2048.
- [242] H. Hou, C. E. Banks, M. Jing, Y. Zhang and X. Ji, *Advanced Materials*, 2015, **27**, 7861–7866.
- [243] B. Cao, H. Liu, B. Xu, Y. Lei, X. Chen and H. Song, *J. Mater. Chem. A*, 2016, **4**, 6472–6478.
- [244] C. Han, K. Han, X. Wang, C. Wang, Q. Li, J. Meng, X. Xu, Q. He, W. Luo, L. Wu and L. Mai, *Nanoscale*, 2018, **10**, 6820–6826.
- [245] Y. Chen, W. Luo, M. Carter, L. Zhou, J. Dai, K. Fu, S. Lacey, T. Li, J. Wan, X. Han, Y. Bao and L. Hu, *Nano Energy*, 2015, **18**, 205–211.
- [246] K. Lei, F. Li, C. Mu, J. Wang, Q. Zhao, C. Chen and J. Chen, *Energy Environ. Sci.*, 2017, **10**, 552–557.
- [247] R. C. Mass, E. Uchaker and G. Cao, *Science China Materials*, 2015, **58**, 715–766.

- 
- [248] Z. Lu, A. Schechter, M. Moshkovich and D. Aurbach, *Journal of Electroanalytical Chemistry*, 1999, **466**, 203 – 217.
- [249] P. Novák, R. Imhof and O. Haas, *Electrochimica Acta*, 1999, **45**, 351 – 367.
- [250] D. Aurbach, Z. Lu, A. Schechter, Y. Gofer, H. Gizbar, R. Turgeman, Y. Cohen, M. Moshkovich and E. Levi, *Nature*, 2000, **407**, 724 EP –.
- [251] T. Ichitsubo, T. Adachi, S. Yagi and T. Doi, *J. Mater. Chem.*, 2011, **21**, 11764–11772.
- [252] H. Tian, T. Gao, X. Li, X. Wang, C. Luo, X. Fan, C. Yang, L. Suo, Z. Ma, W. Han and C. Wang, *Nature Communications*, 2017, **8**, 14083 EP –.
- [253] Z. Zhao-Karger, M. E. Gil Bardaji, O. Fuhr and M. Fichtner, *J. Mater. Chem. A*, 2017, **5**, 10815–10820.
- [254] D. Aurbach, R. Skaletsky and Y. Gofer, *J. Electrochem. Soc.*, 1991, **138**, 3536–3545.
- [255] A. Ponrouch, C. Frontera, F. Bardé and M. R. Palacín, *Nature Materials*, 2015, **15**, 169–172.

*"No one will blame you for giving up. In fact, quitting at this point is a perfectly reasonable response."*

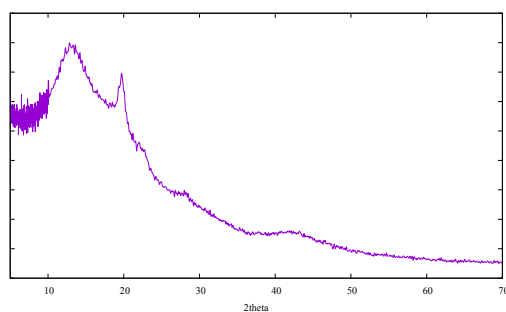
---

—GLaDOS

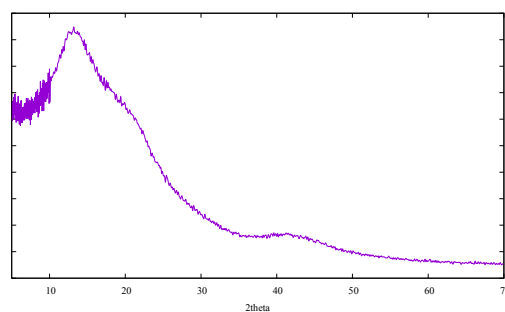
# Appendix A

## Appendix

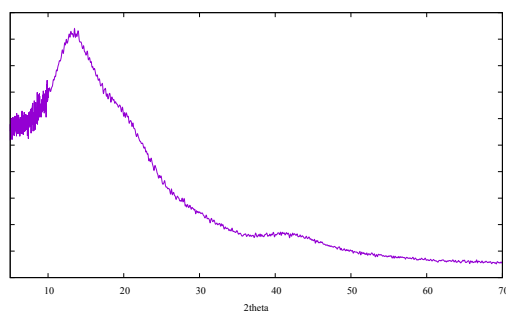
### A.1 Chapter: 3



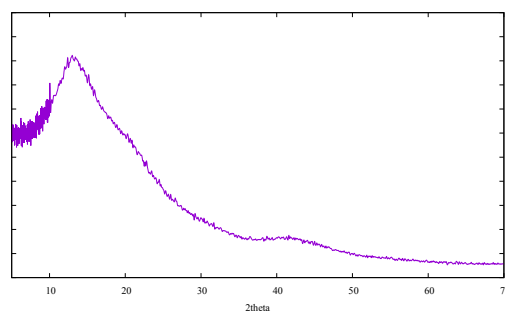
(a) S0



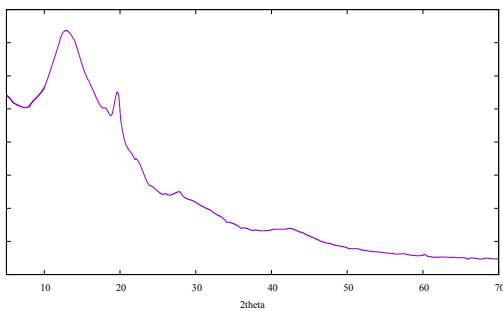
(b) S1



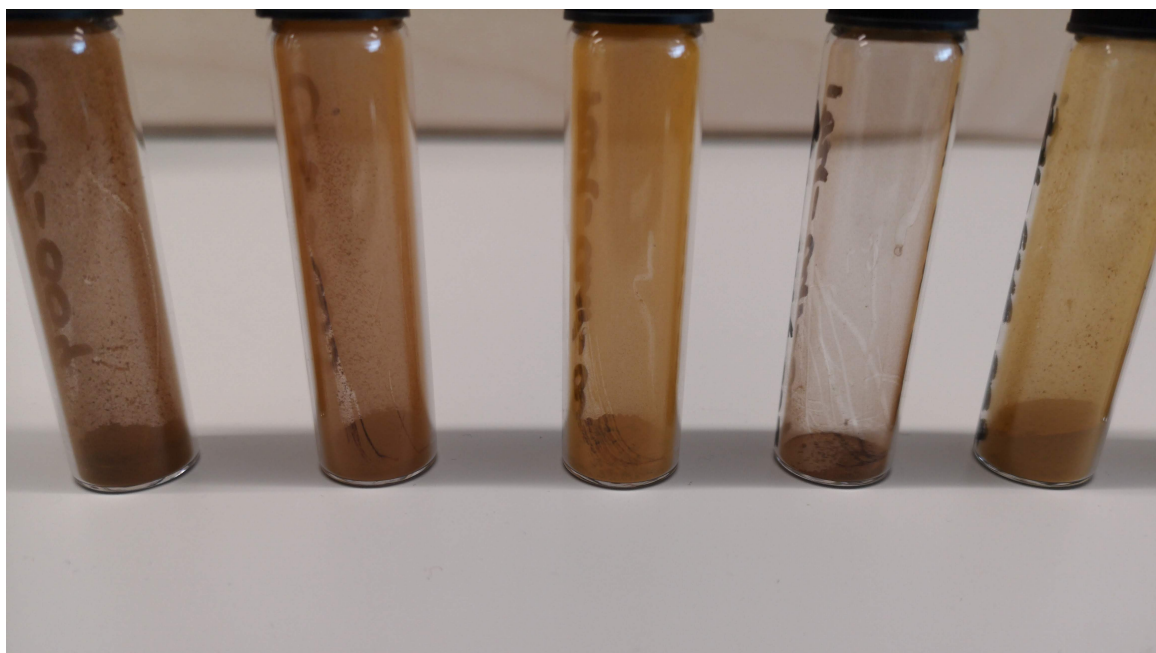
(c) S1



(d) S2



(e) S0

**Figure A.1:** Powder x-ray diffraction patterns of reactions (a) 4 to (e) 8.**Figure A.2:** Product material produced from reactions 4 to 8 (left to right).

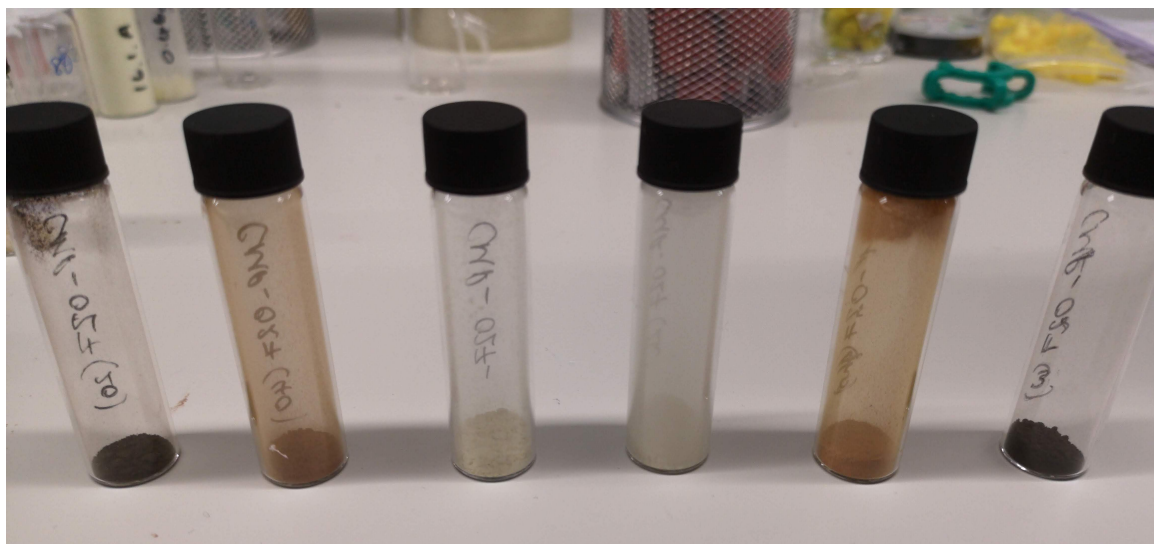


**Figure A.3:** The materials produced from reaction 11. From left to right: 20 minutes, 40 minutes, 60 minutes, 120 minutes, 240 minutes, and 7 days reaction products.

## A.2 Chapter: 4

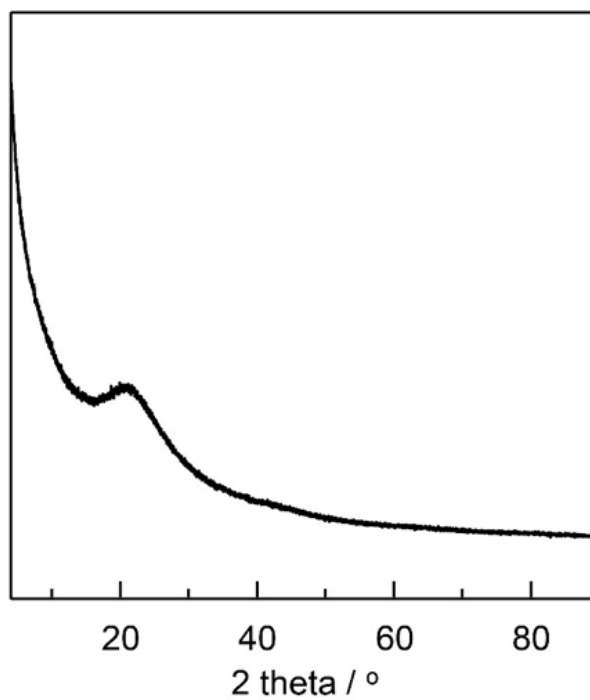


**Figure A.4:** Powder X-ray diffraction pattern of OSPC-1 with Cu target, from 4° to 90°.

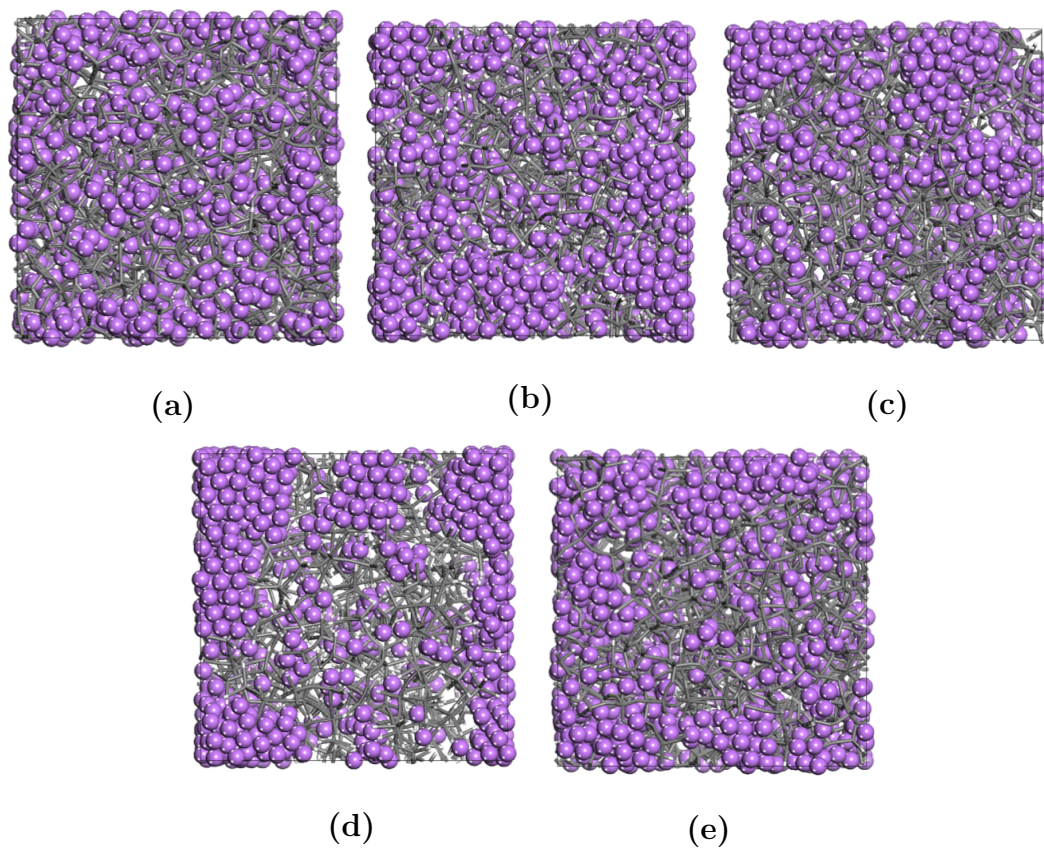
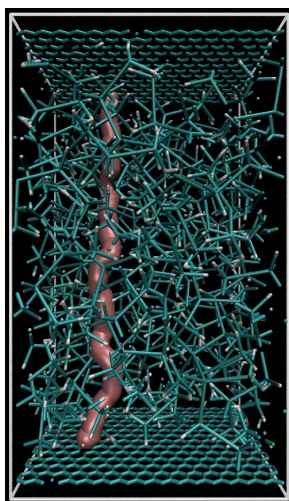
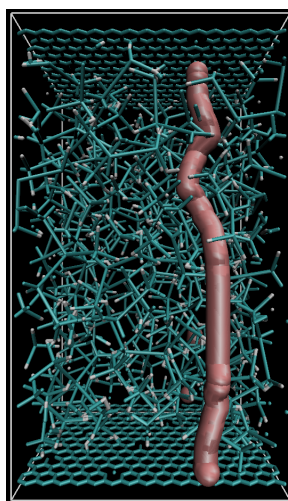


**Figure A.5:** Theoretical capacity of lithium ions (purple) with the OSPC-1 models 1a-e respectively (grey).

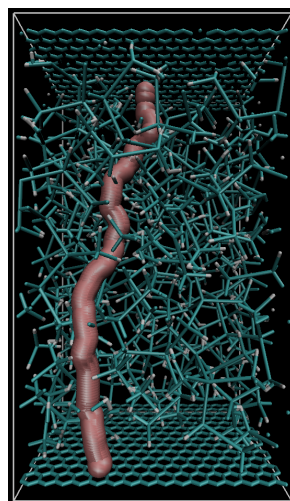




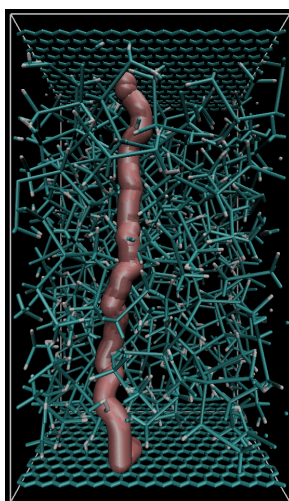
(a) Li2



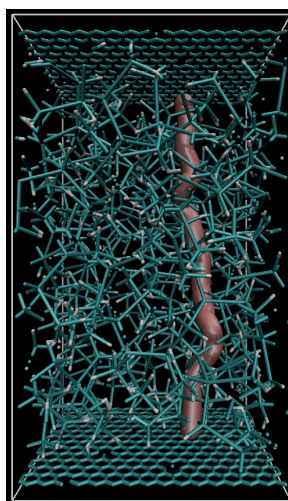
(b) Li3



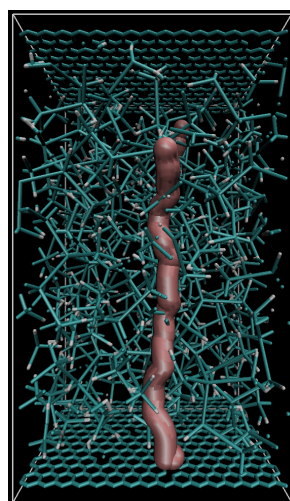
(c) Li4



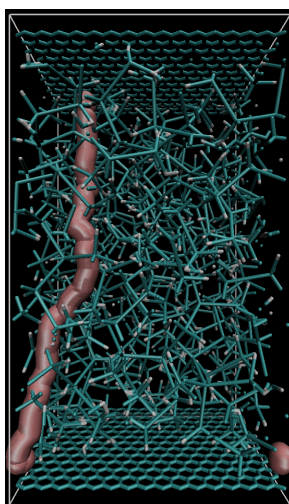
(d) Li5



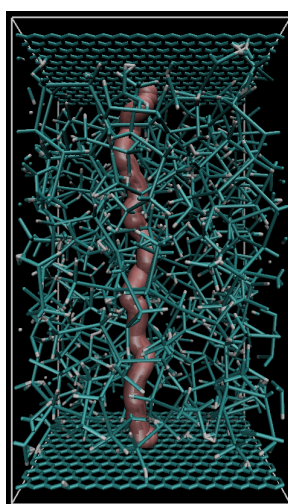
(e) Li6



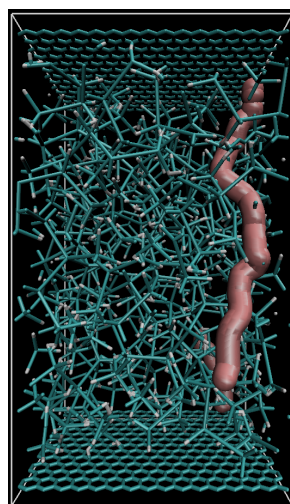
(f) Li7



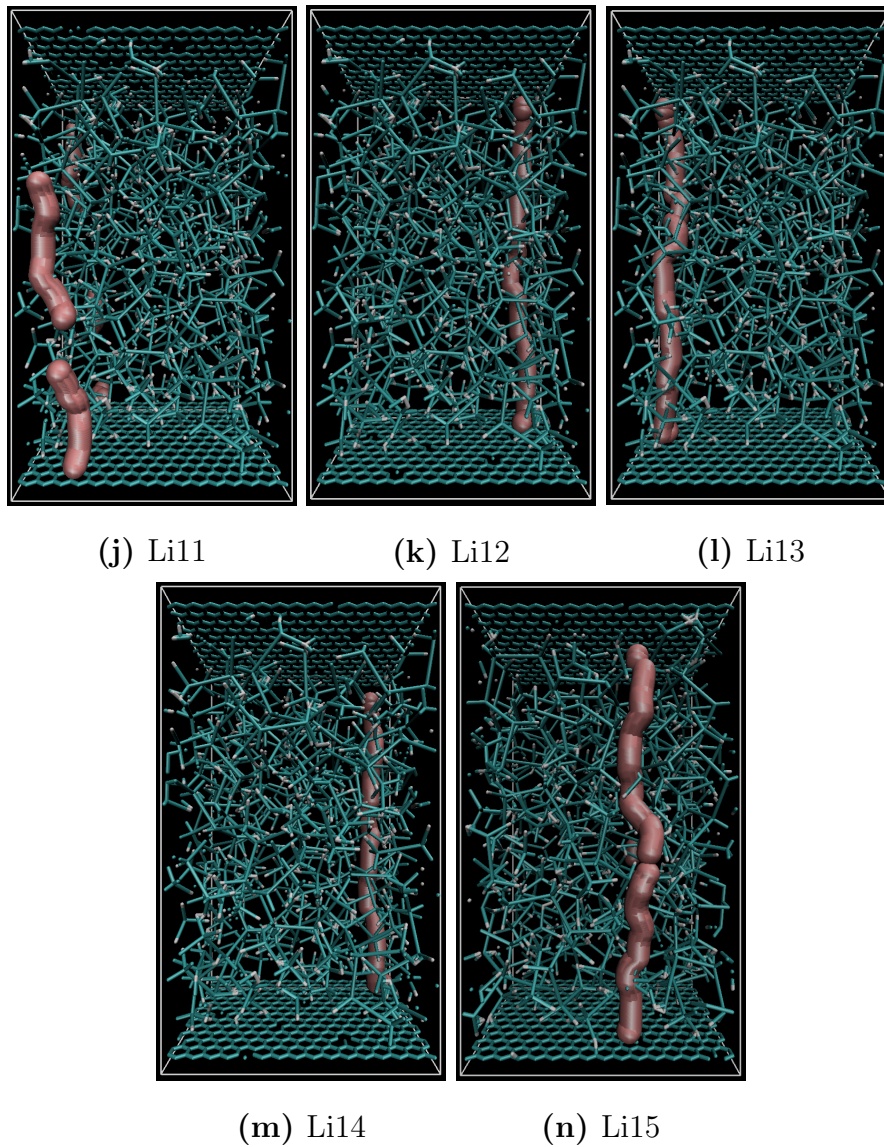
(g) Li8



(h) Li9

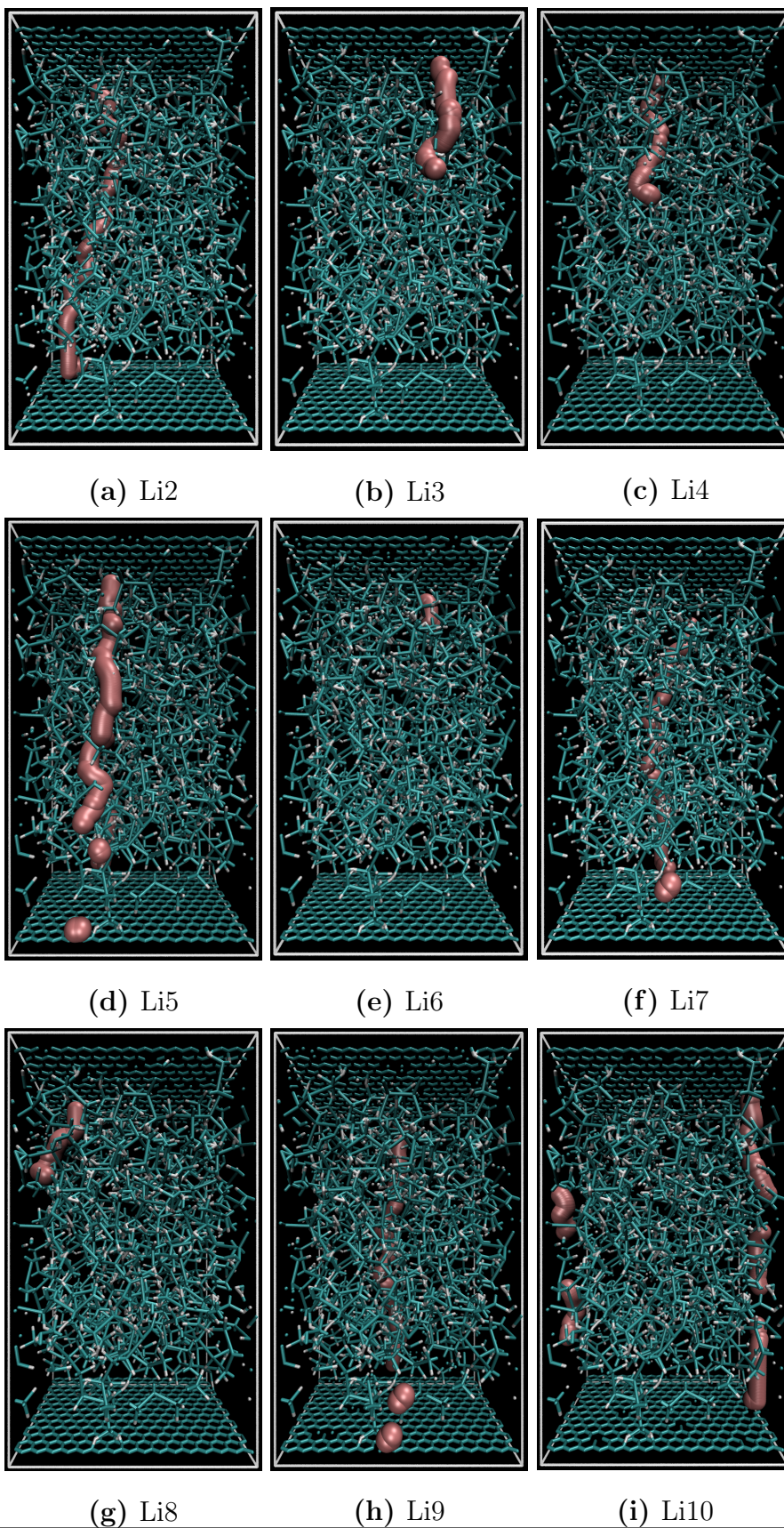


(i) Li10



**Figure A.6:** Diffusion of each individual lithium ion in the OSPC-1 system (a)Li2 - (n)Li15; Each lithium ion pathway extracted from the same simulation, and individual lithium ion coordinates plotted in an overlay for each respected figure.





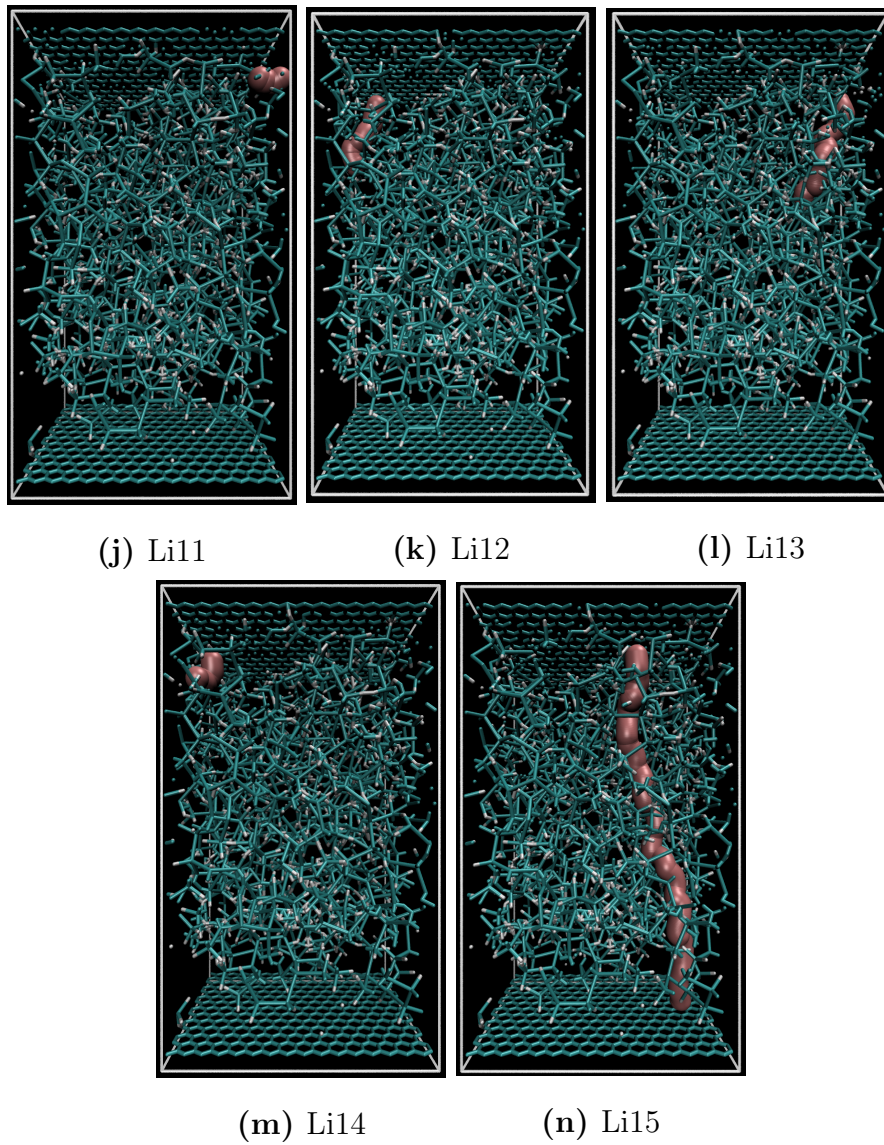
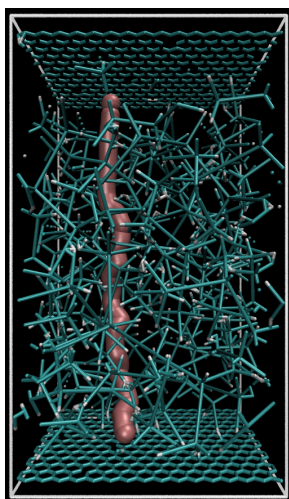
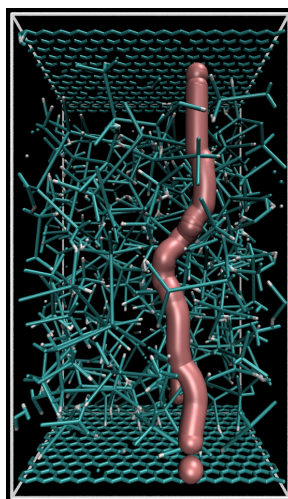


**Figure A.7:** Diffusion of each individual lithium ion in the OSPC-0 system (a)Li2 - (n)Li15

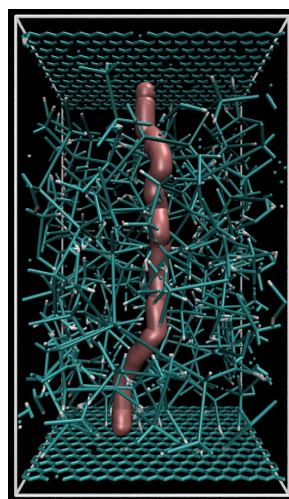




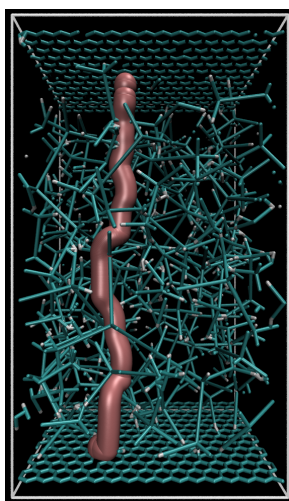
(a) Li2



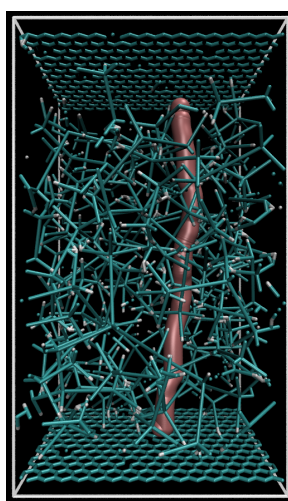
(b) Li3



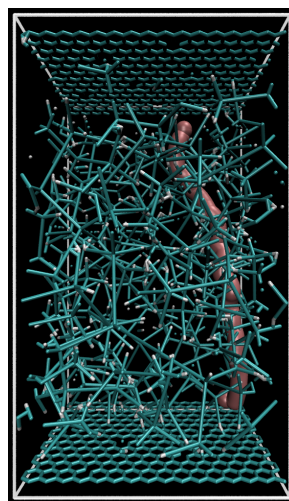
(c) Li4



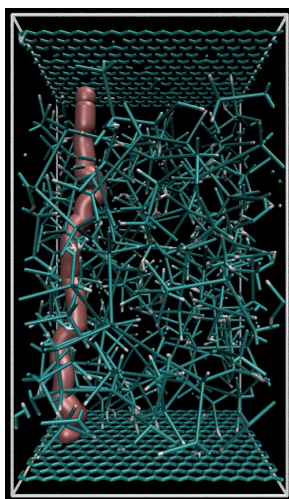
(d) Li5



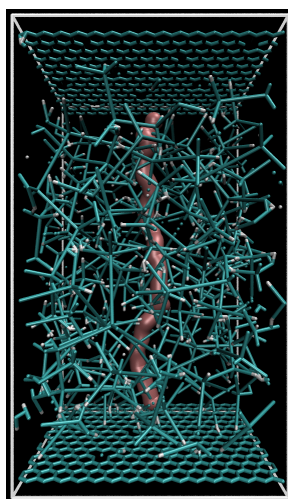
(e) Li6



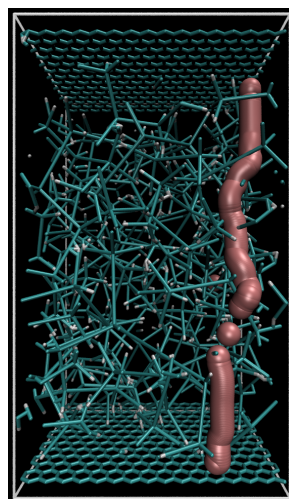
(f) Li7



(g) Li8



(h) Li9



(i) Li10

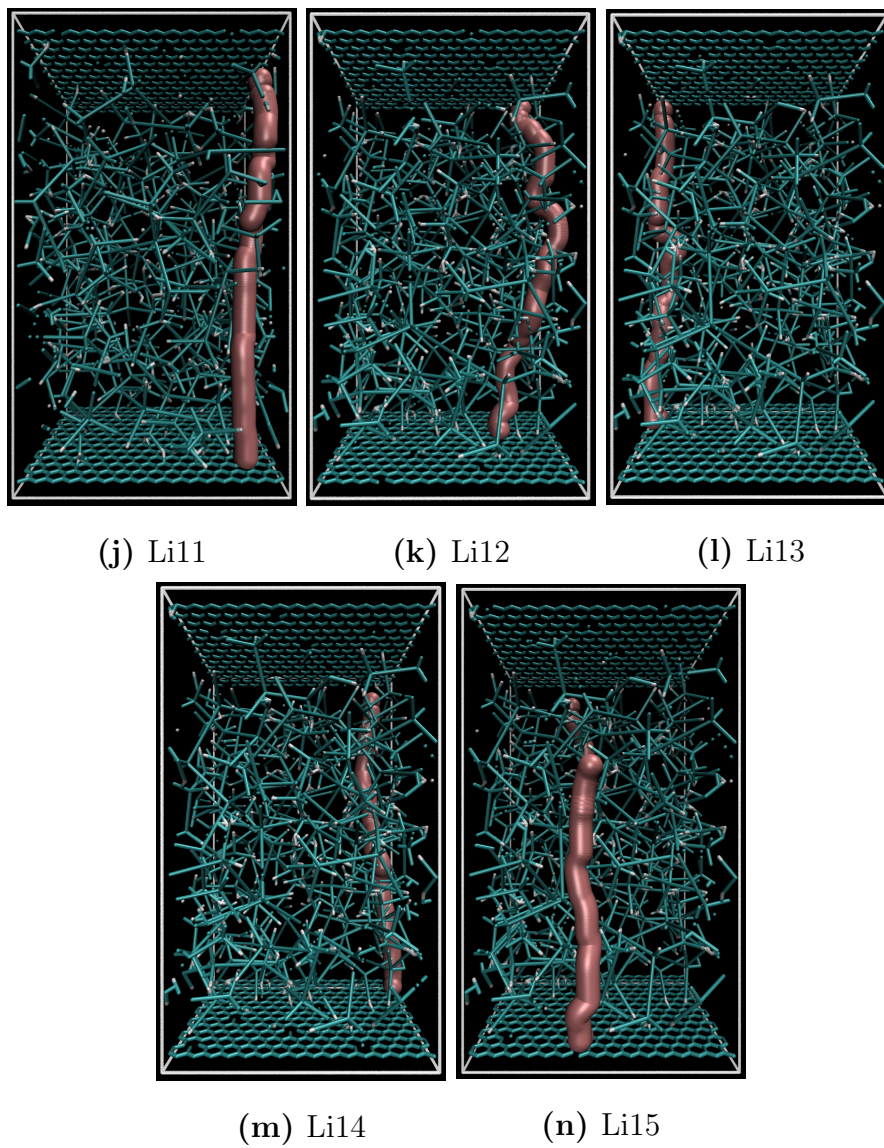
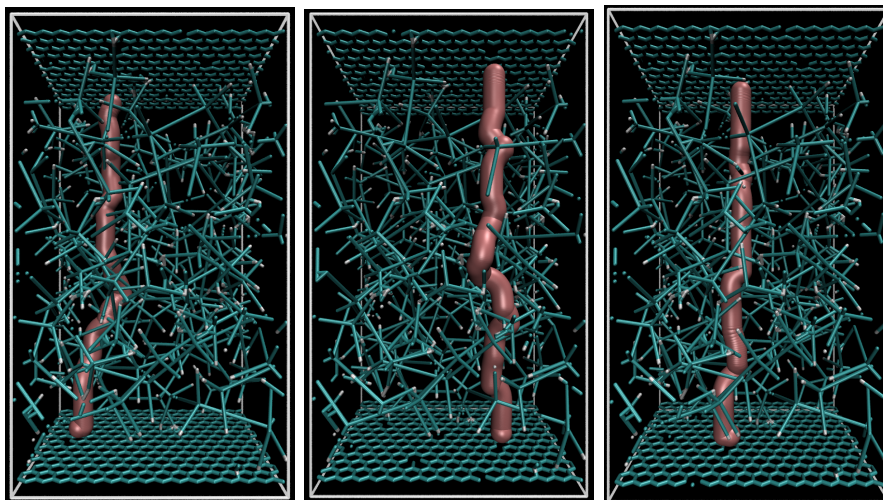


**Figure A.8:** Lithium ion diffusion through the OSPC-2 framework; (a)Li2 - (n)Li15.

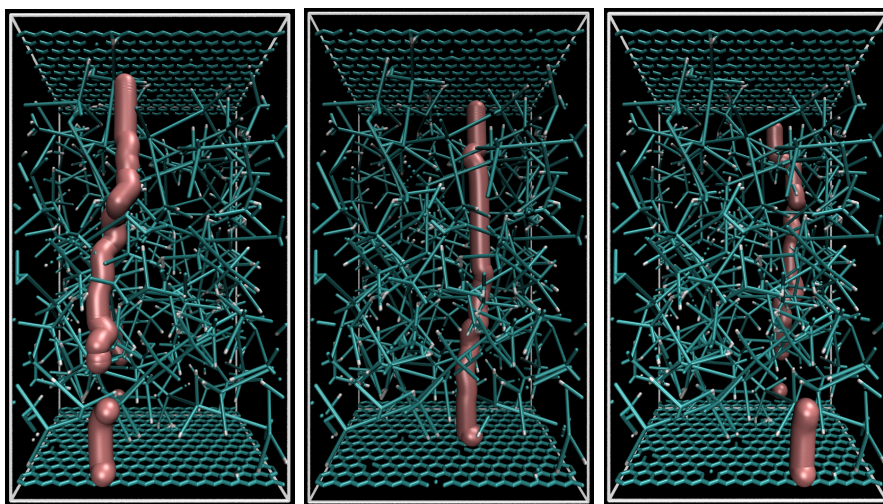




(a) Li2

(b) Li3

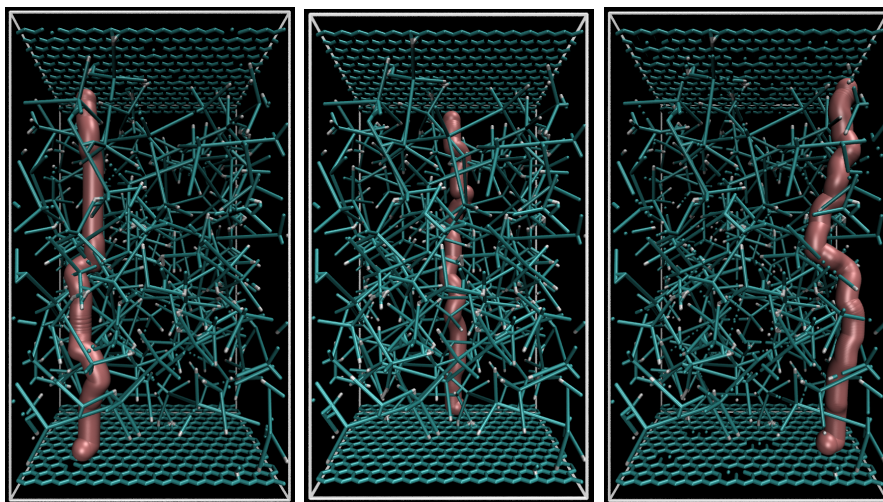
(c) Li4



(d) Li5

(e) Li6

(f) Li7



(g) Li8

(h) Li9

(i) Li10

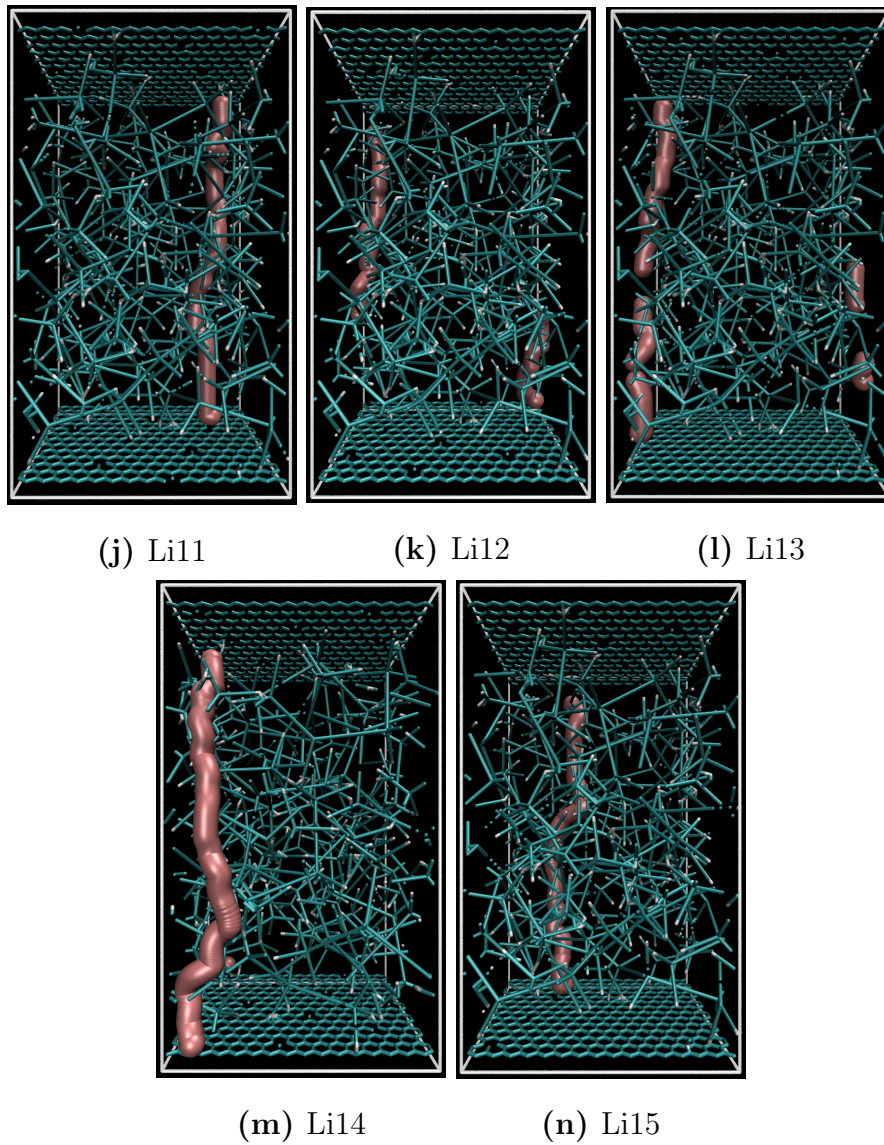
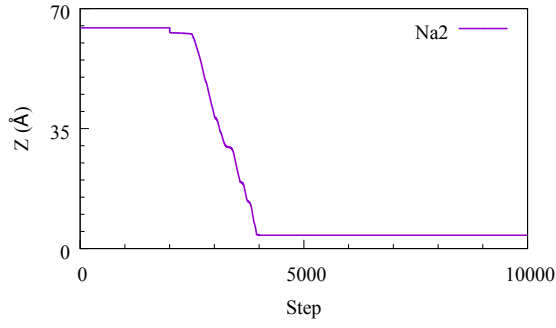


**Figure A.9:** Lithium ion diffusion of each individual ion within the OSPC-3 system; (a)Li1 - (n)Li15

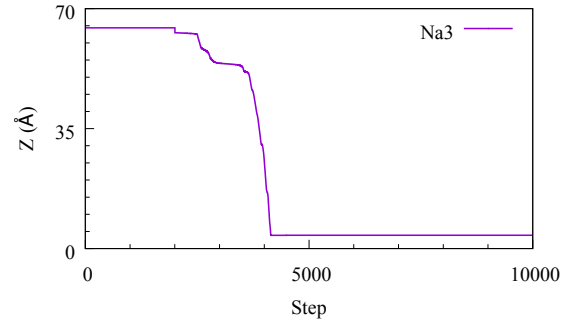


## A.3 Chapter: 5

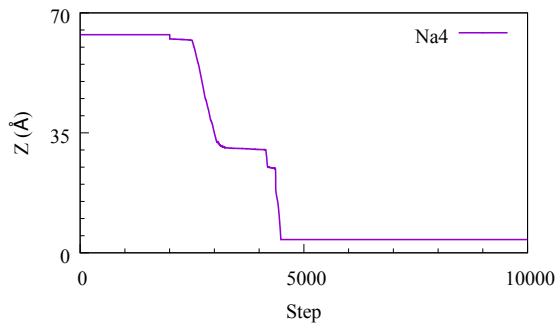
### A.3.1 OSPC-1



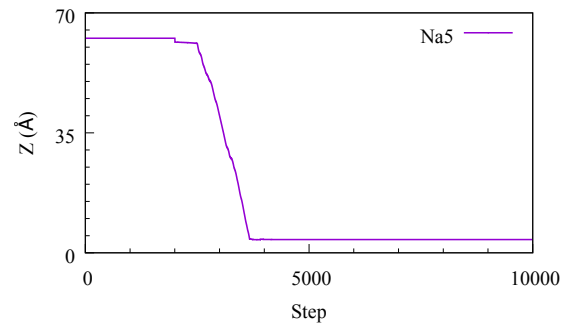
(a) Na2



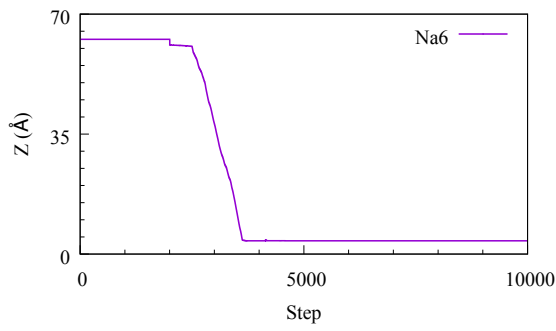
(b) Na3



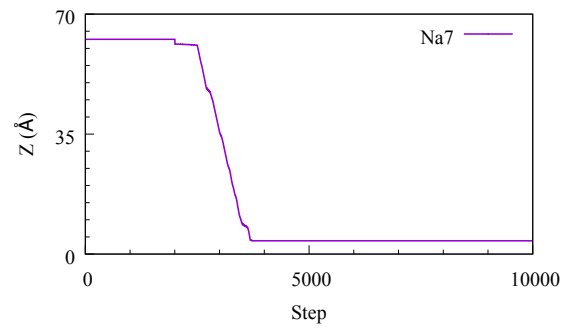
(c) Na4



(d) Na5



(e) Na6



(f) Na7

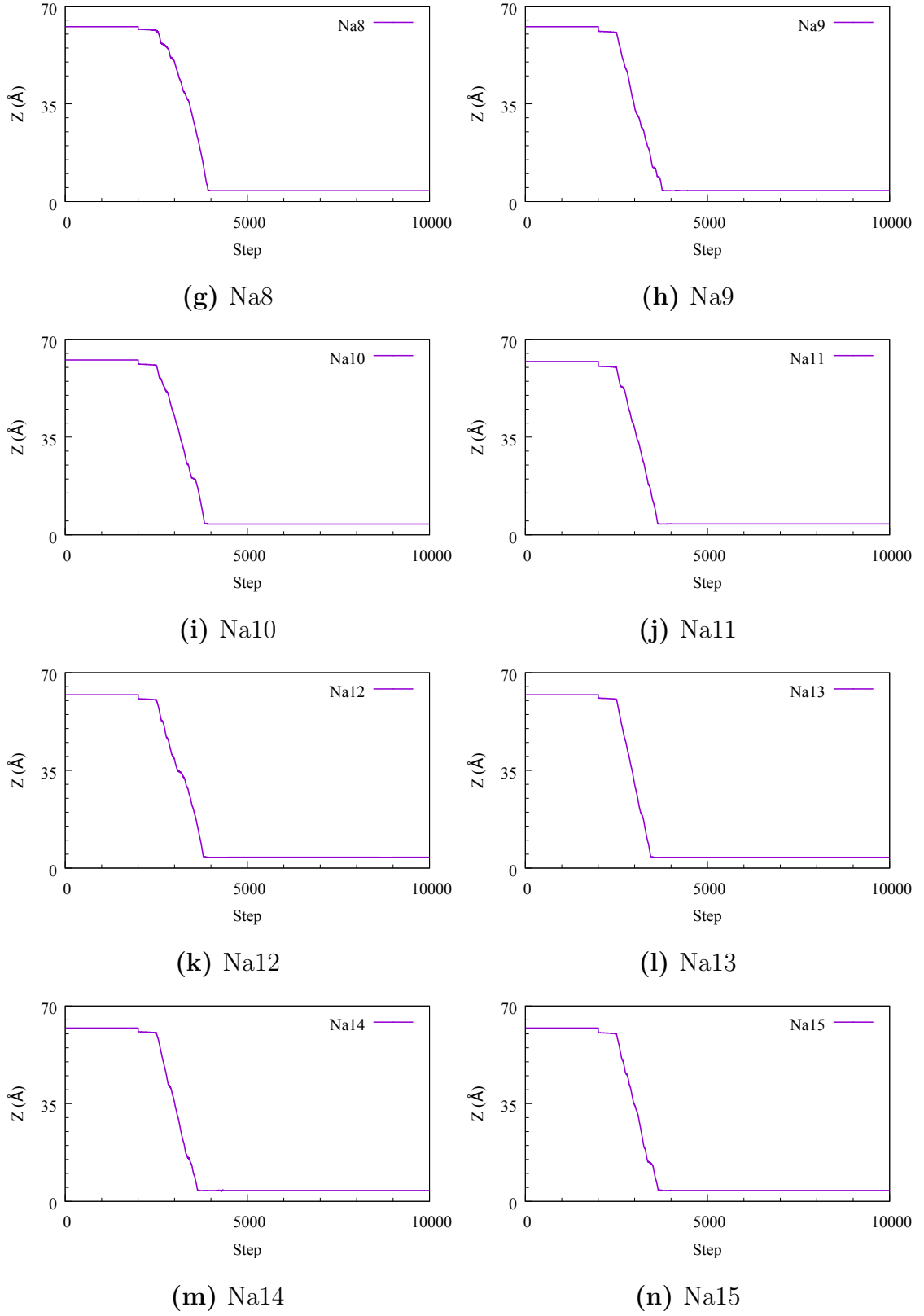
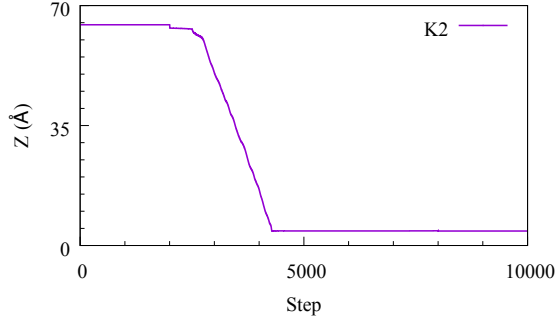
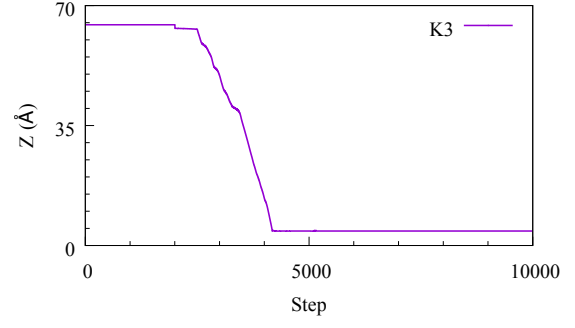


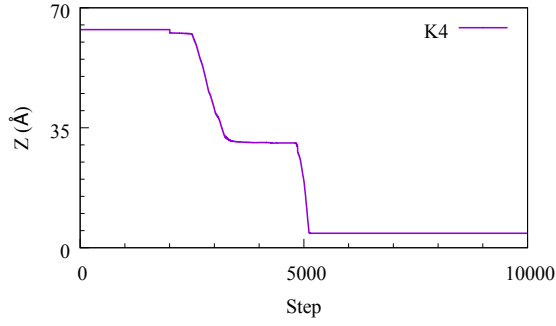
**Figure A.10:** Diffusion plots of the individual sodium ions within the simulation cell of OSPC-1; (a)Na1 - (o)Na15.



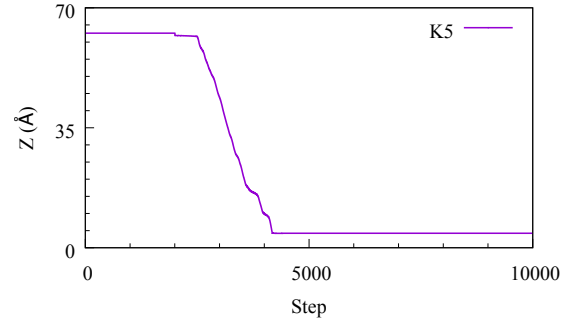
(a) K2



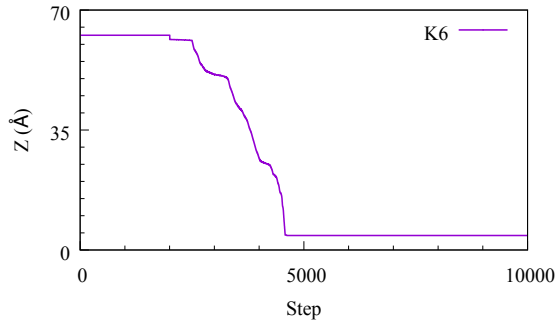
(b) K3



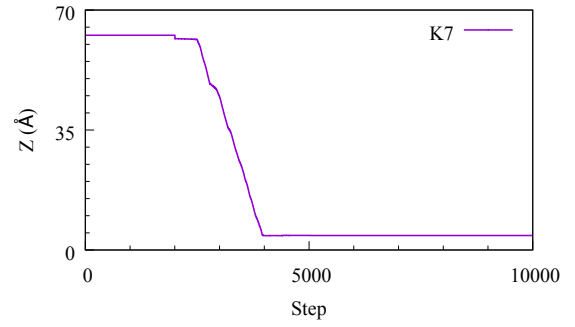
(c) K4



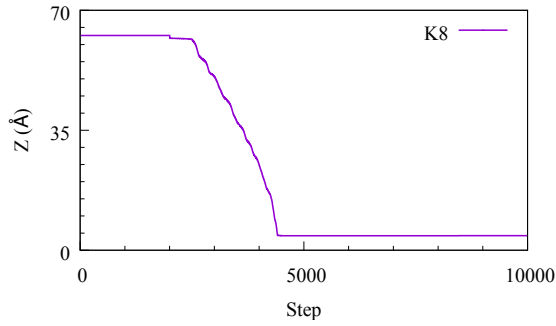
(d) K5



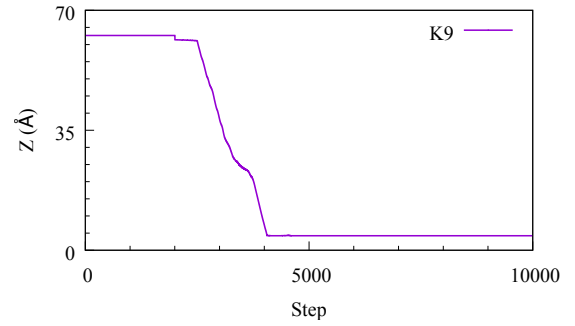
(e) K6



(f) K7



(g) K8



(h) K9

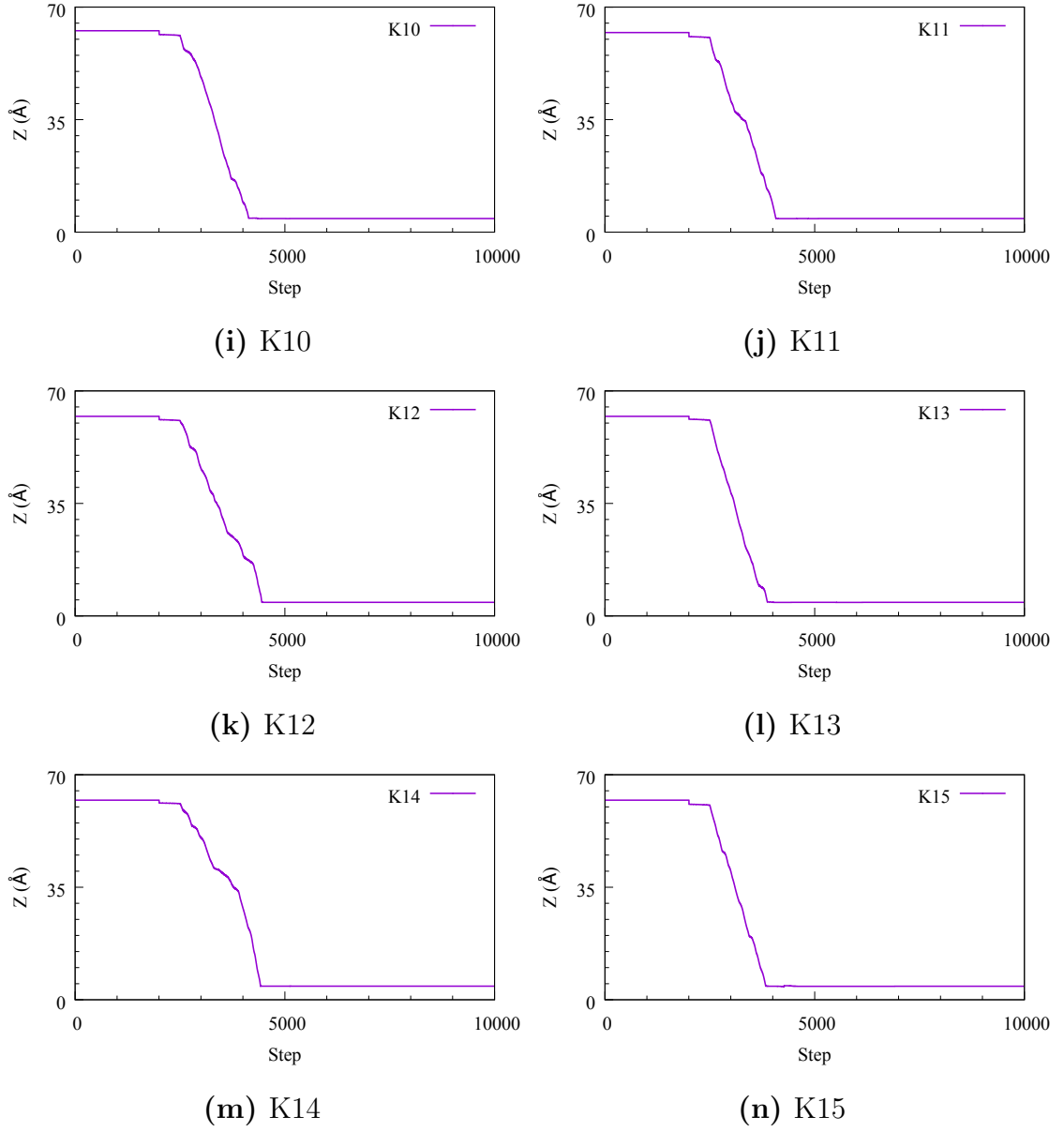
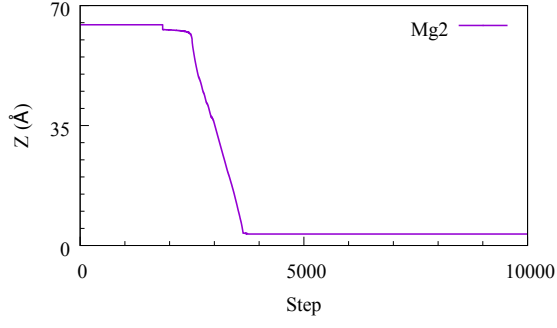
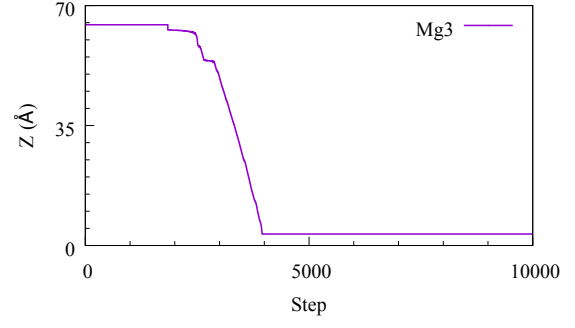


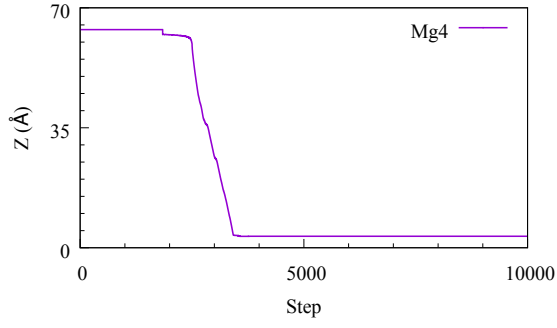
**Figure A.11:** Diffusion plots of the individual potassium ions within the OSPC-1 system; (a)K2 - (n)K15.



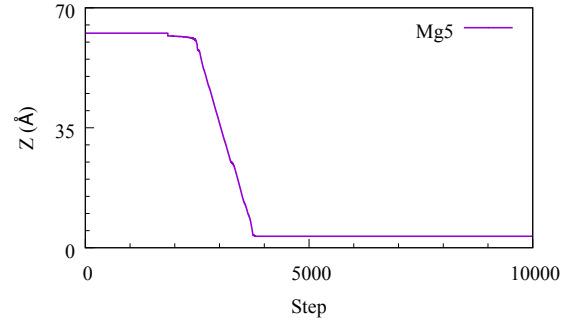
(a) Mg2



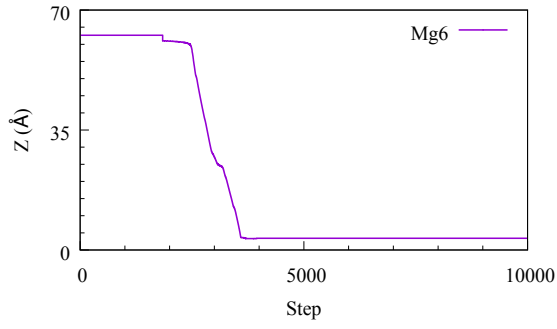
(b) Mg3



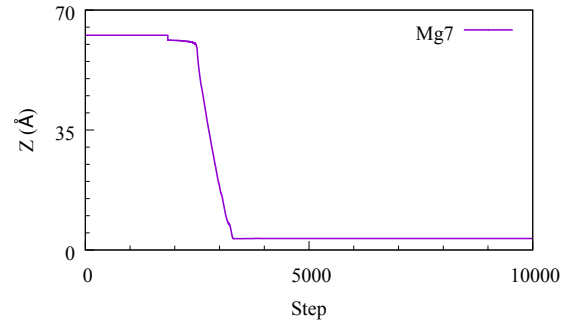
(c) Mg4



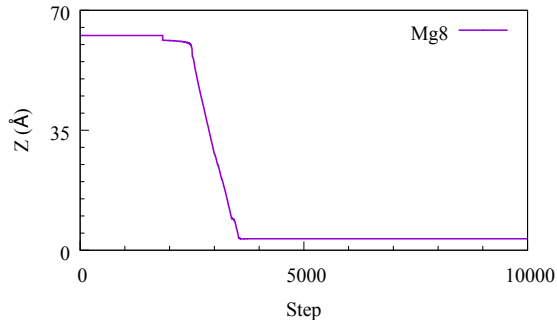
(d) Mg5



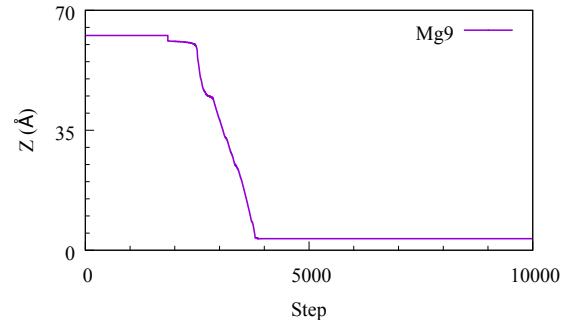
(e) Mg6



(f) Mg7



(g) Mg8



(h) Mg9

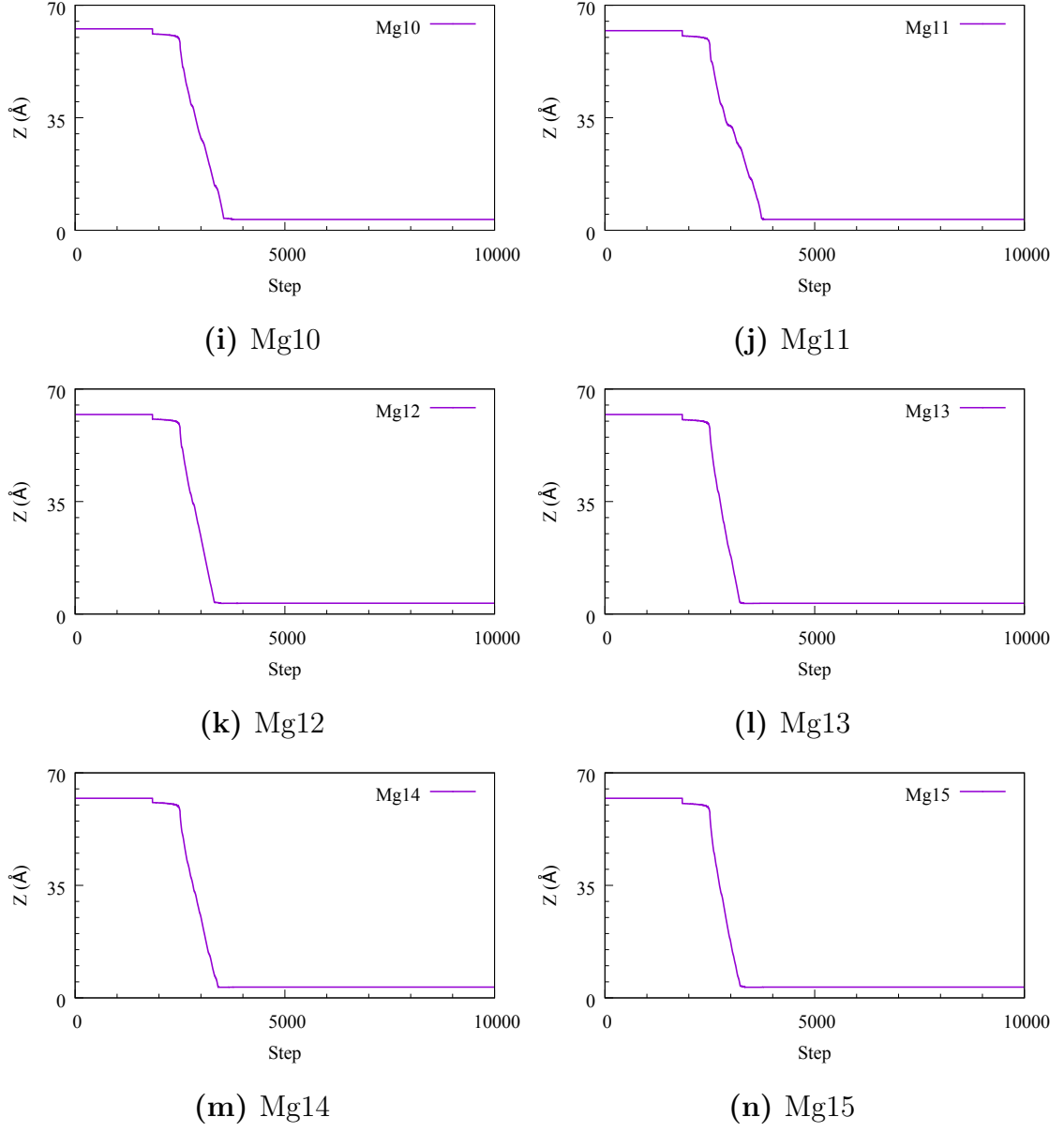
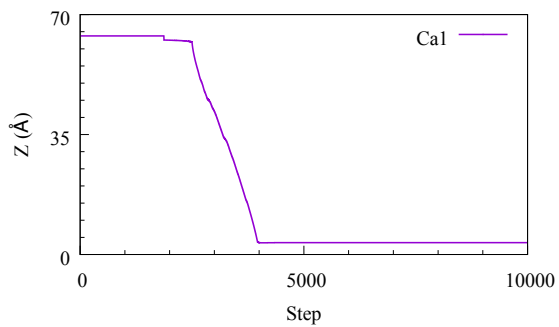
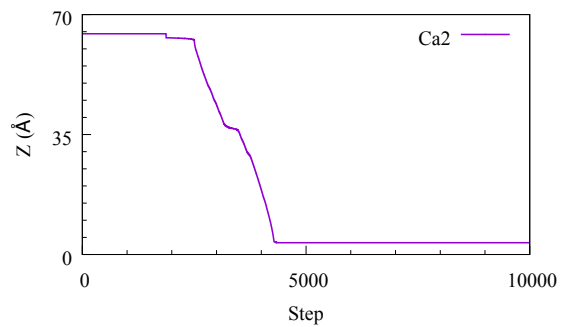


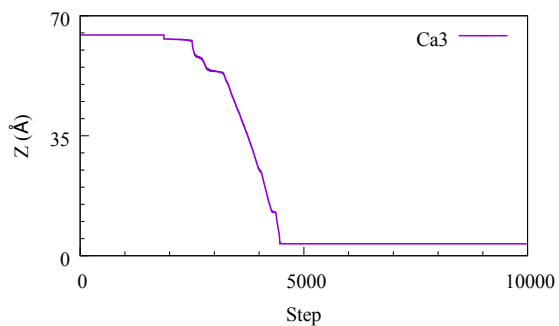
**Figure A.12:** Diffusion plots of the individual magnesium ions within the simulation cell of OSPC-1; (a)Mg2 - (n)Mg15.



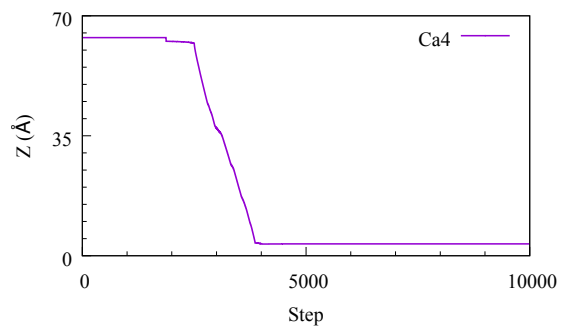
(a) Ca1



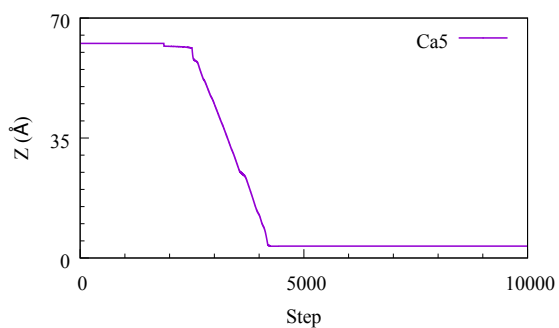
(b) Ca2



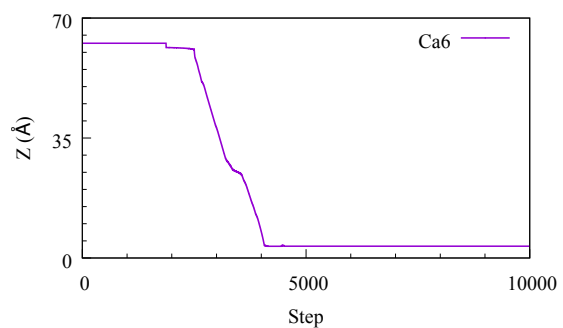
(c) Ca3



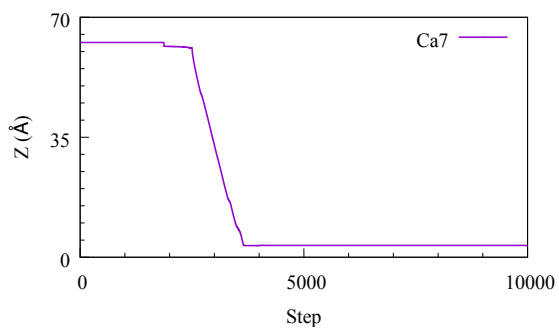
(d) Ca4



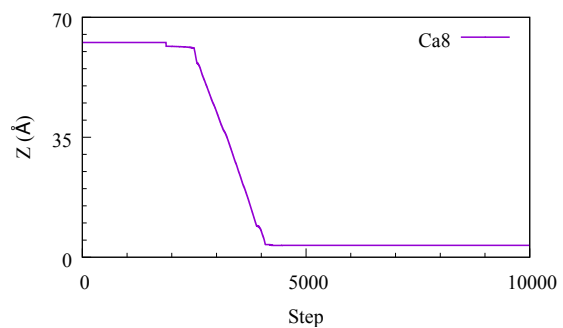
(e) Ca5



(f) Ca6



(g) Ca7



(h) Ca8

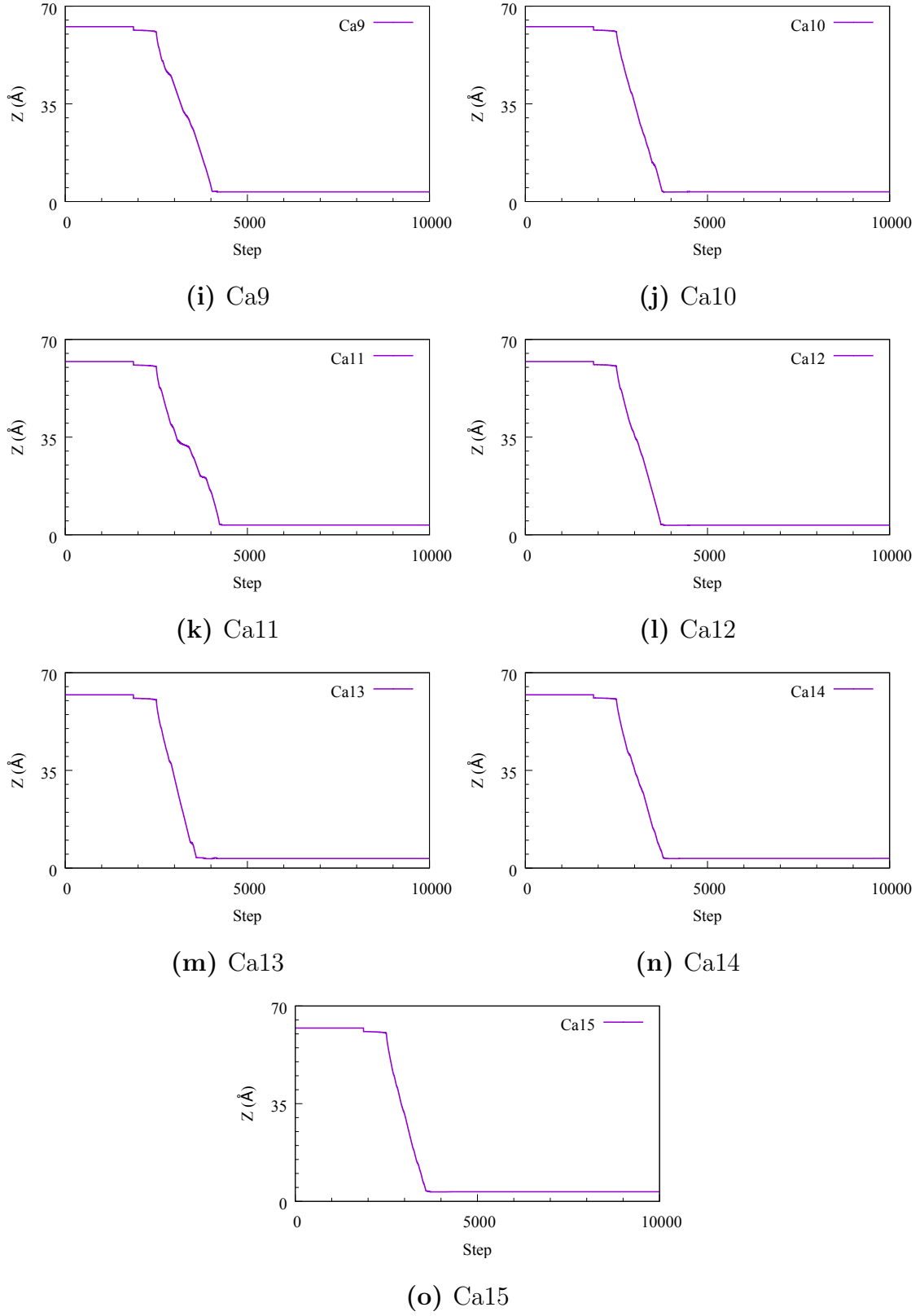
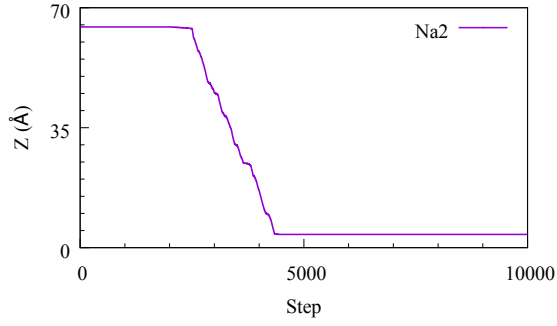


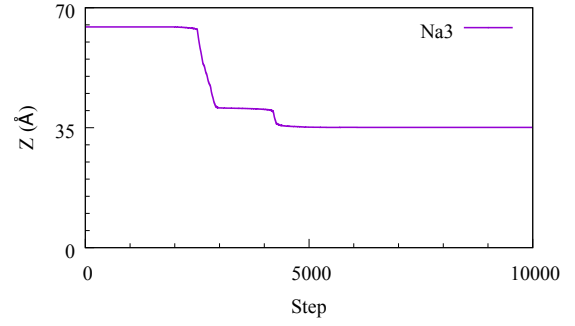
**Figure A.13:** Diffusion plots of the individual calcium ions within the OSPC-1 system; (a)Ca1 - (o) Ca15



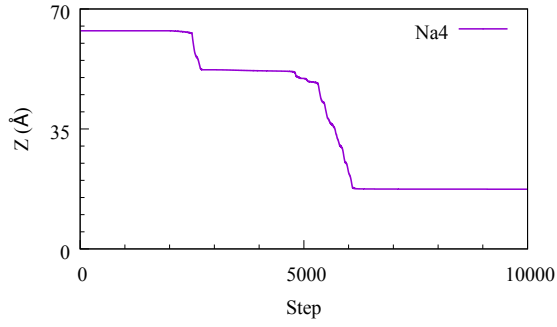
### A.3.2 OSPC-0



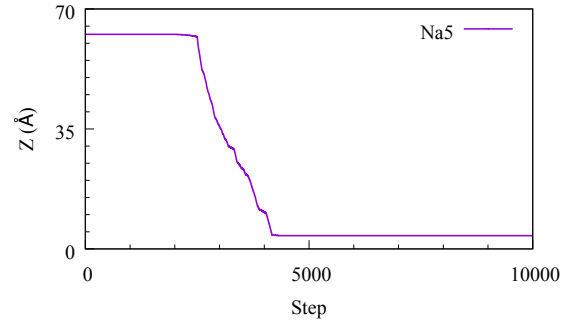
(a) Na2



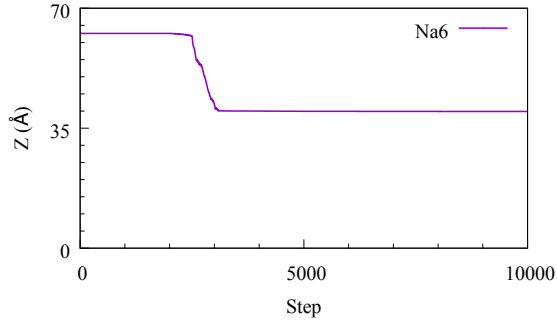
(b) Na3



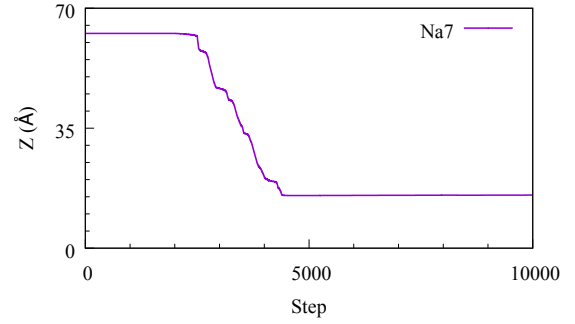
(c) Na4



(d) Na5



(e) Na6



(f) Na7

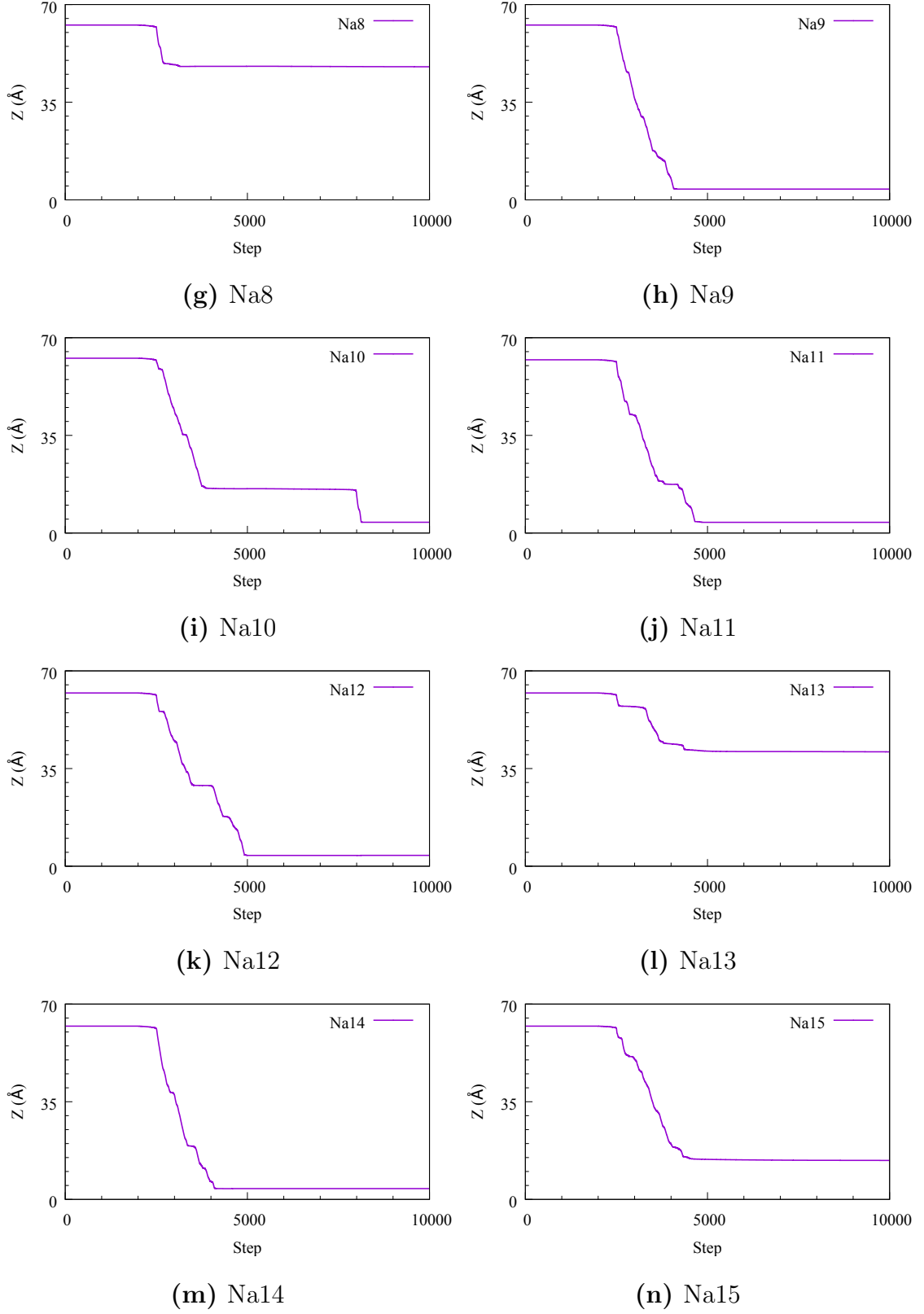
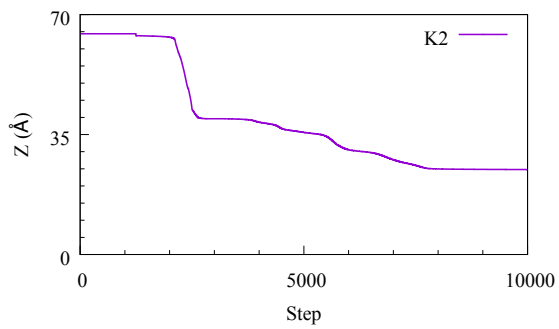
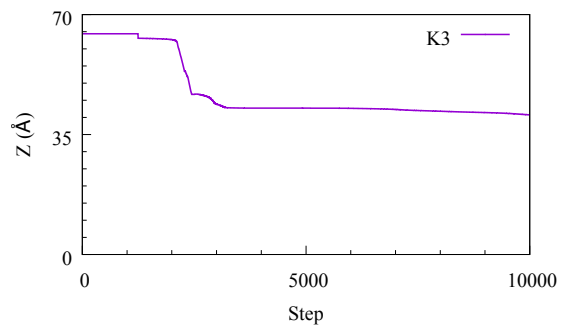


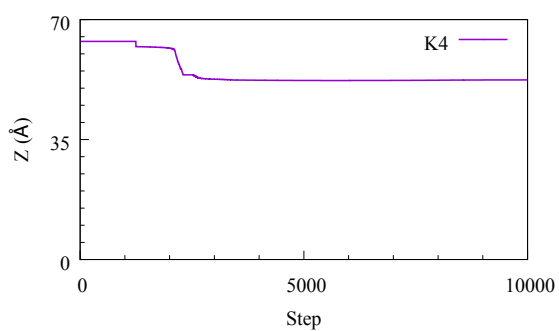
**Figure A.14:** Diffusion plots of the individual sodium ions with the OSPC-0 system; (a)Na1 - (o)Na15.



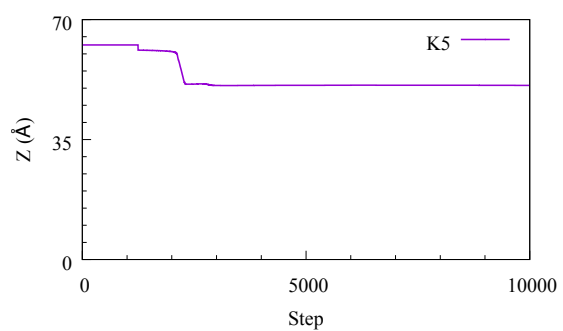
(a) K2



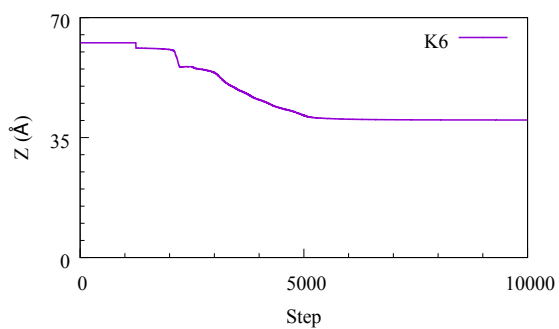
(b) K3



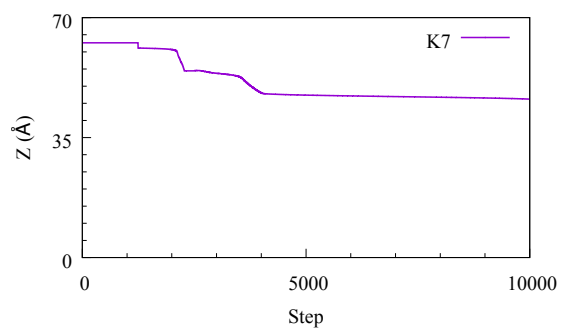
(c) K4



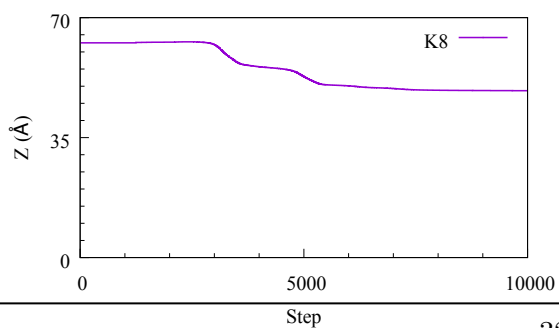
(d) K5



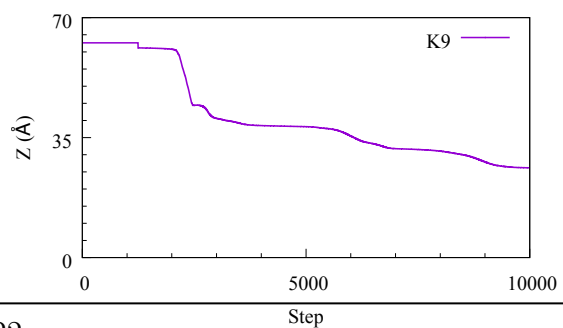
(e) K6



(f) K7



(g) K8



(h) K9

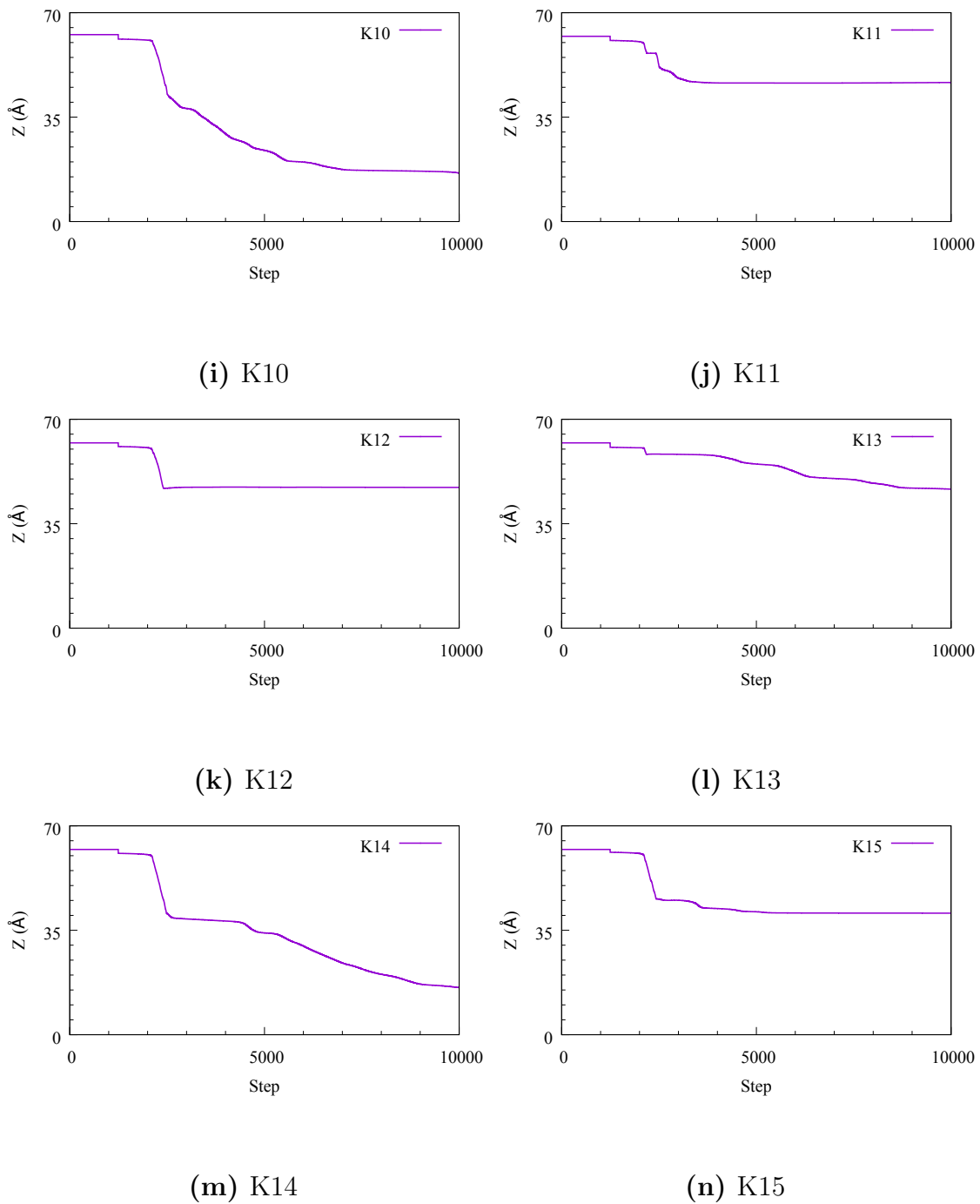
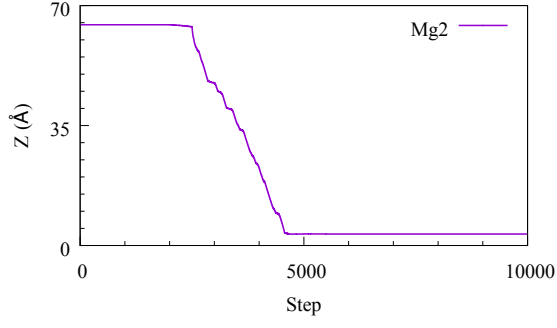
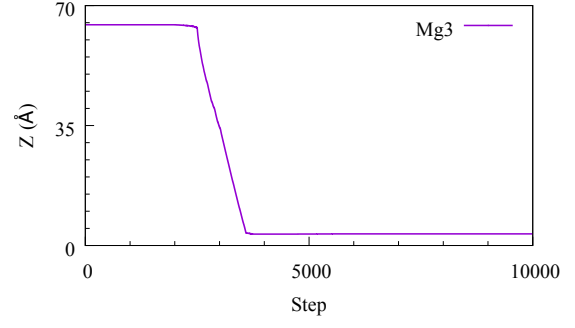


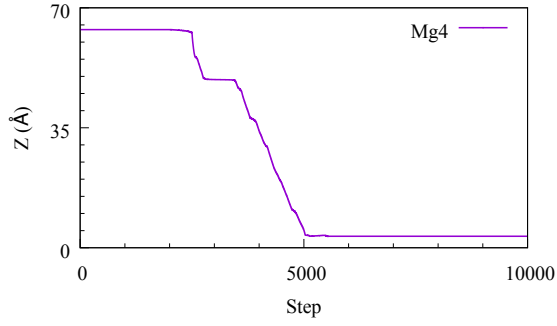
**Figure A.15:** Z-axis movement of the individual potassium ions within the OSPC-0 structure; (a)K1 - (o)K15.



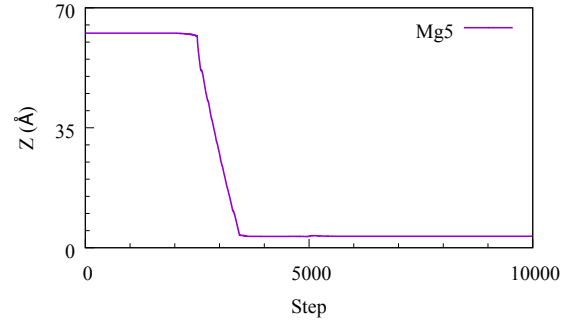
(a) Mg2



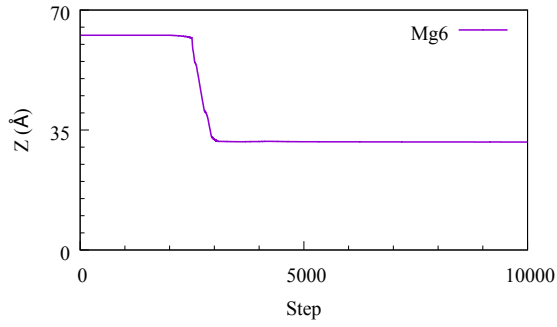
(b) Mg3



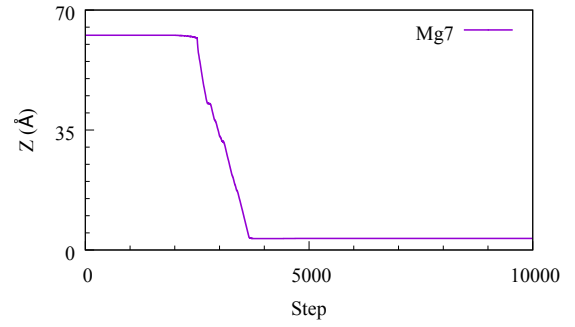
(c) Mg4



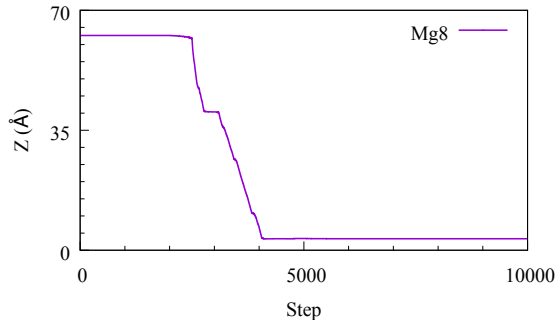
(d) Mg5



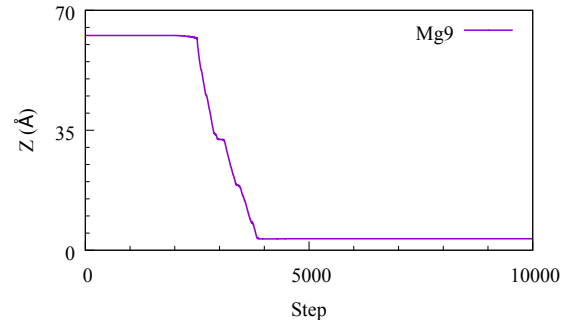
(e) Mg6



(f) Mg7



(g) Mg8



(h) Mg9

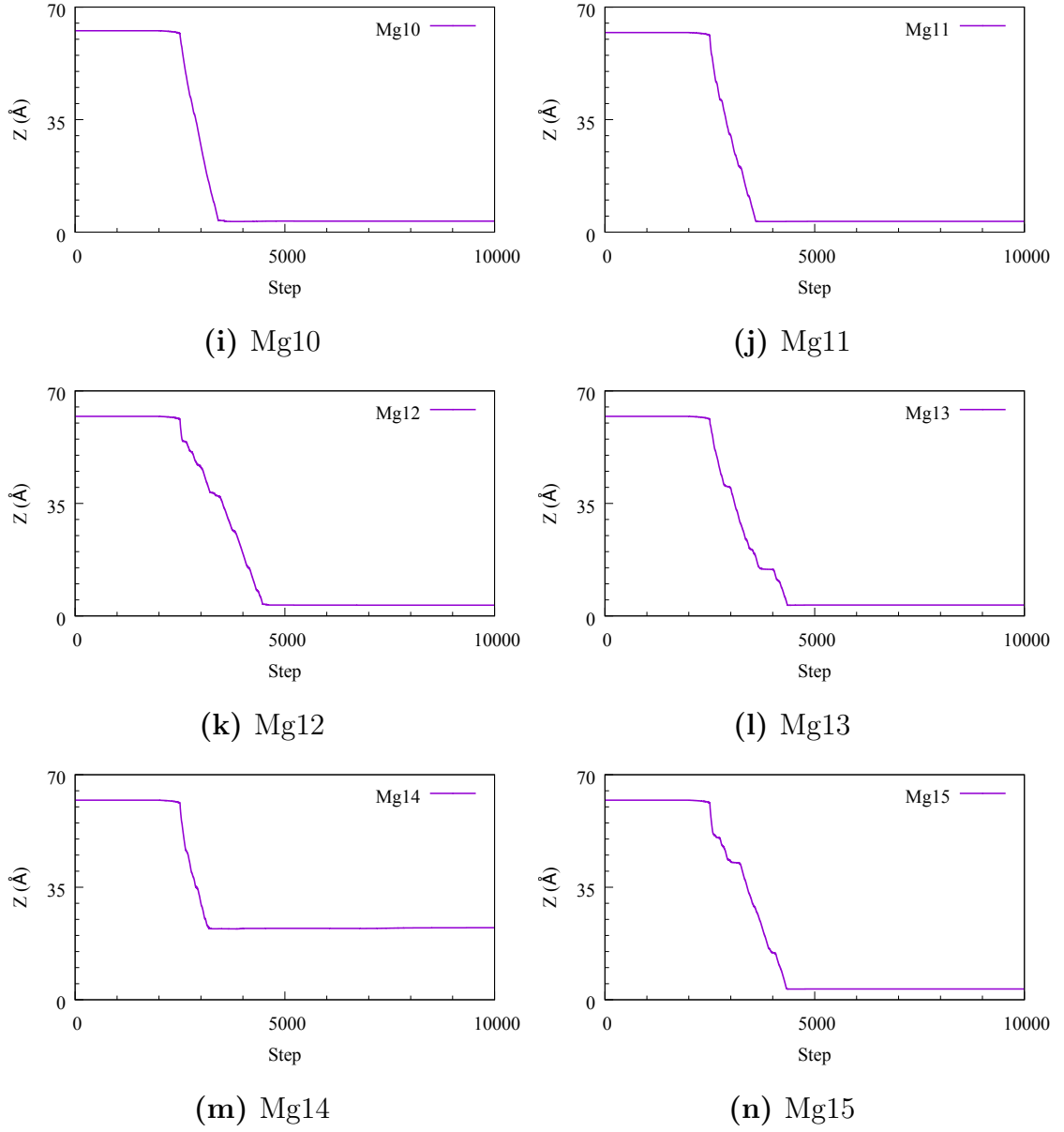
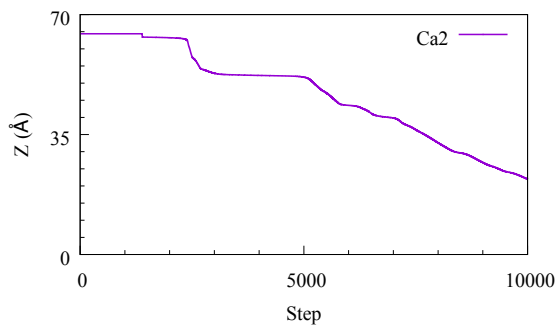
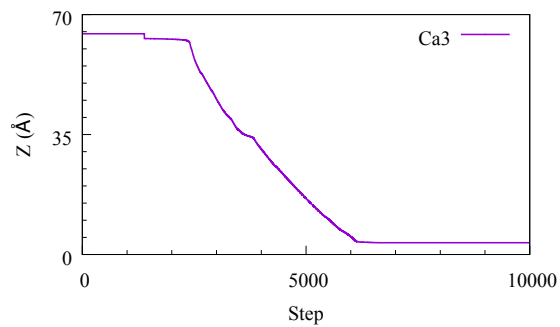


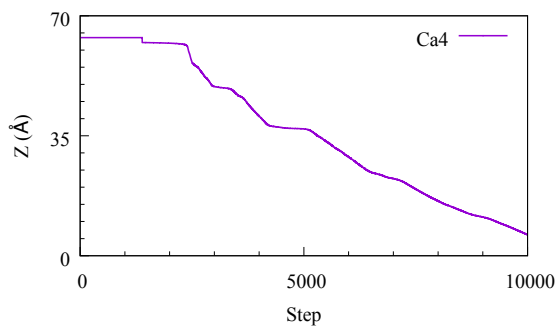
**Figure A.16:** Z-axis movement of the individual magnesium ions within the OSPC-0 structure; (a)Mg1 - (o)Mg15.



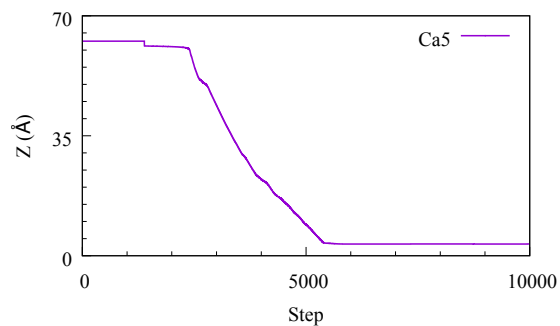
(a) Ca2



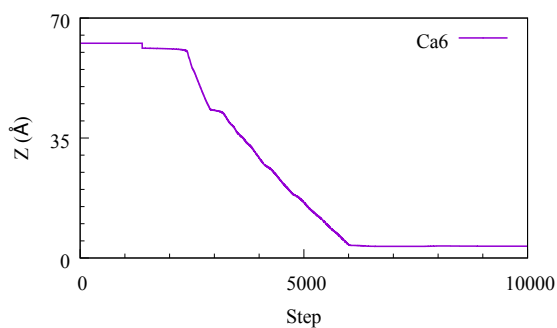
(b) Ca3



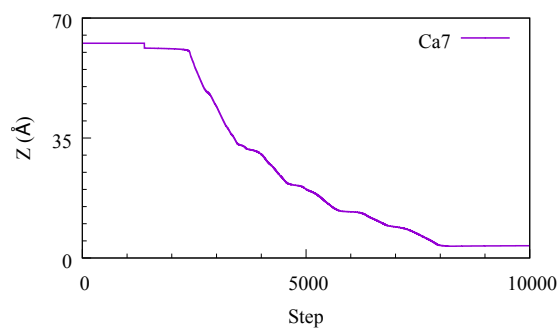
(c) Ca4



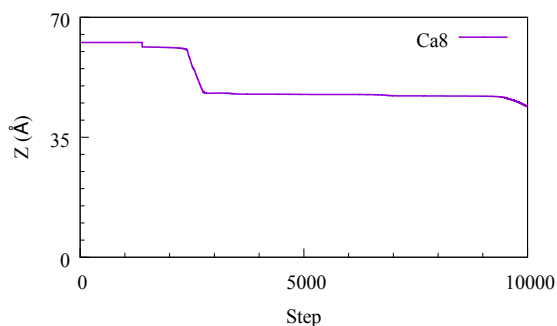
(d) Ca5



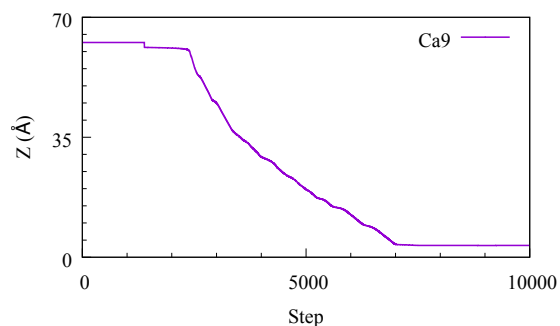
(e) Ca6



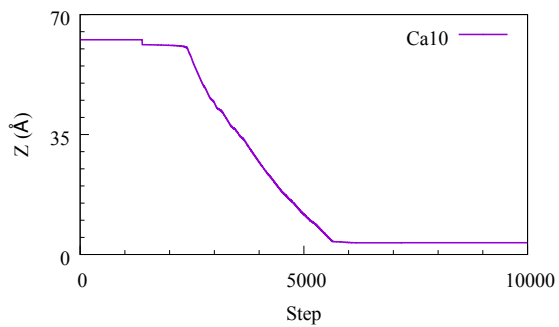
(f) Ca7



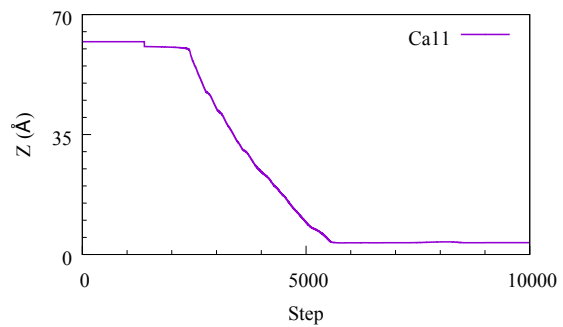
(g) Ca8



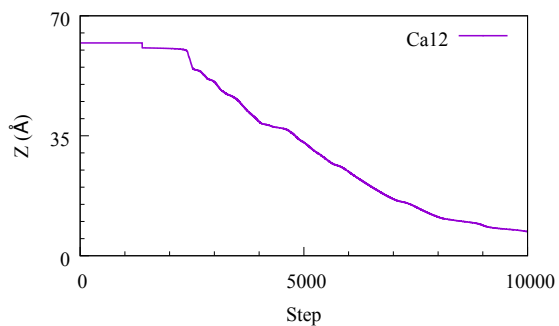
(h) Ca9



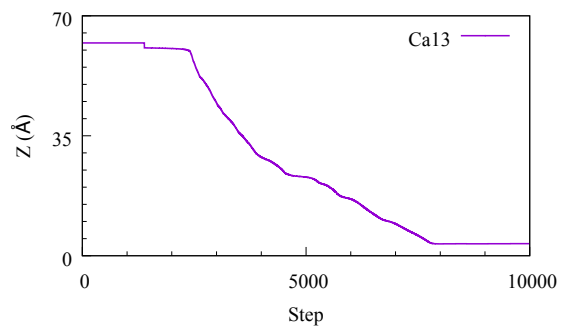
(i) Ca10



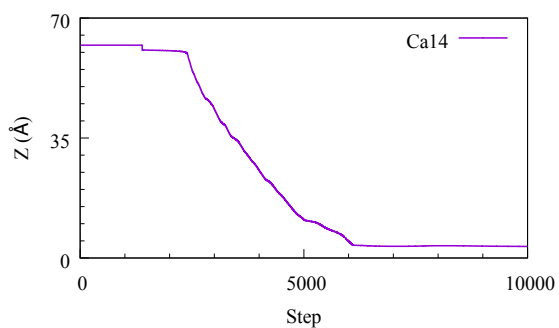
(j) Ca11



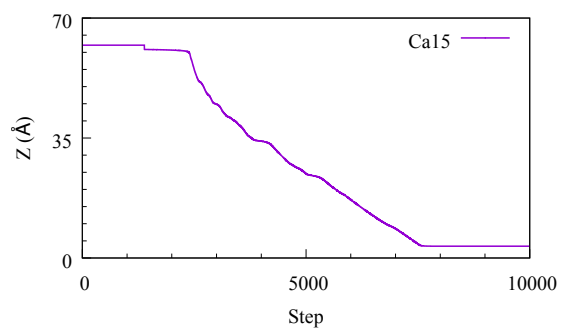
(k) Ca12



(l) Ca13



(m) Ca14



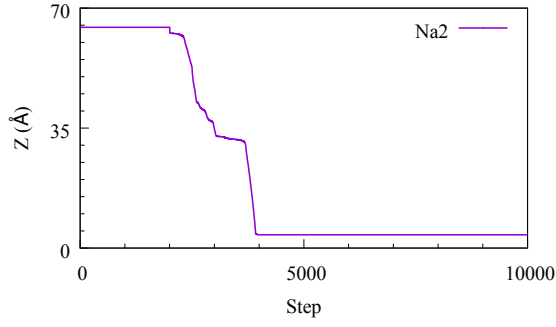
(n) Ca15

**Figure A.17:** Diffusion and z-axis movement of the calcium ions within the OSPC-0 structure.

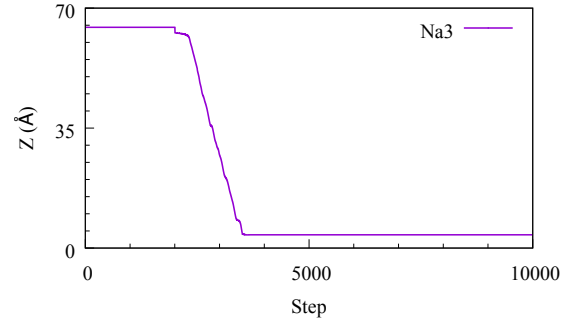




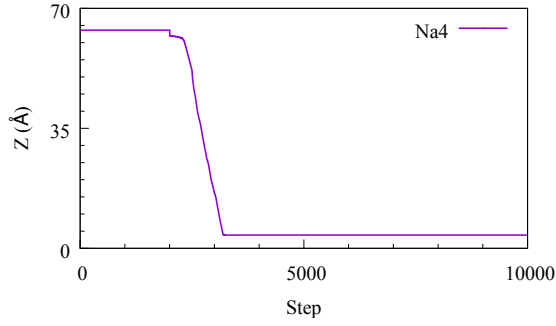
## A.3.3 OSPC-2



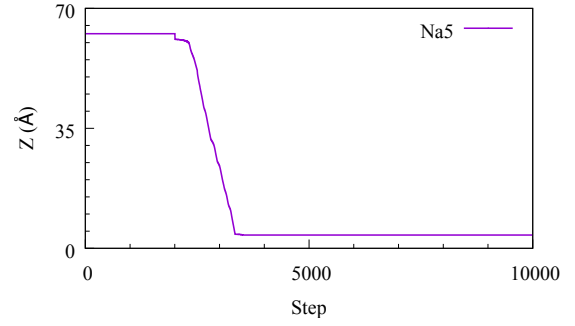
(a) Na2



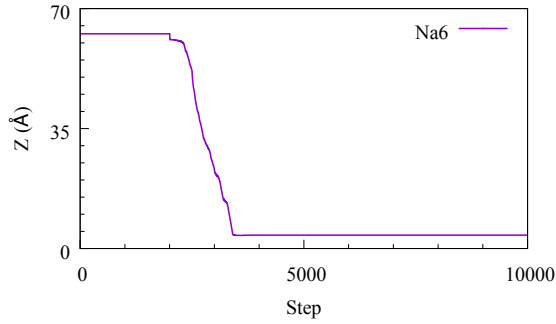
(b) Na3



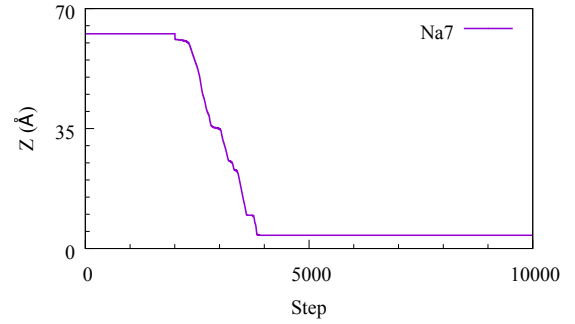
(c) Na4



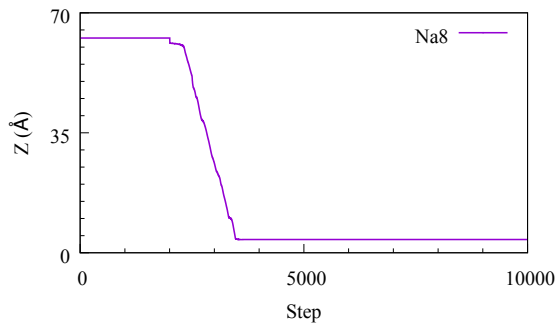
(d) Na5



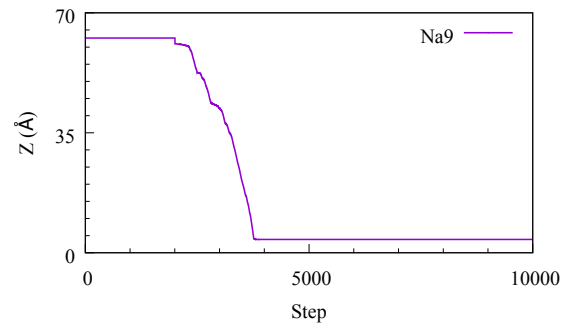
(e) Na6



(f) Na7



(g) Na8



(h) Na9

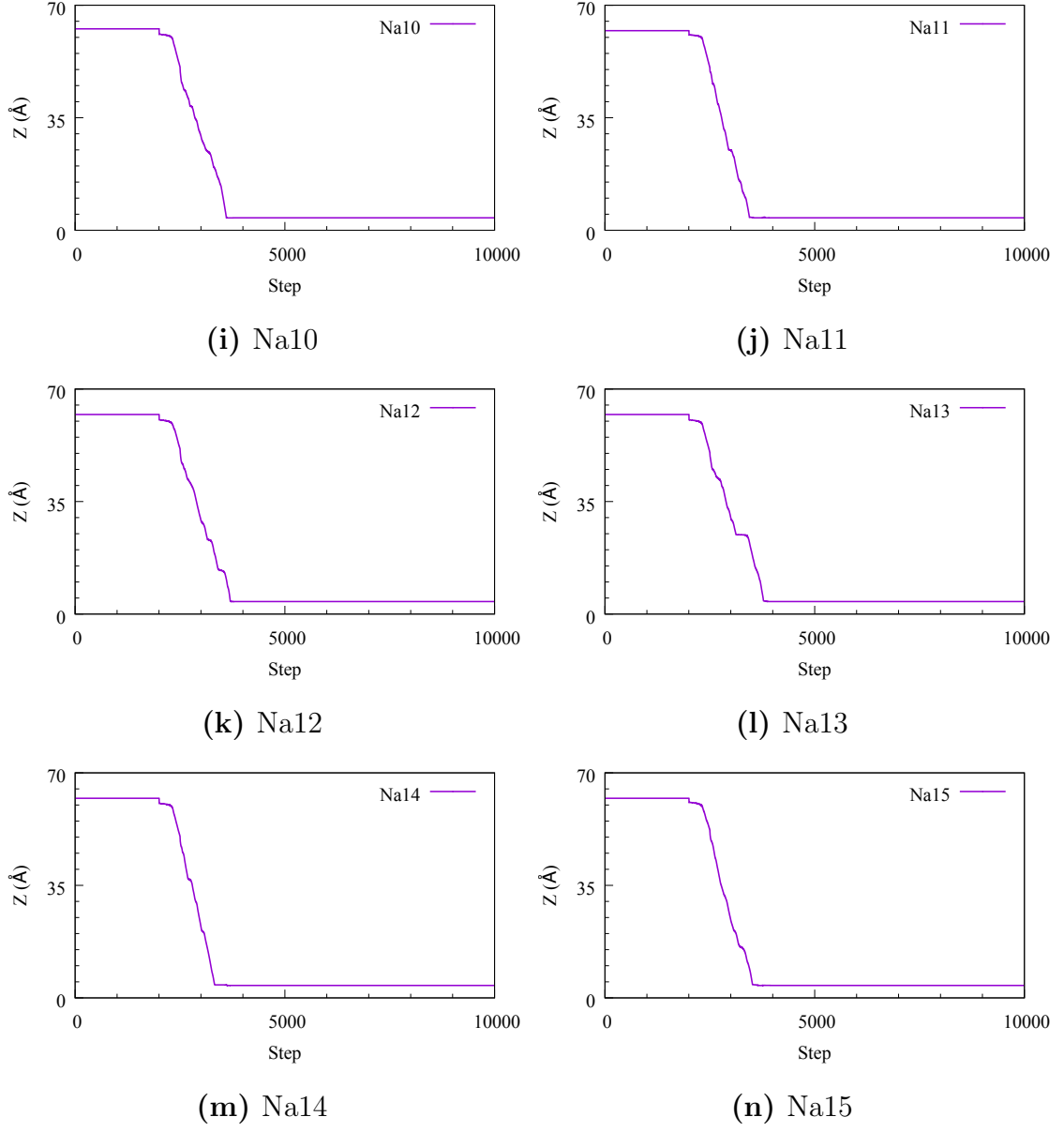
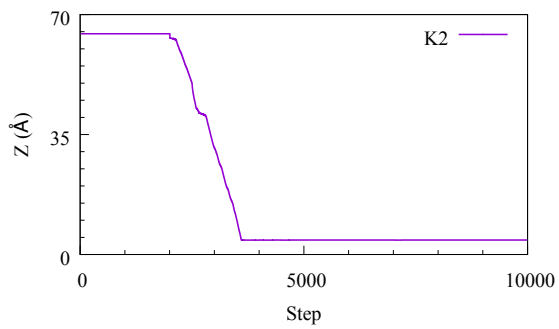
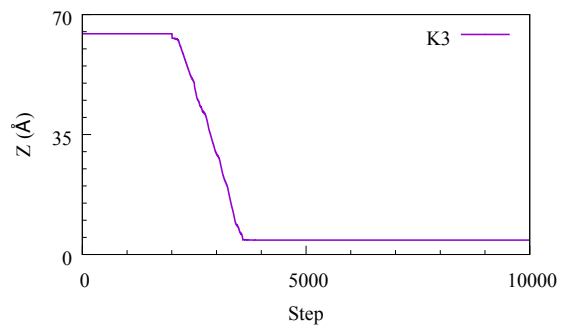


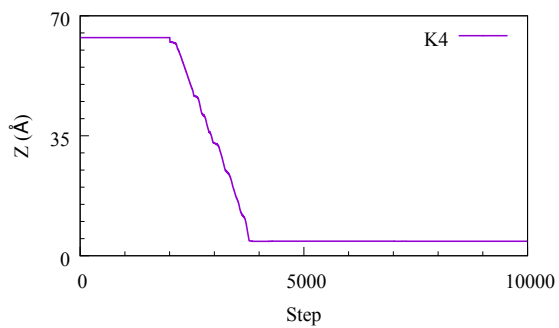
**Figure A.18:** Diffusion plots of the individual sodium ions within the OSCP-0 system; (a)Na1 - (o)Na15.



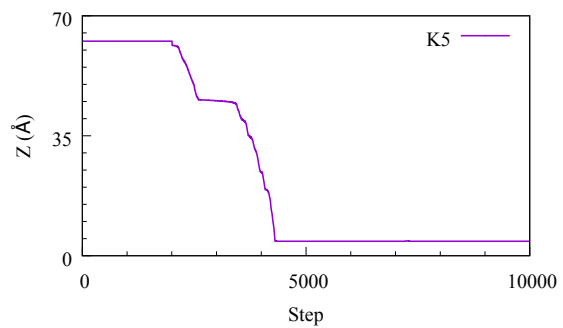
(a) K2



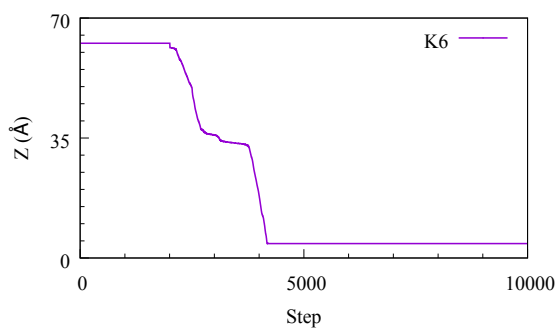
(b) K3



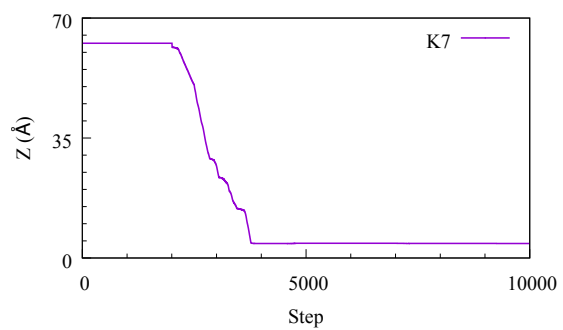
(c) K4



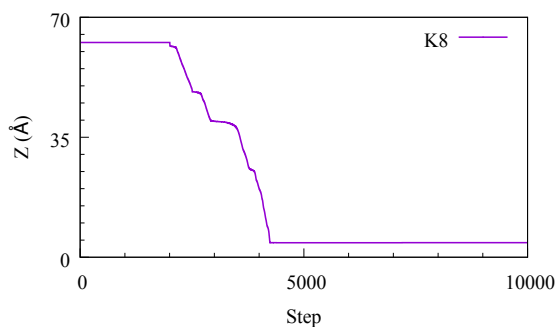
(d) K5



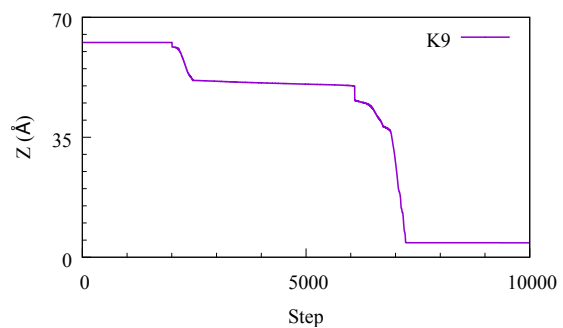
(e) K6



(f) K7



(g) K8



(h) K9

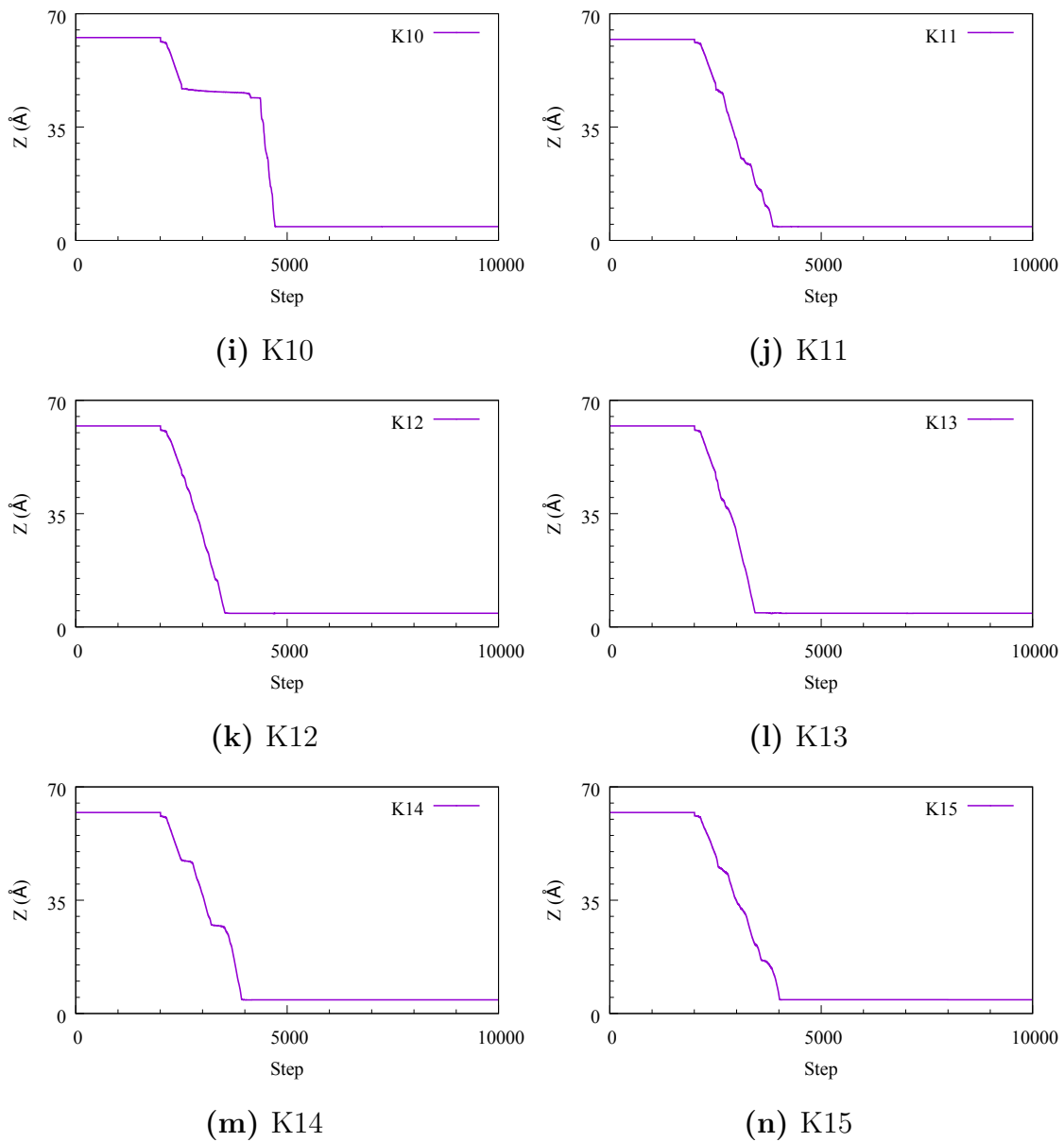
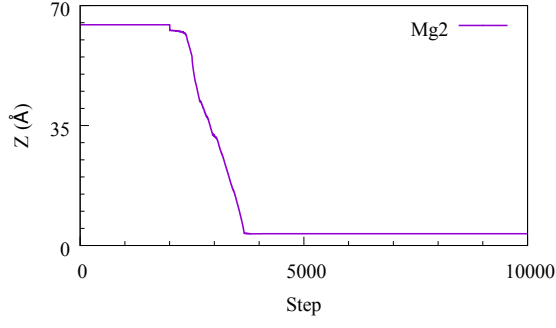
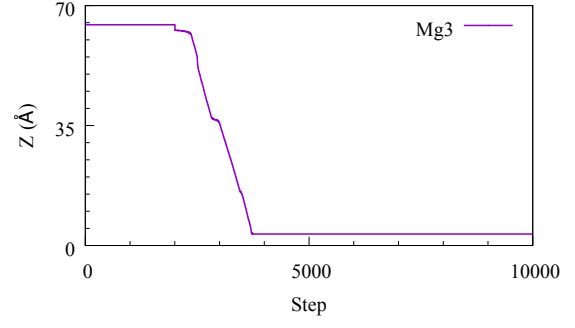


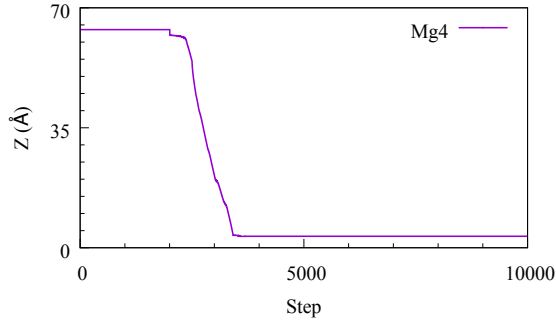
**Figure A.19:** Diffusion and z-axis movement of the individual potassium ions within the OSPC-2 structure. (a)K1 - (o)K15.



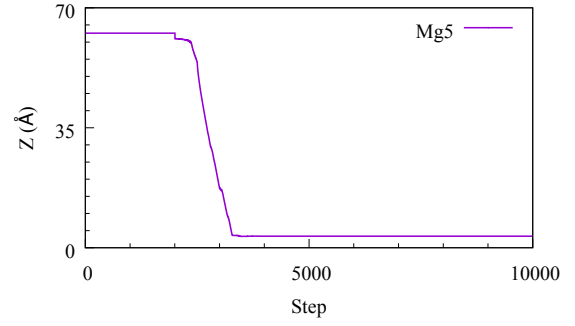
(a) Mg2



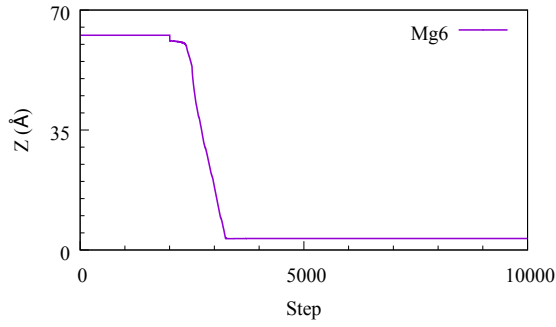
(b) Mg3



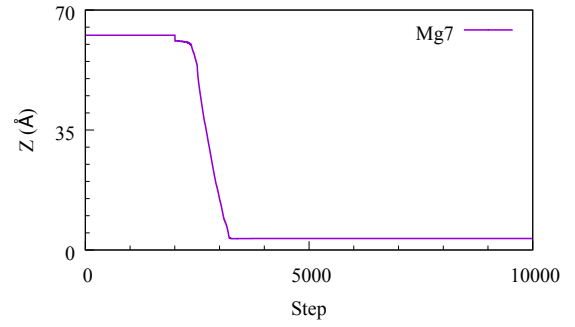
(c) Mg4



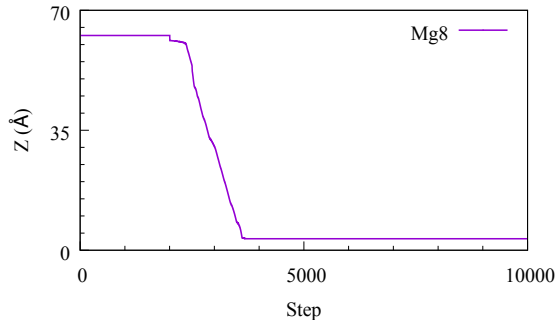
(d) Mg5



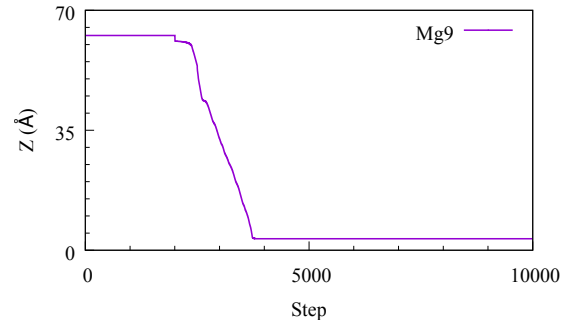
(e) Mg6



(f) Mg7



(g) Mg8



(h) Mg9

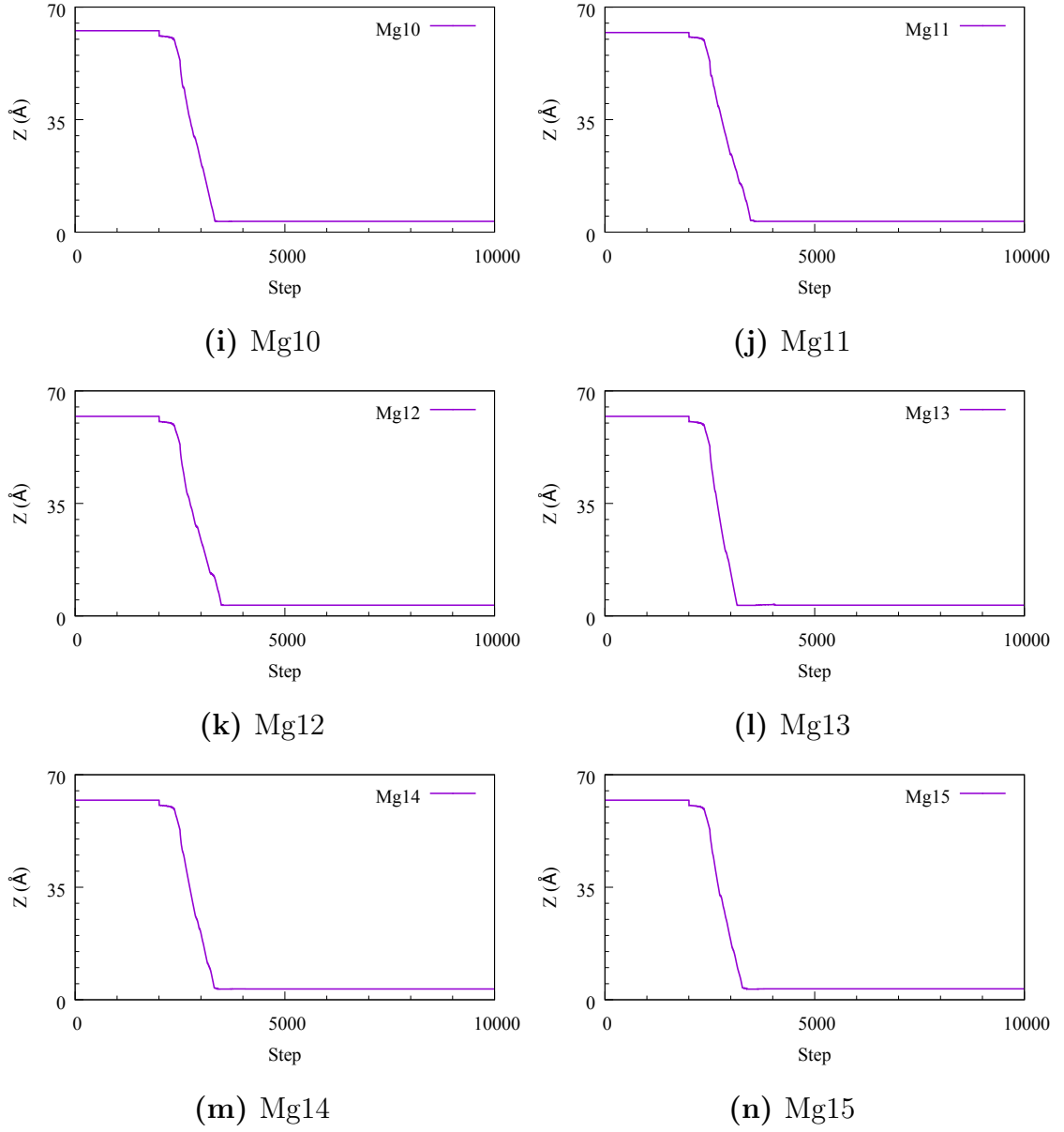
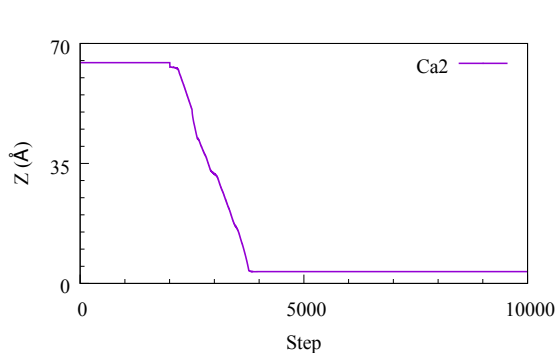
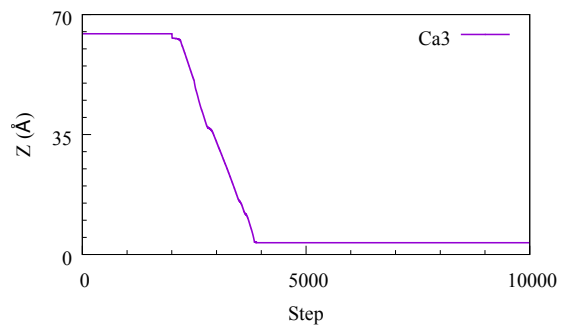


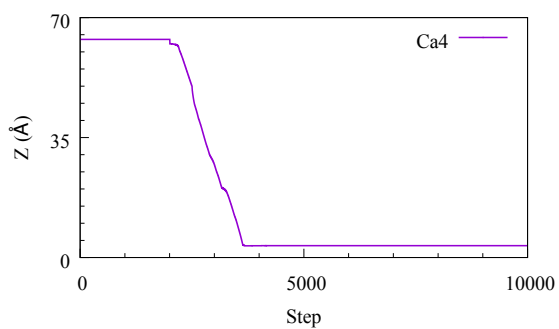
**Figure A.20:** Diffusion and z-axis movement of the individual magnesium ions within the OSPC-2 structure; (a)Mg1 - (o)Mg15.



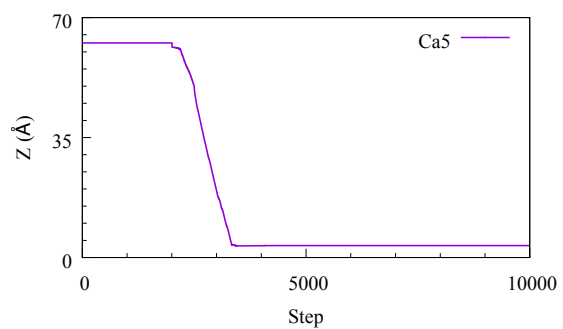
(a) Ca2



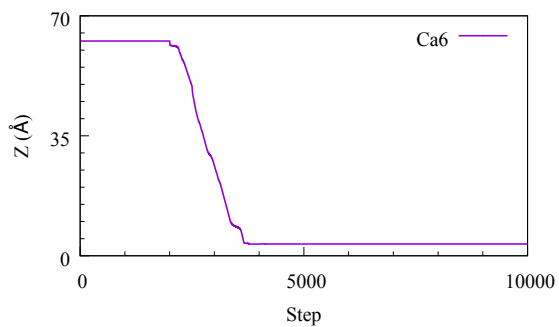
(b) Ca3



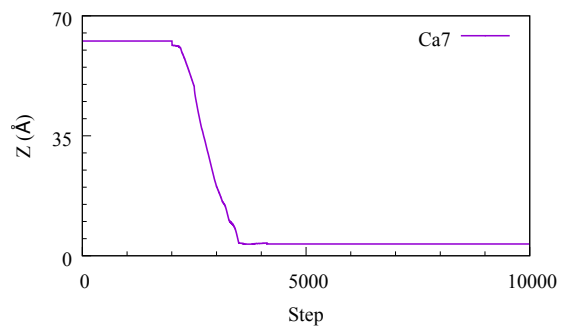
(c) Ca4



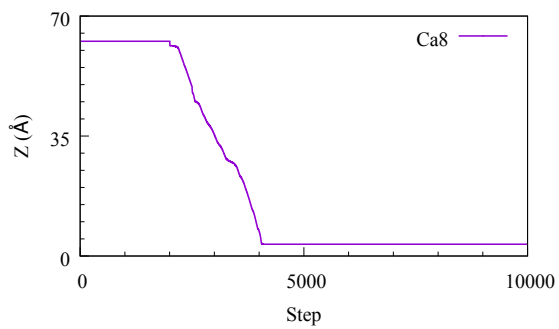
(d) Ca5



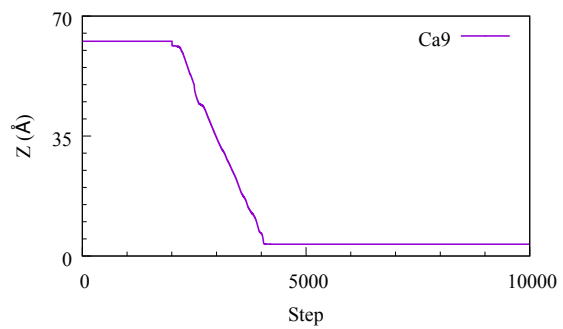
(e) Ca6



(f) Ca7



(g) Ca8



(h) Ca9



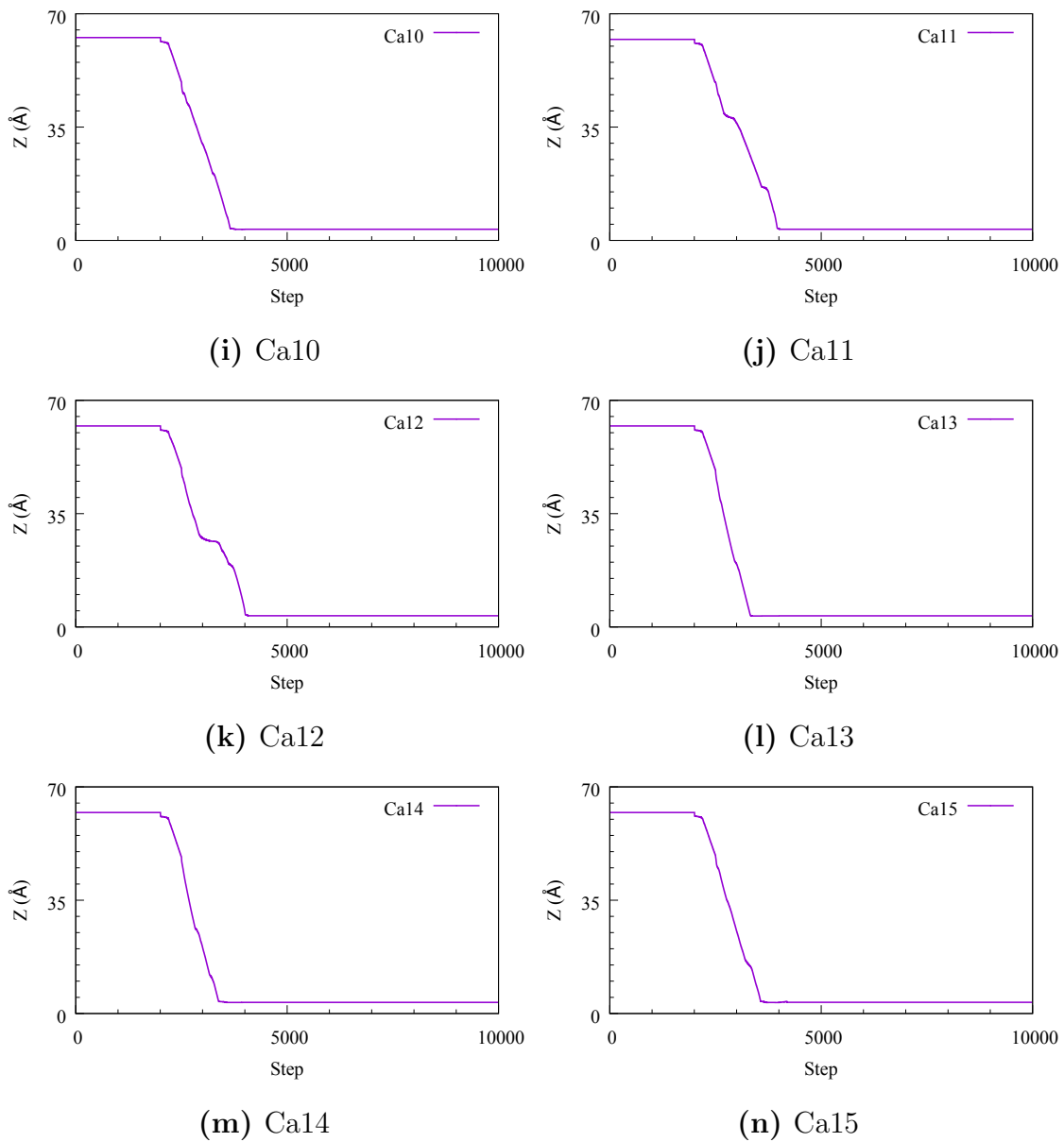
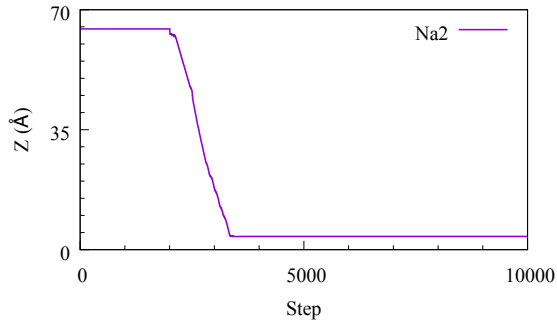
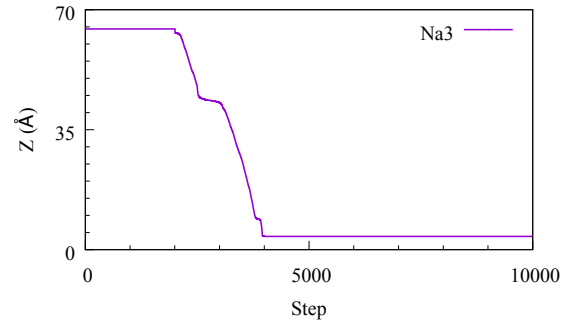


**Figure A.21:** Diffusion and z-axis movement of the individual calcium ions through the OSPC-2 structure. (a)Ca1 - (o)Ca15.

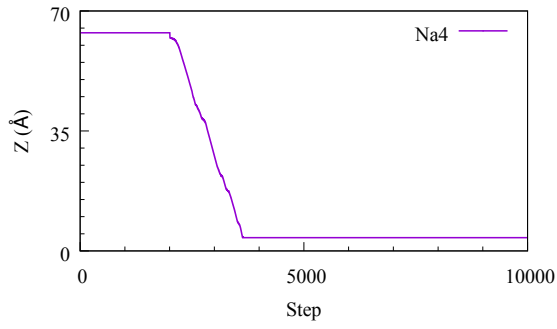
### A.3.4 OSPC-3



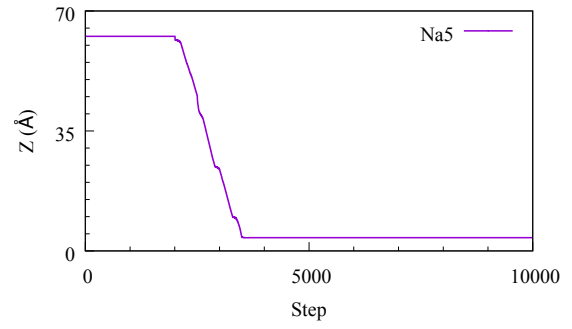
(a) Na2



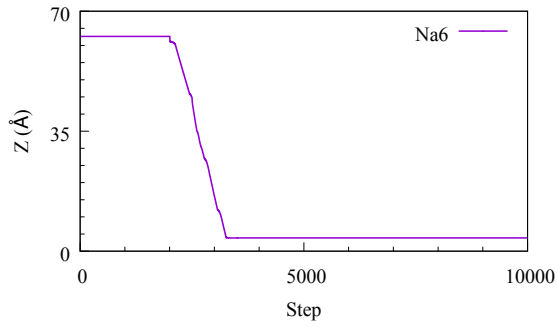
(b) Na3



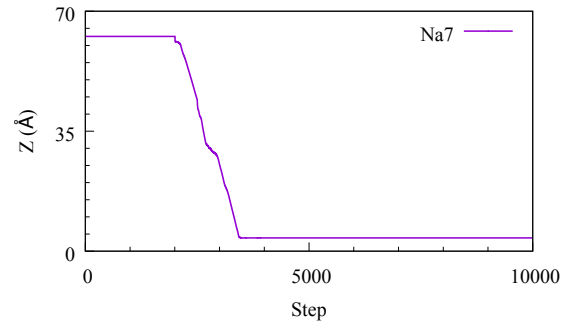
(c) Na4



(d) Na5



(e) Na6



(f) Na7

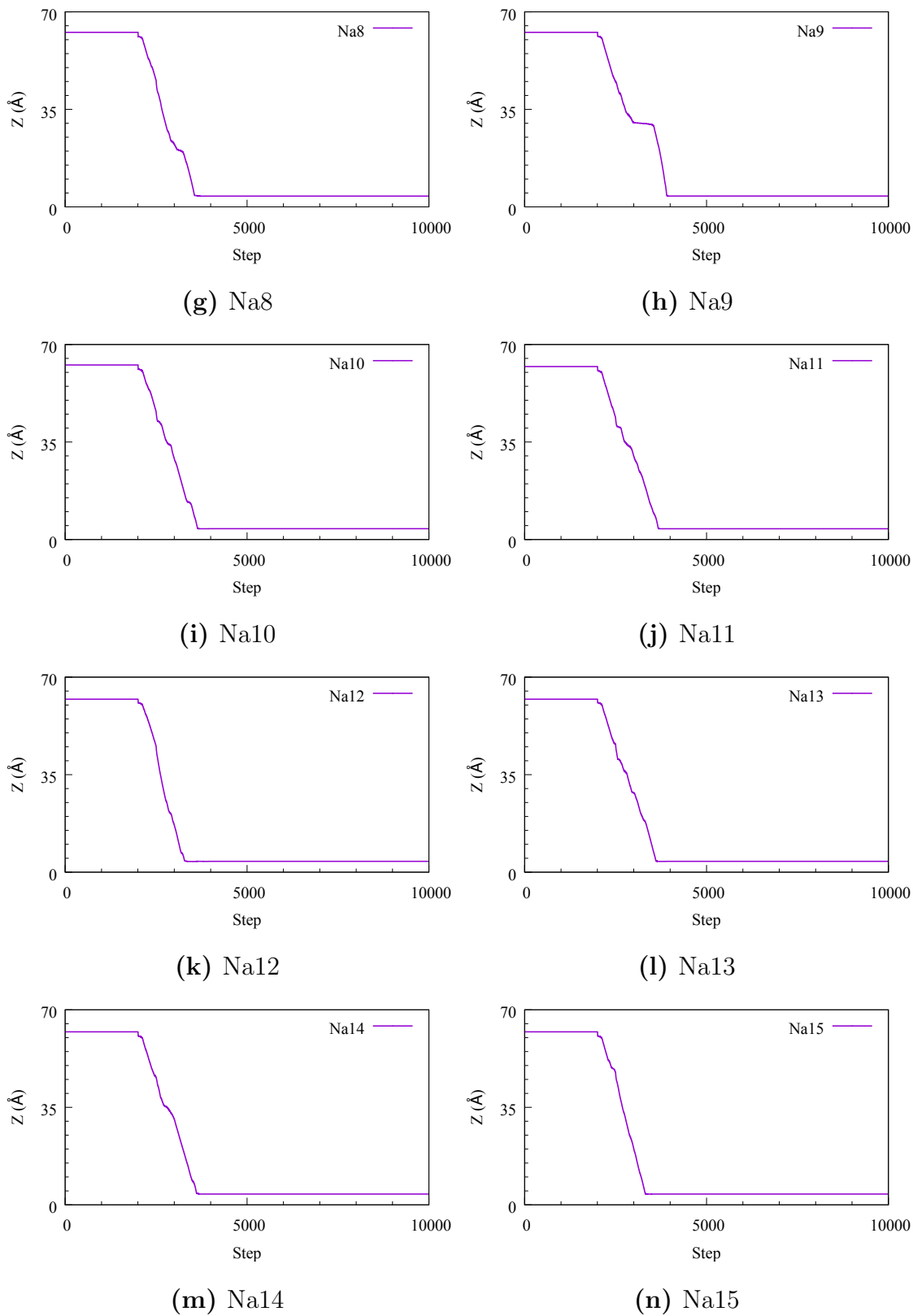
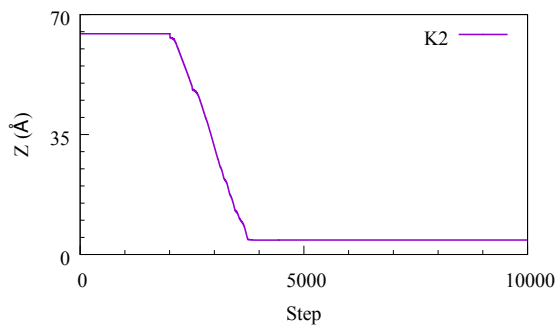
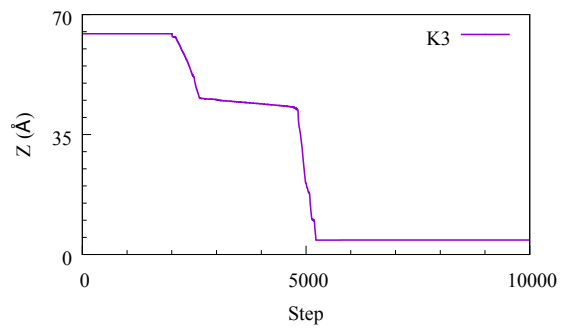


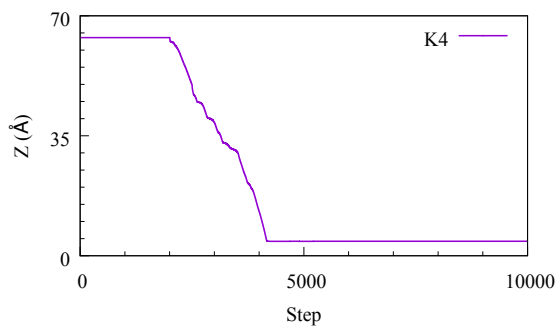
**Figure A.22:** Diffusion and movement of the individual sodium ions through the OSPC-3 structure. (a)Na1 - (o)Na15.



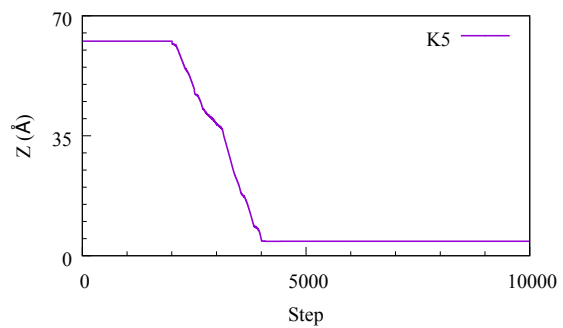
(a) K2



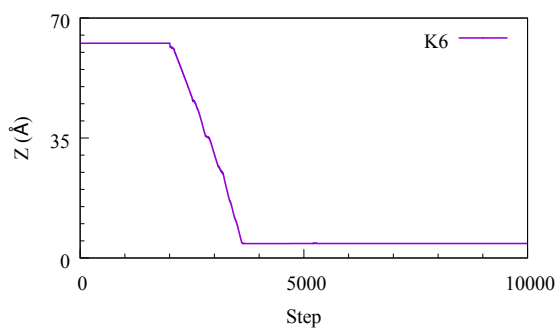
(b) K3



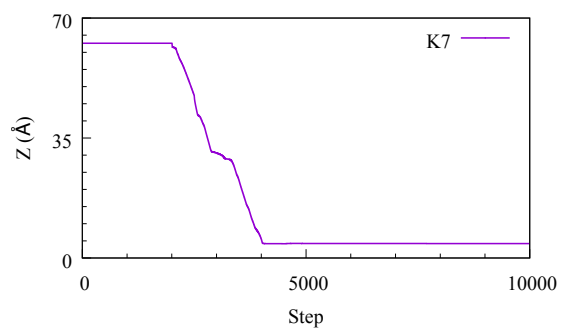
(c) K4



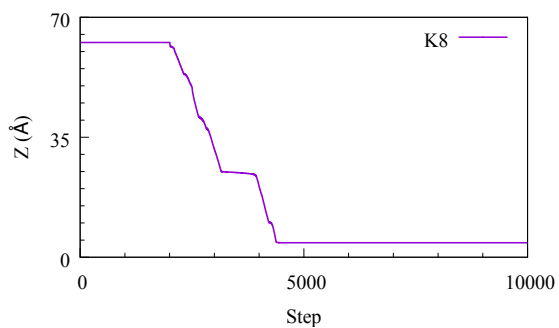
(d) K5



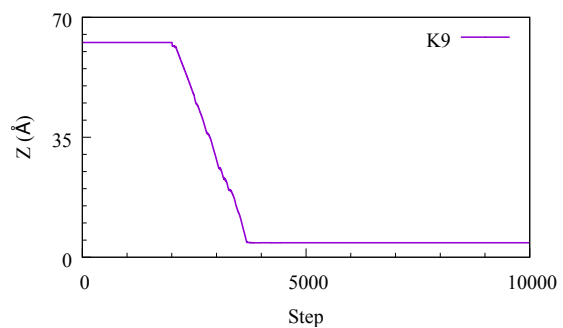
(e) K6



(f) K7



(g) K8



(h) K9

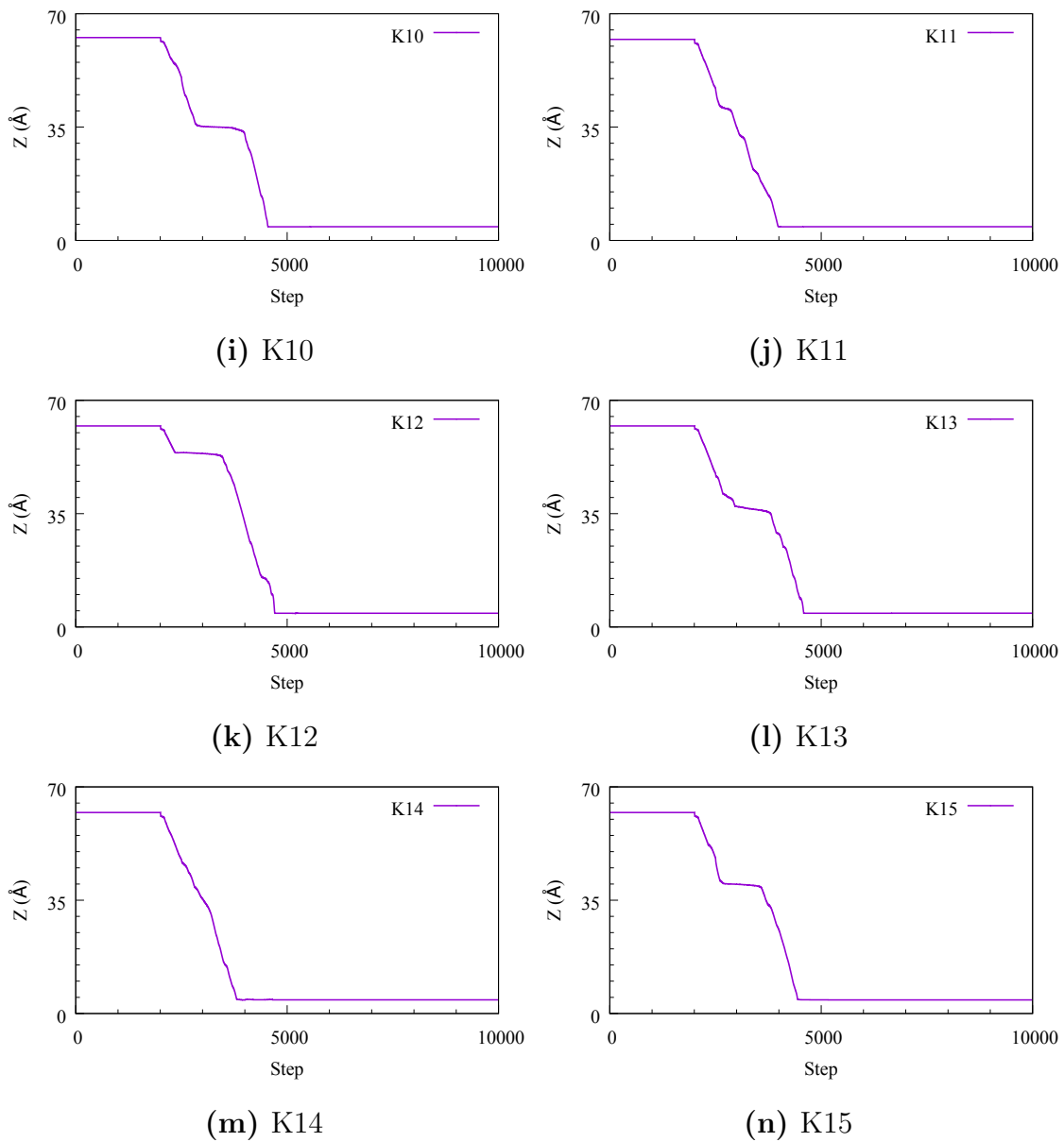
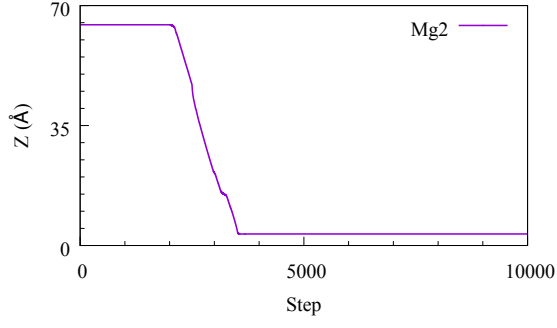
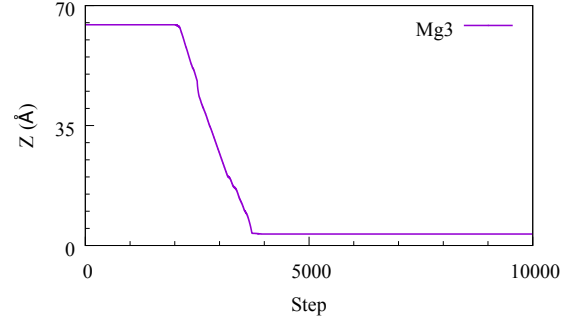


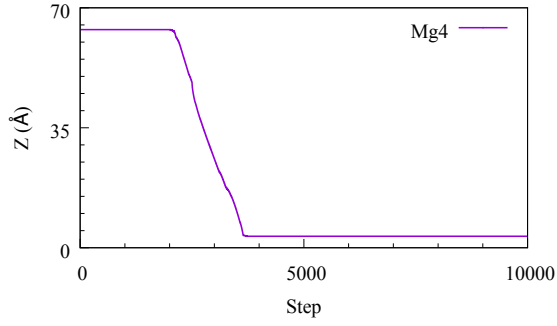
**Figure A.23:** Diffusion and z-axis movement of the individual potassium ions with the OSPC-3 structure. (a)K1 - (o)K15.



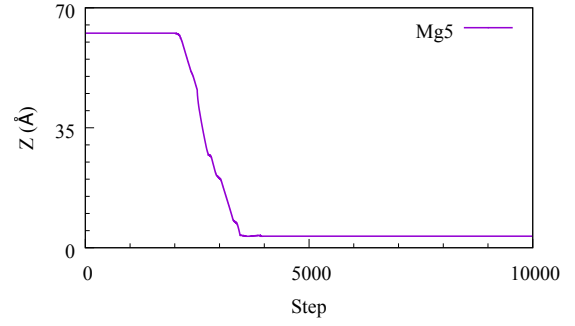
(a) Mg2



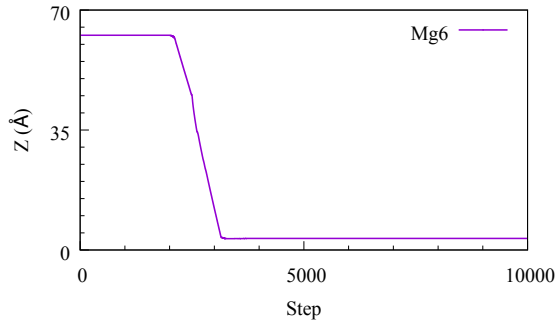
(b) Mg3



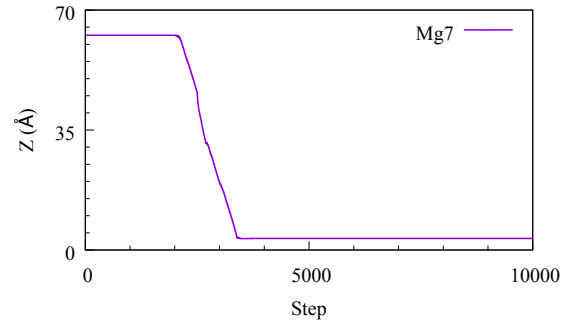
(c) Mg4



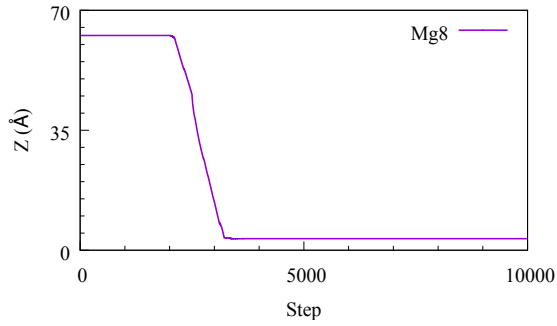
(d) Mg5



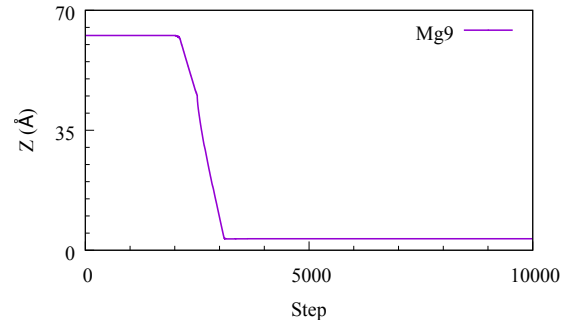
(e) Mg6



(f) Mg7



(g) Mg8



(h) Mg9

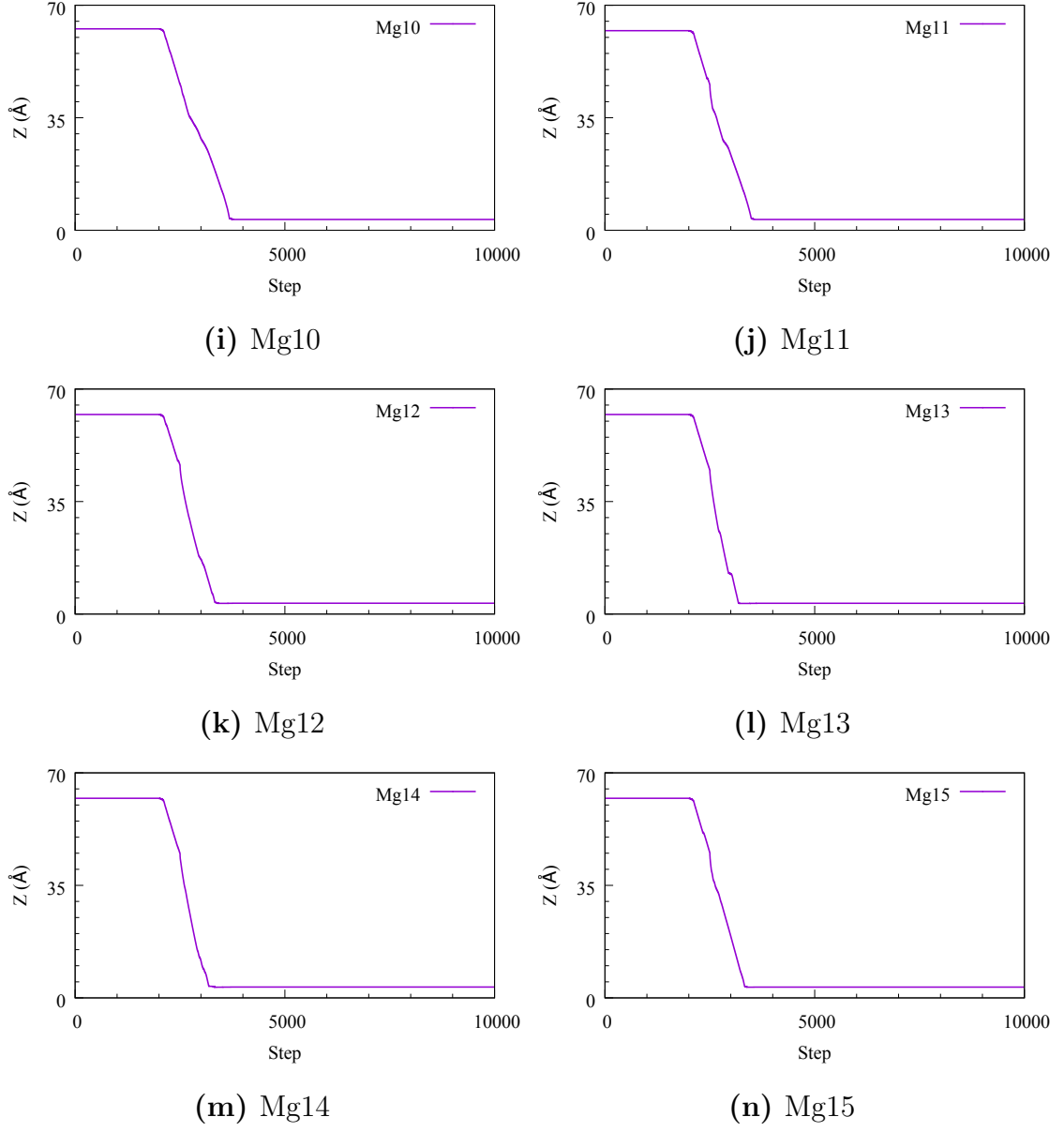
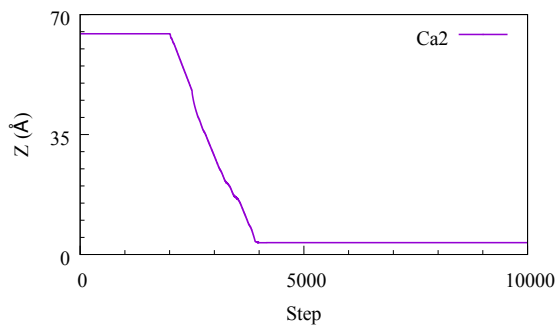
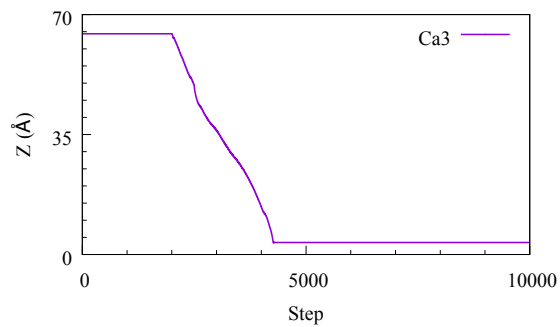


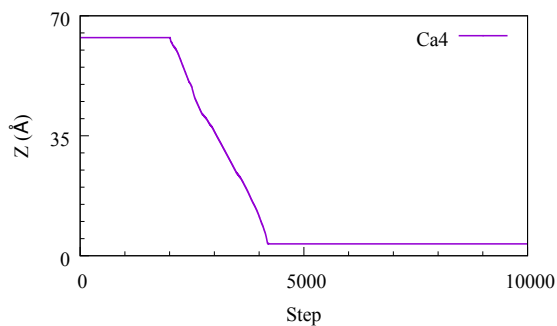
**Figure A.24:** Diffusion and z-axis movement of the individual magnesium ions with the OSP-3 structure. (a)Mg1 - (o)Mg15.



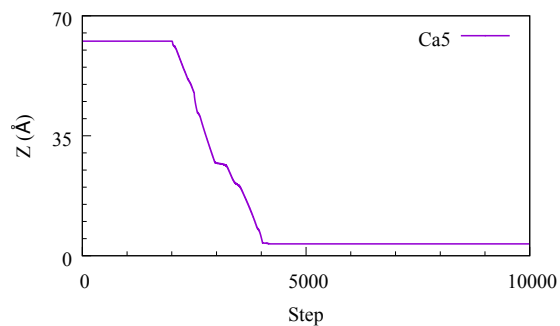
(a) Ca2



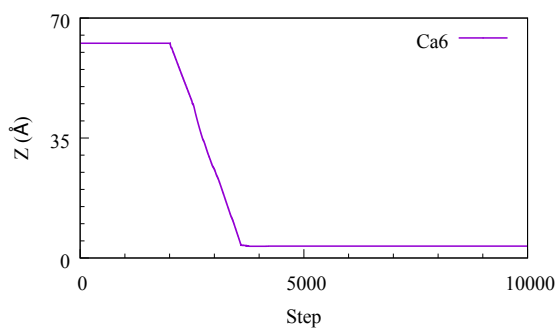
(b) Ca3



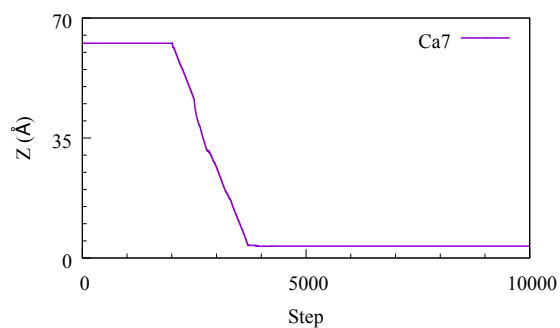
(c) Ca4



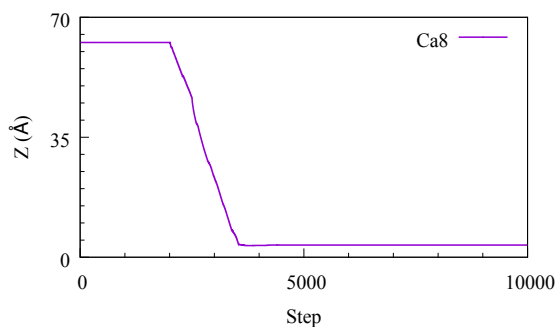
(d) Ca5



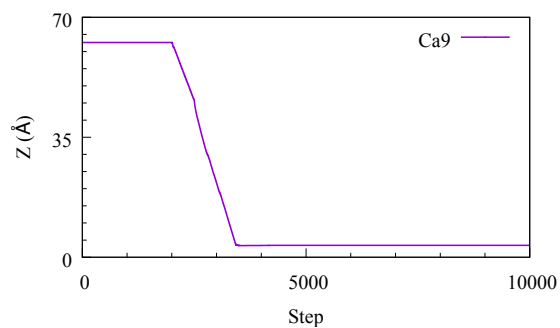
(e) Ca6



(f) Ca7



(g) Ca8



(h) Ca9



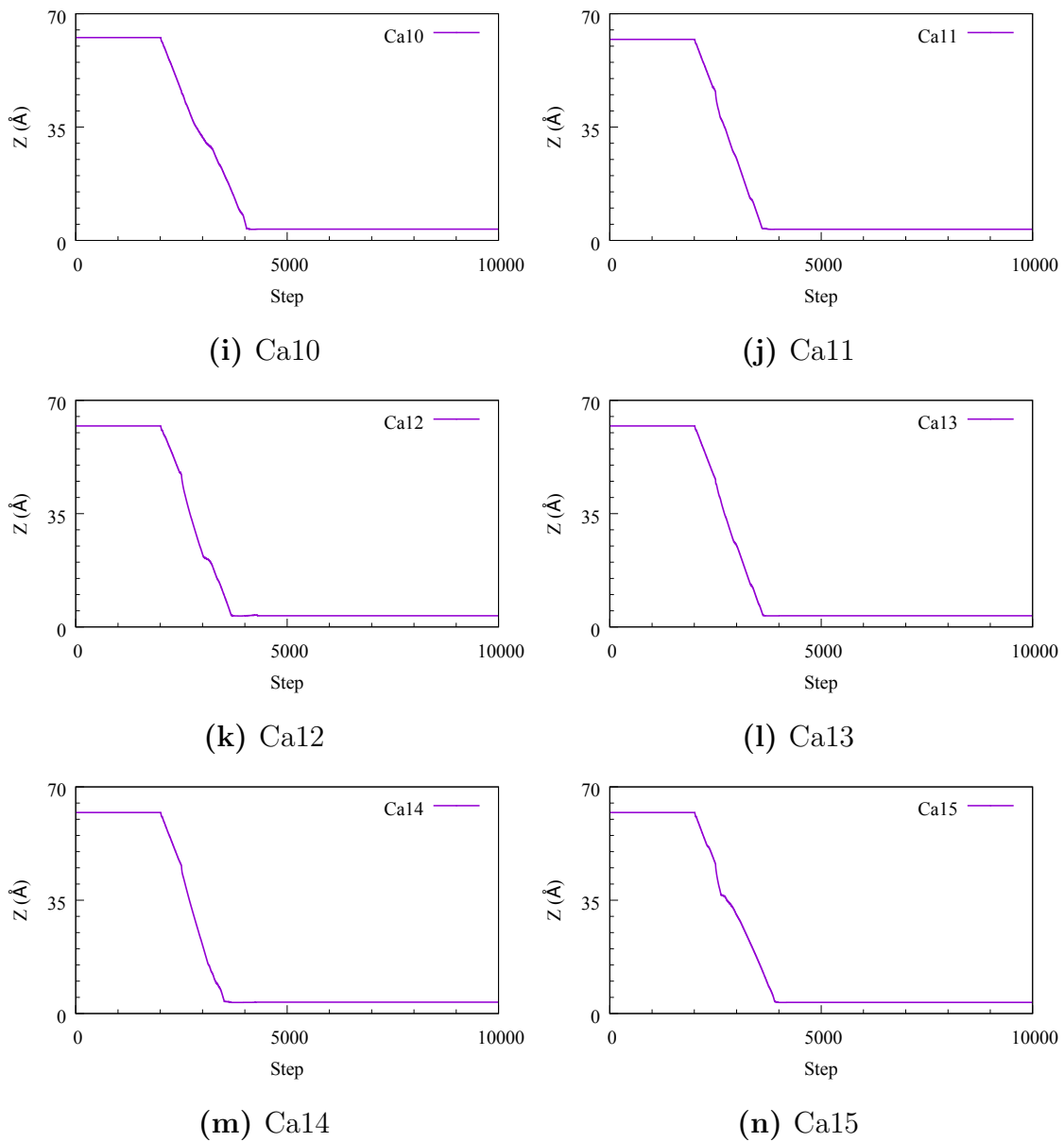


**Figure A.25:** Diffusion and z-axis movement of the individual calcium ions within the OSPC-3 structure. (a)Ca1 - (o)Ca15.